Krishna Mohan Singh
Sushanta Dutta
Sudhakar Subudhi
Nikhil Kumar Singh *Editors*

Fluid Mechanics and Fluid Power, Volume 6

Select Proceedings of FMFP 2022

Springer

Lecture Notes in Mechanical Engineering

Topics in the series include:

- Engineering Design
- Machinery and Machine Elements
- Mechanical Structures and Stress Analysis
- Automotive Engineering
- Engine Technology
- Aerospace Technology and Astronautics
- Nanotechnology and Microengineering
- Control, Robotics, Mechatronics
- MEMS
- Theoretical and Applied Mechanics
- Dynamical Systems, Control
- Fluid Mechanics
- Engineering Thermodynamics, Heat and Mass Transfer
- Manufacturing Engineering and Smart Manufacturing
- Precision Engineering, Instrumentation, Measurement
- Materials Engineering
- Tribology and Surface Technology

Indexed by SCOPUS, EI Compendex, and INSPEC.

All books published in the series are evaluated by Web of Science for the Conference Proceedings Citation Index (CPCI).

To submit a proposal for a monograph, please check our Springer Tracts in Mechanical Engineering at https://link.springer.com/bookseries/11693.

Krishna Mohan Singh · Sushanta Dutta ·
Sudhakar Subudhi · Nikhil Kumar Singh
Editors

Fluid Mechanics and Fluid Power, Volume 6

Select Proceedings of FMFP 2022

Springer

Editors
Krishna Mohan Singh
Department of Mechanical and Industrial
Engineering
IIT Roorkee
Roorkee, Uttarakhand, India

Sudhakar Subudhi
Department of Mechanical and Industrial
Engineering
IIT Roorkee
Roorkee, India

Sushanta Dutta
Department of Mechanical and Industrial
Engineering
IIT Roorkee
Roorkee, Uttarakhand, India

Nikhil Kumar Singh
Department of Mechanical and Industrial
Engineering
IIT Roorkee
Roorkee, Uttarakhand, India

Contents

About the Editors

Prof. Krishna Mohan Singh is Professor in the Department of Mechanical and Industrial Engineering at Indian Institute of Technology (IIT) Roorkee. His research interests include the areas of computational mechanics, development of novel parallel algorithms, meshfree methods, shape and topology optimization, fluid dynamics, DNS/LES of turbulent flows, CAE, computer-aided analysis and design of thermo-fluid and multi-physics systems, computational fluid dynamics, modeling and simulation of flow and heat transfer in turbomachines, transport and energy systems.

Prof. Sushanta Dutta is Professor in the Department of Mechanical and Industrial Engineering at Indian Institute of Technology (IIT) Roorkee. His research interests are in the areas of experimental fluid mechanics, experimental heat transfer, optical measurement techniques, active and passive control of flow field, wake dynamics, turbulence study, Schlieren, HWA, PIV, LCT, PSP, microfluidics and heat transfer augmentation using phase change material.

Prof. Sudhakar Subudhi is Associate Professor in the Department of Mechanical and Industrial Engineering at Indian Institute of Technology (IIT) Roorkee. His research interests are in the area of experimental heat transfer and fluid mechanics, heat transfer enhancement of natural and forced convection in water/nanofluids, natural ventilation and unconventional energy systems.

Dr. Nikhil Kumar Singh is Assistant Professor in the Department of Mechanical and Industrial Engineering at Indian Institute of Technology (IIT) Roorkee. His broad research interests include direct numerical simulations of two-phase flows and phase change, computational fluid dynamics and heat transfer, numerical methods and turbulent flows.

Linear and Nonlinear Simulations of Magnetorotational Instability for the Upcoming DRESDYN-MRI Experiment

Ashish Mishra, George Mamatsashvili, and Frank Stefani

Nomenclature

Re   Reynolds number
Rm   Magnetic Reynolds number
Lu   Lundquist number
Pm   Magnetic Prandtl number
μ   Rotation ratio of outer to inner cylinder
MRI Magnetorotational instability

1 Introduction

Magnetorotational instability (MRI) is considered a prime mechanism in explaining the angular momentum transport in astrophysical disks. However, despite of many efforts, the direct and conclusive evidence of MRI in lab is still elusive.

It is to be noted here that the recent claim by the Princeton group regarding the identification of axisymmetric mode of MRI [1] and the non-axisymmetric mode is still under scrutiny [2]. In their experiment, the axisymmetric mode of MRI and the non-axisymmetric mode appear, surprisingly, very close to each other and at parameters which are significantly lower than the predictions of global linear stability analysis (see Fig. 8 in ref. [2]). The discovery of other versions of MRI such as helical MRI

A. Mishra (✉) · G. Mamatsashvili · F. Stefani
Helmholtz-Zentrum Dresden-Rossendorf, Bautzner Landstr. 400, D-01328 Dresden, Germany
e-mail: a.mishra@hzdr.de

G. Mamatsashvili
Abastumani Astrophysical Observatory, 0301 Abastumani, Georgia

Institute of Geophysics, Tbilisi State University, 0193 Tbilisi, Georgia

(HMRI, [4]) and azimuthal MRI (AMRI, [5]) and their successful detection in the laboratory Taylor–Couette (TC) devices containing liquid metal [9, 13, 15] has paved a way for more sophisticated experiments such as the DRESDYN-MRI experiment [14]. Such a new experiment (Fig. 1b) is presently under construction in the framework of the DREsden Sodium facility for DYNamo and thermohydraulic studies (DRESDYN) at Helmholtz-Zentrum Dresden-Rossendorf (HZDR). In this experiment, we can reach Re $\sim 10^6$, Rm ~ 40, and Lu ~ 10 which theoretically is sufficient for the detection of MRI in laboratory (see Tables 1 and 2 for the physical parameter of the DRESDYN-MRI experiment and the definition of non-dimensional parameters used in this study, respectively). As a preparatory step toward the large-scale MRI experiments within DRESDYN project, we study these instabilities and the connection between them specifically for those ranges of the characteristic parameters of the magnetized Taylor–Couette flow that are achievable in these experiments. We aim, in particular, at a detailed analysis of the axisymmetric MRI and its nonlinear evolution and saturation properties. We also analyze the scaling behavior of the instability with respect to various system parameters.

Fig. 1 **a** A simplified Taylor–Couette flow setup with an imposed helical magnetic field, **b** a schematic view of the new DRESDYN-MRI machine [10]
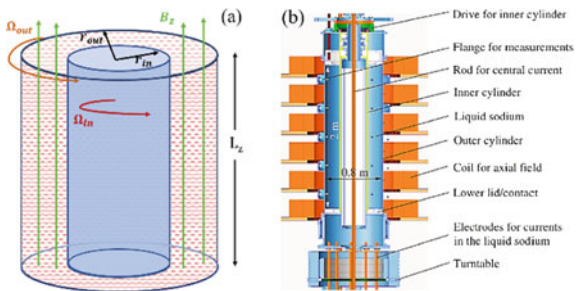
Table 1 Physical parameters of the new DRESDYN-MRI experiment with liquid sodium

Physical parameter	Values
r_{in}	0.2 m
r_{out}	0.4 m
L_z	2 m
Ω_{in}	$\leq 2\pi \cdot 20$ Hz
Ω_{out}	$\leq 2\pi \cdot 6$ Hz
Axial magnetic field (B_{0z})	≤ 150 mT
Current through central rod (I)	≤ 50 kA
Conductivity (σ)	9.5×10^6 S/m
Viscosity (ν)	6.512×10^{-7} m^2/s
Density (ρ)	920 kg/m^3

The material parameters are for a sodium temperature of $T = 130$ °C

Table 2 Non-dimensional system parameters of the DRESDYN-MRI experiment with liquid sodium based on the values in Table 1, assuming material parameters of liquid sodium at $T = 130\,°C$

Dimensionless parameter	Definition	Values
μ	Ω_{out}/Ω_{in}	(0.25, 0.35]
Normalized height	L_z/r_{in}	10
Reynolds number (Re)	$\Omega_{in}\, r^2_{in}/\nu$	$\leq 7.72 \times 10^6$
Magnetic Prandtl number (Pm)	ν/η	7.77×10^{-6}
Magnetic Reynolds number (Rm)	RePm	≤ 40
Lundquist number (Lu)	$B_{0z}\, r_{in}/\sqrt{\rho\mu_0\nu\eta}$	≤ 10

2 Mathematical Setting and Numerical Method

We consider an infinitely long cylindrical Taylor–Couette (TC) setup containing sodium as liquid metal with imposed axial magnetic field B_{0z} as shown in Fig. 1. The equilibrium rotation profile $\Omega(r)$ for a TC setup with inner and outer cylinder with radii r_{in} and r_{out} and angular velocities Ω_{in} and Ω_{out}, is given by:

$$\Omega(r) = C_1 + C_2/r^2, \tag{1}$$

where C_1 and C_2 are,

$$C_1 = (\Omega_{out}r^2_{out} - \Omega_{in}r^2_{in})/\left(r^2_{out} - r^2_{in}\right)$$

$$C_2 = (\Omega_{out}\Omega_{in})r^2_{in}r^2_{out}/\left(r^2_{out} - r^2_{in}\right).$$

The basic MHD equation to study the TC flow is

$$\partial_t u + (u \cdot \nabla u) = -\frac{\nabla P}{\rho} + \frac{(B \cdot \nabla)B}{\rho\mu_0} + \nu\nabla^2 u \tag{2}$$

$$\partial_t B = \nabla \times (u \times B + \eta\nabla^2 B \tag{3}$$

$$\nabla \cdot u = 0, \quad \nabla \cdot B = 0, \tag{4}$$

where ρ, p, ν, μ_0, and η are the density, hydrodynamic pressure, kinematic viscosity, magnetic permeability, and magnetic diffusivity of the fluid between the cylinders, respectively. For linear analysis, the basic MHD Eqs. (2–4) are linearized to form an eigenvalue problem in the radial direction, and the radial structure is solved by the spectral collocation method using Chebyshev polynomials typically up to $N = 30$–40 [4, 5, 8, 10]. The base flow is given by the standard TC profile as in Eq. 1, and the imposed axial magnetic field is used as base field. No-slip boundary condition is

used for velocity, and insulating boundary condition is used for magnetic field with periodic boundary conditions in the axial direction (see [10] for details). For the nonlinear analysis, the cylindrical flow domain is distributed as $(r, \varphi, z) \in [r_{in}, r_{out}] \times [0, 2\pi] \times [0, L_z]$. We used the pseudo-spectral code from Ref. [3] to solve the basic nonlinear MHD Eqs. (2–4) of an incompressible conducting fluid in TC setup. For our setup, we non-dimensionalise length by r_{in} and time by Ω_{in}^{-1} and hence $[r_{in}, r_{out}] \in [1, 2]$ and $L_z = 10$ as the aspect ratio is 10. Chebyshev collocation method is used to distribute the points along radii to achieve higher resolution near the boundaries. We conduct high-resolution study with $N_r = 500$, i.e., finite difference points in the radial direction, and $N_z = 800$, i.e., Fourier modes in the axial direction. This resolution is chosen such that the modes are fully resolved. Since MRI is dominated by $m = 0$ modes, in this analysis, we do not allow other non-axisymmetric modes to grow; hence, N_φ is set to 1. Here, we set minimum wavelength $k_z = 2\pi/L_z$ to allow at least one full wave in the axial domain (see also [11]).

3   Results and Discussion

In order to obtain the region of instability for MRI in Fig. 1a–e, we plot the maximized growth rate over all axial wavenumbers $k_z \geq k_{z,\min}$ of the most unstable axisymmetric mode ($m = 0$) of MRI in (Rm − Lu)-plane for varying μ (= Ω_{out}/Ω_{in}) and fixed β = 0. As aforementioned, we focus our analysis on the Rayleigh stable regime, i.e., $\mu > 0.25$. We observe that the instability region in the (Lu − Rm)-space decreases with increasing μ. The critical Rm and corresponding Lu for $\mu = 0.26$ are at 4.8384 and 1.5220, respectively, as in Fig. 2a, while the same for the Keplerian profile, i.e., $\mu = 0.35$ lie at 16.1714 and 5.0937, respectively, as in Fig. 2e. Since the maximum achievable Rm and Lu in the DRESDYN-MRI experiment are 40 and 10, respectively (cf. Table 2), MRI can be detected successfully in DRESDYN-MRI experiment for all μ in the range (0.25, 0.35]. In Fig. 2f, we plot the marginal instability curve of MRI for various μ in the (Lu, Rm)-plane which clearly shows the monotonic increase of critical Lu and Rm with increasing μ. Our linear analysis shows that the MRI can be unambiguously detected in the upcoming DRESDYN-MRI experiment for μ = 0.26 to more astrophysically relevant quasi-Keplerian flow profile $\mu = 0.35$ [10].

We study the evolution of magnetic energy of the most unstable axisymmetric MRI mode to understand the nonlinear MRI and its saturation behavior in detail in an extensive parameter space. Further, to obtain the scaling laws of various parameters in saturated state, we analyze each point for different Re $\in \{1, 4, 7, 10, 20, 30, 40, 100\} \times 10^3$. This study allows us to concretely understand the behavior of magnetic energy and angular momentum transport of MRI in the exponential and saturated states. To analyze the growth and subsequent nonlinear saturation of axisymmetric MRI modes, in Fig. 3a, we follow the evolution of the volume-integrated total magnetic energy of perturbations, $\mathcal{E}_{mag} = \int_V b^2 \, dV$, where V is the volume of the TC device for μ = 0.27, varying Reynolds numbers Re, and two pairs of (Lu, Rm) = (30, 9) (solid lines) and (Lu, Rm) = 9, 2.5 (dashed lines). In all these cases, the magnetic energy
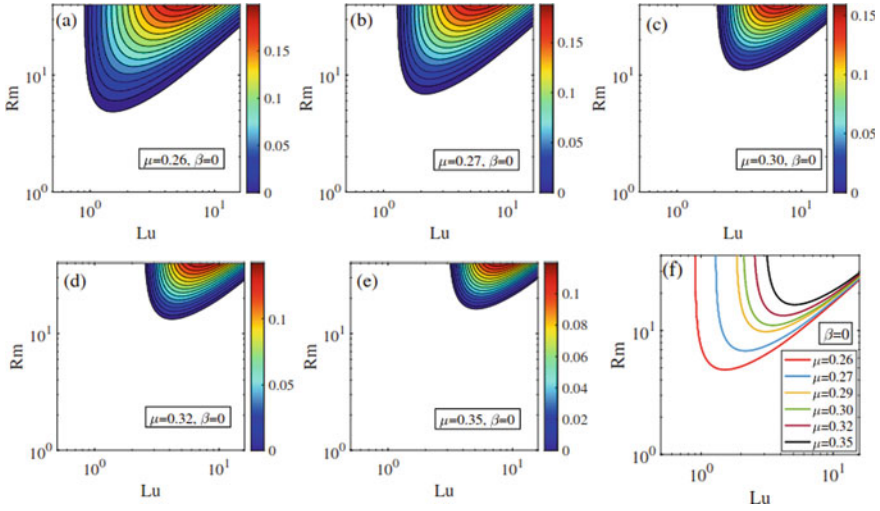
Fig. 2 **a–e** MRI growth rate $\mathrm{Re}(\gamma) \geq 0$ in the (Lu, Rm)-plane, maximized over $k_z \geq k_{z,\min}$, varying μ. **f** The corresponding marginal stability curves for these values of μ, which better indicate a shift of the unstable area to higher Lu and Rm, implying a greater stability for increasing μ [10]

initially grows exponentially with the growth rate predicted by the 1D linear analysis and afterward approaches the saturation state where the energies and stresses remain nearly constant with time. This behavior is consistent with previous nonlinear studies of MRI both at infinite [6, 7] and finite [16, 17] height of the cylinders. Since the magnetic energy of MRI depends mostly on Rm (see also [10]), the exponential growth and saturation energy is smaller for smaller Rm.

In Fig. 3b, we plot the magnetic energy values in the nonlinear saturated state $\hat{\mathcal{E}}_{\mathrm{mag}}$ as a function of Re for various pairs (Lu, Rm), and the black dashed lines show
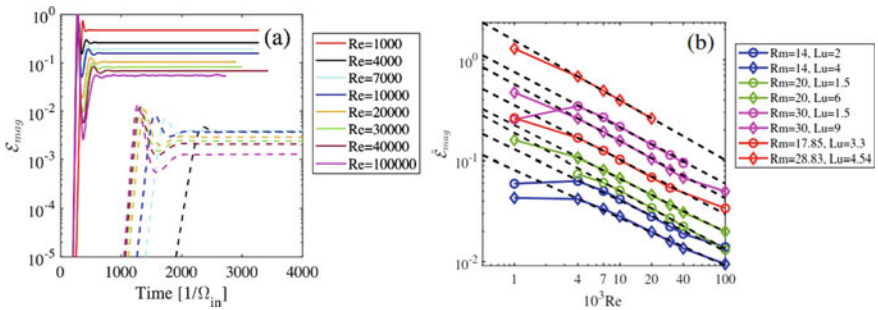
Fig. 3 **a** Time evolution of volume-integrated magnetic energy $\hat{\mathcal{E}}_{\mathrm{mag}}$ for different Re, fixed (Lu, Rm) $= (2.5, 9)$(dashed), $(9, 30)$(solid) and $\mu = 0.27$. **b** Magnetic energy in the saturated state, $\hat{\mathcal{E}}_{\mathrm{mag}}$ as a function of Re for different pairs (Lu, Rm). Black dashed lines are the power law fits of the form Re^a with an average value of the scaling parameter $a \approx -1/2$ [11]

the power law fit. Evidently, for all sets of (Lu, Rm), the saturated magnetic energy decreases with an increase in Re, forming a family of lines with nearly the same slope in the logarithmic scale at Re $\geq$ 4000, where the asymptotic regime appears to be already reached. We numerically fit this dependence with the power law Re^a shown by black dashed lines in Fig. 3b, which are more or less parallel to each other with the common average power law index $a \approx -1/2$. This implies that the magnetic energy in the saturated state follows a power law scaling Re$^{-1/2}$ or, for that matter, Pm$^{1/2}$ as Rm is fixed for all considered pairs (Lu, Rm). This result is consistent with a previously reported scaling law for MRI in a wide-gap TC geometry with endcaps [2]. This result will be important below for extrapolating the values of the magnetic energy from the simulations down to even smaller, experimentally relevant Pm $\sim 10^{-6} - 10^{-5}$. Figure 4a shows the time evolution of normalized torque G/G_{lam} measured on the inner cylinder for $\mu = 0.27$ and different Reynolds numbers Re. Solid lines show the evolution of this torque for Rm = 30, Lu = 9, while the dashed lines correspond to Rm = 9, Lu = 2.5. Since the torque measured in the simulations is normalized using the laminar torque, the minimum torque is equal to 1. It is seen in Fig. 4a that, in contrast to the magnetic energy, G/G_{lam} increases with Re both during the exponential growth at the linear stage and in the saturated state. During the evolution, the torque at inner cylinder G_{in} increases the angular momentum while the torque at outer cylinder G_{out} decreases it, eventually reaching an equilibrium in the saturated quasi-steady state when both torques become equal $G_{\text{in}} = G_{\text{out}}$.

As discussed above, the normalized torque G/G_{lam} determines the effective angular momentum transport in the flow. We can obtain only the turbulent contribution to the torque by subtracting the laminar one, $G/G_{\text{lam}} - 1$, which can be used to determine the scaling with Re. Note that $G/G_{\text{lam}} - 1$ is already normalized and does not depend on the velocity normalization. In Fig. 4b, we plot $G/G_{\text{lam}} - 1$ on the cylinders in the saturated state as a function of Re for different Lu and Rm. The black dashed lines show the power law fitting of the form Re^b where b is the scaling
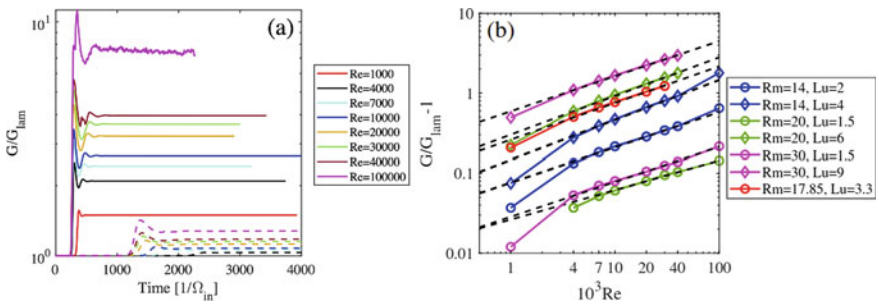
Fig. 4 **a** Time evolution of normalized torque G/G_{lam} for different Re, fixed (Lu, Rm) = (2.5, 9) (dashed), (9, 30) (solid) and $\mu = 0.27$, $k_{z,\text{min}} \geq 2\pi/L_z$. **b** Normalized turbulent torque $G/G_{\text{lam}} - 1$ in the saturated state as a function of Re for different sets of (Lu, Rm). Black dashed lines show the fitting of power law of the form Re^b where b is the scaling parameter. Numerically obtained average scaling parameter $b \approx 0.5$ [11]

exponent. Similar to the saturated magnetic energy, normalized turbulent torque also forms a family of parallel lines for different (Lu, Rm), but unlike the former, it increases with increasing Re. Numerically obtained power law fitting exponent $b \approx$ 0.5 indicates the power law dependence $G/G_{\text{lam}} - 1 \propto \text{Re}^{0.5}$, that is, $\propto \text{Pm}^{-0.5}$ as Rm is fixed. This is consistent with the similar $\text{Re}^{0.5}$ scaling of the torque for MRI at large Re and Rm found by Liu et al. [7].

It is now interesting to investigate the mechanism of transition of MRI from linear growth phase to saturated state. Figure 5 shows one instant of magnetic reconnection for $\mu = 0.27$, Rm = 30, Lu = 9, and Re = 40,000 occurring at time = 359 in the transition region as shown in Fig. 1. As evident from Fig. 5a, the field lines (B_r, B_z) in the (r, z)-plane show the field lines forming an X-type magnetic reconnection region at $z = 5$ and $r = 1.3$. Figure 5b shows the azimuthal current density J_φ in the (r, z)-plane. Evidently, the current density at the site of reconnection is very large indicating the formation of current sheets, thus facilitating as the indicator of magnetic reconnection. Figure 3b shows that the magnetic energy scales with Re. Similarly, kinetic energy also scales with Re. This allows us to estimate the expected value of RMS velocity and magnetic field perturbations in the DRESDYN-MRI experiment for $\mu = 0.27$ and Pm $= 7.77 \times 10^{-6}$ for various sets of (Lu, Rm). Table 3 shows the calculated RMS velocity and magnetic field for different sets of (Lu, Rm). It is clear from the table that the RMS velocity and magnetic field perturbations are larger for larger values of (Lu, Rm). It is interesting to note that the RMS velocity perturbations can vary to as high as 1.3 m/s depending upon (Lu, Rm). Similarly, RMS magnetic field perturbation can vary from 0.2 mT to very high value of 13 mT. These estimated perturbation values of velocity and magnetic field are encouraging as they will allow optimized detection of MRI in the experiment (see also [11]).
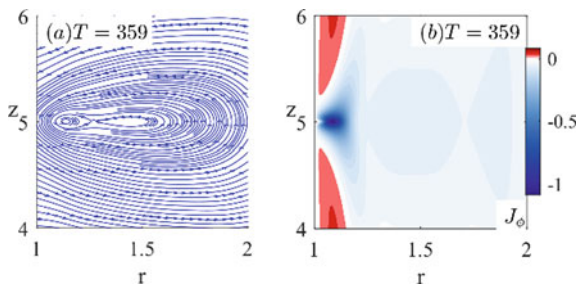
Fig. 5　a Field lines (B_r, B_z) showing magnetic reconnection **b** Azimuthal current density J_φ at the site of magnetic reconnection for $\mu = 0.27$, Rm = 30, Lu = 9 and Re = 40,000 at time = 359 falling in the transition from growth phase to saturation state (see Fig. 3) [11]

Table 3 RMS of the velocity and magnetic field perturbations as estimated from the simulations in the nonlinear saturated state that we can expect in DRESDYN-MRI experiment at $\mu = 0.27$ [11]

(Lu, Rm)	u ($\Omega_{in}r_{in}$)	u (m/s)	b (B0)	b (mT)
(2, 14)	0.0138	0.0808	0.0078	0.222
(4, 14)	0.0437	0.2560	0.0068	0.387
(1.5, 20)	0.0053	0.0443	0.0085	0.181
(6, 20)	0.0745	0.6234	0.0079	0.675
(1.5, 30)	0.0059	0.0740	0.0125	0.267
(9, 30)	0.1047	1.3142	0.1020	13.073

4 Conclusions

In this study, using linear stability analysis, we show that MRI can be conclusively and unambiguously detected in the upcoming DRESDYN-MRI experiment. We extend our linear MRI analysis to study its nonlinear evolution and saturation properties. We numerically solved the fully nonlinear MHD equations in the TC geometry with imposed axial magnetic field only and focused strictly on axisymmetric MRI, i.e., $m = 0$ mode. In this study, we show that for different sets of (Lu, Rm) and fixed μ the magnetic energy in the saturated state and the normalized turbulent torque scales with $Re^{-0.5}$ and $Re^{0.5}$, respectively. Our analysis also shows that the transition of MRI from exponential growth phase to saturation state occurs via magnetic reconnection. Further investigation has shown that these scaling laws hold true for non-axisymmetric modes also (c.f. 12 for details). The scaling law derived here allows us to estimate the values of RMS velocity and magnetic field perturbations expected in the upcoming DRESDYN-MRI experiment and conclusively identify MRI in laboratory.

References

1. Wang Y, Gilson EP, Ebrahimi F, Goodman J, Ji H (2022) Observation of axisymmetric standard magnetorotational instability in the laboratory. Phys Rev Lett 129:115001
2. Wang Y, Gilson EP, Ebrahimi F, Goodman J, Caspary KJ, Winarto HW, Ji H (2022) Identification of a non-axisymmetric mode in laboratory experiments searching for standard magnetorotational instability. Nat Commun 13:4679
3. Guseva A, Willis AP, Hollerbach R, Avila M (2015) Transition to magnetorotational turbulence in Taylor-Couette flow with imposed azimuthal magnetic field. New J Phys 17(9):093018
4. Hollerbach R, Rüdiger G (2005) New type of magnetorotational instability in cylindrical Taylor-Couette flow. Phys Rev Lett 95:124501

5. Hollerbach R, Teeluck V, Rüdiger G (2010) Nonaxisymmetric magnetorotational instabilities in cylindrical Taylor-Couette flow. Phys Rev Lett 104:044502
6. Knobloch E, Julien K (2005) Saturation of the magnetorotational instability. Phys Fluids 17(9):094106–094106–6
7. Liu W, Goodman J, Ji H (2006) Simulations of magnetorotational instability in a magnetized Couette flow. Astrophys J 643(1):306–317
8. Mamatsashvili G, Stefani F, Hollerbach R, Rüdiger G (2019) Two types of axisymmetric helical magnetorotational instability in rotating flows with positive shear. Phys Rev Fluids 4:103905
9. Mishra A, Mamatsashvili G, Galindo V, Stefani F (2021) Convective, absolute and global azimuthal magnetorotational instabilities. J Fluid Mech 922:R4
10. Mishra A, Mamatsashvili G, Stefani F (2022) From helical to standard magnetorotational instability: predictions for upcoming liquid sodium experiments. Phys Rev Fluids 7:064802
11. Mishra A, Mamatsashivili G, Stefani F (2023a) Nonlinear evolution of magnetorotational instability in a magnetized Taylor-Couette flow: Scaling properties and relation to upcoming DRESDYN-MRI experiment. Phys Rev Fluids 8(8) https://doi.org/10.1103/PhysRevFluids.8.083902
12. Mishra A, Mamatsashvili G, Stefani F, (2023b) Non-axisymmetric standard magnetorotational instability in the upcoming DRESDYN-MRI experiments -- linear and nonlinear dynamics. arXiv:2307.16295 https://doi.org/10.48550/arXiv.2307.16295
13. Seilmayer M, Galindo V, Gerbeth G, Gundrum T, Stefani F, Gellert M, Rüdiger G, Schultz M, Hollerbach R (2014) Experimental evidence for nonaxisymmetric magnetorotational instability in a rotating liquid metal exposed to an azimuthal magnetic field. Phys Rev Lett 113(2):024505
14. Stefani F, Gailitis A, Gerbeth G, Giesecke A, Gundrum Th, Rüdiger G, Seilmayer M, Vogt T (2019) The DRESDYN project: liquid metal experiments on dynamo action and magnetorotational instability. Geophys Astrophys Fluid Dyn 113(1–2):51–70
15. Stefani F, Gundrum T, Gerbeth G, Rüdiger G, Schultz M, Szklarski J, Hollerbach R (2006) Experimental evidence for magnetorotational instability in a Taylor-Couette flow under the influence of a helical magnetic field. Phys Rev Lett 97(18):184502
16. Wei X, Ji H, Goodman J, Ebrahimi F, Gilson E, Jenko F, Lackner K (2016) Numerical simulations of the Princeton magnetorotational instability experiment with conducting axial boundaries. Phys Rev E 94(6):063107
17. Winarto H, Ji H, Goodman J, Ebrahimi F, Gilson E, Wang Y (2020) Parameter space mapping of the Princeton magnetorotational instability experiment. Phys Rev E 102(2):023113

Estimation of Inlet Conditions of Fluid Flow in a Thick Pipe Using Inverse Technique

K. Dinesh Reddy and B. Konda Reddy

Nomenclature

h	Heat transfer coefficient (w/m^2 K)
k	Thermal conductivity (w/m K)
MCMC	Markov Chain Monte Carlo
MH	Metropolis–Hastings
r	Radius (m)
v	Velocity (m/s)
T	Temperature (K)
α	Thermal diffusivity (m^2/s)

Subscripts

i	Inlet
in	Inner
out	Outer

K. Dinesh Reddy · B. Konda Reddy (✉)
Department of Mechanical Engineering, IIIT RK Valley, RGUKT AP, YSR Kadapa, India
e-mail: bogala.kondareddy@rguktrkv.ac.in

K. Dinesh Reddy
e-mail: kdineshreddy@rguktrkv.ac.in

1 Introduction

With the rapid rise in the processing power of workstations, the usage of inverse methods for solving heat transfer and fluid flow problems is becoming more popular in theory and practice. This method starts with effects and then calculates the causes. In general, temperature and velocity are the effects, and the thermophysical properties of materials transport coefficient (heat transfer coefficient) and initial and boundary conditions are the causes in thermal sciences. This study is aimed for estimating the inlet parameters like the velocity and temperature of the fluid flowing inside the thick pipe with uniform heat flux applied on its outer surface. Some application in food processing and chemical (Process) industry demands the prior inlet conditions to maintain the desired temperatures on the surface of the thick pipe subjected to uniform heat flux.

2 Literature Review and Objective

For estimating parameters in all engineering and science disciplines, the inverse method is widely practiced today. In heat transfer, the inverse method is used to retrieve thermophysical properties [1, 2], boundary wall heat fluxes [3], and the location and intensity of heat sources [4]. However, inverse problems are ill-posed in nature [5]. The quality of the estimations will be directly affected if any error creeps into the measurements of the experimental data. In literature, deterministic and stochastic techniques are commonly used to solve. Bayesian inference, which is one of the Stochastic-based techniques in inverse heat transfer problems, has advantages, like adding noise in the data and utilizing the prior information while estimating the parameters. In engineering and science, the Bayesian inference applications to estimate parameters are vast. For instance, in the field of engineering, notable researchers like Reddy and Balaji [6], as well as Gnanasekaran and Balaji [7], have utilized Bayesian inference for parameter estimation. Similarly, in the realm of science, authors such as Kaipio and Somersalo [8] and Siekmann et al. [9] have employed Bayesian inference to estimate parameters significantly. In the area of parameter estimation with specific reference to fluid flow through the thick pipe, Kim et al. [10] used an inverse method for estimating thermophysical properties of the fluid flowing in a pipe, and Lu et al. [11] used the inverse method to predict fluctuations in temperature at the inner wall in the pipeline without damaging the integral structure of the pipeline. Han et al. [12] 'estimated the transient convective boundary condition in a horizontal pipe with thermal stratification based on the inverse heat conduction problem,' and Chen et al. [13] used a 'conjugate-based inverse algorithm to estimate unknown space and time-dependent heat transfer rate on the external wall of a pipe system.' Most of the studies on parameter estimation in flow through a pipe with thick wall discussed inverse techniques to estimate unknown heat flux and heat transfer coefficient on the surface. Parameter estimation of fluid flow conditions at

the inlet in flow through the pipe using inverse techniques is rarely reported in the literature. The focus of the present work is to estimate fluid flow conditions at the inlet in flow through a pipe with a thick wall using the inverse technique.

3 Materials and Methods

The present study considers a thick pipe with an internal radius of 10 mm, an outer radius of 20 mm, and a length of 2000 mm. An incompressible fluid flows through the pipe with inlet velocity (v_i) and inlet temperature (T_i). A heat flux of 500 W per unit area is applied uniformly on the pipe's outer surface. Water is used as a working fluid, and the pipe material is mild steel. The schematic representation of the problem with the coordinate system is shown in Fig. 1.

3.1 Forward Model

The governing equations and boundary conditions for the above-described problem are as follows:

Governing Equations

At wall region ($r = r_{in}$ to r_{out}):

$$\frac{1}{r}\frac{\partial}{\partial r}\left(r\frac{\partial T_{(x,r)}}{\partial r}\right) + \frac{\partial}{\partial x}\left(\frac{\partial T_{(x,r)}}{\partial x}\right) = 0. \tag{1}$$

At fluid region ($r = 0$ to r_{in}):

$$\frac{\partial}{\partial x}\left(v_{(x,r)}T_{(x,r)}\right) - \frac{1}{r}\frac{\partial}{\partial r}\left(r\alpha\frac{\partial T_{(x,r)}}{\partial r}\right) = 0. \tag{2}$$
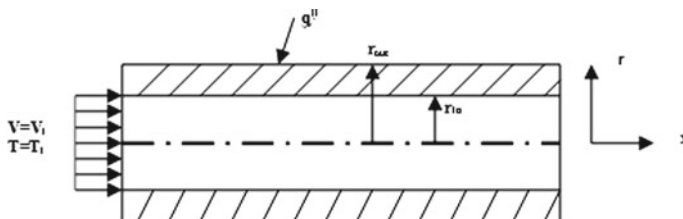
Fig. 1 Schematic diagram of the problem

Boundary Conditions

At heat flux boundary condition ($r = r_{0ut}$):

$$-k\frac{\partial T_{(x,r)}}{\partial r} = h\left(T_{(x,r)} - T_{\infty}\right). \tag{3}$$

At $r = r_{out}$, $q'' = 500$ W/m^2.

At the interference between solid and fluid ($r = r_{in}$),

$$k_f\frac{\partial T_{f(x,r)}}{\partial r} = k_s\frac{\partial T_{s(x,r)}}{\partial r} \Rightarrow T_{f(x,r)} = T_{s(x,r)}. \tag{4}$$

At $x = 0$ and $r = 0$ to r_{in}, $u(0, r) = v_i$, and $T(0, r) = T_i$.

As uniform heat flux is applied on the outer surface, the temperature on the pipe's surface varies along the length of the pipe. The temperature on the surface of the pipe depends on the inlet velocity and inlet temperature of the fluid flowing through the pipe. This dependency of the outer surface temperature of the pipe on the inlet velocity and temperature is used to do the inverse analysis for finding out the inlet parameters.

The temperature distribution on the pipe's outer surface is obtained by running the simulations. COMSOL is used to run the simulations for the two-dimensional steady laminar flow problem. Simulations are run for multiple data sets of inlet velocity and inlet temperature. The information thus obtained is used to fit a nonlinear curve by using Bayesian analysis.

Different nonlinear curves are fitted by considering the variation of surface temperature on the outer surface along the Pipe's length. Among them, the best fit with less error is considered. The best curve fit is as follows:

$$T(x) = a + \left(\frac{b}{v_i^c}\right) \times x^d + T_i, \tag{5}$$

where a, b, c, and d are constants

The estimates of the constants are given in Table 1, and their PPDFs are shown in Fig. 2.

Table 1 Estimation of the constants a, b, c, and d

Constant	Mean	SD	Naive SE
a	0.995	0.0839	1.25e−04
b	12.908	0.116	1.36e−04
c	0.7887	0.01331	1.14e−04
d	0.640	0.01724	1.42e−04
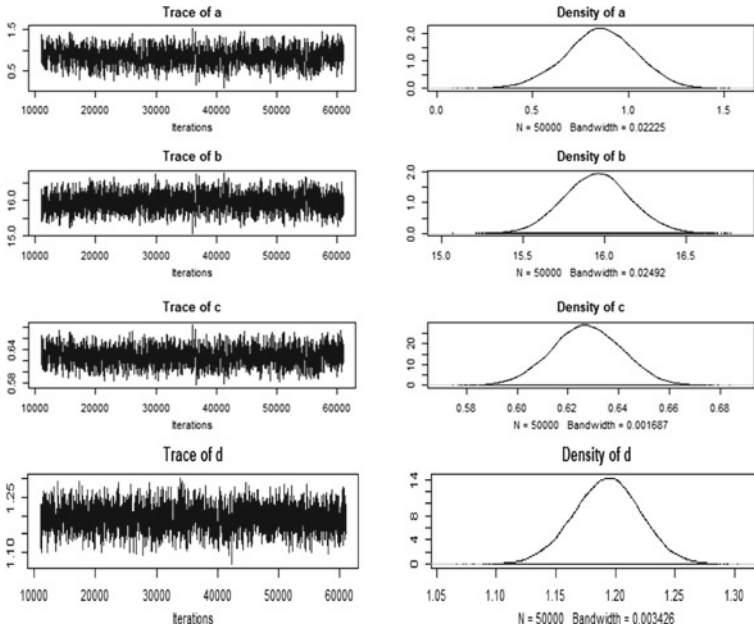
Fig. 2 PPDFs of constants *a*, *b*, *c*, and *d*

3.2 Inverse Model

The present study uses the Bayesian framework to solve the inverse problem. While solving the inverse problem, Eq. 5 is used as a forward model to get the temperature on the surface of the pipe at six points with a distance of 0.1 m, 0.2 m, 0.4 m, 0.8 m, 1.2 m, and 1.6 m, respectively, from the entrance. The simulated temperature data at six equally spaced points in COMSOL is considered as surrogated data by adding noise. The surrogated data thus obtained is considered as measurement data to do the inverse analysis using the Bayesian framework. The values for the parameter 'v_i' and 'T_i' are chosen with an initial guess, and using these initial guess values, and the Metropolis–Hastings (MH) algorithm which is Markov Chain Monte Carlo (MCMC) method, the subsequent samples are generated to solve the problem with the Bayesian inference. Metropolis et al. [14] gave a basic understanding which got MCMC-based MH algorithm.

Table 2 Results of estimation of 'v_i and T_i' with synthetic temperature data with no noise

S. No	Estimated v_i (cm/s)		Estimated T_i (K)	
	Mean	SD	Mean	SD
1	2.84	0.25	318.28	0.318
2	4.25	0.64	323.5	0.223
3	5.43	0.776	345.3	0.315

Synthetic data for v_i and T_i of 2.8 cm/s and 318 K, 4.2 cm/s and 323 K, 5.5 cm/s and 345 K, respectively

Table 3 Results of estimation of 'v_i' and T_i' with synthetic temperature data with 3% noise

S. No	Estimated v_i (cm/s)		Estimated T_i (K)	
	Mean	SD	Mean	SD
1	2.96	0.34	319.23	0.234
2	4.39	0.76	324.8	0.36
3	5.7	0.567	346.1	0.24

Synthetic data for v_i and T_i of 2.3 cm/s and 318 K, 4.2 cm/s and 323 K, 5.5 cm/s and 345 K, respectively

4 Results and Discussion

Estimation of parameters is done with temperature distributions obtained for assumed values of 'v_i' and 'T_i.' Three sets of values for inlet temperature and inlet velocity are considered for this exercise, namely 2.8 cm/s and 318 K, 4.2 cm/s and 323 K, and 5.5 cm/s and 345 K. For a given value of inlet velocity and inlet temperature, the temperature data at six points on the outer surface of the pipe is first obtained from the forward model. This data with no added noise is considered as surrogate experimental data, and parameters 'v_i' and 'T_i' are estimated simultaneously. This is followed by adding 3% white noise to the temperature data obtained from the forward model for a given value of 'v_i' and 'T_i,' and estimations are again performed. Tables 2 and 3 show the results of this exercise. PPDFs of estimated parameters are shown in Fig. 3 with no noise and in Fig. 4 with 3% noise. From Tables 2 and 3, it can be seen that the estimations are perfect with no noise added, while even with a 3% noise, the estimations are accurate to within 5%.

5 Conclusions

Simulations were conducted for 2D fully developed steady-state laminar flow through a thick pipe in COMSOL. The surrogated temperature data is combined with a forward model to retrieve inlet temperature and inlet velocity by working out the
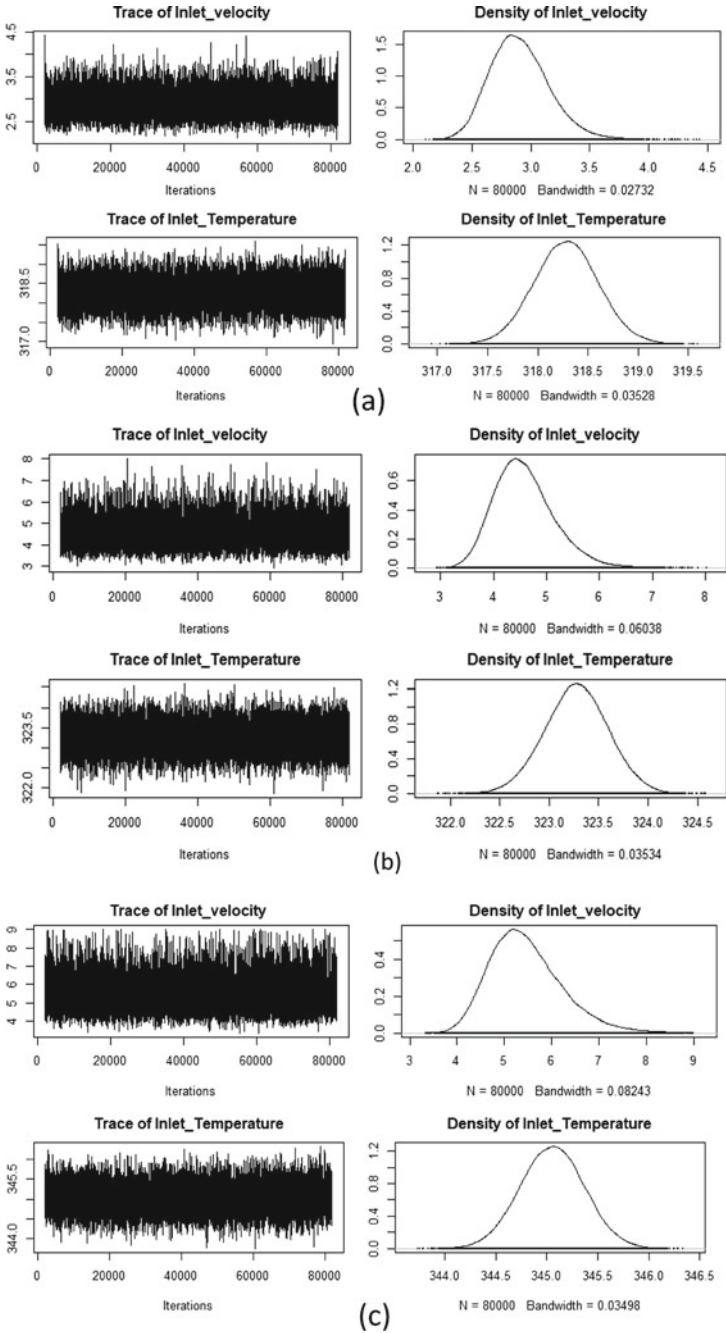
Fig. 3 PPDFs for simultaneous estimation of v_i and T_i for assumed v_i and T_i as **a** 2.8 cm/s and 318 K, **b** 4.2 cm/s and 323 K, and **c** 5.5 cm/s and 345 K with no noise
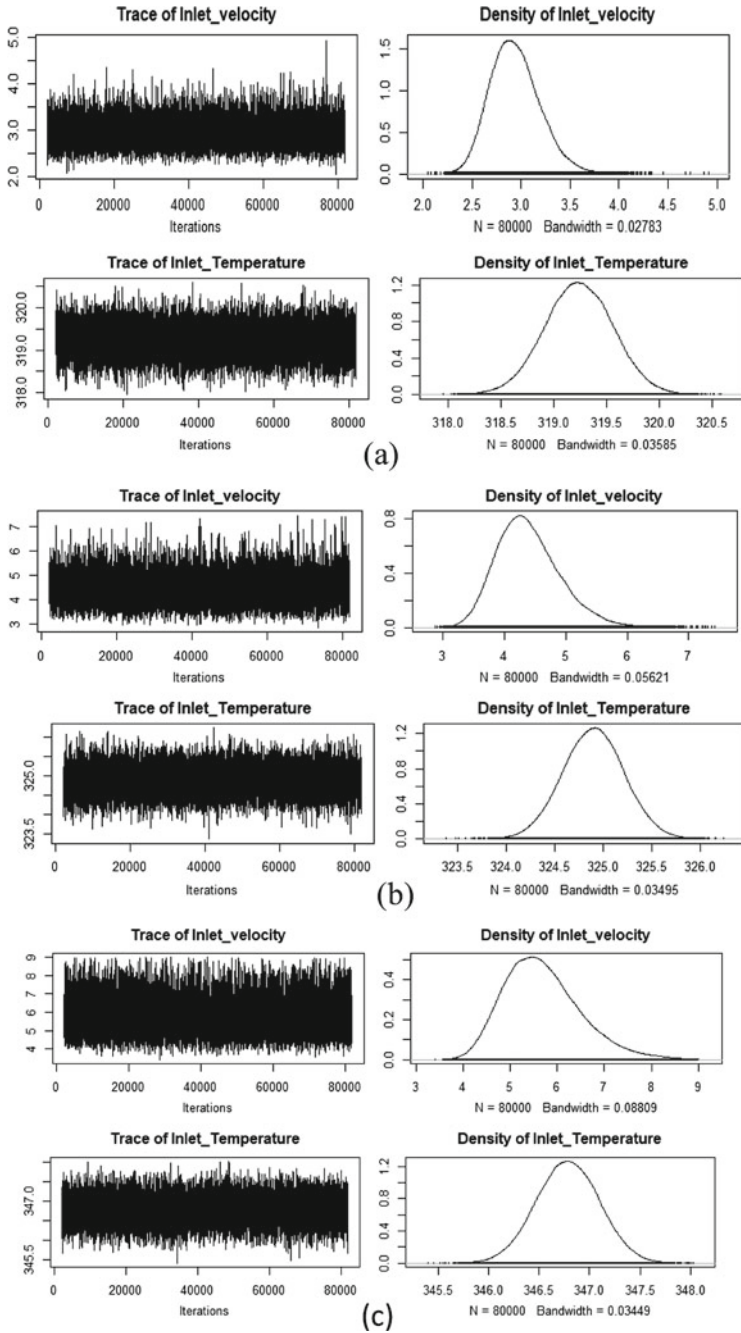
Fig. 4 PPDFs for simultaneous estimation of v_i and T_i for assumed v_i and T_i as **a** 2.8 cm/s and 318 K, **b** 4.2 cm/s and 323 K, and **c** 5.5 cm/s and 345 K with 3% noise

posterior probability density functions (PPDFs) of the inlet temperature and inlet velocity. The values of inlet temperature and velocity were retrieved with good accuracy for both noise-free and noisy cases. As there exists a correlation between inlet velocity and inlet temperature, by changing the priors for the inlet temperature and inlet velocity, a different combination of inlet temperature and inlet velocity can be retrieved according to the situation.

References

1. Huang C-H, Yan J-Y (1995) An inverse problem in simultaneously measuring temperature-dependent thermal conductivity and heat capacity. Int J Heat Mass Transfer 38(18):3433–3441
2. Znaidia S, Mzali F, Sassi L et al (2005) Inverse problem in a porous medium: estimation of effective thermal properties. Inverse Prob Sci Eng 13:581–593. https://doi.org/10.1080/174159 70500098337
3. Mota CAA, Orlande HRB, De Carvalho MOM et al (2010) Bayesian estimation of temperature-dependent thermophysical properties and transient boundary heat flux. Heat Transfer Eng 31:570–580. https://doi.org/10.1080/01457630903425635
4. Ghosh S, Pratihar D, Maiti B et al (2011) Inverse estimation of location of internal heat source in conduction. Inverse Prob Sci Eng 19:337–361. https://doi.org/10.1080/17415977.2011.551876
5. Beck JV, Arnold KJ (1977) Parameter estimation in engineering and science. Wiley series in probability and mathematical statistics. Wiley, New York (NY)
6. Reddy BK, Balaji C (2015) Bayesian estimation of heat flux and thermal diffusivity using liquid crystal thermography. Int J Therm Sci 87:31–48
7. Gnanasekaran N, Balaji C (2013) Markov Chain Monte Carlo (MCMC) approach for the determination of thermal diffusivity using transient fin heat transfer experiments. Int J Therm Sci 63:46–54
8. Kaipio J, Somersalo E (2007) Statistical inverse problems: discretization, model reduction and inverse crimes. J Comput Appl Math 198:493–504
9. Siekmann I, Wagner LE II, Yule D, Fox C, Bryant D, Crampin EJ, Sneyd J (2011) MCMC estimation of Markov models for ion channels. Biophys J 100:1919–1929
10. Kim SK, Lee II W (2002) An inverse method for estimating thermophysical properties of fluid flowing in a circular duct. Int Commun Heat Mass Transfer 29(8):1029–1036. https://doi.org/ 10.1016/S07351933(02)00431-1
11. Lu T, Han WW, Jiang PX, Zhu YH, Wu J, Liu CL (2015) A two-dimensional inverse heat conduction problem for simultaneous estimation of heat convection coefficient, fluid temperature and wall temperature on the inner wall of a pipeline. Prog Nuclear Energ 81:161–168
12. Han WW, Chen HB, Lu T (2019) Estimation of the time-dependent convective boundary condition in a horizontal pipe with thermal stratification based on inverse heat conduction problem. Int J Heat Mass Transf 132:723–730
13. Lih CW, Ching YY, Jin CW, Long LH (2008) Inverse problem of estimating transient heat transfer rate on external wall of forced convection pipe. Energ Convers Manage 49(8):2117–2123
14. Hastings WK (1970) Monte Carlo sampling methods using Markov chains and their applications. Biometrika 57(1):97–109

Effect of Hierarchical Porous Media on Specific Capacity and Energy Density of Li-O$_2$ Battery

T. Ajeesh Mohan, M. Jithin, and Malay K. Das

Nomenclature

A_{ED}	Effective active area of the electrode per volume (m^{-1})
$A_{ED,0}$	Effective active area of the electrode before discharge (m^{-1})
C, ϕ	Concentration (mol/m^3)
$ce_{j\alpha}$	Discrete velocity (m/s)
D	Mass diffusivity (m^2/s)
d_{avg}	Average size of the pores in electrode (m)
E_0	Thermodynamic equilibrium voltage (V)
F	Faraday constant (96,487 C/mol)
g_j	Pseudo-particle distribution (–)
$g_j^{(eq)}$	Equilibrium distribution function (–)
I_{ext}	External current density (A/m^2)
i_0	Exchange current density (A/m^3)
k_{ORR}	Oxygen reduction reaction coefficient (–)
M	Molecular weight (g/mol)
$\dot{m}$	Mass consumption rate (g/m^{3}s)
R_{ORR}	Reaction rate of oxygen reduction reaction (A/m^3)
T	Cell temperature (K)
u_α	Volume-averaged velocity (m/s)
V	Voltage (V)
$V_{Li_2O_2}$	Volume of Li$_2$O$_2$ deposited (m^3)
α_{ORR}	Transfer coefficient of ORR (–)

T. Ajeesh Mohan (✉) · M. Jithin
Department of Mechanical Engineering, Amal Jyothi College of Engineering, Koovappally, Kerala, India
e-mail: tajeeshmohan@gmail.com

M. K. Das
Department of Mechanical Engineering, IIT Kanpur, Kanpur, India

δ_{EL}	Thickness of anode separator layer (m)
$\delta_{Li_2O_2}$	Thickness of the Li_2O_2 precipitate (m)
$\varepsilon_{Li_2O_2}$	Local volume fraction of Li_2O_2 (–)
ε, por	Porosity (–)
ε_0	Initial porosity (–)
η	Overpotential (V)
σ_{EL}	Conductivity of the electrolyte ($\Omega^{-1}\,m^{-1}$)
τ	Tortuosity (–)
τ_ϕ	Dimensionless relaxation time (–)
ω_j	Weight coefficient (–)

1 Introduction

Porous materials are well suitable as the cathode for Li-O_2 and Li-air batteries due to their particular advantages like high specific surface area, large pore volumes, etc. [1]. A high specific surface area leads to a better reaction kinetics through an abundance of exposed active sites and thereby to a higher round-trip efficiency [2]. The pore volume of the battery cathode is critical in accommodating the discharge products and transporting electrolyte and oxygen which have serious effects on overall battery performance [3]. Pore clogging and channel breaking arise as the pores are being filled by discharge products which will result in poor diffusion of oxygen and thereby prevent the good utilization of pores deep in the cathode far away from the inlet [4]. Since a cathode with low porosity seriously inhibits the species transportation, it is logical to think of highly porous materials as cathodes. But as the porosity increases, the specific surface area of the cathode decreases which will result in a reduction of active sites for electrochemical reaction. This, in turn, reduces the reaction kinetics and leads to a lower round-trip efficiency [2]. Hence, we can conclude that an optimum porosity is required to balance diffusion and reaction kinetics and thereby deliver the best output from the Li-O_2 battery.

Hierarchical porous materials are a possible solution for the above-mentioned problems. The cathode can be designed as a nonuniformly porous material with maximum porosity near the oxygen inlet and a step-by-step or continuous reduction of porosity inwards. The higher porosity near the oxygen inlet enhances the diffusion inwards, and the higher surface area in the farther regions ensures better reaction kinetics. Hierarchical porous structures are claimed to improve the discharge capacity as they are effective in accommodating discharge products [2]. Some hierarchically porous cathodes have been synthesized by various researchers and were shown to give better performance [5–9]. Numerical study on Li-O_2 battery is still rare due to the complexities involved despite the outstanding possibilities it offers, but it has gained interest recently due to its advantages. The parameter sensitivity analysis on hierarchical porous cathode done by Jiang et al. [10] is a notable one that claims an improvement in specific capacity with the hierarchical porous cathode.

Usage of LBM for modeling the Li-O_2 battery [11] is also an emerging trend due to the vast advantages that the LBM offers to investigate the Li_2O_2 deposition which is a notable one. However, while dealing with nonuniform porosity, the conventional LBM shows non-negligible numerical errors. The present work uses a recently proposed model by Chen et al. [12] which captures varying porosity using LBM and attempts to capture the porosity variations that arise in the cathode of the lithium-oxygen battery due to the pore filling caused by the reaction product deposition. An in-house code is developed using FORTRAN to carry out the simulations on Li-O_2 battery cathodes with a uniform and hierarchical distribution of initial porosity, and the results are compared.

2 Mathematical Formulation

The LBM model proposed by Chen et al. [12] is used to carry out simulations, since the model handles spatial and temporal variations in diffusion coefficient due to nonuniform porosity distribution in porous media. The concentration field is solved in the porous cathode using the equation given below:

$$\partial_t(\varepsilon\phi) = \nabla_\alpha(D_e\nabla_\alpha\phi). \tag{1}$$

The governing equation is solved using SRT LBM formulation, and the LB evolving equation for concentration field reads:

$$g_j(x_\alpha + ce_{j\alpha}\Delta t, t + \Delta t) - g_j(x_\alpha, t)$$
$$= -\tau_\phi^{-1}\Big[g_j(x_\alpha, t) - g_j^{(eq)}(x_\alpha, t)\Big]. \tag{2}$$

The equilibrium distribution function $g_j^{(eq)}$ is defined as:

$$g_j^{(eq)} = \begin{cases} \phi(\varepsilon - \varepsilon_0) + \omega_j\phi\Big(\varepsilon_0 + \frac{ce_{j\alpha}u_\alpha}{c_s^2}\Big), & j = 0 \\ \omega_j\phi\Big(\varepsilon_0 + \frac{ce_{j\alpha}u_\alpha}{c_s^2}\Big), & j \neq 0 \end{cases}. \tag{3}$$

In order to guarantee numerical stability, generally we chose the minimum value of porosity in the investigated domain as ε_0. The concentration ϕ is obtained by:

$$\phi = \frac{\sum_j g_j}{\varepsilon}, \tag{4}$$

and the effective mass diffusivity D_e is given by:

$$D_e = \varepsilon_0\Big(\tau_\phi - \frac{1}{2}\Big)c_s^2\Delta t. \tag{5}$$

The effective diffusivity is dependent on the local porosity and tortuosity according to the relation:

$$D_e = D_{O_2} \varepsilon^{\tau}. \tag{6}$$

Tortuosity is calculated as:

$$\tau = 1 - 0.77 \ln \varepsilon. \tag{7}$$

The computational domain considered is shown in Fig. 2. Periodic boundary condition is considered in the y-direction. At the right boundary, Dirichlet condition is considered for oxygen concentration. The value of oxygen concentration at the right boundary is calculated according to the relation:

$$\frac{\partial \left(\varepsilon \rho_{EL} C_{O_2} \right)}{\partial t} = \nabla \cdot \left(\rho_{EL} D_e \nabla C_{O_2} \right) + \dot{m}_{O_2}. \tag{8}$$

The consumption rate in species equations of O_2 is:

$$\dot{m}_{O_2} = -\frac{R_{ORR}}{2F} M_{O_2}. \tag{9}$$

Neumann condition is given at the left boundary which represents the interface between porous cathode and the anode separator layer. The calculation of overpotential is carried out according to the model proposed by Li et al. [13] in which the assumption is that the overpotential is uniform throughout the domain at each time instant. The rate of oxygen reduction reaction is calculated according to the equation:

$$R_{ORR} = \left(\frac{C_{Li^+}}{C_{Li^+}^{ref}} \right) \cdot \left(\frac{C_{O_2}}{C_{O_2}^{ref}} \right) \cdot k_{ORR} \cdot A_{ED} \cdot \exp \left(\frac{\alpha_{ORR} F}{RT} \eta \right). \tag{10}$$

Analysis is done under isothermal assumption, and hence, the temperature is fixed as 298 K. The effective active area of electrode per volume, A_{ED} is calculated as:

$$\frac{A_{ED}(t)}{A_{ED,0}} = \frac{\pi \left[d_{avg} - 2\delta_{Li_2O_2}(t) \right]^2}{\pi d_{avg}^2} = \left(1 - \frac{\varepsilon_{Li_2O_2}(t)}{\varepsilon} \right)^{\frac{2}{3}}. \tag{11}$$

Local volume fraction of Li_2O_2, $\varepsilon_{Li_2O_2}$ is calculated from the ORR as:

$$\varepsilon_{Li_2O_2}(t) = \frac{\int R_{ORR} \cdot dt}{2F} \frac{M_{Li_2O_2}}{\rho_{Li_2O_2}}. \tag{12}$$

The ORR coefficient, k_{ORR} is given by:

Fig. 1 Polarization curves for validation of code
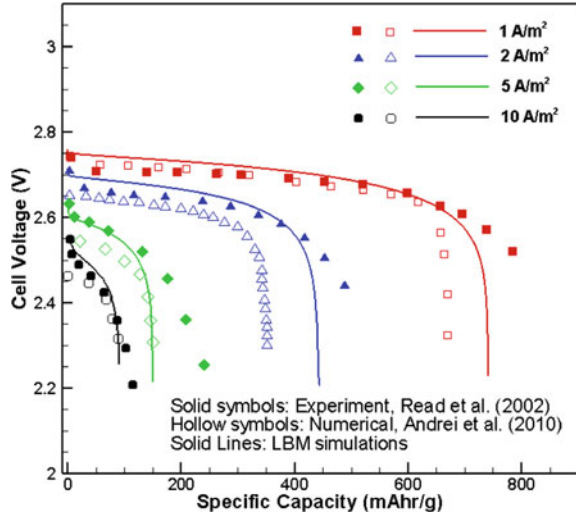
$$k_{ORR} = \begin{cases} i_0 \cdot \left(1 - 0.9\frac{\varepsilon_{Li_2O_2}}{1.63 \times 10^{-6}}\right) & \text{for } \varepsilon_{Li_2O_2} < 1.63 \times 10^{-6} \\ 0.1i_0 & \text{for } \varepsilon_{Li_2O_2} \geq 1.63 \times 10^{-6} \end{cases}. \tag{13}$$

The integration of the ORR rates within the whole computational domain gives the discharge current:

$$I_{ext} = \int_{Electrode} R_{ORR} dx dy. \tag{14}$$

The output voltage of the battery is given by (Fig. 1):

$$V = E_0 - \eta - I_{ext} \times \left(\frac{\delta_{EL}}{\sigma_{EL}}\right). \tag{15}$$

3 Validation

The code developed has been validated against published results from experimental [14] and numerical [15] literature, and the validation plot is given in Fig. 1. The simulations were run for different values of external current densities, and the conditions for the simulations were kept the same as in the literature from which they are compared. It is evident from the figure that the code developed provides credible results as the data got from simulations shows a very good agreement with the published experimental results of Read et al. [14]. The results from our simulations
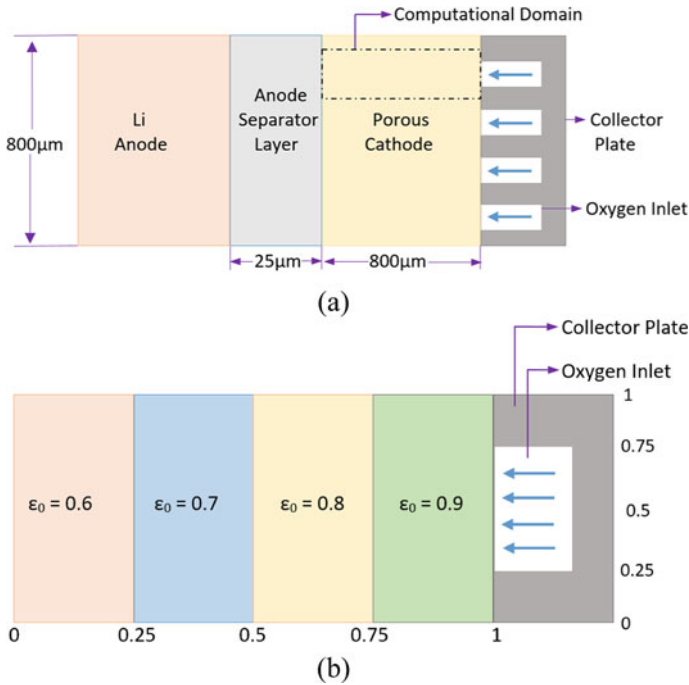
Fig. 2 Schematic diagram of **a** the computational domain considered **b** hierarchical porous media in the cathode

were also compared with the numerical results of Andrei et al. [15], and our results seem quite acceptable.

4 Results and Discussion

Simulations were carried out for three different cases: two cases with uniform initial porosity equal to 0.6 and 0.9, respectively, and one case with a hierarchical initial porosity such that the first 25% of the volume of cathode near the oxygen inlet is set to have an initial porosity equal to 0.9, each of the next adjacent quarter volumes with initial porosity equal to 0.8, 0.7, and 0.6, respectively, as shown in Fig. 2. That is, the hierarchical porous cathode is set to have a decreasing initial porosity from inlet to inwards. The parameters used for simulation were taken from Li et al. [13] and O'Laoire et al. [16].

The variation of output cell voltage with energy density and specific capacity is plotted as given in Fig. 3a, b, respectively. From the plots, it is evident that the hierarchical porous cathode gives a better energy density than the uniform porous cathodes; but at the same time, it fails to give the specific capacity which is offered

by the uniform porous cathode with high initial porosity (0.9 in the present case). The hierarchical porous cathode shows a 6.23% increase in energy density and a 19.97% decrease in specific capacity.

Although energy density and specific capacity are similar properties, energy density quantifies the energy output per unit volume of the cathode, whereas specific capacity quantifies the same per unit mass of the cathode. A battery with high specific capacity can be used where there are strict weight constraints, and that with high energy density can be used where there are strict space constraints. In practical cases, both the weight and space have constraints. A cathode with high uniform initial

Fig. 3 Polarization curves for uniform and hierarchical porous cathodes
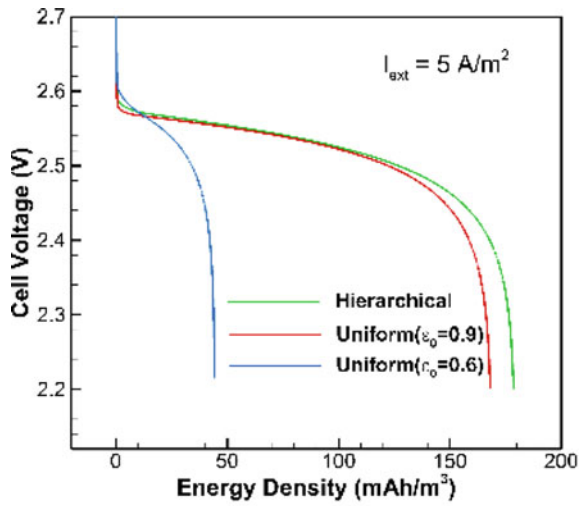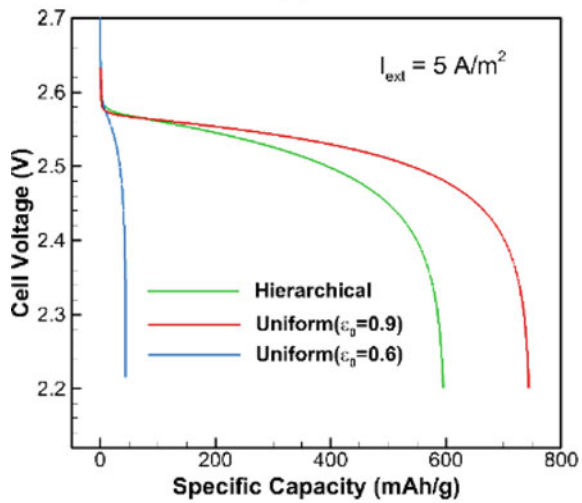
porosity delivers the best specific capacity indicating that it can give the battery with least weight. At the same time, it consumes a large space due to its large volume. As an optimum balance between weight and space requirements, a hierarchical porous cathode stands as the best option.

The uniform porous cathode with low initial porosity (0.6 in the present case) gives poor energy density and specific capacity indicating that for a required capacity of the battery, the weight and space requirements are very high. On the other hand, the hierarchical porous cathode shows more than 12 times (1244%) increase in specific capacity and more than 3 times (346%) increase in energy density compared to this cathode with low uniform initial porosity. Clearly, from the point of view of weight and space requirement, the uniform porous cathode with low initial porosity does not seem to be a good option.

As we have already seen in the first section, a highly porous cathode offers excellent diffusion which ensures the transport of oxygen everywhere in the cathode even at the far ends from the inlet and sufficient space to accommodate discharge products; at the same time, it has to compromise on the reaction kinetics due to the reduction in the exposed active sites for reaction as a result of the low specific surface area of highly porous materials. From Figs. 4a and 7a, it is clear that the porosity at the far end from the inlet of the uniform porous cathode with high initial porosity is slightly decreased, and Figs. 4b and 7b show a nonzero volume of Li_2O_2 deposited at the far end. These factors indicate a good diffusion of oxygen till the far end causing the reaction to take place. From Figs. 6 and 7, we can understand that the reduction in porosity and volume of Li_2O_2 deposited at the far end in a hierarchical porous cathode is slightly less than that of the uniform porous cathode with high initial porosity which is due to the reduction in diffusion caused by the inner layers of lower initial porosity.

We can observe in Fig. 7 that the hierarchical and uniform high porous cathodes follow the same trend in the first quarter volume near the inlet for porosity distribution and Li_2O_2 deposition since both share the same initial porosity. When moving into the next quarter volume, we can see a jump in the volume of Li_2O_2 deposited and a fall in porosity for the hierarchical porous case, whereas the high uniform porous case continues in its gradual path. This is due to an increase in specific surface area and hence in the exposed active sites which enhances the reaction kinetics. These step-by-step jumps in the volume of Li_2O_2 deposited cause an increase in the total volume of Li_2O_2 deposited for the hierarchical porous case compared to the uniform high porous case.

It can be observed from Fig. 7b also, as we can see that the area under the curve is maximum for the hierarchical porous case. The increase in Li_2O_2 deposition proves the increase in reaction kinetics and energy output. Since all three cathodes modeled have the same volume, we can say that the hierarchical porous case gives the best energy density which we have already seen in Fig. 3a.

A cathode with a low uniform initial porosity can offer a high specific surface area, thereby an abundance of exposed active sites for reaction and is capable of providing an excellent reaction kinetics; but on the contrary, oxygen fails to travel much distance from the inlet due to the pure diffusion offered by low porous materials,

Fig. 4 Contour plots for the distribution of porosity and volume of Li_2O_2 deposited in the uniform porous cathode ($\varepsilon_0 = 0.9$) at the end of discharge
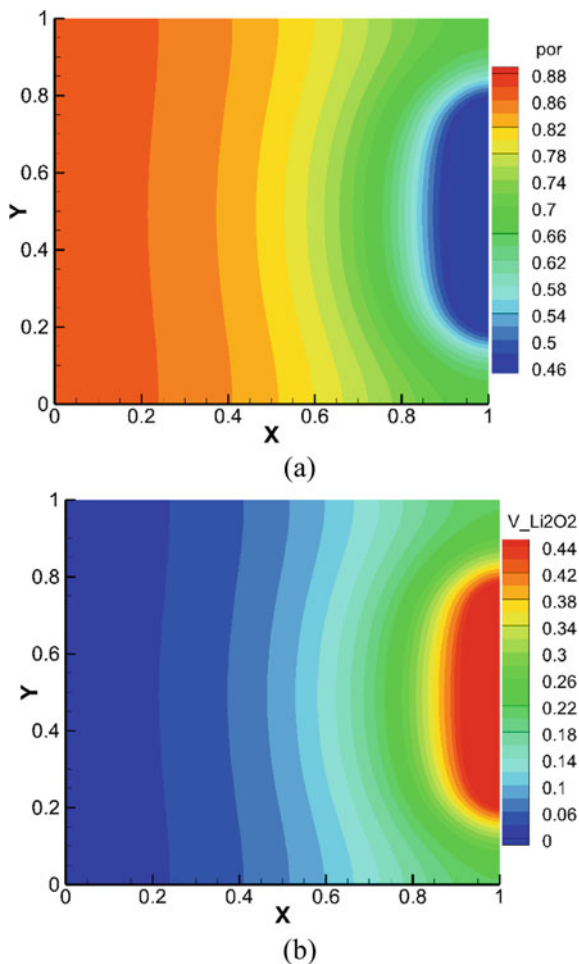
and the active sites deep inside the cathode will end up untouched by oxygen. Also, there is a shortage of voids to accommodate the discharge products for a given volume of the cathode. We can see in Figs. 5a and 7a that the porosity undergoes negligible variation in more than half of the domain at the end of discharge. Figures 5b and 7b show that the volume of Li_2O_2 deposited in those regions is almost zero. This is due to the negligible reaction taking place in those regions even though they offer plenty of exposed active sites. Therefore, the capability of reaction is not being utilized, and it fails to give a good energy density and specific capacity.

A cathode with a hierarchical initial porosity as proposed in this work can offer better energy density than the cathodes with uniform initial porosity even though the specific capacity offered by that is less than that of cathodes with high uniform initial porosity. The improvement in energy density in the hierarchical porous cathode is attained by the balance of diffusion and reaction kinetics. Since the nearby areas of

Fig. 5 Contour plots for the distribution of porosity and volume of Li_2O_2 deposited in the uniform porous cathode ($\varepsilon_0 = 0.6$) at the end of discharge

(a)

(b)
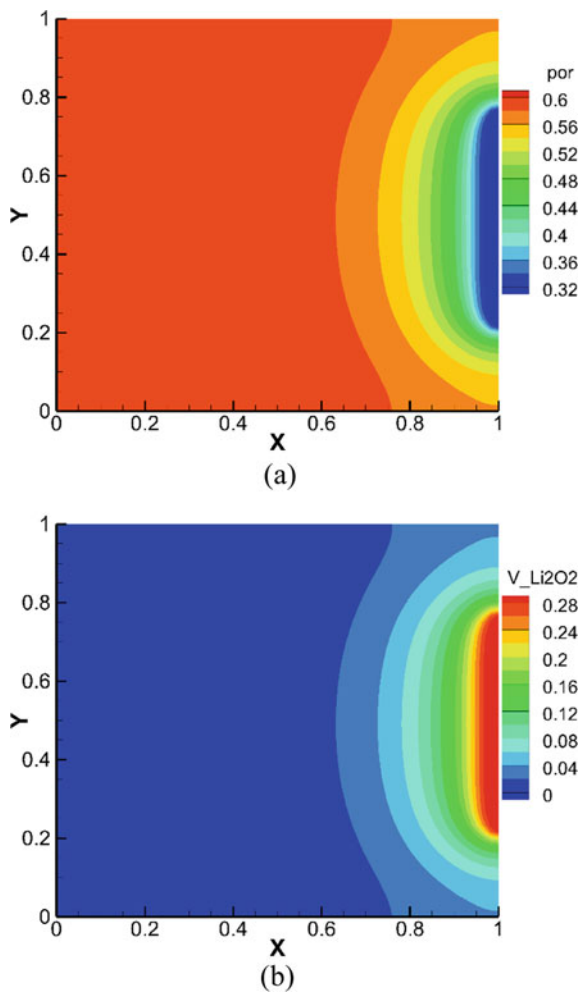
oxygen inlet are high in porosity, oxygen experiences a seamless transport inward. The porosity decreases inwards, and hence, diffusion experiences a reduction as going inwards with an increase in the reaction kinetics due to the increase in surface area. This balance ensures that the maximum of active sites is utilized for reaction, and the best output is delivered by the battery.

Fig. 6 Contour plots for the distribution of porosity and volume of Li_2O_2 deposited in the hierarchical porous cathode ($\varepsilon_0 = 0.6$–0.9) at the end of discharge

(a)

(b)
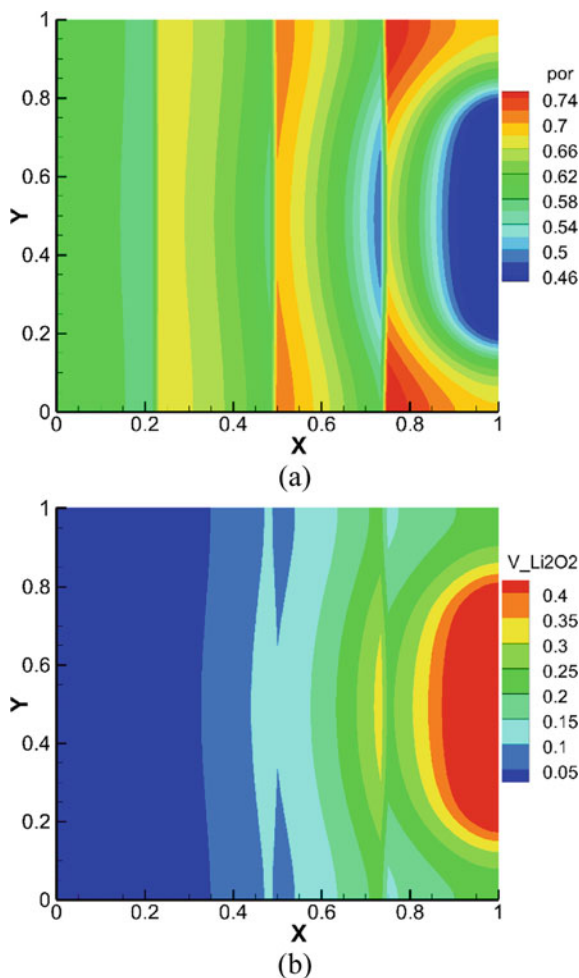
5 Conclusions

Li-O_2 cathodes with uniform and hierarchical initial porosities have been simulated using LBM. Two cases of uniform initial porosities equal to 0.9 and 0.6, respectively, were compared with a case of hierarchical initial porosity consisting of four slabs from 0.6 to 0.9 (maximum near the inlet). The hierarchical porous cathode was found to be balancing the diffusion and reaction kinetics. It provided the maximum energy density, but the uniform porous cathode with high initial porosity (0.9) gave the maximum specific capacity. The uniform porous cathode with low initial porosity (0.6) gave the least energy density and specific capacity. Quantitatively, the hierarchical porous cathode showed a 6.23% increase in energy density and a 19.97% decrease in specific capacity compared to the uniform high porous cathode, whereas it

Fig. 7 Centerline
distribution of porosity and
volume of Li_2O_2 deposited
in uniform and hierarchical
porous cathodes at the end of
discharge
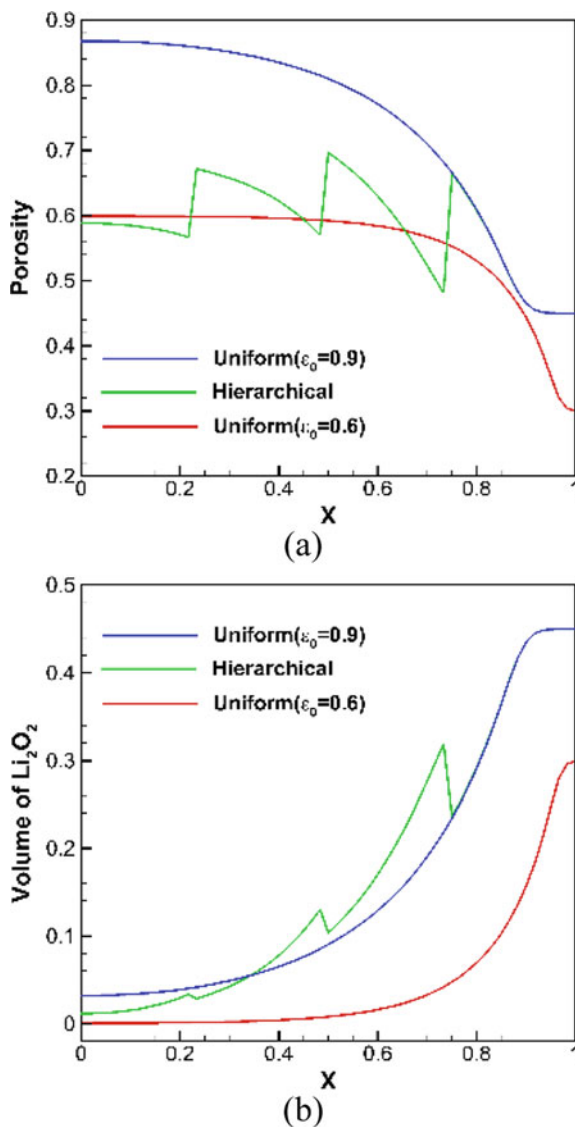
showed a 346% increase in energy density and a 1244% increase in specific capacity
in comparison with the uniform low porous cathode. It is concluded that the hier-
archical porous cathode is highly space efficient due to the better energy density it
offers. Further investigations have to be made to find an optimum distribution of
initial porosity in hierarchical porous cathodes.

References

1. Yang X-Y et al (2017) Hierarchically porous materials: synthesis strategies and structure design. Chem Soc Rev 46(2):481–558
2. Wang H et al (2020) Porous materials applied in nonaqueous Li–O_2 batteries: status and perspectives. Adv Mater 32(44):2002559
3. Li L et al (2015) Hierarchical pore-in-pore and wire-in-wire catalysts for rechargeable Zn– and Li–air batteries with ultra-long cycle life and high cell efficiency. Energ Environ Sci 8(11):3274–3282
4. Das MK, Jithin M (2020) Transport phenomena, electrochemistry and degradation in lithium-oxygen battery. Dynamics and control of energy systems. Springer, pp 433–464
5. Huang J et al (2017) Porous RuO_2 nanosheet/CNT electrodes for DMSO-based Li-O_2 and Li ion O_2 batteries. Energ Storage Mater 8:110–118
6. Lin X et al (2018) An open-structured matrix as oxygen cathode with high catalytic activity and large Li_2O_2 accommodations for lithium-oxygen batteries. Adv Energ Mater 8(18):1800089
7. Lu X et al (2019) 3D Ag/NiO-Fe_2O_3/Ag nanomembranes as carbon-free cathode materials for Li-O_2 batteries. Energ Storage Mater 16:155–162
8. Yuan M et al (2019) Ultrathin two-dimensional metal–organic framework nanosheets with the inherent open active sites as electrocatalysts in aprotic Li–O_2 batteries. ACS Appl Mater Interfaces 11(12):11403–11413
9. Zhang J et al (2016) Facile synthesis of hierarchical porous Co_3O_4 nanoboxes as efficient cathode catalysts for Li–O_2 batteries. J Mater Chem A 4(17):6350–6356
10. Jiang K et al (2020) Parameter sensitivity analysis and cathode structure optimization of a non-aqueous Li–O_2 battery model. J Power Sour 451:227821
11. Jithin M, Das MK, De A (2016) Lattice Boltzmann simulation of lithium peroxide formation in lithium–oxygen battery. J Electrochem Energ Convers Storage 13(3)
12. Chen S, Yang B, Zheng C (2017) Simulation of double diffusive convection in fluid-saturated porous media by lattice Boltzmann method. Int J Heat Mass Transf 108:1501–1510
13. Li X, Faghri A (2012) Optimization of the cathode structure of lithium-air batteries based on a two-dimensional, transient, non-isothermal model. J Electrochem Soc 159(10):A1747
14. Read J (2002) Characterization of the lithium/oxygen organic electrolyte battery. J Electrochem Soc 149(9):A1190
15. Andrei P et al (2010) Some possible approaches for improving the energy density of Li-air batteries. J Electrochem Soc 157(12):A1287
16. O'Laoire CM (2010) Investigations of oxygen reduction reactions in non-aqueous electrolytes and the lithium-air battery. Northeastern University

Development of Tomographic Background-Oriented Schlieren Technique for 3D Density Measurement in Buoyant Plumes

Javed Mohd and Debopam Das

1 Introduction

Several natural and industrial applications involve fluid flows having density variations such as compressible flows, mixing, buoyant plumes, and thermals. Modeling and control of such complex flows require accurate measurement of density. Background-oriented schlieren (BOS) [4, 6, 10] is a density measurement technique in transparent media where the density gradients are related to the refractive index through the Gladstone–Dale relation. In its derivative technique, tomographic-BOS (T-BOS) where the line-integrated density gradients, based on the apparent deflection of a background pattern, from multiple projection angles could be used to reconstruct the instantaneous three-dimensional density field using tomographic algorithms. The analytical tomographic reconstruction technique such as filtered back projection (FBP) based on the Fourier slice theorem suffers from reconstruction accuracy when there are fewer projections. On the other hand, the algebraic reconstruction techniques (ART) which are iterative provide better reconstruction accuracy with limited projection angles and noisy data. Simultaneous iterative reconstruction technique (SIRT), a variation of ART, is used to develop an in-house code to reconstruct the instantaneous density field using the data obtained from BOS measurements.

In the scope of the present work, the developed technique has been applied to study the density dynamics of the buoyant plumes. Buoyant plumes occur in industrial applications such as ventilation and heating, industrial chimneys, and wastewater disposal. The applications in environmental settings include meteorological, oceanographical, and volcanological flows. Currently, MTT [3] model is a widely used theory to predict the behavior of plumes along with many of its derivatives. However, some areas such as the turbulence closure assumption concerning the entrainment

J. Mohd (✉) · D. Das

Department of Aerospace Engineering, IIT Kanpur, Kanpur 208016, India
e-mail: javedm@iitk.ac.in

coefficient, near-field dynamics of the lazy plumes, and the evolution of starting plumes still lack a detailed explanation. During the initial development of plumes, the internal dynamics of the plume head have not been studied.

2   Methodology and Experiments

The experimental setup to generate the buoyant plume used in the present study is shown in Fig. 1. Two mass flow controllers (MFC 1 and MFC 2, Alicat Scientific, MFC-100slpm, MFC-1000slpm) are used to precisely intake the dry He and Air gases which are being supplied from the compressed gas cylinders. These two gases are then mixed in a specially designed mixing chamber and then fed to the settling chamber. In the settling chamber, a sponge layer and honeycomb structure are used to further dampen any remaining flow disturbances and straighten the flow. Finally, the buoyant mixture of He–Air is discharged into the ambience which develops into a buoyant plume. The camera arrangement for BOS measurement of this buoyant plume is shown in Fig. 2. Here, eight cameras (see Table 2 for details) facing a random dotted pattern are placed around the buoyant plume in such a way that the line of sight of the camera and background passes through the center of the measurement volume. The eight cameras are mounted at an angular distance of 22.5° around the measurement volume on a semicircular arc with measurement volume at the center. Each camera is focused on the background pattern which is mounted diagonally opposite of the camera. The plane of the background pattern, lens plane, and sensor plane all are parallel to each other. Hence for calibration, only a scaling factor will be required. The distance between the center of the measurement volume and background as well as between center of measurement volume and camera lens is 600 mm. The background patterns are being illuminated with a high-power flash LED or a laser volumetric illumination. All the eight cameras acquire the images in synchronization at 10 fps with an exposure time of 100 μs.

For this technique such as basic ART [2], simultaneous iterative reconstruction technique (SIRT), simultaneous algebraic reconstruction technique (SART), and

Fig. 1 Experimental setup schematic for generating buoyant plumes
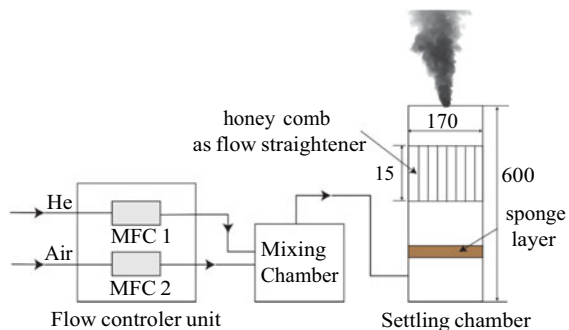
Fig. 2 Schematic showing eight cameras arrangement around the buoyant plume
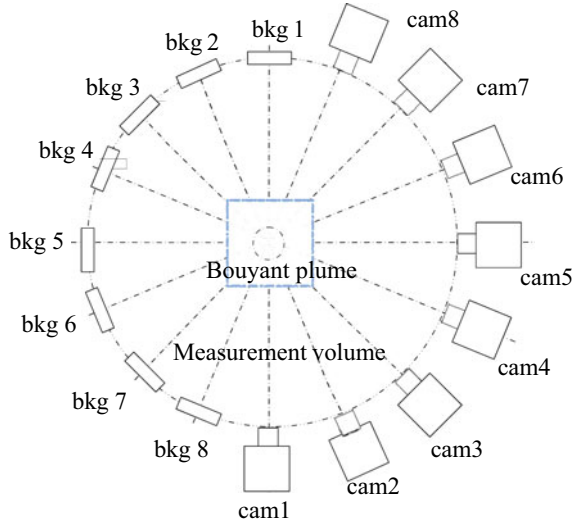
multiplicative algebraic reconstruction technique (MART) [1] will be utilized. A comparative assessment will be made, and the best technique provided the measurement data in present experiment will be used to obtain the 3D unsteady density field.

The data from the experiment is obtained in the form of $\Delta x'$ and $\Delta y'$ displacements of the background pattern. These displacements have been calculated by cross-correlating the images with and without the density gradient in the domain. Knowing other parameters in the setup, the integrated density gradient can be obtained using the following relations:

$$\int_{\zeta_1}^{\zeta_2} \frac{\partial \rho}{\partial y} dz = \frac{n_0 \Delta y'}{G Z_D}$$

$$\int_{\zeta_1}^{\zeta_2} \frac{\partial \rho}{\partial x} dz = \frac{n_0 \Delta x'}{G Z_D} \tag{1}$$

where Z_D is the distance between background and measurement volume [10], G is the Dale–Gladstone constant, and n_0 is the ambient refractive index field. The data, thus, obtained in Eq. 1 can be used for further processing.

Analytical reconstruction algorithms are faster and accurate. However, they do require a large number of noiseless projection data, therefore limiting their use for certain practical applications where it is not possible to acquire projection data at large number of projection angle. Algebraic reconstruction algorithms, on the other hand, can work with fewer projection angles and noisy data. Algebraic techniques

also allow to include prior knowledge during the reconstruction. However, due to their iterative nature, they do require a large computing power.

Unlike ART in SIRT, the solution $\vec{f}$ is not updated after each row calculation, but the corrections for all the rays are averaged, and this averaged value is used to update the solution. This completes the first iteration, and the process keeps on going until a suitable convergence criterion is obtained. SIRT iteration step can be mathematically given as:

$$\vec{f}^{i+1} = \vec{f}^i + \sum_1^M \frac{\left(\frac{(p_i - \vec{w}_i \cdot \vec{f}^{i-1})}{\vec{w}_i \cdot \vec{w}_i} \vec{w}_i \right)}{M} \tag{2}$$

where $\vec{f} = f_1, f_2, f_3, \ldots, f_N$ and $\vec{w}_i = w_1, w_2, w_3, \ldots, w_N$ is ith row of the matrix w_{ij}. The weights w_{ij} has been modeled [9] using Joseph's linear interpolation method. Here, $j = 1$ to N is the total number of unknowns or grid points, and $i = 1$ to M is the total number of projection rays.

The generated He–Air buoyant plume could be characterized by the parameters given in Table 1. The parameters as given in Table 1 are defined as follows:

Density ratio

$$S = \frac{\rho_0}{\rho_\infty}$$

Froud number

$$\mathrm{Fr} = \frac{V_0}{\sqrt{gD}}$$

Reynolds number

Table 1 Details of the experimental cases

Case	S	Re	Fr	Ri
He20Air15	0.51	633	1.03	0.91

Table 2 Details of the imaging and cross-correlation computation

Camera	IMPERX B2320M, 2352 × 1768px
Analysis method	FFT window deformation
Inter. area (pass 1) Inter. area (pass 2)	128 × 128 pixels (50% overlap) 64 × 64 pixels (50% overlap)

Fig. 3 Gaussian fit on the reconstructed density field extracted along the centerline
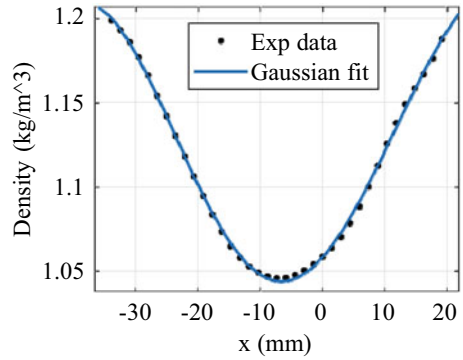
$$\text{Re} = \frac{\rho_0 V_0 D}{\mu_0}$$

Richardson number

$$\text{Ri} = \frac{(\rho_0 - \rho_\infty) g D}{\rho_0 V_0^2}$$

where ρ_0, ρ_∞, V_0, and D are the density of source, density of ambient air, velocity at source, and diameter at source.

2.1 Validation

The reconstructed density field has been validated by fitting a two-term least-square Gaussian curve [5] on the centerline profile from the experimental data. The resulting fit has a R-squared value of 0.999 and is shown in Fig. 3.

3 Results and Discussion

The density gradient projection as obtained by the eight cameras is shown in Fig. 4. These results are obtained after cross-correlation of the background pattern with and without the density gradient. The cross-correlation has been performed using MATLAB-based open-source toolbox-PIVlab [7, 8]. The parameters for cross-correlation computations are given in Table 2.

The density gradient field is then integrated using a Poisson solver with the Neumann boundary conditions. The resulting field represents a line-integrated density field as shown in Fig. 5 for all the eight cameras. Finally, the three-dimensional

Fig. 4 Projected density gradient (represented by contour levels) from eight cameras
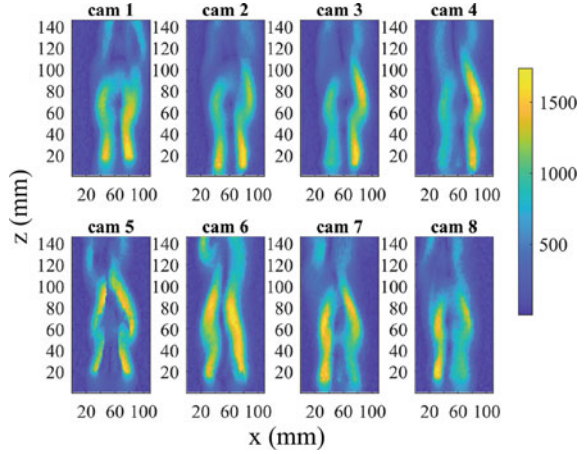
density field is reconstructed using the SIRT technique taking the line-integrated density field of each camera as input. A Dirichlet boundary condition with ambient density is used to correct for the integration constant in the reconstructed data. The reconstruction has been performed in each plan and hence, these planes are stacked up to find the volumetric density field. A visualization of the three-dimensional density field is provided in Fig. 6 using isosurfaces of density magnitude at 0.97, 1, and 1.05 kg/m^3.

Finally, the central line density profile, along y at $z = 73$ mm and $x = 25$ mm, has been extracted from the three-dimensional density field and is plotted in Fig. 7 along with the density gradient which has been obtained by taking derivative of the centerline profile.

Fig. 5 Line-integrated density field (represented by contour levels)
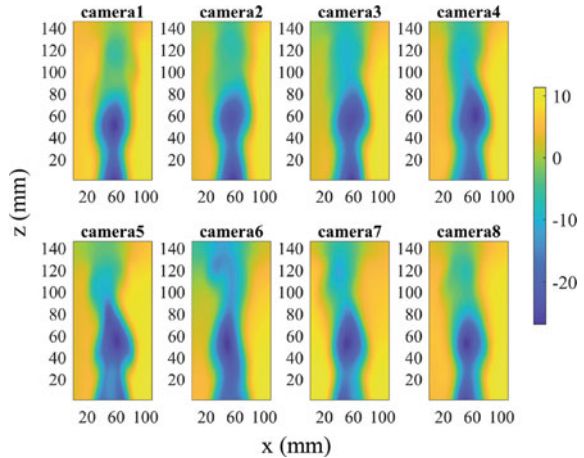
Fig. 6 Reconstructed density field visualized by isosurfaces of density magnitude
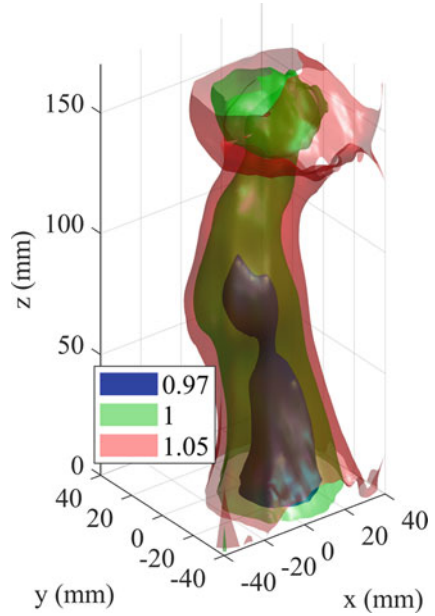
Fig. 7 Centerline density profile
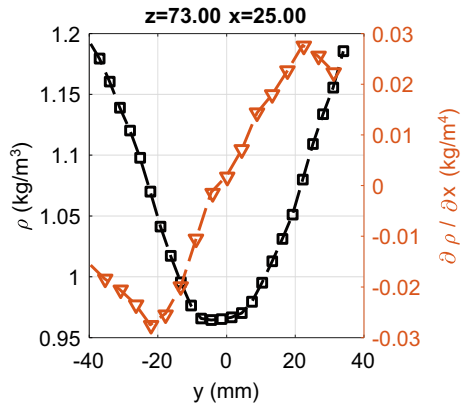
4 Conclusions

This paper demonstrated the proof of the concept measurement for the three-dimensional density in buoyant plumes using tomographic background-oriented schlieren (T-BOS). A MATLAB-based software suit, developed in-house, is employed for data processing and tomographic reconstruction computations. A buoyant plume using a He–Air mixture has been utilized for the measurement and the volumetric density field has been reconstructed. The Gaussian nature of the reconstructed density field has been validated by fitting a least-square Gaussian curve with

an R-squared value of 0.999. The developed technique would be further used to study the density dynamics of the buoyant plumes.

References

1. Munshi P, Mishra D, Muralidhar K (1999) A robust mart algorithm for tomographic applications. Numer Heat Transf Part B Fundam 35(4):485–506
2. Kak AC, Slaney M (1988) Principles of computerized tomographic imaging, vol 33. SIAM
3. Morton BR, Taylor GI, Turner JS (1956) Turbulent gravitational convection from maintained and instantaneous sources. Proc Royal Soc London Ser A Math Phys Sci 234(1196):1–23
4. Raffel M (2015) Background-oriented schlieren (BOS) techniques. Exp Fluids 56(3):1–17
5. Richardson J, Hunt GR (2022) What is the entrainment coefficient of a pure turbulent line plume? J Fluid Mech 934
6. Settles GS, Hargather MJ (2017) A review of recent developments in schlieren and shadowgraph techniques. Meas Sci Technol 28(4):042001
7. Thielicke W, Sonntag R (2021) Particle image velocimetry for MATLAB: accuracy and enhanced algorithms in PIVLab. J Open Res Softw 9(1)
8. Thielicke W, Stamhuis E (2014) PIVLab-towards user-friendly, affordable and accurate digital particle image velocimetry in MATLAB. J Open Res Soft 2(1)
9. van Aarle W, Palenstijn WJ, De Beenhouwer J, Altantzis T, Bals S, Batenburg KJ, Sijbers J (2015) The ASTRA toolbox: a platform for advanced algorithm development in electron tomography. Ultramicroscopy 157:35–47
10. Venkatakrishnan L, Meier GEA (2004) Density measurements using the background oriented schlieren technique. Exp Fluids 37(2):237–247

Aerodynamic Characterization of a Winged Re-entry Vehicle at Select Mach Numbers and Angles of Attack Through CFD Simulations

M. Jathaveda, Kunal Garg, and G. Vidya

Nomenclature

CN	Normal force coefficient (–)
α	Angle of attack (°)
Cmcg	Pitching moment coefficient about cg (–)
Cp	Coefficient of pressure (–)
CA	Axial force coefficient (–)
CL	Lift force coefficient (–)
CD	Drag force coefficient (–)

1 Introduction

Aerodynamic characterization is an important activity in the design and analysis of any launch vehicle, whether it is expendable or reusable. The aerodynamic coefficients are an essential input to the trajectory and control design as well as structural design and analysis. The most challenging aspect of aerodynamic characterization of a reusable launch vehicle is the span of Mach number as well as angle of attack and sideslip, along with control surface deflection. The characterization of the vehicle without control surface deflection gives an idea of the lift coefficient, drag coefficient, lift to drag ratio and the pitching moment coefficient/yawing moment coefficient of the vehicle. Lift coefficient gives an idea of the wing loading along with the angle of attack needed for the same for a given weight of the vehicle. Lift to drag ratio indicates the glide slope angle at subsonic Mach number and gives a measure of

M. Jathaveda · K. Garg · G. Vidya (✉)

Aero Combustion Modelling Division, ADSG, AERO, VSSC, ISRO, Trivandrum 695022, India

e-mail: gvidya18k@gmail.com

cross-range in hypersonic Mach number. The sign of the pitching moment coefficient indicates the direction of control surface deflection needed for trimming the vehicle at the desired angle of attack, the magnitude dictates the extent of control surface deflection and the slope indicates the static stability of the system.

2 Literature Review and Objective

The aerodynamic characteristics of a vehicle are in general, analysed through the use of high-fidelity wind tunnel tests over scaled force and pressure models. The aerodynamic characterization through wind tunnel tests for Space Shuttle Orbiter, X34 and ISRO's winged body re-entry vehicle are given in [1–3]. With the availability of good commercial and in-house CFD software and excellent computing facilities, it is possible to characterize any vehicle within a reasonable turn-around time. Both wind tunnel testing and CFD methods are used for the aerodynamic characterization of PRORA USV [4].

The aerodynamic coefficients of the study configuration at three typical Mach numbers in pitch plane, along with flow features at certain angles of attack, are estimated using *Fluent* CFD simulations and presented here, along with limited validation and code–code comparison. Various flow features in the field and over the body at typical M, α combinations are discussed.

3 Materials and Methods

Figure 1 shows the study configuration. The configuration has a spherical cap joining a slanted ogive nose in the leeward side with, a D-shaped fuselage, double delta wing with elevons at the trailing edge, twin canted vertical tails with rudders at the trailing edge. CFD simulation using commercial package *ANSYS FLUENT* has been carried out for the configuration in wind tunnel scale at $M = 0.3$, 1.1 and 2.0, and angle of attack (α) range of $-5°$ to $25°$ in steps of $5°$. Some of the results for $M = 0.3$ and $M = 2$ are reported in [5, 6]. The sign convention for angle of attack and sideslip is also depicted in Fig. 1.

Fig. 1 Study configuration and sign convention
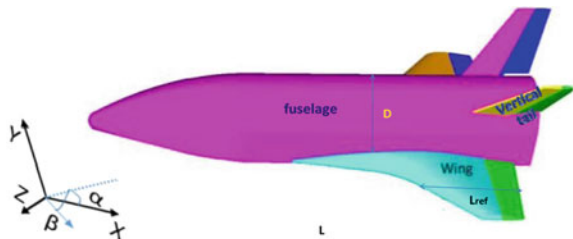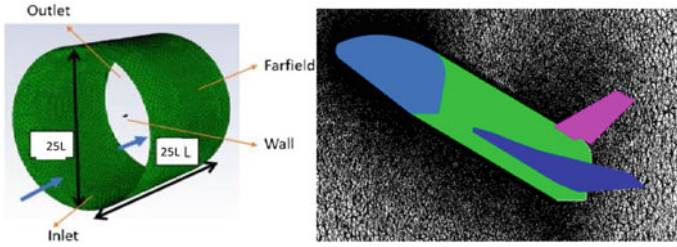
Fig. 2 Computational domain, boundary condition, view of symmetry plane grid along with body
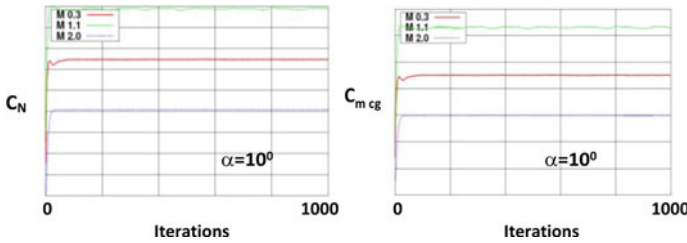
Fig. 3 Convergence of aerodynamic coefficients

The computational domain is cylindrical with length and diameter 25 L, where L is full vehicle length, which is ~6.5D. Far-field boundary condition with body as viscous wall has been used as boundary condition. Unstructured grid with 32.07 million cell count has been made using *ANSYS* mesh. The zoomed mesh in symmetry plane is depicted in Fig. 2, along with the computational domain and boundary conditions. Convergence of aerodynamic normal force and pitching moment coefficients for α = 10° is shown in Fig. 3.

4 Results and Discussion

The scheduled angle of attack profile given in Fig. 4 is reproduced from [7]. This indicates that the angle of attack is always less than 10° from low supersonic Mach number up to low subsonic touchdown. Hence, details of the aerodynamic characteristics are given at typical angles of attack of 0 and 10°. However, the aerodynamic coefficients for the complete vehicle are given for a range of angle of attack.

Fig. 4 Scheduled angle of attack profile from [7]
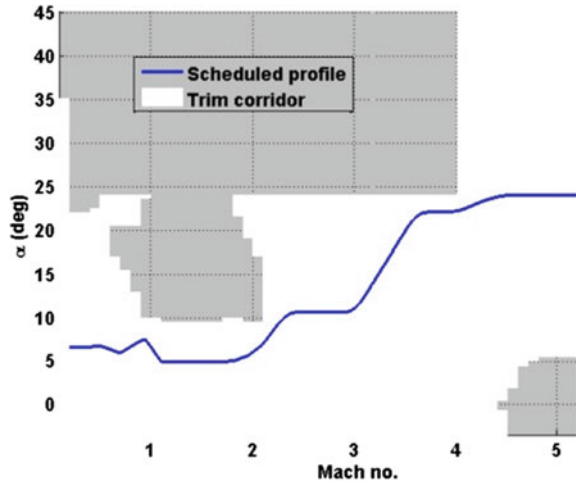
4.1 Symmetry Plane Flow Field

The Mach palette for $M = 0.3$, 1.1 and 2.0 at angle of attack $10°$ is given in Fig. 5. The stagnation regions at the nose cap for all the three cases are visible. The upstream influence ahead of nose cap at $M = 0.3$, shock stand-off at $M = 1.1$ and 2.0, expansion at the cone-cylinder and base, low-speed flow and Mach number deficit in the base region at all Mach numbers are clearly visible. Figure 6 indicates increased level of C_p at the stagnation and also in post-shock region at transonic/supersonic Mach numbers, fall of C_p due to expansion in the cone-cylinder junction and base, suction C_p at the base for all Mach numbers and a clear indication of stagnation point and subsequent overshoot of static pressure in the wake region.

4.2 Base Pressure Coefficient

The fuselage is D shaped for the study configuration. Hence, C_p value at the base region for $\alpha = 10°$ is averaged and presented in Fig. 7 for $M = 0.3$, 1.1, 2.0 along with C_p base for circular cylinder [8] and Space Shuttle Orbiter [9] which has similar fuselage but with flare at the fuselage end. It is observed that the values are not matching for all Mach numbers, but all configurations exhibit maximum suction at transonic Mach number. The base C_p of the study configuration is more negative as compared to circular cylinder but less negative as compared to Space Shuttle Orbiter.
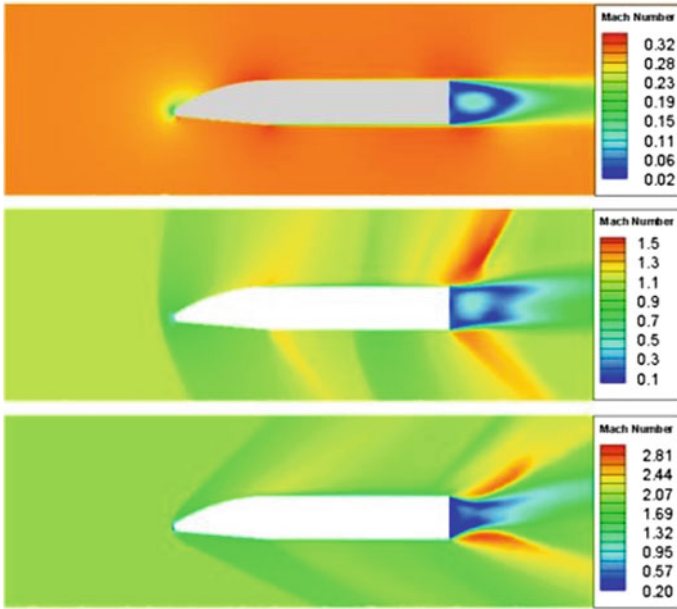
Fig. 5 Symmetry plane Mach palette at $M = 0.3, 1.1, 2.0$ at $\alpha = 10°$
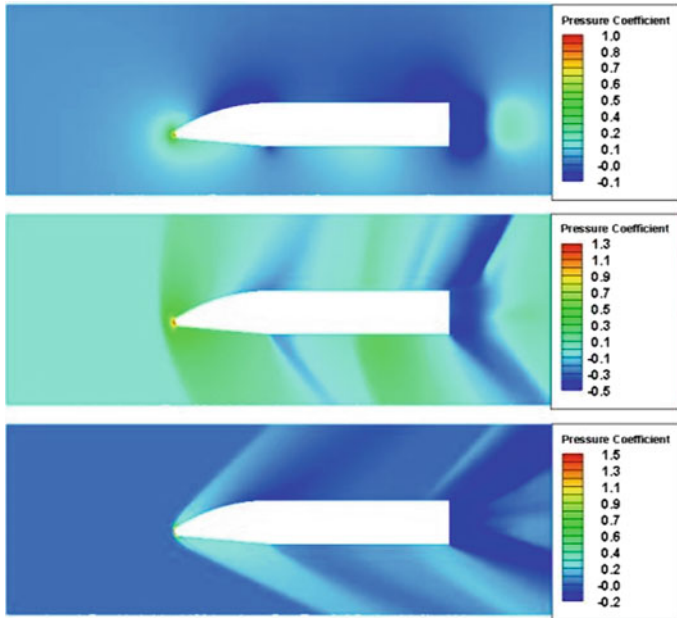
Fig. 6 Symmetry plane C_p palette at $M = 0.3, 1.1, 2.0$ at $\alpha = 10°$
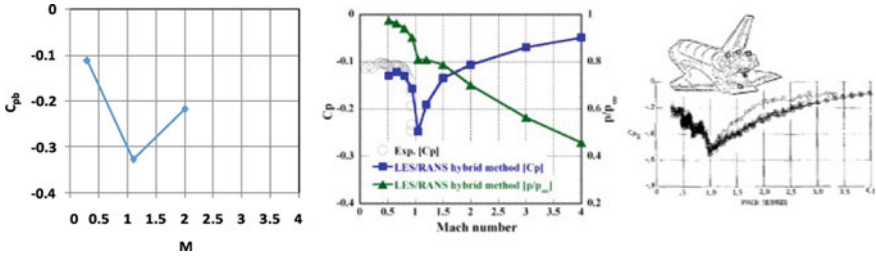
Fig. 7 Base C_p for the study configuration, circular cylinder and Space Shuttle Orbiter

4.3 Pressure Distribution at 0° and 10°

The pressure distribution for $M = 0.3$, 1.1 and 2.0 at $\alpha = 0°$ is presented in Fig. 8. The stagnation pressure (high) pressure is evident in the nose cap and wing leading edge at all Mach numbers. The expansion region on both windward and leeward near the cone-cylinder junction, upper surface of the wing and wing trailing edge are clearly visible.

The pressure distribution for $M = 0.3$, 1.1 and 2.0 at $\alpha = 10°$ is presented in Fig. 9. The stagnation pressure (high) pressure is evident in the nose cap and wing leading edge at all Mach numbers, as in $\alpha = 0°$. There is a decrease in C_p over the leeward side of the wing as well as fuselage. Suction C_p is very high over leeward side of the wing at $M = 0.3$ and 1.1, whereas this is not the case with $M = 2$. In
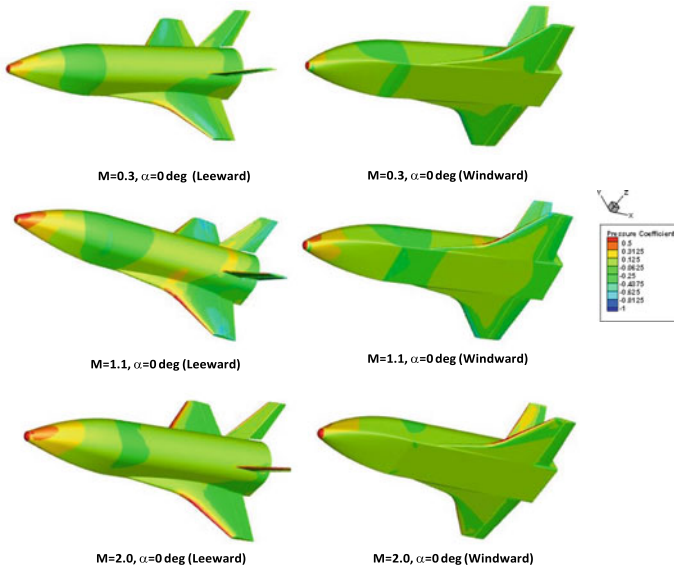
Fig. 8 C_p distribution at $\alpha = 0°$
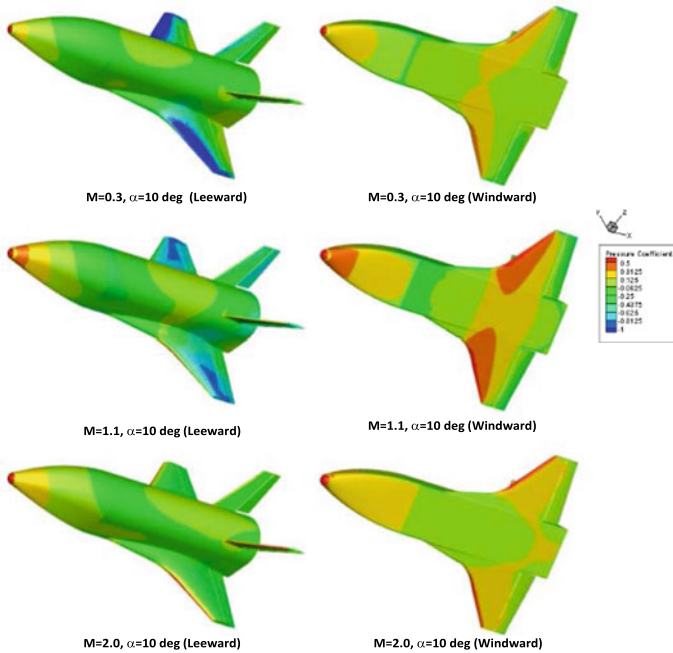
Fig. 9 C_p distribution at $\alpha = 10°$

the windward side, there is an increase in C_p for $\alpha = 10°$, at all Mach numbers, for both fuselage and wing. The interference of the wing on the fuselage is more clearly seen along with the change in pattern with Mach number. The expansion region near the cone-cylinder junction, upper surface of the wing and wing trailing edge are clearly visible. The pressure difference between the windward and leeward sides is the mechanism by which aerodynamic forces are generated at various Mach numbers.

4.4   Surface Streamline Patterns at 0° and 10°

The surface streamlines are plotted and presented in Figs. 10 and 11 for $M = 0.3$, 1.1 and 2.0 at $\alpha = 0°$ and 10°, respectively. The flow is mostly attached over the vehicle at all Mach numbers at $\alpha = 0°$ (Fig. 10).

Streamlines at $\alpha = 10°$ in the windward side, at all Mach numbers, indicate attached flow. Turning off the flow from fuselage symmetry plane towards sides of the fuselage in the nose cone portion is clearly visible. Streamlines in the leeward side indicate the turning due to the angle of attack, on the fuselage side panel, at all Mach numbers. Multiple separation and attachment lines are clearly visible over

M=0.3, α=0 deg   (Leeward)   M=0.3, α=0 deg (Windward)

M=1.1, α=0 deg (Leeward)   M=1.1, α=0 deg (Windward)

M=2.0, α=0 deg (Leeward)   M=2.0, α=0 deg (Windward)
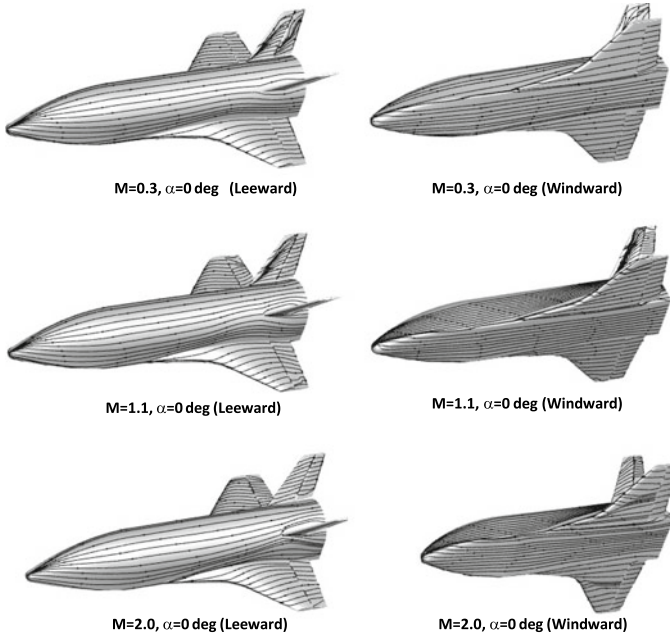
Fig. 10 Surface streamlines at $\alpha = 0°$

M=0.3, α=10 deg   (Leeward)   M=0.3, α=10 deg (Windward)

M=1.1, α=10 deg (Leeward)   M=1.1, α=10 deg (Windward)

M=2.0, α=10 deg (Leeward)   M=2.0, α=10 deg (Windward)
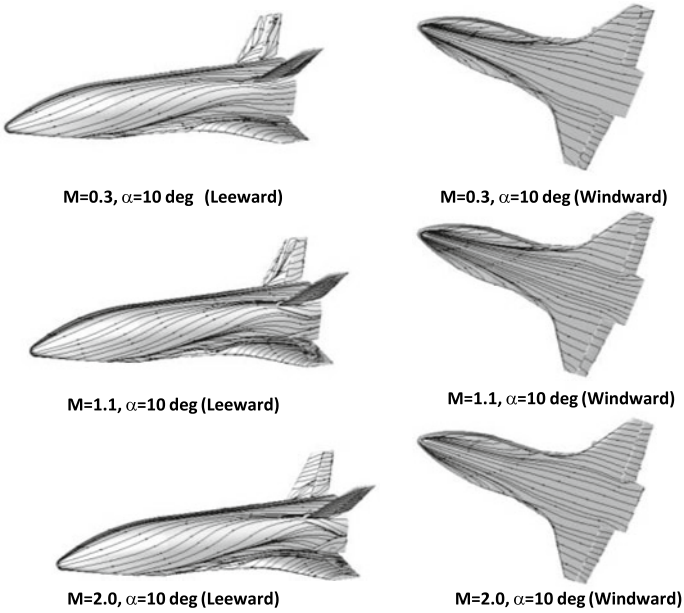
Fig. 11 Surface streamlines at $\alpha = 10°$

fuselage side panel, leeward side of symmetry plane and over the leeward side of the wing and vertical tail.

4.5 Contribution of Various Components to Aerodynamic Coefficients at $\alpha = 0°$ and $10°$

The contribution of fuselage, wing and vertical tail to aerodynamic coefficients at $M = 0.3$, 1.1 and 2.0 are presented in Fig. 12 for $\alpha = 0°$ and $10°$.

Fuselage is the highest contributor to axial force coefficient at all Mach numbers. Wing contributes to axial force coefficient in a negative way at subsonic Mach numbers at angle of attack and this phenomenon is called 'leading edge suction'. The highest value of Axial force coefficient is for the fuselage and it is at $M = 1.1$, $\alpha = 10°$.

Normal force coefficient increases with angle of attack and it is the highest at $10°$ angle of attack for all Mach numbers. Wing is the highest contributor to normal force coefficient at all Mach numbers. The relative contribution of the fuselage increases with Mach number and is maximum at $M = 2$. The highest value of Normal force coefficient is for the wing, and it is at $M = 1.1$, $\alpha = 10°$.

Pitching moment coefficient of the wing is always negative (pitch down), and it becomes more negative with angle of attack. Fuselage contribution becomes more pitch up with increase in angle of attack. The trend of the vertical tail contribution
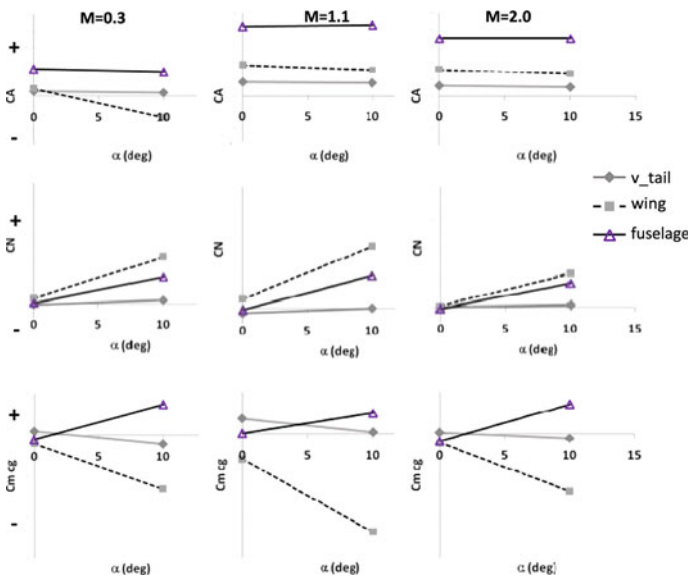
Fig. 12 Contribution of various components to aerodynamic coefficients at $\alpha = 0°$ and $10°$
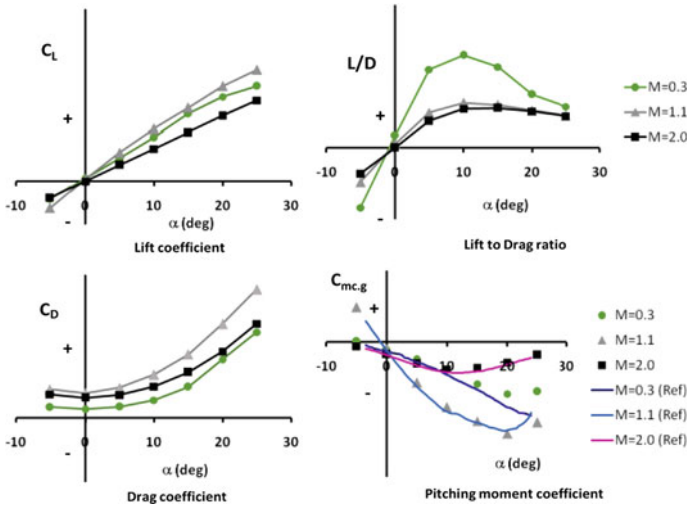
Fig. 13 Aerodynamic coefficients at $M = 0.3, 1.1, 2.0$

is similar to the wing and opposite to that of fuselage. The highest value of pitching moment coefficient is for the wing and it is at $M = 1.1$, $\alpha = 10°$.

4.6 Aerodynamic Coefficients at All Angles of Attack

The aerodynamic coefficients for all Mach numbers and angles of attack are presented in Fig. 13. The axial force and normal force coefficients are in body-axis system, and they are converted to lift and drag coefficient in wind-axis system. Lift, drag and pitching moment coefficients along with lift to drag ratio are presented in Fig. 13.

Lift coefficient increases with angle of attack for all Mach numbers and is the maximum for $M = 1.1$. Linearity of lift coefficient curve drops at higher angles of attack. There is no clear indication of stall. Drag coefficient increases with angle of attack for all Mach numbers in a near-parabolic fashion and is the maximum for $M = 1.1$. Lift to drag ratio increases with angle of attack up to a certain value and falls thereafter. The fall is steeper at $M = 0.3$ as compared to $M = 1.1$ and 2. The maximum value of lift to drag ratio is at $M = 0.3$, $\alpha = 10°$. Pitching moment coefficient is negative (pitch down) for all positive angles of attack. The slope of the pitching moment curve indicates static stability. The configuration is stable at $M = 0.3$ and 1.1 up to $\alpha = 20°$ and becomes unstable thereafter. Vehicle shows instability for $M = 2$ from $\alpha = 10°$ onwards.

The CFD results for pitching moment coefficient are compared with data given in [3, 10]. It is observed that the prediction matches very well for $M = 0.3$ up to $\alpha = 15°$, for $M = 1.1$ up to $\alpha = 20°$ and for $M = 2$ at all angles of attack.
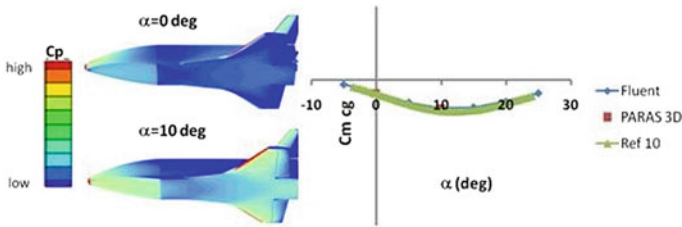
Fig. 14 *PARAS* simulations at $M = 2$ and comparison of pitching moment

Code–code comparison has been carried out using simulation at $M = 2$, using PARAS [11]. Comparison of pitching moment coefficient is shown in Fig. 14 along with C_p distribution over the complete vehicle. Code to code is within 2%. CFD data is lower than data in [10] by 5–10% at $\alpha = 0$ and 10°, respectively.

5   Conclusions

The flow features and aerodynamic characteristics of a wing-body reusable launch vehicle configuration are simulated at three typical Mach numbers at select angles of attack, using Computational Fluid Dynamics simulations. The solver used is *Ansys Fluent* with unstructured grid having 32 million cells. Variations of symmetry plane Mach number and C_p distribution, base pressure coefficient, coefficient of pressure over the study configuration, flow patterns, component contribution to aerodynamic coefficients at select angles of attack are discussed. Lift, drag and pitching moment coefficient along with lift to drag ratio are plotted. The validation of pitching moment coefficient with reference data is brought out. Lift coefficient increases with angle of attack and is the maximum at $M = 1.1$ for a given angle of attack. Drag coefficient varies nonlinearly with angle of attack and is the highest for $M = 1.1$. Lift to drag ratio increases with angle of attack, reaches a maximum around 10° angle of attack and decreases further and is the highest at $M = 0.3$. Pitching moment coefficient curves at $M = 0.3$, 1.1 and 2.0 indicate pitch down moment for all angles of attack. Static stability is present till alpha 20° for M1.1 and 0.3, whereas stability is lost for M2 at alpha above 10° itself. The comparison of pitching moment coefficient with reference data indicates good comparison for M2 at all angles of attack, M1.1 at angle of attack up to 20°, whereas comparison is good for $M = 0.3$ only till 15° angle of attack. Code–code comparison with *PARAS* at $M = 2$ indicates a match within 2%.

References

1. Surber TE, Olsen DC Space Shuttle Orbiter Aerodynamic development. AIAA 74-991
2. Brauckmann GJ X-34 Vehicle Aerodynamic Characteristics. AIAA 98-2531
3. Rao BS, Kurade R, Sivaramakrishnan AE, Ganesan VR Experimental investigation of the flow over an 80/45 rounded leading edge double delta wing-body model. AIAA 2013-0249
4. Rufolo GC, Roncioni P, Marini M, Votta R, Palazzo S Experimental and numerical aerodynamic data integration and aerodatabase development for the PRORA-USV-FTB_1Reusable vehicle. AIAA 2006- 8031
5. Jathaveda M, Garg K, Vidya G, Patil MM, Ashok V (2022) Subsonic aerodynamics of a winged reusable launch vehicle. IIT Kanpur branch, NCAE 2022
6. Jathaveda M, Garg K, Vidya G, Patil MM, Ashok V (2022) Flow features and aerodynamic characteristics of RLV-TD at supersonic Mach number. In: Proceedings of the 1st international conference in fluid thermal and energy systems, 9–11 June 2022, NIT Calicut, Kerala, India
7. Pillai JR et al (2017) Mission design and performance. Curr Sci
8. Kawai S, Fujii K (2004) Computational study of a supersonic base flow using LES/RANS hybrid methodology. AIAA Paper 2004-0068, January 2004
9. Phillips WP, Compton HR Base drag determination for STS flights, pp 1–5. AIAA-83-2719
10. Vidya G, Manokaran K, Ganesan VR, Prasath M, Epuri SK, Balasubramaniam P, Babu C, Subrahmanyam BV, Bandyopadhyay P (2018) Aerodynamic design, characterisation and flight performance of RLV-TD. Curr Sci 114(1):48–63
11. Ashok V, Babu TC (1999) Parallelisation of Navier- Stokes code on a cluster of workstations. In: Lecture notes in computer science, vol 1745. Springer, pp 349–353. https://doi.org/10.1007/978-3-540-46642-0_50

Large Eddy Simulations (LES) of Supercritical Nitrogen Jets

Swapnil Tupkari, Snehasis Chowdhury, Hrishikesh Gadgil, and Vineeth Nair

Nomenclature

D	Injector diameter (m)
t	Time (s)
R	Universal gas constant (J/mol K)
C_p	Constant pressure specific heat capacity (J/mol K)
T	Temperature (K)
ρ	Density (kg/m^3)
u	Velocity (m/s)
τ_{ij}	Viscous stress tensor (Pa)
v	Specific molar volume (m^3/kmol)
a, b	Coefficients in equation of state (–)
ω	Acentric factor (–)
q	Heat flux (W/m^2)
h	Specific enthalpy (J/kg)
e	Specific internal energy (J/kg)
g	Specific free energy (J/kg)
Ψ_h	Isenthalpic compressibility (s^2/m^2)
μ	Viscosity (Pa s)
λ	Thermal conductivity (W/m K)
x	Axial coordinate (m)
r	Radial coordinate (m)
$r_{1/2}$	Jet half-width (m)

S. Tupkari (✉) · S. Chowdhury · H. Gadgil · V. Nair
Department of Aerospace Engineering, Indian Institute of Technology Bombay, Mumbai 400076,
India
e-mail: ftupkari@gmail.com

Subscripts

inj   Injection state
c   Critical state
∞   Ambient state
0   Reference state

1 Introduction

Supercritical combustion for a long period of time has been a topic of concern limited to liquid rocket engines (LRE). However, recent advancements in propulsion technology tend to apply high-pressure combustion in diesel piston engines and gas turbines to achieve greater efficiency with low emission. Hence, clearer understanding of supercritical fluids characteristics and studying their behaviour inside a combustion chamber has now become more important. Computational fluid dynamics (CFD) is proven to be an essential tool to analyse such process efficiently.

Inside a cryogenic rocket engine where the propellants are injected at low temperature but extremely high pressure (transcritical state), the combustion pressure usually reaches 10 MPa or more, which is far above the critical limits of the propellants. Absorbing heat from reaction, the temperature also rises above critical point. This transition of fluid from subcritical temperature to supercritical temperature is characterized by high nonlinearity in thermophysical properties. This nonlinearilty at transition is predominant near critical point, but it remains as pressure goes supercritical and identified as *pseudo-boiling* phenomenon. Therefore, for a CFD simulation, it is a challenge to model these non-idealities accurately. There are several equations of state (EoS) present in literature to model the real gas effects. Among them, cubic EoS proposed by Peng–Robinson (PR) [1] and Soave–Redlich–Kwong (SRK) [2] are shown to be most effective and accurate. However, the cubic EoS show some discrepancy in density prediction near critical point specifically in transcritical side. Therefore, most of recent studies [3, 4] implement PR model, with a volume translation method (VTM) for density correction near critical point.

In experiments of LO_x/LH_2 combustion, Mayer and Tamura [5] have observed clear contrast between subcritical and supercritical injection. Where after subcritical injection, the jet follows a process of breaking into smaller droplets (atomization), and for supercritical injection, the jet forms string-like structures that rapidly dissolve into the environment following a gas-like turbulent diffusion process. Thus, turbulence plays a key role in supercritical mixing, and any numerical study of the same requires choice of suitable turbulence model to capture the shear layer development. Large Eddy Simulation (LES) is one of the most useful tools and has been widely applied in several studies by Oefelein [6], Zong and Yang [7], Schmitt et al. [8], Müller and Pfitzner [3], Oefelein [6] and Bellan et al. [9] in their study have also implemented high-fidelity direct numerical simulation (DNS) for more accurate result. Present

study uses a 3D LES framework realizing the sub-grid scale turbulence with classical Smagorinsky model.

This work is focused on investigating the unsteady mixing characteristics of a supercritical nitrogen jet injected in supercritical environment. A new OpenFOAM solver is developed to study injection and mixing happening at high pressures. It is a step in developing a solver for simulating combustion in LRE. Peng–Robinson equation of state with volume translation method of Harstad et al. [10] is employed to incorporate real gas effects. A modified PISO algorithm along with isenthalpic compressibility is used [3]. The empirical correlations for high-density fluids are used for computing transport properties [11]. This newly developed solver is validated with the experimental results of Mayer et al. [12] as well as numerical results from [3] for N_2. Effect of chamber pressure on mixing layer development is also studied extensively in this paper. Two separate cases of injection pressures 6.9 and 9.3 MPa are considered for this study. Zong and Yang [7] also considered these pressures to study transcritical injection. Current study focuses on supercritical injection for same pressure levels.

2   Mathematical Modelling

2.1   Governing Equations

All the compressible flow equations are described here. Continuity equation:

$$\frac{\partial \rho}{\partial t} + \frac{\partial \rho u_j}{\partial x_j} = 0. \tag{1}$$

Momentum equation ($i = 1, 2, 3$):

$$\frac{\partial \rho u_i}{\partial t} + \frac{\partial \rho u_j u_i}{\partial x_j} = -\frac{\partial p}{\partial x_i} + \frac{\partial \tau_{ij}}{\partial x_j}. \tag{2}$$

Enthalpy equation:

$$\frac{\partial \rho h}{\partial t} + \frac{\partial \rho u_j h}{\partial x_j} = -\frac{\partial q_i}{\partial x_i} - \frac{Dp}{Dt} + \frac{\partial \left(u_i \tau_{ij}\right)}{\partial x_i}. \tag{3}$$

The heat flux is given by:

$$q_j = -\lambda \frac{\partial T}{\partial x_j}.$$

The viscous stress tensor τ_{ij} is given by:

$$\tau_{ij} = \mu \left(\frac{\partial u_i}{\partial x_j} + \frac{\partial u_j}{\partial x_i} \right) - \frac{2}{3} \mu \delta_{ij} \left(\frac{\partial u_k}{\partial x_k} \right).$$

Here, ρ is the density, u_i is the velocity in ith direction, p is thermodynamic pressure, h is enthalpy, μ is molecular viscosity, and δ_{ij} is the Kronecker delta. In OpenFOAM while solving enthalpy Eq. (3), viscous heating term $\left(\partial \left(u_i \tau_{ij} \right) / \partial x_i \right)$ is neglected as it is negligible for low-velocity flows.

2.2 Thermophysical Modelling

The thermophysical modelling used for LES study of cryogenic N_2 jet is described here.

$$p = \frac{RT}{v - b} - \frac{a}{v^2 + 2vb - b} \tag{4}$$

$$a = 0.457235 \frac{R^2 T_c^2}{p_c} \left(1 + \kappa \left(1 - \sqrt{T_r} \right) \right)^2 \tag{5}$$

$$b = 0.077796 \frac{RT_c}{p_c}. \tag{6}$$

In this equation, $v(\mathrm{m^3/kmol})$ is the molar volume, $R(\mathrm{J/kmol\,K})$ is the universal gas constant, intermolecular forces of attraction are taken into account by a, and the reduction of free volume as the molecules have finite volume is considered by b. T_r is the reduced temperature, $T_r = T/T_c$, $\kappa = 0.37464 + 1.54226\omega - 0.26992\omega^2$, here ω is the acentric factor. For nitrogen $\omega_{N_2} = 0.0372$, $p_c = 3.4$ MPa, $T_c = 126.192$ K, and $\rho_c = 313$ kg/m^3. . The Peng–Robinson (PR) equation of state is a cubic equation that cannot predict liquid density accurately close to critical point. In order to correctly predict liquid densities, we use the volume translation method proposed by Harstad et al. [10].

$$v = v_{pr} + \left. \frac{\partial g^0}{\partial p} \right|_T. \tag{7}$$

The internal energy is calculated using departure function formulation.

$$e = e^0 + \int_\infty^v \left[T \left. \frac{\partial p}{\partial T} \right|_v - p \right] dv \tag{8}$$

$$e = e^0 + \frac{1}{2b\sqrt{2}} \left[a - T \frac{\partial a}{\partial T} \right] \ln \left[\frac{v + b \left(1 - \sqrt{2} \right)}{v + b \left(1 + \sqrt{2} \right)} \right]. \tag{9}$$

In this equation, e represents molar internal energy, e^0 is its value at 1 bar pressure, and v indicates molar volume obtained from PR-EoS.

The enthalpy can be calculated in the similar way:

$$h = h^0 + \int_{p^0}^{p} \left[v - T \left. \frac{\partial v}{\partial T} \right|_p \right] \mathrm{d}p \tag{10}$$

$$h = h^0 + pv - RT + \frac{1}{2b\sqrt{2}} \left[a - T \frac{\partial a}{\partial T} \right] \ln \left[\frac{v + b\left(1 - \sqrt{2}\right)}{v + b\left(1 + \sqrt{2}\right)} \right]. \tag{11}$$

We use isenthalpic compressibility for real gas-based PISO algorithm [3].

$$\Psi_h = \left. \frac{\partial \rho}{\partial p} \right|_h = -\frac{1}{v^2} \left. \frac{\partial v}{\partial p} \right|_h. \tag{12}$$

The NASA 9 coefficient polynomials are used for calculating following functions [13]:

$$\frac{C_p^0}{R} = a_1 T^{-2} + a_2 T^{-1} + a_3 + a_4 T + a_5 T^2 + a_6 T^3 + a_7 T^4 \tag{13}$$

$$\frac{H_T^0}{RT} = -a_1 T^{-2} + \frac{a_2 \ln T}{T} + a_3 + \frac{a_4 T}{2} + \frac{a_5 T^2}{3} + \frac{a_6 T^3}{4} + \frac{a_7 T^4}{5} + \frac{a_8}{T} \tag{14}$$

$$\frac{S_T^0}{R} = -\frac{a_1 T^{-2}}{2} - a_2 T^{-1} + a_3 \ln T + a_4 T + \frac{a_5 T^2}{2} + \frac{a_6 T^3}{3} + \frac{a_7 T^4}{4} + a_9 \tag{15}$$

$$\frac{G_T^0}{R} = \frac{H_T^0}{RT} - \frac{S_T^0}{R} = -\frac{a_1 T^{-2}}{2} + \frac{2a_2(1 - \ln T)}{T}$$
$$+ a_3(1 - \ln T) - \frac{a_4 T}{2} - \frac{a_5 T^2}{6} - \frac{a_6 T^3}{12} - \frac{a_7 T^4}{20} + \frac{a_8}{T} - a_9. \tag{16}$$

The transport properties, i.e. viscosity and thermal conductivity, are modelled using empirical correlation of dense fluids by Chung et al. [11]. A new class is added to OpenFOAM in order to use these correlations (Figs. 1 and 2).

2.3   Computational Set Up

Computational domain used in present study is shown in Fig. 1. A hexahedral O-grid is created using OpenFOAM. Axial and radial extent of the domain is 90D and 28D, respectively, where $D = 2.2$ mm is the injector diameter. Grading is used in axial and

Fig. 1 Geometry of the
computational domain used
in present study
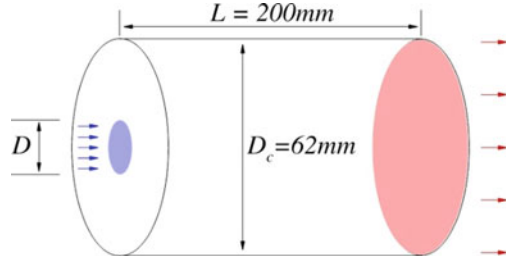
Fig. 2 Meshing
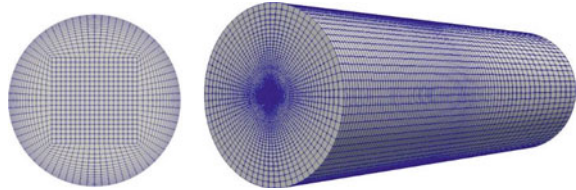
radial directions, whereas no grading is used in azimuthal direction. In order to carry out grid independence study, a number of grid points in axial and radial directions are varied, while azimuthal grid points are unchanged. Three grids with mesh count of 2.1 million, 4.2 million, and 6.5 million cells are used in order to conduct grid independence study for supercritical case with 3.97 MPa pressure. The number of grid points used in axial, radial, and azimuthal directions for different grids is given in Table 1. It was found that 4.2 million mesh gives fairly accurate results and reaches convergence; hence, it has been used in further simulations.

All the boundary conditions used during the simulation are tabulated in Table 2. For pressure *waveTransmissive* (*wT*), boundary condition is used at outlet. N_2 is injected under supercritical condition; at a temperature of 137 K at a velocity of 5.4 m/s, injection pressure is varied as 3.97, 6.9, and 9.3 MPa.

A pipe flow simulation was carried out separately, and developed average velocity profile is given as inlet profile along with *turbulentInlet* boundary condition. Ambient temperature and pressure inside the chamber are kept as 298 K and 3.97 MPa, respectively. So cryogenic N_2 is injected into ambient N_2 inside the chamber.

Table 1 Details of mesh used

Mesh	Axial	Radial	Azi.	Total count
1	400	70	72	2.1 million
2	560	98	72	4.2 million
3	705	123	72	6.5 million

Table 2 Boundary condition specifications

B.C.	p	T	U
Outlet	wT	$\nabla T = 0$	InletOutlet
Inlet	$\nabla p = 0$	137 K	TurbulentInlet
Coflow	$\nabla p = 0$	$\nabla T = 0$	0.1 m/s
Wall	$\nabla p = 0$	298 K	0.1 m/s

3 Results and Discussion

Total run-time of ~ 1 s is considered in present study. It is found that the residuals drop and become range-bound after a short time. Results are saved at an interval of 0.001 s after this initial transient. To allow uniformity in results, the results presented in this paper are for data obtained after 0.3 s, which is well past the time for which transients are present. LES simulations of supercritical N_2 are carried out using newly developed solver. Smagorinsky sub-grid scale (SGS) model is used with second-order spatial discretisation scheme. Euler scheme is used for temporal discretisation.

Simulations are carried out for all grids, and results are compared with benchmark data. Figure 4 shows centreline density plot for supercritical N_2 injection at 3.97 MPa pressure. This axial density matches the experimental results of Mayer et al. [12] as well as with results of Müller et al. [4] fairly well (Fig. 3).

Simulations of higher injection pressure cases are carried out keeping all other boundary conditions unchanged. To observe the mixing characteristics, density distributions for higher-pressure cases are visualized and compared with the baseline case. Figure 5 shows the instantaneous and mean density field for the three cases at a plane of symmetry. With increase in pressure, overall density of jet also increases, which is expected. Isocontour lines are plotted in both mean and instantaneous field for density value of $\rho = (\rho_{\text{inj}} + \rho_\infty)/2$, signifying the potential core boundary. These isolines and axial mean density distributions (Fig. 6) suggest a longer potential core

Fig. 3 Grid independence test carried out using three different meshes with mesh count of 2.1 million, 4.2 million, and 6.5 million cells
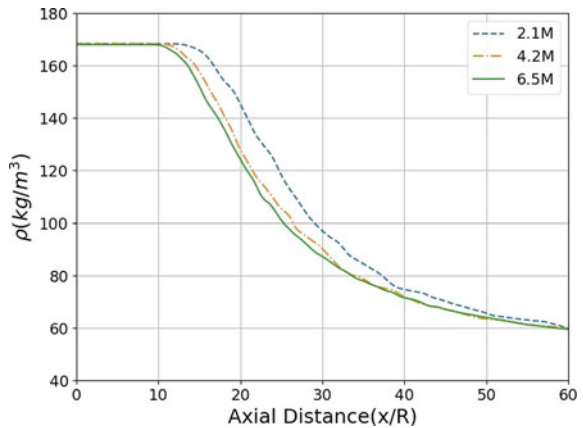
Fig. 4 Average centreline density plot for the supercritical N_2 injection at 3.97 MPa; -o- experimental data
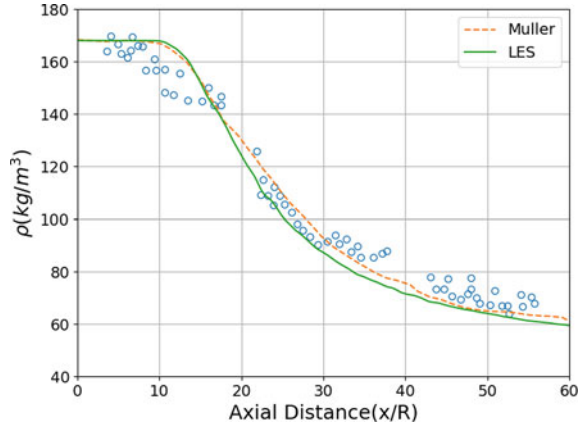
for higher pressures. For 6.9MP, a pressure of the potential core is observed to be 25% longer than that of 3.97 MPa case. However, for 9.3 MPa pressure, the core length drops slightly from 6.9 MPa.

Contours of density gradient (Fig. 7) and vorticity magnitude (Fig. 9) are visualized in logarithmic scale to capture the variations in larger range. Jet breakup mechanism is observed to be highly turbulent in nature. The instantaneous density gradient and vorticity plots show Kelvin–Helmholtz-type vortical structures developed from jet surface establishing the mixing mechanism of supercritical jet.

Higher-density gradient is visible for higher operating pressures. For 6.9 MPa and 9.3 MPa pressure, the maximum mean density gradient is observed to be around 2.7 times and 3.1 times of the baseline, respectively.

This happens possibly due to the injection condition coming closer and crossing the pseudo-boiling line as pressure increases. Higher-density stratification is also responsible for transfer of turbulent kinetic energy from radial direction to axial direction. In literature, this is known as the solid wall effect, that is predominant near critical point or pseudo-boiling point. For this reason, jet break up gets delayed and spreading rate drops in higher-pressure cases to some extent. However, for the maximum pressure case, the spreading rate almost remains unchanged. The spreading rate is visualized by half-width distribution (Fig. 8) which shows earlier growth for 3.97 MPa case, whereas for 6.9 and 9.3 MPa cases, the spreading is delayed and almost similar for both cases. This behaviour can be justified by the weakening of pseudo-boiling at higher pressure which eventually reduces the density stratification effect.

The vorticity contours also show similar trend of spreading behaviour. For the baseline case, the instantaneous flow structure is characterized with strong turbulent eddies, whereas with increasing pressure, the high-density stratification absorbs energy from eddies in shear layer weakening the eddy structure and reducing width of the turbulence dominant region. Therefore, maximum average vorticity also drops as pressure is increased.

Fig. 5 Instantaneous
(above) and mean (below)
density variation; iso-contour
lines for of N_2 jet for
injection pressures 3.97 MPa
(top), 6.9 MPa (middle), and
9.3 MPa (bottom)
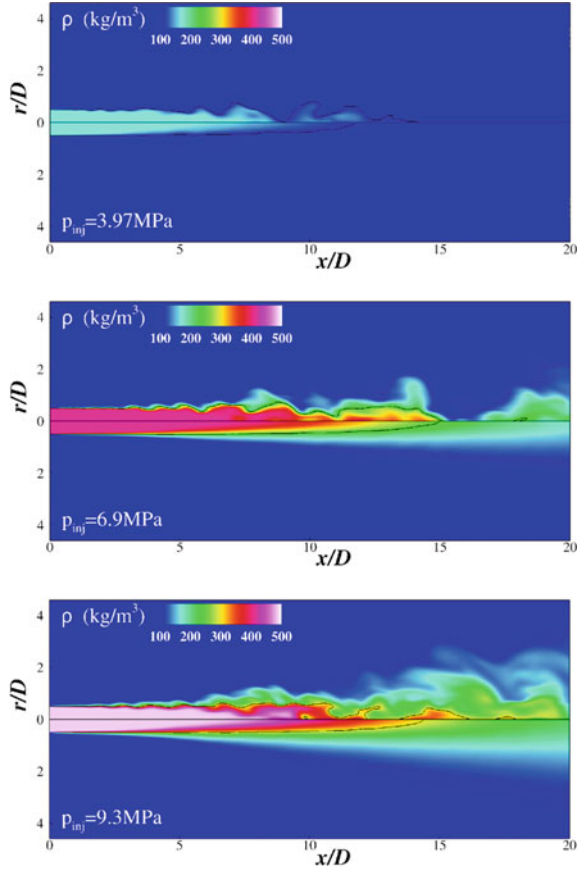
Fig. 6 Average centreline
density variation for different
injection pressures
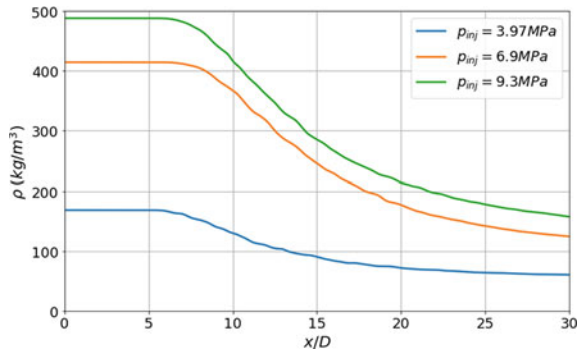
Fig. 7 Instantaneous (above) and mean (below) variation of density gradient for injection pressures 3.97 (top), 6.9 MPa (middle), and 9.3 MPa (bottom)
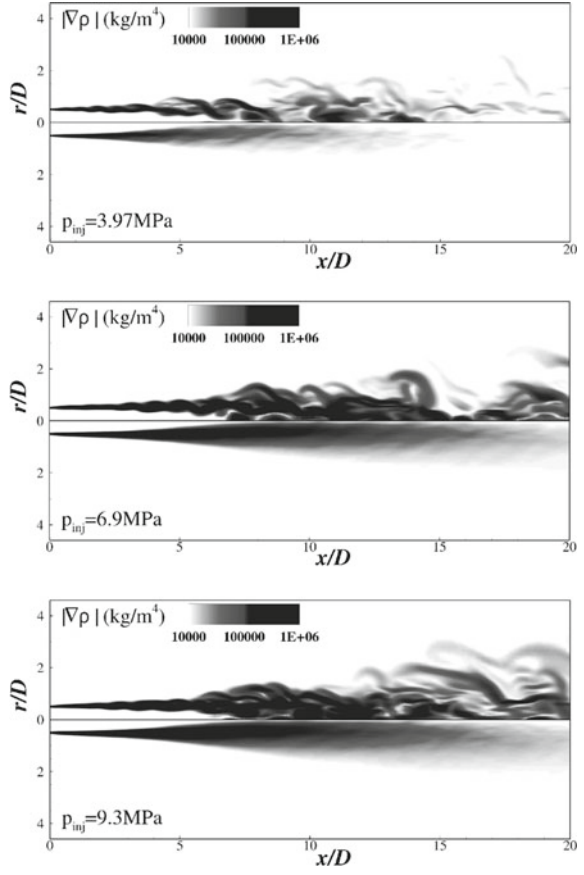
Fig. 8 Jet half-width distribution for different pressure conditions
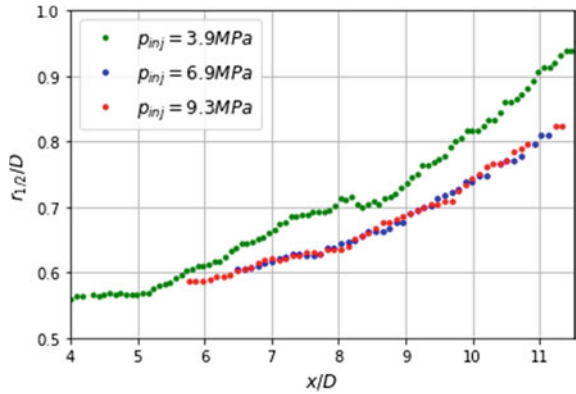
Fig. 9 Instantaneous (above) and mean (below) vorticity field for injection pressures 3.97 MPa (top), 6.9 MPa (middle), and 9.3 MPa (bottom)
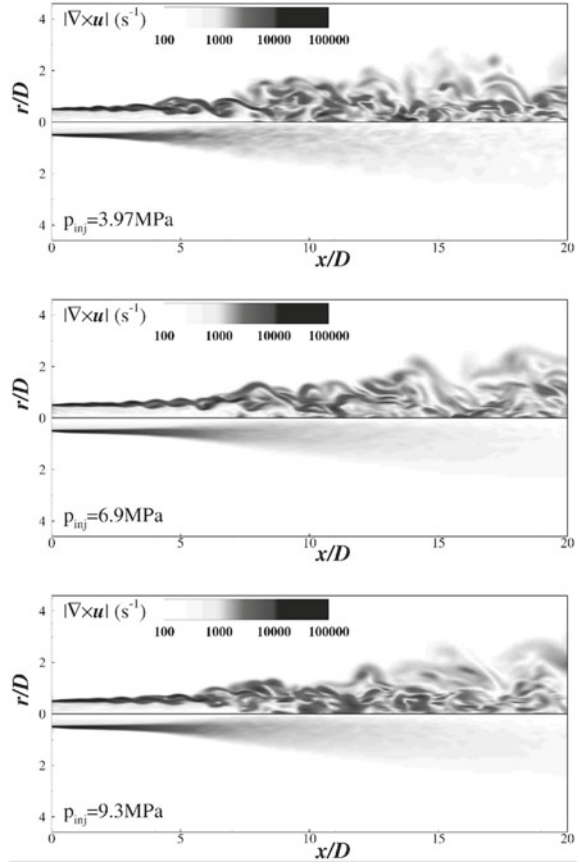
4 Conclusions

A numerical framework is developed using multiple computational models, to study supercritical injection and mixing behaviour. The base line case replicating experiments of Mayer et al. [12] has shown good agreement with experimental as well as with other numerical studies. In the next part of the study, which focused on effects of injection pressure, the following inferences can be drawn:

- With increase in injection pressure while in supercritical phase, the density gradient between jet and surrounding increases and then saturates. This can be justified by the fact that increasing pressure with temperature unchanged makes injection condition cross-pseudo-boiling line while pseudo-boiling itself weakens.
- Higher-density gradient eventually results in a so-called solid wall effect that reduces spreading rate of the jet and increases its core length to some extent.

The observations give an insight that rising injection pressure keeping temperature unchanged eventually reduces jet mixing up to some limit, and it is largely dependent on pseudo-boiling effects. However, effects of temperature might be opposite because of moving away from critical point. This requires further investigations to get a clearer idea.

References

1. Peng DY, Robinson DB (1976) A new two-constant equation of state. Ind Eng Chem Fundam 15(1):59–64
2. Soave G (1972) Equilibrium constants from a modified Redlich-Kwong equation of state. Chem Eng Sci 27(6):1197–1203
3. Müller H, Pfitzner M (2016) Large-eddy simulation of coaxial liquid nitrogen/gaseous hydrogen injection at trans- and supercritical conditions. J Propul Power 32(1)
4. Matheis J, Pfitzner M, Hickel S, Müller H, Niedermeier CA (2016) Large-eddy simulation of nitrogen injection at trans- and supercritical conditions. Phys Fluids 28(015102)
5. Mayer W, Tamura H (1996) Propellant injection in a liquid oxygen/gaseous hydrogen rocket engine. J Propul Power 12(6)
6. Oefelein JC (2006) Mixing and combustion of cryogenic oxygen-hydrogen shear-coaxial jet flames at supercritical pressure. Combust Sci Technol 178(1–3):229–252
7. Zong N, Yang V (2006) Cryogenic fluid jets and mixing layers in transcritical and supercritical environments. Combust Sci Technol 178(1–3):193–227
8. Cuenot B, Poinsot T, Schmitt T, Selle L (2009) Large-eddy simulation of transcritical flows. C. R. Mecanique 337:528–538
9. Bellan J, Miller RS, Harstad KG (2001) Direct numerical simulations of supercritical fluid mixing layers applied to heptane–nitrogen. J Fluid-Mech 436:1–39
10. Bellan J, Harstad KG, Miller RS (1997) Efficient high-pressure state equations. AIChE J 43(6):1605–1610
11. Lee LL, Chung TH, Ajlan M, Starling KE (1988) Generalized multiparameter correlation for nonpolar and polar fluid transport properties. Ind Eng Chem Res 27(4)
12. Branam R, Schneider G, Hussong J, Mayer W, Telaar J (2003) Raman measurements of cryogenic injection at supercritical pressure. Heat Mass Transf 39:709–719
13. Ruscic B, Burcat A (2001) Third millennium ideal gas and condensed phase thermochemical database for combustion. Technion-Israel Institute of Technology Haifa, Israel

Design of Rolling Road for Wind Tunnel Simulation

Anagh S. Bhanu, Manish K. Mathur, Murali R. Cholemari, and Srinivas V. Veeravalli

1 Introduction

Dust dispersion due to vehicular movement can generate particulate pollution. To understand the characteristics of dust dispersion, it is essential to analyse the wake formed behind a moving vehicle. Performing the experiments onsite might not yield good results due to uncontrollable conditions such as wind velocity, wind direction, traffic conditions, etc. These limitations due to uncontrollable environmental conditions can be eliminated by conducting experiments in the wind tunnel. In a relative reference, we can simulate the motion of the vehicle in a wind tunnel where the vehicle is at rest and the air moves around it. The oncoming flow with uniform velocity in the wind tunnel separates at the rear part of the vehicle due to the abrupt change in the vehicle geometry to form a recirculating region. This results in a velocity deficit behind the vehicle to form near and far wakes that extend many vehicle heights downstream [1].

In actual road conditions, the air can be assumed to be stationary, so the formation of the boundary layer is not a concern due to the absence of relative velocity between air and ground. But, in the case of the wind tunnel, the ground is fixed, and the air is moving through the tunnel. This stationary ground will cause the formation of a boundary layer due to the no-slip condition. The formation of the boundary layer at the test section of a wind tunnel is a larger concern for ground effect aerodynamic studies. Lots of previous research have shown that the boundary layer thus formed due to the stationary floor affects the flow field and the dispersion characteristics of road dust near the ground [2–5]. To replicate the actual road condition in the moving vehicle's frame of reference, the boundary layer's growth over the test section floor must be eliminated or mitigated. In addition, the vehicle's wheel rotation must be allowed to achieve exact flow conditions [6]. Wheel rotation has a substantial effect

A. S. Bhanu (✉) · M. K. Mathur · M. R. Cholemari · S. V. Veeravalli
Department of Applied Mechanics, IIT Delhi, New Delhi 110016, India
e-mail: amy217551@am.iitd.ac.in

on the flow, and in the case of particle dispersion, the motion of the wheel plays a very critical role. There are several methods available to avoid boundary layer formation. However, a ground surface moving with the velocity of wind tunnel-free stream can enable vehicle wheel rotation along with eliminating the boundary layer formation.

A rolling road can be considered a modification for the wind tunnel to provide a moving ground condition inside the test section [7]. It is similar to a conveyor belt system with a higher belt speed. The vehicle test model is kept on a flexible rolling road belt encircling driven and driving rollers. Automobile designers frequently use the rolling road to analyse the aerodynamic behaviour of their vehicles to predict how the vehicles will behave on the road. This paper intends to propose a design solution for the rolling road system able to fit the wind tunnel in the Gas Dynamics Lab at IIT Delhi, India, to further develop the capability to study the dispersion characteristics of vehicle wake by providing moving ground conditions to the test section floor of the tunnel. The general design process and design study of the rolling road system are discussed.

2   Methodology

The rolling road consists of a flexible belt stretched across the driver and driven pulleys mounted on a rigid support frame. The power required to run the system is provided by an AC induction motor connected to a driven shaft using a pulley belt drive. The vehicle model is kept on a backing plate above which the rolling road belt slides. Figures 1 and 2 show the illustration of vehicle model in the test section of the wind tunnel resting on the stationary and moving floor, respectively.

The velocity gradient on the stationary floor leads to the boundary layer formation which keeps on growing in the streamwise direction. A rolling road provides a moving surface that eliminates the velocity gradient and hence prevents the boundary layer formation which better simulates actual road conditions. The belt speed of the rolling road must be the same as that of the wind tunnel-free stream. In addition to this,

Fig. 1 Wind Tunnel Simulation with stationary ground
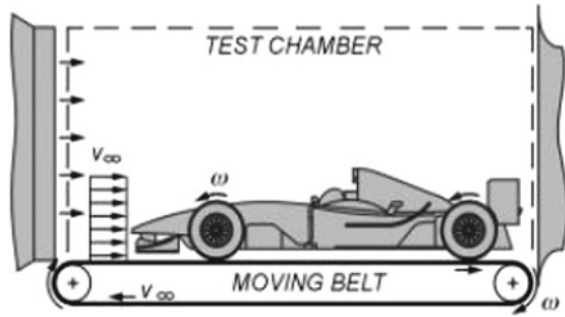
the amount of vibrations induced during the operation of the rolling road must be negligible. During the operation of the system, there is a chance for the rolling road belt to go on either side of the pulley, and there will be a reduction in the belt tension in the long run. Thus, the rolling road design must have provisions for aligning and tensioning the belt. The design of each component of the rolling road is discussed in the following subsections:

2.1 Design of Rolling Road Belt

A single belt rolling road configuration consists of a wide belt whose width is usually more than 1.5 times the width of the testing vehicle model. This belt configuration can cover the entire area below the under-body of the vehicle and the same belt can be used to test vehicle models of a wider range of wheelbase and tracks.

The rolling road belt is one of the most important elements in the system. The selection of belt material is majorly based on the surface finish of the belt and the cost. Steel belt is used in Windshear Rolling Wind Tunnel at Concord in North Carolina [8]. They have a very good surface finish but it is generally used with air-bearing supports which makes the design complicated and expensive. Fabric and polyester belts are generally used in the packaging industry which deals with very low belt speeds up to 1 m/s. They have very a poor surface finish which will induce vibrations in the system.

The rough surface that slides over the backing plate generates a lot of heat due to friction while operating at a speed of 10 m/s which causes premature belt failure. PVC belts are having a very good surface finish, and they are cheap when compared to other belt materials. They induce very less vibrations due to good surface finish and the friction force is also less due to low specific weight. The thickness of the rolling road belt is decided with the help of maximum principal stress failure criteria. Forces acting on the rolling road belt are shown in the free-body diagram of the belt sliding over the backing plate along the direction of wind velocity as shown in Fig. 3. Equations 1–4 are used to decide the thickness t_b of the belt according to failure theory.

Fig. 3 Free-body diagram of rolling road
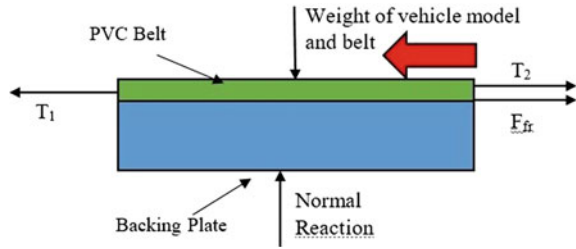
$$T_1 - T_2 = F_{fr} \tag{1}$$

$$\frac{T_1 - T_c}{T_2 - T_c} = e^{\mu\theta} \tag{2}$$

$$T_o = \frac{T_1 + T_2 + 2T_c}{2} \tag{3}$$

$$t_b = \frac{T_o \times FOS}{\sigma \times w}. \tag{4}$$

2.2 Design of Pulley

Rolling road consists of a drive pulley, a driven pulley, and an idler pulley. The rolling road belt forms a closed loop around these pulleys so that it can rotate continuously. The drive pulley is driven by a power transmission unit to propel the belt. For better traction, the drive pulley is usually lagged to avoid slipping of the belt. The driven pulley is located at the endpoint of belt conveyor. The idler pulley is used to provide the rolling road belt with a proper amount of tension by adjusting its position. The anatomy of a pulley is shown in Fig. 4.
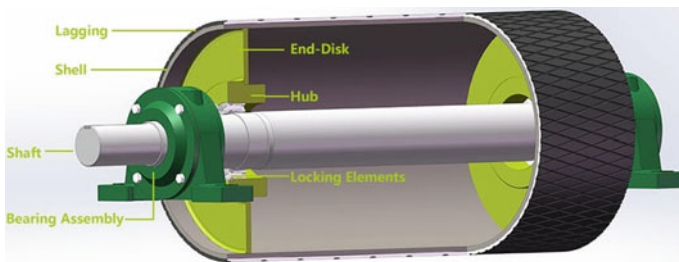
Fig. 4 Components of pulley

It consists of a shell that is in direct contact with the belt. Shell is generally made of a cold rolled sheet of steel or hollow steel tubing. The major share of the weight of rolling road is due to pulleys. The weight of the pulley is decided by the thickness of the shell. So the calculation of shell thickness has to be done precisely to avoid the rolling road becoming heavy. Shell thickness t of the pulley can be calculated using the Eqs. 5–8 given below [9].

$$F_n = 2T_o \sin\left(\frac{\theta_d}{2}\right) \tag{5}$$

$$BM = \frac{F_n \times l}{8} \tag{6}$$

$$Z_b = \frac{BM}{F_b} \tag{7}$$

$$t = \sqrt{\frac{6Z_b}{l}}. \tag{8}$$

Shafts are the rotating elements in the pulley which are designed to withstand all the applied forces from the belt and other components with minimum deflection. They are locked to the hubs of the end disc using locking elements. The shaft is supported on both sides by bearings, and it will be undergoing distributive load due to tension in the rolling road belt in the horizontal direction and the same due to the weight of the roller in the vertical direction. In addition to this, in the case of the driver pulley, there will be point load due to the tension of the belt from the drive unit. The diameter of the shafts is designed by using maximum shear stress failure theory considering all the forces mentioned above using Eqs. 9 and 10.

$$\tau_{max} = \frac{\sigma_y}{2 \times FOS} \tag{9}$$

$$\tau_{max} = \frac{16\sqrt{M^2 + T^2}}{\pi d^3}. \tag{10}$$

The circular disc at both ends of the pulley is called diaphragm plate. It is fabricated from thick steel plates which are welded into the shell at each end to strengthen the drum. These end plates are welded with hubs to accommodate the pulley shaft. The pulley is attached firmly to the shaft via end plates with the help of locking elements. The outer surface of the shell can be covered with rubberised material using vulcanisation. This process is called lagging, and it is usually used on driver pulleys. Lagging is necessary to improve the friction between the rolling road belt and pulley to improve the torque that can be transmitted through it.
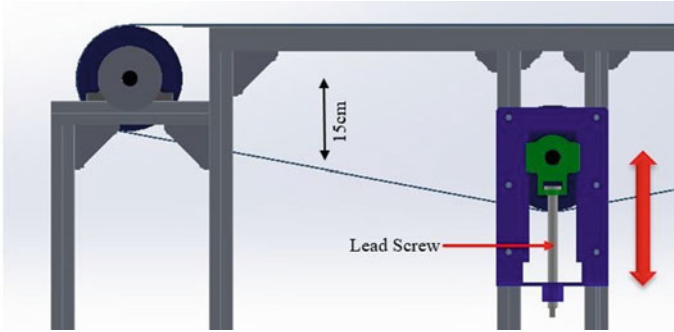
Fig. 5 Arrangement of idler pulley mounted on take-up bearing for tensioning

2.3 Tracking and Tensioning

PVC belt is the flexible element in the rolling road system. Over the period of usage, the belt will undergo permanent deformation due to the tension forces and temperature variations. These deformations cause a reduction in tension resulting in the slipping of the belt. Idler roller mounted on take-up bearing can be used to solve this issue. It can be displaced vertically by turning the lead screw of the take-up bearing as shown in Fig. 5. Tension in the belt can be adjusted by displacing the idler roller as mentioned above.

Though there is enough tension in the belt, it may move either side of the pulley at a higher belt speed. Crowning the drive pulley can be done to avoid the issue of slight misalignment. Severe tracking issues can be eliminated by placing one of the pulleys in an adjustable bearing so that it can be adjusted at the time of misalignment. In this design, the tail pulley is mounted on the pillow block bearing which can be moved along the frame. The driven pulley is adjusted in such a way that it is displaced from the side where the rolling road belt is moving to. This will correct the misalignment in the belt and the length between both sides of the belt is adjusted till the belt is centred.

2.4 Design of Backing Plate

The backing plate lies on top of the rolling road where the vehicle for conducting the experiments is placed. The rolling road belt will be sliding over the backing plate. The plate is subjected to point load due to the weight of the vehicle and a uniformly distributed load due to the weight of the belt. Further, it will undergo friction force in the area where the rolling road belt is sliding over. The plate should have enough flexural modulus so that the maximum deflection at the centre due to bending is in the acceptable range. The thickness of the backing plate has to be decided based on the maximum deflection, stress, and material cost. The minimum thickness for the
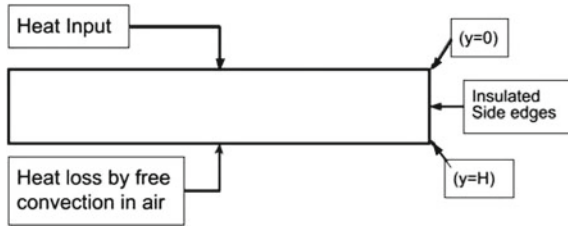
safe design can be obtained by conducting structural analysis on the backing plate using plate theory.

The surface of the backing plate must be extremely smooth so that the heat generated due to friction is minimum. A very high temperature on the backing plate can ruin the life of the rolling road belt. Temperature analysis of the backing the musts be conducted to check whether the maximum temperature formed in the backing plate is well below the working temperature of the belt. Assuming the temperature variation along the length and width is very small than that along the thickness; hence, this heat transfer problem can be reduced to a one-dimensional heat transfer problem as shown in Fig. 6, and the temperature variation along the thickness H can be determined using the Eq. 11 [10].

$$T(y) = Q_{in}\left(\frac{H - y}{k} + \frac{1}{h}\right) + T_\infty \tag{11}$$

where y is the distance along the thickness of the backing plate from the top surface.

The one-dimensional steady-state heat transfer simplification gives information regarding the parameters that affect the temperature along the thickness of the backing plate. To reduce the temperature at any point on the backing plate, the convective heat transfer coefficient h should be increased as much as possible, and thickness H must be reduced as much as reasonably possible.

2.5 Design of Support Frame

The rolling road consists of several components including heavy rotating rollers, a moving belt on the backing plate, and other tensioning and alignment features. The static and dynamic forces produced by all the stationary and moving components must be safely transmitted to the ground without generating any kind of vibrations in the system. The frame must have good strength to support the components, and at the same time, it should be lightweight. Structural analysis has to be carried out to check the maximum combined stress induced in the frame and the maximum deformation of the frame.

2.6 Design of Drive Unit

A motor driving unit has to be designed such that it can overcome all the resistive torque acting on the rolling road. The major share of the driving unit power is consumed by the rolling road belt while working against the friction force between the rolling road belt and the backing plate. In addition to this, the total moment of inertia of all the rotating components has to be considered to calculate the starting torque due to belt acceleration. The motor is designed in such a way that the maximum belt speed occurs at the rated motor shaft rotational speed. A suitable multiplication factor can be chosen to obtain the required belt velocity at the rated motor shaft speed as shown in Eq. 12. Equations 13 and 15 relate the minimum required power and torque required for the motor, calculated according to the rated motor shaft speed. Starting torque vanishes when the rolling road starts working continuously at a particular belt speed [10].

$$\text{Speed ratio} = \frac{\text{Belt}_{\text{speed}} \times 60}{2\pi r_{\text{driver}} \text{motor}_{\text{speed}}} \tag{12}$$

$$T_{\min} = \left(\frac{|F_{\text{fr}}| \text{speed ratio} \times r_{\text{drive}}}{\eta_{\text{drive}}} + I_{\text{drive}} \frac{\omega_{\text{f}} - \omega_{\text{s}}}{\Delta t} \right) \text{sf} \tag{13}$$

$$\omega = \frac{\text{belt}_{\text{speed}}}{r_{\text{drive}}} \tag{14}$$

$$P_{\min} = T_{\min} \frac{\omega}{\text{speed ratio}}. \tag{15}$$

3 Results and Discussion

The isometric view of the rolling road design is shown in Fig. 7. It can be accommodated in the rectangular area of 2 m long and 1 m wide inside the test section. The entire setup is 190 cm long, 99 cm wide and, 107 cm high. The backing plate where the model will be kept is having a dimension of 140×99 cm. Analysis of each component of the rolling road system is discussed in the following subsections.

3.1 Analysis of the Rolling Road Belt

The design of the rolling road belt was done very carefully by considering all the factors mentioned in the previous section. The single belt configuration was chosen for the belt layout in this design as it is flexible with model dimensions. By considering

Fig. 7 Isometric view of the
rolling road system

the costs and benefits of generally used belt materials, it was decided to use endless PVC belts for making the rolling road. Using the principal stress failure criteria, by considering all the forces mentioned in the free-body diagram given in Fig. 3, it was found that the 3-mm-thick 2ply PVC belt will be safe for extreme working conditions.

3.2 Analysis of the Pulleys

Three pulleys of a diameter of 20 cm made of mild steel are used for constructing the rolling road. Pulleys must be manufactured using CNC machines with utmost care to avoid the run out which can cause vibrations. Dynamic balancing has to be carried out on the pulley both along the circumference as well as axially. This is because the centre of mass of the pulleys will not lie on the axis of rotation of the pulleys which will give rise to unbalanced dynamics forces. Each of the pulleys is having a face width of 89 cm which was decided according to space constraints. Shell thickness of the pulleys is selected as 8.8 mm using Eq. 8 which gives an approximate weight of 100 kg for each pulley including other components. Carbon steel of 3 cm diameter is used to make the pulley shaft by considering all the forces mentioned in the previous section and using Eq. 10. The driver pulley is diamond lagged with 1-cm-thick vulcanised neoprene to improve the friction between the belt and pulley. The driven and drive pulleys are placed at a centre distance of 160, and the idler pulley is placed 15 cm vertically below the plane made by the other two pulley centres as shown in Fig. 5.
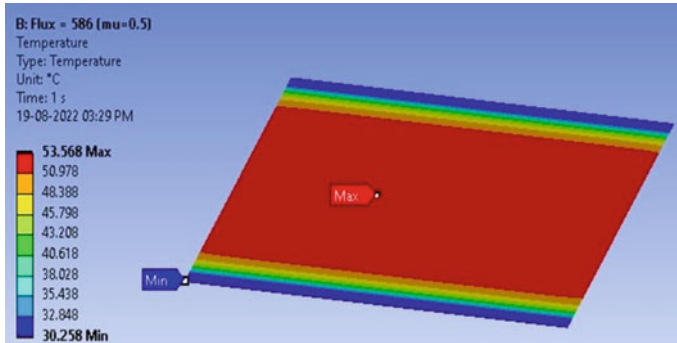
Fig. 8 Temperature distribution on the backing Plate

3.3   Thermal Analysis of the Backing Plate

The temperature generated due to the friction between the rolling road belt and the backing plate was analysed analytically using one-dimensional steady-state heat transfer approximation. This gave a result of maximum temperature of 53.56 °C at the top surface of the backing plate for an input heat flux of 586 W/m². The working temperature of the PVC belt is 80 °C which is well ahead of the analytical result that we have obtained. The analytical solution neglects the heat convection from the areas which are not covered by the belt and the lateral faces which would help to lower the temperature. A two-dimensional steady-state heat transfer analysis was conducted using the finite difference method in ANSYS Steady-State Thermal to determine the maximum temperature formed and compare it with the analytical results. The simulation results shown in Fig. 8 reveal that the maximum temperature formed on the backing plate is 53.54 °C, which is very close to the analytical result.

3.4   Static Structural Analysis of Backing Plate

An effort is put towards the designing of the backing plate where the rolling road belt slides over. Stress analysis was carried out to check whether the backing plate has enough flexural modulus so that it will not bend under the load of the vehicle model and the rolling road belt. Cold-rolled stainless-steel sheet with an area of 140 cm by length and 99 cm by width is used for the backing plate because of its improved surface finish and strength. The maximum deflection was determined using plate theory. The structural analysis result of the stainless-steel sheet shown in Fig. 9 suggests that a 3-mm-thick stainless-steel sheet will take all the load and the maximum deformation on it is 1.5 mm and a maximum bending principal stress of 35 MPa, which is well below the yield point.
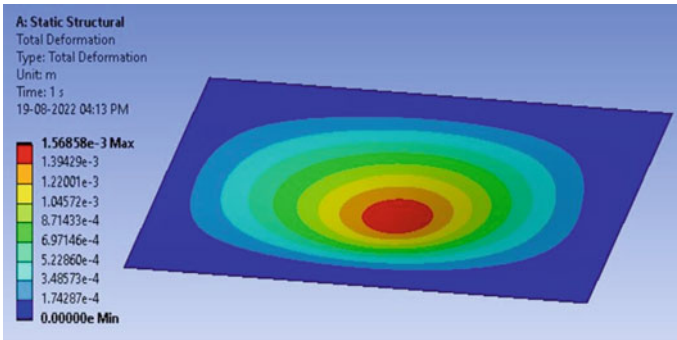
Fig. 9 Structural analysis of the backing plate

3.5 Static Analysis of the Frame

The entire components of the rolling road are mounted on the support frame which is made of an aluminium extrusion profile of modular dimension 4545 mm. Aluminium extrusion profile helps us to make highly structurally efficient members at a low cost. The entire skeleton of the frame which is shown in Fig. 10 can be easily assembled using these profiles. The aluminium profile joints are not permanent; instead, they are done with the help of hammer-head T-bolts and nuts. Static structural analysis of the support frame was conducted to test the safety of the frame which is undergoing loads due to the components of the rolling roads. Figure 11 shows the deformation at different locations of the support frame. The results show that under the loads, the frame undergoes maximum deflection of 0.2 mm and maximum direct stress of 1 MPa which is compressive.

Fig. 10 Isometric view of the frame
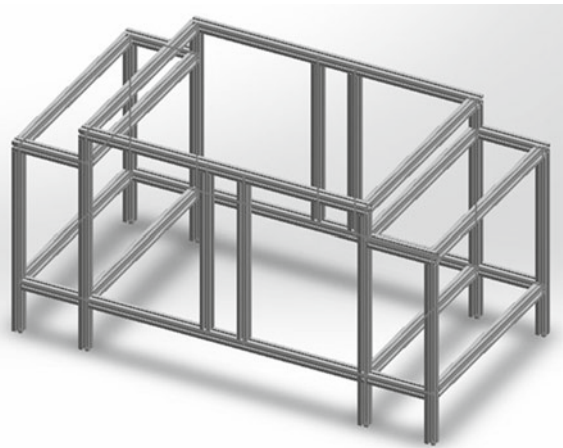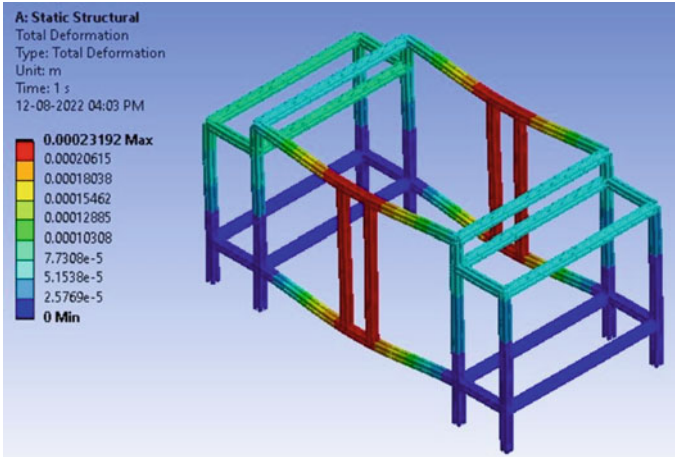
Fig. 11 Static structural analysis of the frame

3.6 Analysis of the Drive Unit

A three-phase AC induction motor is used for providing the power to run the rolling road system. The power from the motor shaft is transferred to the driver pulley of the rolling road with the help of a V-belt pulley system. The minimum torque and power of the motor are calculated using Eqs. 13 and 15 for a speed ratio of 0.95. The power and torque of the motor are calculated for a maximum belt speed of 10 m/s. From the calculation using Eqs. 12–15, the anticipated motor requires a power of 4 kW and 36 Nm torque at an RPM of 1000. A variable frequency drive is coupled with the motor to control the speed of the belt.

4 Conclusion

The specifications of the rolling road setup are given below.

- The rolling road is designed with a belt area of 160 × 89 cm.
- Rolling road belt is made using PVC belt with a the thickness of 3 mm.
- System consists of three pulleys made of mild steel with a diameter of 20 cm. The centre distance between the driven and drive pulley is 160 cm, and the idler pulley is used to provide belt tension
- Tracking and tensioning of the rolling road belt are done using the idler pulley and bearings.
- Rolling road belt slides over the backing plate made of stainless steel with 3 mm thickness.

- Maximum temperature formed on the backing plate is 53.56 °C which is well below the working temperature of the belt.
- Aluminium extrusion profile of modular dimension 45 × 45 mm is used to make the support frame. Static structural analysis shows that the frame undergoes a maximum deflection of 0.2 mm due to the forces.
- A three-phase AC induction motor of 4 kW power and 36 Nm torque at 1000 RPM coupled with a variable frequency drive can be used as the power source for running the system.

The design of rolling road to provide a moving ground surface in the environmental wind tunnel is presented. The ground surface moves with a velocity of the free stream to avoid the formation of the boundary layer and to enable vehicle wheel rotation. The maximum belt speed of 10 m/s is designed to simulate the actual road conditions inside the wind tunnel at Gas Dynamics Lab, IIT Delhi, India. Each component of the design was analysed for safe design in extreme working conditions.

Nomenclature

T_1, T_2	Tension in tight and slack side of belt (N)
T_c	Centrifugal tension of belt (N)
T_o	Initial tension of belt (N)
F_{fr}	Friction force (N)
σ_y	Yield stress (Pa)
w	Width of the belt (m)
μ	Coefficient of friction (–)
θ	Angle of wrap (rad)
BM	Bending moment on the belt (Nm)
l	Pulley face width (mm)
θ_d	Distortion angle (20°) (deg)
fb	Allowable pulley shear stress (Pa)
τ_{max}	Maximum shear stress (Pa)
M	Maximum bending moment on the shaft (Nm)
T	Maximum twisting moment on the shaft (Nm)
d	Diameter of the pulley (m)
r_{drive}	Radius of the driver pulley (m)
η_{drive}	Transmission efficiency (–)
I_{drive}	Moment of inertia of all rotating components (kg m^2)
P_{min}	Minimum motor power (W)
T_{min}	Minimum torque required at the motor (Nm)
ω_f, ω_s	Start and finish angular velocity of the pulley (rad/s)
Δt	Ramp time to accelerate belt speeds (s)
ω	Angular velocity corresponding to belt$_{speed}$ (rad/s)
$T(y)$	Temperature of the backing plate at y (°C)

k	Thermal conductivity of the backing plate (W/mk)
Q_{in}	Input heat flux due to friction (W/m^2)
T_∞	Ambient temperature (°C)

References

1. Li R (2017) Aerodynamic drag reduction of a square-back car model using linear genetic programming and physic-based control, Ph.D. thesis
2. Bearman PW, De Beer D, Hamidy E, Harvey JK (1988) The effect of a moving floor on wind-tunnel simulation of road vehicles. SAE Transactions, pp 200–214
3. Carpentieri M, Kumar P, Robins A (2012) Wind tunnel measurements for dispersion modelling of vehicle wakes. Atmos Environ 62:9–25
4. Hackett JE, Williams JE, Baker JB, Wallis SB (1987) On the influence of ground movement and wheel rotation in tests on modern car shapes. Tech. report, SAE Technical Paper
5. Strachan RK, Knowles K, Lawson NJ (2007) The vortex structure behind an ahmed reference model in the presence of a moving ground plane. Exp Fluids 42(5):659–669
6. Burgin K, Adey PC, Beatham JP (1986) Wind tunnel tests on road vehicle models using a moving belt simulation of ground effect. J Wind Eng Ind Aerodyn 22(2–3):227–236
7. Hucho W-H (1987) Chapter 11—wind tunnels for automobile aerodynamics. In: Hucho W-H (ed) Aerodynamics of road vehicles. Butterworth-Heinemann, pp 398–436
8. Walter J, Bordner J, Nelson B, Boram A (2012) The windshear rolling road wind tunnel. SAE Int J Passenger Cars Mech Syst 5:265–288
9. Mechanical Handling Engineers' Association (1977) Recommended practice for troughed belt conveyors. Mechanical Handling Engineers' Association
10. Edirisinghe R, Mayoral S (2019) On the mechanical design of the rolling road addition to the csuf wind tunnel. SAE Technical Paper Series

Entrainment Characteristics of a Swirling Liquid Jet

Toshan Lal Sahu, Ujjwal Chetan, Prabir Kumar Kar, Saurabh Dhopeshwar, Prasanta Kumar Das, and Rajaram Lakkaraju

1 Introduction

Swirling flow is one of the handfuls of problems in fluid dynamics that involves a wide range of applications in combustion chambers, cyclone separators [1], turbomachines, and nozzle design for spray and coating processes. Better fuel mixing and flame stability can be achieved by providing a swirl to the injected fluid in combustion chambers [2, 3]. Several predictive models and correlations have been reported to estimate the near-field entrainment characteristics [4–6]. Ricou and Spalding [7] investigated the entrainment in axisymmetrical turbulent jets and suggested the following empirical relation:

$$\frac{m}{m_0} = 0.32 \frac{x}{d_0} \left(\frac{\rho_a}{\rho_i} \right)^{\frac{1}{2}},$$

(1)

where m is the total mass flow rate at any cross-section, m_0 is the mass flow rate at the nozzle inlet, d_0 is the nozzle diameter, ρ_a is the density of the ambient fluid, and ρ_i is the density of the injected fluid. The experiments were performed for different combinations of gases having different densities. The authors suggested an entrainment coefficient of 0.32 for all the gases considered within some experimental error. Furthermore, Hill [8] explored the local entrainment rates in the initial developing region of the flow and suggested an entrainment coefficient ranging from 0 to nearly 0.3 in the developing region and 0.32 in the fully developed region.

T. L. Sahu (✉)
Advanced Technology Development Centre, IIT Kharagpur, Kharagpur 721302, India
e-mail: toshansahu.18@gmail.com

U. Chetan · S. Dhopeshwar · P. K. Das · R. Lakkaraju
Department of Mechanical Engineering, IIT Kharagpur, Kharagpur 721302, India

P. K. Kar
Department of Physics, IIT Kanpur, Kanpur 208016, India

Han and Mungal [9] performed direct measurements of entrainment in reacting and non-reacting turbulent jets, where authors explored the impact of flow speed, heat release, and buoyancy on the rate of entrainment and found good agreement with the entrainment coefficients suggested by Ricou and Spalding.

Furthermore, Post et al. [10] explored the near-field entrainment characteristics of gas jets and sprays under diesel conditions. The author compared the entrainment coefficients with some of the other significant works including [8, 11, 12]. In the region where the velocity profiles were self-similar, the entrainment coefficient fell under 10% error compared with entrainment coefficients obtained for other works. Recently, Hassan et al. [13] performed experiment on a free surface plunging jet for Reynolds numbers ranging from 3000 to 10,000 by using time-resolved PIV measurements and claimed that vortex pairing appears on the free surface of the plunging jet, which leads to early bulk entrainment of the fluid. Furthermore, the authors concluded that for a Reynolds number of $Re = 5004$, the entrainment coefficient was equal to 0.2 at a streamwise distance of three times of nozzle diameter, which kept on increasing at further downstream locations up to nine nozzle diameter with an entrainment coefficient of 0.72. Beyond $Re = 9000$, the entrainment rate and coefficient became invariant with the Reynolds number. This independency with the Reynolds number was also consistent with the conclusion made by Ricou and Spalding in which there was no increment in the mass entrainment beyond a Reynolds number $O \sim 25,000$.

Therefore, the present work is inspired to get rich information on the role of swirl strength on entrainment characteristics at moderate Reynolds number. We have carried out three-dimensional numerical simulations using the volume of fluid (VOF) method coupled with adaptive mesh refinement using the open-source code Gerris. Moreover, we have explored the shear layer between the liquid–air interface to see the region of maximum velocity fluctuations to trace the enhanced mixing region. Primarily, we have determined the mass flow rate along the streamwise direction to estimate the mass of air entrained. We have explained the governing differential equation and numerical setup in Sect. 2, entrainment of air and comparison with previous literature in Sect. 3. Finally, the conclusion and summary are presented in Sect. 4.

2 Numerical Methodology

2.1 Governing Differential Equations and Numerical Schemes

A schematic diagram representing the flow domain has been shown in Fig. 1 in which a liquid jet is injected into a quiescent gas phase. The computational domain has a dimension of $50\ D \times 10\ D \times 10\ D$, where D is the diameter of the nozzle from which fluid is emerging. At the entrance, we have applied a uniform injection

velocity U in the x-direction along with an angular velocity U_θ to give solid body rotation to the liquid. At the exit of the domain, we maintained the outflow boundary condition to avoid any reflectional information, i.e., the jet goes out of the domain without introducing any backward propagation. The remaining four walls have been considered solid walls with free slip boundary condition. The boundary walls are considered at a distance of five times the nozzle diameter. In the present study, we have two independent control parameters, namely the axial Reynolds number and swirl number which are characterized by Re and S, respectively. The axial Reynolds number is defined based on nozzle diameter D and the injection velocity U provided at the inlet. Therefore, the axial Reynolds number can be defined as:

$$Re = \frac{\rho_l U D}{\mu_l},\tag{2}$$

where μ_l is the dynamic viscosity of liquid, and ρ_l is the density of the liquid. D is the initial diameter of the jet at nozzle exit. Also, the swirl number has been defined as:

$$S = \frac{U_\theta}{U_i},\tag{3}$$

where $U_\theta = \Omega R$ is the azimuthal velocity applied to the initialized fluid at the nozzle exit, and R is the initial radius of the jet. The minimum length of the pipe for which a solid body rotation can be imparted to the rotating fluid has been prescribed equally
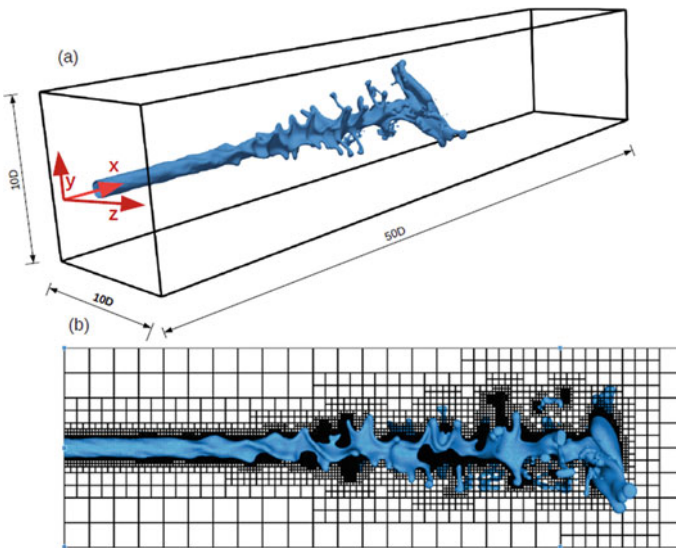
Fig. 1 (**a**) Computational domain with injected liquid at $Re = 50$ and $S = 0.5$ and (**b**) Adaptive mesh refinement (AMR) for a well-resolved interface

to 50 times the diameter of the pipe [14]. This difficulty is implicitly removed when a constant angular velocity Ω is applied at the inlet of the domain. Direct numerical simulations have been performed for the time-dependent, incompressible Navier–Stokes equation. A description of the discretization scheme and other computational methods can be found in [15]. The conservation equations for mass and momentum has been shown in Eqs. 4 and 5.

$$\nabla \cdot (u) = 0 \tag{4}$$

$$\rho \frac{Du}{Dt} = -\nabla p + \nabla \cdot (\mu(\nabla u + \nabla u^T)) + \sigma \kappa \delta_s \hat{n} + \rho g, \tag{5}$$

where $\mathbf{u} = (u, v, w)$ is the fluid velocity. σ is the surface tension coefficient acting at the interface between liquid and air. κ is the radius of curvature, δ_s is the Dirac delta function, and $\hat{n}$ is the outward normal vector to the liquid–air interface. The present study uses the VOF technique to track the interface between the swirling liquid and surrounding air. The volume fraction is represented by α in the volume fraction field transport equation as shown in Eq. 6.

$$\frac{\partial \alpha}{\partial t} + \nabla \cdot (u\alpha) = 0. \tag{6}$$

The surface force has been modeled using the continuum surface force (CSF) approach. The volume fraction field α is 1 when occupied by liquid and 0 when occupied by gas. Therefore, a modified form of density and viscosity is incorporated in the momentum conservation equation, which is given by Eq. 7 as shown below:

$$\rho(\alpha) = \rho_l \alpha + \rho_g (1 - \alpha)$$
$$\mu(\alpha) = \mu_l \alpha + \mu_g (1 - \alpha). \tag{7}$$

The subscripts 'l' and 'g' represent the liquid and gas phases, respectively. The numerical approximation applied for each term in the governing differential equation is second-order accurate in space and time. Octree discretization is employed to discretize spatially. The velocity advection terms have been discretized using the Bell–Colella–Glaz second-order unsplit upwind scheme, which is stable for CFL < 1. The surface tension term is computed using the combination of height function curvature estimation and balanced-force surface tension discretization. Also, adaptive mesh refinement (AMR) technique is applied to dynamically refine the mesh to capture the more delicate flow features at desired locations such as interface between liquid and air. AMR introduces finer meshes based on the vorticity threshold at the interface. The simulations have been carried out for the lower range of Reynolds numbers of $Re = 50$ and $Re = 100$ for five different swirl numbers.

Fig. 2 Variation of Undisturbed Contracted Length l_c with Swirl Parameter χ
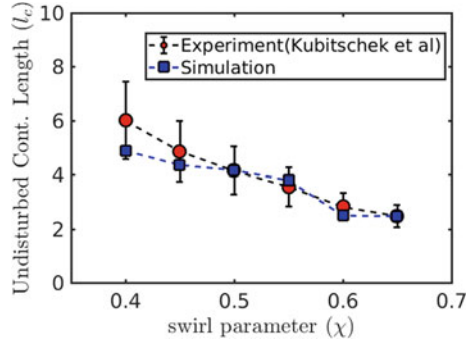
2.2 Validation

The code has been validated against the work of Kubitschek et al. [16]. The authors investigated the different helical modes which appear at the interface of a viscous rotating liquid jet. We have reproduced one of the results in Fig. 2 which shows the variation of undisturbed contracted length with varying Swirl number at a Reynolds number of $Re = 68$. The simulation results are in good agreement with the experimental results and falls under the error bar of experimental data.

3 Results and Discussion

3.1 Entrainment of Air

To explore the entrainment characteristics, we have focused on determining the mass flow rate perpendicular to the jet axis. Numerous measurements have been performed to estimate axial velocity profiles in previous literature under the assumption of self-similar velocity profiles and 2D flow fields. Therefore, we have performed three-dimensional numerical simulations to eliminate these two assumptions in calculating mass flow rate. Especially in the developing region of the flow, the assumption of self-similar velocity profiles leads to overprediction of mass flow rate at any streamwise location. Moreover, there is always uncertainty associated with defining the boundary in the spanwise or radial direction up to which the mass flow rate needs to be calculated. For example, Hassan et al. [13] defined the outer boundary at the location where the velocity drops to 5% of the centerline velocity. Furthermore, to accurately capture the interface, we employed the volume of fluid method with adaptive mesh refinement.

Thus, it was possible to calculate the mass flow rate of liquid and gas phases separately, corresponding to the volume fraction field of $\alpha = 1$ and $\alpha = 0$, respectively. In our study, the density difference between the injected liquid and the ambient fluid

is significant, $O \sim 800$, and therefore, a filtered interface is considered instead of a purely diffused interface. Therefore, at any streamwise location, the total mass flow rate is the sum of the individual mass flow rate of the injected liquid and ambient fluid. The mass entrained between axial stations x measured from the nozzle exit and x_0, which is the location of the entrance of the jet, is given by Eq. 8:

$$\overline{\dot{m}}_{\text{ent}} = \overline{\dot{m}}_x - \overline{\dot{m}}_0$$

$$\dot{m}_{\text{ent}} = \iint\limits_{S} \rho u(x, y, z) \mathrm{d}A - \iint\limits_{S} \rho u(x_0, y, z) \mathrm{d}A, \tag{8}$$

where y_1 and y_2 are the locations of boundaries in the spanwise direction. In the previous literature, entrainment of the ambient phase has been expressed using different terminologies, namely entrainment ratio, entrainment fraction, and entrainment rate interchangeably. Hereafter in, we shall use the term mass entrainment fraction Ψ, which is the ratio of mass entrained at any cross-section normalized by the mass injected at the inlet m_0 defined as:

$$\psi = \frac{\overline{\dot{m}}_x - \overline{\dot{m}}_0}{\overline{\dot{m}}_0}. \tag{9}$$

It can be inferred from Fig. 3a and b that the mass entrainment fraction Ψ does not increase monotonically for both the Reynolds number $Re = 50$ and $Re = 100$ at five different swirl numbers. At low swirl numbers of $S = 0.5$, the entrainment fraction is nearly 0.1 for a streamwise location of $x = 8\,D$, indicating that nearly 10% of the air is entrained. This can be explained with the help of the development and movement of toroidal recirculation zones in the ambient air with evolving time. For $S = 0.5$, the size of the recirculation zone is smaller than that of the recirculation zones observed for a higher swirl number of $S = 1.55$. At higher swirl numbers of $S = 1.55$, the entrainment fraction becomes of the order of 1, indicating that it has entrained mass equal to the initial mass injected nearly at a streamwise location of $5\,D$. Noticeably, the entrainment fraction for the Reynolds number of $Re = 50$ and $Re = 100$ consistently increases for swirl numbers of $S = 1.1$, $S = 1.3$ and $S = 1.55$ up to a streamwise location of nearly four jet diameters as the size and the strength of the recirculation zones grows with higher swirl numbers. Moreover, the accumulation of ambient air on the liquid–air interface can be observed through the instantaneous velocity vector field from animation 1, where the red and blue-colored velocity vectors represent the swirling liquid and ambient air, respectively (Fig. 4). Also, it can be inferred that, because of the development of the recirculation zones, the ambient air is subjected to a toroidal recirculation which tries to shear the liquid–air interface and get entrained inside the liquid vortex core. The isosurface of the concentrated x-vorticity layer can be observed in Fig. 5. It is to be noted that we have removed half of the portion of the isosurface to visualize the shear layers explicitly.
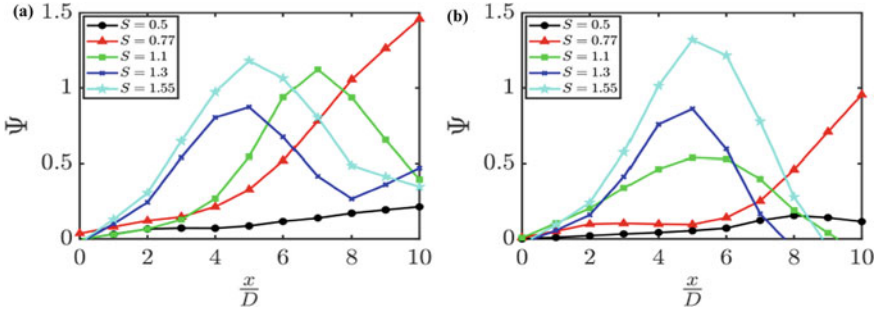
Fig. 3 Mass entrainment fraction for different swirl numbers **a** at $Re = 50$ and **b** at $Re = 100$
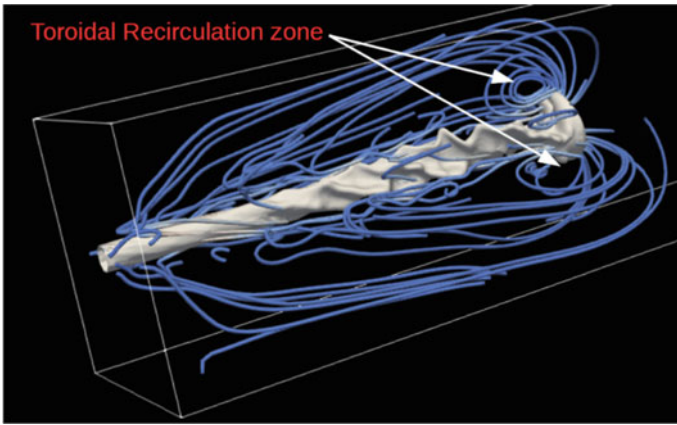
Fig. 4 Three-dimensional toroidal recirculation zones in the ambient fluid for $Re = 50$ and $S = 0.5$

Fig. 5 Shear layers represented by the iso-surfaces of x-vorticity
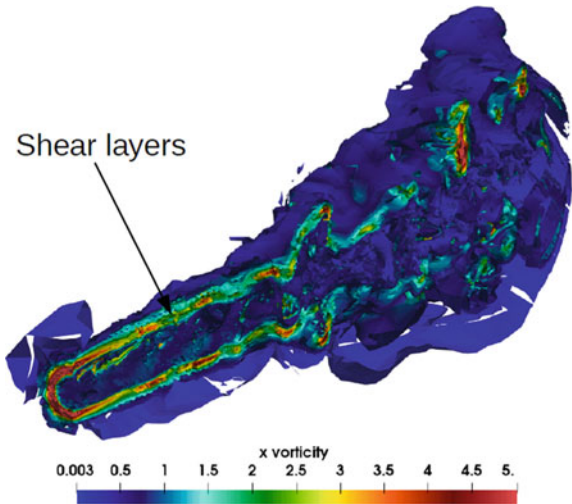
3.2   Calculation of Entrainment Coefficient

A few approaches were made in the previous studies to calculate the entrainment coefficient C_e. Here, we shall use the empirical relation derived by Ricou and Spalding based on their experiments [7]. It is to be noted that these empirical relations are the outcome of the dimensional analysis performed for entrainment in free turbulent jets. Although the experiments were initially performed for turbulent gaseous jets having constant entrainment coefficients, a more general form of the same empirical law can be used for studies involving two-phase jets. For example, Post et al. [10] used a more general form of the empirical expression initially derived by Ricou and Spalding to find the entrainment coefficient in the case of the gas jet and sprays, which is given by the equation below:

$$\frac{m}{m_0} = C_e \frac{x}{d_0} \left(\frac{\rho_a}{\rho_i} \right)^{\frac{1}{2}},$$

where C_e is the entrainment coefficient, ρ_i is the density of the injected fluid, and ρ_a is the density of the ambient fluid. This expression has a limitation that it can only be applied for flow having a constant entrainment coefficient. Therefore, it was necessary to arrive at an expression valid for varying entrainment coefficients.

Moreover, it can also be used for flows involving liquid and two-phase jets. The modified form of the expression applicable at any local streamwise location x is:

$$C_e(x) = \frac{d\overline{\dot{m}}_{ent}}{dx} \frac{d_0}{m_0} \left(\frac{\rho_i}{\rho_a} \right)^{\frac{1}{2}}. \tag{10}$$

Equation 10 has also been used for calculation of the entrainment coefficients in atomized liquid jets including some of the notable works as [17–19]. The entrainment coefficients based on this empirical law have been shown in Fig. 6 for Reynolds number of $Re = 50$ and $Re = 100$. We have observed that the entrainment coefficients do not follow a particular trend. In contrast, the entrainment coefficients lie in the range of 0–0.15, which is smaller than the entrainment coefficients predicted for free axisymmetric turbulent jets, which lie in the range of $0 < C_e < 0.32$.

3.3   Comparison of Entrainment Characteristics with Previous Literature

- Comparison with Turbulent Swirling Jets

Figure 7a shows the comparison of mass entrainment fraction Ψ for two different swirl numbers of 1.1 and 1.3 with some of the notable work in the field of swirling liquid jets. We have chosen these two swirl numbers based on the entrainment studies
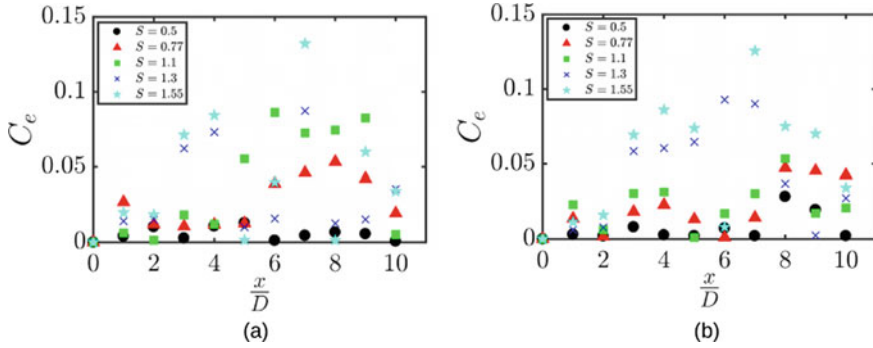
Fig. 6 Local entrainment coefficients C_e with five different swirl numbers for **a** $Re = 50$ and **b** $Re = 100$

available in the previous literature. Park and Shin [20] explored the entrainment characteristics of free swirling jets through schlieren flow visualization. The authors concluded that the entrainment fraction increases with the swirl intensities along the streamwise direction. Moreover, Cozzi et al. [21] explored the impact of swirl strength on the air entrainment characteristics using a model burner to explore the mixing process at Reynolds number of $Re = 21{,}800$. Since most practical applications involving higher entrainment and mixing, such as combustion chambers, operate at $Re \sim 20{,}000$, entrainment and mixing characteristics have been studied for a higher range of Reynolds numbers. It may seem improper to compare the entrainment characteristics of swirling liquid jets having a significant difference in their Reynolds number; however, entrainment studies at moderate Reynolds numbers with higher swirl intensities are limited. Despite a significant difference in the Reynolds numbers, the provision of swirl at a moderate Reynolds number can enhance entrainment characteristics. It can be inferred from Fig. 7a that, up to a distance of five times the nozzle diameter, the rate of entrainment is much lower of the order of one-fourth of the entrainment coefficient obtained by Park and Shin [20, 21] for a similar range of swirl numbers $S = 1.1$ and $S = 1.3$. However, for higher swirl strength of $S = 1.55$, even for $Re = 50$, the entrainment rate becomes comparable with the works by Park and Shin at a distance of nearly 10 nozzle diameters.

- **Comparison with Non-Swirling Free Turbulent Jets and Plunging Jets**

As per the previous studies performed, entrainment and mixing phenomena in non-swirling free turbulent jets and plunging jets have been widely investigated where the entrainment characteristics have been expressed in terms of entrainment coefficient C_e. An exhaustive comparison of the previous literature with present work has been shown in Fig. 7b.

One of the pioneering works in the field of axisymmetric gas jets was performed by Recou and Spalding, and the authors suggested that an entrainment coefficient was
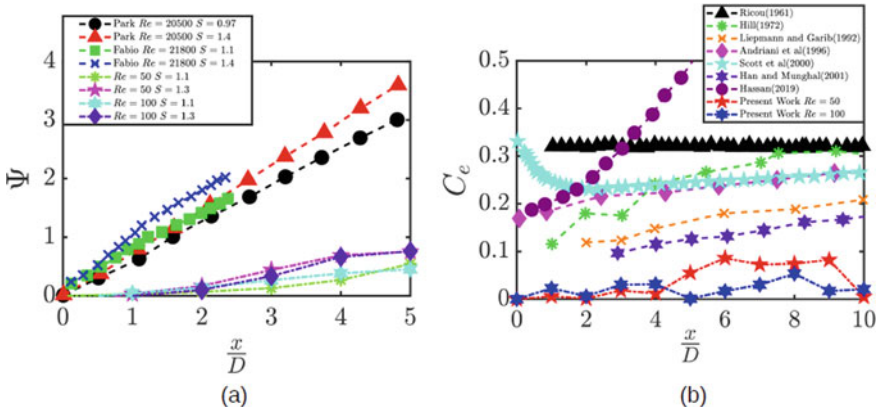
Fig. 7 Comparison of entrainment with previous works: (**a**) Entrainment fraction (Ψ) obtained for turbulent swirling jets, (**b**) entrainment coefficient, (C_e) for non-swirling free turbulent jets

0.32 in the far-field region from the nozzle where the flow was fully developed. Later, Hill [8] explored the entrainment coefficient in the initial region of the axisymmetric turbulent air jet and suggested entrainment coefficients that varied from 0.1 to 0.3 in the developing region and became 0.32 in the fully developed region. Recently, Hassan et al. [13] experimented on a water jet plunging into a quiescent pool of liquid with a free surface. The authors claimed that the entrainment coefficient varied from 0.2 to 0.72 for Reynolds numbers ranging from 5004 to 10,628. Furthermore, entrainment coefficients in some of the other significant works have been shown in Fig. 7. It can be concluded that the entrainment coefficient for $Re = 50$ and $Re = 100$ lies in the range of 0–0.15, which is smaller than the entrainment coefficient generally observed for free turbulent axisymmetric jets and plunging jets.

4 Conclusion

We have explored the entrainment characteristics and development of recirculation zones in a swirling liquid jet using high-fidelity 3D numerical simulations coupled with the VOF technique. The study includes two dimensionless parameters, namely swirl number which varies from $S = 0.5$ to $S = 1.55$ and Reynolds number of $Re = 50$ and $Re = 100$. A systematic study is done through simulations to see the impact of increasing swirl number on the mass of air entrained inside the liquid vortex core. For all ranges of control parameters, we have observed the existence of recirculation zones as one of the prominent features. The recirculation has been traced through streamlines, which attain the shape of a toroid with evolving time. Furthermore, the entrainment fraction consistently increases up to a distance of nearly 5D for all the five swirl numbers for both the Reynolds number of $Re = 50$ and $Re = 100$. At the liquid–air interface, the shearing effect of the recirculation enhances the

entrainment of air inside the bulk liquid core. The entrainment coefficient C_e varied from 0 to 0.15 for the considered range of Reynolds number and swirl number. Also, the entrainment coefficients predicted in the present work are much smaller than the previous coefficients observed for free axisymmetric turbulent jets and plunging jets.

Further research work can be carried out to explore the entrainment characteristics of turbulent swirling jets at high Reynolds numbers. Also, research work is indeed requested from the scientific community to understand the entrainment characteristics, specifically in reacting flows in diesel combustion chambers.

Nomenclature

A	Volume fraction field
C_e	Entrainment coefficient
CFL	Courant–Friedrichs–Lewy criteria
D	Initial diameter of the jet
G	Acceleration due to gravity
κ	Curvature of the interface
m_0	Mass flow rate at the inlet
m_x	Mass flow rate at any axial location 'x'
Re	Reynolds number
ρ_1	Density of liquid
ρ_g	Density of gas
S	Swirl number
Ψ	Entrainment fraction
μ_1	Dynamic viscosity of liquid
μ_g	Dynamic viscosity of gas

References

1. Hoekstra AJ, Derksen JJ, Van Den Akker HEA (1999) An experimental and numerical study of turbulent swirling flow in gas cyclones. Chem Eng Sci 54(13–14):2055–2065. https://doi.org/10.1016/S0009-2509(98)00373-X
2. Syred N, Chigier NA, Beér JM (1971) Flame stabilization in recirculation zones of jets with swirl. Symp Combust 13(1):617–624. https://doi.org/10.1016/S0082-0784(71)80063-2
3. Chen RH, Driscoll JF (1989) The role of the recirculation vortex in improving fuel-air mixing within swirling flames. Symp Combust 22(1):531–540. https://doi.org/10.1016/S0082-0784(89)80060-8
4. Kiger KT, Duncan JH (2011) Air-entrainment mechanisms in plunging jets and breaking waves. Annu Rev Fluid Mech 44:563–596. https://doi.org/10.1146/annurev-fluid-122109-160724

5. Ma J, Oberai AA, Drew DA, Lahey RT, Moraga FJ (2010) A quantitative sub-grid air entrainment model for bubbly flows—plunging jets. Comput Fluids 39(1):77–86. https://doi.org/10.1016/j.compfluid.2009.07.004

6. Harby K, Chiva S, Muñoz-Cobo JL (2014) An experimental study on bubble entrainment and flow characteristics of vertical plunging water jets. Exp Therm Fluid Sci 57:207–220. https://doi.org/10.1016/j.expthermflusci.2014.04.004

7. Ricou FP, Spalding DB (1961) Measurements of entrainment by axisymmetrical turbulent jets. J Fluid Mech 11(1):21–32. https://doi.org/10.1017/S0022112061000834

8. Hill BJ (1972) Measurement of local entrainment rate in the initial region of axisymmetric turbulent air jets. J Fluid Mech 51(4):773–779. https://doi.org/10.1017/S0022112072001351

9. Han D, Mungal MG (2001) Direct measurement of entrainment in reacting/nonreacting turbulent jets. Combust Flame 124(3):370–386. https://doi.org/10.1016/S0010-2180(00)00211-X

10. Post S, Iyer V, Abraham J (2000) A study of near-field entrainment in gas jets and sprays under diesel conditions. J Fluids Eng Trans ASME 122(2):385–395. https://doi.org/10.1115/1.483268

11. Liepmann D, Gharib M (1992) The role of streamwise vorticity in the near-field entrainment of round jets. J Fluid Mech 245:643–668. https://doi.org/10.1017/S0022112092000612

12. Crow SC, Champagne FH (1971) Orderly structure in jet turbulence. J Fluid Mech 48(3):547–591. https://doi.org/10.1017/S0022112071001745

13. Hassan SH, Guo T, Vlachos PP (2019) Flow field evolution and entrainment in a free surface plunging jet. Phys Rev Fluids 4(10):1–17. https://doi.org/10.1103/PhysRevFluids.4.104603

14. Pedley TJ (1969) On the instability of viscous flow in a rapidly rotating pipe. J Fluid Mech 35(1):97–115. https://doi.org/10.1017/S002211206900098X

15. Popinet S (2003) Gerris: A tree-based adaptive solver for the incompressible Euler equations in complex geometries. J Comput Phys 190(2):572–600. https://doi.org/10.1016/S0021-9991(03)00298-5

16. Kubitschek PJ, Weidman DP (2007) Helical instability of a rotating viscous liquid jet. Phys Fluids 19(11). https://doi.org/10.1063/1.2800371

17. Cossali GE (2001) An integral model for gas entrainment into full cone sprays. J Fluid Mech 439:353–366. https://doi.org/10.1017/S0022112001004591

18. Lee TW, Faeth GM (1992) Structure and mixing properties of combusting monopropellant sprays. J Propuls Power 8(2):271–279. https://doi.org/10.2514/3.23474

19. Al Rabadi S, Friedel L, Surma R (2007) Prediction of droplet velocities and rain out in horizontal isothermal free jet flows of air and viscous liquid in stagnant ambient air. Chem Eng Technol 30(11):1546–1563. https://doi.org/10.1002/ceat.200700221

20. Park SH, Shin HD (1993) Measurements of entrainment characteristics of swirling jets. Int J Heat Mass Transf 36(16):4009–4018. https://doi.org/10.1016/0017-9310(93)90151-U

21. Cozzi F, Coghe A, Sharma R (2018) Analysis of local entrainment rate in the initial region of isothermal free swirling jets by Stereo PIV. Exp Therm Fluid Sci 94(January):281–294. https://doi.org/10.1016/j.expthermflusci.2018.01.013

Effect of Damping on Bifurcation and Synchronization Behavior of an Aeroelastic System Under Dynamic Stall

Sourabh Kumar, Dheeraj Tripathi, Ankit Gupta, and J. Venkatramani

1 Introduction

Fluid force interaction on an elastic structure causes various phenomena such as flutter, divergence, and limit cycle oscillations. When nonlinearity enters the system due to substantial deformation, flow separation, friction, etc., elastic structures are known to display unexpected dynamic behavior and the linear theory fails to predict these behaviors. Such behaviors may give rise to aeroelastic instability like stall flutter due to the nonlinearity in the aerodynamic forces and lead to large amplitude limit cycle oscillations (LCOs) [1].

One of the interesting and important aspects of the stability theory of aeroelastic systems is structural damping. Several studies show the effect of structural damping on flutter boundaries of the aeroelastic systems [2–4]. Structural systems exhibit a hardening hysteresis behavior under cyclic loading, and this behavior provides a major contribution to the overall damping within the structure [2]. Lee et al. [2] show that a reasonably large amount of structural damping can eliminate the chaotic motion of the airfoil under Freeplay and preload conditions. Most of these studies consider the linear theory for calculating the aerodynamic loads on the structure except for a few [5]. However, the role of damping on complex nonlinear regimes dominated by vortex shedding and flow separation, and it is in-depth physical explanation is missing in the existing literature. Since damping has the potential to alter stability characteristics and even the phase values of the responses, shifting attention to the response dynamics via synchronization was undertaken recently. Indeed, Raaj et al. [6] and Vishal et al. [7] numerically investigated the responses of aeroelastic system experiencing classical flutter and stall flutter, respectively. They showed that frequency coalescence occurs in a nonlinear aeroelastic system through a frequency

S. Kumar · D. Tripathi · A. Gupta · J. Venkatramani (✉)
Department of Mechanical Engineering, Shiv Nadar IoE, Gautam Buddha Nagar,
Uttar Pradesh 201314, India
e-mail: j.venkatramani@snu.edu.in

locking mechanism if the nonlinearity is structural and through a suppression of natural dynamics mechanism if the nonlinearity is aerodynamic. Additionally, they demonstrate various synchronization routes and PLVs as the indicator of classical and stall flutter oscillations in aeroelastic systems. An experimental study by Tripathi et al. [8] demonstrated various synchronization dynamics namely phase trapping, phase slips, phase flip, etc. for an airfoil exhibiting stall flutter. However, it is worth mentioning that none of the above studies considers the effect of damping on the synchronization of pitch and plunge modes. It is thus important to understand the role of synchronization under dynamic stall conditions upon the inclusion of the damping effects in the aeroelastic system, which is the focus of the present study. The present study focuses on numerically investigating the stall-induced responses of a pitch-plunge aeroelastic system with different structural damping values. The aerodynamic loads on the aeroelastic system are determined using the LB model. The aeroelastic responses of the system are monitored with flow speed as the bifurcation parameter. Subsequently, the synchronization theory is used to explore the coupled interaction between the pitch and plunge modes at various dynamical regimes. The fundamental synchronization features are described through a quantitative measure called phase-locking value (PLV), which is derived from the instantaneous phases of the pitch and plunge modes.

The rest of the paper is structured as follows. The mathematical representation of the aeroelastic system and the accompanying aerodynamic forces is presented in Sect. 2. Section 3 presents the bifurcation behavior, synchronization characteristics, and the corresponding discussions. In Sect. 4, the key findings of this investigation are summarized.

2 Methodology

For the present study, a 2DoF (degree of freedom) aeroelastic system is taken into consideration that exhibits pitch (α) and plunge (ξ) motion through torsional and translational springs, respectively. The aeroelastic equations of motion are [2]:

$$\xi'' + x_\alpha \alpha'' + \frac{2\zeta_\xi \omega}{U}\xi' + \left(\frac{\omega}{U}\right)^2 \xi = \frac{-1}{\pi\mu}C_L(\tau) \tag{1}$$

$$\frac{x_\alpha}{r_\alpha^2}\xi'' + \alpha'' + \frac{2\zeta_\alpha}{U}\alpha' + \frac{1}{U^2}\alpha = \frac{2}{\pi\mu r_\alpha^2}C_M(\tau) \tag{2}$$

Here, ξ is the non-dimensional plunge displacement. The center of mass location is at a distance $x_\alpha b$ along the chord from the elastic axis, where b is the semi-chord length. The other parameters are the ratio of natural frequencies in plunge and pitch (ω), the non-dimensional airspeed (U), airfoil to air mass ratio (μ), and the airfoil radius of gyration r_α, respectively. The coefficients of lift and the pitching moment about the quarter chord of an airfoil are denoted by the symbols C_L and C_M, respectively.

These are modeled as unsteady aerodynamic loads and are obtained from the LB model formulation [9].

The aerodynamic loads in the LB model formulation consist of three components, (i) unsteady attached flow component, (ii) trailing edge separation component, and (iii) vortex shedding component. The aerodynamic loads are obtained individually in each module representing different phases of fluid–structure interaction, and subsequently, the total air loads are calculated by the sum of these components. In order to obtain the aeroelastic responses, the LB model is taken in its state space form (akin to [10]), which has 12 aerodynamic states. The first eight states are used to model the unsteady attached flow module, and the rest four are for flow separation (trailing edge separation and vortex shedding modules). These states are combined with four structural states representing pitch–plunge displacements and their derivatives. Finally, the state vector $x = [x1, x2,…, x16]^T$ is obtained by solving the set of first-order ordinary differential equations $x' = f(x, \hat{\alpha}, q)$, where $\hat{\alpha}$ and q represent the effective angle of incidence and the effective pitch rate, respectively. More details of the LB model can be found in the earlier studies by our co-workers [7, 10].

The synchronization analysis between the pitch and plunge modes is carried out via an analytical signal approach in which, the analytic signal, $\zeta(t) = x(t) + ix_H$ $(t) = A(t)e^{i\phi(t)}$, is a complex quantity. Here, $x(t)$ is the original signal, and $x_H(t)$ is its corresponding Hilbert transform (HT). The terms, $\phi(t)$ and $A(t)$, represent the instantaneous phase and the instantaneous amplitude, respectively. A quantitative value called PLV is obtained from the phase difference (ϕ) of the plunge and pitch modes. A PLV value nearby 1 represents a perfect synchronization while that close to zero represents perfectly asynchronous behavior. A detailed description of the synchronization theory can be found in our previous studies [6–8].

3   Results and Discussion

The state space formulation is solved using the Runge–Kutta algorithm. The structural parameters for the study are same as [11] except the ζ_ξ and ζ_α values and are given in Table 1.

The pitch and plunge responses are obtained, by systematically increasing U from 5 to 7. For different pitch and plunge damping values, the bifurcation behavior and corresponding dynamical regimes are first demonstrated. Next, synchronization measures such as PLV and relative phases between the pitch and plunge modes are used to identify synchrony at various damping values.

Table 1 Structural parameters for the present study

ϖ	μ	r_α	x_α	b
0.2	100	0.5	0.25	0.305

3.1 Effect of Damping on Bifurcation

In this section, we will discuss the impact of various ζ_ξ and ζ_α values on the bifurcation behavior and flutter boundary of the nonlinear aeroelastic system under consideration. First, we analyze the zero damping ($\zeta_\xi = 0$, $\zeta_\alpha = 0$) case (Fig. 1a) and compare the results from the existing literature [7], followed by a detailed analysis of the dynamic responses that are altered as a result of damping. In the case of zero damping, flutter speed (U_{cr}) is 5.7 as shown in Fig. 1a. Additionally, it can be seen from the time history of pitch and plunge motion in Fig. 2a–d that LCOs begin at $U = 5.7$ (Fig. 2a) and transform into aperiodic responses at $U = 5.9$. The x_9 (normal load) versus x_{10} (flow separation) phase plots shown in Fig. 3a–d sequentially show that the commencement of aperiodicity coincides with the first instance of a deep dynamic stall event. Note that, the stall flutter phenomena is defined by the discontinuous boundaries that are present in the LB model, for instance, when x_9 exceeds a critical value (stall onset) and $x_{10} = 0.7$ (separated flow). More information about these limits is found in our previous study [10]. As can be seen in Fig. 3a, the flow is only partially detached at $U = 5.8$ because the x_9 and x_{10} values on one side cross the discontinuity limits. The dynamics is fluctuating between deep and light dynamic stall events (see Fig. 3b and c). At $U = 6.6$, the dynamics completely enter a deep stall regime (see Fig. 3d), and the response of the system begins to become periodic, marking the beginnings of stall flutter LCOs (see Fig. 2d). These results are similar to that reported in [7] and serve as the benchmark for further analysis.

Next, the effect of plunge damping on the nonlinear aeroelastic system's bifurcation behavior and flutter boundary is investigated. Since the ζ_ξ value is increased from 0 to 0.2, the (U_{cr}) remains constant (see Fig. 1c and f). In this situation, deep stall flutter LCOs occur earlier when U approaches 6.2 (see Fig. 2d), but the onset of LCOs and their transition into aperiodic responses are basically the same as in
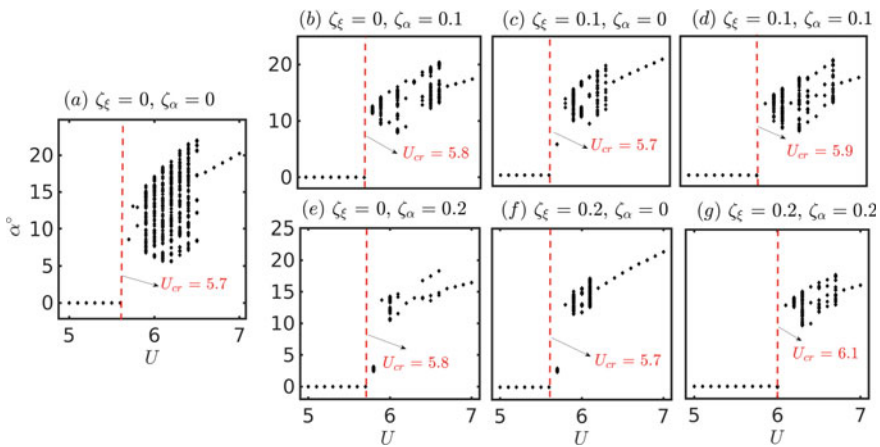
Fig. 1 Bifurcation diagrams with different values of ζ_ξ and ζ_α
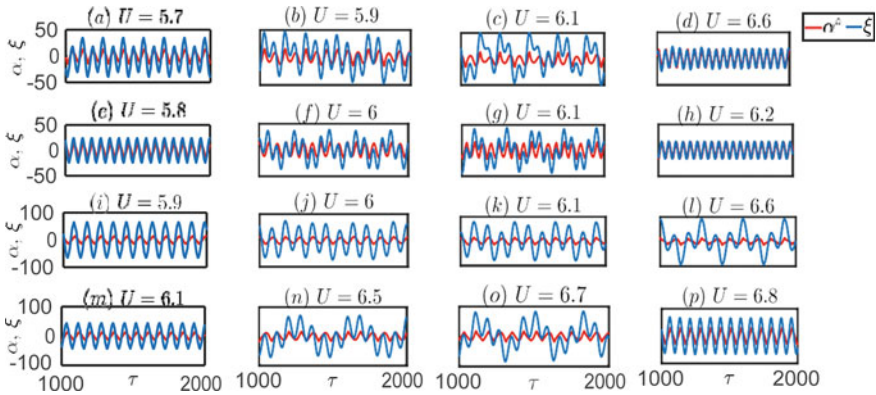
Fig. 2 Overlapped pitch and plunge dynamic responses for: **a–d** $\zeta_\xi = 0$, $\zeta_\alpha = 0$; **e–h** $\zeta_\xi = 0.2$, $\zeta_\alpha = 0$; **i–l** $\zeta_\xi = 0$, $\zeta_\alpha = 0.2$; and **m–p** $\zeta_\xi = 0.2$, $\zeta_\alpha = 0.2$
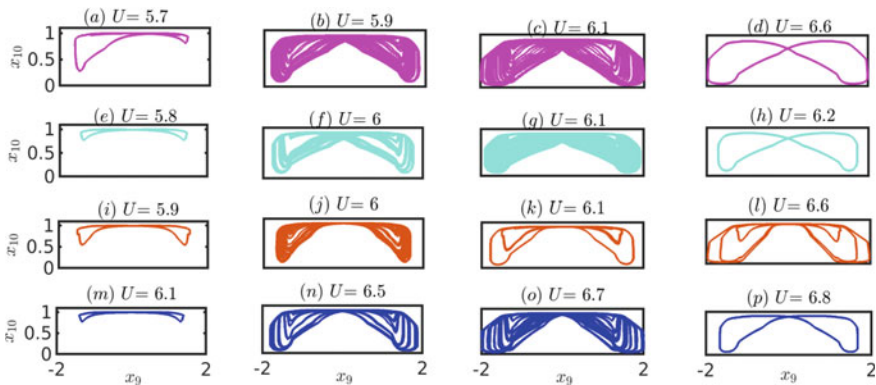
Fig. 3 x_9 versus x_{10} phase plots for: **a–d** $\zeta_\xi = 0$, $\zeta_\alpha = 0$; **e–h** $\zeta_\xi = 0.2$, $\zeta_\alpha = 0$; **i–l** $\zeta_\xi = 0$, $\zeta_\alpha = 0.2$; and **m–p** $\zeta_\xi = 0.2$, $\zeta_\alpha = 0.2$

the zero damping case. According to the accompanying x_9 and x_{10} phase plots, the dynamics reach a deep stall zone (see Fig. 3h). The overall result of increasing plunge damping value is a narrowing of the aperiodic regime and an earlier occurrence of the deep stall flutter event.

Now, we analyzed the effects of ζ_α on the responses of a nonlinear aeroelastic system. It is important to note that, in contrast to the system with zero damping, the bifurcation point has moved to a higher $(U_{cr}) = 5.8$ as we increase the value of $\zeta_\alpha = 0$–0.2 (see Fig. 1b and e). Their corresponding time histories of pitch and plunge motion are shown in Fig. 2i–l. Additionally, it is seen that the deep stall event is delayed to $U = 6.8$ as opposed to $U = 6.6$ in the case of a system with zero damping (see to Fig. 3i–l).

In the final case, we increase both ζ_ξ and ζ_α values to 0-0.2, which caused the (U_{cr}) to postpone from 5.7 to 6.1 (see Fig. 1g). Similar to what we observed in the prior scenario, the commencement of the deep stall event is seen to be delayed until $U = 6.8$ (see Fig. 3m–p).

The results thus far clearly demonstrate that the presence of structural damping in the system affects the system's response behavior and the speed at which stall flutter first appears. The change in dynamic responses, flow separation, and vortex shedding regimes leads the authors to further examine the underlying physical mechanism of such transitions. In the next section, we will discuss the same from a synchronization framework.

3.2 Synchronization Study

This section presents the effect of plunge and pitch damping on the synchronization characteristics of the two modes. To that end, the plot of the PLV with different values of damping under dynamic stall conditions is shown in Figs. 4, 5, and 6. Additionally, the $\Delta\phi$ time variation is also shown in Fig. 7 to visualize the synchronization dynamics qualitatively, albeit selected cases are shown for the sake of brevity.

In the case of zero damping ($\zeta_\xi = 0, \zeta_\alpha = 0$), PLV is 0.99 at $U = 5.8$ (Fig. 4). Note that, while we show the PLV variation from $U = 5.8-7$, the PLV is close to 1 at $U = 5.7$ as well. The phase difference is oscillating but bounded representing synchrony between pitch and plunge modes (see Fig. 7a). Upon increasing the speed, PLV

Fig. 4 Variation of the PLV with flow speed for $\zeta_\xi = 0$–0.2 and $\zeta_\alpha = 0$
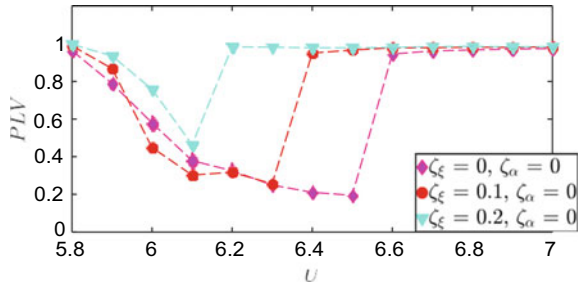
Fig. 5 Variation of the PLV with flow speed for $\zeta_\xi = 0$ and $\zeta_\alpha = 0$–0.2
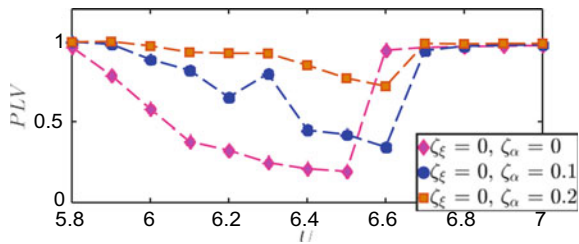
Fig. 6 Variation of the PLV with flow speed for $\zeta_\xi =$ 0–0.2 and $\zeta_\alpha =$ 0–0.2
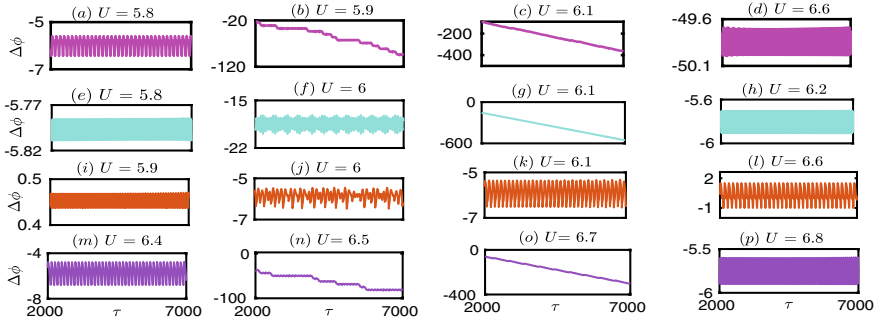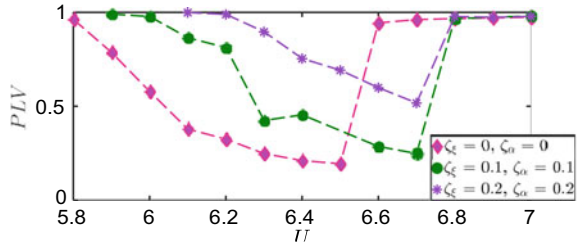
Fig. 7 Relative phase time histories for: **a–d** $\zeta_\xi = 0$, $\zeta_\alpha = 0$; **e–h** $\zeta_\xi = 0.2$, $\zeta_\alpha = 0$; **i–l** $\zeta_\xi = 0$, $\zeta_\alpha = 0.2$; and **m–p** $\zeta_\xi = 0.2$, $\zeta_\alpha = 0.2$

gradually decreases and attains a minimum value of 0.19 at $U = 6.5$. This represents the loss of synchronization, which is also reflected in the $\Delta\phi$ time histories in the form of phase slips in Fig. 7b and phase drifting in Fig. 7c. This type of synchronization between the two modes gives rise to an aperiodic regime (see Figs. 1 and 2b, c). This is attributed to the fact that the aerodynamics is switching between deep and light stall events (see Figs. 3b and c) [11]. At $U = 6.6$, the PLV value again attains a value close to 1, indicating strong synchronization. The corresponding $\Delta\phi$ is bounded and oscillates between a narrow range (see Fig. 7d). Interestingly, $U = 6.6$ is the onset of stall flutter LCOs (see Figs. 1 and 2d), where the dynamics enters in to a deep stall (see Figs. 3d). Upon further increase in flow speed, the PLV approximately remains constant and close to 1 indicating that synchrony persists.

Next, synchronization characteristics are observed in the presence of different damping values in pitch and plunge. When ζ_ξ is raised to 0.1 (keeping $\zeta_\alpha = 0$), PLV variation with flow speed is changed as compared to the undamped case as shown in Fig. 4. At $U = 5.8$, the PLV is close to 1 and decreases with flow speed up to $U = 6.3$. The minimum PLV of 0.25 is obtained at $U = 6.3$, which explains the narrower aperiodic regime (than that of the undamped case) as shown in Fig. 1c. At $U > 6.3$, PLV is close to 1 representing perfect synchronization (corresponding to stall flutter LCOs shown in Fig. 1c). This attributed to the earlier onset of stall flutter LCOs in the presence of plunge damping. When the ζ_ξ value is increased to 0.2 (again keeping $\zeta_\alpha = 0$), it is observed that the asynchronous state is further narrowed (see

Fig. 4). Here, the PLV is close to one at $U = 5.8$ and decreases up to 0.46 till $U = 6.1$ and then attains a constant value close to 1 for $U > 6.2$. The corresponding relative phases variation in Fig. 7e–g also shows a very brief regime of asynchrony (via phase drifting). The perfect synchronization at $U = 6.2$ leads to the earlier onset of stall flutter for $\zeta_\xi = 0.2$ case (see Fig. 1f). Thus, plunge damping majorly impacts the aperiodic regime, and as the plunge damping increases, this regime becomes shorter. Due to this shortening in the aperiodic regime, we observe perfect synchronization leading to stall flutter at lower air speeds.

Next, ζ_α is increased to 0.1 (with $\zeta_\xi = 0$). In this case, PLV is close to one at $U = 5.8$ and first decreases with flow speed up to $U = 6.2$ and then increases slightly at $U = 6.3$ and then again decreases up to $U = 6.6$. Thus, the minimum PLV of 0.35 is attained at $U = 6.6$. At $U > 6.7$, the PLVs are constantly close to 1. Note that, the corresponding aeroelastic response at U—6.7 exhibits stall flutter LCOs (see Fig. 1b). This indicates that stall flutter is postponed compared to the situation of zero damping. Further, ζ_α is increased to 0.2 (with $\zeta_\xi = 0$) (see Fig. 5). In this case, we observe much higher PLV values as compared to earlier cases which indicates that the pitch damping strongly enhances synchronization. The minimum PLV of 0.74 is obtained at $U = 6.6$. The same behavior can also be seen in the $\Delta\phi$ time histories in Fig. 7i–l. Here in all the cases, the phase difference is bounded, and only the range of the bounded fluctuation increases or decreases as the PLV decreases or increases, respectively. In brief, the PLV increases with the pitch damping at any particular flow speed. Additionally, an increment in pitch damping delays the onset of stall flutter.

After analyzing the individual effects of pitch and plunge damping, the investigation is carried forward to the cases where both plunge and pitch damping are considered. For $\zeta_\xi = \zeta_\alpha = 0.1$, we see that PLV remains almost close to 1 up to $U = 6$ and then decreases to a minimum value of 0.24 at $U = 6.7$ (see Fig. 6). For $U > 6.7$, the PLV again attains a value close to 1. Further increasing both ζ_ξ and ζ_α to 0.2, we observe that the perfect synchronization continues to exist up to $U = 6.4$ (see Fig. 7m). After this, we observe a brief regime of asynchrony via phase slip (Fig. 7n) and phase drift (Fig. 7o). At $U = 6.8$, the perfect synchronization is observed again (Fig. 7p). Overall, the combined effect of ζ_ξ and ζ_α leads to the postponement of both the asynchronous regime (corresponding to the aperiodic regime in aeroelastic response) as well as the subsequent synchronized regime (corresponding to stall flutter). Additionally, the PLV increases with an increase in combined damping values.

4   Conclusions

In the paper, a detailed analysis of the effect of structural damping on aeroelastic responses has been presented. This study is the first of its type to examine the impact of damping on the pitch–plunge aeroelastic system by understanding its synchronization characteristics. The salient findings of this study are summarized below:

- Both pitch and plunge damping significantly affect the flutter boundaries. An increase in plunge damping leads to a shorter aperiodic regime while an increase in pitch damping leads to delayed onset of stall flutter.
- At any particular speed, the PLVs are observed to be higher as the damping is increased (in pitch or plunge or both).
- In general, the onset of LCO is marked by a synchronization state (PLV close to 1) which transitions to an aperiodic regime marked by an asynchronous state (PLV gradually decreasing) and subsequently stall flutter via a synchronized state.

The authors believe that a deeper investigation is necessary to fully understand the effect of damping on aeroelastic systems with coupled structural and aerodynamic nonlinearities, which is a fascinating problem to be addressed in the future.

References

1. McCroskey WJ (1981) The phenomenon of dynamic stall. Technical report
2. Lee BHK, Price SJ, San Wong Y (1999) Nonlinear aeroelastic analysis of airfoils: bifurcation and chaos. Prog Aeros Sci 35 (3):205–334
3. Lottati I (1986) The role of structural and aerodynamic damping on the aeroelastic behavior of wings. J Aircr 23(7):606–608
4. Luongo A, D'Annibale F (2017) Nonlinear hysteretic damping effects on the post-critical behaviour of the visco-elastic beck's beam. Math Mech Solids 22(6):1347–1365
5. Jayatilake S, Titurus B (2022) Nonlinear aeroelastic analy sis of a damped elasticaaerofoil system. Nonlinear Dyn 109:1–24
6. Raaj A, Venkatramani J, Mondal S (2019) Synchro nization of pitch and plunge motions during intermittency route to aeroelastic flutter, Chaos. Interdisc J Nonlinear Sci 29(4):043129
7. Vishal S, Raaj A, Bose C, Venkatramani J (2021) Routes to synchronization in a pitch–plunge aeroelastic system with coupled structural and aerodynamic nonlinearities. Int J Non-Linear Mech 135:103766
8. Tripathi D, Shreenivas R, Bose C, Mondal S, Venkatramani J (2022) Experimental investigation on the synchronization characteristics of a pitch-plunge aeroelastic system exhibiting stall flutter, Chaos. Interdisc J Nonlinear Sci 32(7):073114
9. Gordon Leishman J, Beddoes TS (1989) A semi-empirical model for dynamic stall. J Am Helicopter Soc 34(3):3–17
10. Bethi RV, Gali SV, Venkatramani J (2020) Response analysis of a pitch–plunge airfoil with structural and aerodynamic nonlinearities subjected to randomly fluctuating flows. J Fluids Struct **92**:102820
11. Tripathi D, Vishal S, Bose C, Venkatramani J (2022) Stall-induced fatigue damage in nonlinear aeroelastic systems under stochastic inflow: numerical and experimental analyses. Int J Non-Linear Mech 142:104003

Wave-Structure Interaction Dynamics of a Point Absorber Wave Energy Converter

Suman Kumar, Navneet Kumar, and Abdus Samad

1 Introduction

Renewable energy sources can be used to reduce CO_2 emissions [1] and can assist countries with low fossil fuel reserves. Especially India, which imports about one-fourth of the oil and gas required in the country. Only exploring and exploiting such energy can help in sustainable development.

One such energy source is the ocean. Ocean water can give tidal, wave, and thermal energy. India's 7500 km long coastline has an average wave energy harness potential of about 5 to 10 kW/m, and the total potential is about 40 GW [2]. However, the technology has not matured yet [3]. Among several concepts of such energy, a point absorber (PA)-based wave energy converter (WEC) can be an option where water depth is more than a few meters.

A PA has a doughnut-shaped buoy and a vertical cylindrical shaped spar. The spar can be fixed on the seabed or floating. Waves give heaving motion to the buoy, while the spar passing through the buoy is almost motionless. Hence, they get relative motion. Instead of fixing it to the seabed, the bottom end of the spar is attached to a heave plate. The plate resists spar movement with waves. The spar can be 10 to 20 m long, and the buoy diameter can be 1/6th of the wavelength. The energy to be harvested depends upon the wave height and the wavelength. It is a challenging job to tune the system as per the wave frequency as there is a seasonal variation, etc., in the wave frequency.

A simple and compact design of a WEC makes it better for fabrication and installation [4]. An axisymmetric design allows it to capture energy in all directions and

S. Kumar (✉)
Virya Paramita Energy Pvt. Ltd., Visakhapatnam, Andhra Pradesh 530016, India
e-mail: sumanrajak123k@gmail.com

N. Kumar · A. Samad
Wave Energy and Fluids Engineering Laboratory, Department of Ocean Engineering, IIT Madras, Chennai 600036, India

Fig. 1 PA wave energy
converter
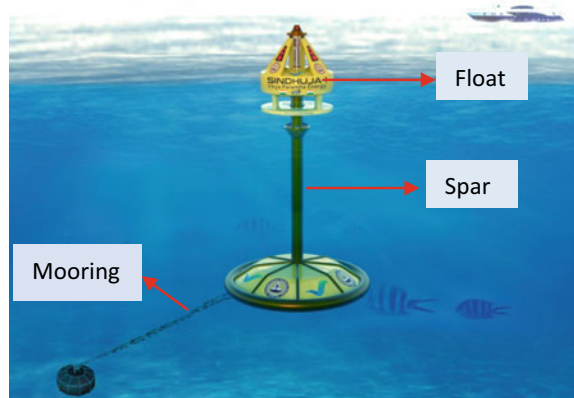
is suitable for short wave periods and low amplitudes [5]. There are single-body and
two-body PAs. A two-body point absorber can be installed at any water depth with
a suitable mooring configuration.

A two-body PA developed at IIT Madras is shown in Fig. 1. Factors, such as
float geometry, power take-off (PTO) mechanism, mooring dynamics, etc., affect the
device's performance and power output. The system absorbs power better when its
natural frequency coincides with the wave frequency [6].

The device disturbs incoming waves and alters the wave field [7]. Therefore,
an analysis with wave-structure interaction (WSI) becomes inevitable to know the
system behavior in the water. The WSI analysis can evaluate system response
parameters such as mooring dynamics, natural frequency, and power output [6].

In 1885, Leavitt [8] patented a PA which has a heaving buoy, a rack, and pinion
gear to compress air using wave energy. Later, ample work [9–11] was reported.
Table 1 presents the recent studies on PA hydrodynamics [12–20]. Except for one
article [19], none has included system load in their work.

Kamarlouei et al. [12] analyzed the hydrodynamic performance of a PA attached
to a spring mechanism. Sun and Zhang [13] studied the control and optimum tuning
of an integrated offshore wave-wind hybrid PA system. Furthermore, parametric
optimization was performed on system modal frequencies. Likewise, several numer-
ical and experimental works on dynamics, control, optimization, and fluid–structure
interaction were carried out [14–20]. Literature shows that the WSI needs to be
studied to understand the device's response. Studying the wave-structure interaction
dynamics of the suggested float shape is the goal of the current effort.

In the present work, to study the wave-structure interaction dynamics and asso-
ciated hydrodynamic coefficients the BEM tool was used. These coefficients can be
used to calculate the system responses. It is presented the static design load on the
structure, which can be used for structural stress analysis.

Table 1 Summary of recent research on PA WECs

Author/s	Hydrodynamics	Design load	Applications
Kamarlouei et al. [12]	✓	×	Hybrid device, performance
Sun and Zhang [13]	✓	×	Control, hybrid devices, performance
Bonovas et al. [14]	✓	×	Array effects, performance
Shami et al. [15]	✓	×	Nonlinear hydrodynamics, performance
Sheng et al. [16]	✓	×	Hydrodynamics, performance
Avalos and Estefen [17]	✓	×	Latching control, hydrodynamics, viscous drag
Haider et al. [18]	✓	×	Control, hydrodynamics, power take-off
Rij et al. [19]	✓	✓	Hydrodynamics, structural loads
Martin et al. [20]	✓	×	Performance, power take-off, structural

2 Materials and Methods

The linear potential theory modeled the fluid-body interaction to understand the system's hydrodynamics. The potential theory implies that fluid is inviscid, irrotational, and incompressible. Figure 2 shows the physical model in the infinite fluid domain of water depth h. The proposed geometry has maximum diameter D and static draft d.

Assuming potential flow theory, a velocity potential is introduced in the flow field, which is defined as:

$$\varphi(x, y, z, t) = Re\left[(\varphi_1 + \varphi_d + u_i \varphi_{ri})e^{-i\omega t}\right] \tag{1}$$

Fig. 2 Sketch of wave structure interaction with float
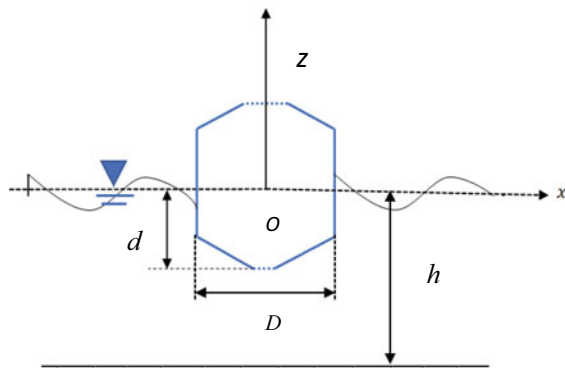
where φ_1 denotes the incident wave potential. Diffraction and unit radiation potential are φ_d and φ_{ri}, respectively. u_i stands for body velocity in heave. The different potentials follow the linear superposition principle. The governing equation of flow physics and associated parameters are presented below.

The radiation and diffraction potentials meet the following boundary conditions according to the linear potential theory [21]:

$$\nabla^2 \varphi_{(d,r)} = 0, \quad (x, y, z) \in \Omega \tag{2}$$

$$\frac{\partial \varphi_{(d,r)}}{\partial z} - \frac{\omega^2}{g} \varphi_{(d,r)} = 0, \quad z = 0 \tag{3}$$

$$\frac{\partial \varphi_{(d,r)}}{\partial z} = 0, \quad z = -h \tag{4}$$

$$\varphi_{(d,r)} = O\left(\frac{1}{\sqrt{R}} e^{ik_0 R}\right), \quad R = \sqrt{x^2 + y^2} \rightarrow \infty \tag{5}$$

where Ω denotes the infinite fluid field, g is the acceleration due to gravity, and ω, k_0 stands for incident wave frequency and wave number, respectively.

The boundary integral equation produced φ_d and φ_r and derived from Green's function as shown below.

$$\alpha(p)\varphi(p) = \iint_s [G(p, q)\varphi_n(q) - \varphi(q)G_n(p, q)]ds \tag{6}$$

where $G(p, q)$ is the free surface Green's function concerning field point $p(x, y, z)$ and a source point q. Figure 3 shows the buoy geometry selected for numerical analysis.

Fig. 3 Geometry used for BEM analysis
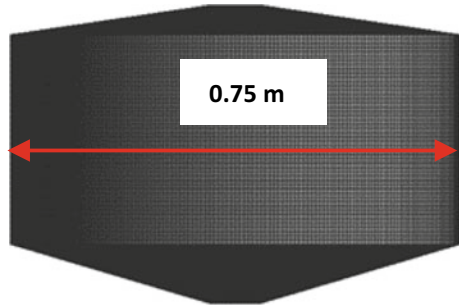
3 Results and Discussion

3.1 Hydrodynamic Coefficients and Forces

Figure 4 shows the different hydrodynamic coefficients such as scaled added mass, radiation damping coefficients, and response amplitude operator (RAO) obtained from BEM analysis. To know the system responses, it is essential to calculate frequency-dependent hydrodynamic coefficients, including various forces acting on the floating body. While the floating body is in motion, the fluid surrounding the body also moves due to inertia, known as an added mass force. The added mass generally affects geometry and body aspect ratio [22]. It is clear from Fig. 4a that at 1.2 rad/s, the added mass attains a minimum value, which further increases with an increase in wave frequency. This is due to the presence of a hole made for spar passage.

Similarly, the radiation damping coefficient is an important index to evaluate radiation forces imposed on hydrodynamic bodies. Figure 4b depicts the variation of radiation damping coefficients with incident wave frequency. With the increase in
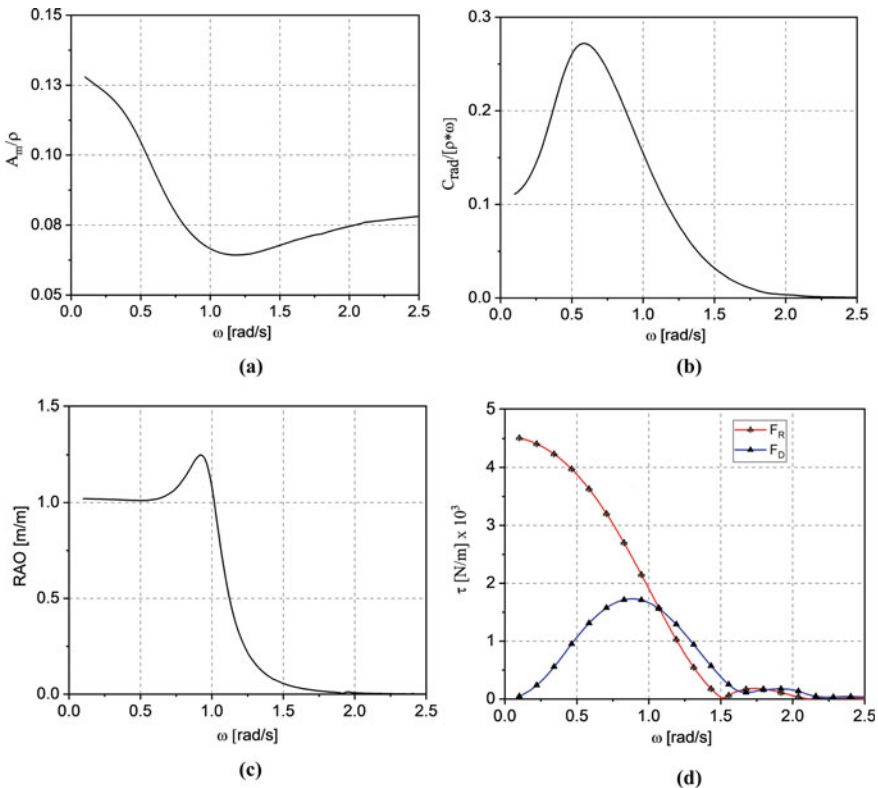
Fig. 4 Hydrodynamic coefficients and forces

Fig. 5 Structure pressure for
0.1 Hz at wave amplitude
0.25 m

N/m^2
69.0
66.7
64.5
62.3
60.1
57.8
55.6
53.4
51.1
48.9
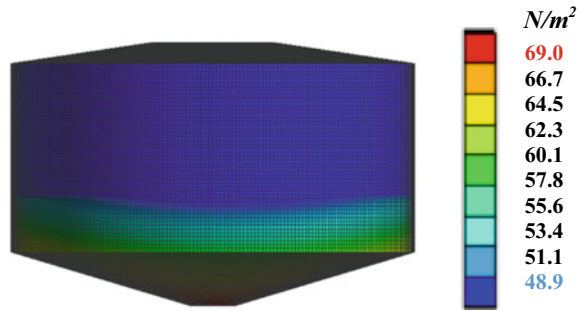
frequency, the damping coefficient increases; however, it decreases after a maximum
value of 0.6 rad/s. Figure 4c shows the RAO plot, which describes the body response
with incident wave amplitude. At zero frequency (no wave), the body has a unity
RAO value. It increases with wave frequency, further attains a maximum value, and
decreases to zero for wave frequency higher than 2 rad/s. Other than hydrostatic force,
a net effect that arises due to buoyancy and gravity, two other hydrodynamic forces
are Froude–Krylov and diffraction forces. They both together give the excitation
force. Figure 4d shows these forces separately with wave frequency. The diffraction
force is zero at zero frequency as there is no wave. As the body attains motion slowly
with an increase in wave frequency, the diffraction force decreases after a particular
frequency. It is also important to note that initially, Froude–Krylov's force decreases
with an increase in frequency; after a specific frequency, it is almost zero.

The floating body subjected to wave action experiences hydrostatic and hydro-
dynamic surface pressure. The structure pressure was evaluated for different wave
amplitude and frequencies. The pressure contour for one such condition is shown
in Fig. 5. The structure experiences a maximum pressure of 69 Pa near the mean
sea water level (MSWL) as this location takes the most load. Figure 6 shows the
shear load variation on the body concerning the center position. It can be useful in
structural stress analysis.

4   Conclusions

The present study proposes and applies a framework for implementing BEM anal-
ysis. The hydrodynamic coefficients are investigated by solving boundary integral
equations through the boundary element method to understand the fluid–structure
interaction of a floating buoy with a conical base.

- The diffraction and Froude–Krylov force are calculated for a given frequency
  range.
- The surface pressure on the proposed geometry is evaluated for given wave
  parameters.

Fig. 6 Structure shear force for 0.1 Hz at wave amplitude 0.25 m
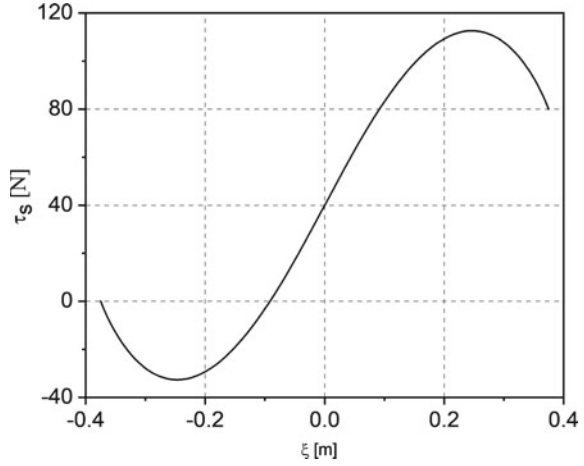
- The static shear force is approximately 112 N at 0.24 m from the mean line.

Nomenclature

A_m Added mass (kg)
C_rad Radiation damping coefficient (N-s/m)
D Float maximum diameter (m)
d Static draft (m)
F_D Diffraction force (N)
F_R Froude–Krylov force (N)
G Green function (–)
g Acceleration due to gravity (m/s^2)
h Water depth (m)
k_0 Wave number (m^{-1})
p Field point (–)
q Source point (–)
u_i Body velocity in heave (m/s)
ω Wave frequency (rad/s)
ρ Sea water density (kg/m^3)
Ω Infinite fluid field (–)
φ Velocity potential (m^2/s)

φ_I Incident wave potential (m^2/s)

φ_d Diffraction velocity potential (m^2/s)

φ_{ri} Unit radiation potential (–)

References

1. Andrew RM, Peters GP (2021) The global carbon project's fossil CO_2 emissions dataset. https://doi.org/10.5281/ZENODO.5569235
2. Rusu E, Onea F (2018) A review of the technologies for wave energy extraction. Clean Energy 2:10–19. https://doi.org/10.1093/ce/zky003
3. Isaacs JD, Schmitt WR (2016) Ocean energy: forms and prospects. American Association for the Advancement of Science Stable. http://www.jstor.org/stable/1684169. Accessed 23 May 2016 13 (25 UTC 2016;207:265–73).
4. Drew B, Plummer AR, Sahinkaya MN (2009) A review of wave energy converter technology. Proc Inst Mech Eng Part A J Power Energy 223:887–902. https://doi.org/10.1243/09576509JPE782
5. Faiz J, Ebrahimi-Salari M (2011) Comparison of the performance of two direct wave energy conversion systems: Archimedes wave swing and power buoy. J Marine Sci Appl 10(4):419–428. https://doi.org/10.1007/s11804-011-1087-9
6. Faizal M, Ahmed MR, Lee YH (2014) A design outline for floating point absorber wave energy converters. Adv Mech Eng. https://doi.org/10.1155/2014/846097
7. Amabili M (2004) The theory and practice of hydrodynamics and vibration by S.K. Chakrabarti, World Scientific, Singapore, 2002, pp. xviii+464, ISBN 981-02-4921-7. J Sound Vib 270:1091. https://doi.org/10.1016/j.jsv.2003.12.003
8. Leavitt C (1885) Mechanism for utilizing wave-power. U.S. Patent US321229A
9. Falnes J (1995) On non-causal impulse response functions related to propagating water waves. Appl Ocean Res 17:379–389. https://doi.org/10.1016/S0141-1187(96)00007-7
10. https://tracxn.com/d/trending-themes/Startups-in-Wave-Energy-Convertor
11. Al Shami E, Zhang R, Wang X (2019) Point absorber wave energy harvesters: a review of recent developments. Energies 12. https://doi.org/10.3390/en12010047
12. Kamarlouei M, Hallak TS, Gaspar JF, Soares CG (2022) Evaluation of the stiffness mechanism on the performance of a hinged wave energy converter. J Offshore Mech Arct Eng 144:1–8. https://doi.org/10.1115/1.4054791
13. Sun T, Zhang Z (2022) Optimal control and performance evaluation of an inerter-based point absorber wave energy converter. Ocean Eng 259:111883
14. Bonovas M, Magkouris A, Belibassakis K (2002) A modified mild-slope model for the hydrodynamic analysis of arrays of heaving WECs in variable bathymetry regions. Fluids 7:183. https://doi.org/10.3390/fluids7060183
15. Al Shami E, Wang Z, Wang X (2021) Non-linear dynamic simulations of two-body wave energy converters via identification of viscous drag coefficients of different shapes of the submerged body based on numerical wave tank CFD simulation. Renew Energy 179:983–997. https://doi.org/10.1016/j.renene.2021.07.068
16. Sheng W, Tapoglou E, Ma X, Taylor CJ, Dorrell R, Parsons DR et al (2022) Time-domain implementation and analyses of multi-motion modes of floating structures. J Marine Sci Eng 10:662. https://doi.org/10.3390/jmse10050662
17. Avalos GOG, Estefen SF (2021) Viscous effect for heaving cylindrical point absorbers controlled by a latching control system and a novel approach to viscous force. J Ocean Eng Marine Energy 7:363–378. https://doi.org/10.1007/s40722-021-00205-y

18. Haider AS, Brekken TKA, McCall A (2021) Real-time nonlinear model predictive controller for multiple degrees of freedom wave energy converters with non-ideal power take-off. J Marine Sci Eng 9:890. https://doi.org/10.3390/jmse9080890
19. Van Rij J, Yu YH, Guo Y (2017) Structural loads analysis for wave energy converters. Int Conf Offshore Mech Arctic Eng OMAE 10. https://doi.org/10.1115/OMAE2017-62139
20. Martin D, Li X, Chen CA, Thiagarajan K, Ngo K, Parker R et al (2020) Numerical analysis and wave tank validation on the optimal design of a two-body wave energy converter. Renew Energy 145:632–41. https://doi.org/10.1016/j.renene.2019.05.109
21. Xu Q, Li Y, Yu YH, Ding B, Jiang Z, Lin Z et al (2019) Experimental and numerical investigations of a two-body floating-point absorber wave energy converter in regular waves. J Fluids Struct 91:102613. https://doi.org/10.1016/j.jfluidstructs.2019.03.006
22. Zhang S, Pedersen PT, Villavicencio R (2019) Probability and mechanics of ship collision and grounding. Butterworth-Heinemann

Temporal Interpolation of Flow Fields for Knocking Combustion Using CNN

Bhavesh Shamnani, Ayush Jaiswal, Bhavna, Mahir Goel, Mayank Shukla, Neetu Tiwari, and Ajit Kumar Dubey

1 Introduction

More than one billion vehicles worldwide, and more than 60% are equipped with gasoline spark ignition (SI) engines. However, the biggest obstacle to further development of highly efficient SI engines is their knocking tendency. Therefore, this phenomenon must be thoroughly understood to meet future energy requirements.

Knocking, in an internal combustion engine [1], creates sharp sounds caused by premature combustion of part of the compressed air–fuel mixture in the cylinder. In a non-knocking engine cycle, the charge burns with the flame front progressing smoothly from the point of ignition across the combustion chamber. The pre-ignition phenomenon during the knocking cycle leads to high-amplitude waves that can cause erosion of the combustion chamber surface and rough, inefficient operation.

Therefore, knock-in high-efficiency engines must be well understood to meet future fuel economy and emission regulations.

Knocking is a complex multi-scale, multi-physics phenomenon which needs understanding of the kinetics of combustion, pressure wave effect as well as turbulent flow and heat transfer. Its inception occurs on very fast time scales. The engine is usually not very accessible to record time evolution of flow, temperature and species for a complete understanding. One alternative is numerical simulations. Over past two decades, 1D direct numerical simulations (DNS) which resolves pressure wave evolution with consideration of detailed chemical kinetics have been performed. Multidimensional DNS with detailed kinetics requires an enormous computing time and memory. The current study utilizes a multidimensional simulation data to test and develop AI models to aid knocking research.

B. Shamnani (✉) · A. Jaiswal · Bhavna · M. Goel · M. Shukla · N. Tiwari · A. K. Dubey
Department of Mechanical and Industrial Engineering, IIT Roorkee, Roorkee 247667, India
e-mail: bhavesh_c@me.iitr.ac.in

2   Literature Review and Objective

Recently, a two-dimensional direct numerical simulation (DNS) of knocking phenomena for a laboratory experiment has been carried out [2]. It reproduces the results for the knocking time and flow field evolution accurately, considering the detailed chemical kinetics coupled with fluid dynamics. Conducting such laboratory-scale 2D simulations poses huge computational costs for higher hydrocarbon fuels and requires larger computing facilities.

Our current study utilizes the 2D-DNS results to test and develop CNN-based models to create image frames between two instants. This will help in improving the time resolution of the experimental flow field images taken during knocking combustion. This analysis would also provide guidelines for low-fidelity simulations with reduced computational requirements and higher accuracy and offer the researcher a better representation of the fine details in the knocking phenomenon with less cost. Different frame interpolation models perform differently given the type of DNS data and frame rate. Hence, exploring all potential models is crucial before arriving at the results. This study also aims at developing a methodology to produce the best results given data of flow fields with time.

3   Methodology

Images were obtained from computed density gradient fields generated from 2D-DNS results. 2D-DNS was performed with the latest reduced kinetics, which was realized by using in-house efficient solver, MACKS combined with compressible flow solver PeleC using AFINITY supercomputer at Tohoku University Japan. 2D-DNS replicated the experiments conducted by a research group at Kyushu University, Japan, with a constant volume chamber ($14 \times 14 \times 80$ mm) using a stoichiometric n-C_7H_{16}/O_2/Ar mixture where O_2 and Ar mole fraction ratio of 21:79 at engine-like condition [3]. From the comparison of the pressure histories, it was found that the two-dimensional simulation was able to reproduce the characteristic events such as the ignition and propagation of flame, cool flame ignition and the knock onset observed in the experiment [4]. From the comparison of the computational density gradient fields with experimental Schlieren images, the two-dimensional simulation was also able to reproduce the overall flame shape transitions observed in the experiment until the knock onset.

For the image interpolation methods, we require the datasets which come from the simulated knocking phenomenon; the aim was to explore and employ various ML models for video frame interpolation with excellent results after the literature review; we came across several potential methods to achieve our objective. In this study, we converged on three such forms of video frame interpolation, namely Adaptive Separable Convolution (AdaSepConv), Real-time Intermediate Flow Estimation (RIFE) and Image Averaging Technique (IAT).

3.1 Generating Dataset

A 2D-DNS of stoichiometric n-C_7H_{16}/O_2/Ar mixture at the engine-like condition with the latest reduced SIP isooctane kinetics was used for our study [1]. A simulated video provided in supplementary data files with this paper has been used to extract the individual frames and label them as the i.png, where i runs from the start to the last frame. The frames also need to be cropped down to the part depicting the flow of pressure waves so that our model does not learn unnecessary noises.

3.2 Video Frame Interpolation via Adaptive Separable

Convolution

This method directly estimates a convolution kernel and uses it to convolve the two frames to interpolate the pixel colour. Generally, frame interpolation algorithms involve a two-step process of estimating the motion and pixel synthesis.

This method provides a robust algorithm that combines these two processes' convolution steps to interpolate two images [5].

For example, we can locate the associated pixels for the pixel (x, y) in the input images I_1 and I_2 and then interpolate the colour from these related pixels. In order to create a high-quality interpolation result, this step frequently also entails resampling pictures I_1 and I_2 to obtain the equivalent values $I_1(x_1, y_1)$ and $I_2(x_2, y_2)$—especially when (x_1, y_1) and (x_2, y_2) are not integer positions, as shown in Fig. 1. This two-step process may be compromised if the optical flow is unpredictable as a result of occlusion, motion blur or texture loss.

In order to solve the problem, motion estimation and pixel synthesis must be combined into a single step. Pixel interpolation must then be defined as a local convolution over patches in the input pictures I_1 and I_2. As seen in Fig. 2 suitable kernel K can be convolved across input patches P1(x, y) and P2(x, y) that are also centred at (x, y) in the appropriate input images to determine the colour of the pixel (x, y) in the target image that has to be interpolated. For pixel creation, the convolutional
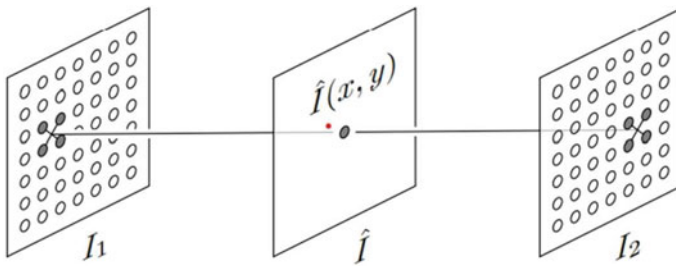
Fig. 1 Interpolation by motion estimation and pixel synthesis
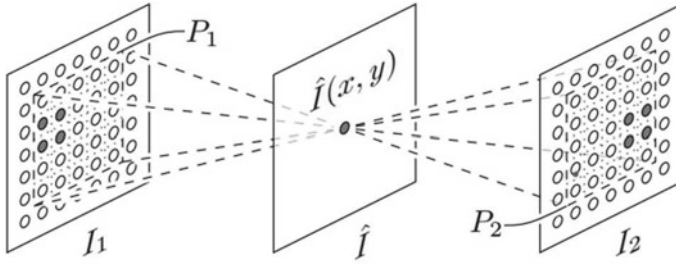
Fig. 2 Interpolation by convolution

kernel K captures both motion and resampling coefficients. There are a few benefits to representing pixel interpolation via convolution. First of all, the single-step approach, which combines motion estimation with pixel synthesis, offers a more reliable answer than the two-step method. Second, the flexibility offered by the convolution kernel enables it to take into consideration and deal with complex situations like occlusion.

3.3   RIFE: Real-Time Intermediate Flow Estimation for Video Frame Interpolation

Many contemporary flow-based VFI techniques initially estimate the bidirectional optical flows before scaling and reversing them to approximation intermediate flows, resulting in distortions on motion borders and intricate pipelines. With significantly greater speed, RIFE [6] employs a neural network called IFNet that can directly predict the intermediary flows from coarse to fine.

IFBlocks only employ 3×3 convolution and deconvolution as building blocks, which are effective on devices with limited resources. They do not feature costly operators such as cost volume.

Given two input frames I_0, I_1 and temporal encoding t (timestep encoded as a separate channel), we directly feed them into the IFNet to approximate intermediate flows $F_{t \to 0}$, $F_{t \to 1}$ and the fusion map M. A privileged teacher uses a unique IFBlock throughout the training phase to improve the students' results based on ground reality. The instructor model and the student model are jointly trained using the reconstruction loss from scratch. The teacher can better direct the pupil to study because their estimates are more accurate (Fig. 3).

3.4   Image Averaging Technique (IAT)

Image averaging is an image processing technique that is often employed to extract some information by creating intermediate frame.
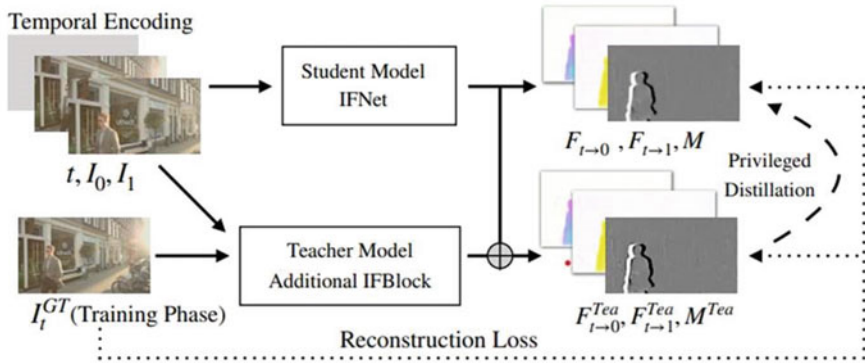
Fig. 3 Overview of RIFE pipeline

The algorithm operates by computing an average or arithmetic mean ($N = 2$) of the intensity values (I) for each pixel position (x, y) in a set of captured images from the same scene or view field.

$$A(N, x, y) = \frac{1}{N} \cdot \sum_{i=1}^{N} I(i, x, y)$$

3.5 Structural Similarity Index Measure (SSIM)

A method used for forecasting the perceived quality of images and other digital images and videos is the structural similarity index measure (SSIM) [7]. SSIM is a tool for calculating how similar two images are to one another. The SSIM index is a complete reference metric, meaning that the initial uncompressed or distortion-free image serves as the baseline for measuring or predicting image quality. To derive the final index, SSIM extracts three features from an image, namely.

1. **Luminance**: Luminance is derived by averaging the pixel values in an image, given as:

$$\mu_x = \frac{1}{N} \sum_{i=1}^{N} x_i$$

Luminance comparison function $l(x, y)$ becomes the function of μ_x and μ_y.
2. **Contrast**: It is calculated as obtaining the standard deviation of the image's pixel.

$$\sigma_x = \sqrt{\frac{1}{N-1} \sum_{i=1}^{N} (x_i - \mu_x)^2}$$

Contrast comparison $c(x, y)$ is then the comparison of σ_x and σ_y.

3. **Structure**: The signal is normalized with its own standard deviation to make two comparison signals which have a unit standard deviation.

$$\frac{x - \mu_x}{\sigma_x}$$

and

$$\frac{y - \mu_y}{\sigma_y}.$$

Structure comparison $s(x, y)$ is taken on the above expressions. The final formula is derived from combining three components to give the similarity measure:

$$S(x, y) = f(l(x, y), c(x, y), s(x, y)).$$

The dependencies of this method are python and pip. It also requires some tools like scikit-image, OpenCV and imutils. Following this, the logic to compare the images will involve using the SSIM method on each interpolated image and its corresponding original.

The SSIM obtained for these images can be used in several ways. It can be plotted on a graph to highlight the variation in accuracy as the process progresses, or it can be averaged to show the overall accuracy of our model.

4 Results and Discussion

Images are interpolated from both models and stored in a separate directory. To objectively establish the performance of these models, we have relied on the SSIM to compare the similarity between the ground truth and the interpolated image.

Figure 4 compares the original image to that of the interpolated images obtained from AdaSepConv, RIFE and IAT models.

4.1 SSIM for AdaSepConv, RIFE and IAT

After successfully obtaining the interpolated images from the AdaSepConv, RIFE and IAT models, we compared them with the original (ground truth) images. The performance is calculated using the structural similarity index measure (SSIM). The window size chosen for the SSIM was 3. The results thus obtained are plotted in Figs. 5, 6 and 7 for AdaSepConv, RIFE and IAT, respectively.

(a)

(b)

(c)

(d)
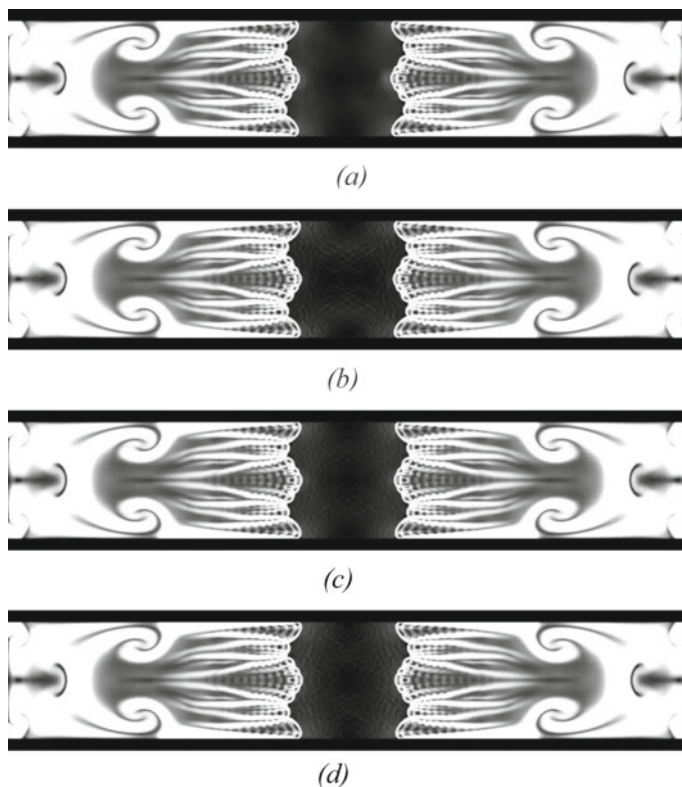
Fig. 4 Prediction for **a** AdaSepConv **b** RIFE, **c** IAT, **d** Actual image

Fig. 5 Adaptive separable convolution
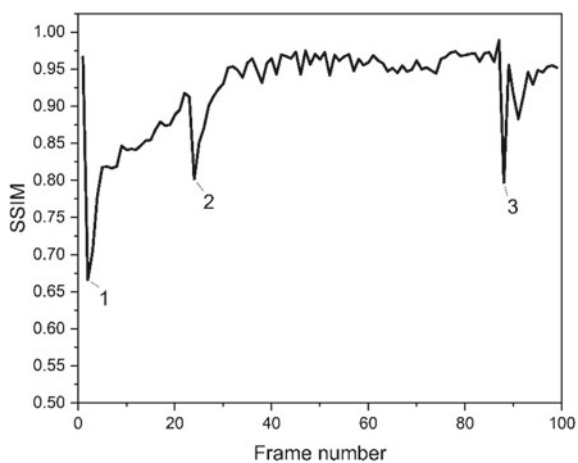
Fig. 6 RIFE
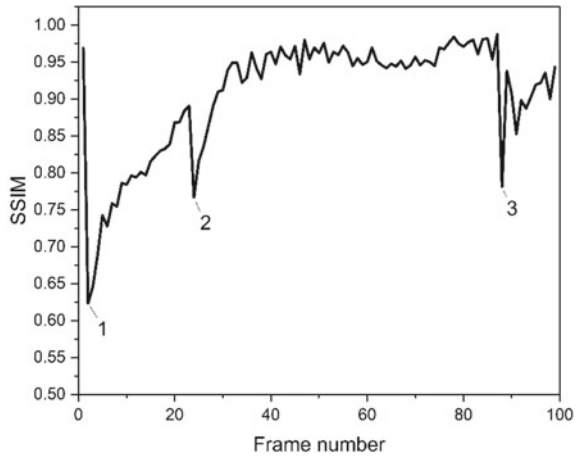
Fig. 7 IAT
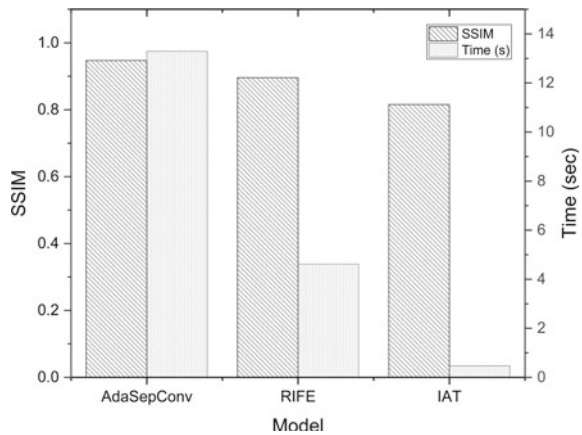
Figures 5, 6 and 7 show that the SSIM dips at the start and end of the simulation. This is attributed to the fact that wave propagation often causes sharp changes at the beginning; hence, those regions are not adequately captured by the interpolated frames. Ultimately, the simulation knocking occurs; therefore, the models do not capture the abrupt changes in the next pressure wave.

In Figs. 5, 6 and 7, the points marked by 1, 2 and 3 signify flame ignition, cool flame ignition in the end-gas and knock onset in the end-gas, respectively. The dip in accuracy at these points is due to the transition between the above-mentioned phases and signifies the abrupt change in the captured states.

Table 1 Trade-off between accuracy and time for AdaSepConv, RIFE and IAT models

Model	SSIM	Time (s)
AdaSepConv	0.947	13.29
RIFE	0.896	4.62
IAT	0.814	0.46

4.2 Computational Time

This section presents the computational time required by each model when interpolating between the same ith and $(i+1)$th to obtain the $(i+1)$th frame. Computational time becomes essential as the resource constraint system does not have the luxury of running the computationally expensive models in a stipulated time. AdaSepConv takes 13.29 s, RIFE executes in 4.62 s and IAT executes in 0.46 s.

5 Conclusions

The growing need to understand the knocking phenomenon in an engine leads us to explore the data-driven methodology to enhance the resolution of the simulation videos. This would aid researchers working in the resource constraints environments to carry forward with the same quantum of work as highly sophisticated computers. Such work can also help reduce the carbon footprint from excessively high computational analysis. If knocking is understood to improve the engine's efficiency, then carbon emission can also be checked.

Based on the current study, AdaSepConv outperformed the RIFE and IAT models regarding the similarity index. However, equal weightage should be given to the computational time involved. In that sense, IAT beat the AdaSepConv and RIFE by a considerable difference.

The overall SSIM averaged over the entire simulation period and the time expended is presented in Table 1. A dip in SSIM is observed at three instants corresponding to initial flame ignition, cool flame ignition in the end-gas and knock onset in end-gas. These three instants represent the times when flow characteristics change quickly.

This work can further be improved by studying various video flow interpolation models and applying such models to the different sets of phenomena apart from the pressure waves, such as density variation, temperature propagation and mass fraction along the combustion chamber.

References

1. Zhi W, Liu H, Reitz RD (2017) Knocking combustion in spark-ignition engines. Prog Energy Combust Sci 61:78–112
2. Morii Y, Dubey AK, Nakarmura H, Maruta K (2021) Two-dimensional laboratory-scale DNS for knocking experiment using n-heptane at engine-like condition. Combust Flame 223:330–336
3. Terashima H, Koshi M (2015) Mechanism of strong pressure wave generation in end-gas autoignition during knocking combustion. Combust Flame 162:1944–1956
4. Kono K, Shinya R, Tanaka S, Nagano Y, Kitagawa T (2017) Study on knock phenomena during flame propagation in a constant volume vessel. In: 55th symposium on combustion
5. Niklaus S, Mai L, Liu F (2017) Video frame interpolation via adaptive convolution. ICCV
6. Huang Z, Zhang T, Heng W, Shi B, Zhou S (2020) RIFE: real-time intermediate flow estimation for video frame interpolation
7. Wang Z, Bovik AC, Sheikh HR, Simoncelli EP (2004) Image quality assessment: from error visibility to structural similarity. IEEE Trans Image Process 13(4):600–612

Experimental Investigation on Vertical Farming Structure Equipped with Electronic Controls

Anansh Gupta, Falguni Charde, Prakhar Adarsh, Lalit Chacharkar, Mahesh Gaudar, and Pramod P. Kothmire

1 Introduction

As the world's population is growing rapidly, there is an enormous demand for food, which is partially met due to a scarcity of fertile land. Other factors such as natural resource depletion due to urbanization, earth erosion, and various forms of contamination also have an impact on farming lands in developing countries such as India. A good environment, fertile land, adequate water supply, and so on are examples of favorable conditions for food cultivation [1]. Farmers must transit from traditional farming to vertical farming as agricultural lands become scarce. Vertical farming is a new trend that aims to reduce the burden of food scarcity. This technique, which incorporates soil-free growing technologies, attempts to alleviate strain on traditional agricultural land by farming upwards rather than outwards [2]. There are various methods by which one can grow the plants in a vertical farm with the use of soil or without the use of soil such as aquaponics [3], aeroponics [4], and hydroponics [5]. It is particularly useful in urban environments. These vertical farm techniques can help offices and societies to reduce CO_2 emissions [6]. This technique can be a very beneficial method to Indian farmers as it has a higher yield, pesticide-free, requires very little soil, and can save a lot of money.

Crops suited for vertical farming are lettuce, spinach, tropical leafy vegetables, salad leaves, herbs, and so on. The appropriate temperature needed is just the normal ambient temperature (21–27 °C) [7]. Here, we have constructed a structure which is portable, easy to cultivate the crops, and easy to handle. Loamy soil is used here as it has plenty of organic matter which is required for the fast growth of the crop, and also, the nutrient content in the crops is high [8]. Since there is no sunlight present at

A. Gupta (✉) · F. Charde · P. Adarsh · L. Chacharkar · P. P. Kothmire
School of Mechanical Engineering, MIT Academy of Engineering, Alandi, Pune 412105, India
e-mail: aagupta@mitaoe.ac.in

M. Gaudar
School of Electrical Engineering, MIT Academy of Engineering, Alandi, Pune 412105, India

the night time or even inside of a house or farm, the appropriate lighting conditions of different wavelengths are used which significantly influence plant growth. Blue and red colors are best suited for increasing the growth rate [9]. Since led emits a low level of thermal radiation having no hot electrodes, a high running life and also no high voltage ballasts make it a practical alternative of sunlight [10]. The system can be automated to work more efficiently with the help of IoT. Different sensors are used to collect data, which is then analyzed to make decisions based on the requirements

2 Literature Review and Objective

The main aspects to consider when designing a vertical farm are structure, nutrition media, lighting, and sustainability features. There are different types to implement vertical farming such as green roof construction, green wall construction, and green facade construction. Vertical farming technology can ensure crop production year-round in non-tropical regions [11], and the production is much more efficient than land-based farming [12]. As vertical farming is an indoor technology the space is utilized efficiently and more crops are yielded in vertical farming [13]. Also, the freshwater usage is low in case of vertical farming as the crops are cultivated in a closed and controlled environment. Soil moisture is another factor contributing toward the growth of plants [14]. Some of the challenges faced in the implementation of the vertical farming system are the limited number of crops that can be grown economically. The leafy greens and herbs remain the primary crop due to the rapid growth cycle. Another major challenge is the very high demand of energy as natural lights are replaced by led lights, and it must be working for at least 12–16 hours a day [15].

With this work, the focus will be on the various factors that must be considered while designing a vertical farming structure. This study explains the design steps, analysis, and manufacturing and provides a comprehensive overview of all of these aspects in order to improve vertical farm understanding and design. Apart from the above investigations, there are some gaps like lack of study of different wavelengths of light, ineffective arrangement of crops, etc. This study focuses on (1) comparative study between the conventional farming setup and vertical farming setup; (2) the effect of different wavelengths of lights on the plant growth; (3) incorporation of Internet of things in order to optimize the vertical farming setup.

Table 1 Electronic components specifications used in project

Sr. No	Components	Specifications
1	Arduino Uno R3	Microcontroller
2	Moisture sensor	LM393, 3.3–5 V
3	RGB led strip lights	12 V operating voltage, 5 m length
4	4-channel relay	Electrically operated switch
5	Pumps	5–12 V DC

3 Materials and Methods

3.1 AEIOU Analysis

This analysis gives a complete overview about the activities and the user associated with the system of vertical farming. Important terminologies related to vertical farming are growing media, nutrient content, growth monitoring, source of light. Each of these plays a major role in the efficiency of vertical farming. The outcomes of this analysis display the current gaps in vertical farming which include the protection of plants from insects, handling of structure, monitoring of plants, and nutrition management (Table 1).

3.2 Design of Models

Different CAD geometries were created, and simulations were run in order to find the optimal geometry which consumes less space and gives better yield.

3.2.1 Initial Model

Figure 1 displays the initial model designed for vertical farming. Key features of this model are proper water circulation and effective light conditioning. Each layer of the model contains two crop trays, which increases the amount of crop grown in a given area. The trays are designed in such a way that they can be drawn out from the structure. This feature makes the model easy to clean. Also, this model is space efficient. Apart from these, there are some limitations of the model such as proper moisture content in soil, effective ventilation of the model.

Fig. 1 Initial model for
vertical farming
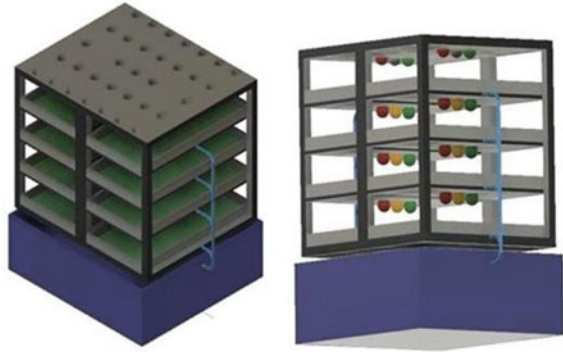
3.2.2 Final Model

Figure 2 shows an overview of the final model, wherein Fig. 2a represents a single unit of stack of the model, Fig. 2b gives the CAD representation of the model, and Fig. 2c shows the image of the final assembly implemented. Key features of this design are proper water circulation, effective ventilation, portable, proper light arrangement, and mechanical stability. Each layer of the model consists of four equally shaped components. The dimensions of the components are based on the plant to be grown. The system is created such that it consumes as little space as possible with maximum yield output. This structure can be used in balconies and living rooms.

(a)   (b)   (c)
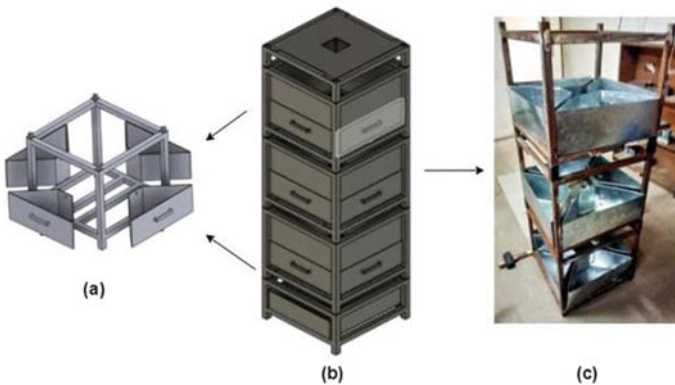
Fig. 2 **a** Single unit of stack, **b** CAD representation of final model and **c** final assembly of fabricated model

3.3 Numerical Analysis

3.3.1 Boundary Conditions

After finalizing the model, the structural analysis of the model was performed. The boundary conditions are: material used is polyethylene terephthalate (PET), and aluminum alloy. Estimated load on each tray is 15 kg. Therefore, a load of 150N was applied in each tray in order to perform the stress analysis. And also the bottom of the structure was kept fixed.

3.3.2 Structural Analysis

The obtained results are showing color distribution of stress analysis of structure, having slight red color at the base of each stack. This showed that if the user wants to increase the weight by adding soil and respective crop, the model needs to be re-evaluated and should be modified according to the user by increasing the thickness of base. Meshing and stress distribution of the final model are shown in Fig. 3.

The software used for performing the analysis is ANSYS static structural module. After applying the boundary conditions, the contours that appear for the structural analysis show us how the structure will behave under the assigned load. The areas with maximum bending moment. The higher stress region is represented by red in the contour plot, while the lower stress region is represented by blue. These contours show us that the distribution of load is even.
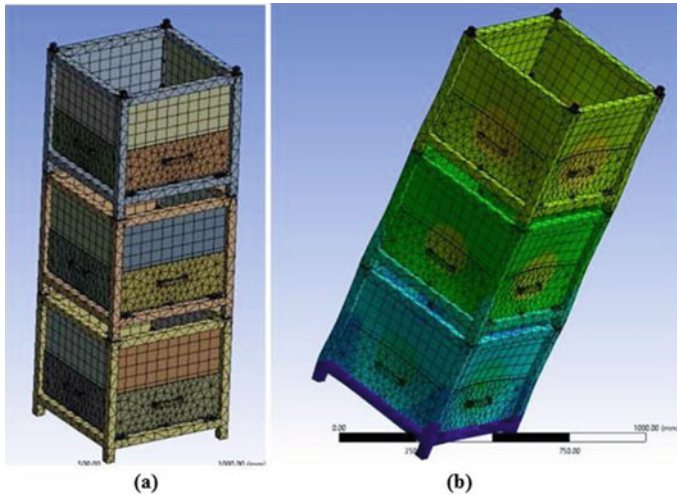
Fig. 3 **a** Meshing and **b** stress distribution on each stack

3.3.3 Air Velocity Analysis

In order to study the airflow velocity distribution around a single stack of the final structure, airflow analysis was performed in ANSYS R16.2. The geometry was simplified first, and then mesh was generated. The boundary conditions were given as the velocity of inlet air equal to 0.8 m/s. The following contours were obtained during the post-processing.

From the above results, we see that the average velocity magnitude across the stack where the soil will be placed is 0.372 m/s which is well within the specified range for natural ventilation of the crop. Also, considering the forced ventilation in the room via ceiling fans will also contribute well. This shows that the oxygen content in the soil will be maintained throughout and there will not be any lack of oxygen during photosynthesis like in any other conventional setup of farming.

4   Results and Discussion

Plants use sunlight, water, and carbon dioxide to produce oxygen and energy in the form of sugar in a process known as photosynthesis. Therefore, oxygen is a by-product of photosynthesis rather than being necessary for it. All plants require oxygen to undergo cellular respiration, which is essential to their life. Additionally to release oxygen as a consequence of photosynthesis, plants also take oxygen from the environment.

The proposed model consists of two stacks, each consisting of four units. Each unit consists of a bitter gourd plant. Each stack has a source of different led lights, i.e. blue and purple lights as shown in Fig. 4. When a plant is given monochromatic light (single light color), the rate of absorption of blue light by chlorophyll is maximum which also increases the rate of photosynthesis, thus increasing the amount of oxygen in the setup environment (Fig. 5).

Plants also increase the content of carbon dioxide in the environment via the respiration process. With carbon dioxide and oxygen enrichment, we see increased product quality and higher yield. Also use of coco peat soil helps in increasing the number of air pockets, which helps in supplying the oxygen to the root of plants.

Daily observations are taken related to the growth of the plants. Heights are noted from the day 1 of the plantations. Some observations are made during the data collection of the plants. The observations are as follows:

1. Plant height growth is quite good during the first two days, and after that, it is gradually increasing.
2. Some plants have shown the yellowing of the leaves on the third–fourth day.
3. The yellowness of plants can be tackled with adequate supply of nutrients such as magnesium and potassium.
4. Some plants are getting new branches from the fifth day.

Fig. 4 Fabricated setup with blue and purple lights
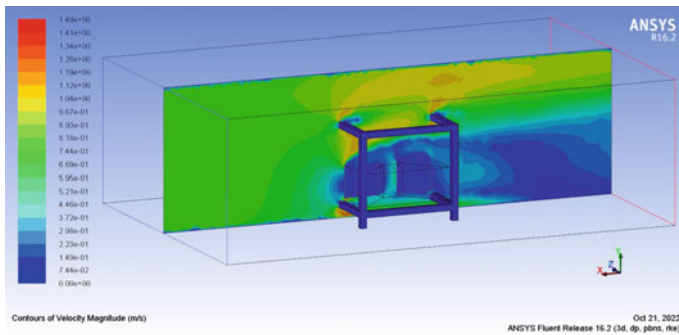
Fig. 5 Air flow analysis: velocity magnitude contour

Figure 6 shows the growth rate of plants named L1, L2, L3C, and L4. The notations are given on the basis of their location in the model, where L stands for lower stack and U stands for upper stack. L3C means the plant is in the lower stack and has a mixture of coco peat soil in it. The plants are placed under purple led lights. *X*-axis represents the date of reading taken, and *Y*-axis represents height of plant in centimeters (cm).

The growth of the plants is observed to be faster in the presence of artificial light as compared to natural sunlight. It can be seen that the growth of a plant under purple light is around 10–17 cm. The selected plant, i.e. bitter gourd, is a creeper type of plant whose growth is measured by its length rather than width. The maximum growth observed under purple lights is 17cm, i.e. of L4. The observations are based on the readings taken in the period of 14–15 days.

Fig. 6 Growth of plants in case of purple lights
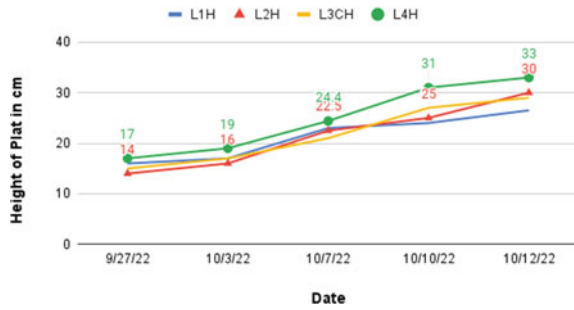
Fig. 7 Growth of plants in case of blue lights
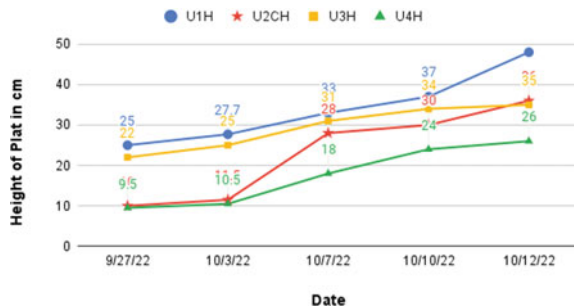
Figure 7 shows the growth rate of plants named U1, U2C, U3 and U4. U2C here means the plant is on the upper stack, and it consists of a mixture of coco peat soil in it. Each stack consists of a plant which has coco peat soil mixed in it. The plants are placed under blue led lights. Blue photons drive the photosynthetic reaction. *X*-axis represents the date of reading taken, and *Y*-axis represents height of plant in centimeters (cm).

The growth of plants is gradually increasing after 2–3 days of being planted. There is a sudden increase in the growth of U2C, consisting of coco peat soil, after the first 4 days. Coco peat helps plants to be healthy due to its antifungal properties. Growth of plants observed in case of blue lights is around 20–26 cm, which is more as compared to plants in case of blue lights, which we will see in the next graph.

Figure 8 shows a comparison between the growth of plants in purple lights and blue lights. Average height of the plants on a particular day is taken and plotted in order to compare the results of two lights. The *X*-axis denotes the date of the reading, and the *Y*-axis represents the height of the plant in cm.

It can be clearly seen that blue lights play an important role in the growth of plants. Growth of plants is more in the case of blue lights as compared to purple lights. The plants have shown sudden increase after 4–5 days of being planted. During the last days of observations, it was seen that the plants under blue lights were growing 3–4 cm per day which shows the impact of blue lights on plants. Blue lights have a wavelength in the range of 440–460 nm, which makes it best for photosynthesis. The

Fig. 8 Comparison of growth of plants in case of blue lights and purple lights
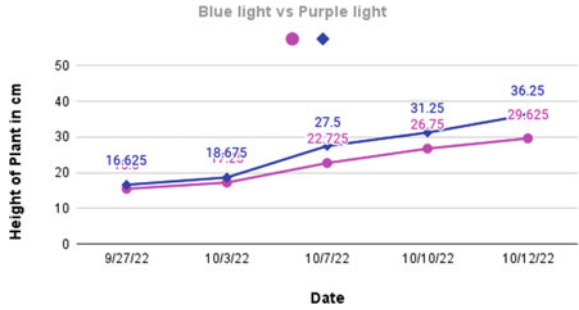
Fig. 9 Plant growth with respect to soil
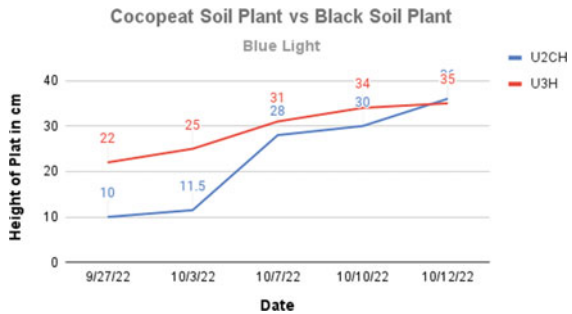
results clearly give an overview of the effect of blue lights as compared to purple lights.

As we are more focused on Blue lights now let us have a comparison between a plant consisting of coco peat mixture and a normal black soil plant. Figure 9 shows a comparison of growth of plants with respect to the soil. The coco peat soil plant, i.e. U2C, is compared with another plant consisting of black soil, i.e. U3. The X-axis denotes the date of reading, and the Y-axis denotes the height of the plant in cm.

The above-displayed line chart clearly states that the growth of the plant is more in case of coco peat soil. Coco peat soil prevents the plant from fungals. Taking a look at readings we can clearly say that the coco peat soil plant has a sudden increase in its growth. Furthermore, it has crossed the height of a normal black soil plant. Also, coco peat has some more features like more water-holding capacity, more efficiency. Little amount of coco peat soil is required to mix in the soil, and it will last a long time.

The above results were based on the growth of plants on the basis of different lights and different soils. We also need to compare these results with the plants that are grown in sunlight. Figure 10 shows a comparison of the plants grown in two different lights and sunlight. One plant reading from each stack, i.e. L1, U1 is taken and plotted on the graph. The X-axis represents the date of reading, and the Y-axis denotes the height of the plant in cm.

The result focuses on comparing the growth in artificial and natural light. From the line chart displayed above, we can say that the growth of plants in blue light is

Fig. 10 Plant growth comparison between artificial lights and natural light
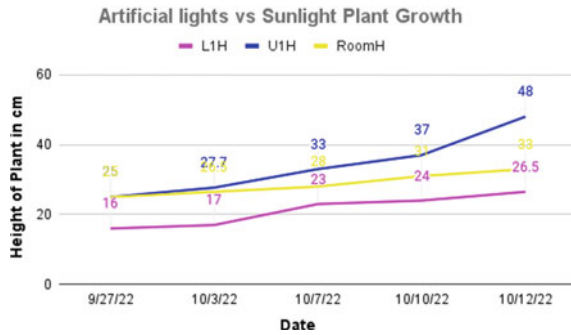
Fig. 11 Area covered by plants in blue lights vs purple lights
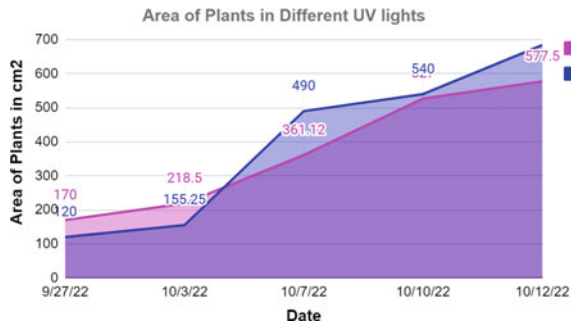
greater than in sunlight. It is because of the continuous supply of blue light. Sunlight is only available at daytime, which affects the growth of plants. As the wavelength range of Blue light lies between 440 and 460 nm, it is considered best for the growth of plants in their early stages. Blue photons are important for photosynthesis.

We can also compare the results based on the area the plant has covered. Area is calculated as a product of plant's length and its width, i.e. distance between the end nodes of two opposite leaves. Figure 11 shows the area covered by plants in different artificial lights. Area of the plant is plotted on the *Y*-axis, whereas date of reading is represented on *X*-axis.

We can clearly see that blue lights are more efficient as compared to purple lights for the early stage of the plant. The sudden increase in the area of plants under blue lights and then gradually increasing and crossing the purple light plants covered area approves our results (Figs. 12 and 13).

5   Conclusions

Major conclusions which can be made from the above results are listed below:

1.   Blue light plants have shown excellent growth as compared to purple light plants.
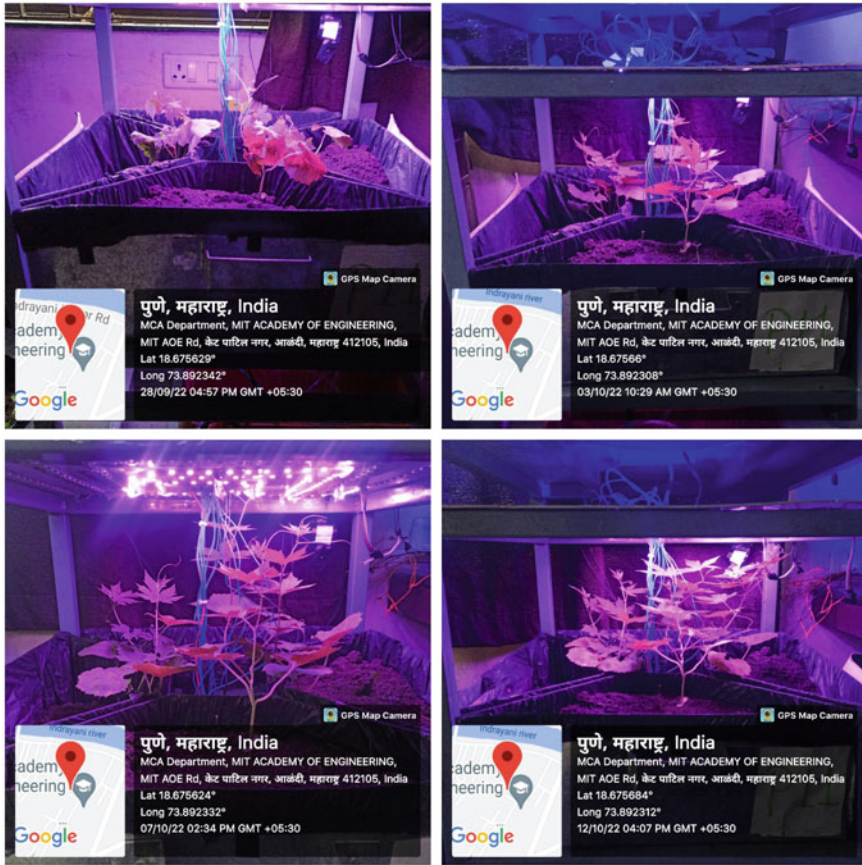
Fig. 12 Plant growth observed under purple lights

2. Mixing of coco peat soil in black soil has increased the plant growth.
3. There is a sudden increase in the growth of plants under blue lights after the first 4 days.
4. Blue lights are more efficient for growth of plants in their early stages.
5. Blue photons play a major role in photosynthesis.
6. Results can also be approved by the area covered, which is more in case of blue lights.

Considering the vertical farm and conventional farm, the distribution of sunlight across all the crops in a conventional farm is considered uniform, while in case of vertical farm, the upper stacks are more exposed to the sun than the lower stacks. This results in faster growth of plants in conventional farming than in vertical farms with respect to sunlight. In conventional farming, the water distribution is done through techniques such as drip irrigation or sprinkler systems.
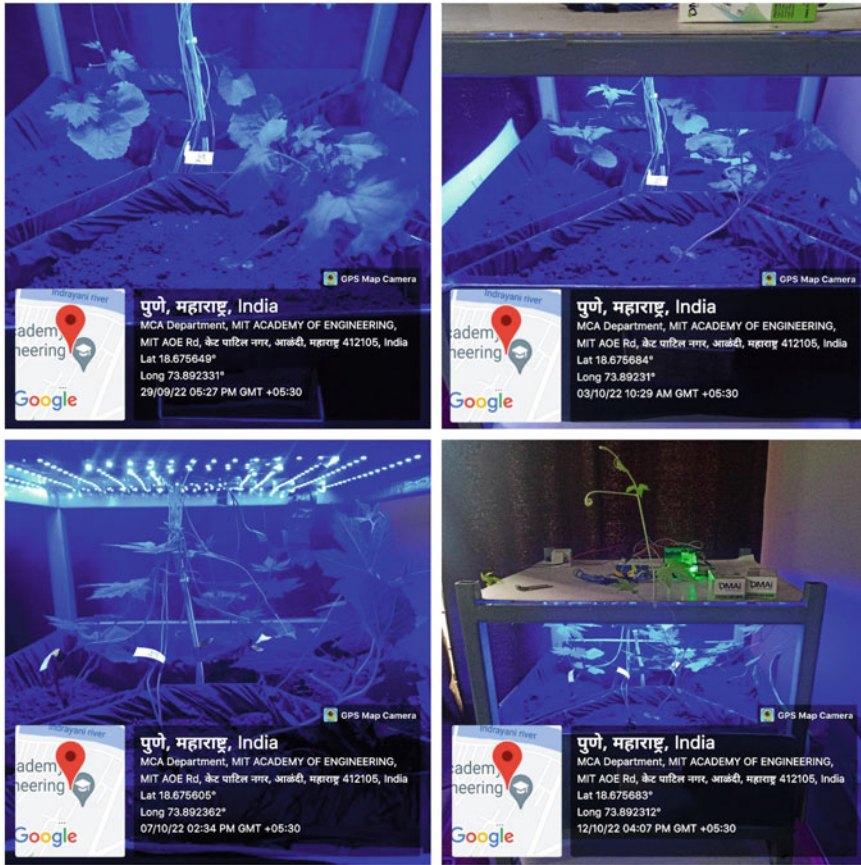
Fig. 13 Plant growth observed under blue lights

This results in excess moisture in the soil, while in the case of vertical farms, the amount of water that flows into each stack is monitored using a moisture sensor, and once the required amount of moisture is reached, the water supply is stopped. Hence forming an automated water supply system. The use of IoT has helped in monitoring and analyzing the data of the moisture sensor.

The above study concludes that the fabricated vertical farming structure is more efficient and cost-effective as compared to traditional farming. The inculcation of artificial lights promotes the growth of the crops; with the addition of IoT systems, the moisture level in soil is maintained to optimum requirement, and hence, better crop yield is obtained. By performing this investigation, we come to know that there is a significant role of different wavelengths of light on the growth of the plants. Here, we observed that the blue light shows more effective results than purple light in terms of the overall growth of the plant and increment of the area of the leaves.

Also, it can be noticed that coco peat has shown more effective results as compared to the black soil.

References

1. Sonawane MS (2018) Status of vertical farming in India. Int Arch App Sci Technol 9:122–125
2. Banerjee C, Adenauer L (2014) Up, up and away! The economics of vertical farming. J Anim Sci 2:40–60
3. König B et al (2018). Analysis of aquaponics as an emerging technological innovation system. J Clean Prod 180:232–243. https://doi.org/10.1016/j.jclepro.2018.01.037
4. Lakhiar IA, Gao J, Syed TN, Chandio FA, Buttar NA (2018) Modern plant cultivation technologies in agriculture under controlled environment: a review on aeroponics. J Plant Interact 13(1):338–352. https://doi.org/10.1080/17429145.2018.1472308
5. Sharma N, Acharya S, Kumar K, Singh N, Chaurasia O (2019) Hydroponics as an advanced technique for vegetable production: an overview. J Soil Water Conserv 17:364–371. https://doi.org/10.5958/2455-7145.2018.00056.5
6. Makino A, Mae T (1999) Photosynthesis and plant growth at elevated levels of CO_2. Plant Cell Physiol 40(10):999–1006. https://doi.org/10.1093/oxfordjournals.pcp.a029493
7. Papasolomontos A, Baudoin W, Lutaladio N, Castilla N, Baeza E, Montero J, Teitel M, Lopez J, Kacira M, Kittas C, Katsoulas N, Bartzanas T, Bakker S, Leonardi C, Maggio A, Gallardo M, Thompson R, Fernandez MD, Abou Hadid A, Patsalos K (2013) Good Agricultural Practices for greenhouse vegetable crops. In: Principles for Mediterranean climate areas
8. Schwamberger E, Sims J (1991) Effects of soil pH, nitrogen source, phosphorus, and molybdenum on early growth and mineral nutrition of burley tobacco. Commun Soil Sci Plant Anal 22(7–8):641–657
9. Yusof SSS, Thamrin NM, Nordin MK, Yusoff ASM, Sidik NJ (2016) Effect of artificial lighting on *Typhonium flagelliforme* for indoor vertical farming. In: 2016 IEEE international conference on automatic control and intelligent systems (I2CACIS), pp 7–10. https://doi.org/10.1109/I2CACIS.2016.7885280
10. Bin Ismail MIH, Thamrin NM (2017) Iot implementation for indoor vertical farming watering system. In: 2017 international conference on electrical, electronics and system engineering (ICEESE), pp 89–94. https://doi.org/10.1109/ICEESE.2017.8298388
11. Urban farming construction model on the vertical building envelope to support the green buildings development in Sleman, Indonesia. In: The 3rd international conference on sustainable civil engineering structures and construction materials—sustainable structures for future generations (Proc Eng 171:258–264). https://doi.org/10.1016/j.proeng.2017.01.333
12. Birkby J (2016) Vertical farming. ATTRA Sustain Agric 2:1–12
13. Avgoustaki DD, Xydis G (2020) Indoor vertical farming in the urban nexus context: business growth and resource savings. Sustainability 12(5):1965
14. Veihmeyer F, Hendrickson A (1950) Soil moisture in relation to plant growth. Annu Rev Plant Physiol 1(1):285–304
15. Besthorn F (2013) Vertical farming: social work and sustainable urban agriculture in an age of global food crises. Aust Social Work 66. https://doi.org/10.1080/0312407X.2012.716448

Improvement in Sealing Effectiveness of Air Curtains Using Positive Buoyancy

Tanmay Agrawal, Narsing K. Jha, and Vamsi K. Chalamalla

1 Introduction

The prevalence of buoyancy-induced density gradients is quite common in building flow applications, e.g., consider a doorway across which the fluids are maintained at different temperature levels. As a result, a driving force is manifested, which leads to bulk fluid transport across the door. To counter such exchange flows, air curtains (AC) are generally installed in the vicinity of a doorway to facilitate aerodynamic sealing. In addition to this inhibition, they also allow free passage for the building occupants without imposing a physical obstruction, thereby making them usable in a multitude of situations. Their other common applications include shopping complexes, food plazas, refrigerated cabinets, medical facilities, restriction of smoke in tunnel fires, etc. A typical AC installation utilizes a planar (rectangular) nozzle in which the air supply is sent by a blower after necessary flow conditioning. The supplied fluid can be taken either from within the room/building under consideration or from its ambient. Most usually, these installations are downward blowing, and in such cases, the air curtain impinges vertically on the floor. In other installations, the AC jet could be upward or sideways blowing with some angular tilt from the doorway. A brief comparison of various such arrangements was explored numerically by Gonçalves et al. [1] around a decade ago.

While the initial patent for the air curtain technology dates back to the early twentieth century, it was only in the late 1960s that the performance of AC was first quantified systematically by Hayes and Stoecker [2]. They measured velocity and temperature profiles along the air curtain axis in a full-scale experimental setup. Based on these measurements, they defined a dimensionless parameter, referred to as the deflection modulus, D_m, representing the ratio of the initial momentum flux contained within the AC jet and the 'stack-effect' induced transverse force as a result

T. Agrawal (✉) · N. K. Jha · V. K. Chalamalla
Department of Applied Mechanics, IIT Delhi, Hauz Khas, New Delhi 110016, India
e-mail: tanmay.agrawal@am.iitd.ac.in

of buoyancy difference. Mathematically, D_m is written as.

$$D_m = \frac{\rho_0 b_o u_0^2}{g H^2 (\rho_d - \rho_l)} = \frac{b_o u_0^2}{g H^2 \left(\frac{T_o}{T_d} - \frac{T_o}{T_l} \right)}, \tag{1}$$

where the subscripts o, l and d are associated with the curtain, light and dense fluids, respectively. T denotes the fluid temperature, and its density, ρ, has been obtained using the ideal gas law. The rectangular nozzle has a width, b_o, and the mean exit velocity is represented as u_o, assuming a top-hat distribution. Lastly, H denotes the doorway height, and g refers to the gravitational acceleration. Hayes and Stoecker demonstrated that the stability of an AC installation could be assessed based on the 'reach' of the planar jet, which can be characterized through D_m. If the jet fluid impinges on the other side of the doorway, i.e., the floor of the room when the AC is downwards blowing, it is said to be stable and is deemed unstable (or breakthrough) otherwise. This transition from an unstable installation to a stable AC occurs at a minimum deflection modulus, $D_{m, min}$, the value of which is affected by the geometrical aspects (b_o, H) as well as the operating conditions (ρ_0, ρ_l, ρ_d). Other pathways of fluid leakage, e.g., windows for natural ventilation, etc., can also affect this critical value of D_m.

In the presence of a stack effect where $\rho_l \neq \rho_d$, the performance of an air curtain is measured by estimating the sealing effectiveness, E. Physically, E represents the exchange flow suppression obtained after employing an air curtain in comparison with that of an open-door scenario, i.e.,

$$E = 1 - \frac{q}{q_{OD}} \tag{2}$$

Here, q is the volumetric exchange flow rate through the door with the air curtain installed, whereas q_{OD} denotes the open-door-based exchange flow rate. Thus, the effectiveness of unity corresponds to a perfectly sealed doorway where the infiltration of the ambient fluid has been completely brought down. On the other hand, a value of zero suggests an absence of an air curtain, i.e., an open-door situation. The existing literature suggests that AC can inhibit up to ~80% of the total buoyancy-driven exchange flow across a doorway [1–8].

In a typical installation, the air curtain feeds on the fluid in its vicinity, i.e., the blower sucks in the indoor fluid when the AC is installed inside the building space and vice versa. Most usually, this supply fluid does not undergo any thermal treatment before being sent to the nozzle exit and is thus neutrally buoyant for the surrounding fluid. In the present study, we numerically investigate the relevance of positive buoyancy in the context of air curtain flows; i.e., the density of the air curtain fluid is larger than that of the surrounding fluid. From a thermodynamic perspective, we consider the case when the supply fluid is cooled before blowing vertically downwards through the AC nozzle. This situation was first studied experimentally by Howell and Shibata [9], who also observed a minimum deflection modulus below

which the air curtain was not effective towards aerodynamic sealing. The dynamical aspects of a 'negatively' buoyant air curtain were recently pursued by Frank and Linden [10] where the air curtain was lighter than the ambient fluids. To the best of the authors' knowledge, there hasn't been any study investigating the performance of positively buoyant AC using numerical methods. Therefore, this work primarily focuses on estimating the sealing effectiveness of such air curtain installations using two-dimensional (2D) Reynolds-averaged Navier–Stokes (RANS) simulations. We seek to understand the influence of operating conditions (through varying D_m) on the effectiveness of these positively buoyant AC.

The computational setup and methodology are discussed briefly in Sect. 2. The results obtained from the present simulations are presented in Sect. 3. We first present the temperature distribution in the computational domain for different operating conditions, followed by the estimates of sealing effectiveness. Lastly, we present estimates of jet spillage in the building space in the presence of a transverse buoyancy. Further, considerations of fluid mixing and flow structures are a work in progress and are not included in the current paper.

2 Methodology

Reynolds-averaged Navier–Stokes (RANS) formulation has been adopted to numerically simulate the positively buoyant air curtains. Herein, any instantaneous quantity is decomposed in its mean value and a fluctuating part. In all the simulations reported, water is chosen as the working fluid to facilitate a direct comparison with the experimental data (described later) obtained for the neutrally buoyant AC. In practical situations, different densities required in the flow can be achieved using dissolved salts (ocean), thermal gradients (atmosphere), suspended particles, etc. For the present simulations, we employ temperature inhomogeneities to create the required density difference, and the corresponding temperature levels are chosen to reflect the thermal comfort requirement in the Indian subcontinental situation. The fluid is assumed to be incompressible, and the density differences are small such that the Boussinesq approximation can be adopted. The following equations are numerically solved to simulate positively buoyant AC:

$$\frac{\partial \overline{u_i}}{\partial x_i} = 0$$

$$\rho \frac{\partial \overline{u_i}}{\partial t} + \rho \overline{u_k} \frac{\partial \overline{u_i}}{\partial x_k} = -\frac{\partial \overline{p}}{\partial x_k} + \frac{\partial}{\partial x_k}\left[\mu \frac{\partial \overline{u_i}}{\partial x_k} - \rho \overline{u_i' u_k'}\right]$$

$$\frac{\partial \overline{T}}{\partial t} + \overline{u_k} \frac{\partial \overline{T}}{\partial x_k} = \frac{\partial}{\partial x_k}\left[\kappa \frac{\partial \overline{T}}{\partial x_k} - \overline{u_i' T'}\right].$$

These are mathematical representations of the conservation of mass, momentum and energy, respectively. Here, u_i, p and T represent the ith velocity component ($i = 1, 2$), pressure and the temperature, respectively. The symbols x_i and t denote the ith spatial coordinate and time. μ represents the dynamic viscosity of the fluid, ρ, its density, and κ denotes the thermal diffusivity. In these equations, an overbar represents an averaged (or mean) quantity, while a superscripted prime ($'$) represents the corresponding fluctuating quantity. The unclosed terms in these equations, e.g., $\overline{\rho u_i' u_k'}$, $\overline{u_i' T'}$, are modelled using the renormalization group (RNG) $k - \epsilon$ turbulence model [11]. We use the RNG $k - \epsilon$ model over other turbulence closure models based on its superiority to simulate plane turbulent jets as was suggested by the extensive RANS simulations conducted by Khayrullina et al. [12].

A. Computational Setup and Boundary Conditions

As described in the preceding section, we study the positively buoyant AC using RANS-based two-dimensional numerical simulations. Towards this, the computational box employed in this study, the size of which is $L = 2.1$ m, $H = 0.35$ m, along with the corresponding boundary conditions, is shown in Fig. 1. For the present simulations, the space under consideration (indoor) that requires sealing spans from the left wall $x = 0$) to the domain centre $x = 1.05$ m) and is initially filled with a cold fluid ($T = 25°C$). An air curtain is provided at the top, just inside the building space, that blows air at a temperature lesser or equal to that of the indoor fluid. In this work, we report simulations with the jet temperatures ranging between 15 and 25°C. Outside the doorway, a warm fluid ($T = 45$ °C) fills in the rest of the computational domain, thus resulting in a reduced gravity, $g' = g \frac{\Delta \rho}{\rho_{av}} \approx 6.7$ cm/s^2. Here, ρ_{av} is taken as the average density of the indoor and outdoor fluid densities. This setup replicates the temperature levels prevalent in the Indian subcontinent in summer situations and thus seeks optimization of the thermal comfort of building occupants using air curtains. We use ten grid points across the nozzle width at the AC exit based on the recommendation of [13] and a grid independence study (not shown) where the jet statistics were evaluated and compared with the data available in the literature. In order to resolve the spatial instabilities in the air curtain jet and the sharp density gradient at the doorway location, the central region of the domain is locally refined symmetrically (refer to the hatched region in Fig. 1). This local refinement allows accurate estimation of the volumetric exchange that primarily initiates at the centre of the domain as a result of initial horizontal stratification. At the jet exit, which °C supplied, and the supply temperature is systematically varied to study its effect on the temperature distribution in the indoor space and the corresponding sealing effectiveness. The resulting doorway height to nozzle width ratio, $\frac{H}{b}$, is fixed at 84 in our simulations which is similar to that of real-scale air curtain installations [3]. The side walls of the computational domain are assigned as outflows to simulate a large ambient situation. We also conducted some simulations using a 'pressure-outlet' boundary condition, and no significant differences were observed in bulk flow estimates. All the other walls of the computational domain are treated as insulated with no slip and no fluid penetration across them.
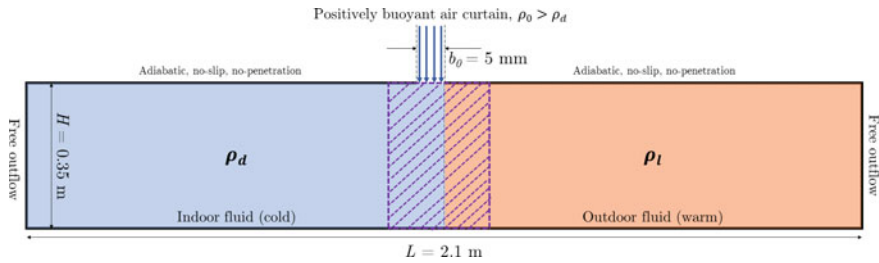
Fig. 1 Schematic of the simulated domain and the corresponding boundary conditions (not per scale)

B. Solver Settings

The ANSYS FLUENT package is used to solve the governing equations of fluid flow and heat transfer. We employ a second-order upwind scheme to approximate the spatial derivatives present in the advective and viscous terms of the governing equations and that associated with the turbulence model. To discretize the temporal field, a first-order implicit method is used, and the time step requirement is constrained by the CFL number of 0.8. The coupled algorithm is used to link the pressure and velocity fields in these incompressible simulations. Three different jet temperatures are simulated in the present work: 15, 20, and 25 °C that results in the reduced gravity between the indoor and curtain fluid, $g' = g \frac{\Delta \rho_{IC}}{\rho_o}$ of approx. 2 cm/s^2, 1 cm/s^2 and 0. For each of these cases, eight simulations are conducted at various values of D_m ranging between 0.05 and 1.5. An additional simulation is also conducted without an air curtain installed, i.e., $D_m = 0$. This scenario is formally known as a lock-exchange flow (LEF) [14] and has been used as a base case for comparison with the air curtain cases. The exchange flow associated with the LEF case is mathematically evaluated as q_{OD}, whereas that with the AC installations is estimated as q (refer Eq. 2). Thus, a total of 25 distinct simulations are reported in this paper.

3 Results and Discussion

The results from the present simulations are now discussed. The adopted simulation methodology based on the 2D RANS simulation and the RNG $k - \epsilon$ turbulence model was first validated against the analytical solution and data available in the literature. The validation was performed for the cases of a pure jet (equivalent to an air curtain under isothermal conditions) and that of a neutrally buoyant air curtain where the buoyancy difference between the air curtain and indoor fluid is zero. These validation metrics are discussed in detail in Agrawal et al. [8] and are not presented here. Overall, a good agreement is observed using the adopted computational methodology.

A. Effect of Deflection Modulus

First, we present the temperature distribution in the computational domain for different values of deflection modulus to illustrate the effect of jet 'strength' on the

aerodynamic sealing in a qualitative way. Figure 2 shows the temperature contours for the cases of D_m of 0, 0.1, 0.4 and 1.5 when the jet inlet temperature is 15 °C. The corresponding no AC case, i.e., the LEF scenario, as illustrated in the top panel, allows a free exchange of the two fluids across the doorway. This results in a gradual increment in the room temperature following convection-driven bulk transport, mixing and thermal diffusion, which is highly undesirable from a thermal comfort perspective. In comparison, when an air curtain is installed, this exchange is significantly suppressed, as shown in the other panels.
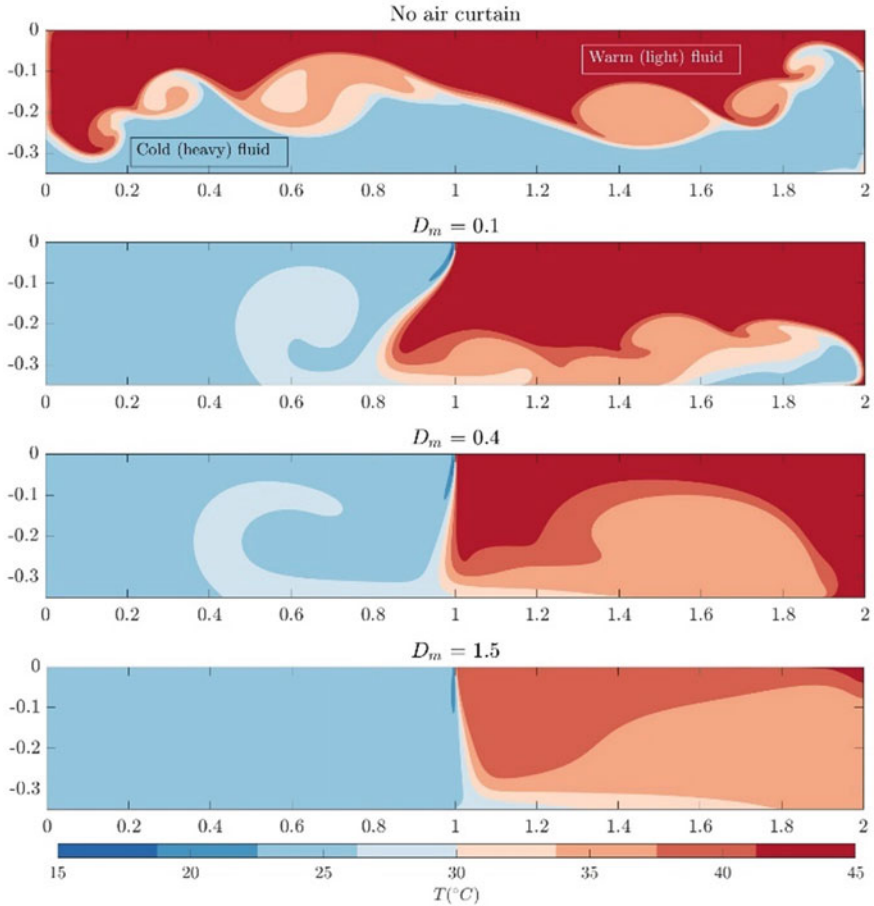
Fig. 2 Temperature distribution (°C) in the domain for different values of D_m at $t^* = t\sqrt{\frac{g'}{H}} = 7$ and with $T_0 = 15$ °C

When the jet is relatively weaker ($D_{\mathrm{m}} \leq 0.1$), it deflects towards the dense fluid owing to buoyancy and pressure forces and also allows some buoyancy-driven exfiltration (see the blue patch beyond $x > 1.6$ m in the second panel). Such AC installations are usually termed unstable or breakthrough as they do not impose a complete sealing across the height of the doorway. Irrespective of the magnitude of positive buoyancy imposed at the jet exit, we observe similar behaviour of positively buoyant AC at small values of D_{m} which is consistent with their neutrally buoyant counterpart. In the present study, we increase the initial jet momentum flux to increase D_{m} and observe that the jet impinges almost vertically on the floor at higher values of D_{m} (see the third and fourth panels). This ensures proper sealing across the doorway, and the air curtain installation is deemed *stable*. No exfiltration is observed at these values of deflection modulus, and the primary source of bulk fluid transport appears to stem from the fluid entrainment and turbulent mixing along the edges of the jet and near the impingement region. When the deflection modulus increases; further, it can be observed that the fluid is very well mixed as compared to the other cases. The quantitative implications of the deflection modulus on sealing effectiveness are discussed in the next section.

B. Sealing Effectiveness

Based on Eq. 2, the performance of an air curtain is obtained using the fraction of exchange flow that it suppresses as compared to the case of a doorway with no air curtain installed. In the absence of an AC, the volumetric exchange can be theoretically estimated using the orifice equation as:

$$q_{\mathrm{OD}} = \frac{1}{3} C_{\mathrm{d}} A \sqrt{g' H}.$$

Here, C_{d} represents the coefficient of discharge, and A is the cross-sectional area available at the exchange site and is taken as the doorway height for the present 2D computations. The exchange flow, q_{OD}, obtained from our simulations for the case of $Q = 0$, results in a C_{d} of 0.56, which agrees very well with the empirical estimate of 0.6 for a rectangular orifice. To estimate the exchange flow in the presence of an air curtain, we use the mass conservation in the indoor space [6]:

$$q = \frac{V_{\mathrm{o}}}{t} \left(\frac{\rho_{\mathrm{d}} - \overline{\rho}}{\rho_{\mathrm{d}} - \rho_{\mathrm{l}}} \right) + \beta Q \left(\frac{\rho_0 - \overline{\rho}}{\rho_{\mathrm{d}} - \rho_{\mathrm{l}}} \right).$$

Here, V_0 is the constant volume of the indoor space, and Q denotes the volumetric flow rate (in m²/s) supplied by the AC per unit width. β represents the spillage fraction of the AC jet fluid inside the room after impingement on the floor. We take β as 0.5 following the discussion in [6]. Lastly, $\overline{\rho}$ is the mean fluid density inside the room at any time instant t.

The sealing effectiveness estimates for all the simulations reported in the present study are shown in Fig. 3a and also compared with the experimental estimates of Jha et al. [6] who measured the effectiveness of neutrally buoyant AC using bulk

density measurement techniques. First, it can be seen that a good agreement exists between the present neutrally buoyant AC and those of Jha et al. While the RANS simulations overpredict the quantitative values by a certain amount, especially at higher deflection modulus, the overall behaviour with varying D_m is captured well. At low values of deflection modulus, owing to jet deflection, the effectiveness is rather small for the breakthrough case. Once the D_m increases, the sealing becomes more prominent. We obtain the peak effectiveness in the range of $D_m \approx 0.2$–0.4, which is similar to that of experimental results. Upon increasing the deflection modulus further, there is a gradual decrease in E, which is usually attributed to more mixing in the computational domain due to turbulence. In comparison with the neutrally buoyant AC, upon supplying the air curtain fluid with positive buoyancy, we observe an increase in sealing effectiveness. This is because the additional buoyancy in the AC jet assists in maintaining the indoor fluid density (temperature), and as a result, the corresponding density difference, $\rho_d - \overline{\rho}$, decreases, resulting in larger effectiveness. In extreme cases, it is also possible that the added buoyancy in the air curtain can nullify the effects of fluid transport from the outdoor space. However, that possibility was not explored in the present study and could be considered in future studies.

As illustrated in Fig. 3b, the percentage increase in the sealing effectiveness, as compared to its neutrally buoyant counterpart, is a weak function of D_m when the air curtain is stable ($D_m > 0.1$). For smaller values of D_m, the relatively higher ΔE is due to the deflection of positively buoyant air curtain inside the room, which increases the mean indoor fluid density. For the cases of T_0 being 15 and 20 °C, we calculate the maximum relative increment in the effectiveness of stable AC to be of the order of ~10%. Whereas the maximum sealing effectiveness is found to be 5% larger than its corresponding value for a neutrally buoyant air curtain. This maximum is achieved at the deflection modulus of approximately 0.4.

3.1 Fractional Spillage of the AC Jet

In this section, we present estimates of β for the case of positively buoyant AC for varying deflection modulus. To compute this, we introduce a passive scalar in the air curtain jet and compute the mean spatial concentration of this scalar in the computational domain. In isothermal case, i.e., $\rho_l = \rho_d = \rho_0$, the jet divides itself symmetrically across the doorway, i.e., $\beta = 0.5$, if the outlets are symmetrical. However, it is known that the transverse buoyancy affects the longitudinal path travelled by jet, especially at lower values of D_m (see the second panel in Fig. 2). Therefore, the fractional spillage, β, might differ from the isothermal value of 0.5 if the effect of transverse buoyancy is substantial. The estimates of β are inherently difficult to obtain through experiments due to the number of species involved in such measurements. Generally, either salt or heat is used to create density differences required for the initial horizontal stratification. If detailed quantitative information is sought, then other scalars, for example, a fluorescent dye to measure the scalar field, are also

Fig. 3 Sealing effectiveness of the positively buoyant air curtains
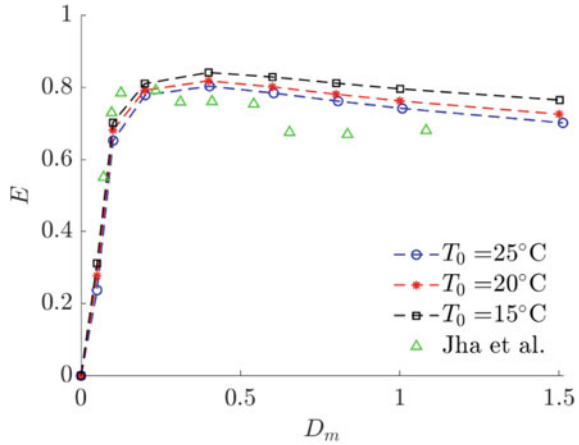
(a) **Effectiveness as a function of deflection modulus for all the present simulations.**
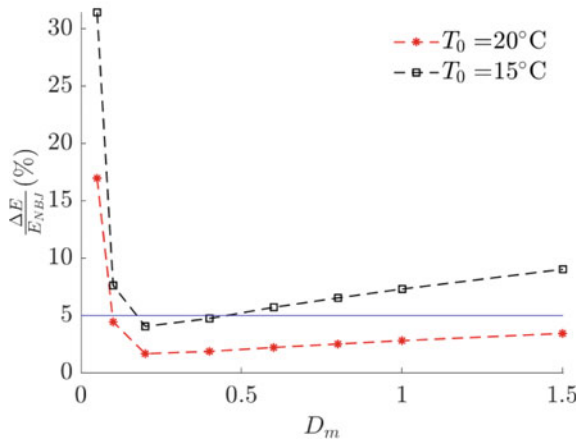
(b) **Percentage increase in effectiveness as compared to the neutrally buoyant AC.**

used. However, direct measurements of a passive scalar to compute β have not been reported to the best of our knowledge.

Figure 4 shows the variation of the spillage fraction, β, for various deflection modulus for the case of $T_0 = 15\,^\circ\text{C}$. The unusually high value of β at low D_m of 0.1 is due to the jet deflection (refer to the Fig. 2). However, once the air curtain is stable, the nominally assumed value of $\beta = 0.5$ appears to be a reasonable estimate. In the range of deflection modulus between 0.4 and 1.5, this does not introduce an error of more than 5% in the estimates of sealing effectiveness. An interesting observation from Fig. 4 is that β reduces slightly with an increase in D_m. This might be attributed to the different density fluids in the computational domain in which the air curtain

Fig. 4 Spillage fraction, β, for different values of D_m with $T_0 = 15\ ^\circ\mathrm{C}$
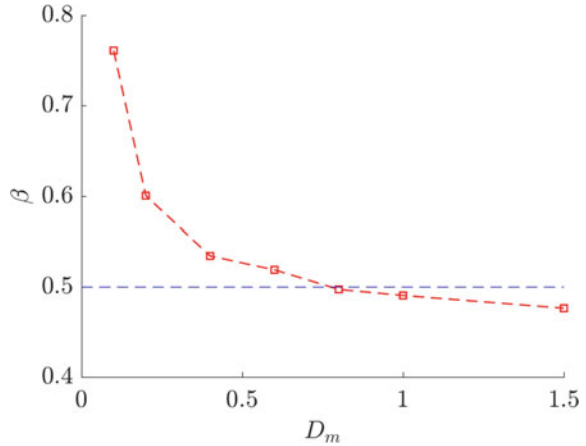
jet penetrates. Consider the indoor space, for example, where the effective density difference for the incoming jet $\rho_0 - \rho_\mathrm{d}$, is smaller than its ambient counterpart, $\rho_0 - \rho_\mathrm{l}$. This results in a larger penetrating force in the outside space and, thus, a smaller β.

4   Conclusions

This paper reported 2D simulations of positively buoyant air curtain flows using the Reynolds-averaged Navier–Stokes (RANS) methodology. The computations employed the RNG $k - \epsilon$ model for turbulence closure and were performed in ANSYS FLUENT. The sealing effectiveness of air curtains was estimated using these simulations for a range of deflection modulus between 0.05 and 1.5 and for three different jet temperature levels. It was shown that the sealing effectiveness increased as the extent of positive buoyancy increased. In comparison with the neutrally buoyant case, the peak effectiveness of the positively buoyant AC was found to be 5% larger, whereas the maximum increment was computed to be ~10%. The jet spillage fraction was also estimated by introducing a passive scalar in the air curtain jet. It was observed that the isothermal value of 0.5 does not introduce errors of more than 5% in the computation of sealing effectiveness when the deflection modulus is larger than ~ 0.4.

Nomenclature

Re   Reynolds number
β Spillage fraction
t^* Dimensionless time

D_m	Deflection modulus
E	Sealing effectiveness
C_d	Coefficient of discharge
A	Cross-sectional area (m^2)
T	Time (s)
b_0	Nozzle width at exit (m)
H	Doorway height (m)
P	Density (kg/m^3)
u_0	Nozzle velocity at exit (m/s)
P	Pressure (Pa)
T_0	Exit jet temperature (K)
Q	Exchange flow rate (m^3/s)
q_{OD}	Exchange flow without air curtain (m^3/s)
g'	Reduced gravity (m/s^2)
μ	Dynamic viscosity (Pa s)

References

1. Gonçalves JC, Costa JJ, Figueiredo AR, Lopes AMG (2012) CFD modelling of aerodynamic sealing by vertical and horizontal air curtains. Energy Build 52:153–160
2. Hayes FC, Stoecker WF (1969) Design data for air curtains. ASHRAE Trans 75(2):168–180
3. Costa JJ, Oliveira LA, Silva MCG (2006) Energy savings by aerodynamic sealing with a downward-blowing plane air curtain—a numerical approach. Energy Build 38(10):1182–1193
4. Foster AM, Swain MJ, Barrett R, D'Agaro P, Ketteringham LP, James SJ (2007) Three-dimensional effects of an air curtain used to restrict cold room infiltration. Appl Math Model 31(6):1109–1123
5. Frank D, Linden PF (2014) The effectiveness of an air curtain in the doorway of a ventilated building. J Fluid Mech 756:130–164
6. Jha NK, Frank D, Linden PF (2021) Contaminant transport by human passage through an air curtain separating two sections of a corridor: part I—uniform ambient temperature. Energy Build 236:110818
7. Jha NK, Frank D, Darracq L, Linden PF (2021) Contaminant transport by human passage through an air curtain separating two sections of a corridor: Part II—two zones at different temperatures. Energy Build 236:110728
8. Agrawal T, Jha NK, Chalamalla VK (2021) Towards understanding air curtain flows using RANS based numerical simulations. In: Proceedings of the 26thNational and 4th International ISHMT-ASTFE Heat and Mass Transfer Conference December 17–20, 2021, IIT Madras, Chennai-600036, Tamil Nadu, India. Begel House Inc
9. Howell RH, Shibata M (1980) Optimum heat transfer through turbulent recirculated plane air curtains. ASHRAE Trans 2567:188–200
10. Frank D, Linden PF (2015) The effects of an opposing buoyancy force on the performance of an air curtain in the doorway of a building. Energy Build 96:20–29
11. Yakhot VSASTBCG, Orszag SA, Thangam S, Gatski TB, Speziale C (1992) Development of turbulence models for shear flows by a double expansion technique. Phys Fluids A 4(7):1510–1520
12. Khayrullina A, van Hooff T, Blocken B, van Heijst G (2019) Validation of steady RANS modelling of isothermal plane turbulent impinging jets at moderate Reynolds numbers. Eur J Mech B Fluids 75:228–243

13. Krajewski G, Węgrzyński W (2015) Air curtain as a barrier for smoke in case of fire: numerical modelling. Bull Pol Acad Sci Techn Sci 63:145–153
14. Agrawal T, Ramesh B, Zimmerman SJ, Philip J, Klewicki JC (2021) Probing the high mixing efficiency events in a lock-exchange flow through simultaneous velocity and temperature measurements. Phys Fluids 33(1):016605

Numerical Studies to Assess the Effect of Simulated Recombiner on Helium Distribution and Mixing in a Scale Down Containment Facility, CSF

Nandan Saha, B. Gera, V. Verma, and J. Chattopadhyay

1 Introduction

Release of hydrogen into the containment building is possible in water-cooled nuclear reactors during the postulated severe accident (SA) conditions. This hydrogen may create a highly combustible hydrogen-air mixture inside the containment building upon mixes with the containment atmosphere. Depending on the prevailing thermal hydraulic conditions, unfortunate ignition of this combustible mixture may threaten the integrity of the containment building. This may cause uncontrolled release of radioactivity in the environment as seen in the recent Fukushima (2011) accident [1]. Hence, effective management of this hydrogen is a major safety challenge for the containment safety designers. As a hydrogen mitigation majors, Passive Catalytic Recombiner Devices (PCRDs) are being deployed in Indian reactors. To find the suitable positions and the required number of PCRDs, transient three-dimensional (3D) hydrogen concentration scenarios following an accident sequence should be known as priori. In this regard, CFD-based simulations are required to be performed. However, before performing the actual reactor calculations, validation exercise must be performed.

For performing validation exercise, experimental data on hydrogen distribution with and without PCRD is must. However, performing hydrogen distribution experiments in actual containment scale is impossible. Highly combustible nature of hydrogen gas makes it further difficult. Worldwide different facilities are commissioned to perform hydrogen distribution studies at different scales. Among the facilities, LSCF (AECL) [2], THAI [3], PANDA [4], MISTRA [4, 5], etc., are very important from reactor safety perspective. A multi-compartment scaled-down containment facility is commissioned in BARC for thermal hydraulic study. This facility is known

N. Saha (✉) · B. Gera · V. Verma · J. Chattopadhyay
Reactor Safety Division, Bhabha Atomic Research Centre, Mumbai 400085, India
e-mail: nsaha@barc.gov.in

as Containment Studies Facility (CSF) [6] which is approximately 1:250 volumetrically scaled-down model of a standard 220 MWe Indian Pressurized Heavy Water Reactor (PHWR) containment building. Handling large quantities of hydrogen poses major safety concern. Due to this, it is a standard practice worldwide [2, 4] to use helium as a surrogate gas to hydrogen in all the distribution studies. To simulate the PCRD induced flow and its effect on helium mixing characteristics, simulated PCRDs are used. In simulated PCRDs, catalyst plates are replaced with heater plates to mimic the same heat release rate. In CSF also, helium distribution experiments with and without simulated recombiner devices are being performed. Before performing the experiments, blind CFD simulations have been performed. The results of blind simulations are presented here.

In the context of reactor safety, several CFD-based hydrogen/helium distribution studies are available in the literature [7–10]. Most of the literature are aimed at performing validation studies before going for actual reactor calculations. The major aim is to develop a CFD code or to validate a commercially available code for accurate containment calculations. In this present work, commercially available code CFD-ACE+ is used for helium distribution simulation in CSF geometry with and without the simulated PCRDs as part of blind exercise. In this paper, the details of the CSF geometry, various parameters, modelling approaches, simulation results and findings are presented.

2   Problem Description and Modelling

CSF is a multi-compartment containment structure having internal diameter of 5.7 m and height of 7.15 m as shown in Fig. 1a. CSF consists of four levels. The upper three levels represent the V1 volume while the basement represents the V2 volume of PHWR. V1 and V2 volume are connected via several vent pipes. In the present study, the V2 volume is isolated from V1 volume. Hence, only V1 volume is modelled as shown in Fig. 1a. The V1 volume consists of three levels, e.g. ground floor, first floor and the dome area. The ground floor has two compartments (R1 and R2) in half cylindrical shape representing fuelling machine vaults with another annular compartment R10 surrounding them. The helium is injected in this R1 compartment. Hence for helium distribution study, the CSF volume above the ground floor which is the floor of injection room is considered. The first floor that has two quarter cylindrical rooms, R3 and R4, represents steam generator vaults and pump rooms, situated directly above the rooms R1 and R2, respectively. In between R3 and R4, R5 and R6 compartments are situated in the first floor. Above first floor, the entire dome shape area is representing the containment dome (R7) of 220 MW$_e$ PHWR. The annular space behind R3 is designated as R8 while the annular space behind R4 is designated as R9. R5, R6, R8 and R9 are directly connected to the dome at the top. The ground floor annular space behind R1 and R2 are designated as R10. Ground floor and the first floor are connected via 8 rectangular openings situated in the annulus. Different compartments of CSF are interconnected through several

openings as shown in Fig. 1a, b. Openings between R1 and R2 are closed in all the simulations as in actual case where the fuelling machine vaults are isolated. Helium injected in R1 can only can only escape through top horizontal opening between R1 and R3. The dimensional details are shown in Fig. 1a. The total internal volume of the V1 region of CSF is ~150 m³.

In this present study, CFD-based numerical studies have been performed to assess the effect of simulated recombiner on the helium distribution and mixing behaviour
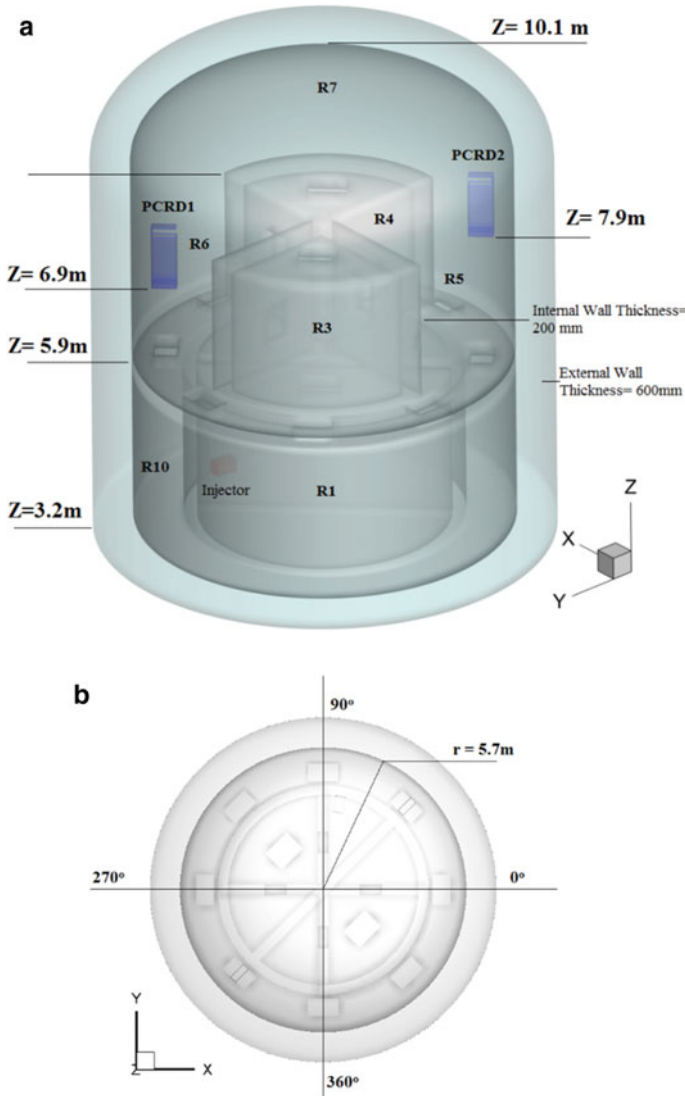
Fig. 1 a 3D geometry of CSF with both the PCRD. **b** Top view of CSF

in CSF geometry. In the simulated Passive Catalytic Recombiner Devices (PCRDs), the catalyst plates are replaced with heater plates to mimic the same heat release rate and thereby the same kind of thermally induced flow. In this work, the helium distribution simulations have been carried out first without the PCRD's. The details of helium injection for the simulated cases are presented in Table 1. The helium is injected in the R1 compartment injection position (elevation 1170 mm) as depicted in Fig. 1a. The helium is injected for 20 min at a rate of 600 SLPM with an injector having cross-sectional area of 0.2 m × 0.2 m. The total helium injected is equivalent to the homogeneous concentration of 8% v/v of the entire V1 volume. After that simulation has been carried out in the presence of two PCRD devices (PCRD1 and PCRD 2) and the distribution behaviour is compared with the first case where no PCRD is placed in CSF. The geometry of the PCRD is shown in Fig. 2 while the positions of both the PCRDs inside CSF are shown in Fig. 1a. Both the PCRDs are operated in a similar manner for a total duration of 40 min, with time varying heat release rate as described in Table 2. Selected important locations data (helium concentration, temperature, velocity) have been presented and compared here. The coordinates of the monitoring points are provided in Table 3.

Helium distribution in a multi-compartment geometry like CSF requires solution of 3D transient mass, momentum and species transport equation. In addition, energy

Table 1 Case details

Simulation No	PCRD	Injection	Mesh size
Case 1	No	600 SLPM @ 20 min (0.2 m × 0.2 m)	8.5 lacs
Case 1HA	Yes (approach 1)		13.88 lacs
Case 2HB	Yes (approach 2)		

Fig. 2 PCRD geometry
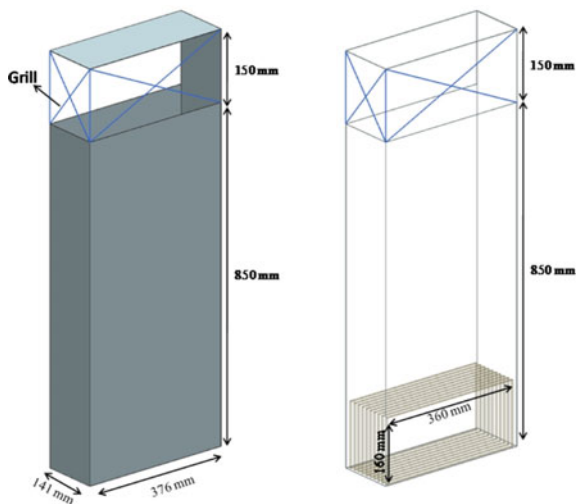
Table 2 Heater power of individual PCRD with time

Time (min)	Total heater power (kW)
0–11	1
11–18	3
18–22	5
22–29	3
29–40	1

Table 3 Monitor locations

Sl. No.	Location	R (m)	θ	Z (m)
Helium concentration				
1	R1	0.856	173.3	5.2
2	Dome	0	0	10.1
3	Annulus ground floor	2.46	90	4.15
4	Annulus 1st floor	2.47	337.6	7.05
5	Hor. opening b/w R1 and R3	1.1	135	5.9
Temperature				
6	Dome	0	0	10.1
7	PCRD1 inlet plane	2.37	45	6.9
8	PCRD2 inlet plane	2.37	225	7.9
Velocity				
7	PCRD1 inlet plane	2.37	45	6.9
8	PCRD2 inlet plane	2.37	225	7.9
9	0.1 m below of PCRD1 inlet plane	2.37	45	6.8
10	0.1 m below of PCRD2 inlet plane	2.37	225	7.8

equation is also required to be solved simultaneously for cases with PCRDs. In this kind of simulation, buoyancy plays a very important role due to continuous release of lighter gas into the domain and also due to the continuous release of heat in different location. In addition, an appropriate turbulence model with relevant source terms is essential to correctly predict the turbulent diffusion.

Each PCRD consists of ten heater plates (each 10 mm thick). Modelling of all the plates with PCRD box (2 mm thick wall) will substantially increase the mesh size and also the computational time. Considering the large geometries of CSF and large simulation time, it can be understand that detailed modelling of PCRDs in containment is computationally very expensive and not reasonable. Hence, in this work, all the PCRD plates of each PCRD are lumped into a single heat generating control volume (hot section). Two approaches are used here for simulating PCRD's. In first approach (Case 1HA), the entire heat source is dumped in the fluid control volume and neither solid plate's thermal inertia nor the pressure drop across the plates are modelled. In second approach (Case 1HB), the lumped plate volume is

considered as a porous zone where appropriate pressure drop and the thermal inertia of the plates are considered. It is to be mentioned here that the solid and gas volume in the porous zone are considered to be in thermal equilibrium with each other in simulation Case H1B.

In this work, all the simulations are carried out in commercial CFD software CFD-ACE+. Standard k–ε turbulence model with standard wall function is used for turbulence modelling. Heat transfer in the concrete volume has been modelled to account for its thermal inertia. Convective boundary condition has been used at the outer containment wall. First order discretization scheme is used for all the terms. In all the simulations, it is considered that the CSF domain is filled with quiescent air before helium injection into the domain. Hence, all three velocity components are initialized with zero value while the turbulence levels are initialized with very low value. Initial pressure and initial temperature are set to 101,325 Pa and 303 K, respectively. Ideal gas law is used for density calculation while mass diffusivity is considered constant for each species. Appropriate mixing laws have been used for calculating mixture properties available in CFD-ACE+ software.

3   Results and Discussion

In this section, the results of simulations are presented and compared to understand the effect of simulated recombiner on helium distribution. In this paper, total three simulations are presented. The first case (Case 1) involves helium injection for 20 min followed by diffusion phase of 20 min. In the second simulation (Case 1HA), helium is injected at the same rate for 20 min in the presence of two simulated PCRDs. The PCRDs are operated for 40 min with time varying heat rate as per Table 2. In third case (Case 1HB), the second case is repeated with different modelling approach for the simulated PCRD as described earlier. In the subsequent section, the comparison between two modelling approaches of PCRD (Case 1HA and Case 1HB) is presented along with the effect of simulated recombiner in CSF geometry. The localized mesh refinement near injection and near all the openings (especially vertical ones) are very crucial for buoyancy-driven flows (helium jet and plume) and taken care of in this study. In case where recombiners are presents, further mesh refinement in and around the PCRD positions are carried out to capture the thermally induced flow better.

In Fig. 3, the helium concentration in the injection room, R1 has been presented for all the three cases. It can be seen that there is a difference in predicted helium distribution between Case 1HA (approach 1) and Case 1HB (approach 2). To better interpret the results, first cases with PCRDs are compared among each other before assessing the effect of simulated recombiner in helium mixing.

In Fig. 4, the temperature transient at the dome location (250 mm below the top most point) is presented for Case1HA and Case1HB. As the effect of plate thermal inertia is not considered in Case1HA, the peak temperature comes significantly higher compare to Case1HB. In Case1HB, the heater section of PCRD are considered as porous media with appropriate porosity and pressure drop value applicable for the

Fig. 3 Variation of helium conc. in injection room, R1 (Monitor point 1)
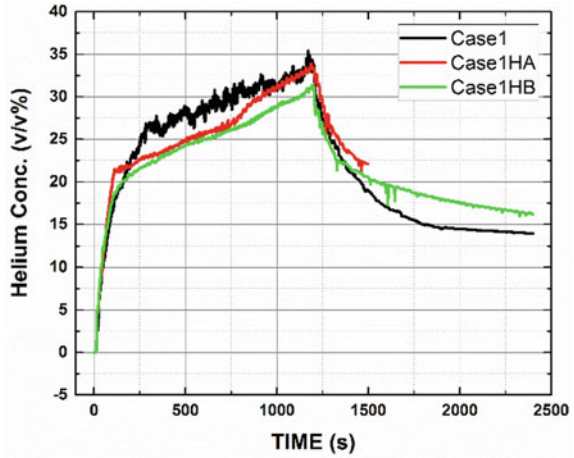
PCRD geometry shown in Fig. 2. The heat capacity of individual heater plates is 303 J/K while the mass of each plate is 0.670 kg. The comparison shows the importance of thermal inertia of the recombiner plates in calculating actual heat addition to the gases. However, in present case the inertia of PCRD boxes are not considered due to inherent limitation of CFD-ACE+ software in thin wall modelling in parallel computation.

In Fig. 5, the inlet and outlet temperature of PCRD have been compared for the Cases1HA and 1HB. In Case1HA, there is a large fluctuation at start of every change in heat rate unlike Case1HB due to the absence of solid plate's inertia. Though the out let temperature is almost similar at the outlet monitor point the inlet temperature is higher in Case1HA due to higher heat addition to the atmosphere. As these two are point temperature data, contour plots are presented in Figs. 6, 7 for Case1HA and

Fig. 4 Temperature transients at dome
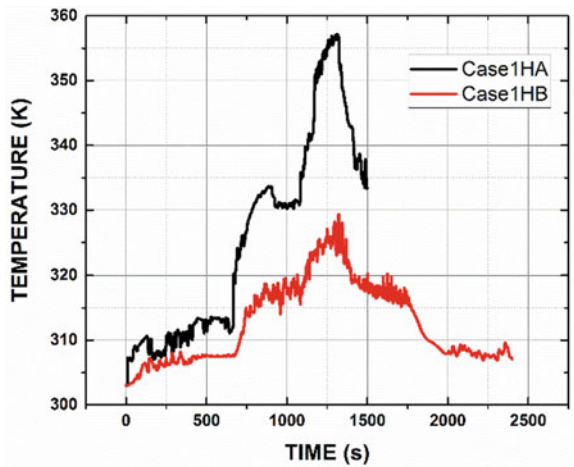
Case1HB, respectively, to get a more comprehensive scenario. It can be seen that Case1HA predicts non-uniform and large localized temperature within the recombiner unlike Case1HB. In Fig. 8, the Z velocity data has been presented at the point which is 0.1 m below the inlet plane. It can be seen that the velocity is higher in Case1HA as more heat is added to the gas volume in that approach. The fluctuations in velocity are very prominent at the inlet of PCRDs as the PCRDs are placed directly above the openings. Comparisons between the two modelling approach of PCRD, distinctly shows the improvement in the results in the Case1HB.

In Figs. 9 and 10, the Z velocity has been presented at 0.1 m below the inlet and just at the inlet respectively for Case1HB. It can be seen that the velocity becomes more unidirectional just at the inlet and also the magnitude increases due the presence of porous zone (porosity reduces the available flow area) (Fig. 11). This is presented in a more clear way in the Fig. 12 where velocity vector plot around the PCRD has

Fig. 5 Temperature at inlet and outlet of PCRD2
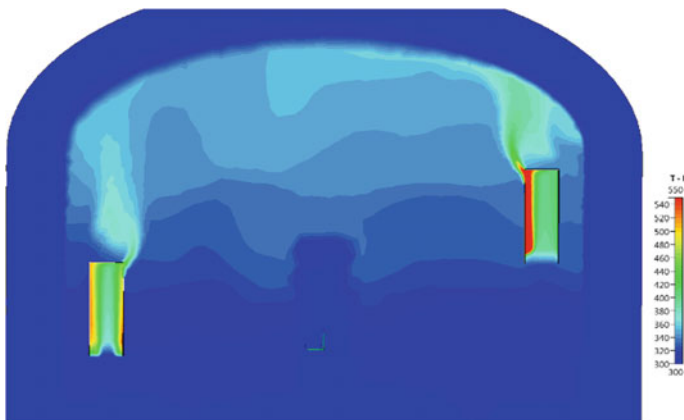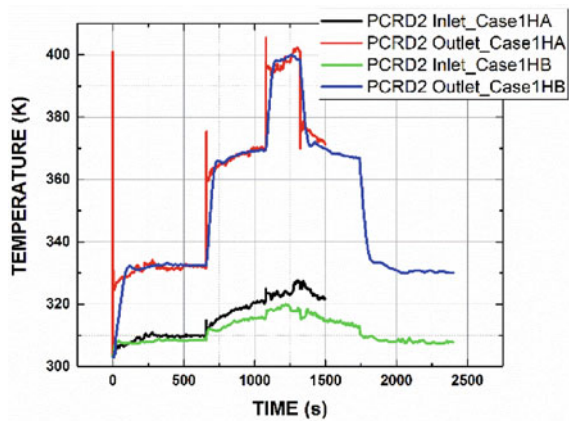
Fig. 6 Temperature contour at heater plane at 22 min for Case 1HA
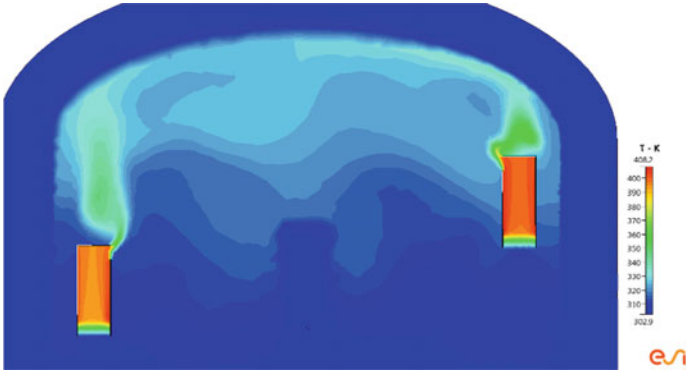
Fig. 7 Temperature contour at heater plane at 22 min for Case 1HB

Fig. 8 Z velocity at 0.1 m
below the PCRD2 Inlet
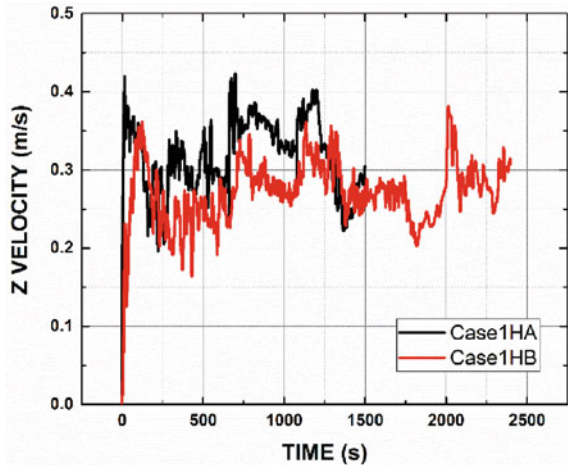
been shown. It can also be seen that the fluctuations are more at the inlet of PCRD1 as the PCRD1 is placed 1 m above the opening while the PCRD2 is placed 2 m above. Moreover, the fluctuations at inlet are more at low power and it decreases significantly at high power when higher driving force is available.

Now with the background of fundamental difference between these two approaches, the impact on helium distribution is presented in the following sections. In Fig. 3, it can be seen that the predicted peak concentration in the injection room is less due to operation of heater. However, the concentration is higher in post injection phase with heater operation. To understand this, the helium concentration at other location need to be looked at first. In Figs. 12, 13 and 14 helium concentration are presented for dome (250 mm below the top most point), first floor annulus and ground floor annulus. It can be seen that in all the cases the peak concentration comes lower when the heater is in operation. Moreover, the long-term concentration approaches

Fig. 9 Comparison of *Z* velocity at 0.1 m below the PCRDs inlet for Case 1HB
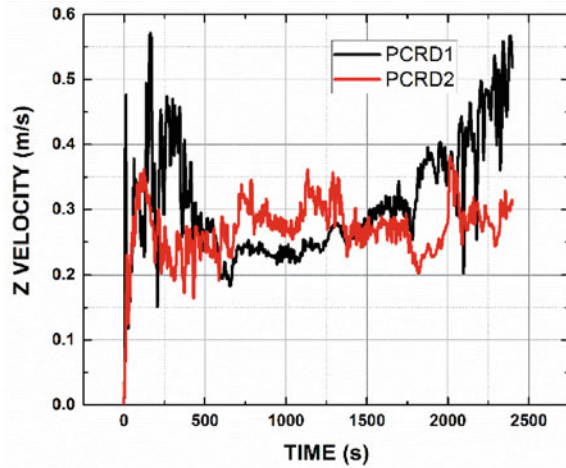
Fig. 10 Comparison of *Z* velocity just at inlet plane of PCRDs for Case 1HB
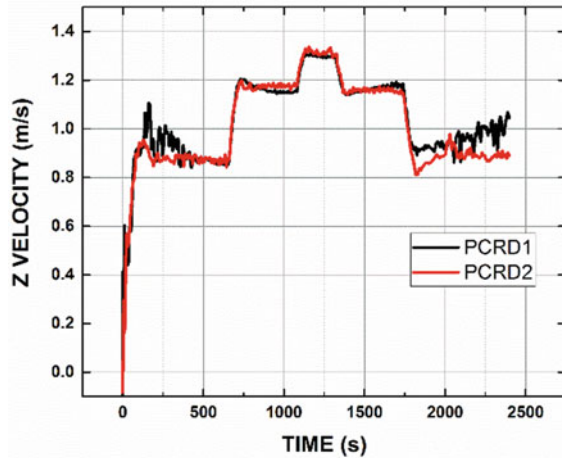
towards the equilibrium concentration faster. But the effect of heater is more prominent in first floor and dome area due to its direct interconnection and the placement of heater. The ground floor mixing is also affected significantly as the PCRDs are placed just above the openings connecting ground floor and first floor. However, the concentrations takes more time to approach the equilibrium concentration of 8% v/v in the compartment R1, R2, R3 and R4. In Fig. 15, the large fluctuations in the helium concentration at the horizontal opening between R1 and R3 can be observed. This depicts the classical ceiling jet behaviour in buoyancy-driven flows near openings. It can be seen that the operation of simulated PCRD dampens this oscillating jet behaviour.

Fig. 11 Velocity vector, PCRD2 at 22 min (Case 1HB)
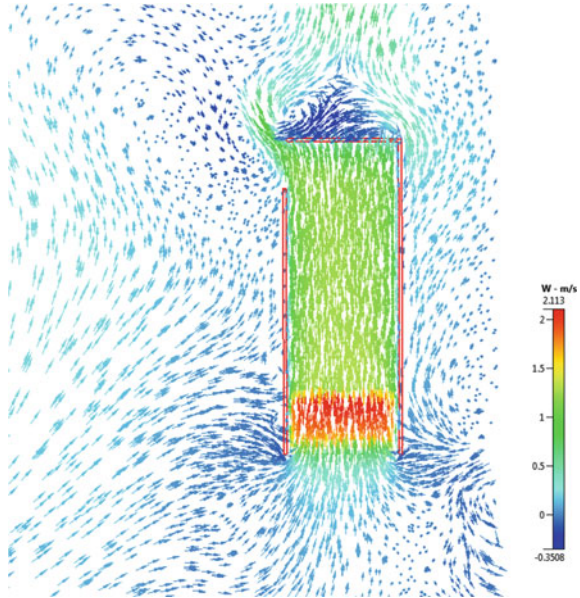
Fig. 12 Helium conc. at dome
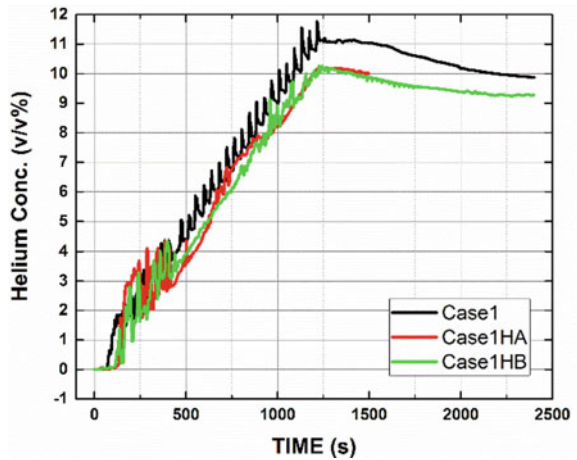
It can be concluded here that this kind of lighter gas distribution studies in the presence of simulated recombiner in large multi-compartment scaled-down geometry provides a very important insight into the effect of PCRD operation in helium mixing. The helium distribution characteristics in presence of simulated recombiner device are presented in terms of concentration, temperature and velocity with probable explanations. As the facility is volumetrically scaled, hence the scaled-down length scale is not appropriate for accurately simulating the buoyancy driven flows. Hence, the extent of effect cannot be simulated. However, this kind of exercise is very much

Fig. 13 Helium conc. in
first floor annulus
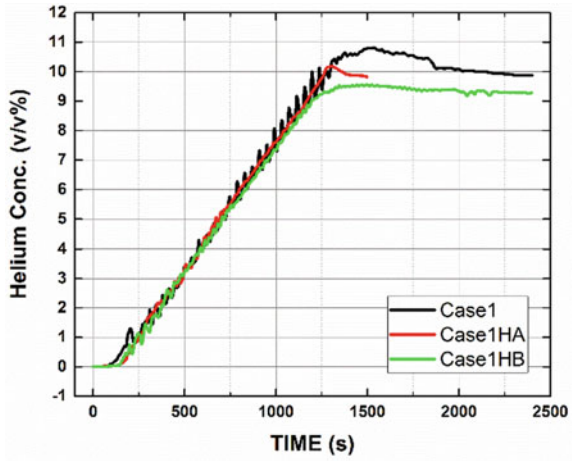
Fig. 14 Helium conc. in
ground floor annulus
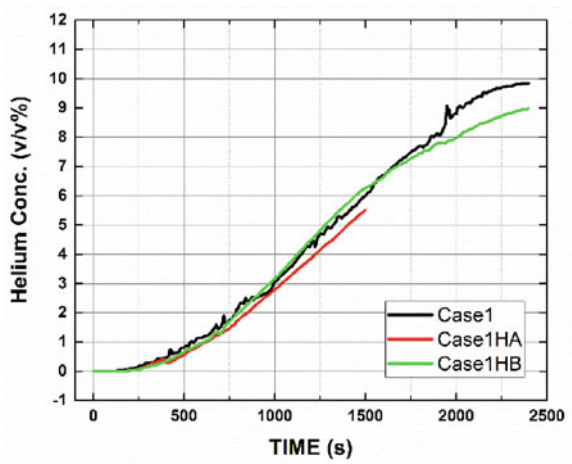
important to gain experience before performing actual reactor calculations. Based on
present finding, experiments will be performed in this facility and simulations will
be carried out again in future for validation exercise.

4   Conclusions

In this present blind CFD exercise, the effect of simulated recombiner device on
helium distribution and mixing is investigated in CSF geometry. Several impor-
tant characteristics are identified which will help in planning future experiments.
It is shown here that the porous media consideration is very effective in modelling

Fig. 15 Helium conc. in horizontal openings between R1 and R3
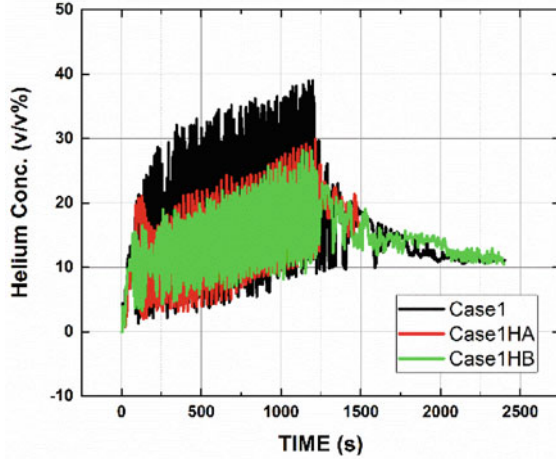
multiple PCRDs within the CFD framework with reasonable mesh size. It is found here that the placement of PCRD is very important and is directly influences the mixing characteristics. This kind of studies must be performed before experiment to find optimum number and correct location of PCRDs to get maximum efficiency of PCRDs. In present case, the porous zone of PCRD is modelled with thermal equilibrium model which is available in CFD-ACE+ software as standard. In future, thermal non-equilibrium model in porous media will be implemented to improve the accuracy. In future, the effect of PCRD box thermal inertia will also be investigated.

References

1. TEPCO (2012) Fukushima Nuclear Accident Analysis Report
2. Krause M (2007) Hydrogen Program at AECL, S3–1. In: The 2nd European Review Meeting on Severe Accident Research (ERMSAR-2007) Forschungszentrum Karlsruhe GmbH (FZK), Germany, 12–14 June 2007
3. OECD/NEA THAI Project (2010) Hydrogen and fission product issues relevant for containment safety assessment under severe accident conditions. Final Report: NEA/CSNI/R(2010)3.
4. Kljenak I, Andreani M (2012) OECD, OECD/SETH-2 Project PANDA and MISTRA Experiments Final Summary Report, Paris
5. Studer E, Magnaud JP, Dabbene F, Tkatschenko I (2007) International standard problem on containment thermal hydraulics ISP47: step-1 results from the MISTRA exercise. Nucl Eng Des 237:536–551
6. Thangamani I, Gera B, Verma V, Chattopadhyay J (2019) Design basis report on CSF, RSD Report, RSD/CSS/016/12/2019
7. Royl P, Rochholz H, Breitung W, Travis JR, Necker G (2000) Analysis of steam and hydrogen distributions with PAR mitigation in NPP containments. Nucl Eng Des 202:231–248
8. Prabhudharwadkar DM, Iyer KN, Mohan N, Bajaj SS, Markandeya SG (2011) Simulation of hydrogen distribution in an Indian Nuclear Reactor Containment. Nucl Eng Des 241:832–842

9. Visser DC, Houkema M, Siccama NB, Komen EMJ (2012) Validation of a FLUENT CFD model for hydrogen distribution in containment. Nucl Eng Des 245:161–171
10. Kudriakov S, Dabbene F, Studer E, Beccantini A, Magnaud JP, Paillère H, Bentaib A, Bleyer A, Malet J, Porcheron E, Carol C (2008) The TONUS CFD code for hydrogen risk analysis: physical models, numerical schemes and validation matrix. Nucl Eng Des 238:551–565

Design and Development of Thermoplastic Microfluidic Device for Argentometric Mohr Method

R. Rahul, V. Aishwarya, Prasad Nikhil, R. S. Mini, and S. Kumar Ranjith

1 Introduction

About 97% of water on earth cannot be used directly as drinking water due to high salinity. Moreover, the water available for drinking purposes is strongly affected by population growth, urbanization and industrialization in most countries. Water pollution has adverse effects on public health, causing about numerous deaths every day [1]. Unchecked and illegal disposal of organic and inorganic waste to water bodies from both commercial and residential sources is the primary source of water pollution. Such primary pollutants contributed to the presence of harmful chemicals in surface water, such as toxic metals, essential minerals and pathogenic organisms [2]. In addition to that, sewage, soil runoff and landfills contribute significantly to water pollution. Water quality is primarily affected by nutrient absorption, toxic metals, pharmaceutical and natural pollutants. These factors must be within allowable limits, which otherwise affect human health as well as aquatic ecosystems. One of the most prevalent inorganic anions in water and wastewater is chloride (Cl^-) ion. Calcium, magnesium and sodium salts contain Cl^- ion. The natural water is contaminated with Cl^- ion from different sources like layers of rocks, some salt

R. Rahul (✉) · N. Prasad · S. Kumar Ranjith
Micro/Nanofluidics Research Laboratory, Department of Mechanical Engineering, College of Engineering Trivandrum, Thiruvananthapuram, Kerala, India
e-mail: rahulraveendran1818@gmail.com

R. S. Mini
Department of Mechanical Engineering, College of Engineering Trivandrum, Thiruvananthapuram, Kerala 695016, India

V. Aishwarya
Department of Civil Engineering, College of Engineering Trivandrum, Thiruvananthapuram, Kerala 695016, India

R. Rahul
APJ Abdul Kalam Technological University, Thiruvananthapuram, Kerala 695016, India

deposits, sediments, sewage, and road salt infiltration [3]. A high chloride level may injure developing plants and damage steel pipelines and structures. The secondary drinking water standard of 250 mg/L is designed to signal problems with the quality of water. Existing chloride monitoring techniques involve complex equipment, longer processing times, and highly trained professionals, which makes these techniques complicated and tedious. Towards the realization of a mobile device, sensitive and selective water quality control system is required. In this regard, microfluidic [4] based devices are highly promising [5, 6]. Several researchers [7, 8] performed extensive research on the development and application of microfluidic devices for detecting water contaminants. The microfluidics-based lab on a chip (LOC), device delivers fast results, is inexpensive and highly sensitive analysers with considerable productivity [9–13]. Mohr method is the standard method for chloride ion detection. The present study focuses to conduct the Mohr method of chloride detection in LOC device. In order to gain a better understanding of chloride detection in LOC, flow visualization of Mohr procedure on two different microfluidic channels is conducted. The primary goal of this work is to visualize the basic flow mixing behaviour of silver nitrate ($AgNO_3$), sodium chloride (NaCl) and potassium chromate (K_2CrO_4) in two microchannels of different size and nature. Next, to conduct the volumetric study of Mohr method on-chip with varying flow rate and concentration. As part of the study, microchip fabrication and standard Mohr chloride detection test are conducted.

2 Methodology

This section describes in detail about the fabrication of polymethyl methacrylate (PMMA) microchannels, off-chip Mohr chloride detection theory, and the flow mixing behaviour of chloride monitoring in LOC. For the fabrication of microchips, PMMA with a thickness of 2 mm is used. The reagents used for the off-chip and on-chip chloride detection are sodium chloride, potassium chromate and silver nitrate. In Mohr chloride detection, the basic titration theory is used to obtain the volume of an unknown sample. For that, the colourimetric change is observed with change in sample volume. Furthermore, the same reagents and identical proportions are used for the on-chip flow mixing characterization. The chip is manufactured using a micro CNC milling operation and thermally bonded at a pressure of 220 kPa. For the flow visualization of chloride, a CCD camera and an inverted brightfield microscope are used. The complete workflow of the chloride detection by on-chip and off-chip methods is shown in Fig. 1.

A. **PMMA Microchip Fabrication**

This section describes the steps involved in the fabrication of PMMA LOC device. The PMMA is chosen as the material for the base and cover layer due to its transparency, and it requires less time for preparation. The fabrication technique used for the proposed LOC device is computer numerical control (CNC) micromilling. At first, the VCarve application is used to create the microchannel design, and the output
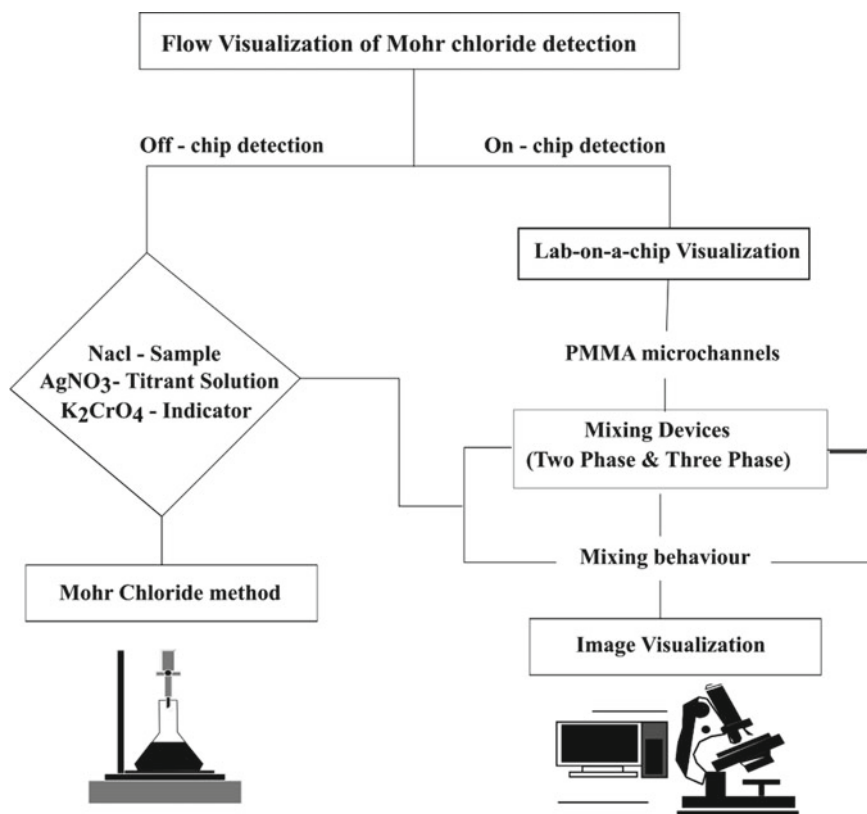
Fig. 1 Workflow of Mohr chloride detection visualization under off-chip and on-chip conditions

numerical code is used to drive the CNC device. A tungsten carbide tool is used to mill channels on a 2 mm-thick PMMA sheet. Isopropyl alcohol is used to clean the machined microchannel base and cover plates. The PMMA sheet is trimmed to the required dimensions using a laser cutting tool (Epilog Engraver, USA). For the bonding procedure, thermal bonding mechanism is employed between the cover and base layer of milled PMMA sheets. The maximum pressure applied to both layers is 220 kPa, by using a compression spring force (CSF) mechanism [14]. The entire assembly is heated in a muffle furnace (3 kW) for 120 mins at 95 °C. The input and outlet connections of the PMMA device are made from soft, flexible capillary tubes. The fabricated PMMA microchips are shown in Fig. 2.

B. **Off-Chip Mohr Chloride Detection**

In Mohr chloride detection method, silver nitrate solution is used as the titrant and potassium chromate are used as the indicators. When a chloride-containing water sample is titrated against a silver nitrate solution in the presence of an indicator, the chlorides precipitate as white silver chloride.
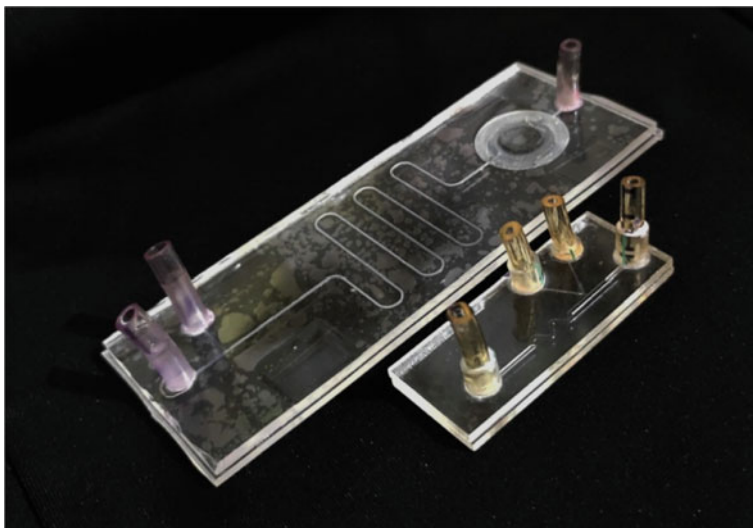
Fig. 2 Fabricated PMMA microchips for flow visualization

$$Ag^+ + Cl^- \Leftrightarrow AgCl$$
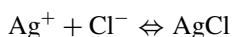
At the end point of titration, white precipitate changes to reddish brown precipitate. By that time entire AgCl precipitates and the reddish brown colour is the indication of silver chromate.

$$2Ag^+ + CrO^{2-} \Leftrightarrow Ag_2CrO_4$$
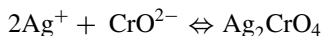
Apparatus used for chloride test are conical flask, burette, pipette and measuring cylinder. To identify the mass of chloride ion in water sample, 20 ml of measured sample NaCl (0.004 Normality) is taken and 1.0 ml 1% of indicator solution (potassium chromate) is added to it. The resulting solution turned light yellow with the addition of K_2CrO_4. The solution is then titrated with a standard silver nitrate solution (normality: 0.0141). With the addition of silver nitrate, a white precipitate is formed and the colour changes to faint reddish brown once the entire chloride is precipitated (Fig. 3). The amount of titrant expended is used for the final calculation.

C. **On-Chip Chloride Detection**

For on-chip detection of chloride ions, two PMMA microchips with varying dimensions are used (Fig. 4). The same procedure of the Mohr test is carried out in the fabricated microchannels.
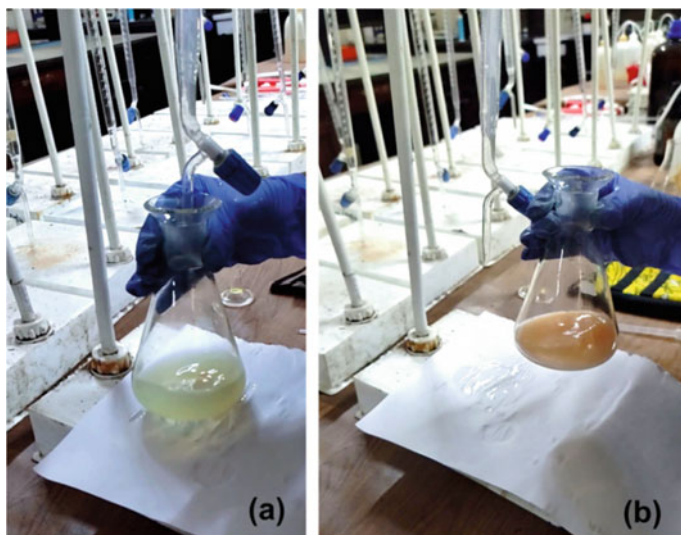
Fig. 3 Off-chip Mohr chloride titration method **a** before and **b** after required volume of silver nitrate is added
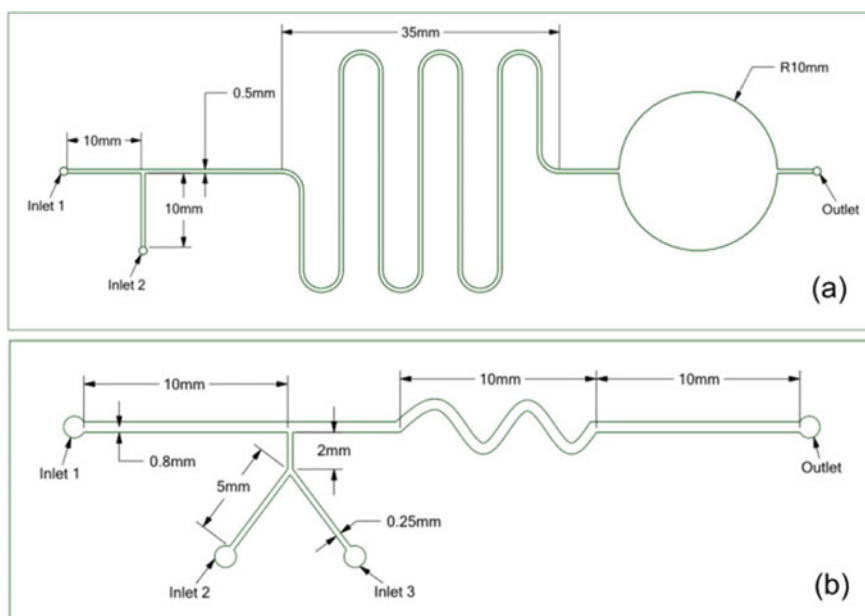
Fig. 4 Schematic diagram of **a** two-phase and **b** three-phase microchannel configuration used for fluid mixing visualization of chloride test

3 Results and Discussion

This section deals with the experimental results and flow visualization characterization of Mohr chloride test.

A. Estimation of Chloride (Mohr Method)

The experimental observation of the Mohr method using standard NaCl solution and silver nitrate solution is listed in Table 1. Determination of the mass of chloride ion per litre of water (0.004N NaCl) using one of the observations is written below.

Volume of water sample $V_1 = 20$ ml; Volume of $AgNO_3$ solution $V_2 = 20.7$ ml; Normality of $AgNO_3 = N_2 = 0.0141$ N.

At the end point of titration, number of NaCl equivalents in the solution is equal to the number of $AgNO_3$ equivalents in the solution.

Normality of chloride ion in the sample,

$$N_1 = V_2 N_2 / V_1.$$

Mass of chloride ion per litre of the sample,

$$= N_1 \text{ equivalent weight of chlorine.}$$
$$= N_1 35.46 \times 1000 = 517.48 \text{ mg/L.}$$

B. Flow Visualization and Chloride Ion Detection in Fabricated PMMA Microchips

(1) *Flow visualization of two-phase mixing device:* To understand the mixing behaviour of the Mohr test at a microscale, two separate PMMA microchips are considered in this study. The volume and width of the microchannels are different for both cases. For two-phase visualization study, a microchip with dimension 120 mm × 50 mm × 4 mm and channel width 500 μm is used. The two-phase and three-phase reagents mixing device is schematically illustrated in Fig. 4. The mixing phenomena are investigated using a bright-field inverted microscope with a CCD camera, as illustrated in Fig. 5a. For the two-phase mixing study, a solution of standard NaCl and 1.0 ml 1% of indicator solution (potassium chromate) is supplied to the inlet 2 with a flow rate of 10 μl/min, and silver nitrate is introduced to the inlet 1 with 10 μl/min flow rate using

Table 1 Volume of reagents used for Mohr method

Sl. No.	V_1 (ml)	Initial reading	Final reading	V_2 (ml)
1	20	0	20.7	20.7

microinjection pumps (NE4002X and KDS Legato 111 Makes) (see Fig. 5b). The observed behaviour of chloride test is shown in Fig. 5b–j.

At the T junction, two fluids interact with a constant flow velocity (10 μl/ min), and as a result, the interface between the two fluids shows a dark thin line over a certain period of time. This is due to the formation of white silver chloride precipitate. In most cases, the precipitation of silver chloride hinders the passage of light, and in microscope, it appears as dark. However, complete mixing occurs in the serpentine mixing zone (Fig. 5e–g), and the colourimetric change observed is same as that of the off-chip conditions. The tail end of the chip shows a reddish brown colour, which indicates silver chromate formation at a microscale (Fig. 5i, j). When the flow velocity of both inlets is changed, the colour intensity over the channel length is also varied. Typically, at a constant flow rate, the thickness of the silver chloride layer increases with time interval, as illustrated in Fig. 6. For the visualization of Mohr method on LOC device, varying flow rates of silver nitrate solution are analysed. The average value of flow rate at which the maximum colour intensity of reddish brown is achieved is 10 μl/min and is at 2 min. The mixing performance of the fabricated PMMA microchip depends on the side wall (Re $\geq$ 50) roughness [15, 16] and the number of turns in the serpentine microchannel [17].

(2) *Flow visualization of three-phase mixing device:* A microchannel with three inlets is employed for this study, and it is schematically illustrated in Fig. 7. In connection with that, a microchip with size of 50 mm $\times$ 20 mm $\times$ 4 mm, microchip and channel width 800 and 250 μm is used. Standard sodium chloride
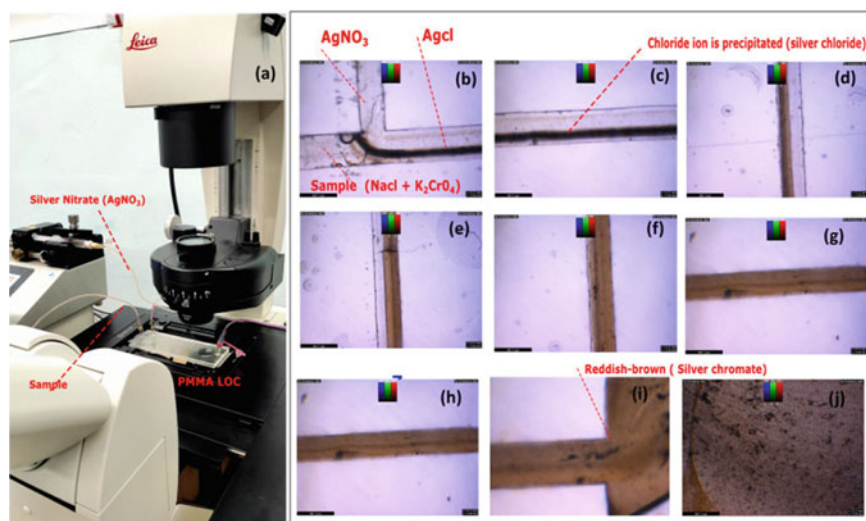
Fig. 5 Flow visualization of Mohr method on two-phase mixing device. **a** Experimental set-up of on-chip detection. **b–j** Mixing phenomena at different locations captured with a CCD camera
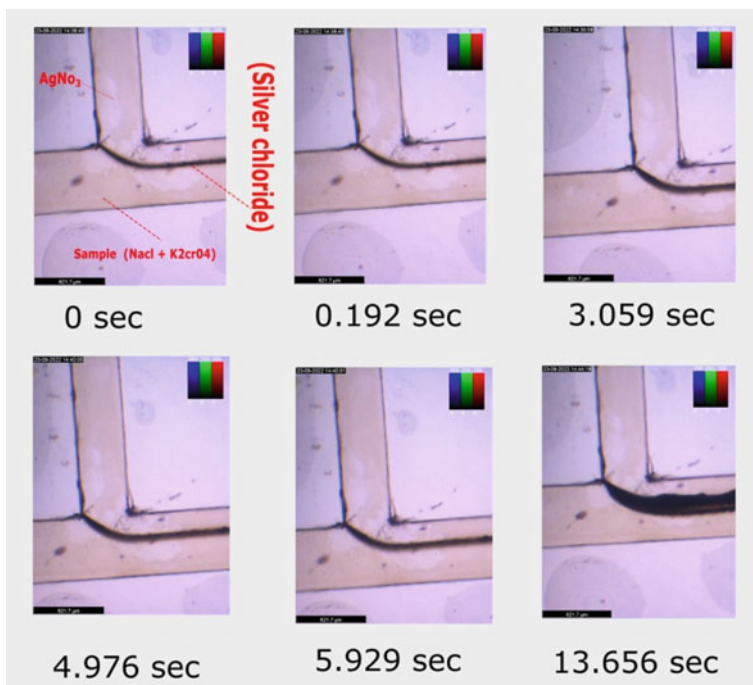
Fig. 6 Visualization of silver chloride precipitation at different time intervals in a 500 μm width two-phase mixing device (sample at 90 μl/min and silver nitrate at 20 μl/min)

and potassium chromate indicator are introduced through inlet 2 (250 μm) and inlet 3 (250 μm) respectively with a constant flow rate, and through inlet 1 (800 μm) silver nitrite solution is passed (see Fig. 7a). The mixing behaviour is visualized in Fig. 7. At the Y junction dark patches are observed, which is the indication of silver chloride and towards the end of serpentine channel reddish brown precipitates are observed. As mentioned earlier, reddish brown precipitate is due to the formation of silver chromate.

4 Conclusions

In this paper, a microfluidic chip is designed and fabricated and the argentometric Mohr method is demonstrated on the chip. As per IS:10500-2012, maximum acceptable limit of chloride content in drinking water is 250 mg/L and it is 1000 mg/L in the water used for purposes other than drinking. This pilot work focused on the visualization of Mohr method on LOC. Visualization of Mohr method on two different variants of microchips is done with varying flow rate, and the volumetric estimation of chloride content from image data is planned as the future work. The
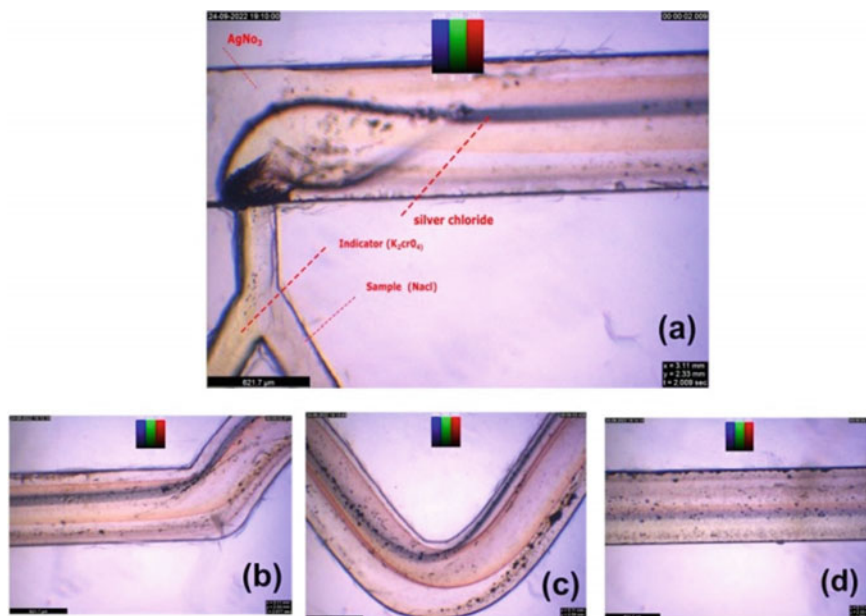
Fig. 7 Visualization of chloride detection in three-phase mixing device in which the flow rate of silver nitrate is 300 μl/min and the flow rate of sample and indicator are 90 μl/min

proposed LOC is designed to handle more volume of fluid than paper microfluidic-based strips. The auxiliary device for pumping and imaging in this pilot work can easily be replaced with capillary pumping mechanism and image sensing to adhere to portability constraints.

Nomenclature

V_1 Volume of water sample (ml)
V_2 Volume of silver nitrate sample (ml)
N_1 Normality of silver nitrate (N)
N_2 Normality of chloride ion (N)

References

1. Rai PK, Islam M, Gupta A (2022) Microfluidic devices for the detection of contamination in water samples: A review. Sens Actuat A 347:113926
2. Thio SK, Bae SW, Park S-Y (2022) Lab on a smartphone (los): a smartphone-integrated, plasmonic-enhanced optoelectrowetting (oew) platform for on-chip water quality monitoring through lamp assays. Sens Actuat B Chem 358:131543
3. Wu D, Hu Y, Liu Y, Zhang R (2021) Review of chloride ion detection technology in water. Appl Sci 11(23):11137
4. Bragheri F, Vázquez RM, Osellame R (2020) Microfluidics. In: Three-dimensional microfabrication using two-photon polymerization. Elsevier, Amsterdam, pp 493–526
5. Asiri AM et al. (2020) Nanosensor Technologies for Environmental Monitoring. Springer, Berlin
6. Gallah N, Besbes K (2016) Electroosmotic micropump analysis for lab on chip water quality monitoring. In: 2016 13th International Multi-Conference on Systems, Signals and Devices (SSD). IEEE, pp 330–335
7. Kulthong K, Srisung S, Boonpavanitchakul K, Kangwansupamonkon W, Maniratanachote R (2010) Determination of silver nanoparticle release from antibacterial fabrics into artificial sweat. Particle Fibre Toxicol 7(1):1–9
8. Kapoor A, Balasubramanian S, Muthamilselvi P, Vaishampayan V, Prabhakar S (2020) Lab-on-a-chip devices for water quality monitoring. In: Inamuddin AMA (ed) Nanosensor technologies for environmental monitoring. Springer, Cham, pp 455–469
9. Jin J-H, Kim JH, Lee SK, Choi SJ, Park CW, Min NK (2018) A fully integrated paper-microfluidic electrochemical device for simultaneous analysis of physiologic blood ions. Sensors 18(1):104
10. Giannitsis AT (2011) Microfabrication of biomedical lab-on-chip devices. a review. Eston J Eng 17(2):109
11. Sengupta J, Adhikari A, Hussain CM (2021) Graphene-based analytical lab-on-chip devices for detection of viruses: A review. Carbon Trends 4:100072
12. Zhu Z, Frey O, Ottoz DS, Rudolf F, Hierlemann A (2012) Microfluidic single-cell cultivation chip with controllable immobi-lization and selective release of yeast cells. Lab Chip 12(5):906–915
13. Novell M, Guinovart T, Blondeau P, Rius FX, Andrade FJ (2014) A paper-based potentiometric cell for decentralized monitoring of li levels in whole blood. Lab Chip 14(7):1308–1314
14. Arjun A, Ajith R, KumarRanjith S (2020) Mixing characterization of binary-coalesced droplets in microchannels using deep neural network. Biomicrofluidics 14(3):034111
15. Wang X, Liu Z, Yang Y, Cai Y, Song Q, Wang B (2022) Effects of sidewall roughness on mixing performance of zigzag microchannels. Chem Eng Process Process Intensif 179:109057
16. Pravinraj T, Patrikar R (2018) Modeling and characterization of surface roughness effect on fluid flow in a polydimethylsiloxane microchannel using a fractal based lattice boltzmann method. AIP Adv 8(6):065112
17. Clark J, Kaufman M, Fodor PS (2018) Mixing enhancement in serpentine micromixers with a non-rectangular cross-section. Micromachines 9(3):107

Normal Collision of a Single-Dipole of Vortices with a Flat Boundary

Shivakumar Kandre and Dhiraj V. Patil

1 Introduction

The two-dimensional (2D) bounded flows feature the phenomenon of vortex-wall interactions and the formation of structures due to the detachment of viscous boundary layers. The vortex interactions with no-slip walls are encountered in practical applications such as interaction of aircraft trailing vortices with the ground and large-scale vortex interactions with coasts and landscapes. The small-scale structures form dipoles with the primary vortex and advect over the entire domain. The formation of secondary vortices strongly affects the evolution of 2D decaying turbulence [1, 2]. Hence, it is important to study the influence of rigid boundaries on the vortex dynamics to characterize the vortex-wall interactions.

The numerical simulations are carried out in the past to investigate the physics that encountered during the vortex-wall interactions [3–6]. Primarily, Orlandi [3] investigated the effect of bounded domain which is initialized using Lamb dipoles using stream functions, on the generation of secondary and tertiary vortices at the wall. The frequent and multiple rebounds of the dipoles are due to the production of vorticity at the wall. The formed dipolar vortices take circular trajectory far from the boundaries. The no-slip wall is the source of vorticity production at the boundary. Clercx and van Heijst [4] quantified the enstrophy production for oblique and normal dipole-wall collision in a square domain. The dissipation of kinetic energy and palinstrophy computed and the physics associated with the vortex-wall interactions are further studied. The shielded monopolar vortices particularly for higher Re values are analysed in [5]. Trajectory of the dipole for the stress-free and no-slip boundaries are given, and vorticity at the wall for several dipole-wall collision time is quantified.

S. Kandre · D. V. Patil (✉)

Department of Mechanical, Materials and Aerospace Engineering, IIT Dharwad, Dharwad 580008, Karnataka, India

e-mail: dhiraj@iitdh.ac.in

Recently, Peterson and Porfiri [6] have studied the impact of semi-infinite rigid plate and its tip on the dipole interaction. The vortex shedding is observed at the tip of semi-infinite rigid plate. Recently, similar work carried out by using lattice Boltzmann method [7, 8]. The monopole, dipole and tripoles of vortices are observed during the interaction of co-rotating isolated vortices based on the inter-vortical distance at low Reynolds number in a two-dimensional (2D) square domain [7]. The vortex-wall interaction problem is investigated with dipole propelling towards slip boundaries [8].

In this work, the vortex-wall interactions with no-slip boundaries are studied numerically in a square domain using the lattice Boltzmann method with a Bhat-nagar–Gross–Krook (BGK) collision model. In order to capture the vortex-wall interactions accurately, the simulations are performed with 2048^2 grid points with second-order accurate non-equilibrium bounce-back condition for solid-wall boundaries. The paper is organized as follows, mathematical formulations, initial arrangement of isolated monopolar vortices and the validation of LB algorithm are given in Sect. 2, the results obtained for normal collision of dipole with wall are discussed in Sect. 3 and conclusions are given in Sect. 4.

2 Methodology

The kinetic-theory-based lattice Boltzmann (LB) method is employed which captures the evolution of distribution functions at each lattice point using an iterative procedure of local collisions and near-neighbour shift [9–12]. The easy implementation of the boundary conditions, parallel algorithm and explicit nature help LBM to get attention over the conventional CFD method. The LB equation with a single relaxation time (SRT) or BGK collision model [13] is,

$$f_i(\boldsymbol{x} + \boldsymbol{e_i}\Delta t, t + \Delta t) = f_i(\boldsymbol{x}, t) - \frac{\Delta t}{\tau}\big(f_i(\boldsymbol{x}, t) - f_i^{\text{eq}}(x, t)\big), \qquad (1)$$

where f_i is a particle density distribution function along ith lattice direction, $\boldsymbol{e_i}$ is lattice velocity vector, and Δt is time step. The two-dimensional nine discrete velocity (D2Q9) lattice structure is employed for the simulations with its corresponding lattice velocities. The f_i^{eq} in Eq. (1) is the equilibrium distribution function governed by the discrete Maxwell–Boltzmann distribution with terms upto $O(\text{Ma}^2)$.

$$f_i^{eq} = w_i \rho \left[1 + 3\frac{\boldsymbol{e_i} \cdot \boldsymbol{u}}{c^2} + \frac{9}{2}\frac{(\boldsymbol{e_i} \cdot \boldsymbol{u})^2}{c^4} - \frac{3}{2}\frac{\boldsymbol{u} \cdot \boldsymbol{u}}{c^2} \right]. \qquad (2)$$

Here, $c = \Delta x/\Delta t = 1$ is a lattice speed. The relaxation time, τ is related to kinematic viscosity using the Chapman–Enskog expansion. The density and momentum are computed as zeroth- and first-order moments of the distribution function.

$$\tau = \left(\frac{\nu}{c_s^2} + \frac{1}{2}\right); \quad \rho = \sum_{i=0}^{N-1} f_i(\boldsymbol{x}, t); \quad \rho\boldsymbol{u} = \sum_{i=0}^{N-1} f_i(\boldsymbol{x}, t)\boldsymbol{e_i} \tag{3}$$

The 2D bounded vortex flows are characterized by the vortex-wall interactions and formation of thin boundary layers due to the shear effect induced by the no-slip wall. In order to quantify the impact of the vortex-wall interaction on the vortex dynamics, three global quantities are studied. These are kinetic energy of the flow, $E(t)$, enstrophy, $\Omega(t)$ and palinstrophy, $P(t)$. The $P(t)$ is a measure of vorticity gradients.

$$E(t) = \frac{1}{2} \int_D [u_x^2 + v_y^2] \mathrm{d}A; \tag{4}$$

$$\Omega(t) = \frac{1}{2} \int_D [\omega_z^2] \mathrm{d}A; \tag{5}$$

$$P(t) = \frac{1}{2} \int_D |\nabla\omega_z|^2 \mathrm{d}A. \tag{6}$$

Problem Description and Validation

The normal dipole-wall interactions are studied in a square domain $[0, 2] \times [0, 2]$ using lattice Boltzmann method. The flow is initialized with two isolated Gaussian monopolar counter-rotating vortices at the centre of the domain with 0.2 separation distance. Two isolated monopoles are introduced at the location of $\boldsymbol{x} = (0.9, 1)$ and $\boldsymbol{x} = (1.1, 1)$ and arranged in such a way that dipole travels towards the bottom boundary of the domain. The no-slip condition is applied for all the boundaries. Initial arrangement and domain configuration are shown in Fig. 1. The vorticity is distributed to each of the monopolar vortexes as,

$$\omega_z = \omega_e \left(1 - (r/r_0)^2\right) \exp\left(-(r/r_0)^2\right). \tag{7}$$

where r_0 is the dimensionless vortex radius (where the vorticity changes its sign) which is set to 0.1, r is the distance from the centre of the monopole, and ω_e is the vorticity extreme of the monopolar vortex. The velocity fields to achieve the isolated monopoles are expressed as,

$$u_x = \frac{1}{2}|\omega_e|(y - y_1)\exp\left(-(r_1/r_0)^2\right) - \frac{1}{2}|\omega_e|(y - y_2)\exp\left(-(r_2/r_0)^2\right) \tag{8}$$

$$u_y = -\frac{1}{2}|\omega_e|(x - x_1)\exp\left(-(r_1/r_0)^2\right) + \frac{1}{2}|\omega_e|(x - x_2)\exp\left(-(r_2/r_0)^2\right) \tag{9}$$

Here, $r_1 = \sqrt{(x - x_1)^2 + (y - y_1)^2}$, and $r_2 = \sqrt{(x - x_2)^2 + (y - y_2)^2}$.

Fig. 1 Initial arrangement
of isolated monopoles with
the computational domain
configurations
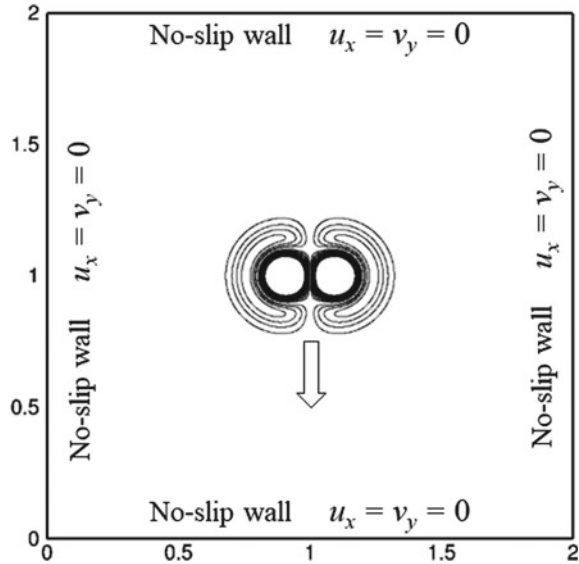
The Reynolds number of the flow is defined as,

$$\text{Re} = \frac{u_{\text{rms}} w}{\nu},$$

where, u_{rms} velocity is considered as characteristic velocity of the flow, w is the half width of the domain and ν is non-dimensional kinematic viscosity. The time coordinate is non-dimensionalized using convective velocity (w/u_{rms}).

A second-order accurate, non-equilibrium bounceback extrapolation method is used to compute the unknown distribution functions at the no-slip boundaries. The unknowns at the boundaries are computed by equalizing its f_i^{neq} with f_i^{neq} of immediate fluid node in the discrete velocity direction. The simulations are performed with 2048^2 grid points.

The algorithm is validated with the available literature data [8], where, the normalized kinetic energy and enstrophy are compared for $\text{Re} = 2500$. The temporal evolution of $\Omega(t)/\Omega_0$ and $E(t)/E_0$ is compared in Figs. 2 and 3, respectively. It is observed that the higher grid resolution and second-order accurate boundary conditions are able to capture the vortex-wall interactions accurately and results are well compared with the literature data.
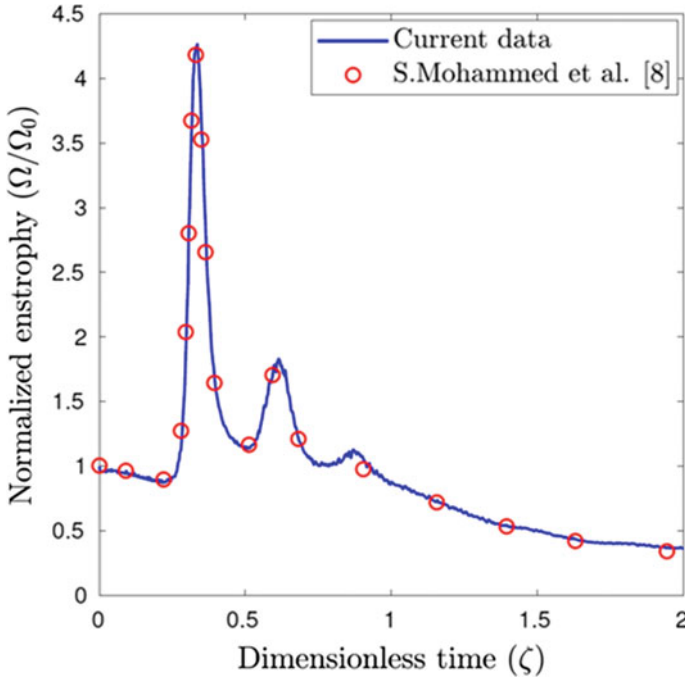
Fig. 2 Evolution of enstrophy compared with the literature data at Re = 2500

3 Results and Discussion

Here, the physics associated with the normal collision of the dipole with a wall for Reynolds numbers from 625 to 5000 is discussed. Figure 4 shows the vorticity snapshots at Re = 5000 for series of vortex-wall interaction events. The boundary layers of counter-vorticity forms and its magnitude increases as the dipole approach the wall. The dipole halves separate from each other once the dipole reaches the boundary. The halves move in the opposite direction. The process is followed by the formation of thin vortex filaments and secondary vortices due to the detachment of the boundary layers. These secondary vortices form new asymmetric dipole with the primary vortex and move along the circular trajectory. Such process leads to the second time collision of dipoles with the no-slip boundary.

The tertiary dipole is formed when the vortex pair collide for the second time. Thus, multiple small-scale structures of positive and negative vorticity are formed due to the frequent and multiple detachments from the wall. The subsequent interactions cause strength or vorticity magnitude of the vortices to reduce and the energy to decay continuously.

The vorticity magnitude is extracted at the wall ($y = 0$) at the time of first and second collision of the dipole to quantify the impact of Re variations on the production of vorticity. The corresponding vorticity profiles are given in Fig. 5a, b. It is deduced
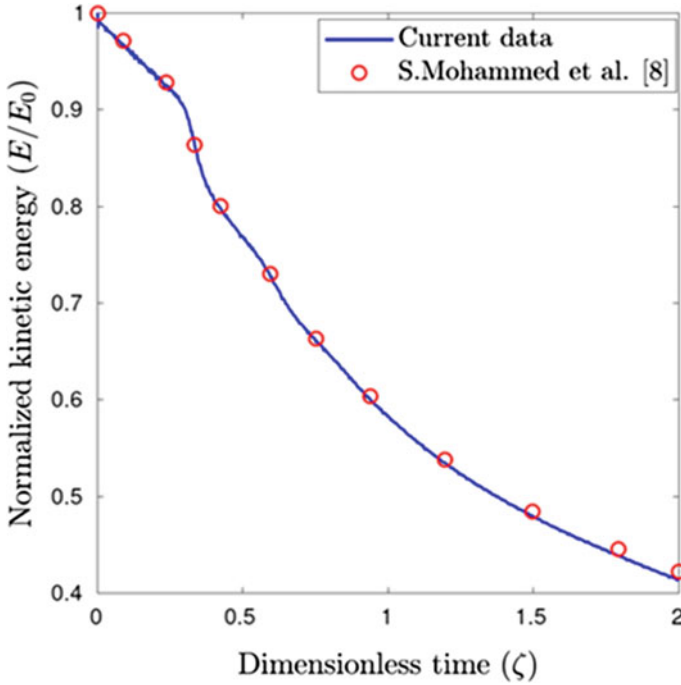
Fig. 3 Evolution of kinetic energy compared with the literature data at Re = 2500

from the profiles that the vorticity production is larger for large Re, and it reduces gradually with the Re of the flow. The symmetric behaviour can also be seen in the vorticity profile since the data is extracted over the domain length. The vorticity snapshots in Fig. 4 capture the domain length from $x = 0.4$ to 1.6. The fluctuations of vorticity productions in the case of Re = 5000 (see Fig. 5b) represent the formation of multiple small-scale secondary vortices near the boundary. The location of vortex-wall interaction points changes. Further, the relationship between Re and maximum vorticity production at the wall is studied for various Reynolds numbers (varies from Re = 200 to 5000). The corresponding line plot is shown in Fig. 6 particularly for the first-time collision. It is found that the maximum vorticity production at the wall varies logarithmically with the Reynolds numbers.

In order to further underpin the physics for the vortex-wall interactions, the global flow quantities such as $E(t)$, $\Omega(t)$ and $P(t)$ are measured for all the Re variations. The corresponding temporal evolutions are given in Figs. 7, 8 and 9, respectively. The quantities are normalized with the corresponding value at $\zeta = 0$. The decay rate of kinetic energy is directly proportional to the enstrophy (i.e. square of the vorticity) variations. Hence, the study of enstrophy evolution is important. The peaks observed in the enstrophy curves indicate the generation of intense vorticity at the no-slip wall. The first peak corresponds to the first dipole-wall collision, and collision at the second time is represented by the second peak. The intense vorticity is produced in
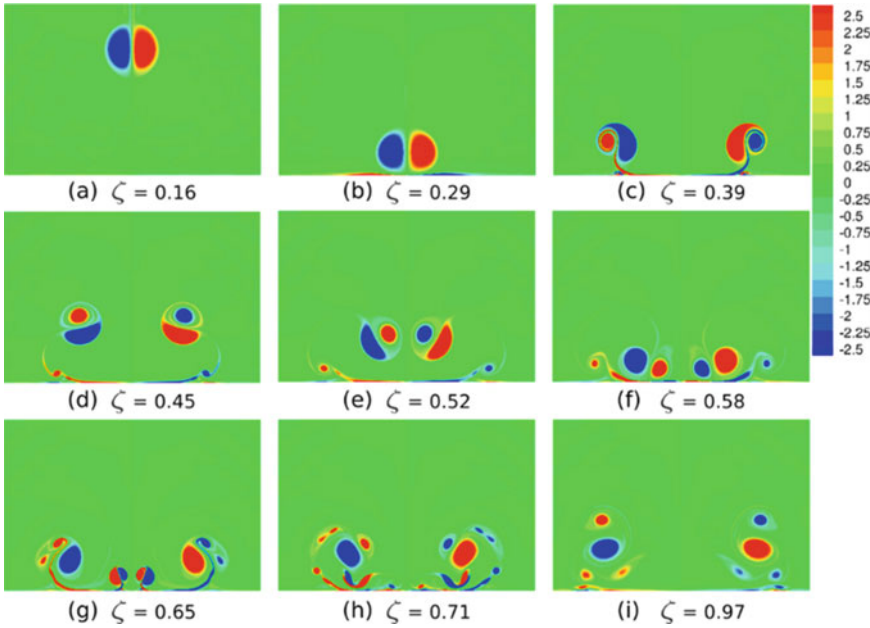
Fig. 4 Vorticity snapshots of the dipole-wall interactions captured at Re = 5000
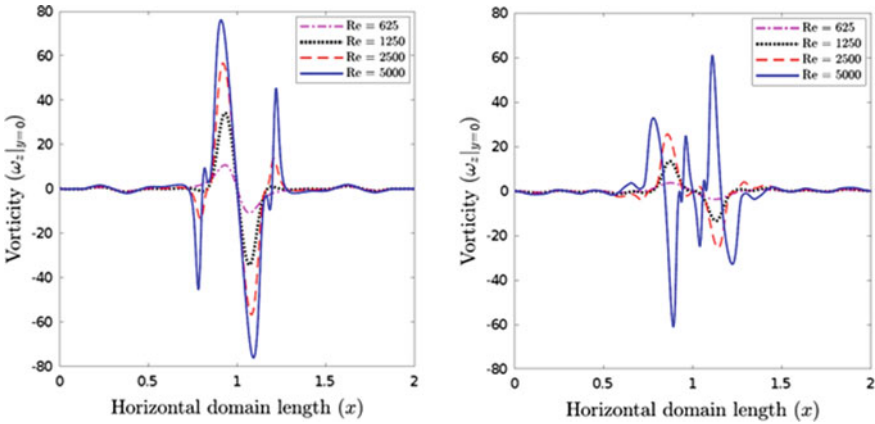
Fig. 5 Vorticity production at the boundary ($y = 0$) for: **a** first-time collision ($\zeta = 0.32$), **b** second-time collision ($\zeta = 0.62$)

the boundary layer during the first collision and is the source of total enstrophy. The peaks achieve maximum value with Reynolds number. One collision with the wall is observed for the Re = 625. The evolution of the total enstrophy for normal collision of the bounded domain can be an integral equation [5].
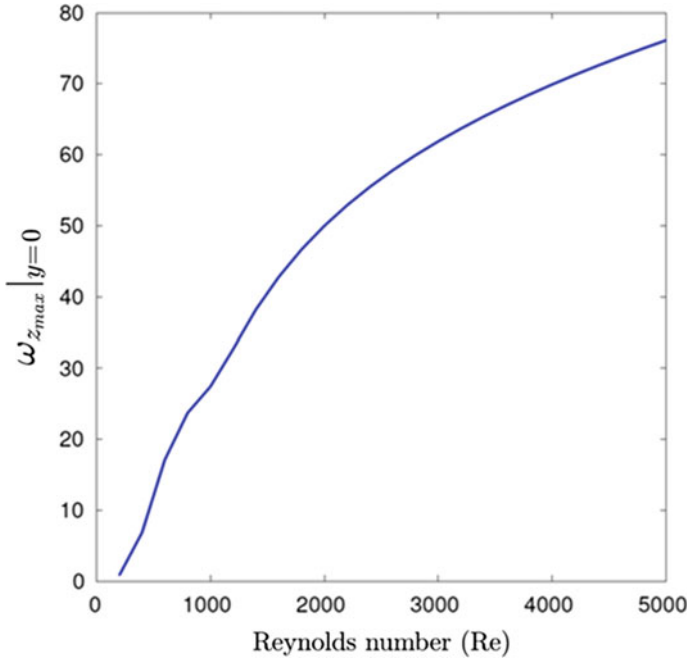
Fig. 6 Maximum vorticity production at the boundary ($y = 0$) as a function of Re for first collision ($\zeta = 0.32$)

The kinetic energy decays monotonously as a function of Re values. It decays faster for an increased enstrophy during the first and second vortex-wall collision. The change in the total kinetic energy depends on the evolution of total enstrophy [5]. The palinstrophy is the measure of vorticity gradient, and it is maximum during the dipole-wall collisions which makes the vortex to deform and induces strain effect to it. The appearance of two peaks in palinstrophy curves can be seen in Fig. 9.

4   Conclusions

The physics associated with the normal collision of a single-dipole of vortices with a flat boundary are studied in a square computational domain using LB-BGK approach and 2048^2 grid nodes. The studies are carried out for various Re values from 625 to 5000. No-slip boundary condition is a main cause of vorticity production at the wall. The production becomes intense at the time of dipole-wall collision. The detachment of the boundary layer forms new asymmetric dipole with the primary vortex and follows the circular trajectory before colliding again with the wall. Multiple small-scale vortices are formed close to the wall for large Reynolds number after the second collision. In the case of Re < 5000, the detached layer rolled up and resulted in the
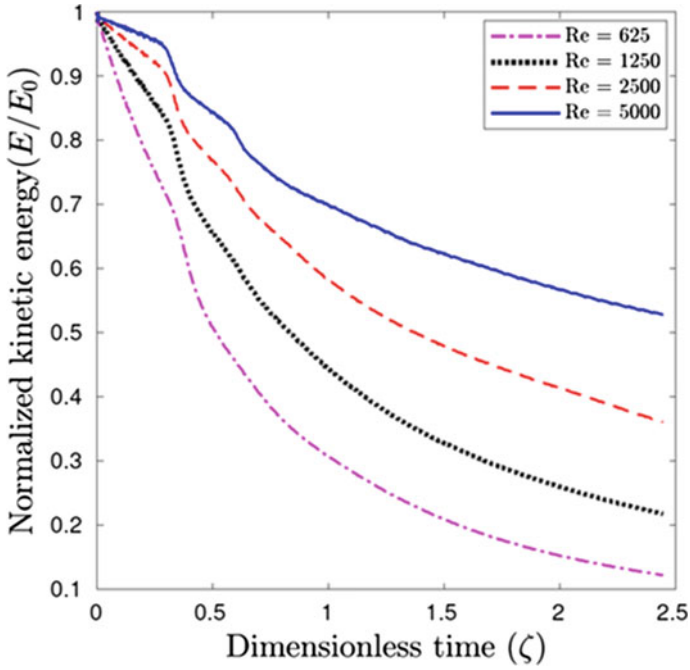
Fig. 7 Evolution of normalized kinetic energy as a function of Reynolds numbers
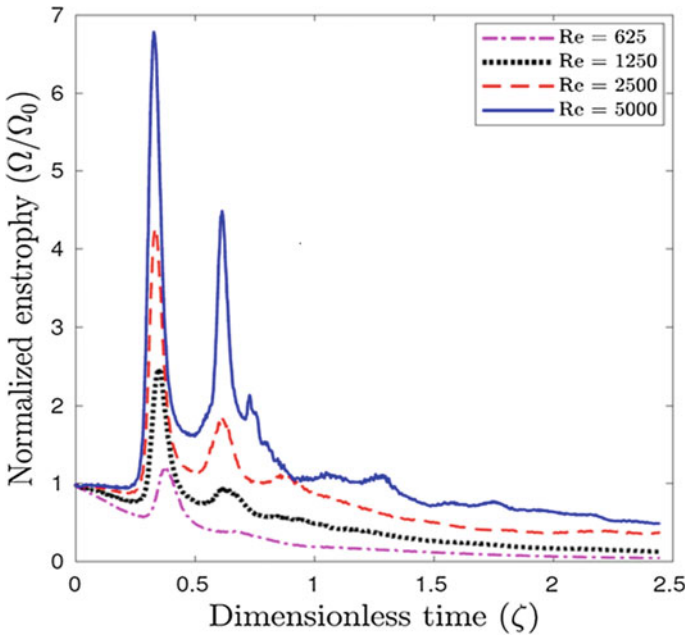
Fig. 8 Evolution of normalized enstrophy as a function of Reynolds numbers
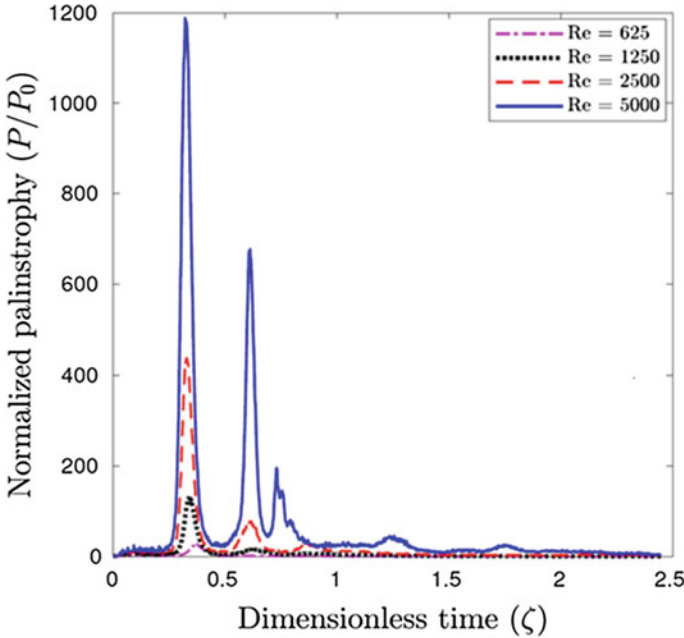
Fig. 9 Evolution of normalized palinstrophy as a function of Reynolds numbers

formation of single vortex. The vorticity production is quantified by extracting the data at $y = 0$ along the entire horizontal length of the domain. The magnitude of the peaks depends on the collision events and reduce with decrease in the Re value. The impact of no-slip boundary and Re variations on the vortex-wall interactions are further studied with the help of global quantities $E(t)$, $\Omega(t)$ and $P(t)$. The large vorticity production at the boundary during the collision makes the enstrophy reach its maximum value. The enstrophy peaks diminish with Re values. The decay rate of kinetic energy is directly influenced by the enstrophy changes, and it decays faster during the vortex-wall interactions. The generation of vorticity gradients during the vortex-wall collision is represented by the appearance of peaks in the palinstrophy curves.

Nomenclature

ζ Dimensionless time
Re   Reynolds number
u_{rms} Root-mean-square velocity

ν	Kinematic viscosity
w	Half width of the domain
ω_z	Vorticity in z-direction
Ω	Enstrophy
P	Palinstrophy
E	Kinetic energy
ω_e	Vorticity extreme

References

1. Clercx HJH, Nielsen AH (2000) Vortex statistics for turbulence in a container with rigid boundaries. Phys Rev Lett 85(4):752
2. Clercx HJH, Van Heijst GJF (2000) Energy spectra for decaying 2d turbulence in a bounded domain. Phys Rev Lett 85(2):306
3. Orlandi P (1990) Vortex dipole rebound from a wall. Phys Fluid Dyn 2(8):1429–1436
4. Clercx HJH, van Heijst GJF (2002) Dissipation of kinetic energy in two-dimensional bounded flows. Phys Rev E 65(6):066305
5. Kramer W, Clercx HJH, Van Heijst GJF (2007) Vorticity dynamics of a dipole colliding with a no-slip wall. Phys Fluids 19(12):126603
6. Peterson SD, Porfiri M (2013) Impact of a vortex dipole with a semi-infinite rigid plate. Phys Fluids 25(9):093103
7. Toth G, Hazi G (2010) Merging of shielded gaussian vortices and formation of a tripole at low Reynolds numbers. Phys Fluids 22(5):053101
8. Mohammed S, Graham DI, Reis T (2020) Modeling the effects of slip on dipole–wall collision problems using a lattice Boltzmann equation method. Phys Fluids 32(2):025104
9. Patil DV, Lakshmisha KN, Rogg B (2006) Lattice Boltzmann simulation of lid-driven flow in deep cavities. Comput Fluids 35(10):1116–1125
10. Gawas AS, Patil DV (2019) Rayleigh-Bénard type natural convection heat transfer in two-dimensional geometries. Appl Therm Eng 153:543–555
11. Bisht M, Kumar P, Patil DV (2021) Non-Newtonian power-law fluid flow over obstacles embedded inside a cavity. Phys Fluids 33(4):043111
12. Gawas AS, Patil DV (2022) Natural convection heat transfer with anisotropic thermal diffusion for tilted two-dimensional cavities. Int J Heat Mass Transf 194:123000
13. He X, Luo L-S (1997) A priori derivation of the lattice Boltzmann equation. Phys Rev E 55(6):R6333

Study on the Impact of Fin Diameter on Thermal and Hydraulic Behaviour of Annular Finned Tubes in Crossflow Using 3D CFD Simulations

Mohit Raje and Amit Dhiman

1 Introduction and Literature Review

The thermal process industry often uses a crossflow heat exchanger with water or air as thermal carriers. The heat transfer coefficient of air is 10–50 times smaller than other fluids [1]. Such low heat transfer coefficient values significantly alter the total heat transfer. Extended surfaces, known as fins, are used on heat exchangers to overcome this issue. Such types of heat exchangers are commonly used as evaporators and condensers in the refrigeration and air-conditioning industry [2].

Because of their direct use in process industries, these heat exchangers have been studied for decades. Watel et al. [3] studied a single-finned tube's flow and thermal behaviour in crossflow. In their study, Reynolds number was varied from $2550 < Re < 42,000$, and fin spacing varied from 2 to 40 mm. For crossflow over a staggered tube bank, Nir [4] gave correlations for friction factor and heat transfer. These experimental correlations are valid for $30 < Re < 10,000$. An experimental study by Gianolio and Cuti [5] correlated the case of forced and induced drafts. They also gave a correction factor if the number of tube rows used is less than six. Pis'mennyi [6] gave correlations for convective heat transfer of tube bundles in crossflow. Their correlations use bundle shape parameter, which considers different geometry parameters.

Recent advancements in computational techniques helped researchers to get a better insight into the problem. A study of unsteady forced convection over radial fins was carried out by Bouzari and Ghazanfarian [7]. They investigated the impact of fin number, fin height and fin location on Strouhal number, drag coefficient and

M. Raje · A. Dhiman (✉)

Department of Chemical Engineering, IIT Roorkee, 247667, Roorkee, Uttarakhand, India

e-mail: amit.dhiman@ch.iitr.ac.in

M. Raje

e-mail: mpradeepraje@ch.iitr.ac.in

Nusselt number. Mon and Gross [8] and Mon [9] used three-dimensional (3D) numerical analysis to study the effect of fin spacing on a staggered and in-line tube array of finned tubes using the RNG k–ε turbulence model. In their study, the fin spacing was altered from $1.6 \leq s \leq 4$ mm, and the Reynolds number range was $8.6 \times 10^3 \leq Re \leq 4.3 \times 10^4$. They concluded that the formation of the horseshoe vortex at the fin-tube interface significantly affects the thermal interactions. Nemati and Moghimi [10] studied different turbulence models for flow over annular finned tubes in crossflow and showed that the transition SST model gives better results with available experimental correlations. A study on shape optimisation for the heat exchanger having a finned tube was carried out by Nemati et al. [11]. A comparative study of the thermal–hydraulic performance of various plate-fin and tube-fin heat exchangers was carried out by Kumar et al. [12]. Their study recommended the use of circular fins to reduce operating costs. Studies on novel fin shapes are available in the literature [13–15].

The current study focuses on the effect of fin diameter over four-row staggered tubes in crossflow using three-dimensional simulations. Studying the impact of fin diameter on the thermo-hydraulic behaviour of finned tubes is essential. This is because, on the one hand, it provides higher heat transfer surface area, but it causes additional flow restriction, which directly affects the pressure drop.

2 Problem Description and Meshing

2.1 Computational Domain

CFD studies are done for the crossflow of air over an annular finned tube. Working fluid (air) with constant physical properties is used to investigate the thermal and hydrodynamic behaviour. The array has four circular finned tubes arranged in a staggered manner. The tube and fin are made of aluminium such that the tube diameter is d and fin diameter is D. Longitudinal and transverse tube pitch was taken as S_l and S_t, respectively. The upstream and downstream distances are taken as $2.8d$ and $8d$, respectively [16]. Figure 1 shows the illustration of the computational domain.
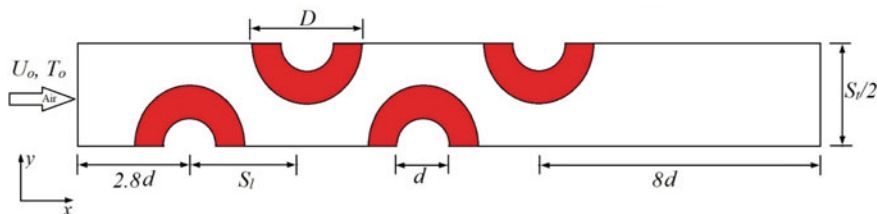
Fig. 1 Illustration of computational domain along x–y plane

2.2 Governing Equations

The flow of air over annular finned tubes is three-dimensional, unsteady, turbulent and incompressible. Reynolds averaged Navier–Stokes (RANS) equations implemented in this study (Eqs. 1–3) are taken from the literature [17–19] and are given as:

Continuity equation:

$$\frac{\partial \rho}{\partial t} + \frac{\partial}{\partial x_i}(\rho u_i) = 0. \tag{1}$$

Momentum balance equation:

$$\frac{\partial}{\partial t}(u_i) + \frac{\partial}{\partial x_j}(u_i u_j) = -\frac{1}{\rho}\frac{\partial p}{\partial x_i} + \frac{\partial}{\partial x_j}\left[\nu\left(\frac{\partial u_i}{\partial x_j} + \frac{\partial u_j}{\partial x_i} - \frac{2}{3}\delta_{ij}\frac{\partial u_\ell}{\partial x_\ell}\right)\right]$$
$$+ \frac{1}{\rho}\frac{\partial}{\partial x'_j}\left(-\rho\overline{u'_i u'_j}\right), \tag{2}$$

where $(-\rho u'_i u'_j)$ are the Reynolds stresses.

The energy equation is given as follows:

$$\frac{\partial}{\partial t}(\rho E) + \frac{\partial}{\partial x_i}(u_i(\rho E + p)) = \frac{\partial}{\partial x_i}\left(k_{\text{eff}}\frac{\partial T}{\partial x_i}\right). \tag{3}$$

The equation for conduction inside the fins is given as follows:

$$\rho c_p \frac{\partial T}{\partial t} = k_s\left(\frac{\partial^2 T}{\partial x_i^2}\right) \tag{4}$$

where subscripts i and j in the above-mentioned equations represent spatial directions, δ_{ij} is Kronecker delta, and the effective thermal conductivity is represented as k_{eff}.

Reynolds stresses mentioned above are modelled using the transition SST model [18], which is an augmentation over the k–ω model [17]. Literature [10, 11] justifies the applicability of this model for the current problem under consideration. Additional information about this model is available in the above-mentioned literature.

2.3 Boundary Conditions

The following boundary conditions are used to solve the governing equations previously described.

- At the inlet, constant velocity (*x*-direction) and constant temperature (T_o) of air are specified.
- Zero-gauge pressure at the outlet of computational domain.
- Heat flux and velocity components at symmetry surfaces are zero.
- At the tube wall surface, no-slip condition with constant wall temperature (T_w) is applied.
- No-slip condition is applied at the fin–fluid interface, along with convection from the fin.

2.4 Mesh Generation and Solution Algorithm

ANSYS meshing software R18.1 [19] is employed for the discretisation of the computational domain. Near the solid surfaces, fine meshing was done to capture the boundary layer effect. A structured mesh was made in the region between fins, while an unstructured mesh was made in the remaining domain. The resulting mesh has average skewness of 4.1×10^{-2}, an average aspect ratio of 9.7, an average value of *y*+ is well below 2 and a minimum grid size of 0.05 mm. Figure 2 shows the mesh of the computational domain. Numerical simulations are performed for annular finned tubes arranged in a staggered array for various fin diameters. The present study is carried out in the Reynolds number range of $4630 \leq Re \leq 9260$. Finite volume-based solver ANSYS Fluent [19] is used to solve the unsteady turbulent flow. The physical properties of air are considered constant. PISO scheme is implemented for pressure–velocity coupling, and the second-order upwind scheme is adopted to discretise the continuity, energy and momentum equations. In contrast, a second-order implicit scheme is used for transient formulation. The convergence criteria for the energy equation is set to 10^{-10}, whereas for other equations, it is set to 10^{-09}.

3 Output Parameters

The equation for the overall heat transfer from the tube bank is

$$Q = \dot{H}_{\text{out}} - \dot{H}_{\text{in}} \tag{5}$$
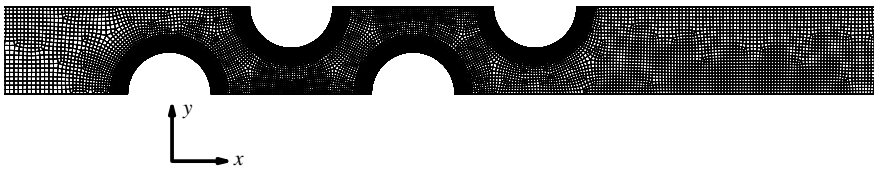
Fig. 2 Mesh of the computational domain along *x*–*y* plane

where $\dot{H}_{\text{out}}$ and $\dot{H}_{\text{in}}$ are flow rates of enthalpy at the outlet and inlet of the tube bundle, respectively, obtained from ANSYS Fluent [19]. Taking A_f as fin surface area, A_t as tube surface area and η as fin efficiency, we can determine the air-side heat transfer from Eq. (6).

$$h = \frac{Q}{(A_t + \eta A_f)\theta}$$ (6)

The log-mean temperature difference (θ) is defined as

$$\theta = \frac{T_0 - T_{\text{out}}}{\ln\left(\frac{T_0 - T_w}{T_{\text{out}} - T_w}\right)}.$$ (7)

An iterative procedure to get the fin efficiency is adopted from Mon and Gross [8]. The Nusselt number is calculated as

$$\text{Nu} = \frac{hd}{k}.$$ (8)

The expression for Reynolds number (Re) is given by Eq. (9).

$$\text{Re} = \frac{d u_{\text{max}} \rho}{\mu}.$$ (9)

4 Grid Independence and Validation

4.1 Grid Independence

Four different grids having 180,250, 221,952, 250,712 and 295,874 control volumes were considered for grid independence test. The results of different grids were compared with the most refined grid consisting of 295,874 control volumes. These results are shown in Table 1. It is clear that the grid with 221,952 control volumes is preferable considering accuracy and computational time and therefore used in this study.

Table 1 Grid independence test at $Re = 9260$ and $D = 34$ mm

No. of control volumes	Nu	Deviation	ΔP	Deviation
180,250	77.79	−2.83%	60.47	−1.76%
221,952	76.38	−0.97%	59.81	−0.65%
250,712	76.04	−0.52%	59.59	−0.27%
295,874	75.65	–	59.43	–

4.2   Validation

To test the accuracy of the current numerical scheme, present findings were compared to the previously available experimental data from literature [5] and are shown in Fig. 3. For Nusselt number, the maximum deviation was 9.4% and for the Euler number, it was 9.2%. According to the literature [12, 20], deviations within ±15% are acceptable when computational results are compared with experimental data. This approves the accuracy of the current model.

5   Results and Discussion

This section discusses the thermal and hydraulic behaviour of the annular finned tubes in detail. Studies are carried out to determine how pressure drop, heat transfer rate and heat transfer coefficient are affected by fin diameter and Reynolds number. In addition, the fin surface temperature distribution is obtained to get more insight into the thermal behaviour of fins.

Figure 4 illustrates how the heat transfer rate varies with the Reynolds number for various tube sizes. We see that the heat transfer is affected by fin diameter since the increase in fin diameter will increase the available heat transfer area. Also, at a higher value of the Reynolds number, an increment in flow velocity contributes to the heat transfer rate. The heat transfer is nearly 29% higher when the fin diameter changes from 34 to 38 mm at the lowest value of *Re,* whereas this change is nearly 19% at the highest Reynolds number.

In Fig. 5, a plot of the heat transfer coefficient versus Reynolds number for varying tube diameters is shown. For all scenarios, the heat transfer coefficient rises with *Re*. This is mainly caused by increased heat transfer rate at a superior Reynolds number (as shown in Fig. 4). The heat transfer coefficient increases by roughly 61% as the Reynolds number rises from the lowest to the highest value for the fin diameter of 34 mm and for fin diameter of 38 mm it increases by 57%. At $Re = 4630$, the heat transfer coefficient is nearly 12% higher when the fin diameter increases from 34 to 36 mm. Whereas it increases by nearly 9% at $Re = 9260$.

Pressure drop is used as an essential parameter to analyse the hydrodynamic behaviour of any crossflow heat exchanger. Knowledge of pressure drop helps in determining the pumping requirements. Figure 6 depicts the plot of pressure drop

Fig. 3 Comparison of current results with experimental data from literature [5]: **a** Nusselt number and **b** Euler number

(a)

(b)
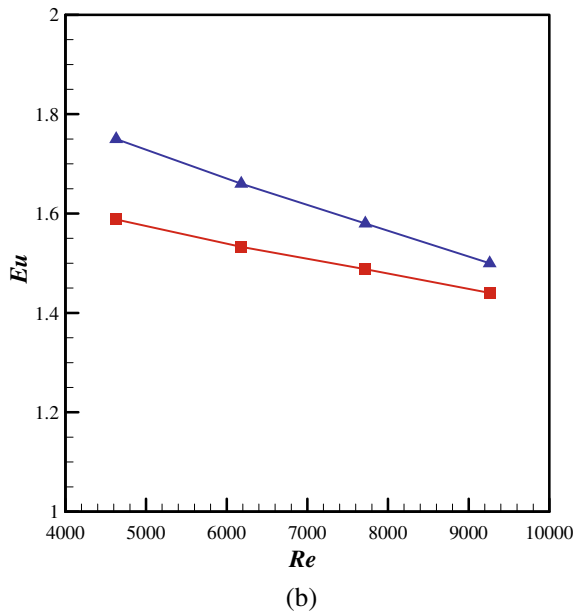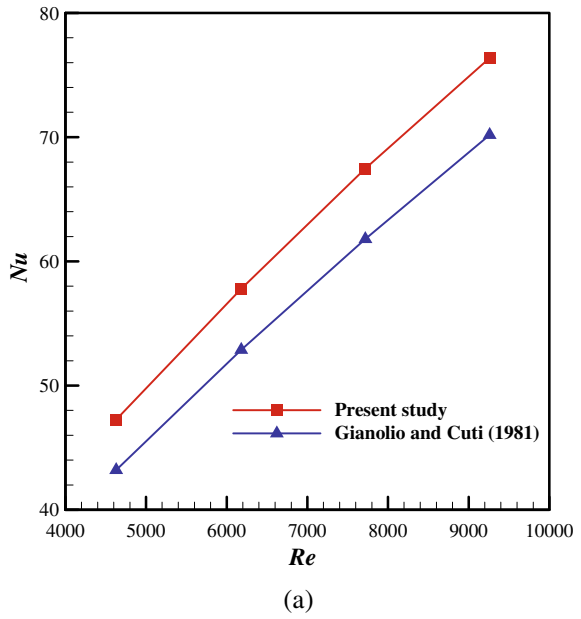
Fig. 4 Heat transfer rate
against Reynolds number at
various fin diameter values
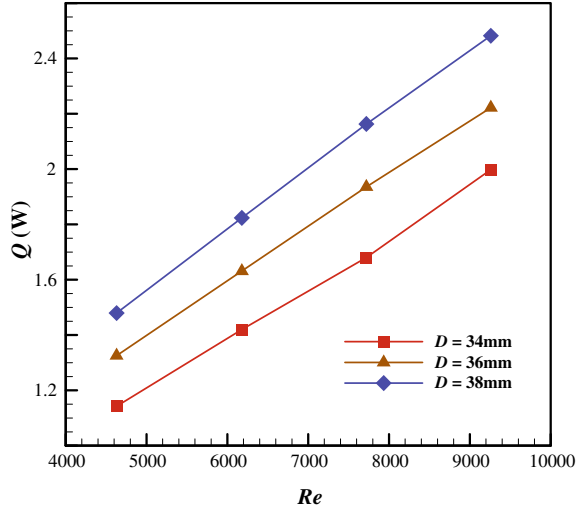
Fig. 5 Heat transfer
coefficient against Reynolds
number at various fin
diameter values
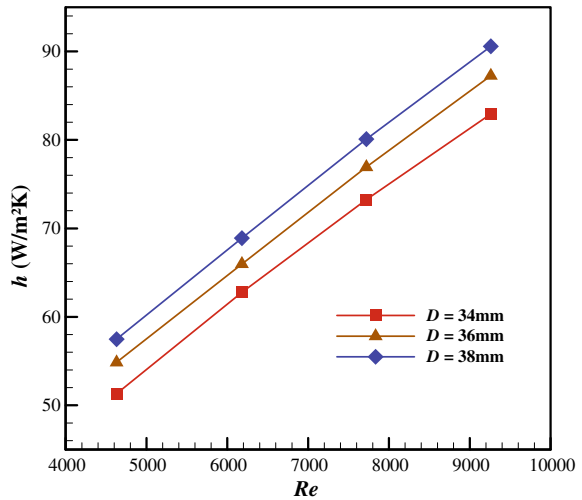
against the Reynolds number with variation in fin diameter. It is evident that the
pressure drop increases with the Reynolds number at all values of the fin diameter
owing to an increment in velocity. The pressure drop increases by nearly 9–12%
at the highest and the lowest Reynolds number, respectively, when the fin diameter
increases from 34 to 38 mm. At a particular value of the Reynolds number, when the
fin diameter is augmented, it intensifies the skin friction factor, contributing to the
escalation of pressure drop.

The illustration of the change in fin surface temperature for the maximum and
minimum Reynolds number at different fin diameters for the first finned tube is

Fig. 6 Pressure drop against Reynolds number at various fin diameter values
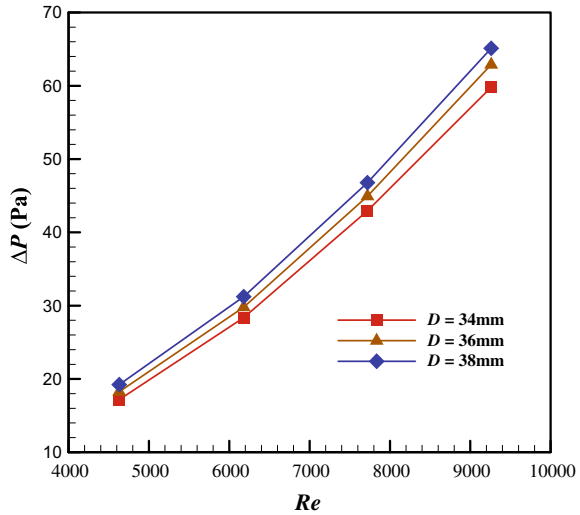
shown in Fig. 7. It is noticeable from the figure that the maximum temperature difference is along the radial direction. Additionally, the frontal portion of the fin exhibits greater temperature gradients than the back portion. The temperature at the downstream section is nearly the same as the tube surface temperature. However, as the Reynolds number and fin diameter increase, the region of lower temperature at the downstream section decreases. The surface temperature distribution on succeeding rows has similar behaviour and is not shown here for brevity. It is worth mentioning here that the upstream side temperature of the second row is higher than any other rows. This is because higher velocity flow impinges on the upstream section of this finned tube.

6 Conclusions

Three-dimensional computations are performed for the staggered alignment of annular finned tubes in cross-flow. The impact of fin diameter on thermal and hydrodynamic parameters is investigated using the transition SST turbulence model. The key conclusions from this research are as follows:

- The heat transfer rate increases according to the Reynolds number and fin diameter. The heat transfer rate rises by nearly 19% and 29% when the fin diameter is enlarged at the highest and the lowest Reynolds number values, respectively.
- The heat transfer coefficient, an important factor used to quantify thermal performance, also shows the same trend as the heat transfer rate when plotted against Reynolds number. The heat transfer coefficient surges by nearly 61% when the Reynolds number is increased from its minimum value to its maximum value
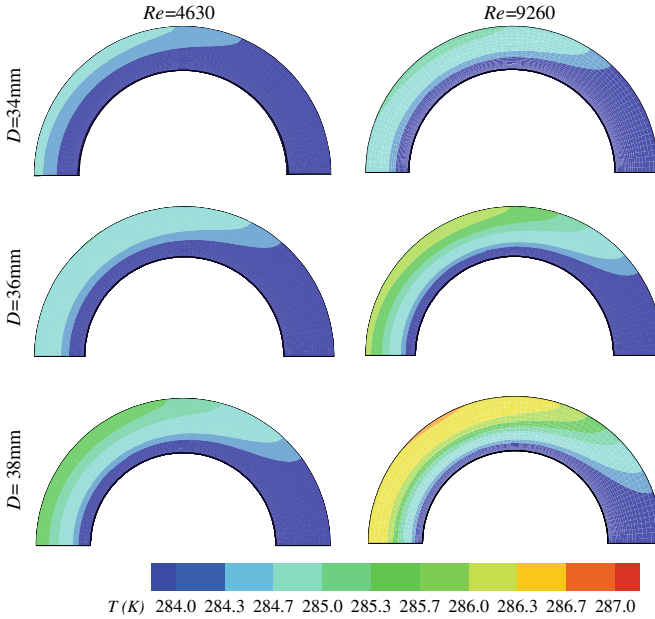
Fig. 7 Fin surface temperature distribution at the maximum and minimum Reynolds number at various values of fin diameter

when the diameter of the fin equals 34 mm. Nevertheless, for a fin diameter of 38 mm, it surges by nearly 57%.

- Pressure drop increases with the Reynolds number and the fin diameter owing to the increased velocity and increased skin friction factor, respectively. This increase is nearly 9–12% at the highest and the lowest value of the Reynolds number.
- The downstream side of the fin has a temperature that is almost identical to the surface temperature of the tube. Albeit this region of lower temperature decreases with Reynolds number and fin diameter, it is clear that this section will contribute the least in heat transfer.
- Based on these results, it is undoubtedly deduced that the higher fin diameter values give higher heat transfer but at the expense of pressure drop.

Nomenclature

A_f	Fin surface area (m^2)
A_t	Tube surface area (m^2)
d	Tube diameter (mm)
D	Fin diameter (mm)
Eu	Euler number

h	Heat transfer coefficient (W/m^2 K)
$\dot{H}$	Enthalpy flow rate (W)
k	Thermal conductivity (W/m K)
Nu	Nusselt number
ΔP	Pressure drop (Pa)
Q	Heat transfer rate (W)
Re	Reynolds number
S_l	Longitudinal tube pitch (mm)
S_t	Transverse tube pitch (mm)
T	Temperature (K)
u_{max}	Maximum velocity (m/s)
ρ	Density (kg/m^3)
υ	Kinematic viscosity (m^2/s)
μ	Viscosity (kg/m s)
η	Fin efficiency
θ	Log mean temperature difference

References

1. Webb RL (1980) Air-side heat transfer in finned tube heat exchangers. Heat Transfer Eng 1(3):33–49
2. Shah RK, Sekuli DP (2003) Fundamentals of Heat Exchanger Design, 1st edn. Wiley, New York, pp 41–44
3. Watel B, Harmand S, Desmet B (1999) Influence of flow velocity and fin spacing on the forced convective heat transfer from an annular-finned tube. Int J Ser B Fluids Thermal Eng 42(1):56–64
4. Nir A (1991) Heat transfer and friction factor correlations for crossflow over staggered finned tube banks. Heat Transfer Eng 12(1):43–58
5. Gianolio E, Cuti F (1981) Heat transfer coefficients and pressure drops for air coolers with different numbers of rows under induced and forced draft. Heat Transfer Eng 3(1):38–48
6. Pis'mennyi EN (2011) An asymptotic approach to generalising the experimental data on convective heat transfer of tube bundles in crossflow. Int J Heat Mass Transf 54(19–20):4235–4246
7. Bouzari S, Ghazanfarian J (2017) Unsteady forced convection over cylinder with radial fins in cross flow. Appl Therm Eng 112:214–225
8. Mon MS, Gross U (2004) Numerical study of fin-spacing effects in annular-finned tube heat exchangers. Int J Heat Mass Transf 47(8–9):1953–1964
9. Mon MS (2003) Numerical investigation of air-side heat transfer and pressure drop in circular finned-tube heat exchangers. Doctoral Thesis, Technische Universitat Bergakademie Freiberg, Germany
10. Nemati H, Moghimi M (2014) Numerical study of flow over annular-finned tube heat exchangers by different turbulent models. CFD Lett 6(3):101–112
11. Nemati H, Moghimi MA, Sapin P, Markides CN (2020) Shape optimisation of air-cooled finned-tube heat exchangers. Int J Therm Sci 150:106233
12. Kumar A, Joshi JB, Nayak AK (2017) A comparison of thermal-hydraulic performance of various fin patterns using 3D CFD simulations. Int J Heat Mass Transf 109:336–356

13. Anoop B, Balaji C, Velusamy K (2015) A characteristic correlation for heat transfer over serrated finned tubes. Ann Nucl Energy 85:1052–1065
14. Unger S, Beyer M, Gruber S, Willner R, Hampel U (2019) Experimental study on the air-side thermal-flow performance of additively manufactured heat exchangers with novel fin designs. Int J Therm Sci 146:106074
15. Bošnjaković M, Muhič S, Čikić A (2020) Experimental testing of the heat exchanger with star-shaped fins. Int J Heat Mass Transf 149:119190
16. Raje M, Dhiman A. Three-dimensional analysis of the thermal and hydraulic performance of finned and un-finned tubes in a staggered array. Therm Sci Eng Prog (submitted)
17. Menter FR, Kuntz M, Langtry R (2003) Ten years of industrial experience with the SST turbulence model. Turbul Heat Mass Transf 4(1):625–632
18. Menter FR, Langtry R, Völker S (2006) Transition modelling for general purpose CFD codes. Flow Turbul Combust 77(1–4):277–303
19. Ansys Fluent Users Guide, Release 18.0 (2017)
20. Asif M, Chaturvedi R, Dhiman A (2021) Heat transfer enhancement from in-line and staggered arrays of cylinders in a heat exchanger using alumina–water nanofluid. J Therm Sci Eng Appl 13(4):041025

Rigid-Vortex Configurations of Four Point Vortices

Sreethin Sreedharan Kallyadan and Priyanka Shukla

1 Introduction

Analogous to the point mass approximation used in celestial mechanics, the point vortex model [1] is a discrete vortex model widely used to study the motion of mutually interacting vortices in a two-dimensional incompressible ideal fluid. In this model, a vortex is identified as a delta distribution of vorticity, which induces a radially symmetric azimuthal velocity field. The magnitude of this velocity is proportional to the vortex strength (circulation), and it decays inversely with the distance from the vortex. When multiple point vortices are present, each vortex will move according to the superposition of velocity fields induced by the other vortices giving rise to complex fluid motions. The N-vortex problems, the problem on the motion of N interacting point vortices, help us to gain insights into the elementary processes that govern the mixing and transport in turbulent flows [2]. For a comprehensive review of the point vortex model and its applications, the reader may refer to [3, 4].

The governing equations of a system of N point vortices ($\alpha = 1, 2, \ldots, N$) of circulations $\Gamma_\alpha \in \mathbb{R}$ and coordinates $(x_\alpha(t), y_\alpha(t)) \in \mathbb{R}^2$ at time t on the unbounded plane is

$$\frac{\mathrm{d}x_\alpha}{\mathrm{d}t} = \frac{-1}{2\pi} \sum_{\beta=1}^{N}{}' \Gamma_\beta \frac{(y_\alpha - y_\beta)}{l_{\alpha\beta}^2},$$

$$\frac{\mathrm{d}y_\alpha}{\mathrm{d}t} = \frac{1}{2\pi} \sum_{\beta=1}^{N}{}' \Gamma_\beta \frac{(x_\alpha - x_\beta)}{l_{\alpha\beta}^2}, \tag{1}$$

S. S. Kallyadan (✉) · P. Shukla
Department of Mathematics, IIT Madras, Chennai 600036, India
e-mail: sreethin2@gmail.com

where $l_{\alpha\beta} = \sqrt{(x_\alpha - x_\beta)^2 + (y_\alpha - y_\beta)^2}$ denotes the distance between α and β vortices, and the primed sum is used to indicate that the $\beta = \alpha$ case is excluded from the summation (see Ref. [4] for more details). Since the point vortex Eq. (1) are undefined if any one of the $N(N-1)/2$ inter-vortex distances $l_{\alpha\beta}$ is zero, we shall always assume that the initial vortex coordinates $k_\alpha = (x_\alpha, y_\alpha)|_{t=0}$ are distinct.

For certain initial vortex positions, referred to as the rigid vortex configurations, the resulting vortex motion is such that the inter-vortex distances remain constant throughout the motion, and the collection of vortices moves as a rigid body. The importance of the rigid vortex configurations stems from the fact that they represent the critical points of vortex interaction energy subjected to a constant linear and angular momentum [5]. Hence, a vortex system slows down as it approaches any rigid vortex solutions, resulting in them being observed as coherent and persistent patterns in two-dimensional flows [5–10]. The three-vortex problem is fully understood [11–14], and in particular, it is known that the equilateral triangle configuration is the only non-collinear rigid vortex configuration possible. While the number of rigid vortex configurations in a four-vortex system is known to be finite for prescribed values of circulations [15], it is not understood how these vortex configurations are geometrically distributed in the space of all possible initial vortex positions. Since the configuration space is more than three-dimensional, visualizing and understanding their distribution is difficult. The present work is devoted to addressing this challenge.

While there are multiple numerical approaches present in the literature to find rigid vortex configurations for prescribed values of circulations [16–18], the linear formulation proposed by Newton and Chamoun [18] enables one to find them purely in terms of vortex configurations without the prior knowledge of circulations. In this approach, one first derives the following expression for the squared inter-vortex distance derivative using (1) (see Chapter 2 of Ref. [4]),

$$\frac{d}{dt}(l_{\alpha\beta}^2) = \frac{2}{\pi} \sum_{\gamma=1}^{N} {}'' \Gamma_\gamma A_{\alpha\beta\gamma} \left(\frac{1}{l_{\beta\gamma}^2} - \frac{1}{l_{\alpha\gamma}^2} \right), \tag{2}$$

where the double primed sum is used to indicate that the two cases $\gamma = \alpha$ and $\gamma = \beta$ are excluded from the summation, and

$$A_{\alpha\beta\gamma} = \frac{1}{2} \big[(x_\beta - x_\alpha)(y_\beta - y_\gamma) - (x_\beta - x_\gamma)(y_\beta - y_\alpha) \big] \tag{3}$$

represents the (signed) area of the triangle $\Delta_{\alpha\beta\gamma}$ obtained by joining the three-vortex coordinates (x_α, y_α), (x_β, y_β), and (x_γ, y_γ) in that specific order. Since rigid vortex configurations are equilibrium points of the phase plane constituted by the inter-vortex distances, and because (2) is linear in circulations, the condition for constant inter-vortex distances $d/dt(l_{\alpha\beta}^2) = 0$ initially can be thus expressed as a matrix system,

$$M\Gamma = 0, \tag{4}$$

where $M = M(k_\alpha)$ is the $N(N-1)/2 \times N$ configuration matrix whose entries are in terms of the initial vortex position and $\Gamma = [\Gamma_1, \Gamma_2, \ldots, \Gamma_N]^{\mathrm{T}}$ is the set of circulations as a column vector. Therefore, the only possible circulations that can be assigned to a geometric arrangement of vortices such that they lead to a rigid vortex motion are the null space elements of its associated configuration matrix. The notion of configuration matrix was used to find individual rigid vortex configurations in Ref. [18]. In the present work, we shall use this concept to analyze the distribution of rigid close approximation of a rigid vortex configuration for some nonzero choice of circulation set.

This paper is organized as follows. In Sect. 2, we define an error function using the singular values associated with the configuration matrix to numerically quantify the distance from a generic vortex configuration to a rigid vortex configuration. The error function is used to illustrate the distribution of rigid vortex configurations and to explain the different possible cases exhaustively in Sect. 3. Finally, in Sect. 4, we summarize our findings.

2 Methodology

Without loss of generality (WLOG), we may assume that $k_1 = (0, 0), \quad k_2 = (1, 0)$ by appropriately choosing the origin, orienting, and scaling the axes. Let us denote the initial locations of the third and fourth vortices by $k_3 = (a, b)$ and $k_4 = (x, y)$, respectively. We shall assume that (a, b) is a fixed parameter and (x, y) is a free variable; i.e., we are interested in which all (x, y) yield a rigid vortex configuration for a fixed choice of (a, b). From the linear formulation (4), we have the configuration matrix M to be $2/\pi$ times

$$\begin{pmatrix} 0 & 0 & A_{123}\left(\frac{1}{l_{23}^2} - \frac{1}{l_{13}^2}\right) & A_{124}\left(\frac{1}{l_{24}^2} - \frac{1}{l_{14}^2}\right) \\ 0 & A_{132}\left(\frac{1}{l_{23}^2} - 1\right) & 0 & A_{134}\left(\frac{1}{l_{34}^2} - \frac{1}{l_{14}^2}\right) \\ 0 & A_{142}\left(\frac{1}{l_{24}^2} - 1\right) & A_{143}\left(\frac{1}{l_{34}^2} - \frac{1}{l_{13}^2}\right) & 0 \\ A_{231}\left(\frac{1}{l_{13}^2} - 1\right) & 0 & 0 & A_{234}\left(\frac{1}{l_{34}^2} - \frac{1}{l_{24}^2}\right) \\ A_{241}\left(\frac{1}{l_{14}^2} - 1\right) & 0 & A_{243}\left(\frac{1}{l_{34}^2} - \frac{1}{l_{23}^2}\right) & 0 \\ A_{341}\left(\frac{1}{l_{14}^2} - \frac{1}{l_{13}^2}\right) & A_{342}\left(\frac{1}{l_{24}^2} - \frac{1}{l_{23}^2}\right) & 0 & 0 \end{pmatrix}$$

where the entries are in terms of *a, b* and *x, y*. Clearly, $\Gamma = [0, 0, 0, 0]^{\mathrm{T}}$ trivially yields $M\Gamma = 0$. Necessitating not all circulation are zero implies that M must have at least one of the singular values (the eigenvalues of the matrix $M^{\mathrm{T}}M$, see [18]) zero. Therefore, for a given configuration, we can associate an error

$$E(x, y) = \frac{\sigma_{\min}}{\sigma_{\max}},$$

where $\sigma_{\min}$ and $\sigma_{\max}$ are the smallest and largest singular values associated with the configuration matrix M. Note that singular values are always non-negative, and a near zero value of $E(x, y)$ implies that the vortex configuration is a close approximation of a rigid vortex configuration for some nonzero choice of circulation set.

3 Results and Discussion

Depending on the type of vortex triangle formed by the first three vortices ($\alpha = 1, 2, 3$), we may subdivide the different parametric cases into three.

- Equilateral triangle case ($l_{13} = l_{23} = 1$)
- Isosceles triangle case ($l_{13} = l_{23} \neq 1$, or $l_{13} = 1$, $l_{23} \neq 1$ or $l_{23} = 1$, $l_{13} \neq 1$)
- Non-isosceles triangle case ($l_{13} \neq l_{23} \neq 1$).

A. Equilateral Triangle Case

The parametric case, where (a, b) is such that $l_{13} = l_{23} = l_{12} = 1$ is a degenerate case, as explained below. WLOG we may assume $(a, b) = (1, \sqrt{3})/2$. The matrix M can be simplified to show that irrespective of the value of (x, y), for the choice of circulations

$$\Gamma_1 = -\frac{\left(\frac{1}{l_{34}^2} - 1\right)\left(\sqrt{3}(x - 1) + y\right)}{2\left(\frac{1}{l_{14}^2} - 1\right)y},$$

$$\Gamma_2 = \frac{\left(\frac{1}{l_{34}^2} - 1\right)\left(\sqrt{3}x - y\right)}{2\left(\frac{1}{l_{24}^2} - 1\right)y},$$

$$\Gamma_3 = 1,$$

$$\Gamma_4 = 0,$$

All vortex configurations lead to rigid vortex motion. Therefore, in a four-vortex configuration, if any three vortices form an equilateral triangle, it is a rigid vortex configuration for the appropriate choice of circulations.

B. Isosceles Triangle Case

Suppose that the vortex triangle obtained by joining the location of the first three vortices is an isosceles triangle and not an equilateral triangle. By appropriately indexing the three vortices, we may assume that $l_{13} = l_{23} \neq 1$. Therefore, we must have $a = 0.5$ and $b \neq \sqrt{3}/2$. The distribution of $\log(E)$ versus (x, y), the initial location of the fourth vortex, is illustrated for the representative case $(a, b) =$

Fig. 1 Density plot of $\log(E)$ for $(a, b) = (0.5, 0.5)$
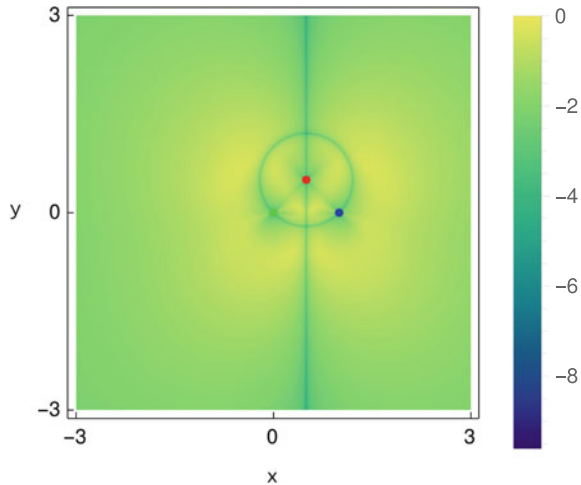
$(0.5, 0.5)$ in Fig. 1. The location of the first three vortices is marked by green, blue and red dots, respectively. It can be seen that the rigid vortex configurations exist as a one-dimensional continuum, wherein the fourth vortex initial position, $k_4 = (x, y)$, varies continuously over (i) a circle centered at (a, b) with a radius $l_{13} = \sqrt{a^2 + b^2}$ and (ii) the $x = 1/2$ line. Each point on the circle represents the trivial case in which vortices indexed 1, 2 and 4 are equidistant from the third vortex at (a, b). The triviality of the configuration is because we can always choose $\Gamma_3 = 1$ and all other vortex circulations to be zero, resulting in vortices 1, 2 and 4 becoming passive tracers with the associated rigid vortex motion being the simple uniform circular motion around the third vortex. Note that the above arguments hold true for any b.

Substituting $a = 0.5 = x$ and simplifying the configuration matrix M, we see that the following choice of circulations would yield a rigid vortex configuration irrespective of the third and fourth initial vortex coordinates on the $x = 1/2$ line.

$$\Gamma_1 = 1,$$
$$\Gamma_2 = 1,$$
$$\Gamma_3 = \frac{2y(4y^2 - 3)(b - y)(1 + 4b^2)}{(1 + 4y^2)(4y^2 - 8by - 1)},$$
$$\Gamma_4 = \frac{2b(4b^2 - 3)(y - b)(1 + 4y^2)}{(1 + 4b^2)(4b^2 - 8by - 1)},$$

C. **Non-isosceles Triangle Case**

The non-isosceles triangle case represents the most generic case, and the configuration matrix cannot be analytically simplified anymore. The density plot of $\log(E)$ for the representative case $(a, b) = (0, 2)$ is shown in Fig. 2.

Fig. 2 Density plot of
$\log(E)$ for $(a, b) = (0, 2)$
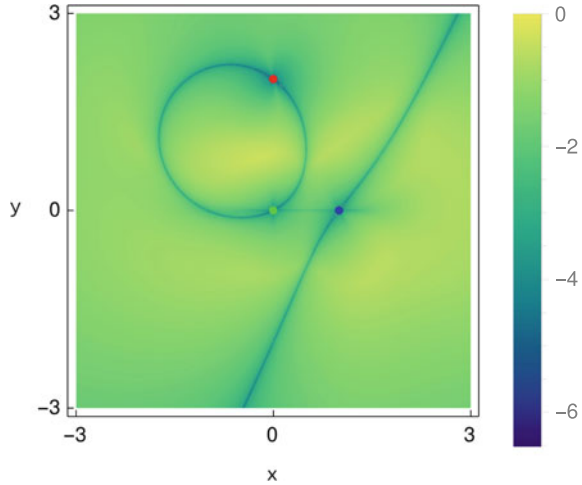
It can be seen that the rigid vortex configurations still exist as one-dimensional continua consisting of a bounded and unbounded component. However, unlike the isosceles triangle case, the two components do not have any intersections. Moreover, the bounded component is no longer a circle but a simple closed curve. The $x = 1/2$ straight line component is also replaced by a curved unbounded line.

Let us investigate what happens to the two components when we approach one of the singular cases l_{13} or l_{23} approaching zero with respect to the parameter (a, b). It suffices to only consider the case of l_{13} tending to zero because of the reflective symmetry of the vortex configurations along the $x = 1/2$ line. We consider $(a, b) = (0.25, 0)$ for the density plot in Fig. 3. It can be seen that the bounded component of the continuum shrinks down in size as l_{13} tends to zero.

Fig. 3 Density plot of
$\log(E)$ for $(a, b) = (0.25, 0)$
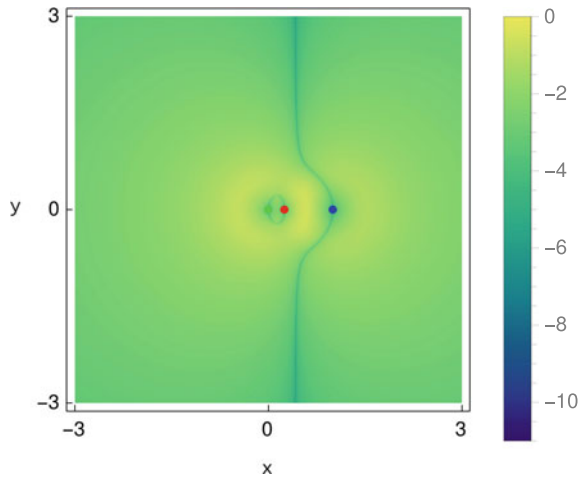
It is worth noting that the bounded component of the rigid vortex continua contains two singular configurations, wherein the coordinate of the fourth vortex coincides with one of the other two vortex locations. Such singular continua of rigid vortex configurations were studied by O'Neil [19]. The present manuscript asserts that this singular nature is a fundamental property of the continua of rigid vortex configurations when $N > 3$.

4 Conclusions

The initial vortex arrangements that lead to rigid vortex motion of four point vortices are systematically illustrated and analyzed. The different parametric cases are subdivided into three as (i) equilateral triangle case, (ii) isosceles triangle case, and (iii) non-isosceles triangle case, based on the type of vortex triangle obtained by joining the first two vortices at $(0, 0)$ and $(1, 0)$ with the third vortex.

If the location of the third vortex in the configuration is such that it forms an equilateral triangle, then irrespective of where the fourth vortex is located, there is at least one choice of non-trivial circulations for which the resulting motion is a rigid vortex motion.

On the other hand, if the vortex triangle is an isosceles triangle, the locations of the fourth vortex for which the resultant configuration is a rigid vortex configuration consists of a circle passing through the two vortices and a straight line. A choice of circulations for the rigid vortex configurations in the continua is also analytically given.

Lastly, when the vortex triangle has no symmetry, then the collection of fourth vortex locations in the rigid vortex configurations for a fixed third vortex location is again continua consisting of a bounded simple closed curve and an unbounded curved line. The two components are disconnected, unlike the isosceles triangle case. Moreover, as the location of the third vortex approaches any of the first two vortices, the bounded component shrinks in size.

Apart from the five-vortex example provided by Roberts [20], it is still not known whether there are more examples of continua of rigid vortex configurations wherein the associated circulations remain constant. A robust analysis of the non-isosceles case focusing on how the circulations vary along the bounded and unbounded continua may provide important insights in this regard.

Nomenclature

(x_α, y_α) Cartesian coordinate of the α-vortex
Γ_α Circulation of the α-vortex
k_α Initial vortex position of the α-vortex
$l_{\alpha\beta}$ Distance between α and β vortices

(a, b) Initial location of the third vortex
(x, y) Initial location of the fourth vortex

References

1. Helmhollz H (1858) Uber integrale der hydrodynamischen gleichungen, welche den wirbel-bewegungen entsprechen. J Reine Angew Math 25–55
2. Aref H (1983) Integrable, chaotic, and turbulent vortex motion in two-dimensional flows. Annu Rev Fluid Mech 15(1):345–389
3. Aref H (2007) Point vortex dynamics: a classical mathematics playground. J Math Phys 48:065401
4. Newton PK (2013) The N-vortex problem: analytical techniques, vol 145. Springer, Cham
5. Aref H, Newton PK, Stremler MA, Tokieda T, Vainchtein DL (2002) Vortex crystals. Technical report. Department of Theoretical and Applied Mechanics (UIUC)
6. Yarmchuk E, Gordon M, Packard R (1979) Observation of stationary vortex arrays in rotating superfluid helium. Phys Rev Lett 43(3):214
7. Durkin D, Fajans J (2000) Experiments on two-dimensional vortex patterns. Phys Fluids 12(2):289–293
8. Kossin JP, Schubert WH (2004) Mesovortices in hurricane isabel. Bull Am Meteorol Soc 85(2):151–153
9. Grassi D, Adriani A, Moriconi M, Mura A, Tabataba-Vakili F, Ingersoll A, Orton G, Hansen C, Altieri F et al (2018) First estimate of wind fields in the Jupiter polar regions from Jiram-Juno images. J Geophys Res Planets 123(6):1511–1524
10. Di Labbio G, Ait Abderrahmane H, Fayed M, Ng HD (2020) Transitions between systems of satellite vortices in a rotating fluid. Phys. Fluids 32(10):101701
11. Grobli W (1877) Specielle Probleme uber die Bewegung geradliniger paralleler Wirbelfaden, vol 8. Druck von Zurcher und Furrer
12. Synge J (1949) On the motion of three vortices. Can J Math 1(3):257–270
13. Novikov E (1975) Dynamics and statistics of a system of vortices. Zh Eksp Teor Fiz 68(1868–188):2
14. Aref H (1979) Motion of three vortices. Phys Fluids 22(3):393–400
15. Hampton M, Moeckel R (2009) Finiteness of stationary configurations of the four-vortex problem. Trans Amer Math Soc 361(3):1317–1332
16. Campbell LJ, Ziff RM (1979) Vortex patterns and energies in a rotating superfluid. Phys Rev B 20:1886–1902
17. Aref H, Vainchtein DL (1998) Point vortices exhibit asymmetric equilibria. Nature 392(6678):769–770
18. Newton PK, Chamoun G (2007) Construction of point vortex equilibria via Brownian ratchets. *Proc R Soc Lond Ser A Math Phys Eng Sci* 463(2082):1525–1540
19. O'Neil KA (2013) Singular continuation of point vortex relative equilibria on the plane and sphere. Nonlinearity 26(3):777–804
20. Roberts GE (1999) A continuum of relative equilibria in the five-body problem. Phys D Nonlinear Phenom 127(3):141–145

Simulation of Blow-Down Through Two-Phase Flow Module and Orifice in HTHP Loop Using RELAP5/MOD 3.2

A. Moorthi, Niraj Uttam, K. Prem Sai, and I. V. N. S. Kamaraju

1 Introduction

During a LOCA in a water-cooled reactor, the steam-water mixture rushes through the opening of the pressure boundary. The blow-down rate is a function of the size of the opening and pressure and temperature of coolant [1, 2]. The flow can be single phase or two phase. Experimental investigations of blow-down through different sizes of orifices are proposed to be conducted in the high-temperature and high-pressure (HTHP) loop facility available at Kalpakkam [3]. In this facility, studies were conducted on Blow-down through orifices [4] and delayed neutron (DN) tubes earlier [5]. Further elaborate studies are planned by installing homogenizer and two-phase flowmeter (TPFM) along with the orifices.

2 Description of HTHP Loop

The high-temperature and high-pressure loop consists of a test vessel, nitrogen gas cushioned pressurizer, purification loop, canned motor pump, heating system, cooling tower and associated piping and instrumentation. The total volume of the HTHP loop works out to be about 1.5 m^3. The loop is filled with DM water and the pressurizer is kept initially at a pressure of 70 bar and level 1.5 m from the bottom at room temperature condition. From the bypass line of the HTHP loop, the blow-down line is extended to the homogenizer and two-phase flowmeter and then to the flow restricting orifice for the proposed experiments as shown in Fig. 1. By switching the heating system on, the temperature of water in the loop rises, causing rise in water

A. Moorthi (✉) · N. Uttam · K. Prem Sai · I. V. N. S. Kamaraju
Bhabha Atomic Research Centre Facilities, Kalpakkam 603127, India
e-mail: drmoorthi77@gmail.com

Fig. 1 Isometric view of HTHP loop with TPFM and FRO on the blow-down line
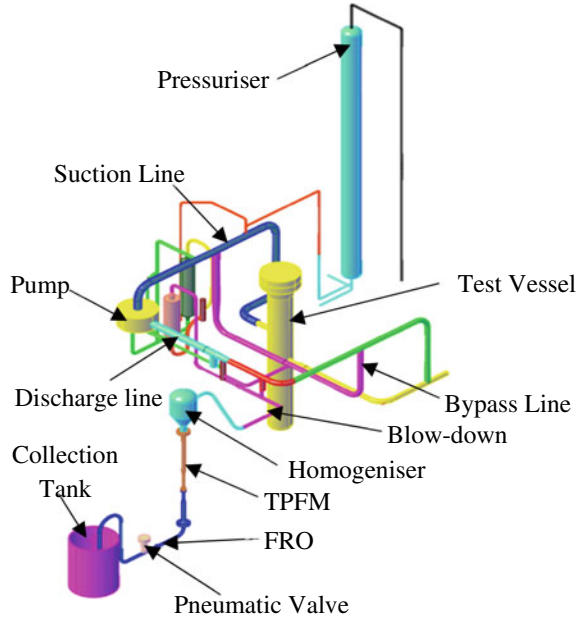
level by swelling and pressure rise in the pressurizer. After attaining the desired pressure 120 bar and temperature 300 °C, a quick opening (pneumatic) valve is opened to initiate the blow-down of the subcooled water through the orifice. The downstream of the orifice is lead to a partially filled collection tank through 2″ line, which is immersed in water. The blow-down steam-water mixture gets condensed in the collection tank. The TPFM measures the two-phase flow by gamma ray attenuation method and finally mass is balanced to calculate the flow rates. Before taking up the proposed experiments, simulation studies are carried out to ensure the feasibility to use the HTHP loop for this work.

3 Analyses Using RELAP5/MOD 3.2

3.1 Modelling of High-Temperature Loop Using RELAP5

The analyses of different blow-down cases are carried out using RELAP5/MOD 3.2 code [6]. The nodalization of high-temperature loop is shown in Figs. 2 and 3. During the nodalization of HTHP loop, the volume and the thermal capacity of the loop are carefully considered to simulate the actual loop data by considering the details of the individual components such as size, length, area, volume and number of control volumes. Initially, the flow restricting orifice (FRO) is modelled as control volume of length 3.5 mm having an area equivalent to the size of orifice. As the

Fig. 2 Model of HTHP loop
in RELAP5/MOD 3.2 for the
simulation of blow-down
through TPFM and FRO
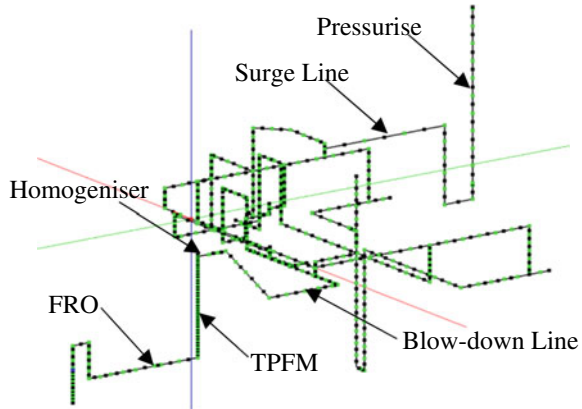
blow-down rates increase, due to two-phase flow formation, very small time steps ($<10^{-4}$ s) are required for the analysis to keep it within Courant limit. Hence, for the sizes higher than 5 mm, FRO is modelled as junction component with an area equivalent to the FRO size. The isolation valve in the surge line connecting the loop to pressurizer is modelled as a junction with the reduced area. It acts like an orifice of area equivalent to 5 mm diameter. The pneumatic valve is modelled as motorized valve with valve opening and closing rate of 33.3%/sec. The abrupt area change model is used wherever the change in area is involved.

The initial conditions of the loop like temperature and pressure are taken based on the test cases. The entire loop and its heat structures, except pressurizer, are given uniform temperature. The pressurizer is kept at low temperature. The initial level of the pressurizer is specified as 3.938 m for all the cases. Only the initial loop pressure and temperatures are specified.

In the analysis, for first 10 s the initial conditions are maintained. At the 10th second, the pneumatic valve starts opening to initiate blow-down and is fully opened by the 13th second. The valve starts closing at 77th second and at 80th second it fully closed, ending the blow-down; i.e., the blow-down is for about 70 s. The valve closing in 3 s is simulated using a trip card. The analysis is continued for some more time (50 s) in order to stabilize of the loop parameters. The values of mass fluxes, pressures and temperatures at pressurizer line, two-phase flow metering device and blow-down line locations are plotted.

In the analysis, for first 10 s the initial conditions are maintained. At the 10th second, the pneumatic valve starts opening to initiate blow-down and is fully opened by the 13th second. The valve starts closing at 77th second and at 80th second it fully closed, ending the blow-down; i.e. the blow-down is for about 70 s. The valve closing in 3 s is simulated using a trip card. The analysis is continued for some more time (50 s) in order to stabilize of the loop parameters. The values of mass fluxes, pressures and temperatures at different locations are plotted. The locations are; pressurizer line, two-phase flow metering device and blow-down line.
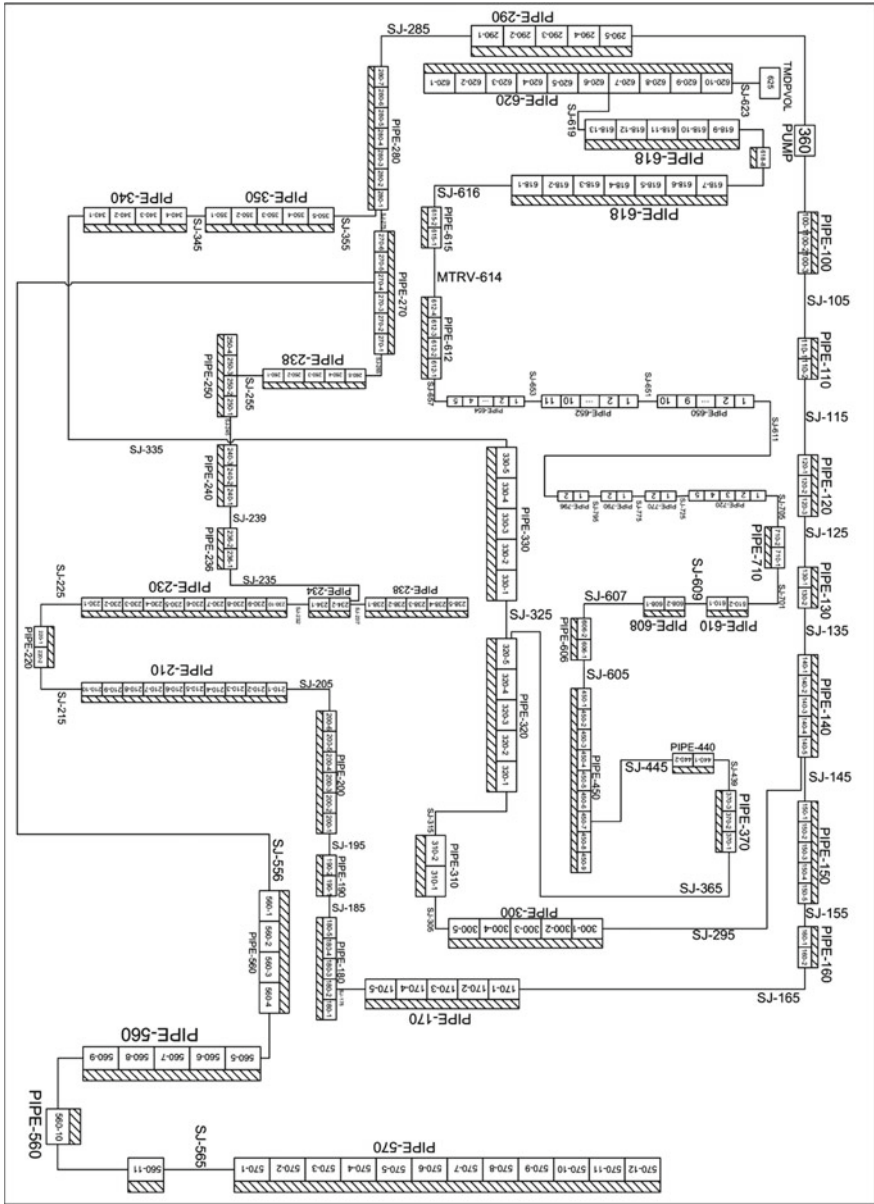
Fig. 3 Nodalization of HTHP Loop in RELAP5/MOD 3.2 with TPFM and FRO for blow-down analysis

3.2 Analysis Cases

In the experimental case, the loop is heated to a desired temperature and pressure by pump heat and heaters before starting the blow-down. In the analysis, these conditions are given as the initial conditions and the loop is initialized with the test pressure and temperature before starting the blow-down in the RELAP analysis. The initial loop pressures considered for the analyses are 120, 110 and 100 bar and the initial loop temperatures are 300, 290 and 280 °C, respectively. The quick-acting pneumatic valve is modelled as motorized valve with opening and closing time of 3 s. The downstream of the orifice is connected to a 50NB sch. 40 pipe and its other end is immersed in water in a tank partially filled with water. The tank is kept on weighting scale. The analysis of blow-down is carried out through orifices of different sizes (3.0, 3.5, 4.0, 4.5, 5.0, 6.0, 7.0, 8.0, 9.0 and 10.0 mm). The initial pressure and temperature considered for the analysis of the different cases are given in Table 2. The pipelines of the loop are modelled as heat structures. The heat structures of the blow-down line and the homogenizer and the TPFM are not modelled in the present analysis. Abrupt area change model is used in the analysis for the pressure loss due to area change. Only one TPFM module (M2) is considered in the present analysis.

4 Results and Discussion

In all the simulations of transients, the loop is initialized with starting temperature and pressure. The important parameters such as the pressurizer pressure, loop pressure and temperature, pressure and temperature of the fluid in the upstream of the flow restricting orifice and the TPFM are plotted. The mass flow through the isolation valve in the surge line, mass flow through the TPFM and the mass flow through the FRO are also estimated. The typical pressure drop across the FRO at the average blow-down rate and the corresponding pressure drop across the TPFM and isolation valve are reported for comparison. The quality of water in the blow-down line and the loop is also estimated. The summary of the results of the simulations is given in Tables 1, 2 and 3. The expected average blow-down rates and the maximum inventory loss for 70 s of the blow-down through different sizes of the orifices are given in Table 3. The important parameters such as the loop pressure, temperature and the mass flow rates during the course of the transients are plotted for specific size of an orifice (3 and 10 mm) at a given initial pressure and temperature of the loop in Figs. 4, 5, 6, 7, 8 and 9. The expected inventory loss for 70 s blow-down for different sizes of orifice at 120, 110 and 100 bar and at different temperatures is shown in Figs. 10, 11 and 12.

Table 1 Summary of the results of blow-down through 3.0 mm orifice with TPFM

Pin (bar)	Tin (°C)	P_{final} (bar)		T_{FRO}	Mass flow rate (kg/s)		
		P_{prz}	P_{loop}	(°C)	Initial	Final	Avg
120	300	102.5	89.1	298.7	0.557	0.380	0.445
	290	101.7	86.2	288.7	0.564	0.450	0.501
	280	102.0	86.5	279.2	0.571	0.490	0.517
110	300	95.5	85.2	299.0	0.511	0.333	0.393
	290	94.6	81.4	288.9	0.539	0.408	0.460
	280	93.9	79.7	279.0	0.545	0.469	0.496
100	300	88.5	85.0	299.4	0.444	0.287	0.340
	290	87.3	77.0	289.1	0.512	0.360	0.410
	280	86.5	74.1	279.1	0.519	0.424	0.464

Table 2 Summary of the results of blow-down through 10.0 mm orifice with TPFM

Pin (bar)	Tin (°C)	P_{final} (bar)		T_{FRO}	Mass flow rate (kg/s)		
		P_{prz}	P_{loop}	(°C)	Initial	Final	Avg
120	300	98.1	75.9	253.0	2.365	3.370	2.735
	290	95.3	66.3	232.3	2.644	3.480	2.610
	280	93.1	57.6	219.3	2.866	3.367	2.420
110	300	92.7	76.6	248.0	2.087	3.528	2.614
	290	89.7	67.3	237.7	2.398	3.399	2.540
	280	87.3	58.1	222.4	2.640	3.329	2.360
100	300	87.5	77.6	272.7	1.728	2.736	2.376
	290	84.0	67.1	243.8	2.122	3.241	2.440
	280	81.5	58.5	226.4	2.391	3.268	2.310

4.1 Blow-Down Through 3.0 mm Orifice

The summary of the results for the simulation of blow-down through 3.0 mm orifice size with TPFM-M2 is given in Table 3. The data of loop pressure, temperature and mass flow through FRO and other locations are plotted in Figs. 4, 5 and 6 for different initial pressure and temperature conditions. The trends of the transients for loop initial pressure and temperature of 120 bar and 300 °C are shown in Fig. 5. It is found that the average mass flow rate during the blow-down is varied from 0.517 to 0.34 kg/s. The average blow-down rates decrease with decrease in the initial pressure of the loop as expected. For a given initial pressure, the average blow-down rate increases with decrease in the initial temperature. Single phase blow-down takes place in this case. Only in the case of 100 bar and 300 °C case, two-phase blow-down starts after 38 s. and continues at constant pressure corresponding to its saturation condition. The summary of the results of blow-down through 3.0 mm orifice case

Table 3 Expected average blow-down rates through different sizes of orifice and total inventory loss

Sl. No	Pin (bar)	Tin (°C)	Average blow-down rate (kg/s) for different sizes of orifice									
			3.0	3.5	4.0	4.5	5.0	6.0	7.0	8.0	9.0	10.0
1	120	300	0.44	0.53	0.61	0.87	0.78	1.11	1.60	2.06	2.44	2.73
2		290	0.50	0.60	0.68	0.76	0.80	1.02	1.46	1.90	2.29	2.61
3		280	0.52	0.65	0.75	0.82	0.88	1.02	1.30	1.73	2.11	2.42
4	110	300	0.39	0.48	0.56	0.70	0.73	1.06	1.52	1.97	2.34	2.61
5		290	0.46	0.55	0.62	0.69	0.74	0.97	1.40	1.84	2.23	2.54
6		280	0.50	0.61	0.69	0.76	0.78	0.92	1.26	1.68	2.05	2.36
7	100	300	0.34	0.41	0.55	0.65	0.70	1.00	1.43	1.85	2.18	2.38
8		290	0.41	0.49	0.55	0.55	0.69	0.92	1.35	1.77	2.15	2.44
9		280	0.46	0.56	0.62	0.70	0.69	0.86	1.21	1.63	1.99	2.31
Minimum (kg/s)			0.34	0.41	0.55	0.55	0.69	0.86	1.21	1.63	1.99	2.31
Maximum (kg/s)			0.52	0.65	0.75	0.87	0.88	1.11	1.60	2.06	2.44	2.73
Avgerage (kg/s)			0.45	0.54	0.63	0.72	0.76	0.99	1.39	1.83	2.20	2.49
Min. inventory loss (kg)			23.80	28.95	38.64	38.64	48.28	59.92	84.66	114.10	139.30	161.70
Max. inventory loss (kg)			26.19	45.74	52.44	57.67	61.29	74.49	106.72	138.21	163.86	183.00
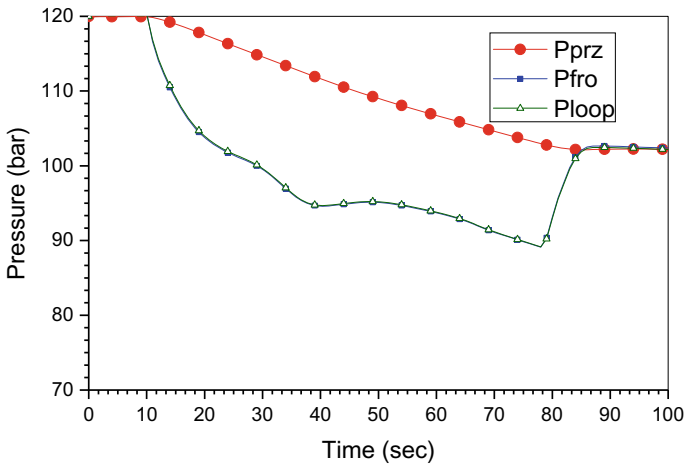
Fig. 4 Loop pressure for blow-down through 3.0 mm orifice at 300 °C and 120 bar initial condition
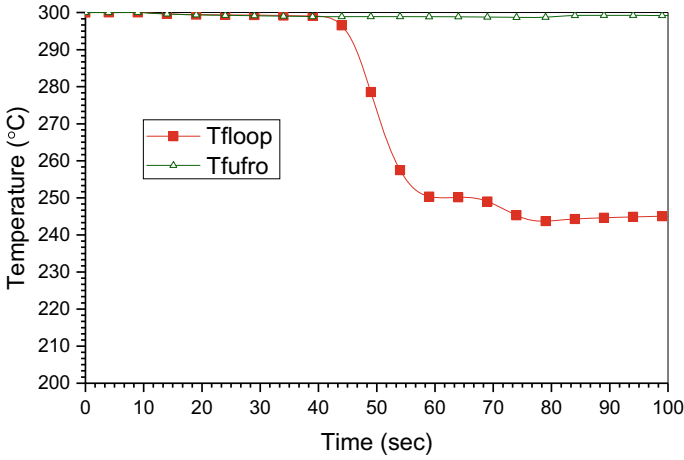
Fig. 5 Loop temperature for blow-down through 3.0 mm orifice at 300 °C and 120 bar initial condition
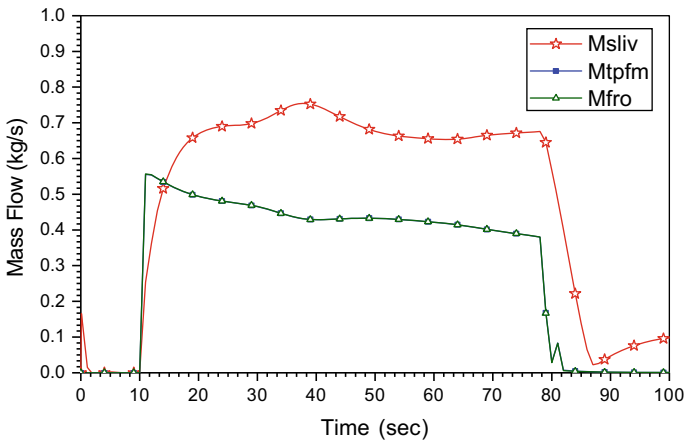
Fig. 6 Loop mass flow rate for blow-down through 3.0 mm orifice at 300 °C and 120 bar initial condition

is given in Table 1. The temperature of the water remains almost same as that of initial temperature and is less by 1.3 °C. The reduction in loop pressure is in the range 18.3–11.5 bar from the initial value and that of loop temperature is in the range 58.8–41.0 °C from the initial temperature during this transient. The overall inventory loss from the loop is varied from 23.8 to 36.19 kg for different initial pressure and temperature during the blow-down.
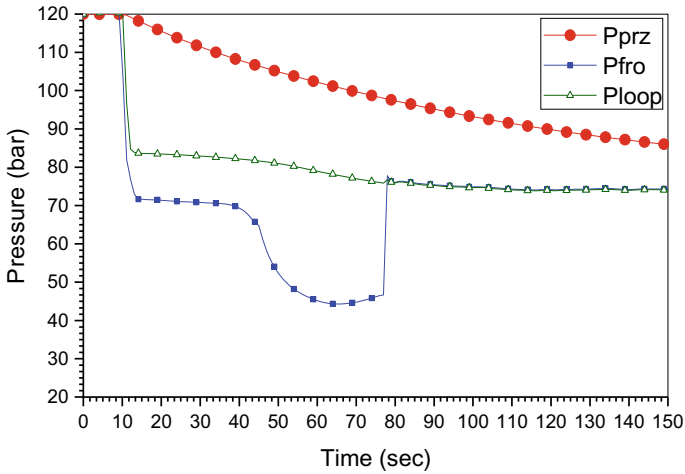
Fig. 7 Loop pressure for blow-down through 10.0 mm orifice at 300 °C and 120 bar initial condition
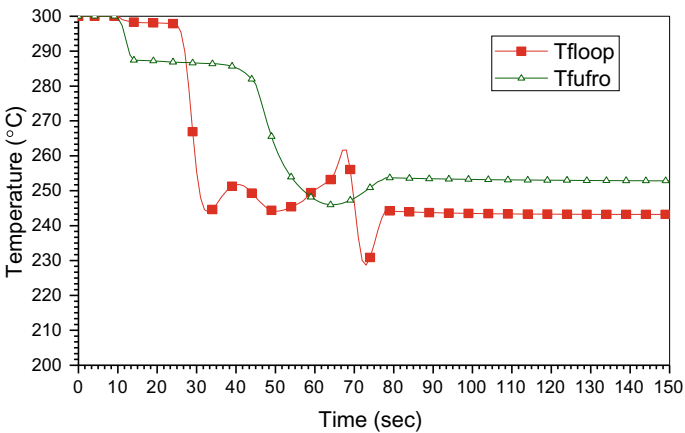
Fig. 8 Loop temperature for blow-down through 10.0 mm orifice at 300 °C and 120 bar initial condition

4.2 Blow-Down Through 10.0 mm Orifice

The summary of the results for the simulation of blow-down through 10.0 mm orifice size with TPFM-M2 is given in Table 2. The transient data of loop pressure, temperature and mass flow through flow restricting orifice and other locations are plotted in Figs. 7, 8 and 9 for 120 bar and 300 °C initial pressure and temperature conditions. In this transient, the loop gets depressurized to its saturated condition within 5 s
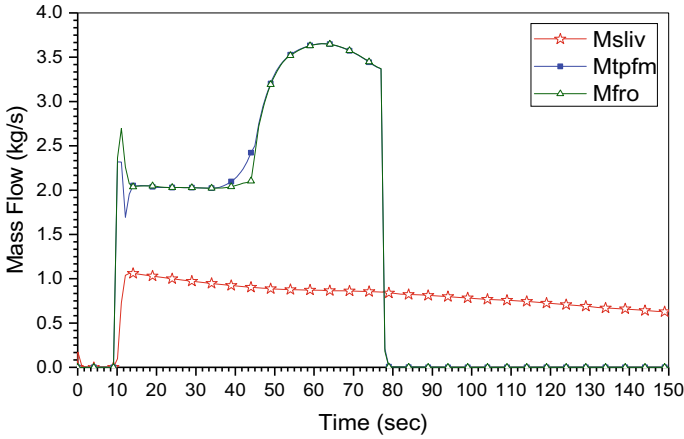
Fig. 9 Loop mass flow rate for blow-down through 10.0 mm orifice at 300 °C and 120 bar initial condition
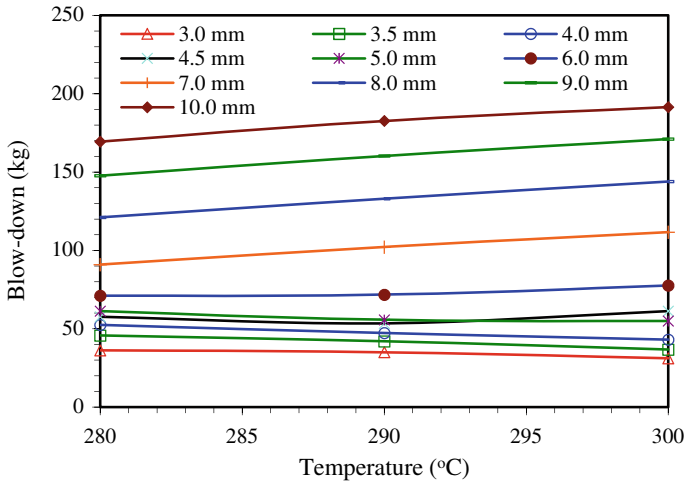
Fig. 10 Expected loss of inventory for 70 s blow-down for different sizes of orifice at 120 bar at different temperature

from the opening of pneumatic valve. The blow-down temperature is observed to be slightly reduced (by ~12 °C) from the initial loop temperature and remains the same for about 35 s. A steep reduction in the blow-down temperatures is observed at the end of the transient (last 35 s before closing the pneumatic valve), the blow-down temperature is reduced by about 60.7 °C at 280 °C and 120 bar to 27.3 °C at 300 °C and 100 bar pressure. As the blow-down temperature reduces at the end of the transient, the corresponding increase in the blow-down rate and the corresponding reduction in the pressure in the upstream of flow restricting orifice are observed. The
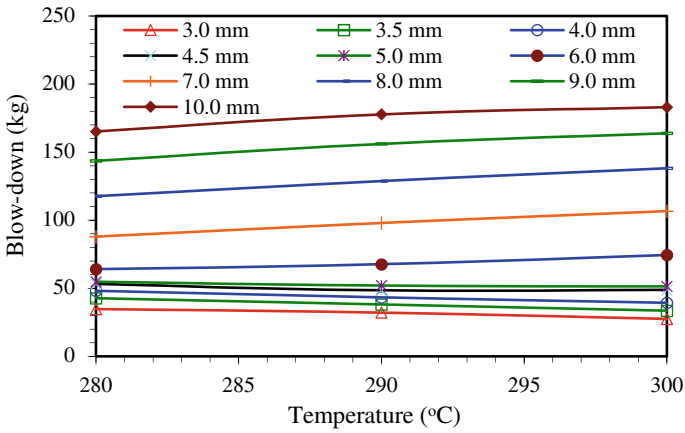
Fig. 11 Expected loss of inventory for 70 s blow-down for different sizes of orifice at 110 bar at different temperature
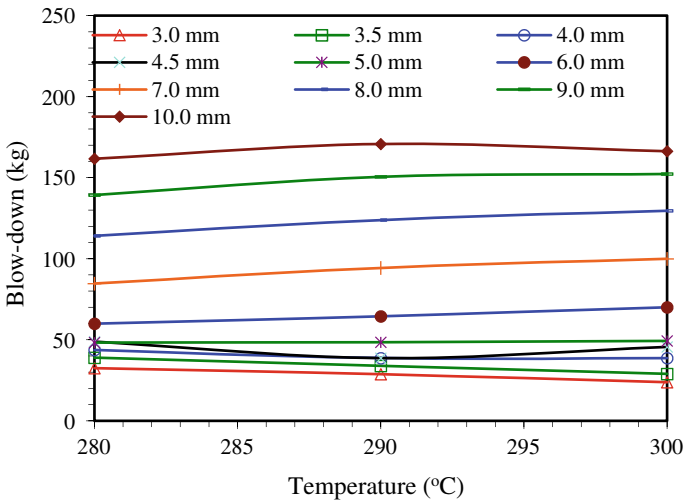
Fig. 12 Expected loss of inventory for 70 s blow-down for different sizes of orifice at 100 bar at different temperature

average mass flow rate during the blow-down is varied from 2.614 to 2.310 kg/s. The overall inventory loss from the loop for 3.5 mm orifice is varied from 161.70 to 183.00 kg for different blow-down cases analysed.

4.3 Summary of Two-Phase Blow-Down Analysis

The summary of results for this case with TPFM-M2 is given in Table 3. The transient data of loop pressure, temperature and mass flow through FRO and other locations are plotted in Figs. 10, 11 and 12 for different initial pressure and temperature conditions. The trends of the transients for loop initial pressure of 120 bar and for three different temperatures 300, 290 and 280 °C are shown in Fig. 10. Similarly, the results at 110 bar and at three temperatures are shown in Fig. 11 and for 100 bar case is shown in Fig. 12.

From the analytical results, the following observations are made.

i. The flow rate and pressure fall during blow-down are dependent on the mass of nitrogen present in the pressurizer which expands during blow-down. The mass is a function of the initial pressure and the gas space volume. In this case, the gas space volume is kept same.

ii. The pressure fall in the loop is in the range of 5 bar to 25 bar after the blow-down. The pressure stabilization takes place in the loop after some time. The pressure fall in pressurizer is not as sharp as the loop due to the high flow resistance in the surge line during blow-down.

iii. In general, it is observed that the blow-down rates increase with the increase in the size of the orifice. For a given size of the orifice and temperature, the blow-down rates increase with the increase in the loop pressure.

iv. For a given pressure and orifice size, in general, the blow-down rates increase with increase in the initial loop temperature. As the flow between the loop and the pressurizer is restricted by the size of the isolation valve (equivalent to 5 mm orifice), there is a mismatch between the blow-down flow rate and the flow rate from the pressurizer. Due to this, for FRO sizes up to 5 mm, the blow-down rate is almost constant or decreases slightly. The blow-down takes place at single phase conditions. As the FRO size increases above 5 mm, the make-up from pressurizer is less than the blow-down rate and hence the loop gets quickly depressurized to the saturated condition corresponding to the initial temperature of the loop. The blown rates are constant for some time and then increases as two-phase flow takes place. The period of two-phase blow-down increases with increase in the size of the FRO.

5 Conclusions

The following conclusions were made from the results of blow-down analyses,

i The results of blow-down analysis through different sizes of the orifice indicate that the blow-down rate is from 0.35 kg/s for 3 mm orifice size to 3.0 kg/s for 10 mm size orifice.

ii The pressurizer surge line isolation valve is restricting the cold-water flow coming into the loop for higher size orifices. As the size of the orifice increases, the blow-down rates also increase and the loop gets de-pressurized faster.

iii Two-phase conditions occur in the loop and discharge continues at constant loop pressure corresponding to the loop temperature.

iv It is observed that the loop supports the utilization of TPFM-M2 spool for blow-down through the orifice sizes considered. As the loop volume is less (~1.5 m^3), the loop gets depressurized very fast, thereby restricting the blow-down rates.

Nomenclature

FRO	Flow restricting orifice
M	Mass flow rate (kg/s)
p	Pressure (bar)
prz	Pressurizer
sliv	Surge line isolation valve
T_{floop}	Temperature of fluid in the loop main pipeline
T_{fufro}	Temperature of the fluid in the upstream of fro
TPFM	Two-phase flow metering device

References

1. Ardron KH, Furness RA (1976) A study of the critical flow models used in reactor blowdown analysis. Nuclear Eng Des 39(2–3):257–66
2. Nigmatulin BI, Soplenkov KI (1987) Critical steady-state blowdown of flashing water through tubes. Nuclear Eng Des 99:85–92
3. Moorthi A, Uttam N, Prem Sai K, Krishna Murthy KCK, Ravi KV (2011) Study of high temperature loop heating experiment using Relap5/Mod 3.2. In: Proceedings of the 21st National and 10th ISHMT-ASME heat and mass transfer conference. IIT Madras. India (ISHMT_IND_12_30)
4. Moorthi A, Uttam N, Prem Sai K, Krishna Murthy KCK, Ravi KV (2014) Blowdown of subcooled and near saturated water through DN tube. New Horizons in Nuclear Reactor Thermal Hydraulics and Safety, Mumbai
5. Moorthi A, Uttam N, Prem Sai K, Krishna Murthy KCK, Ravi KV (2014) Blow down of subcooled water through orifices. New Horizons in Nuclear Reactor Thermal Hydraulics and Safety, Mumbai
6. Relap5/Mod 3.2 Code Manual-Volume-II user guideline and input manual. NUREG/CR/5535

Numerical Simulation of Flow Through Sump Pump

Ravikant Kumar, Ruchi Khare, and Ashish Singh

1 Introduction

In sump and intake models, the usual aim is to achieve smooth, steady approach flow conditions so that obstructions and velocities are high enough to cause air entrainment. By a proper intake sump design, uniform flow can be led to the vertical pumps and the performance of the pump in fact enhanced. The Hydraulic Institute Standards specify general guidelines for the design of sumps. The site constraints usually call for a deviation from the Standards. It then becomes essential to investigate the sump to ensure smooth flow over the entire flow range of the pumps.

The location of intake structure should be such that it may provide swirl-free and uniform flow. The intake which is nearer to the free surface is considered to be more economical, because it is easily accessible for maintenance.

2 Literature Review and Objective

The CFD simulation is done to identify the different kinds of vortex structures that may appear in a pump sump. The physical model test consists of a simple geometry, with the pump situated within eccentricity of 3% of the sump width from the centre of the sump passage [1]. The CFD model can be used to study the effect of various parameters and hence can become an important tool for the optimization of pump sump geometry. In CFD, the building of the scale model is replaced with a virtual representation. Also, the process of physically recording results is replaced with the running of a simulation on the computer. During experimental investigation, formation or air entrainment was observed at LWL and same was rectified by modified

R. Kumar (✉) · R. Khare · A. Singh
Department of Civil Engineering, MANIT Bhopal, Bhopal 462003, India
e-mail: ravikantkumarmanit@gmail.com

the height of the existing curtain wall. The main objective is to carry out numerical simulation of a circular and rectangular multiple suction intake wells and analyses the swirl generation and vorticity in the pumping intake under different operating conditions and also to study velocity and pressure distribution in various parts of pump sump.

3   Geometry and Mesh Generation

For flow analysis in a vertical intake structure, 3D geometric modelling of whole of the intake structure space is required which includes sump suction pipe and bell mouth. The modelled intake structure in the present work consists of a rectangular and a circular sump well consisting of three pumps, of different arrangements for the study of the behaviour of various operating conditions.

The geometry of the vertical multiple pump intake, it is obtained to design the whole vertical intake space within a single domain. Therefore, the whole design contains bell mouth and sump suction pipes. The whole design is modelled in the Ansys ICEM 16.1 consisting of inlet, outlets, suction pipes, and bell mouths. Optimization of geometry in Ansys ICEM CFD is carried out. Two different shapes that is the rectangular and circular sump wells with three suction pipes in each case are prepared (Figs. 1, 2, 3 and 4; Tables 1 and 2).

Fig. 1 Complete assembly of rectangular intake well
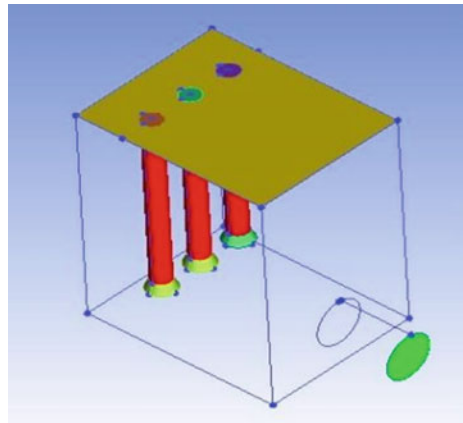
Fig. 2 Complete assembly
of circular intake well
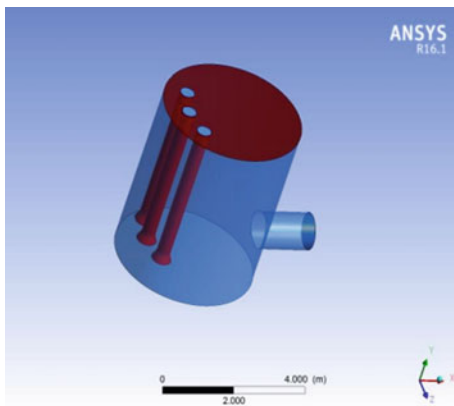
Fig. 3 Mesh generation of
rectangular intake structure
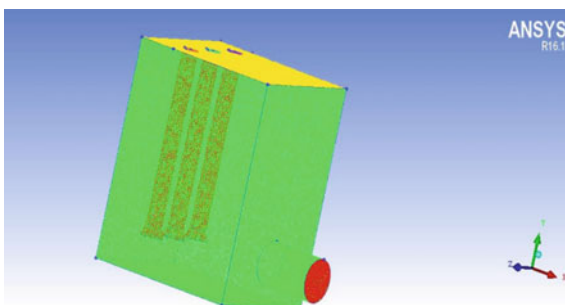
Fig. 4 Mesh generated in
circular intake
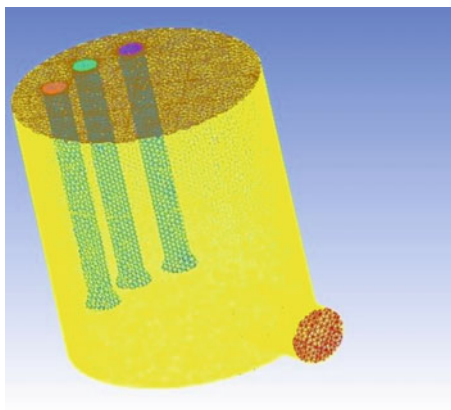
Table 1 Specifications of rectangular vertical intake structure model

Height of intake	5 m
Bell mouth diameter	0.59 m
Number of suction pipe	3
Number of bell mouth	3
Inlet diameter of intake	1 m
Length of inlet pipe	1.5 m
Diameter of each suction pipe	0.4 m

Table 2 Specifications of circular vertical intake structure model

Height of intake	5 m
Bell mouth diameter	0.59 m
Number of suction pipe	3
Number of bell mouth	3
Inlet diameter of intake	1 m
Length of inlet pipe	1.5 m
Diameter of each suction pipe	0.4 m
Diameter of intake well	2.02 m

3.1 Boundary Conditions

In the present study of vertical pump intake structure numerical flow simulations have been carried out for a varying deign parameters and mass flow rate.

4 Results and Discussions

Geometrical modelling tests are considered as highly reliable way to assess pump intake designs in comparison to theoretical modelling. Computational fluid dynamics 3D flow simulation has the ability of providing much more detailed information of the flow field at a least of the cost and time required for the model study (Table 3).

Table 3 Details of different conditions of intake well used for analysis

Case 1	Rectangular intake well, pump1 and 3 are in running condition
Case 2	Rectangular intake well, pump 1 and 2 are in running condition
Case 3	Circular intake well, pump 1 and 3 are in running condition
Case 4	Circular intake well, pump 1 and 2 are in running condition

Fig. 5 Swirl angles with respect to location in suction pipes for outlet 1 & 3
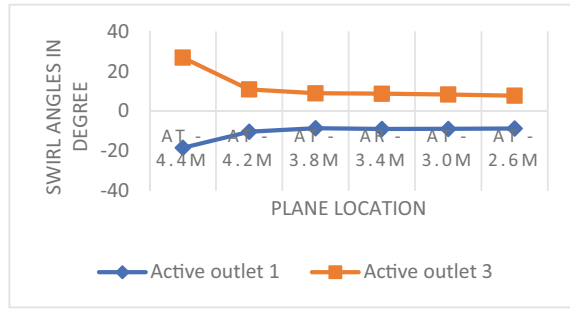
4.1 Swirl Analysis for Rectangular Intake

In the design of the rectangular intake the suction pipes are installed as of two of them are working and one is taken as standby. Further tests are performed for the calculation of tangential velocities, axial velocities, swirl angles, and velocity curls for each of the working suction pipes (Fig. 5).

The quantitative results are compared for pump 1 and pump 3 suction pipe and suction pipe 3 at working condition in the form of the swirl angles taken at an appropriate interval of 0.59 m from the bell mouth opening to the impellers eye. The average directional vorticity 0.61° is calculated at each defined planes created with in each suction pipes at definite intervals. It was found the swirl angle in suction pipes of both pumps is in opposite direction it is because of their symmetrical location from the inlet pipe of intake well.

The quantitative results are compared with suction pipe 1 and suction pipe 2 at working condition and swirl angles taken at an interval of 0.40 m from the bell mouth opening to the impellers eye and also one surface is taken below bell mouth. The average directional vorticity is calculated at each defined planes created with in each suction pipes at definite intervals. It was found the in suction pipe 1 the swirl angle is coming negative to show the direction and in suction pipe 3 the swirl angle is coming as positive showing the opposite direction. The variation of swirl angles at different sections of pump1 and pump2 suction pipes is shown in Fig. 6.

4.2 Swirl Analysis for Circular Intake

In the design of the circular intake the suction pipes are installed as of two of them are working and one is taken as standby as worked in rectangular intake. Further tests are performed for the calculation of tangential velocities, axial velocities, swirl angles, and velocity curls for each of the working suction outlets (Fig. 7).

The quantitative results are compared with suction outlet 1 and suction outlet 3 at working condition in the form of the swirl angles taken at an appropriate interval of 0.40 m from the bell mouth opening to the impellers eye. The average directional

Fig. 6 Swirl angles with respect to location in suction pipes for outlet 1 & 2
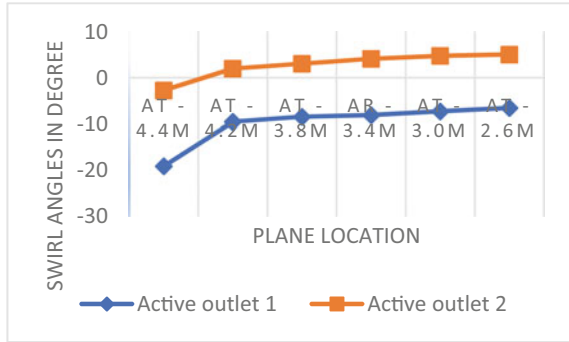
Fig. 7 Swirl angles with respect to location in suction pipes for outlet 1 & 3
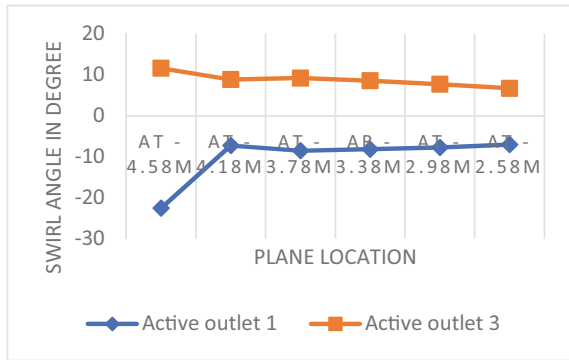
vorticity is calculated at each defined planes created with in each suction pipes at definite intervals. It was found the in suction outlet 1 the swirl angle is coming negative to show the direction and in suction outlet 3 the swirl angle is coming as positive showing the opposite direction flow of fluid (Fig. 8).

The quantitative results are compared with suction outlet 1 and suction outlet 2 at working condition and swirl angles taken at an interval of 0.40 m from the bell

Fig. 8 Swirl angles with respect to location in suction pipes for outlet 1 & 2
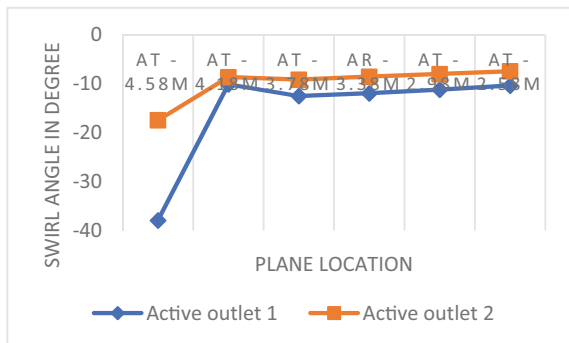
Fig. 9 Streamlines suction
outlet 1 & 3 active
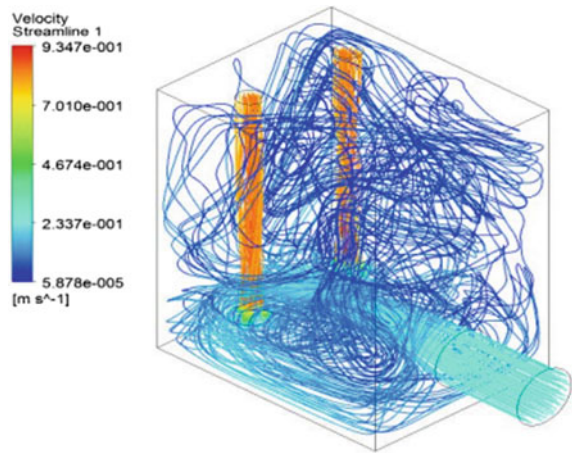
mouth opening to the impellers eye and also one surface is taken below bell mouth.
The average directional vorticity is calculated at each defined planes created with in
each suction pipes at definite intervals. It was found in the suction outlet 1 the swirl
angle is coming negative to show the direction and in suction outlet 3 the swirl angle
is coming as positive showing the opposite direction Comparable results are plotted
showing swirl angles under working suction 1 and suction 2. It was found that at
initial just below the suction bell mouth the swirl angle, velocities are higher showing
sudden increase in values and fluctuation in graph as compared to that further defined
surface for calculation of swirl angles.

4.3 Streamlines of Case 1 and Case 2

Variation of velocities streamlines of complete assembly of a rectangular pump intake
at uniform inlet condition of 1.5 atmospheric with varying operating suction outlets.
Figures 9 and 10 show the working suction pipes 1 & 3 and 1 & 2, respectively.
Showing swirl generation.

4.4 Streamlines of Case 3 and Case 4

Variation of velocities streamlines of complete assembly of a Circular pump intake
at uniform inlet condition of 1.5 atmospheric with varying operating suction outlets.
Figures 11 and 12 show the working suction pipes 1 & 3 and 1 & 2, respectively.
Showing swirl generation.

Fig. 10 Velocity streamlines
suction outlet 1 & 2 active
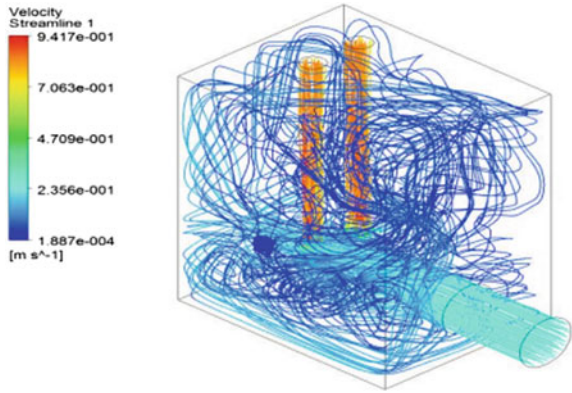
Fig. 11 Velocity streamlines
suction outlet 1 & 3 active
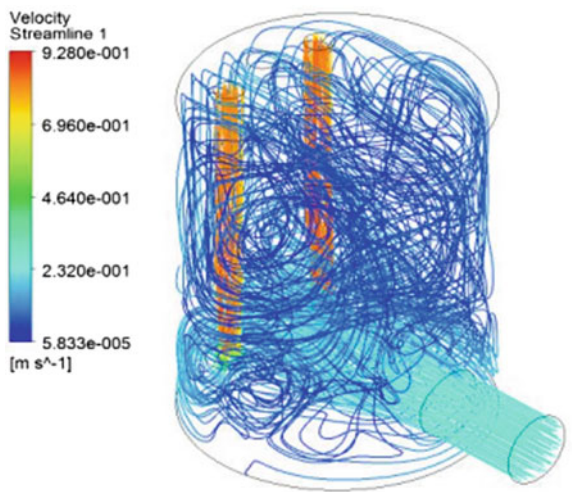
Fig. 12 Velocity streamlines
suction outlet 1 & 2 active
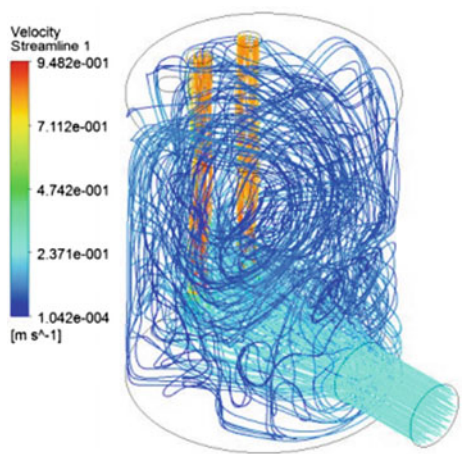
4.5 Velocities **u**, v *and* **w** *Analysis*

According to the above tabular value obtained at a location of 0.6 m from the bottom of the pump intake from 0 to 3.2 m, line drawn passing through the centre of the bell mouth. It was clear from the graphical representation of above data that the fluctuation of velocities in *u*, *v* and *w* direction is smooth (Tables 4 and 5).

According to the above tabular value obtained at a location of 0.6 m from the bottom of the pump intake from 0 to 3.2 m, line drawn passing through the centre of the bell mouth. It was clear from the graphical representation of above data that the fluctuation of velocities in *u*, *v* and *w* direction is not smooth. Found most fluctuation near the 2nd suction outlet (Table 6).

According to the above tabular value obtained at a location of 0.6 m from the bottom of the pump intake from 0 to 3.2 m, line drawn passing through the 2 centre

Table 4 Velocities in *u*, *v* and *w* direction w.r.t Z-0 to 3.2 (m) case 1

Z (m)	Velocity u (m s^{-1})	Velocity v (m s^{-1})	Velocity w (m s^{-1})
0	0.19	0.11	− 0.01
0.4	0.13	− 0.06	− 0.08
0.7	0.02	0.19	0.09
1.1	− 0.1	0.02	0.16
1.4	− 0.17	− 0.03	0.05
1.8	− 0.26	− 0.04	0.01
2.2	− 0.19	0.01	− 0.06
2.5	− 0.08	0.02	− 0.01
2.9	0.07	0.06	0.08
3.2	0.11	0.05	0

Table 5 Velocities in *u*, *v* and *w* direction w.r.t Z-0 to 3.2 (m) of case 2

Z (m)	Velocity u (m s^{-1})	Velocity v (m s^{-1})	Velocity w (m s^{-1})
0	0.12	− 0.02	0
0.4	− 0.01	− 0.01	− 0.04
0.7	− 0.03	0	− 0.02
1.1	− 0.07	0.04	− 0.01
1.4	− 0.16	0.13	− 0.06
1.8	− 0.08	0.12	0.07
2.2	− 0.13	0.02	− 0.05
2.5	0.04	0.21	− 0.03
2.9	0.08	− 0.03	0.06
3.2	0.13	− 0.01	0

Table 6 Velocities in *u*, *v* and *w* direction w.r.t Z-0 to 3.2 (m) of case 3

Z (m)	Velocity u (m s^{-1})	Velocity v (m s^{-1})	Velocity w (m s^{-1})
0	0.09	− 0.07	0.04
0.4	− 0.01	− 0.06	− 0.09
0.7	0.07	0.46	− 0.03
1.1	− 0.18	0.07	0.28
1.4	− 0.14	− 0.05	0.03
1.8	0.01	− 0.04	− 0.01
2.2	− 0.04	− 0.05	− 0.26
2.5	0.09	0.46	− 0.02
2.9	0.01	− 0.05	0.02
3.2	0.16	− 0.05	− 0.11

of the bell mouth. It was clear from the graphical representation of above data that the fluctuation of velocities in *u*, *v* and *w* direction is smooth and uniform at 0 and 3.2. Velocity *v* increases at centre of the bell mouth (Table 7).

According to the above tabular value obtained at a location of 0.6 m from the bottom of the pump intake from 0 to 3.2 m, line drawn passing through the centre of the bell mouth. It was clear from the graphical representation of above data that the fluctuation of velocities in u, v and w direction is also smooth, and from 0 to 1 m, there are almost linear velocities.

Table 7 Velocities in *u*, *v* and *w* direction w.r.t Z-0 to 3.2 (m)

Z (m)	Velocity u (m s^{-1})	Velocity v (m s^{-1})	Velocity w (m s^{-1})
0	− 0.01	0.05	0
0.4	0	0.02	0.01
0.7	− 0.02	0.01	− 0.03
1.1	− 0.04	− 0.03	− 0.04
1.4	− 0.36	0.05	− 0.17
1.8	− 0.25	0.2	0.14
2.2	− 0.09	0.07	− 0.26
2.5	0.21	0.45	0.08
2.9	0	− 0.09	0.05
3.2	0.11	− 0.06	− 0.07

5 Conclusions

From the above study on swirling flow in sump with multiple pump intakes of rectangular and circular pump intake structure, it has been observed that the location and operating conditions of the suction pipe in sump geometry affect local and global intake performance parameters significantly. The following conclusions have been drawn from the tabular and graphical results. In case of rectangular pump intake, it was found in the suction outlet 1 the swirl angle is coming negative to show the direction and in suction outlet 3 the swirl angle is coming as positive showing the opposite direction. When the suction outlet 1 and 2 working of rectangular intake it was observed that there is no such variation in swirl angles both are nearly identical. In case of circular pump intake, the variation in swirling angles is smooth and non-fluctuating. It is observed from the graphs that the swirl angles just below the opening of bell mouth are much higher than the angles inside the suction pipes in all cases of rectangular and circular pump intakes because of high swirl at the suction inlet. As moving from opening of bell mouth to suction pipes the velocity decreases. From the computation analysis of velocity streamlines, Cases of circular pump intake the streamlines are smooth because, no corner or edges in the geometry. Maximum swirl angle obtained in case rectangular intake is found to be 28.826° which is obtained just below the bell mouth at a depth of 0.2 m from bell mouth opening. Maximum swirl angle obtained in case of circular intake is found to be 32.35° which is obtained just below the bell mouth at 4 m from bell mouth opening. In velocities u, v and w analysis with respect to Z from 0 to 3.2 m the velocity variation is smooth in case, when the suction outlet 1 & 3 working. In velocities u, v and w analysis with respect to Z from 0 to 3.2 m the velocity variation is fluctuating near the second suction inlets, when suction outlets 1 & 2 working. Where as in case of circular pump intake the velocities u, v and w variation are almost same and no fluctuation is observed below the non-working suction inlets.

References

1. Lucino C, Liscia S, Duro G (2010) Vortex detection in pump sumps by means of CFD. In: XXIV Latin American congress on hydraulics
2. Okumura T, Kamemoto K, Matsui J (2007) CFD prediction and Model experiments on suction vortices in Pump Sump. In: The 9th international conference of fluid machinery, AICFM-053

Estimation of Free Floating Characteristics of a Close Coupled Canard Based on Computational Studies

R. J. Pathanjali, Muralidhar Madhusudan, B. Praveen Kumar, T. Shubhangi, V. Sundara Pandian, and D. Narayan

1 Introduction

Certain modern fighter aircraft has been designed with delta wings and a close coupled canard to enhance maneuvering and supersonic performance. The canard design, in addition to meeting conventional design targets, has to cater to various scenarios in its failure case too. A close-coupled canard configuration will be typically integrated with a lifting canard, wherein the canard lift is used to complement the wing lift for optimal performance. In such a configuration, if the canard actuation system fails during flight at a particular angle of attack, there are two possible situations. In the first scenario, the canard due to its inherent weathercock stability, may float and align itself with the free stream flow. In the second situation, the canard may get stabilized at one of its extreme deflections. Other variations of the second scenario are also possible. However, our design intent is on the first scenario, wherein upon the failure of the actuation system, the canard should try to align itself to the local free stream angle. This is a favourable case for aircraft stability because a typical unstable aircraft with loss of canard lift ahead of the aircraft centre of gravity will tend to become stable aircraft and hence safer to control and land. Therefore, it is essential to understand the behaviour of the free floating canard at various Mach (M)–angle of attack (AoA) regime in the flight envelope.

The need to understand the floating characteristics of a control surface especially canard had been studied earlier in open literature [1–3]. Gumusboga [1] and Altug had modelled the aerodynamic effects of asymmetric elevator failures in the F-16 Aircraft and reported the control surface deflections required for common types of control surface failures such as freezing, floating and loss of effectiveness. Hollinger [2] had studied about the canard hinge moment and longitudinal stability of a 1/7

R. J. Pathanjali (✉) · M. Madhusudan · B. Praveen Kumar · T. Shubhangi · V. Sundara Pandian · D. Narayan
Aeronautical Development Agency, Bangalore 560017, India
e-mail: pathanaero@gmail.com

scale model of the Convair B-58 in a free-flight investigation and presented that the canard hinge moment is very small when the canard hinge axis is located near to the centre of pressure. It has also been mentioned that the variation of canard hinge moment with AoA is minimal in the transonic and supersonic Mach numbers, and it was almost constant at the higher Mach numbers. Kraus [3] had studied about the estimation of free floating characteristics of canard for a delta-canard configuration of an aircraft at high angle of attack and estimated the favourable location of pivot axis, for stabilizing the aircraft in case of a failure. This paper builds upon these open literatures by studying the effect of canard floating by using CFD studies. This paper compiles the CFD studies carried out to understand the canard behaviour at transonic and supersonic conditions to determine whether it satisfies the floating requirements.

2 Configuration and Computational Details

The configuration of the generic fighter aircraft with close coupled canard is studied in this paper as shown in Fig. 1. The generic fighter aircraft is a delta wing configuration with two missiles at the wing tips. The canard is swept back, and the canard flow couples closely with the flow over the delta wing to enhance the lift characteristics of the aircraft. The geometric details of the canard are shown in Fig. 2. The canard hinge is kept at a location such that it subdivides the canard with roughly one-third of the area ahead of the hinge axis and two-thirds behind the hinge axis. However, a major portion of the leading edge of the canard is ahead of the hinge. The root chord of the canard is the reference line on which all parameters are studied in this paper.

CFD studies were carried out using full aircraft configuration as shown in Fig. 1. The mesh was generated in ANSYS ICEMCFD and solved for RANS equations in Metacomp CFD++ solver. RANS equations with SST turbulence model were used for prediction of flow features. The post-processing of the flow field is carried out in Tecplot. The canard location on the aircraft had been fixed based on the aerodynamic requirements taking into account of all the allied system constraints. The canard hinge location and actuator have been fixed based on the requirement to have minimal power for actuation for the planned operational schedule. The canard hinge is fixed at 66.4% of the root chord with the main aim of having the smallest possible actuator, as shown in Fig. 2. The canard operating range is from + 20° to 20° in flight, wherein + 20° indicates the position of canard with leading edge down by 20° and − 20° indicates that canard has been positioned with leading edge up by 20°. Major flow features and hinge moments are explained with 0°, + 10° and 10° deflections of canard for better understanding.

Fig. 1 Basic aircraft wing
and canard sweep details
with canard
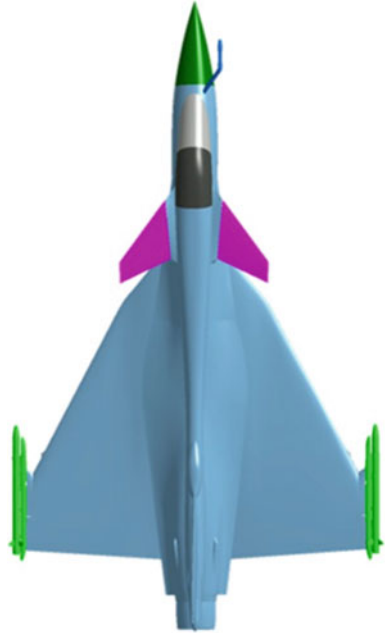
Fig. 2 Canard hinge
location and canard area
forward and aft of hinge
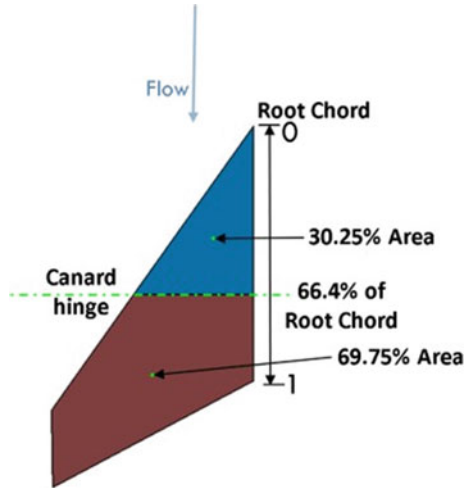
3 Hinge Moment Characteristics of Canard

To understand the hinge moment characteristics of the canard, extensive CFD studies were carried for the full aircraft configuration along with canard for various conditions. The mesh used for this study had been evolved over the years for capturing

the desired wing and canard vortices and extensive density regions have been used to capture the canard leading edge vortex as well as the wing vortex. The mesh distribution on a section over the aircraft is shown in Fig. 3. Validation studies have been carried out between CFD and experimental data for the canard configuration as shown in Figs. 4 and 5. The experimental results shown in this paper were obtained from carrying out tests of scaled aircraft model in a closed circuit wind tunnel facility. The free stream conditions in the test facility are $M = 0.9$ and Reynolds number per unit length of 3.25 million/ft. The ΔCL and ΔCm were obtained from both CFD and wind tunnel by taking the difference between the lift and pitching moment for two configurations—one with canard and one without canard. The comparison shows a close match with the experimental results throughout the range of angles of attack except for an outlier point in the ΔCL curve. For the present study, the hinge moments have been extracted from the configuration with canard from CFD with the above-validated grid generation philosophy. All the aerodynamic forces and the moments have been integrated over a single canard surface and resolved along the hinge axis. However, for better understanding, the forces and moments have been shown along various points of the root chord (X/C) (root chord values normalized from 0 to 1 for convenience). The value of $X/C = 0$ indicates the leading edge of the root chord, and a value of $X/C = 1$ represents the trailing edge of the root chord as shown in Fig. 2.

The hinge moments on the canard from CFD studies for various canard deflections at $M = 0.9$ and $M = 1.3$ are shown in Figs. 6 and 7, respectively. A positive hinge moment indicates that the moment about the canard hinge axis is trying to cause the leading edge of canard to go up. A negative hinge moment tends to rotate the canard leading edge down. From Fig. 6, it can be seen for $M = 0.9$ that at extreme $+ 20°$ deflection of canard, the canard hinge moment is positive for most of the AoA which indicates that when the canard is deflected leading edge down by $+ 20°$, its hinge moment is in such a way that the canard leading edge tends to rotate up in case of actuator failure. Similarly, the hinge moments at $- 20°$ deflection of canard
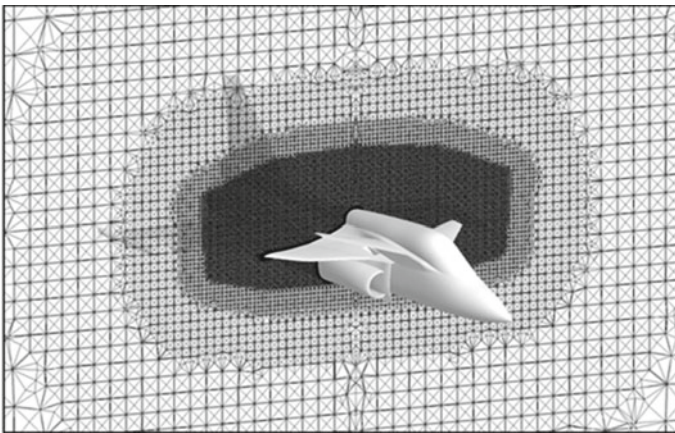
Fig. 3 Representative RANS mesh used for CFD studies
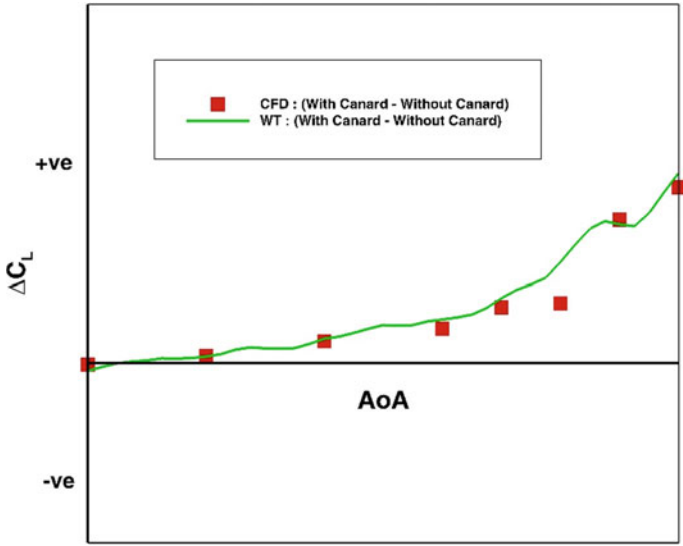
Fig. 4 Validation of CL from CFD with wind tunnel results for $M = 0.9$
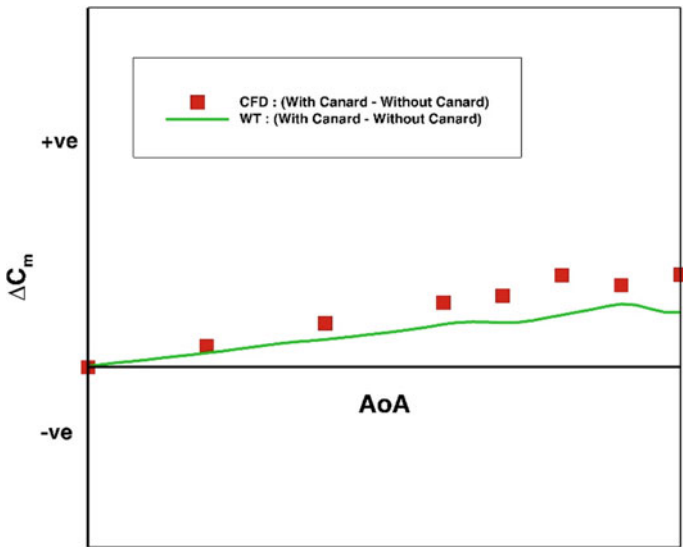
Fig. 5 Validation of Cm from CFD with wind tunnel results for $M = 0.9$

tend to rotate the canard leading edge down. This is a definitive indication of the canard floating characteristics, wherein if the canard fails during its extreme positive deflection, it tends to rotate back towards neutral, and when it fails during the extreme negative deflection, it tends to rotate back down towards the neutral again. Using the same analogy, any failure at intermediate locations of canard will also tend to rotate the canard back to a particular neutral position. The approximate angle for the canard to float can be obtained by interpolating the canard deflections for zero hinge moment as shown in Fig. 8.

It can be seen from Fig. 8 that the canard floating angle is increasing with AoA, i.e. as the AoA increases the canard is trying to align itself more closely with the free stream. The explanation for this favourable trend in canard hinge moment characteristics can be obtained from detailed post-processing of CFD data. The variation of canard hinge moment across the normalized root chord of canard (X/C) is shown in Fig. 9. The hinge is kept at 0.664 (66.4% X/C) as shown by the vertical line. The hinge moments are plotted for $M = 0.9$ at AoA $= 0°$ for three canard deflections. The hinge moment is positive for positive deflection of canard, if the hinge is located at very low X/C and vice versa. It indicates that a reasonably forward hinge for positive canard deflections will be stabilizing as it tends to rotate the canard leading edge to go up typically. Similarly, a reasonably backward hinge will be destabilizing in the sense that a positive canard deflection gives a negative hinge moment (wherein it
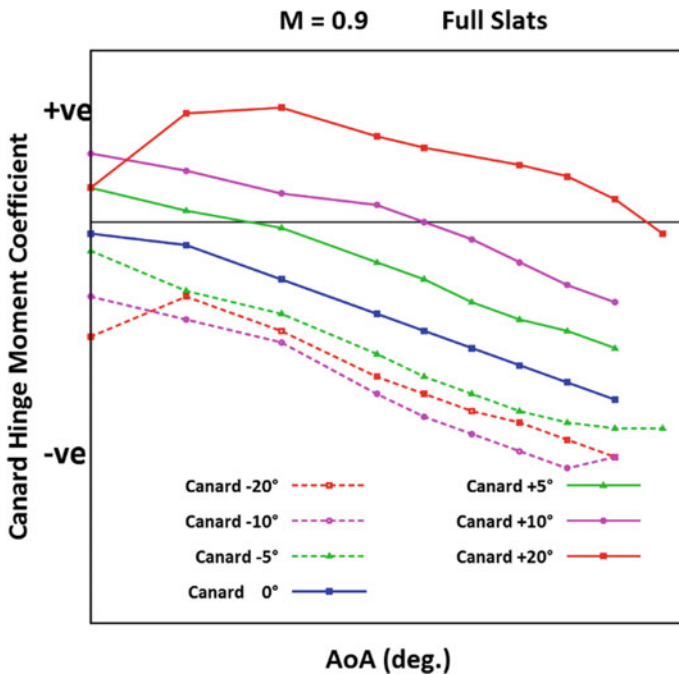
Fig. 6 Hinge moment coefficient for canard from CFD at $M = 0.9$
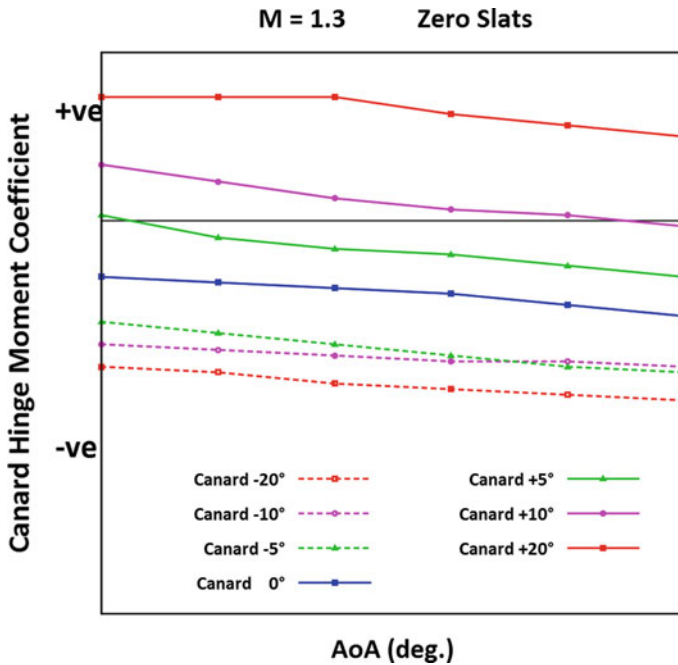
Fig. 7 Hinge moment coefficient for canard from CFD at $M = 1.3$

tends to rotate the canard leading edge to move towards a more positive deflection, i.e. away from neutral). The classical textbooks on stability and control [4] discuss the variation in hinge moments with control surface deflections extensively. For the present study, the canard deflection of $-10°$ and $+10°$ in Fig. 9 confirms the above typical trends. There is a particular location on the X/C where the hinge moment of all the deflections is almost zero. The canard deflection of $-10°$ and $+10°$ intersects the Zero hinge moment line at approximately around 0.725 X/C. This point where the hinge moment is zero is the point where the resultant force acts on the canard (Centre of pressure, COP). In that regard, the position of the hinge (for the present case at 0.664 X/C) ahead of this COP will always tend to provide a favourable hinge moment of the canard.

The hinge moment characteristics are analysed for other AoA for canard deflection of $+10°$ and $-10°$ and shown in Figs. 10, 11 and 12. The trend in hinge moments with AoA is grouped in the range of three AoA regimes. In the linear low AoA regime, the leading edge down deflection of canard $+10°$ is almost parallel (dotted lines). With increase in AoA to around $5°–10°$ AoA, the zero hinge moment point is seen behind the COP. A similar trend is observed for mid and high AoA ranges also. The corresponding plot of variation in hinge moment and the location of COP for $M = 1.3$ at AoA $= 0°$ are shown in Fig. 13 and at a higher AoA in Fig. 14. The hinge moment characteristics are plotted with respect to the canard deflection with varying AoA for $M = 0.9$ and $M = 1.3$ in Figs. 15 and 16. This positive slope of the trend
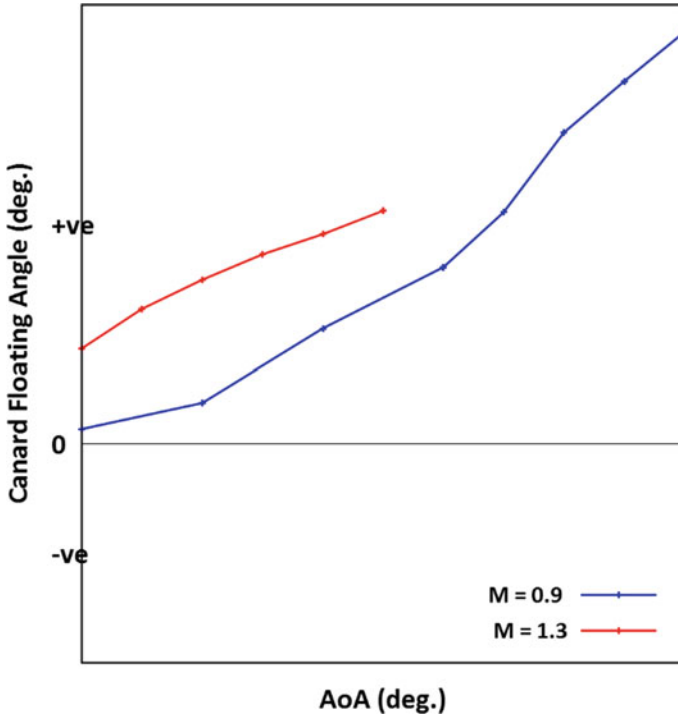
Fig. 8 Approximate angle for float of the canard during actuator failure

Fig. 9 Hinge moment
variation with canard root *X/
C*
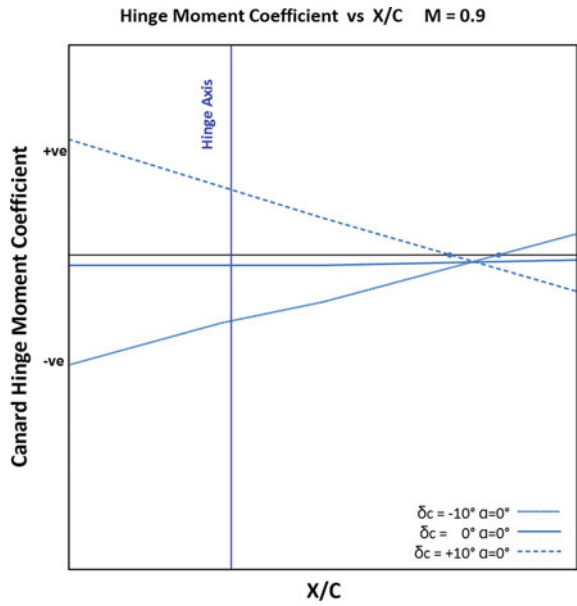
Fig. 10 Hinge moment for
varying AoA at $M = 0.9$
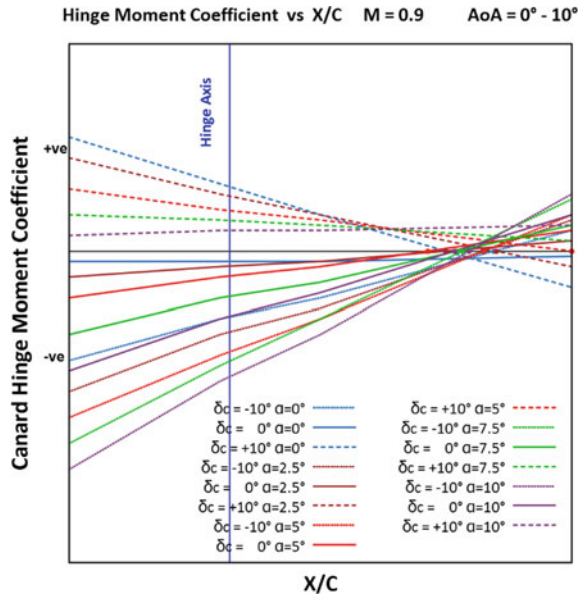
seen in Figs. 15 and 16 is a definitive indication that the canard will float at all AoA.
The positive slope of the curve and its intersection with the zero hinge moment axis
indicates that there is only one unique neutral position where the canard will come
to stabilize during floating. The contours of coefficient of pressure (Cp) and canard
hinge moment coefficient (CHM) for $M = 0.9$ and $M = 1.3$ are given in Figs. 17, 18,
19 and 20. It can be seen that the region of low pressure (high suction) is concentrated
along the top side of the leading edge of the canard for $M = 0.9$. Also, the suction
is distributed along most of the canard surface, thereby maintaining sufficient lift in
the rear portion of the canard. This can also be seen from Fig. 18 where the dark blue
region at the rear of the canard on the top surface is consistently stronger to make
the canard align closely with the free stream.

The flow field is slightly different for $M = 1.3$ as seen from Figs. 19 and 20,
wherein the shock pattern influences the forces on the canard. The leading edge
shock creates a high-pressure region on the top surface of the canard. However, the
trailing edge low pressure on the top surface of the canard is quite strong to make
the canard float at all AoA. The contours from CFD solutions help us to understand
the reasons for canard floating at transonic and supersonic regimes.

Fig. 11 Hinge moment for varying AoA at $M = 0.9$
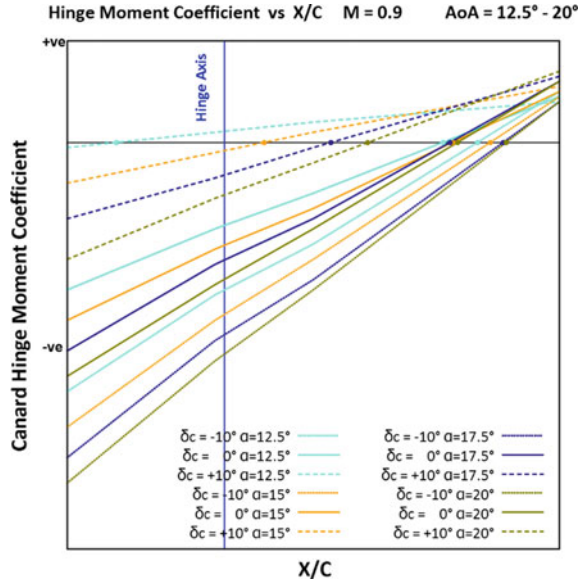
Fig. 12 Hinge moment for varying AoA at $M = 0.9$
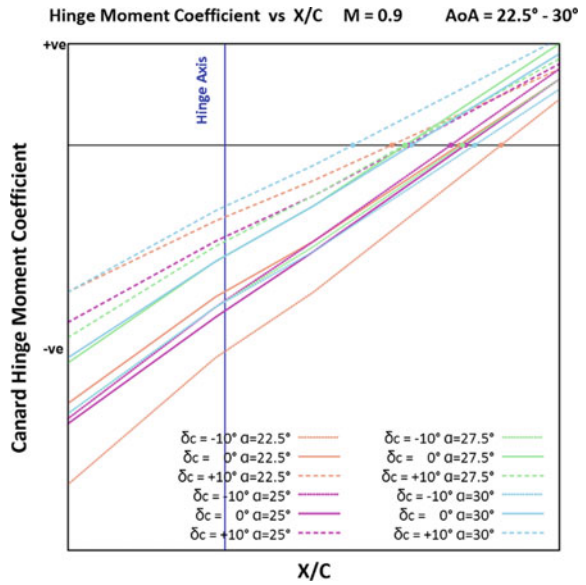
Fig. 13 Hinge moment variation with canard root X/C at $M = 1.3$
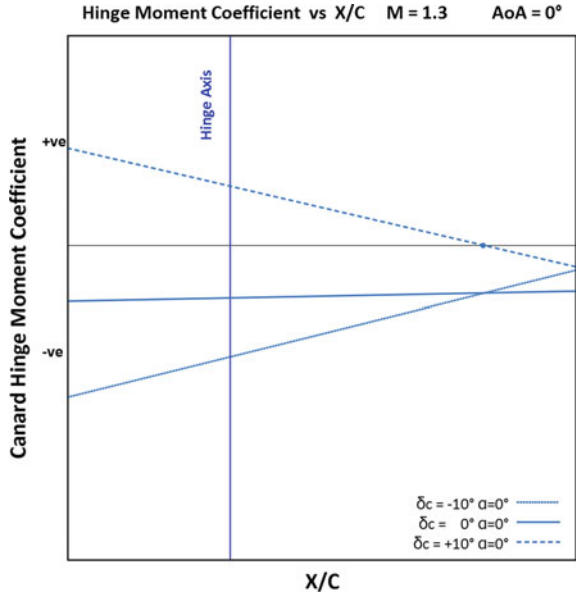
Fig. 14 Hinge moment variation with canard root X/C at $M = 1.3$
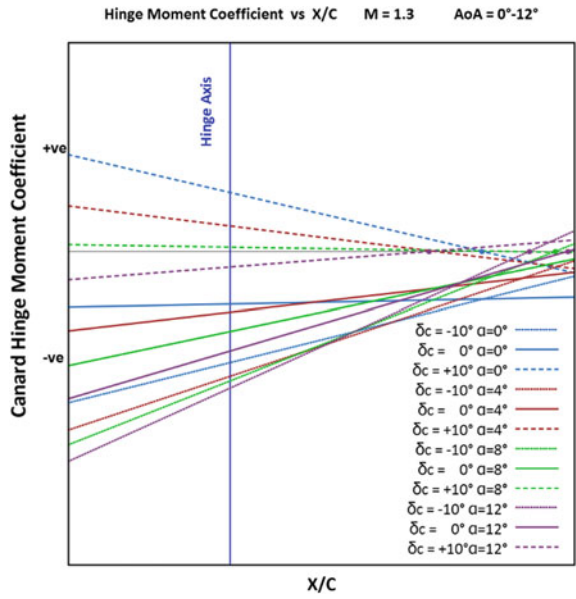
Fig. 15 Canard hinge moment coefficient with canard deflection for $M = 0.9$ for various AoA
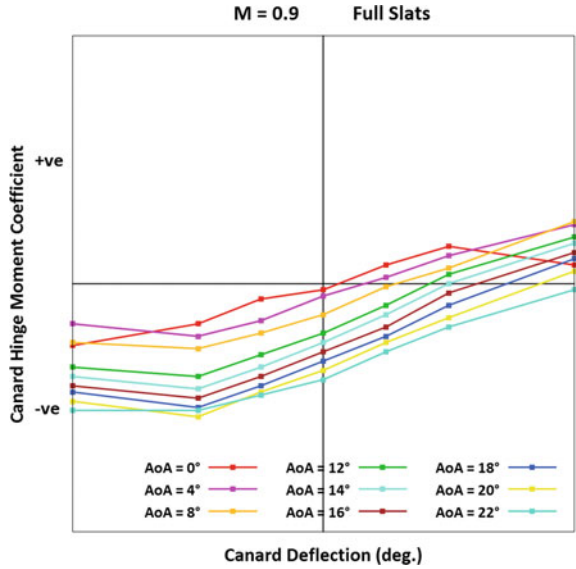
Fig. 16 Canard hinge moment coefficient with canard deflection for $M = 1.3$ for various AoA
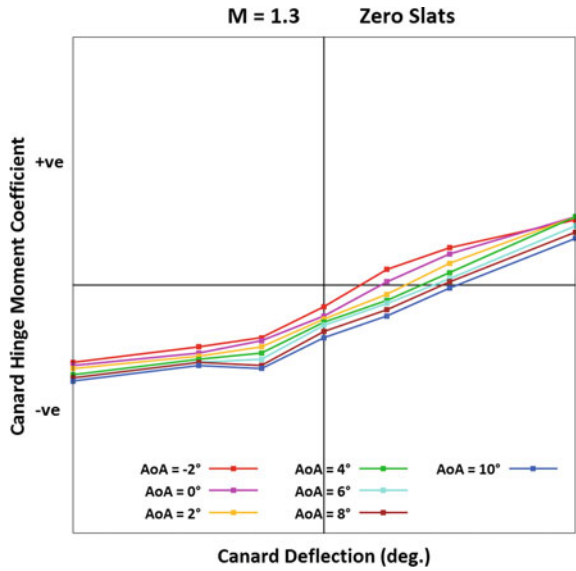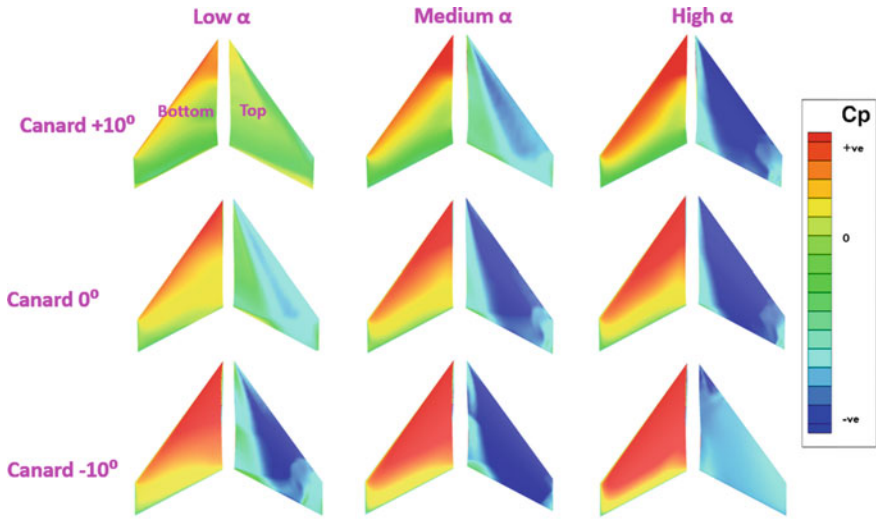
Fig. 17 Cp contours on the top and bottom surface of the canard for $M = 0.9$
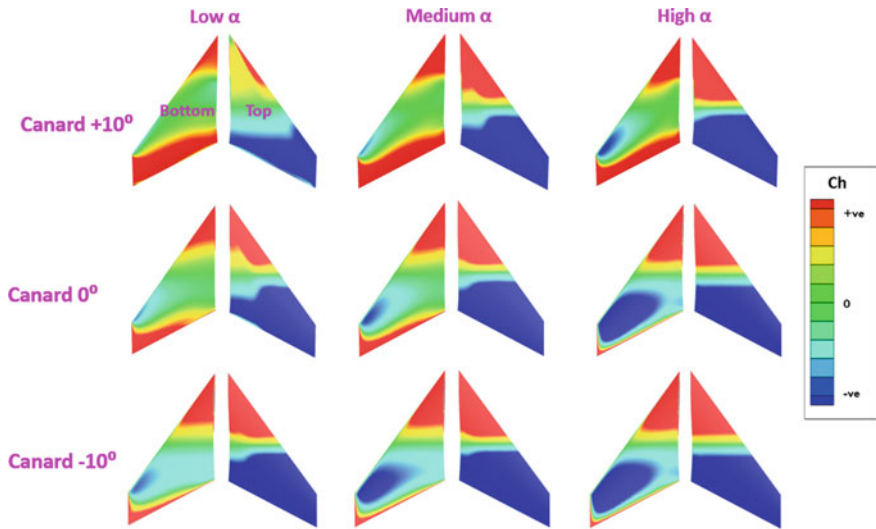
Fig. 18 Hinge moment contours on the top and bottom surface of the canard for $M = 0.9$
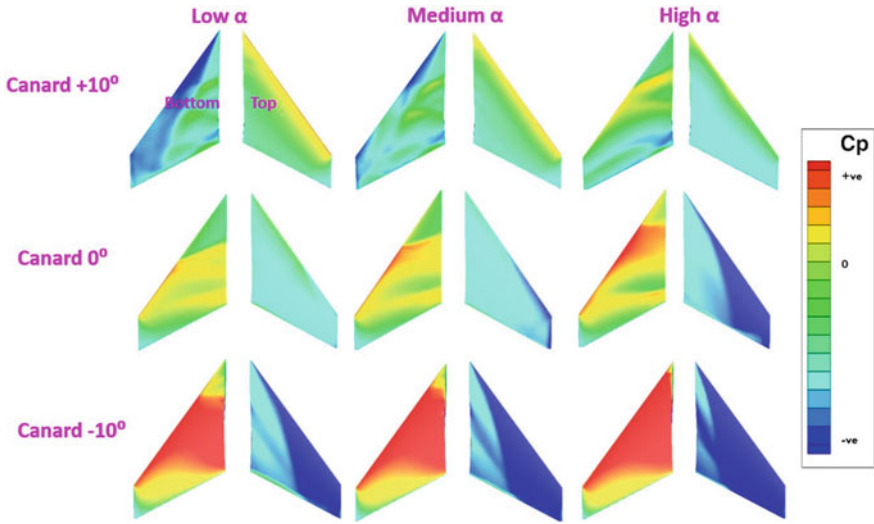
Fig. 19 Cp contours on the top and bottom surface of the canard for $M = 1.3$
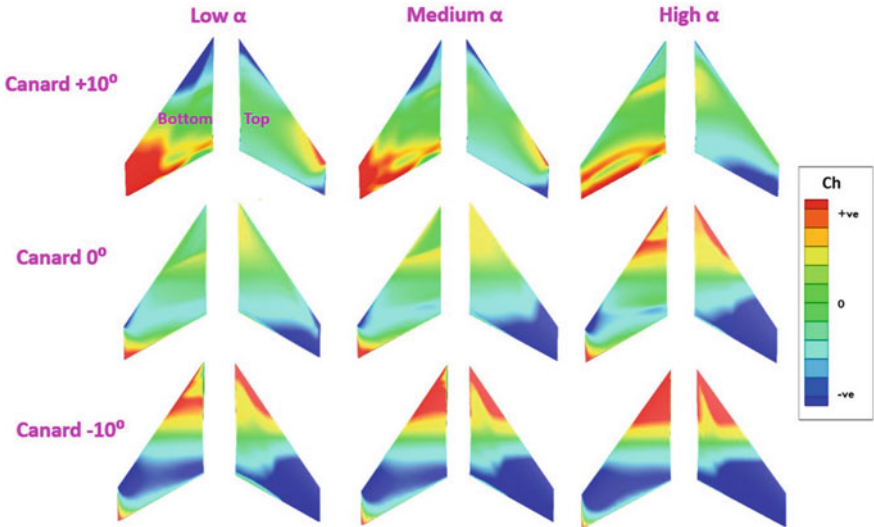
Fig. 20 Hinge moment contours on the top and bottom surface of the canard for $M = 1.3$

4 Conclusion

RANS studies have been used to estimate the hinge moments of a close coupled canard and thereby derive its free floating characteristics in case of canard actuation system failure. CFD studies have been carried out for all canard deflections, and

the trend in the hinge moments for canard deflections of $0°$, $-10°$ and $+10°$ has been used to understand the reasons for canard floating, in case of failure. It has been seen from the CFD studies that the slope and magnitude of the hinge moments and the movement of centre of pressure give a good indication of the free floating characteristics of canard.

Nomenclature

AoA   Angle of attack (°)
CHM   Coefficient of hinge moment (–)
COP   Centre of pressure (m)
Cp   Coefficient of pressure (–)
M   Mach number (–)
Re   Reynolds number (–)

References

1. Gumusboga I, Iftar A (2010) Modeling of asymmetric elevator failures in the F-16 aircraft. AIAA SciTech forum, San Diego, California
2. Hollinger JA (1969) Canard hinge moments and longitudinal stability of a 1/7 scale model of the Convair B-58 external store in a free-flight investigation at Mach numbers from 0.94 to 2.58
3. Kraus W (1980) Delta canard configuration at high angle of attack, 12–17 Oct 1980
4. Perkins CD, Hage RE (1949) Airplane performance stability and control, Jan 1949

The Study on Working Fluid for Cold Gas Reaction Control System and Its Expansion Time in Regulated and Non-regulated Conditions

G. Kesava Vishnu and Vishnu Suresh Nair

1 Introduction

A rocket stage operating with a single engine is capable of creating pitch and yaw moments by gimballing the engine. Gimballing the engine moves the thrust axis away from vehicle axis which creates moment across pitch and yaw planes. A tangential force is required to create moment across roll axis [2]. Tangential force can be created by deflecting fins or by utilizing thrusters in the tangential direction. Fin deflection control would only be effective in regions of high dynamic pressure sufficient to create a lifting force on the control surfaces. Normally used types of thrusters in a launch vehicle are (Fig. 1),

1. Mono-propellant thrusters.
2. Bi-propellant thrusters.
3. Cold gas thrusters.
4. Miniature Solid motors.

A fine control of the thrust and pulse width is difficult with solid motors. Table 1 shows the comparison between mono-propellant, bi-propellant and cold gas systems. Mono-propellant system requires propellant tank, propellant acquisition system, tank pressurization system and catalyst. The tank pressurization system includes gas bottles and pressure regulators. The system performance degrades over time due to catalytic poisoning. Bi-propellant systems require separate propellant storage, feed and control systems for fuel and oxidizer which adds to system complexity. Mono-propellant and bi-propellant thrusters are complex when compared to cold gas systems [1]. Cold gas feed system requires a propellant tank and a regulator. Cold gas propulsion system has already been used in spacecrafts to achieve attitude and orbital control. It has been used in COS-B, OTS, EURECA, ASTRO-SPAS, HIPPARCOS,

G. Kesava Vishnu (✉) · V. S. Nair
Liquid Propulsion Systems Centre (LPSC), Valiamala, ISRO, Thiruvananthapuram 695047, India
e-mail: gkesava97@gmail.com
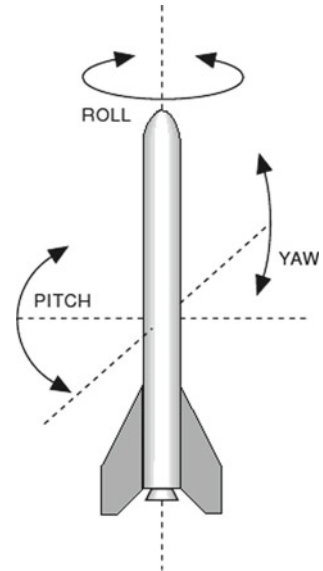
EX-OSAT and STRV-1C and 1D. It was also used on the Dutch SLOSHSAT, which was launched in 2005 [3]. The technology of cold gas propulsion for spacecraft applications is available with STERER, Marotta and Moog (USA), DASA (Germany), Rafael (Israel) and Bradford Engineering (The Netherlands) [4]. Using the system for launch vehicles requires additional design considerations. The ambient pressure of a launch vehicle varies during the course of ascent. So, the thrust delivered by the thruster changes due to variation in the thrust coefficient. The control logic shall be enabled to accommodate this variation in specific impulse. When compared to spacecrafts, launch vehicle thrusters require higher thrust to create a roll moment. Even though the total impulse requirement is nearly same for launch vehicles and satellites, the operating duration is shorter for launch vehicles.

Table 1 Comparison of different mono-propellant, bi-propellant and cold gas system

Spec	Bi	Mono	Cold gas
Isp (s)	190	< 180	60–140
System complexity	High	Medium	Less
No. of design tests	High	Medium	Less
Mass	Low	Medium	High

Fig. 2 Eight thruster configuration (top view)
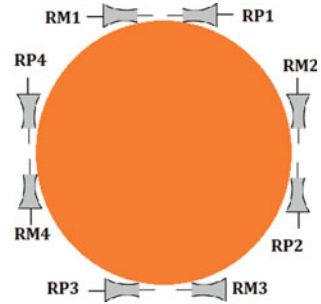
2 Thruster Configuration

Figure 2 shows the thruster configuration. A pair of thrusters are kept, facing 180° apart, on each side of axes. In total, eight thrusters are required to create roll moments in both directions. Even though the primary objective of the reaction control system is to cater roll requirements, it can also be used for pitch and yaw manoeuvers. It can be achieved by the selection of thruster firing configuration. Table 2 shows the firing configuration for roll, pitch and yaw control. Pitch and yaw manoeuvers are possible when the plane of thruster placement is away from the centre of gravity (CG) of the vehicle. When the CG of the vehicle is below the thruster plane, firing the RP2 and RM4 pushes the vehicle towards pitch plus direction, whereas when the CG is above the thruster plane, firing the RP2 and RM4 pushes the vehicle towards pitch minus direction. Similarly, the firing configurations are listed in Table 2 for pitch and yaw manoeuvers, the effectiveness of the thruster firing depends on the distance between the thruster plane and CG. The pitch moment generated is maximum when the thruster plane is at the highest distance from the vehicle CG. Hence, it is always better to position the thruster plane in the topmost point of the vehicle.

3 Cold Gas System

In a cold gas propulsion system, the working fluid is stored at high pressure and expanded through thrusters. This will give the required control thrust for the vehicle. In the system, combustion is not involved. Various choices of gases can be considered for the working fluid. Gases like nitrogen, helium are commonly used [3, 5].

Neon and argon can also be used as working fluids. Higher molecular weight of the working gas is desirable for cold gas system as the medium with the higher molecular weight gives the maximum total impulse for a given storage pressure and volume. Hugo Nguyen et al. discussed the possible propellant choice for cold gas system [4]. Molecular weight is considered as the base parameter for the choice of propellants. Critical temperature and critical pressure also have a major role in its choice. The liquid–vapour saturation curve of the working medium should not be crossed during

Table 2 Thrusters firing versus possible manoeuvers

S. No.	Manoeuver	Simul. firing of thrusters
1	Roll plus	RP1, RP2, RP3, RP4
2	Roll minus	RM1, RM2, RM3, RM4
When CG is below the thruster's plane		
3	Pitch plus	RP2, RM4
4	Pitch minus	RM2, RP4
5	Yaw plus	RM1, RP3
6	Yaw minus	RP1, RM3
When CG is above the thruster's plane		
7	Pitch plus	RM2, RP4
8	Pitch minus	RP2, RM4
9	Yaw plus	RP1, RM3
10	Yaw minus	RM1, RP3

isentropic expansion to ensure that phase change is avoided. If the curve is crossed during expansion, the working medium would liquify and thruster wouldn't be able to produce the required thrust. Figures 3, 4 and 5 show the liquid–vapour saturation curve versus isentropic expansion curve from 300 to 10 bar for nitrogen, helium and methane gases respectively. 300 bar pressure and 300 K temperature are taken as the initial conditions. From Fig. 3, we can see that the temperature after isentropic expansion is well above liquid–vapour saturation curve at any given pressure. Only at pressures below the operating requirement, temperature after isentropic expansion is getting closer to the saturation temperature. Whereas, in Fig. 5, it is observed that for methane, liquid–vapour saturation temperature is higher than the temperature after isentropic expansion for a given pressure. As a result, methane gas liquefies during expansion leading to loss of thrust. Helium's saturation temperature is far away from isentropic expansion temperature when compared to nitrogen. But on the other hand, helium has higher cost and lower molecular weight when compared to nitrogen. Hence, by considering operational and cost-effectiveness, gaseous nitrogen is the better working fluid for cold gas thrusters.

4 Major Components

Atul Mishra et al. discussed the basic system configuration in which the high-pressure cold gas is regulated to low pressure on two steps [5]. The choice of number of regulators depends on the regulating capacity.

The major components were gas bottles, fill and vent valve, regulator and thrusters. Mojtaba Ghasemi et al. detailed each subsystems [6]. Figure 6 shows the components of a cold gas system [6]. It includes the tank for storing gas, fill and drain valve
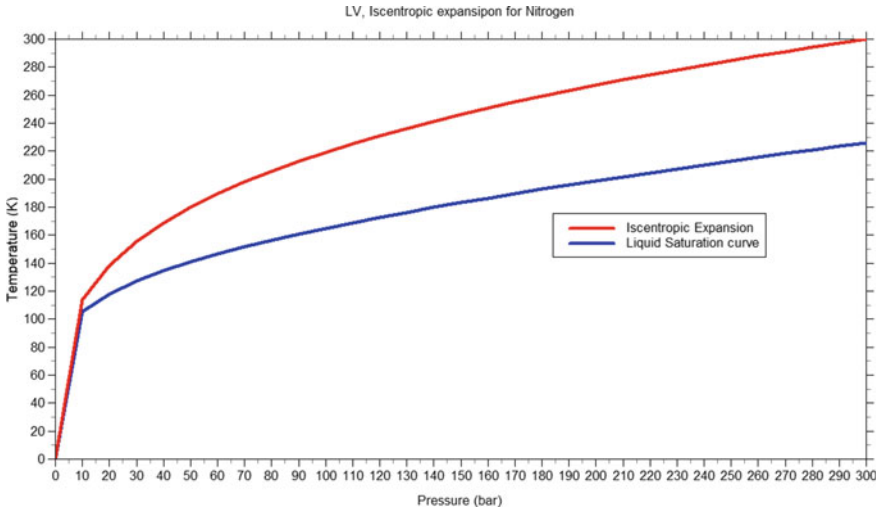
Fig. 3 Liquid vapour saturation-isentropic expansion curve for nitrogen
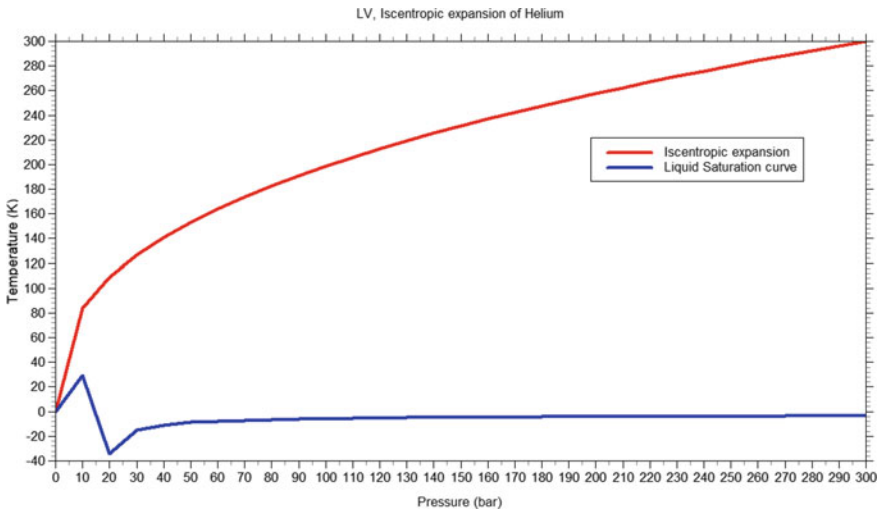
Fig. 4 Liquid vapour saturation-isentropic expansion curve for helium

for filling the gas to the bottle, isolation valve between bottle and regulator, pressure regulator which regulates the high-pressure gas to the required pressure, relief valve, thruster valves which act as a gate for thruster inlet and thrusters. Apart from these fluid components, pressure transducers are used to measure bottle pressure and regulated pressure.
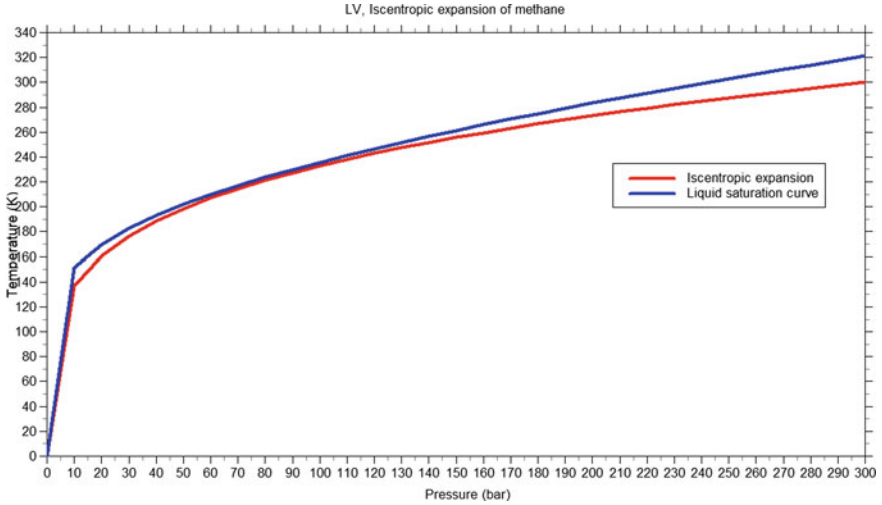
Fig. 5 Liquid vapour saturation-isentropic expansion curve for methane
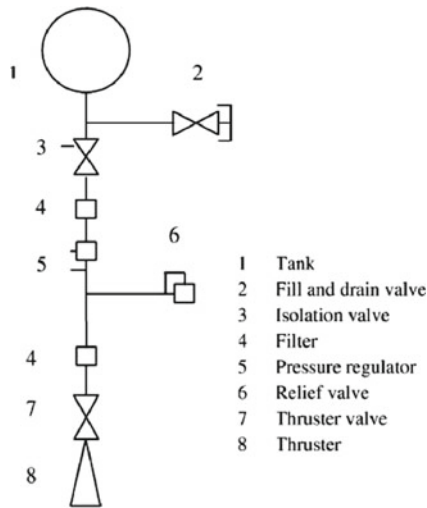
Fig. 6 List of components in cold gas system [6]

5 Regulated Mode Versus Non-regulated Mode

The gas which is stored at higher pressure can be fed to thrusters in two different ways. One, with regulation and the other, without regulation. In the regulated mode, the thrusters will experience a constant pressure till the regulator reaches its limit of

regulation. Below a certain upstream pressure, the pressure regulator enters blow-down mode. The blow-down regime is determined by the orifice diameter used in the regulator whereas the mass flow rate is determined by the effective thruster throat diameter. As the inlet pressure to the thruster is constant in the regulated mode, the thrust produced by the thruster is constant, assuming the thrust coefficient remains constant. Figure 7 shows the schematic of gas feed system with pressure regulator.

In non-regulated mode, there is no pressure regulator downstream of the gas bottle. The high-pressure gas is directly fed to the thrusters. The effective throat diameter of the thruster controls the mass flow rate during firing. As the inlet pressure to the thruster changes continuously, the thrust produced by the thruster also changes continuously. Figure 8 shows the schematic of thruster fed system without pressure regulator.

The major difference between regulated and non-regulated fed system comes with mass flow rate of the cold gas. In regulated fed system, the total process can be divided into two regimes namely,

1. Regulated or steady-state regime.
2. Blow-down or unsteady regime.

Under regulated or steady stage regime, pressure downstream of regulator is maintained constant irrespective of the inlet pressure to regulator. As the thruster throat is in choked condition, the mass flow rate which is constant can be computed as follows,

$$
\dot{m}_R = \frac{A_{NT} P_t}{\sqrt{T_t}} \times \sqrt{\frac{\gamma}{R}} \times \frac{\gamma+1}{2}^{-\frac{\gamma+1}{2(\gamma-1)}}
\tag{1}
$$

where

P_t Chamber pressure of Nozzle

Fig. 7 Cold gas system with pressure regulator
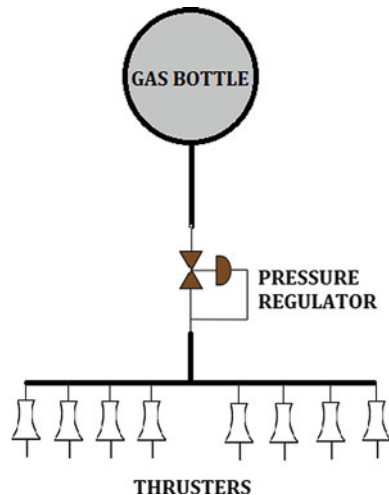
Fig. 8 Cold gas system
without pressure regulator
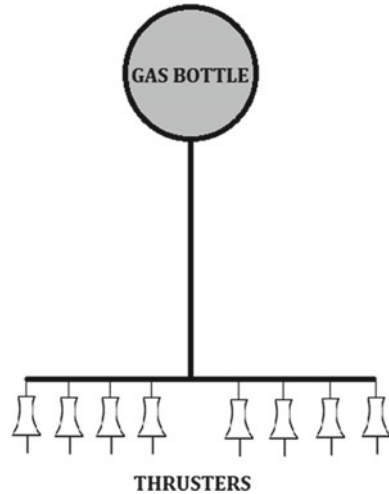
T_t Temperature of cold gas medium
A_{NT} Area of Throat
R Gas constant of a gas
γ Iscentropic constant of a gas.

During blow-down regime, the regulator is fully open, which means the regulator acts as an orifice. Now the mass flow rate is controlled by regulator orifice. As the inlet pressure of regulator/orifice continuously decreases, the mass flow rate also decreases which results in the decrease in thrust delivered by the thrusters.

$$\dot{m}_{BL} = \frac{A_{RO} P_{PR}}{\sqrt{T_t}} \times \sqrt{\frac{\gamma}{R}} \times \frac{\gamma+1}{2}^{-\frac{\gamma+1}{2(\gamma-1)}} \tag{2}$$

P_{PR} Inlet pressure of regulator orifice
A_{RO} Area of regulator orifice.

In a non-regulated feed system, the pressure from bottle is directly fed to thrusters. In this case, the flow is directly controlled by nozzle throat. So the mass flow rate can be calculated as follows by assuming isentropic expansion,

$$\dot{m}_{NR} = \frac{A_{NT} P_R}{\sqrt{T_t}} \times \sqrt{\frac{\gamma}{R}} \times \frac{\gamma+1}{2}^{-\frac{\gamma+1}{2(\gamma-1)}} \tag{3}$$

P_R Pressure at nozzle throat
A_{NT} Area of nozzle throat.

Assuming ideal gas and isentropic expansion,

$$PV = M_b RT \tag{4}$$

$$T = CP^{\frac{\gamma-1}{\gamma}} \tag{5}$$

The rate at which the bottle pressure changes depends on whether the process is regulated or non-regulated. In real case scenario, the stored gas expands in a polytropic process. Arthur S. Iberall derived the effective gamma for isentropic expansion of real gases [7]. He derived a relationship between effective α and γ. The relation depends on the state function and initial state [7]. In the current study, it is assumed that the gas expansion follows the ideal isentropic expansion process.

$$M_b = M - m_e \tag{6}$$

$$\frac{\mathrm{d}m_e}{\mathrm{d}t} = \dot{m} \tag{7}$$

where

M_b Mass of gas inside the gas bottle at given time
M Initial mass of gas inside bottle
m_e Total mass of gas expelled from bottle at given time.

By differentiating Eq. 4,

$$V\frac{\mathrm{d}P}{\mathrm{d}t} = RT\frac{\mathrm{d}M_b}{\mathrm{d}t} + M_b R\frac{\mathrm{d}T}{\mathrm{d}t} \tag{8}$$

Using Eqs. 4 and 6 in Eq. 8

$$V\frac{\mathrm{d}P}{\mathrm{d}t} = RT\dot{m} + \frac{PV}{T}\frac{\mathrm{d}T}{\mathrm{d}t} \tag{9}$$

Using Eq. 5 in Eq. 9

$$V\frac{\mathrm{d}P}{\mathrm{d}t} = -RC\dot{m}P^{\frac{\gamma-1}{\gamma}} + \frac{P^{\frac{1}{\gamma}}V}{C}\frac{\mathrm{d}T}{\mathrm{d}t} \tag{10}$$

And also, by using Eq. 5,

$$\frac{\mathrm{d}T}{\mathrm{d}t} = \frac{\gamma-1}{\gamma}CP^{\frac{-1}{\gamma}} \tag{11}$$

Using Eq. 11 in Eq. 10,

$$V\frac{\mathrm{d}P}{\mathrm{d}t} = -RC\dot{m}P^{\frac{\gamma-1}{\gamma}} + V\frac{\gamma-1}{\gamma}\frac{\mathrm{d}P}{\mathrm{d}t} \tag{12}$$

$$\frac{V}{\gamma}\frac{\mathrm{d}P}{\mathrm{d}t} = -RC\dot{m}P^{\frac{\gamma-1}{\gamma}}. \tag{13}$$

For regulated or steady-state flow,

$$\text{Let } K = \frac{-RC\dot{m}\gamma}{V}.$$

So Eq. 13 becomes,

$$P^{\frac{1-\gamma}{\gamma}}\mathrm{d}P = -K\mathrm{d}t \tag{14}$$

By integration $P(P_1 \text{ to } P_2)$ and $t(0 \text{ to } t)$

$$\gamma\left[P_2^{\frac{1}{\gamma}} - P_1^{\frac{1}{\gamma}}\right] = -Kt. \tag{15}$$

For non-regulated flow, $\dot{m}$ is a function of bottle pressure (2),

$$\text{Let } S = \sqrt{\frac{\gamma}{R}} \times \frac{\gamma+1}{2}^{\frac{-(\gamma+1)}{2(\gamma-1)}}A.$$

Using Eq. 2,

$$\dot{m} = \frac{SP}{\sqrt{T}}$$

Using Eq. 5,

$$\dot{m} = \frac{S}{\sqrt{C}}P^{\frac{\gamma+1}{2\gamma}}. \tag{16}$$

Substituting Eq. 16 in Eq. 13

$$\frac{V}{\gamma}\frac{\mathrm{d}P}{\mathrm{d}t} = -R\sqrt{C}SP^{\frac{3\gamma-1}{2\gamma}}. \tag{17}$$

Let $K_1 = \frac{-R\gamma\sqrt{C}S}{V}$,

$$\frac{\mathrm{d}P}{\mathrm{d}t} = -K_1P^{\frac{3\gamma-1}{2\gamma}}. \tag{18}$$

By integration $P(P_1 \text{ to } P_2)$ and $t(0 \text{ to } t)$

$$\frac{2\gamma}{1-\gamma}\left[P_2^{\frac{-(1-\gamma)}{2\gamma}} - P_1^{\frac{-(1-\gamma)}{2\gamma}}\right] = -K_1 t \tag{19}$$

6 Test Case

Considering the system is used in a launch vehicle, a study case is considered. The specifications for the same are mentioned in Table 3. From the observation made from Sect. 3, nitrogen gas is considered as the working fluid. Using 117.5-L gas bottle, nitrogen gas is stored at 300 bar (a). A total mass of 40 kg nitrogen is stored in the bottle. Time taken for expansion from 300 to 30 bar is calculated for regulated and non-regulated modes. Considering the simultaneous firing of four thrusters at a time, the effective area of thrusters is as follows:

$$D_{\text{eff}} = 2 \times D_{\text{throat}} = 8.4 \text{ mm.}$$

For non-regulated flow, by using Eq. 3

$$m_{\text{NR}} = \frac{P_R}{\sqrt{T_t}} \times 2.18617 \times 10^{-6}.$$

Figure 9 represents the variation of mass flow rate with bottle pressure in non-regulated mode of operation. It can be observed that at 300 bar, the mass flow rate of 3.75 kg/s and at 30 bar, mass flow rate of 0.5 kg/s. As the bottle pressure decreases, mass flow rate also decreases, which leads to a proportional decrease in thrust produced. Using isentropic expansion relation, it is found that for the area ratio of 9.41, the exit Mach no is around 3.86. Using the exit Mach no, the thrust produced by the thrusters is calculated. Figure 10 shows the variation of thrust delivered with respect to pressure. At 300 bar, the thrust was about 680 N and at 30 bar, the thrust is about 490 N. Whereas in regulated flow condition, the pressure at the inlet of thruster is constant which results in constant thrust.

Figure 11 shows the variation of mass flow rate with respect to bottle pressure for regulated feed condition. In the regulated mode, a regulator is used to regulate the bottle pressure to the desired operating pressure. The working fluid at the regulated

Table 3 Case study specifications

S. No.	Parameter	Specification
1	Thruster configuration	8 thruster configurations
2	Thruster throat diameter	4.2 mm
3	Mission duration	75 s
4	Volume of gas storage	117.5 L
5	Total impulse required	8000 N s
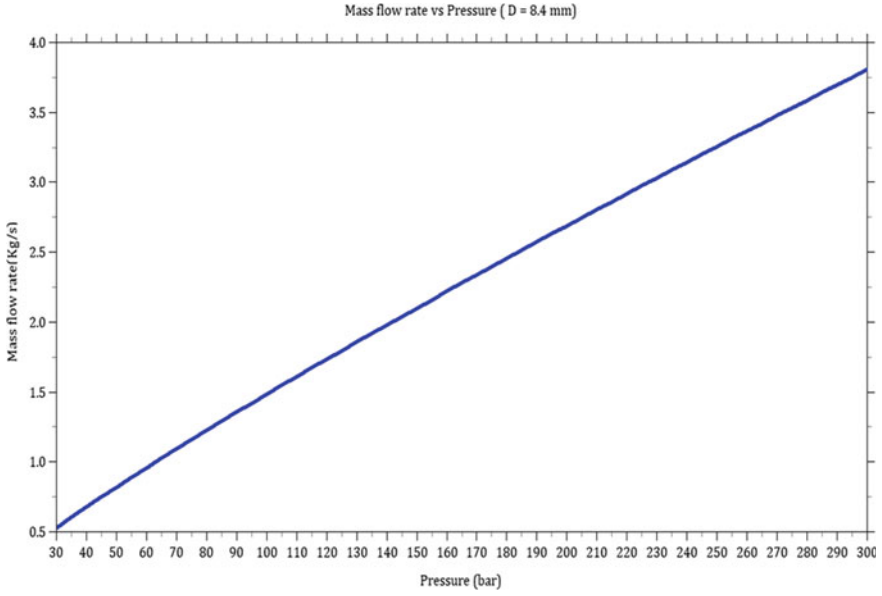
Mass flow rate vs Pressure (D = 8.4 mm)

Fig. 9 Variation of mass flow rate with respect to bottle pressure in non-regulated mode condition

Variation of Thrust vs bottle pressure
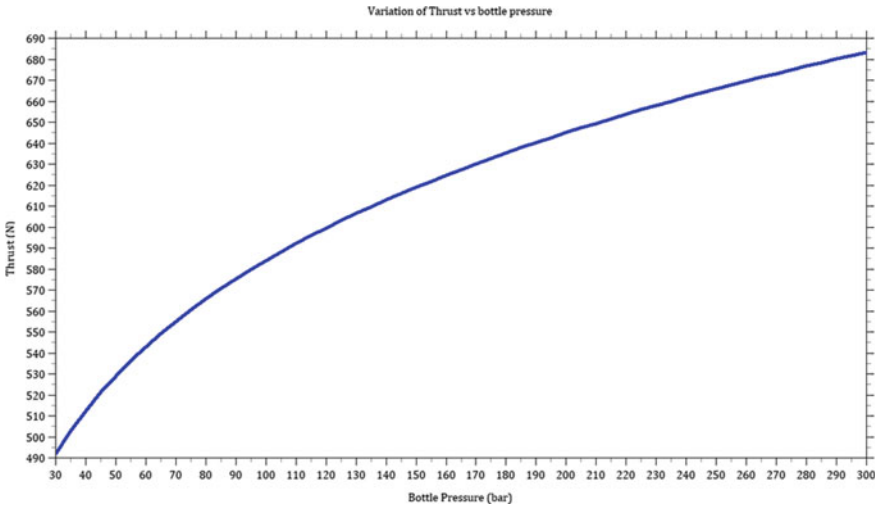
Fig. 10 Variation of thrust with respect to bottle pressure in non-regulated mode condition
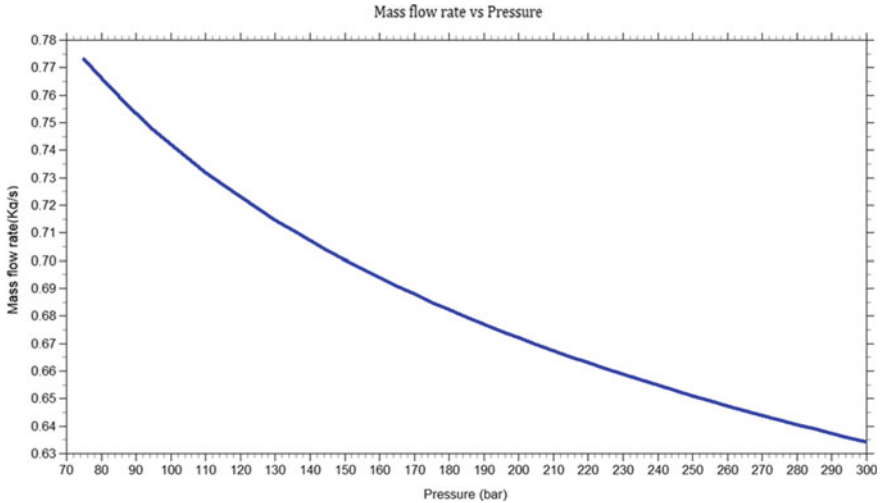
Fig. 11 Variation of mass flow rate with respect to bottle pressure in regulated mode condition

pressure is fed to the thrusters. In the current study, the regulator outlet is fixed at 50 bar for a range of inlet pressures. 70 bar is assumed as the minimum inlet pressure for regulation. From Fig. 11 it can be noticed that the mass flow rate varies from 0.64 to 0.77 kg/s. This variation is observed only due to the change in gas temperature due to isentropic expansion in the bottle. The change in mass flow rate is less when compared to the non-regulated mode. The thrust produced in this condition also nearly remains constant.

Using Eq. 15, the time taken for the bottle pressure to expand from 300 to 70 bar is calculated for regulated mode. Considering the average mass flow rate of 0.7050 kg/ s, the time taken is around 36 s. As the total duration of the mission is 75, 36 s of continuous operation will be sufficient since the thrusters would be operated in pulsed mode. The time required for the expansion of gas from 300 to 70 bar in non-regulated mode is calculated using Eq. 19 and is found to be 12 s.

The time taken for non-regulated feed system is almost one-third of the time taken by the regulated system. This implies at the start of the flight, the pulse duration required to do a manoeuver is less for non-regulated mode when compared to regulated system. This is due to the higher chamber pressure at the thruster. But, considering the overall utilization, feed system with a regulated mode is preferable to non-regulated mode. In non-regulated mode, all the thrusters, thruster valves, feedlines and joints have to be designed for 300 bar pressure. Whereas in regulated mode, fluid elements downstream to the regulator need to be designed only for a lower operating pressure. By considering overall uniform performance and proper usage of gas, regulated mode is selected for the reaction control system.

7   Conclusion

Reaction control system is a thruster-based system used to perform the required control manoeuvers. For a launch vehicle, out of all possible options studied, cold gas thrusters working with nitrogen are the most efficient and economical. In cold gas system, the working medium can be directly fed into thrusters with and without regulation. A test case, where each thruster is having 4.2 mm as throat diameter, where gaseous nitrogen is stored at 300 bar in 117.5 L volume is studied to assess the characteristics of regulated mode and non-regulated mode of operation. The time taken for the bottle pressure to reach 70 bar from 300 bar is around 12 s for non-regulated mode and 36 s for regulated mode. Under regulated mode, the thrust generated is constant, whereas in non-regulated mode, the thrust generated varies with time. For a launch vehicle, cold gas-based reaction control system with regulator is preferred due to less complexity, less cost and uniform performance throughout [5].

Nomenclature

RCS Reaction control system (–)
γ Specific heat ratio (–)
R Gas constant (kJ/kg K)
$\dot{m}$ Mass flow rate (kg/s)

References

1. Sutton GP, Biblarz O. Rocket propulsion element
2. Anderson JD. Fundamentals of aerodynamics
3. Acosta J, Cardin JM. Design and test of an economical cold gas propulsion system, USU conference on small satellites
4. Nguyen H, Kohler J, Stenmark L (2007) The merits of cold gas micro propulsion in state of the art of space missions, IAC 02
5. Mishra AA, Mohite A (2020) A detailed study and analysis of cold gas propulsion system. IRJET 07:10
6. Ghasemi M, Rezaeiha A (2011) Design and development of a flight-model cold gas propulsion system, ISTS2011
7. Iberall AS. The effective 'gamma' for isentropic expansions of real gases, 194

Flow Falling from Slit and Circular Hole Over a Horizontal Cylinder

R. Rajan, B. P. Akherya, Javed Mohd., D. Poddar, G. Wadhwa, S. Saha, and D. Das

1 Introduction

Circular cylinders play an important role in heat mitigation in the cross-flow tubular heat exchangers which are used in domestic and industrial applications. Falling film finds application in a variety of industries mainly in food processing industries because of the high rates of heat transfer existing between the falling liquid film and the horizontal cylinders [1]. Therefore, it is crucial to investigate the wetting area of the film formed on the horizontal cylinder which in turn affects the heat transfer characteristics. Also, falling film flow pattern is sensitive to the initial wetting condition [2].

Different studies have shown the dependency of liquid flow rate on the flow behaviour and the heat transfer. More study is needed to understand the mechanism of the flow pattern and the heat transfer over a horizontal tube. Mitrovic [3] studied experimentally the heat transfer and the mechanism of the flow from a horizontal heated tube to a falling subcooled liquid film. The experimental results indicated that the flow pattern depends not only on the film Reynolds number, Re, but also on the tube spacing.

For laminar falling film flow on horizontal tube, Rogers [4] developed a non-dimensional equation with the laminar film thickness at any position as function of Re, Archimedes number, Ar, and the angular position on the horizontal tube. Rogers and Goindi [5] later measured experimentally the film thickness of water falling on a large diameter horizontal tube. The measured thickness of laminar falling films were compared with the theoretical values, and a new predicted correlation of the film thickness was developed.

R. Rajan (✉) · B. P. Akherya · J. Mohd. · D. Poddar · D. Das
Department of Aerospace Engineering, IIT Kanpur, Kanpur 208016, India
e-mail: rrajan20@iitk.ac.in

G. Wadhwa · S. Saha
Department of Aerospace Engineering, IIT Kharagpur, Kharagpur 721302, India

$$\left(\frac{\delta}{d}\right)_{\min} = 1.186\,\mathrm{Re}^{1/3}\mathrm{Ar}^{-1/3} \tag{1}$$

In this paper, an experimental study is carried out using various concentrations of sugar solution to identify the projected area of film falling over a horizontal cylinder. Projected area is associated with the wetting area of the surface, which in turn decides the heat transfer characteristics of flow over a surface. The relationship among different controlling parameters like diameter of the cylinder, jet diameter just before impact and the projected area is explored. The falling film is generated through a damper reservoir having a hole or a slit at bottom. MATLAB edge detection algorithm is used to calculate the projected area by image processing technique and Buckingham Pi theorem is used to identify the influence of various parameters on the wetting area.

2 Experimental Setup

A schematic illustration of the experimental apparatus used for the present study is shown in Fig. 1. An overhead tank based on Marriott's bottle principle is used to supply the sugar solution for the experiment at a constant flow rate. The Mariotte reservoir is placed on a precision weighing scale (Citizon CG 6102, readability or least-count 0.01 g), which, in turn, is placed on a laboratory jack. A camera (IMPERX B2320M, 2352 × 1768 px) records the scale reading at 10 Hz during the experiment. The recorded scale images were further analyzed to get the mass flow rate. The overhead tank is connected to the nozzle via a flexible PVC pipe through a compressor ball valve. This valve and the laboratory jack are used to control the flow rate [6].

A horizontal cylinder of length 164 mm and diameter 35.06 mm is taken for the experiment. Sugar solution of four different concentrations is used for conducting the experiment. A damper reservoir of dimensions (172 × 62 × 58) mm having a slit (60 × 4) mm or hole (10 mm diameter) is taken as shown in Fig. 2 and the flow is allowed to fall on the top of horizontally placed cylinder through either slit/hole provided on the damper reservoir. A high-speed 4 MP camera is used for recording

Fig. 1 Experimental setup
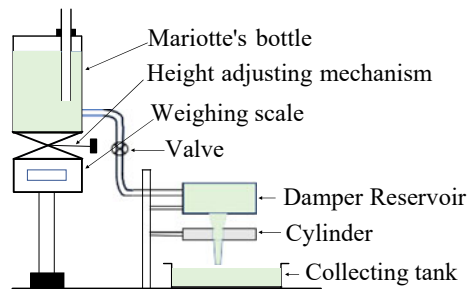
Fig. 2 Damper reservoir
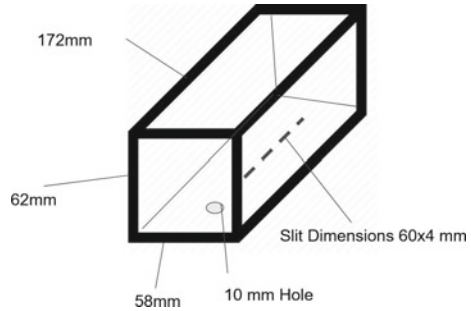
the decrease in weight of sugar solution in Marriott's bottle and thereby finding the flow rate. Another DSLR camera (Nikon 5100, 16 MP) is used for recording the flow over the surface of horizontal cylinder. The field of view for imaging has been illuminated with a diffused light, produced by a 1000-W halogen lamp, passing through a paper sheet in the background. Sugar solution of 16.11, 19.37, 23.9 and 28.32% of concentration (weight by weight) is used in this experiment. At the time of performing experiments, the flow rate was adjusted using a valve and a particular concentrated sugar solution was allowed to fall over the horizontal cylinder through the damper reservoir. The leakage in damper reservoir is avoided by filling the sugar solution inside the reservoir after doing proper levelling of damper.

3 Results

For each concentration, the flow of the sugar solution over the horizontal cylinder was recorded for increasing mass flow. Sufficient time was allowed to be passed so that any unsteady disturbances get mitigated. The image was acquired after ensuring the steady-state flow. Four selected representative images for hole and slit case are shown in Fig. 7. These recorded images were analysed for the calculation of wetting area formed by the flow of sugar solution over a horizontal cylinder using MATLAB. However, for the slit case with C3 concentration it was not possible to calculate the wetting area due to unstable and bifurcated film formation, and therefore, this particular case was not considered for further analysis.

3.1 Image Processing

Buckingham Π theorem was used to identify the non-dimensional numbers required to describe the wetting area on the surface of cylinder. The physical properties required for the description of the wetting area were D_i, V_i, ρ, μ, σ and D_c. Where V_i is the film velocity just before the impact calculated using mass flow rate and

Table 1 Properties of sugar solution

	Concentration (% w/w)	Surface tension (mN/m)	Viscosity (Pa s)	Density (g/cc)
C1	23.9	70.35	0.215	1.274
C2	19.37	67.5	0.125	1.206
C3	16.11	67	0.013	1.158
C4	28.32	70.4	0.278	1.294

cross-sectional area at that location. The non-dimensional numbers identified were capillary number ($(V_i \cdots \mu)/\sigma$), Reynold's number ($(V_i * D_c * \rho)/\mu$), Diameter ratio (D_i/D_c), i.e. ratio of diameter of the jet just before the impact with cylinder and the diameter of the cylinder, and the non-dimensionalized wetting area ($A_w/(D_c)^2$).

The physical properties of the sugar solution, the mass flow rate for the hole, and the mass flow rate for the slit are given in Tables 1, 2, and 3, respectively. The image processing was needed to be done to measure the wetting area on the cylinder and the diameter (in case of hole) and width and depth (in case of slit) for the calculation of the identified non-dimensional numbers. For this, a MATLAB edge detection algorithm was used, and the algorithm first selects and calculates the wetting area and jet diameter. Figure 3 shows original image of the wetting area on the cylinder, and Fig. 4 shows image identified by the edge detection algorithm, both images are similar; hence, the area calculated is accurate. Similarly, the cross-section of the jet was measured using MATLAB algorithm. Non-dimensional numbers were calculated for both hole and slit cases using the measured properties of the fluid and the fluid flow. The calculated wetting area has been plotted with diameter ratio (Fig. 6), Re (Fig. 7) and Ca (Fig. 8). Please note that the wetting area in the present paper is the projected wetting area (Fig. 4).

3.2 Discussion

It was found that the non-dimensionalized wetting area varies linearly with the diameter ratio for both hole and slit as shown in Fig. 6. In case of slit the hydraulic diameter at impact is used as D_i. In the present experiments, the diameter ratio for circular jet achieved is much smaller ($\approx 10\times$) than that of the slit cases. A rapid increase in wetting area is observed at low diameter ratio in case of circular geometry in comparison to slit geometry. The reason for such linear increase will be investigated in future work.

A polynomial of degree 1 was fitted to the data as shown in Fig. 6, with an r-square value of 0.76 and (write value here) for hole and slit, respectively. The obtained scaling relations for hole and slit are given in Eqs. 2 and 3, respectively.

$$\frac{A_w}{D_c^2} = 5.32 \ \frac{D_i}{D_c} - 0.14 \tag{2}$$

Table 2 Mass flow rate at different concentrations for jet through a hole

Concentration (% w/w)	Mass flow rate (g/s)	
C1	q1	49.54
	q2	34.76
	q3	39.46
	q4	20.93
	q8	3.05
	q9	0.778
C2	q1	81.47
	q2	42.06
	q3	20.08
	q4	8.69
	q6	2.01
C3	q1	2.90
	q3	19.18
	q4	47.63
C4	q1	37.23
	q2	2.64
	q4	8.92
	q5	21.04

Table 3 Mass flow rate at different concentrations for jet through a slit

Concentration (% w/w)	Mass flow rate (g/s)	
C1	q1	49.51
	q2	34.13
	q3	38.51
	q4	21.65
C2	q2	42.06
	q4	8.69
C4	q1	12.42
	q3	24.21
	q4	36.91
	q5	37.23

$$\frac{A_w}{D_c^2} = 0.82 \ \frac{D_i}{D_c} + 0.31 \tag{3}$$

Wetting area with Re for the hole case is plotted in Fig. 7a, where for each concentration the wetting area increases with Re; however, the data for all the concentration

Fig. 3 Original image of the fluid flow over horizontal cylinder used for wetting area calculation

Fig. 4 Wetting area extracted from the image shown in 3 using edge detection algorithm
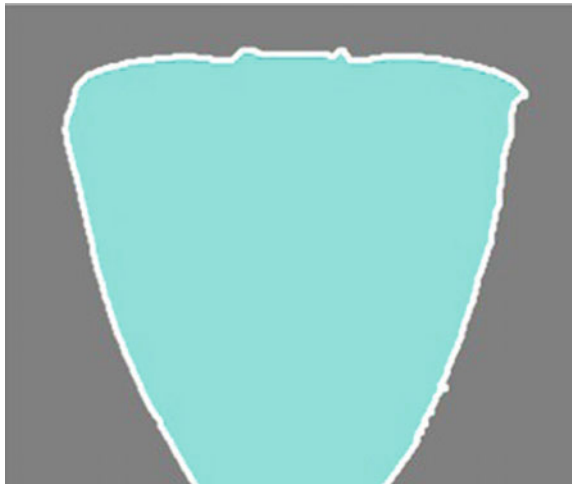
does not seem to follow a unified scaling. This might be due to the irrelevantly selected length and velocity scale for the calculation of Re. On the other hand, the wetting area is decreasing with the Re for the slit case as seen in Fig. 7b. Finally, the wetting area variation with Ca is plotted in Fig. 8. For concentrations C1, C2 and C4, the Ca the wetting area increases with Ca as shown in Fig. 8a. However for the slit case (Fig. 8b), wetting area decreases with Ca. The complete functional relationship between wetting areas, D_i/D_c, Re and Ca would be explored in future studies.
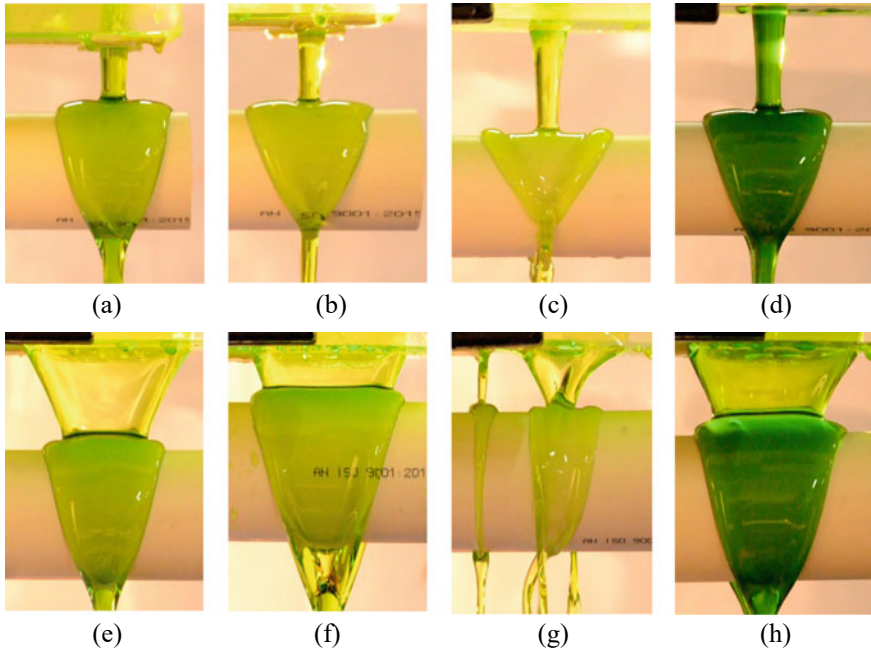
Fig. 5 Representative images for hole **a** C1, q3 **b** C2, q3 **c** C3, q3 **d** C4, q1 and for slit **e** C1, q2 **f** C2, q2 **g** C3, q1 **h** C4, q4

4 Conclusions

The wetting area formed by the flow of sugar solution over a horizontal cylinder was calculated using MATLAB image processing technique. Direct proportional relationship is obtained between the wetting area and the diameter ratio, i.e., the wetting area on the horizontal cylinder increases linearly with increase in the diameter of the jet for both the cases, hole and slit as given in Eqs. 2 and 3. The scaling relation found in this present study could be used to optimize more efficient heat exchangers.

Fig. 6 Wetting area versus
diameter ratio plot
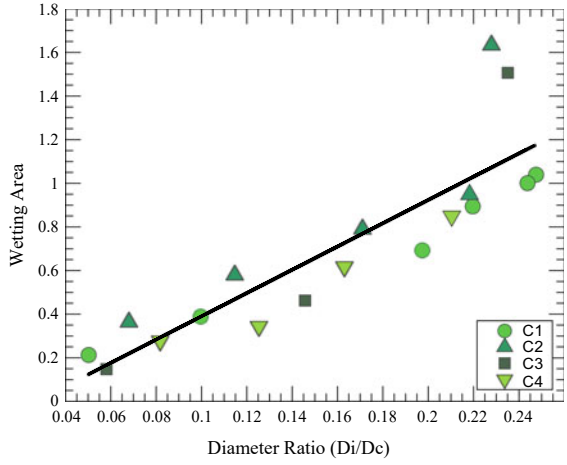
(a) Fluid flow through hole.
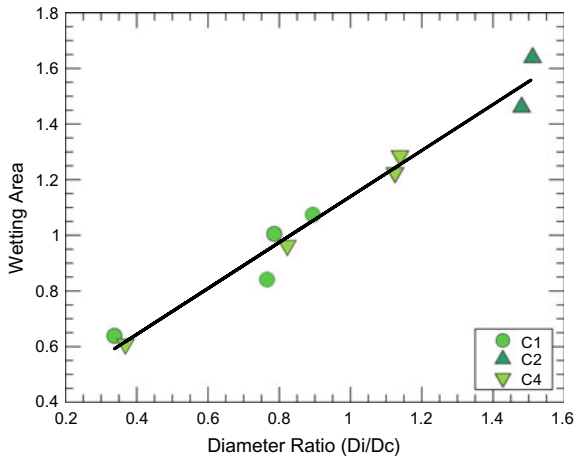
(b) Fluid flow through slit.

Fig. 7 Wetting area versus
Reynolds number plot
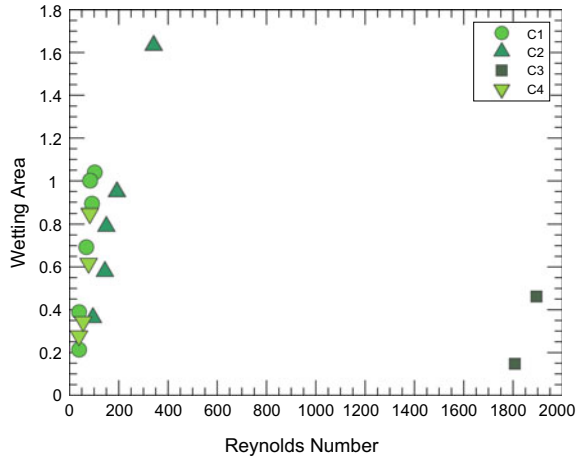
(a) Fluid flow through hole.
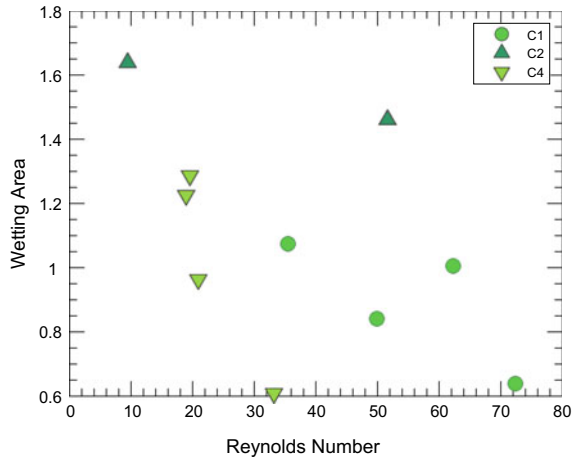
(b) Fluid flow through slit.

Fig. 8 Wetting area versus capillary number plot
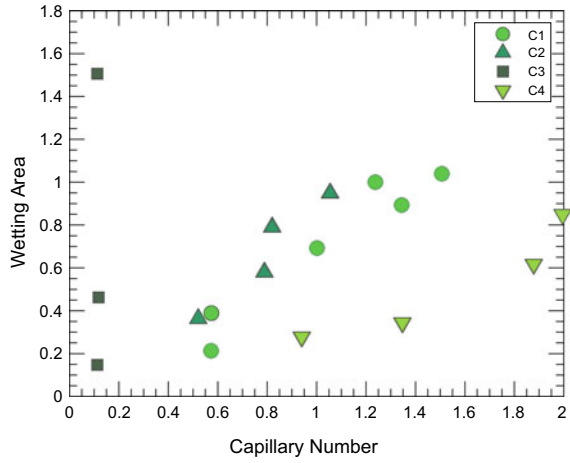
(a) Fluid flow through hole.
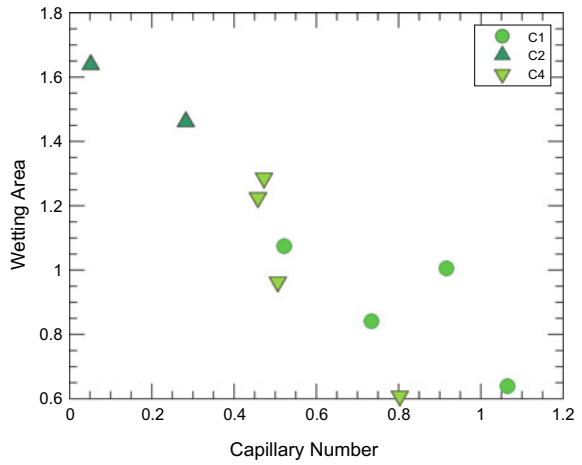
(b) Fluid flow through slit.

Nomenclature

D_i Jet diameter before impact (m)

V_i Velocity of the fluid flow (m/s)
ρ Density of the fluid (kg/m^3)
μ Viscosity of the fluid (Pa s)
σ Surface tension (N/m)
D_c Diameter of the cylinder (m)
Re   Reynold's Number (–)
δ Liquid film thickness (m)
d Tube diameter (m)

References

1. Chung H, Wusiman K, Kim S, Nasan B, Afrianto H, Rehman H, Choi D, Jeong H (2012) Liquid film falling behaviour on horizontal circular cylinder. J Central South Univ 19(5):1353–1358
2. Ding H, Xie P, Ingham D, Ma L, Pourkashanian M (2018) Flow behaviour of drop and jet modes of a laminar falling film on horizontal tubes. Int J Heat Mass Transf 124:929–942
3. Mitrovic J (1986) Influence of tube spacing and flow rate on heat transfer from a horizontal tube to a falling liquid film. In: International heat transfer conference digital library. Begel House Inc.
4. Rogers JT (1981) Laminar falling film flow and heat transfer characteristics on horizontal tubes. Can J Chem Eng 59(2):213–222
5. Rogers JT, Goindi SS (1989) Experimental laminar falling film heat transfer coefficients on a large diameter horizontal tube. Can J Chem Eng 67(4):560–568
6. Mohd J, Yadav A, Das D (2022) Open inverted bell and bell formation during the washing of vials. Phys Fluids 34:042126

Study of Separation Lines and Flow Patterns in 3D Boundary Layer Over Sphere Using Experimental and Numerical Analysis

G. Vasanth Kumar and Rinku Mukherjee

1 Introduction

Figure 1 was taken at the water tunnel facility here at Indian Institute of Technology, Madras. Here one can identify flow separation near the top and bottom sections of cylinder. For a two-dimensional flow, flow separation is generally taken to be the point, where the shear stress τ goes to zero. For three-dimensional flow, instead of a separation point, we have a separation line. The present work is aimed at identifying separation line and its relation with Re for sphere using experimental and numerical methods.

Flow past the sphere is studied in detail for very low Reynolds number flows and analytical methods to calculate aerodynamic forces acting on the sphere is well documented in literature [1]. At high Re, flow past sphere becomes complex and predicting flow separation, taking into consideration the free-stream velocity, turbulence, surface roughness, etc., is very challenging. Fornberg [2] carried out numerical calculations for flow past sphere till Re = 5000 and made observations on the wake patterns. In 2008, a report was published for flow past sphere from laminar regime Re till turbulent regime [3]. The report used Fluent commercial software to compute the flow properties, separation angle, drag coefficient, etc., and compared it with experimental results. Report stated that the commercial CFD package was able to correctly simulate flow past bluff bodies over range of Re.

The concept of using vector fields and critical point in the flow field to study separation can be attributed to Legendre's work in 1956 [4, 5]. Detailed review of the work done prior to 1980s is given by Dallmann [6]. The paper explores flow topology, wall shear, and the relation to three-dimensional separation. Tobak and Peake made striking observations on the role of experiments, particularly flow visualization, to study flow patterns and separation [7]. Three types of patterns in flow separation

G. Vasanth Kumar (✉) · R. Mukherjee
Department of Applied Mechanics, IIT Madras, Chennai 600036, India
e-mail: am18d007@smail.iitm.ac.in

Fig. 1 Flow past cylinder in water tunnel

(based on friction lines originating or not-originating from saddle point) was given by Gary Chapman and Yates in 1991 [8]. Paper by Patel [9] rightly points out the practical difficulty of using flow topology for turbulent flow since the laminar flow produces clear flow structure and are relatively simpler to observe as well as interpret. Recent work by Jean Delery gives a very detailed explanation of critical point theory and types of flow topology associated with different geometries [4].

2 Methodology

2.1 Experimental Analysis

Oil flow visualization tool was used to observe skin-friction lines over surface of sphere and identify regions of separation. Experiment was carried out at low speed wind tunnel with a test section dimension of 0.5 m × 0.5 m × 1.5 m as shown in Fig. 2. Initial experiments were carried out with sphere made of plastic. Friction lines over the surface was influenced by the surface roughness, so the model was discarded, and new model made of steel was fabricated with a smooth finish. Sphere ($\phi = 75$ mm) made of steel was mounted in the test section as shown in Fig. 3, and trial runs were made to ensure that the vibration in tunnel doesn't alter flow patterns over the surface.

Oil mixture is composition of *Titanium Dioxide*, *Oleic Acid*, and *pump oil*. A fixed volume of the three ingredients is mixed thoroughly and sprayed as fine droplets over the entire surface of the sphere. Advantage of using oil-based mixture is that the composition doesn't get dry or is altered when left in open atmosphere—only air flow flowing over the surface for a period of time leaves a pattern over the surface.

Fig. 2 Sub-sonic wind tunnel

Fig. 3 Steel sphere model

In the present work, wind tunnel is run for 10 min continuously at a set velocity for the skin-friction lines to form and photograph for observation.

Experiments were carried out for five different rpms between 450 and 800 in wind tunnel with same composition of oil mixture. Tunnel was run for the same duration at given rpm, and then final patterns were photographed. Experiment was repeated for 600 rpm and observation from repeated runs yielded similar results.

rpm	500	600	700	800	900
Velocity (m/s)	13.8	16.5	19.5	22.19	24.91
Re ($\times 10^5$)	0.68	0.81	0.96	1.1	1.2

2.2 Numerical Analysis

Numerical simulations were carried out in Ansys (ver 2021 R1) using the same model dimension as in case of experimental method. Flow domain was set such that the flow condition near infinity (domain boundary) attained free-stream velocity.

Model and flow domain is shown in Fig. 4a and the generated mesh in Fig. 4b. Mesh was generated such that the AR was below 25 at all locations and the wall Y-plus was monitored to ensure the value remained under unity for the turbulence model. In the present work, SST-k-ω turbulence model was used with turbulence intensity in free-stream limited to 1%. Boundary condition used for the calculation is shown in Fig. 4c, d. Numerical simulations were carried out for same set of Reynolds number as in case of experiments ranging from 0.02 to 0.1 million. Grid Independence was performed and results are shown in Fig. 5. Based on the variation of drag coefficient, 10^5 number of mesh elements were used for all the simulation with inflation layer over sphere surface to capture the boundary layer. Wall y-plus is plotted over the mid-section of sphere as shown in Fig. 6. Wall y-plus value is kept below unity at locations close to the sphere as suggested in literature.

(a) **Flow Domain**

(b) **Generated Mesh**

(c) **Inlet and wall BC**

(d) **Outlet and sphere BC**
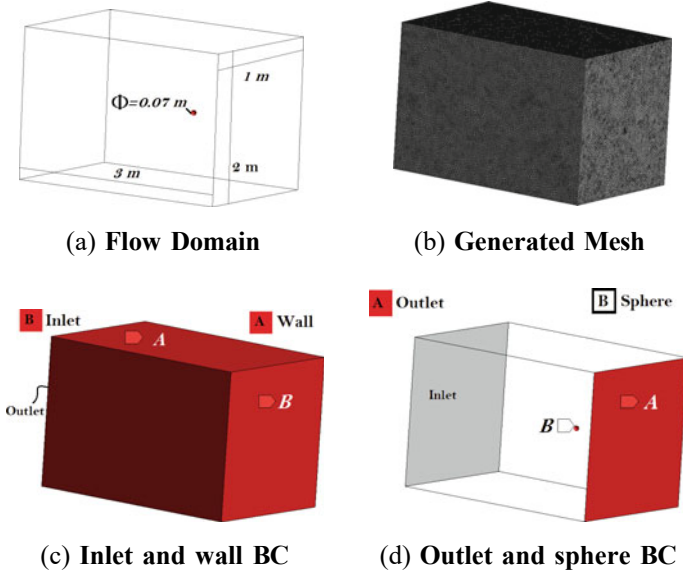
Fig. 4 Numerical set-up—flow past sphere

Fig. 5 Grid independence study
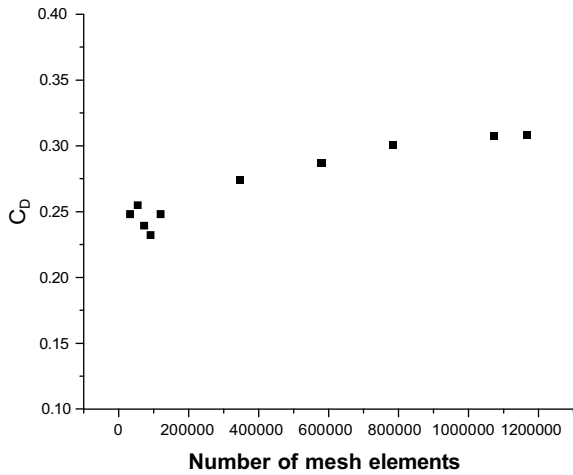
Fig. 6 Wall y-plus over sphere
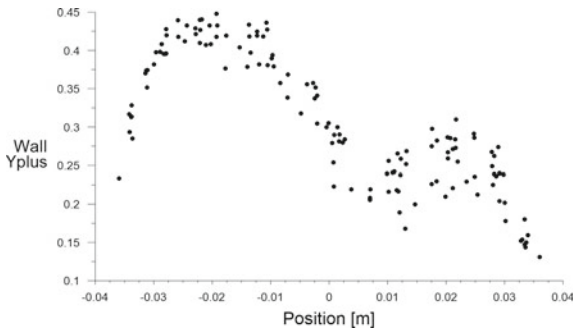
3 Results and Discussion

3.1 Experimental Results

Oil was allowed to settle and results were photographed after running the tunnel for duration of 10–12 min.

Figure 7a, c gives the flow pattern for different velocity corresponding to tunnel rpm of 550 and 700. From the results, it was observed that the area near stagnation point is reducing with increase in Re. A similar trend was observed with increase in rpm till 850 corresponding to velocity of 22 m/s. A quantitative description of this phenomenon is obtained in numerical analysis by plotting velocity profile near stagnation point as shown in Fig. 11.

Figure 7b shows line of separation (at 15 m/s) appears to be aligned at an angle to meridian of the sphere. Increase in velocity influences the separation line as seen in Fig. 7d. From the figure, one can see that the separation line is slightly pushed back

(a)   (b)

(c)   (d)
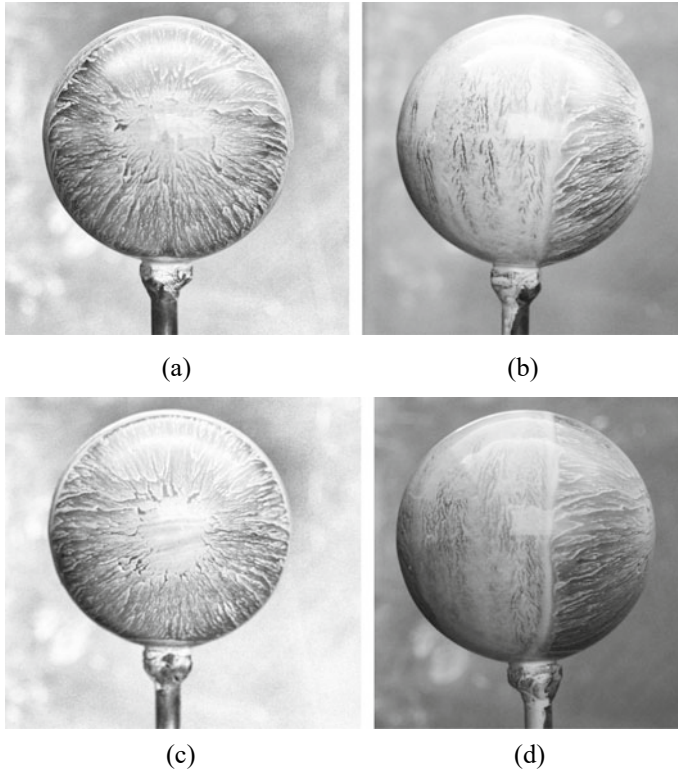
Fig. 7 **a**, **c** Skin-friction lines and **b**, **d** region of separation **a**, **b** $U_\infty = 15.3$ m/s **c**, **d** $U_\infty = 19.5$ m/s

compared to flow at 15 m/s. Figure 8 gives the point of separation near top, middle, and the bottom section of sphere at 19.5 m/s. As mentioned already, radius of sphere is 7.5 cm with origin fixed at center of the sphere—hence, separation near top occurs near 4.5 cm (or 0.75 cm from origin), slightly away from the center plane of sphere. As we come down to the middle section, separation line is slightly ahead compared to separation near top. Near the bottom point of sphere, separation moves toward the center plane. From these results, it is observed that the location of separation points over surface of sphere is varying with location. It remains to be seen if the separation line has a linear relationship with location on the sphere.

Figure 10 gives comparison of separation location at 550 rpm as well as 700 rpm. At 700 rpm, flow separates at 4.5 cm, whereas the separation point is slightly ahead in case of flow at 550 rpm. Slope of separation line is less in case of 700 rpm flow since the flow separation near bottom is very close to 4.5 cm line compared to flow at 550 rpm as seen in Fig. 10 (700 rpm bottom).

It is also observed that the rearward movement of separation line is pronounced during initial change in rpm from 450 till 600 and then the movement gradually

Fig. 8 Separation line for sphere at 700 rpm
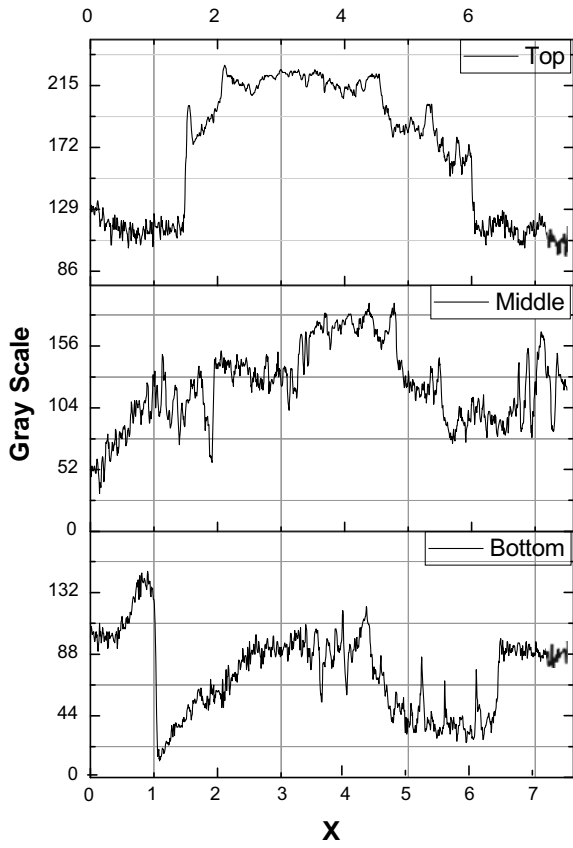
Fig. 9 Separation point location on sphere
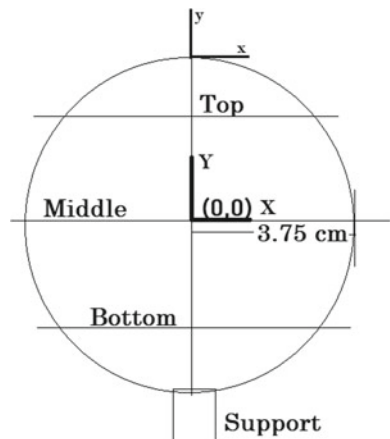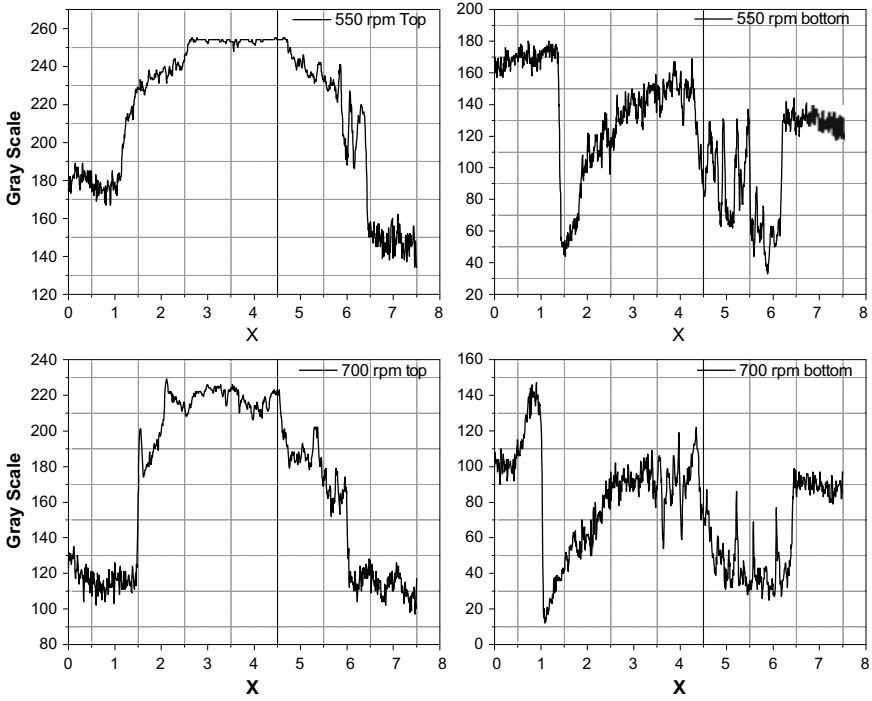
Fig. 10 Separation region—550 and 700 rpm
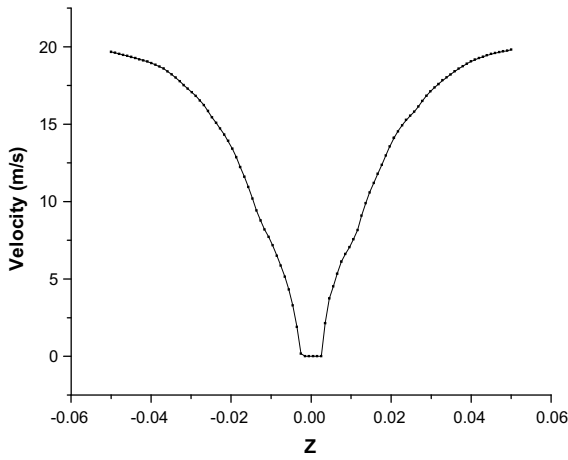
Fig. 11 Velocity profile near stagnation point
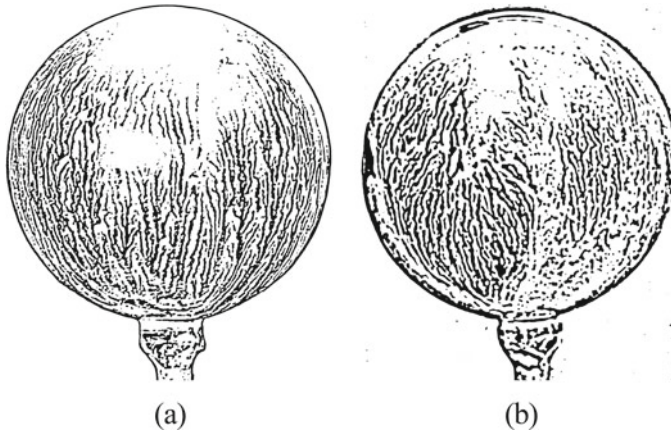
Fig. 12 Rear section of sphere at **a** 550 rpm and **b** 700 rpm

slows down as observed during experiments with different rpm. Another interesting observation from line of separation is the thickening of the separation line due to small region of re-circulation. During the experiment, oil gradually accumulated near separation region and began to move to and from the line from where onset of separation began (Fig. 11).

The second objective of the paper is to find flow patterns and relate the patterns to flow separation. Figure 12a, b was obtained from oil flow visualization results using *Mexican hat filter* in ImageJ software. One of the challenges faced during flow visualization was that the smooth sphere requires high viscous oil for the pattern to form but a high viscous oil doesn't mimic the flow to necessary level of accuracy. The accumulated oil near separation region starts to flow the moment tunnel is turned off. Oil also moves down due to gravity even when the tunnel is running. Attempts will be made in the future to better visualize flow patterns using oil flow with different mixtures used in proportion. To study the flow patterns, numerical analysis was carried out in Ansys and will be discussed in detail in next section.

3.2 Numerical Results

In this paper, numerical simulation for Re $\approx 0.075 \times 10^6$ and $\approx 0.1 \times 10^6$ is reported and compared with experimental results. To verify the validity of results, drag coefficient was calculated from numerical simulations for a few Re. The results are tabulated in Table 1, where we see that the drag coefficient reduces with increase in Re as reported in literature [10].

$$C_D = \frac{2F_D}{\rho v^2 S}$$

Table 1 Drag coefficient versus Re for sphere

Velocity (m/s)	Re	C_D
5	0.025E+06	0.42
15	0.075E+06	0.34
20	0.1E+06	0.31
30	1.55E+05	0.27

where 'S' is the frontal surface area given by $\pi d^2/4$.

Separation line for the sphere from numerical analysis is shown in Fig. 14a. The result matches with the experimental observation shown in Fig. 7b. Comparison of numerical results at different velocity (Figs. 13a and 14a) from numerical simulation also agrees with experimentally observed phenomenon of separation line moving backward with increase in velocity.

As comparison of numerical result with experiments has given a good match, we take up Figs. 13 and 14 for analysis. Rear section of sphere shown Fig. 13c shows the saddle point singularity. The orientation of saddle point singularity changes with increase in velocity as seen in Fig. 14c. Focus point is seen in both case of 15 m/s as well as 20 m/s seen in Figs. 13d and 14d—we have two foci for 20 m/s flow close to surface of sphere compared to single focus for 15 m/s case. Eventually, saddle point strength appears to reduce as we move away from the surface of sphere as expected. The focus points for 15 m/s flow start to drift apart in less space than 20 m/s case as seen in Figs. 13f and 14f.

To precisely find the location of the separation point over the surface of the sphere, velocity profile was plotted at different x-location on either side of pole of the sphere. From Fig. 15, there is a flow separation at $x' = 0.006$ m from the center as shown in Fig. 9 and progressively flow remains detached as we move along positive x-axis.

At $x' = -0.005$ m, we can see the flow is attached. This is agreeing with experimental result where we see that the flow is not separating at the meridian but at a distance slightly away as seen in Fig. 8. It is also interesting to note that the re-circulation zone near the separation line observed in experiment is seen in numerical results as the velocity sees an increase and a dip after flow crosses $x' = 0.006$ m.

4 Conclusions

The objective of present work was to study relation of separation line for spherical geometry and Re. Initially, oil flow visualization was carried out to identify location of separation along the vertical plane (meridian) and to study re-circulation region from the traces of oil patterns. Experiments were carried out for different Re and some of the results are presented in the paper. Numerical simulations were carried out to find the flow pattern at rear section of the sphere and obtain singularity points that are striking feature for a separated flow due to its nonlinear nature. Results obtained from numerical analysis were compared with experimental results. Finally,

(a) **Separation line along meridian of sphere**

(b) **Wall Shear stress at separation region**

(c) **Velocity contour at 0.001m offset from sphere**

(d) **Velocity contour at 0.005m offset from sphere**

(e) **Velocity contour at 0.007m offset from sphere**

(f) **Velocity contour at 0.01m offset from sphere**
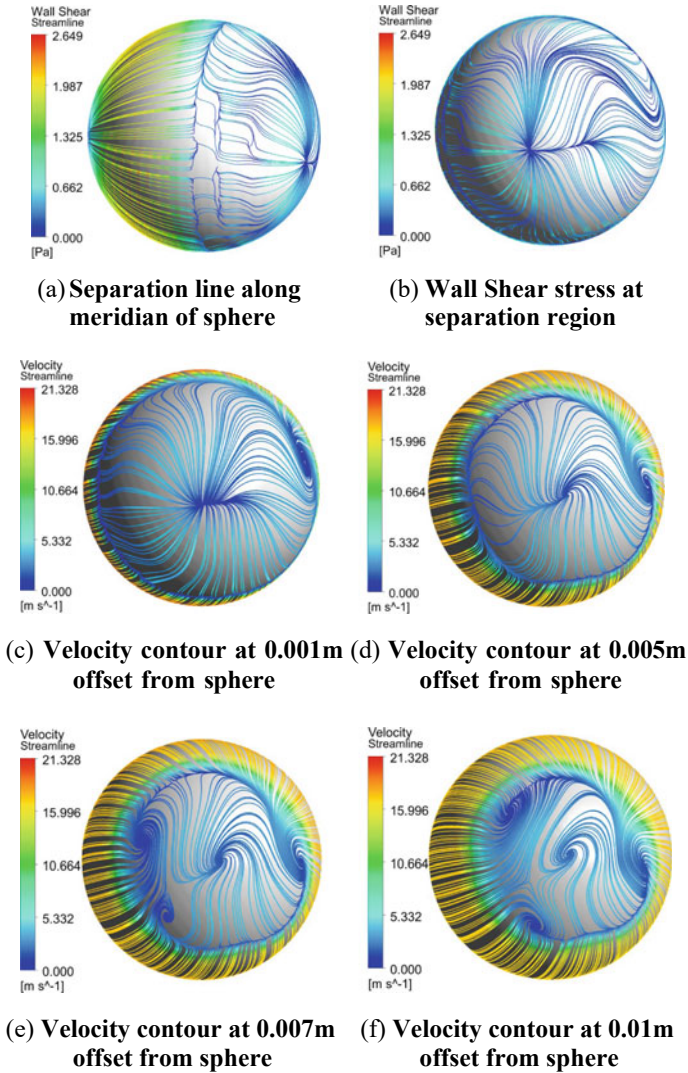
Fig. 13 Results from numerical simulation-$U_\infty = 15$ m/s

some of the critical points for flow past sphere with free-stream velocity of $U_\infty = 15$ m/s and 20 m/s were briefly discussed. The critical points of separated region doesn't vary with change in velocity. It remains to be seen if the results hold good for very low Reynolds number flows and also study the patterns near drag-crisis Re to get additional insights in nature of flow separation in three-dimensional flows.

(a) **Separation line along meridian of sphere**

(b) **Wall Shear stress at separation region**

(c) **Velocity contour at 0.001m offset from sphere**

(d) **Velocity contour at 0.005m offset from sphere**

(e) **Velocity contour at 0.007m offset from sphere**

(f) **Velocity contour at 0.01m offset from sphere**
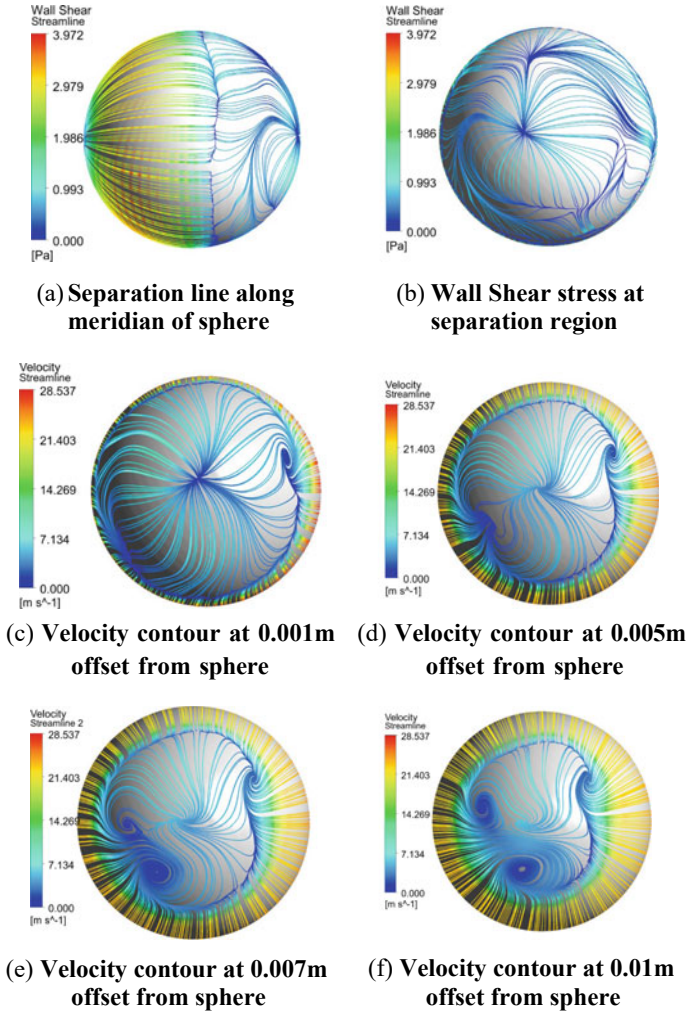
Fig. 14 Results from numerical simulation-$U_\infty = 20$ m/s

Fig. 15 Velocity profile over top surface of sphere
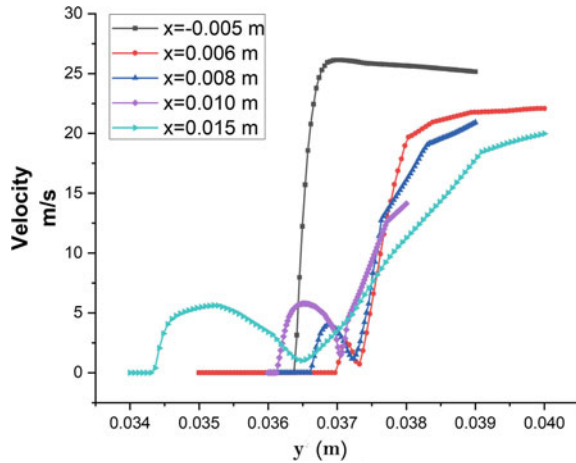
Nomenclature

ϕ	Diameter of model (m)
rpm	Revolution per minute (–)
AR	Dissipation (–)
k	Turbulent kinetic energy (m^2 s^{-2})
ω	Turbulence dissipation rate (m^2 s^3)
SST	Shear stress transport (–)
Re	Reynolds number (–)
C_D	Drag coefficient (–)

References

1. Kim S, Karrila SJ (1991) Microhydrodynamics principles and selected applications, chap 3, 1 edn., Dover Publications, New York, p 50
2. Fornberg B (1988) Steady viscous flow past a sphere at high Reynolds numbers. J Fluid Mech 190:471–489
3. Jones DB, Clarke DA (2008) Simulation of flow past a sphere using the fluent code. Tech. report, Defense Technical Information Center
4. Délery J (2013) Three-dimensional separated flow topology: critical points, separation lines and vortical structures, chap 6, 6 edn. Wiley-ISTE, London, UK, p 389
5. Surana A, Grunberg O, Haller G (2006) Exact theory of three-dimensional flow separation. Part 1. Steady separation. J Fluid Mech 564:57–103
6. Dallmann U (1988) Three-dimensional vortex structures and vorticity topology. Fluid Dyn Res 3(1–4):183–189
7. Tobak M, Peake DJ (1982) Topology of three-dimensional separated flows. Annu Rev Fluid Mech 14(1):61–85

8. Chapman GT, Yates LA (1991) Topology of flow separation on three-dimensional bodies. Appl Mech Rev 44(7):329–345
9. Patel VC (1993) Three-dimensional flow separation. Sadhana 18(3):553–574
10. Anderson JD (2017) Fundamentals of aerodynamics, chap 6, 6 edn. McGraw Hill, New York, p 389

Thermal Hydraulic Analysis of Vitrified Waste Product Storage Vault

H. Sreeju, Amit K. Chauhan, M. Thamaraiselvan, M. Rajendrakumar, G. Suneel, M. P. Pradeep, and J. K. Gayen

1 Introduction

The strategy adopted for managing high level waste (HLW) is immobilization followed by interim storage and disposal. Immobilization is carried out by vitrification of HLW into glass matrix using a joule heated ceramic melter (JHCM). Vitrified waste product (VWP) is interimly stored under surveillance for 30 years so that the decay heat produced by the radioisotopes would reduce and integrity of VWP is ensured.

The radioactive waste produced in fuel cycle generates heat. The highly radioactive liquid waste constitutes approximately 97% of all fission products and isotopes. Storage of highly radioactive liquid waste is requiring continuous service. Due to the difficulties in storing radioactive liquid waste, vitrification of radioactive liquid waste is adopted. Vitrification is the process of converting radioactive liquid waste into an inert solidified borosilicate glass matrix. VWP is contained in stainless steel canisters and is kept under surveillance to reduce decay heat and ensure the integrity of the VWP. The decay of radioisotopes vitrified in the glass will result in a considerable amount of heat generation within the glass matrix. The maximum expected heat load is 1.8 kW per VWP. So, the VWP needs to be cooled for a considerable amount of time. To avoid recrystallization of the glass matrix, the maximum glass temperature should be maintained below 500 °C [1].

The storage units are resting vertically between upper plenum and lower plenum. The air inlet temperature is 35°C. Maximum allowable surface bulk temperature of concrete for a nuclear waste storage facility is 65 °C [1]. The decay heat from canisters is removed by air induced by natural convection due to a 100 m stack.

H. Sreeju (✉) · M. Thamaraiselvan · G. Suneel · M. P. Pradeep · J. K. Gayen
Bhabha Atomic Research Centre, Kalpakkam 603102, India
e-mail: sreejuh@igcar.gov.in

A. K. Chauhan · M. Rajendrakumar
Indira Gandhi Centre for Atomic Research, Kalpakkam 603102, India
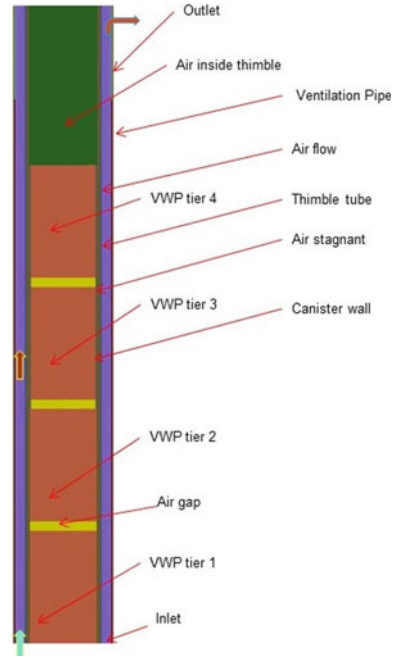
The supply air corridor and exhaust plenum are provided for guiding air into the vault and from the vault to the stack. Air is guided through ventilation pipe around thimble tubes to ensure cooling of canisters. The storage of VWP is described by Fig. 1. Ventilation pipes are connected to the air inlet plenum. The thimble tubes are arranged to have uniform rectangular pitch between subsequent tubes.

2 Literature Review and Objective

The literature pertaining to cooling of VWP in a storage facility is limited. A detailed review of such facilities was not available in reported literature. Verma et al. [2] conducted experimental and numerical analysis for a VWP storage module. The set-up consists of 20 number of storage units stored in an array of 5 × 4. The stack is of 20 m height. Electrical heaters were provided for generating heat. Experimental and theoretical results were found to be in good agreement. For the above setup and uniform heating condition, it was found out that 1D analysis is adequate. Verma et al. [3] performed a numerical analysis of the VWP storage vault. For the pertinent parameters, including stack and duct dimensions, plenum height, etc., parametric studies have been done. CFD code was used to obtain a detailed canister temperature profile. Also investigated are the effects of natural convection within the canister and between the thimble and canister. It was discovered that the temperature at

the canister centreline drops by 20.5 °C due to the natural convection. Maximum centreline temperature is found to be 476 °C for an annulus flow velocity of 1.9 m/s.

A numerical analysis of the nuclear fuel storage vault was performed by Vivek et al. [1] to improve ventilation performance by optimizing the location of interconnecting ducts. The air flow through the vault was examined to determine the various connecting duct configurations. With a rise in the aspect ratio of interconnected ducts, the air exchange rate and heat removal efficiency through the vault dropped. Although square ducts were superior at removing heat, circular vents offer a better air exchange rate. The smoothing of duct edges increased air velocity by reducing flow losses (such as frictional losses and losses due to duct bends). Attaching nozzles to the supply end of the ducts improves the air jet's ability to penetrate the fuel enclosure.

Chen et al. [4] conducted experimental studies investigating the performance of eight turbulence models in an enclosed environment. According to the survey, the inflow jet caused a lot of turbulence in the space. The wall reduced the air turbulence in the room. The heated box's buoyancy increased air recirculation, increasing velocity and turbulence levels. The study discovered that while specific Reynolds Averaged Navier Stokes (RANS) models performed well for straight forward flows. This study demonstrates the sophisticated capabilities of the large eddy simulation (LES) and detached eddy simulation (DES) models for addressing airflow in enclosed spaces.

The extensive literature survey carried out shows that CFD analysis of VWP storage vaults with heat generating medium is not conducted yet. The heat generation rate and annulus velocity are varied to obtain maximum centreline temperature and temperature distribution at various operating conditions. Moreover, the outlet blockage situation is also simulated. The study will be helpful in management of nuclear waste storage facility in an optimized way.

3   Methodology

The 3D model consists of vitrified waste product, canister walls, thimble tubes and ventilation pipes. The VWP is stored in a canister of height 1950 mm and diameter 355 mm. Canister is stacked in 4 tiers. Heat removal from canister is predominantly due to air flowing between thimble and ventilation pipe. However, natural convection flow would exist due to the temperature gradient in the thimble.

It is essential to validate the methodology adopted using a generic CFD code for aforementioned thermal hydraulics problem. The validation was carried out against the available experimental data by Chen et al. [4].

A room of size 2.44 m × 2.44 m × 2.44 m was chosen as the computational domain. A cubical heat generating body of size 1.22 m × 1.22 m × 1.22 m was placed at the centre of the room. A total of 700 W heat is generated. Inlet air supply is 0.01m^3/s through a plenum of opening height of 0.03 m. The outlet is an opening of height 0.08 m.

The analysis results were compared with the data obtained from experimental measurement and CFD study. The location (Point A) used for comparison is 1.2192 m from the inlet and 0.2286 m from the side wall. Graphs were plotted for ($T - T_{min}/T_{max} - T_{min}$) as shown in Fig. 2 and U/U_{max} as shown in Fig. 3 along a vertical line on the point *A*.

The CFD result obtained from thermal hydraulics simulation agrees well with the experimental data and also compares closely against CFD results of Wang and Chen [4].

The 3D model of VWSF vault consists of vitrified waste product, canister walls, thimble tubes, ventilation pipes and concrete walls of the vault as shown in Fig. 4. Inlet plenum is also modelled for studying the air flow distribution at different locations of the storage vault.

Fig. 2 Temperature profile
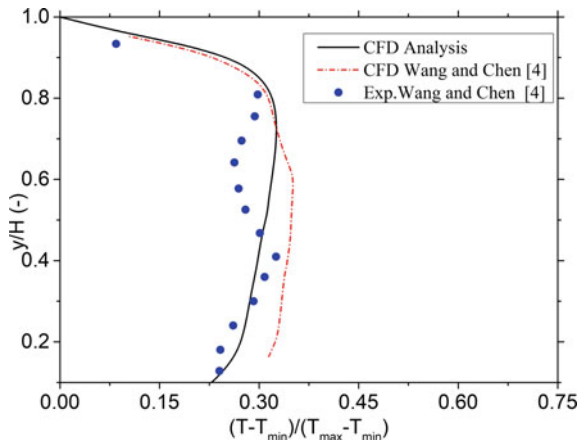
Fig. 3 Velocity profile
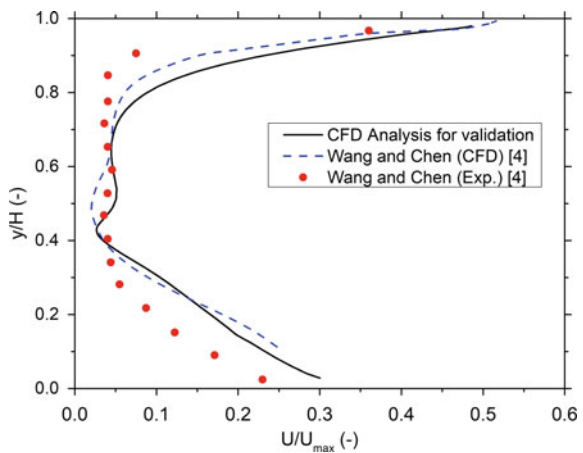
Fig. 4 Model of vault
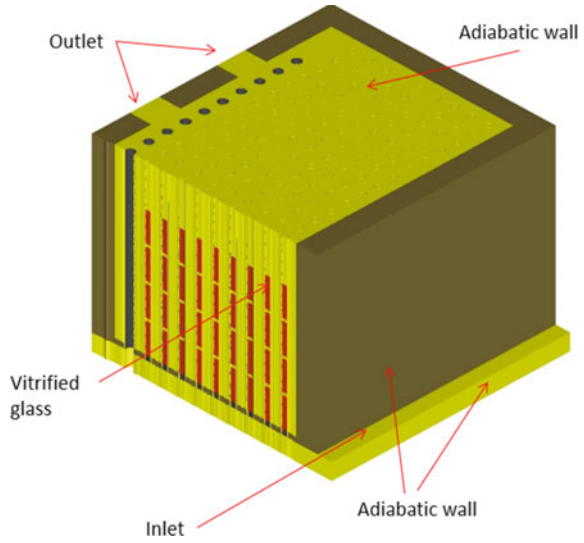
Full scale three-dimensional models were used for obtaining the temperature and velocity profiles. Analysis was carried out by solving the continuity, momentum and energy equation. Buoyancy is modelled using Boussinesq equation.

$$\text{Continuity equation: } \nabla.(\rho \overline{u}) = 0, \tag{1}$$

$$\text{Momentum equation: } \nabla.(\rho \overline{uu}) = -\nabla P + \nabla.(\mu \nabla \overline{u}) + \overline{F}, \tag{2}$$

$$\text{Energy Equation: } \rho C_p [\overline{u}.\nabla T] = \nabla.(K \nabla T) + \dddot{q}, \tag{3}$$

$$\text{Boussinesq Equation: } \rho = \rho_0 [1 - \beta(T - T_0)]. \tag{4}$$

Grid sensitivity test is carried out to optimize the size of 3D mesh in the computational domain. Mesh with 21.5×10^6 elements is selected based on the comparison of temperature along VWP centreline as shown in Fig. 5.

A generalized commercial CFD code Fluent 19.2 is used for modelling fluid flow and heat transfer. Turbulence model sensitivity test is also carried out to select the best model to predict the turbulence behaviour in the computational domain. Standard k–ϵ model is selected for the current problem based on the comparison of other turbulence model carried out as shown in Figs. 6 and 7.

The outer walls of the model were assumed to be adiabatic. No-slip boundary condition is imposed on all walls of the domain. The inlets and outlets of the model were specified as velocity inlet and pressure outlet for single thimble case, while the inlet was specified as mass flow inlet for the case of full vault. As the steel canister is

Fig. 5 Turbulence sensitivity test
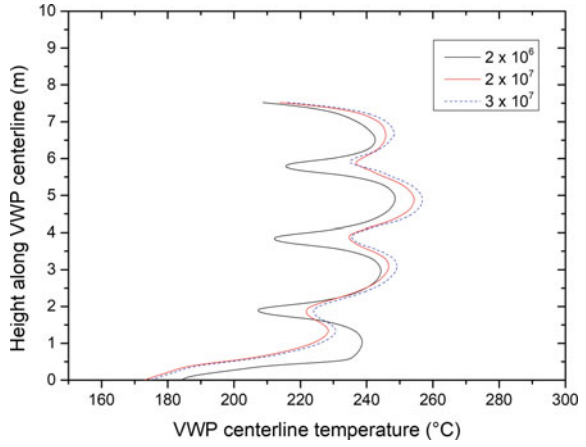
Fig. 6 Variation of temperature along centreline
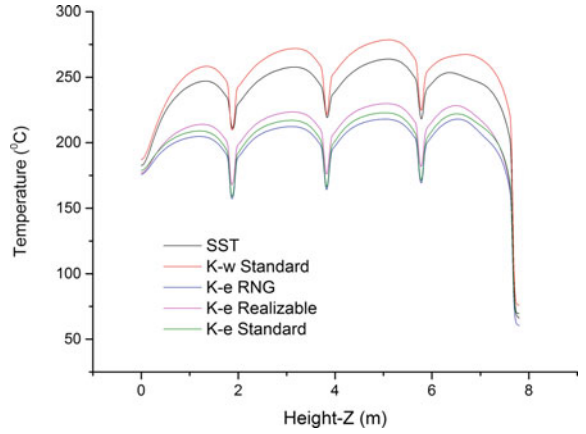
Fig. 7 Radial temperature profile from centreline
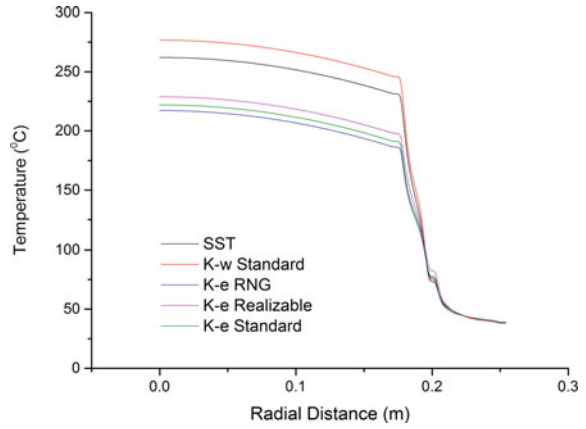
not fully filled before sealing the top using a steel lid, air pockets are present between glass and canister lid. This space is considered while modelling the domain.

4 Results and Discussion

Calorimetric experiments were carried out at VWSF hot cell for determining the heat generation rate of VWP. This can be used for estimating the heat load of vault. The VWP is found to be generating a heat load of 0.6–1 kW. A detailed analysis of the thimble tube under different operating parameters was carried out based on air velocity of the stack at different power levels. The model provides an in depth understanding of temperature profile of glass, canister, thimble tubes, ventilation pipe and vault wall. The effect of air above topmost canister is analysed. The maximum centreline temperature is found to be lowered by 14 °C due to the natural convection cooling provided by the air above the fourth canister. The velocity vector is shown in Fig. 8.

The different single thimble cases analysed are case A1: heat generation rate per VWP 0.8 kW, case A2: heat generation rate per VWP 1 kW and case A3: heat generation rate per VWP 1.8 kW. The effect of radiative heat transfer is considered in all the three cases. Cases without considering radiative heat transfer are B1: heat

Fig. 8 Velocity vector and temperature profile
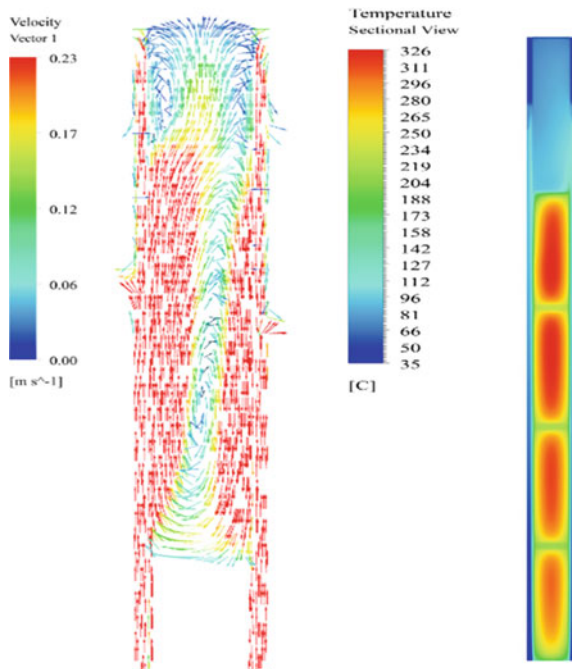
Fig. 9 Centreline
temperature at various
conditions
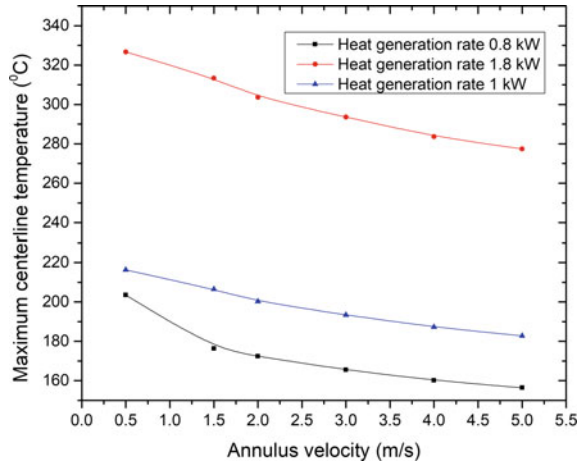
generation rate per VWP 0.8 kW, case B2: heat generation rate per VWP 1 kW, case
B3: heat generation rate per VWP 1.8 kW. The analysis carried out on the full vault
model consists of case F1: flow analysis at full vault at various outlet pressures and
case F2: full vault with heat generation rate per VWP 0.8 kW. The annulus air velocity
is varied from 0.5 to 5 m/s for Cases A and B so as to obtain temperature profile of
VWP, canister, thimble tube and ventilation pipe. Maximum centreline temperature
of VWP for Cases A1, A2 and A3 at various annulus velocity is shown in Fig. 9.

For a canister with heat output of 0.8 kW (Case A1) maximum centreline temper-
ature is found to be 203.46 °C at an annulus velocity of 0.5 m/s as depicted in Fig. 10.
For a canister with heat output of 1 kW (Case A2), maximum centreline temperature
is found to be 216.28 °C at an annulus velocity of 0.5 m/s as depicted in Fig. 11. For
a canister with heat output of 1.8 kW (Case A3), maximum centreline temperature is
found to be 326 °C at an annulus velocity of 0.5 m/s as depicted in Fig. 12. The Cases
A1, A2 and A3 show that the VWP, canister, thimble tube and ventilation pipe are
observed to be sufficiently cooled even at low mass flowrates. The graphs shown in
Figs. 10, 11 and 12 can be used to find out the temperature of VWP, canister, thimble
tube and ventilation pipe at different operating conditions.

Effect of heat transfer due to radiation was studied. Effects of radiative heat transfer
are neglected in the case (Case B1) to study the effect of convection and conduction
in cooling the VWP. Similarly, analysis was conducted for same power level with
radiative heat transfer (Case A1). The maximum centreline temperature occurs in
the VWP located in topmost (fourth) tier when effects of radiative heat transfer is
considered, shown in Fig. 14. The maximum centreline temperature obtained for all
the four tier VWP as shown in Figs. 13 and 14. The third canister depicts maximum
centreline temperature when the effects of radiative heat transfer is negligible as
shown in Fig. 13. It is attributed to the cooling obtained due to circulation of air
at the top canister. At high annulus velocity, forced convection is predominant and

Fig. 10 Temperature of components at $Q = 0.8$ kW
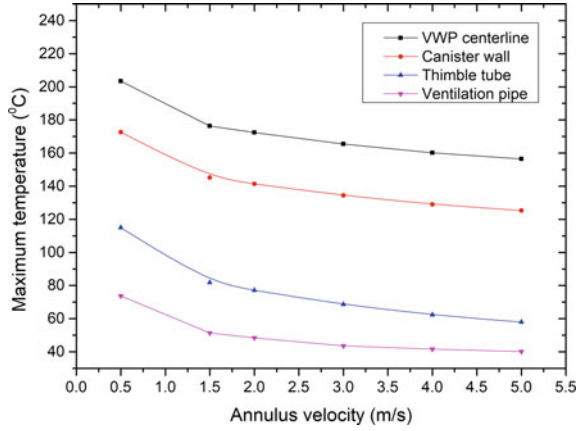
Fig. 11 Temperature of components at $Q = 1$ kW
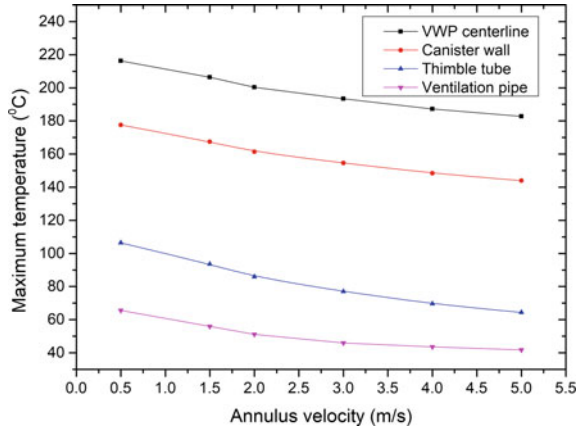
Fig. 12 Temperature of components at $Q = 1.8$ kW
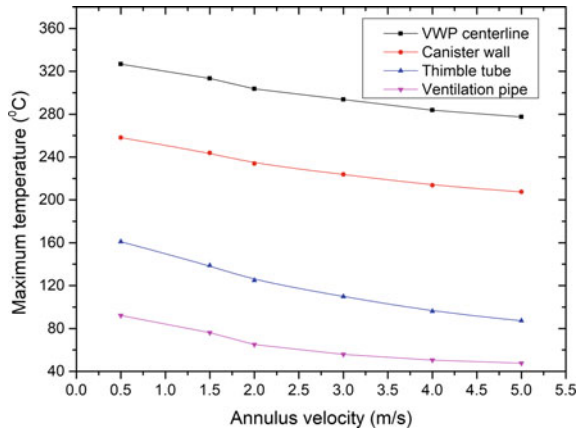
topmost canister depicts maximum centre line temperature. This effect is shown in Figs. 13 and 14.

Numerical analysis was carried out for the full vault model. The storage vault is provided with two outlets. Flow through vault was simulated at different outlet pressures for normal and flow blockage condition (Case F1). The blockage of one of the two vault outlet can cause a drop-in flow rate by 20–22% depending on outlet pressure. This is shown in Fig. 15. The outlets are having same area. One of the outlets is located near to the concrete hatch block due to which some space is free of thimble tubes near to that outlet. Blockage in the outlet located near the hatch block is more concerning than the other outlet as this region has fewer thimbles which create resistance to flow (Fig. 16).

The capacity of vault is 544 canisters. The loading pattern of interest is the case where the vault is loaded with 504 canisters. Rest of the 40 location is not filled. VWP is assumed to be generating a power output of 0.8 kW (Case F2). The temperature of

Fig. 13 Centreline temperature Case B1
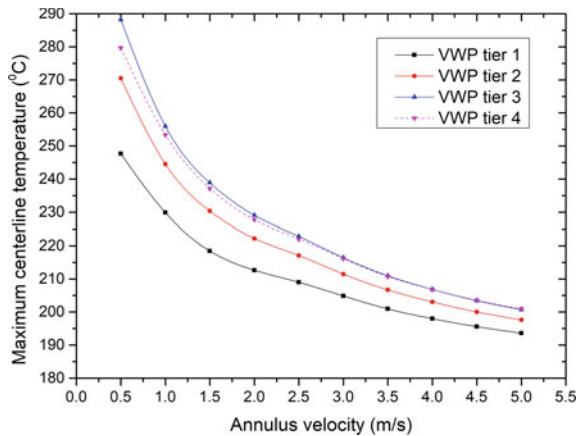
Fig. 14 Centreline temperature Case A1
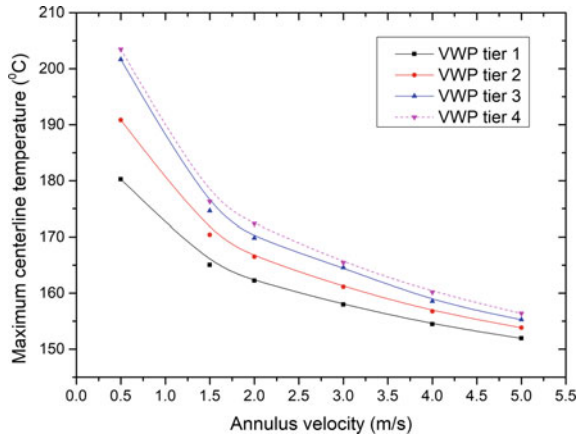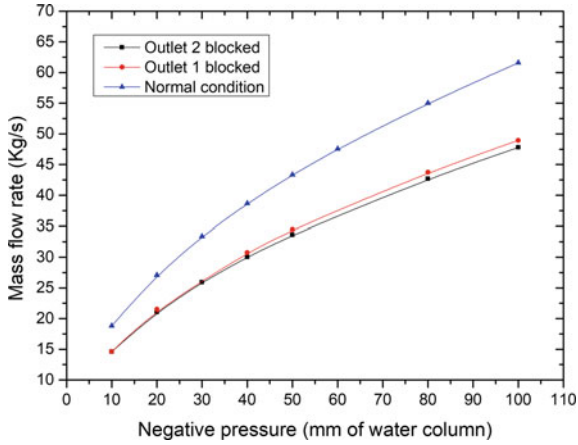
Fig. 15 Mass flow during outlet blockage
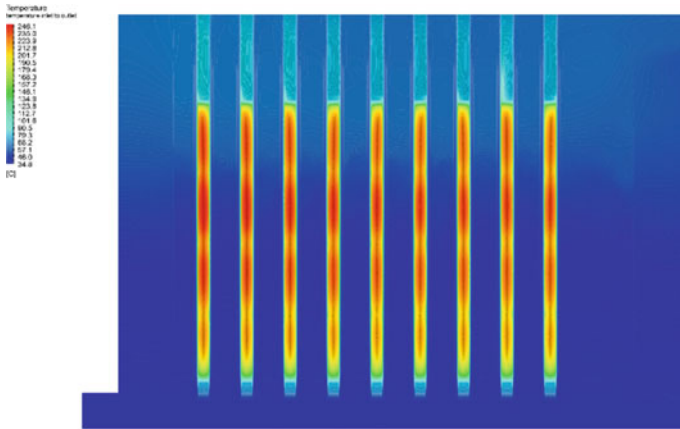
Fig. 16 Temperature profile of vault

vault walls is found to be within acceptable limit of 65 °C. VWP stored in locations away from outlet is expected to have maximum temperature when the vault is filled with 504 canisters. Maximum centreline temperature is 252.5 °C.

The ventilation parameters like air inlet temperature, humidity and wind speed are recorded regularly. The wind speed at ground level is measured and wind speed at stack top is calculated using Hellman method. The model is in agreement with experimental data obtained during partial filling of vault with canisters.

5   Conclusions

In this work, numerical study was carried out on (1) a single thimble model at various operating conditions and (2) full vault model, at expected loading condition. Based on the simulations carried out, the salient conclusions drawn are

- When the annular velocity of cooling air is 0.5 m/s, the maximum centreline temperature for Case A1 is 203.46 °C, for Case A2 is 216.28 °C and for Case A3 is 326 °C. The canister wall, thimble tube and ventilation pipes are cooled sufficiently ensuring safe operating condition.
- The maximum centreline temperature occurs in VWP on tier 3 or tier 4 depending on annulus flow velocity, heat generation rate and extend of radiative heat transfer.
- The maximum centreline temperature is observed at the topmost location of VWP (fourth) tier, when effects of radiative heat transfer are considered.
- With increase in annular velocity, forced convection effect is predominant, and hence, maximum centre line temperature is observed in the topmost canister.
- The blockage in one of the two vault's outlets can cause a drop-in flow rate by 20–22% depending on outlet pressure.
- In case of fully loaded vault, maximum centreline temperature is 252.5 °C, when it operates under normal condition of 0.8 kW heat load per VWP. Canisters located near the outlet witnesses lower temperature compared to those located near the inlet. Thus, the recommended VWP loading pattern is from inlet plenum to outlet plenum.

The numerical model gives sufficient insights for optimizing different operating variables for safe storage of the conditioned waste product. The model will be useful in optimizing the designs of the future facilities.

Nomenclature

HLW	High level waste (–)
VWP	Vitrified waste product (–)
JHCM	Joule heated ceramic melter (–)
RANS	Reynolds averaged Navier Stokes (–)
LES	Large eddy simulation (–)
DES	Detached eddy simulation (–)
VWSF	Vitrified waste storage facility (–)
SST	Shear stress transport model (–)
RNG	Re-normalization group (–)
C_p	Specific heat (J/Kg K)

T	Temperature (k)
ρ	Density (kg/m^3)
ρ_0	Density at reference temperature (kg/m^3)
β	Thermal expansion coefficient (1/K)
ϵ	Turbulence dissipation rate (m^2/s^3)
ω	Specific dissipation rate (1/s)
μ	Dynamic viscosity (kg/m s)
k	Turbulent kinetic energy (m^2/s^2)
K	Thermal conductivity (W/m K)
F	Body force (kg m s^2)
u	Velocity (m/s)
q	Heat generation rate (W/m^3)

References

1. Mishra VK, Panda SK, Sen B, Maiya M, Rao B (2022) Numerical analysis of forced convection heat transfer in a nuclear fuel storage vault. Int J Therm Sci 173:107429
2. Verma V, Ghosh A, Kushwaha H (2002) Simulated model studies for solid waste storage surveillance facility. Nucl Eng Des 211(2):121–138
3. Verma V, Singh RK, Vaze KK (2013) Thermal analysis of VWSB-IP1 at Tarapur. Kerntechnik 78(5):411–421
4. Wang M, Chen Q (2009) Assessment of various turbulence models for transitional flows in an enclosed environment (RP-1271). HVAC&R Res 15(6):1099–1119

Numerical Investigation of Pressure Drops and MHD Flow Through Sudden Expansion in the Presence of an Inclined Magnetic Field

Sunil Dodkey and Narendra Gajbhiye

1 Introduction

In a thermonuclear reactor, the fusion of two isotopes of hydrogen atoms (deuterium and tritium) is achieved in a device called a tokomak. The fusion produces a helium atom along with high-energy neutrons. Strong magnetic fields are required to control and maintain the plasma of the fusion reaction, which is at a high temperature (10^8 K). To prevent damage to the reactor, a fusion blanket is introduced between the plasma and the magnetic coil to absorb the neutrons and cool the device. A liquid metal like lead–lithium eutectic is used as the coolant which circulates through the blanket. For cooling of the blanket, a powerful magnetic field must be passed through by the liquid metal, which is used to magnetically limit the reaction of plasma at elevated temperatures in a fusion reactor core. In the blanket, channels are key elements for distributing the flow of liquid metal from the inlet of the blanket to several channels with abrupt expansion and contraction. Therefore, the liquid metal flows give rise to the 3D MHD effect, and hence, the additional pressure drops. The electrical conductivity of the channel causes the electrical coupling to the adjacent fluid motion; therefore, liquid metal flow suffers a large pressure drop caused by the 3D MHD effect in sudden expansion and contraction, electrical coupling, and movement in the existence of a high magnetic field, etc.

S. Dodkey (✉) · N. Gajbhiye
Department of Mechanical Engineering, Maulana Azad National Institute of Technology Bhopal, Bhopal, Madhya Pradesh 462021, India
e-mail: sdodkey.nitb@gmail.com

2   Literature Review and Objective

The liquid metal fed to the blanket undergoes sudden expansion and, therefore, the rise of the 3D MHD effect. In recent years, researchers' focus has been on minimizing the pressure drop due to the MHD effect. Some of the studies include

An experimental investigation in sudden expansion with an electrically conducting duct wall at a high Hartmann number was done by Buhler et al. [1]. They reported an additional pressure drop at the expansion due to the 3D effect of flow distribution. Mistrangelo and Buhler [2] numerically simulated the flow of liquid metal in a sudden rectangular expansion at a moderate magnetic field (up to Ha = 1000) using a commercial CFX code. They reported similar effects and the formation of vortices behind the expansion.

The effect of the different orientations of the magnetic field on the sudden expansion for the lower Hartmann number (0–100) in sudden expansion was studied by Praveen and Eswaran [3]. The authors reported the effect of magnetic strength on the circulation length in terms of asymmetry growth. Feng et al. [4] numerically simulated the effects of different expansion lengths and expansion ratios in sudden expansion using the OpenFOAM platform. First, the code was validated with ALEX and KIT experiments. The authors reported that an increase in the expansion length increased the total pressure drop.

Morley et al. [5] numerically simulated the liquid metal flow in a sudden expansion with multiple manifolds. They found that a magnetic field makes the liquid metal distribution more uniformly distributed than without a magnetic field. Rhode et al. [6] numerically determined the 3D MHD pressure drop correlation for the 3D sudden expansion and validated it with their previous study.

Kumamaru et al. [7] conducted a numerical simulation to study the magneto-hydrodynamic (MHD) flows through a rectangular channel with abrupt expansion to evaluate the pressure drop caused by the sudden expansion. A set of Hartman numbers, the Reynolds number, and the magnetic Reynolds number were used to determine the 3D MHD effect and pressure drop for expansion in both the parallel and perpendicular directions to the employed magnetic field. A numerical analysis of the 3D MHD effect was also carried out by Kumamaru et al. [8] to determine the pressure drop caused by the sudden shrinkage.

The natural convection flow and heat transfer in a suddenly expanding cavity with a strong magnetic field have been numerically studied by Singh and Gohil [9] using an OpenFOAM solver.

The aim of the present study is to numerically investigate the effect of an inclined magnetic field on the pressure drop and behavior of the magnetohydrodynamic flow of liquid metal through a sudden expansion channel. The inclination of the magnetic field reported in present study ranges from $\theta = 0°$ to $90°$. The Hartman number ranges from 5 to 20 and Reynolds number up to 200.

3 Methodology

3.1 Geometry

The numerical domain considered in the present study is shown in Fig. 1. Numerical investigations are carried for the fixed expansion ratio of ER $= 3$ and length ratio of 2. The mesh is generated using the Ansys ICEM CFD tool. A multi-block meshing is used which is shown in Fig. 2.
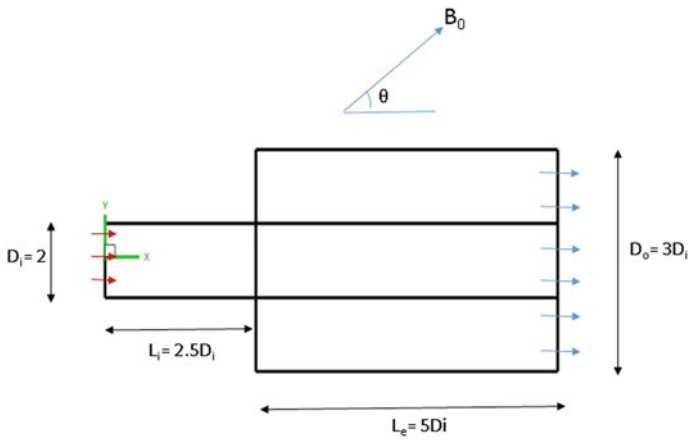
Fig. 1 Schematic of the numerical domain

Fig. 2 Multiblock grid pattern
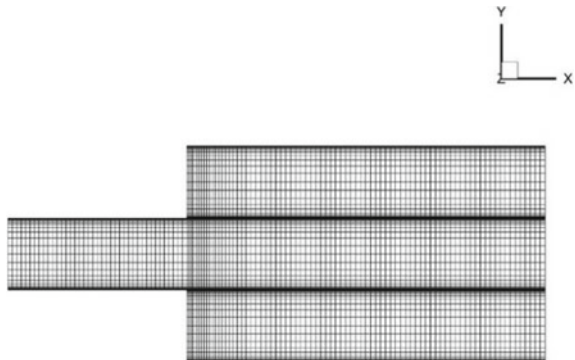
3.2 Grid Independence Test

The grid-independent study is carried out at different grid sizes, as shown in Table 1, for a fixed inclination angle of $\theta = 45°$, Re $= 100$, Ha $= 20$. The grid independence results are shown in Fig. 3. It is seen from the figure that grid sizes G_5 and G_6 show negligible variation in the velocity profile. Therefore, grid G_5 is considered for further simulation.

The present study has been carried out using a 3-D robust code Anupravaha CFD solver. The numerical code is created using the finite volume method. The code reads input in cgns format and produces an output in cgns file. This code has been benchmarked and validated with various published results [10].

Table 1 Grid patterns

Grids	Number of grid points		
	X-direction		Y-direction
	Upstream section	Expanded section	
G_1	71	141	71
G_2	61	121	71
G_3	51	101	71
G_4	41	81	41
G_5	31	81	41
G_6	21	81	41

Fig. 3 Grid independent test at Re $= 100$, Ha $= 20$, $\theta = 45°$
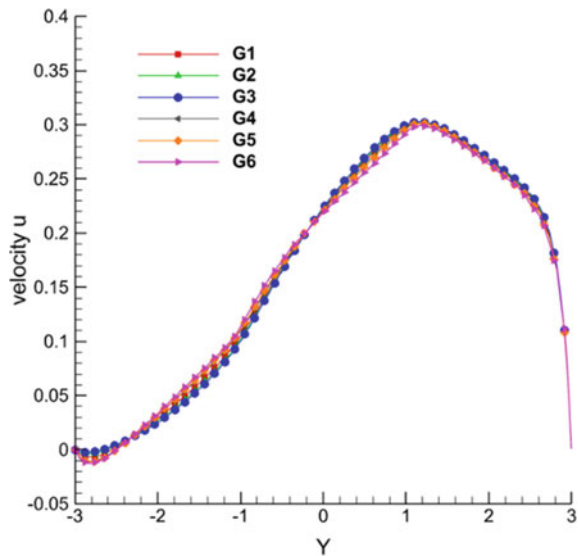
3.3 Governing Equations

The non-dimensional governing equations for magnetohydrodynamic flow are as follows:

Continuity equation:

$$\nabla.\vec{u} = 0. \tag{1}$$

Navier-Stokes equation:

$$\frac{\partial \vec{u}}{\partial t} + (\vec{u}.\nabla)\vec{u} = \nabla P + \frac{1}{\text{Re}}\nabla.\vec{u} + N(J \times B). \tag{2}$$

Ohm's Law:

$$J = \sigma(-\nabla\varnothing) + \vec{u} \times B. \tag{3}$$

Poisson equation:

$$\nabla^2\varnothing = \nabla(\vec{u} \times B). \tag{4}$$

In the above equations, symbols $\vec{u}$, B, $\varnothing$, and P represent the velocity field, magnetic field, electrical potential, and pressure field, respectively.

In the present study, three non-dimensional number appears Hartmann number (Ha), which is the ratio of Lorentz force to viscous force, Reynolds number (Re) which is the ratio of inertia force to viscous force and interaction parameter(N), which is the ratio of Lorentz force to inertia force.

3.4 Boundary Conditions

The following boundary conditions are specified at various sections of the computational domain:

Inlet

$$U = 2 \text{ m/s} \quad v = 0; \quad \partial p/\partial n = 0; \quad \partial\varnothing/\partial n = 0.$$

Outlet

$$\partial\vec{u}/\partial n = 0; \quad P = 0; \quad \partial\varnothing/\partial n = 0.$$

Walls

$$u = 0, v = 0; \quad \partial p / \partial n = 0; \quad \partial \varnothing / \partial n = 0.$$

4 Results and Discussion

The numerical simulations were performed at various Reynold numbers (Re = 50–200) and Hartmann numbers (Ha = 0–20) for different inclination angles ranging from 0° to 90° to study the effect of orientations of inclined magnetic field on the pressure drop and flow behavior of liquid metal.

4.1 Effect of Inclined Magnetic Field on MHD Flow

The variation in the u component of velocity in the transverse direction at $x = 14.25$ is shown in Fig. 4 for Ha = 20 Re = 100. A flattened velocity profile is seen at $\theta = 90°$ because of the high Lorentz force, which suppresses the core velocity. On decreasing the angle of inclination, the value of Lorentz force decreases as the current density starts to align in the magnetic direction. At an inclination of $\theta = 0°$, the magnetic field is in direction of current density; hence, the parabolic velocity is observed. The velocity contour realizing flow behavior at various angles $\theta = 0°–90°$ is shown in Fig. 5.

Fig. 4 Variation of u velocity along Y direction at Re = 100, Ha = 20
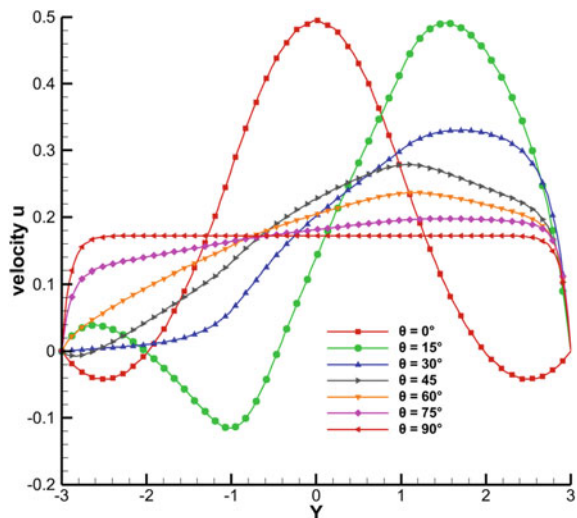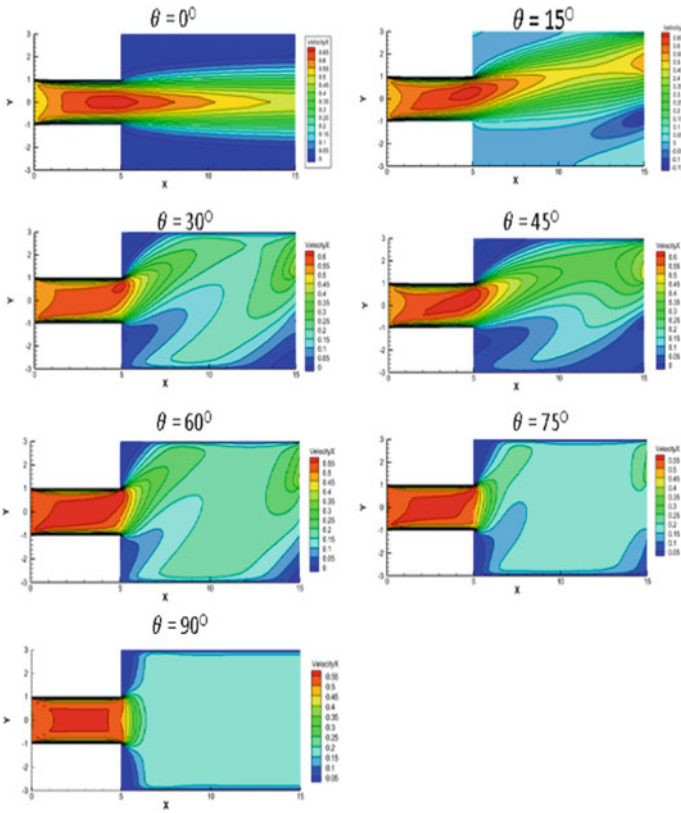
Fig. 5 Velocity contours for different inclinations

In Fig. 6, the pressure variation in x-direction for inclined magnetic field at different angles from $\theta = 0°$–$90°$ is plotted. It is seen that with the increase incli-nation angle, pressure drop increases. The pressure contour at different inclination angles is shown in Fig. 7; it shows a similar behavior as seen in Fig. 6.

4.2 Effects of Hartmann Number

The velocity profile at different Hartmann numbers is plotted in Fig. 8. At Ha = 0, velocity is parabolic in nature with highest and lowest peak values. On increasing the Hartmann number, the flow gets suppressed because of an increase in the magnitude Lorentz force ($F_L = \sigma B^2 u$). The velocity and pressure contour at different Hartmann numbers are shown in Figs. 9 and 11, respectively. Pressure distribution at different Ha is plotted in Fig.10.

Fig. 6 Pressure variation at different angles
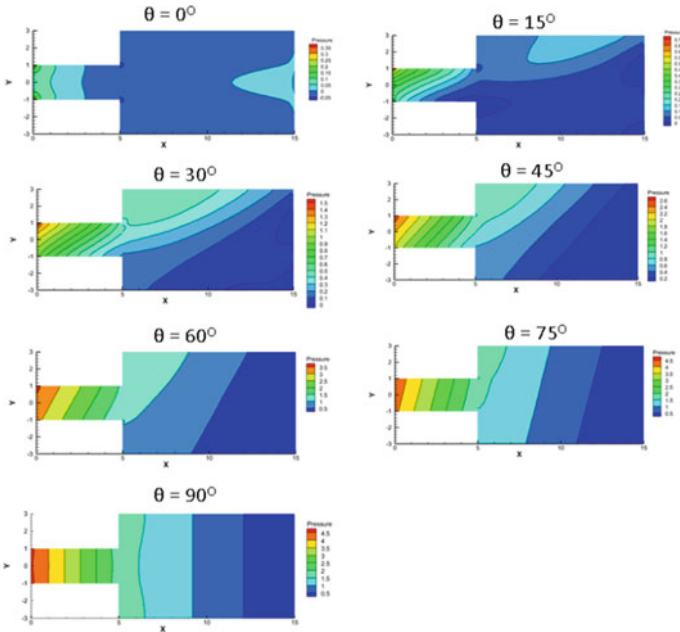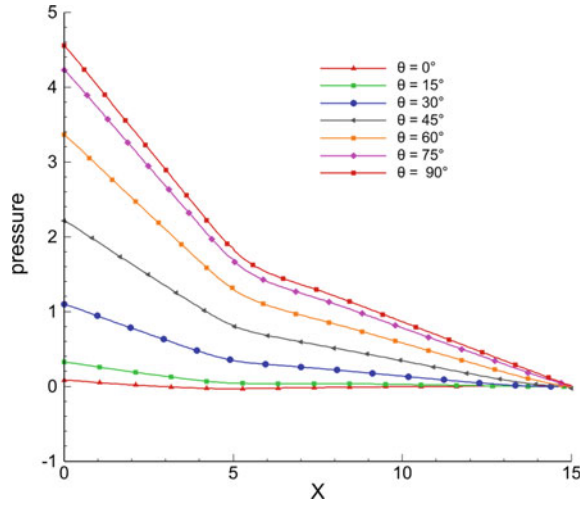
Fig. 7 Pressure contour at different angles

An increase in pressure drop is seen for all the Hartmann numbers. A pressure drop increases steeply before the expanded section, and its steepness decreases in the expanded section due to the formation of circulation zones.

Fig. 8 MHD effect at different Hartmann numbers
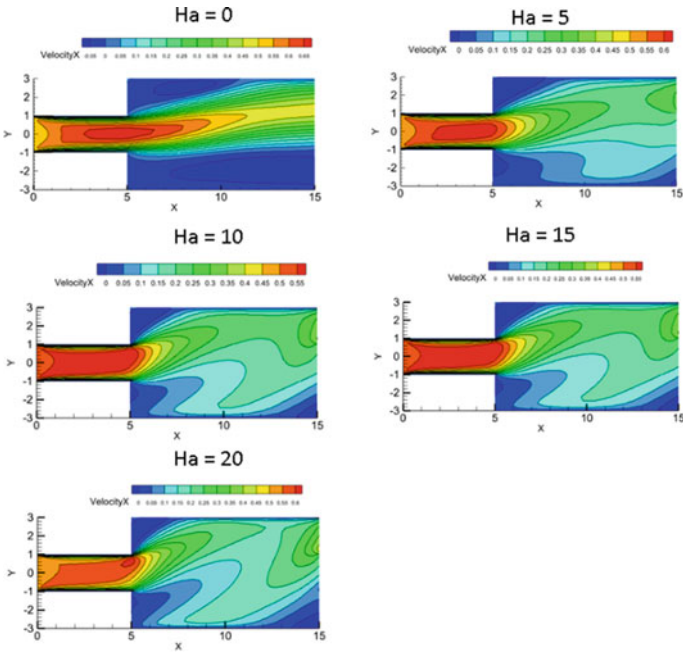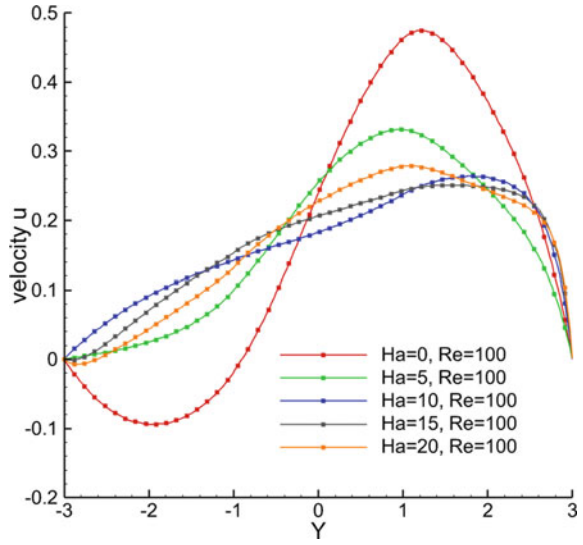
Fig. 9 Velocity contour at different Ha

Fig. 10 Pressure
distribution for different
Hartmann numbers
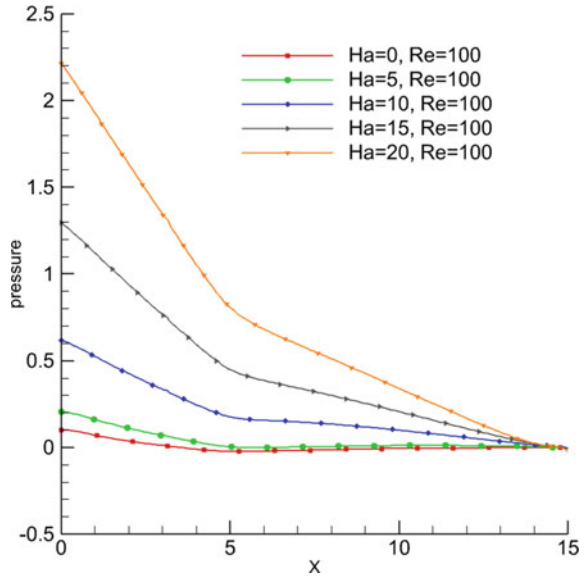
Fig. 11 Pressure contour at
different Ha
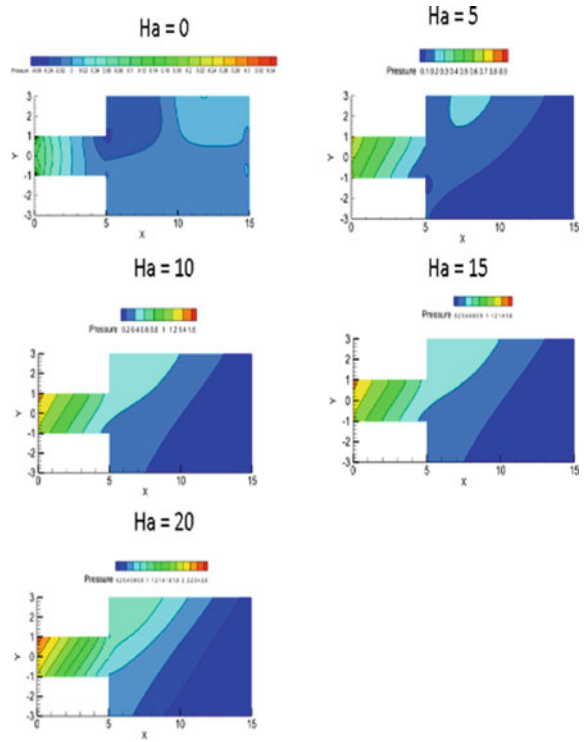
Fig. 12 MHD effect at different Reynolds numbers
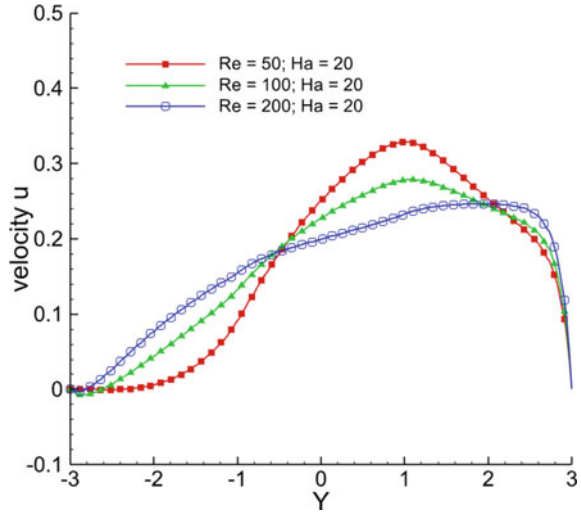
4.3 Effects of Reynolds Number

The effect of Reynolds number on the MHD flow is studied for the fixed Hartmann number of Ha = 20 in this section. The velocity profile at different Re and its contours are plotted in Figs. 12 and 13, respectively. An increase in Reynolds number increases the inertia force, which dominates over the Lorentz force; hence, a smooth velocity profile is observed for Re = 200.

The pressure drop and pressure contours are also shown in Figs. 14 and 15, respectively. It is observed from the figure that the pressure drop decreases with an increase in the Reynolds number.

5 Conclusions

A numerical study of MHD flow through a sudden expansion channel is carried out using an in-house 3D CFD solver. It is seen that the pressure drop increases with an increase in the inclination angle, and the highest-pressure drop is noticed at 90°. The velocity was found to decrease with an increase in the Hartmann number. It is also observed that pressure drop decreases with an increase in Reynolds number at a fixed Hartmann number.

Fig. 13 Velocity contour at different Re
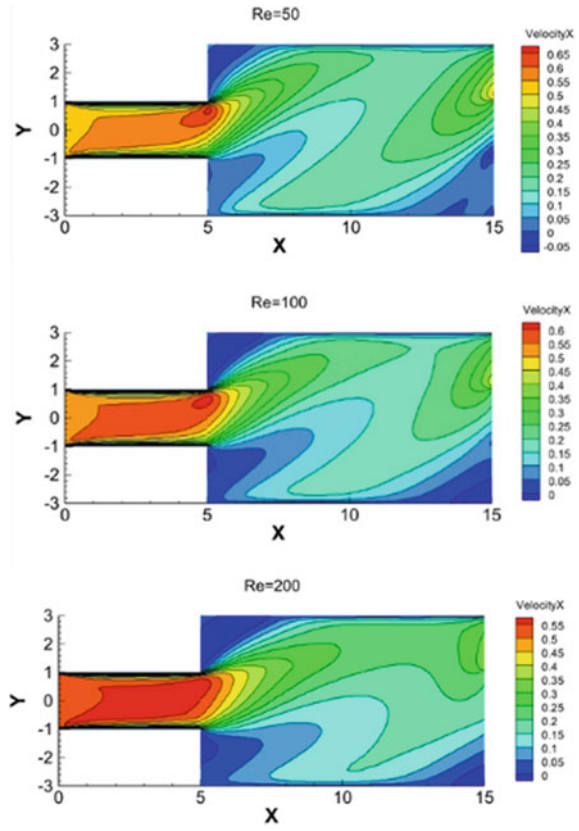
Fig. 14 Pressure variation pattern for different Reynolds numbers
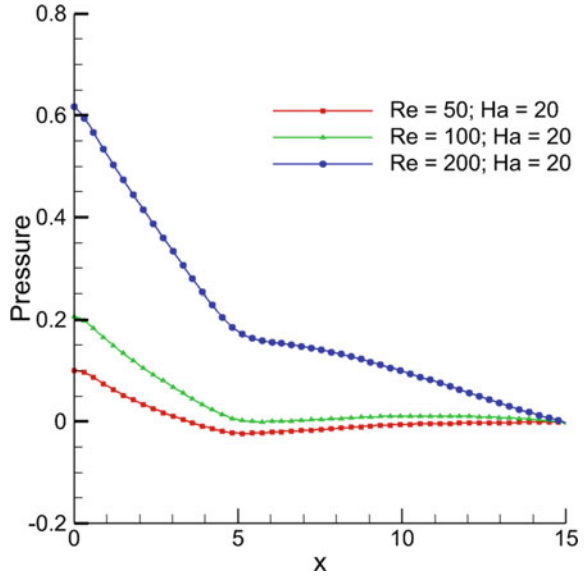
Fig. 15 Pressure contour at different Re
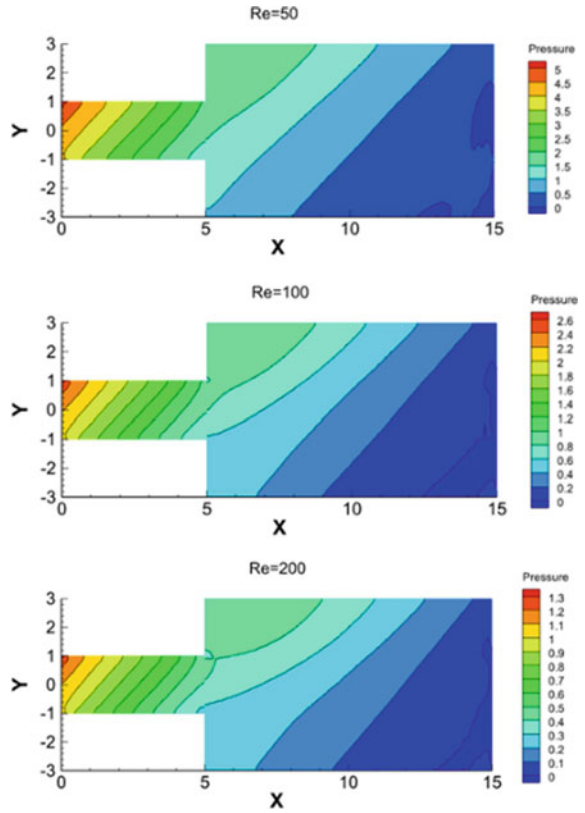
NOMENCLATURE

Ha   Hartmann number (–)
Re   Reynold number (–)
ER   Expansion ratio (–)
ρ Density (kg/m^3)
σ Electrical conductivity (Siemens/s)
μ Kinematic viscosity (kg/m s)
u Velocity component in the x-direction (m/s)
v Velocity component in the y-direction (m/s)
J Current density
B Magnetic field (tesla)
P Pressure (pa)

References

1. Bühler L, Horanyi S, Arbogast E (2007) Experimental investigation of liquid-metal flows through a sudden expansion at fusion-relevant Hartmann numbers. Fusion Eng Des 82(15–24):2239–2245
2. Mistrangelo C, Bühler L (2007) Numerical Investigation of liquid metal flows in rectangular sudden expansions. Fusion Eng Des 82(15–24):2176–2182
3. Praveen T, Eswaran V (2017) Transition to asymmetric flow in a symmetric sudden expansion: hydrodynamics and MHD cases. Comput Fluids 148:103–120
4. Feng J, He Q, Chen H, Ye M (2016) Numerical investigation of magnetohydrodynamic flow through sudden expansion pipes in liquid metal blankets. Fusion Eng Des 109:1360–1364
5. Morley NB, Ni MJ, Munipalli R, Huang P, Abdou MA (2008) MHD simulations of liquid metal flow through a toroidally oriented manifold. Fusion Eng Des 83(7–9):1335–1339
6. Rhodes TJ, Smolentsev S, Abdou M (2018) Magnetohydrodynamic pressure drop and flow balancing of liquid metal flow in a prototypic fusion blanket manifold. Phys Fluids 30(5):057101
7. Kumamaru H (2017) Numerical analyses on liquid-metal magnetohydrodynamic flow in sudden channel expansion. J Nucl Sci Technol 54(2):242–252
8. Kumamaru H (2017) Numerical analyses on liquid-metal magnetohydrodynamic flow in sudden channel contraction. J Nucl Sci Technol 54(12):1300–1309
9. Singh RJ, Gohil TB (2020) Numerical analysis of unsteady natural convection flow and heat transfer in the existence of Lorentz force in the suddenly expanded cavity using open FOAM. J Therm Sci 29(6):1513–1530
10. Gajbhiye NL, Throvagunta P, Eswaran V (2018) Validation and verification of a robust 3-D MHD code. Fusion Eng Des 128:7–22

Air Lubrication on a Flat Plate in a Steady Water Stream

N. David and Yeunwoo Cho

1 Introduction

The topology of injected air underneath the surface of a barge at various combinations of free-stream velocity, air injection rates, vent diameter and air injection angle with respect to the free-stream was observed and two types of air cavities namely, lambda-type and delta-type were found [2]. They showed that the sweep angle increases with the increase in the free-stream velocity at a given air injection rate and that the sweep angle decreases with the increase in the air injection rate at a given free-stream velocity. The injected air through 1 mm vent on the surface of NACA 0010 hydrofoil at various angles of inclination of the hydrofoil, free-stream velocities and air injection rates were observed, and various jet states such as cloudy-puff state, stable-buoyant jet, unstable jet, buoyant-bifurcating jet states were found [3]. They also showed that the jet angle, jet width, jet thickness and jet effective diameter were a function of Reynolds number, Froude number and air injection coefficient. The hull of the scaled model of a carrier was air injected through two air injection slots, and they observed a total resistance decrease as much as 26% when the air injection rate was increased at constant model velocity [4]. Surface shear stress measurements were performed on a flat plate and a model of a carrier in a towing tank and the percentage of drag reduction for various air layer thickness were found [5]. They also showed that the power required to drive the flat plate in a towing tank was of considerably small magnitude for a flat plate with a cavity underneath its surface with

N. David

Department of Aerospace Engineering, Hindustan Institute of Technology and Science, Chennai, Tamil Nadu, India

Y. Cho (✉)
Department of Mechanical Engineering, Korea Advanced Institute of Science and Technology, Daejeon, South Korea
e-mail: ywoocho@kaist.ac.kr

air injection turned on. Using VoF method and Eulerian Multiphase model in STAR-CCM, it has been shown that a considerable reduction in drag upon air injection for various scaled air layer thicknesses underneath a flat plate [6].

Drag experienced by a hydrofoil at various angles of inclination and water depths at several free-stream velocities when subjected to air injection has been studied numerically using VoF method and RANS solver in OpenFOAM [7]. Linear normal mode stability analysis has been used to find an expression for the jet velocity for the air layer formed between water and a wall surface [8]. A considerable resistance reduction on the model ship in a towing tank facility has been found upon air injection at various towing speeds, when compared with the bare hull resistance [9]. Local skin-friction measurements have been performed on a smooth flat plate with air injection through pores, and a significant percentage of drag reduction with the increase in the air injection rate was observed in a constant velocity free-stream of water [10]. Frictional resistance on a full scale experiment ship was measured using shear force sensors on the hull surface [11]. They observed that the time series of the measured shearing force showed a sudden drop upon switching-on of the air injector/blower.

2 Methodology

One million tetrahedral mesh elements were used for all the simulations; the maximum cell squish in the computational domain was 0.46; the maximum cell skewness was 0.44 and the maximum aspect ratio was 5.23. The inlet boundary condition was set as velocity inlet with the constant velocity along the x-direction. The outlet is set as pressure outlet, and symmetry boundary condition is set on one of the planes. In order to save the computational time, mass flow inlet boundary condition is given to the air vents underneath the flat plate, and the flat plate is given no-slip boundary condition. Pressure-based, transient solver is used for the simulations with volume of fluid (VoF) method for the air-water two-phase flow. SST $k\omega$ turbulent model is used for the simulations using pressure-velocity coupled solution scheme. Second-order upwind method is used for the momentum, turbulent kinetic energy and turbulent dissipation rates. The time step, Δt used in the unsteady computations was 0.00025 s, and the first cell distance in the boundary layer region was fixed to be 0.15 mm so that the courant number was within non-diverging limits. The flat plates considered in the analysis have a length of 330 mm, width of 400 mm and a thickness of 8 mm. The air vents have a diameter of 15 mm, positioned in uniform azimuthal spacings apart from each other on a reference circle of diameter 95 mm. The convergence of residuals of the order of $\mathcal{O}(10^{-3})$ was obtained. Finest possible spatial resolution was used with eight inflation layers in the boundary layer region of about 30 mm normal to flat plate, for the time step that was fixed at a computationally practical value of 0.00025 s. The spatial resolution and the time step were such that the Courant number was a non-diverging, stable value over time. Any further fine mesh refinement for the given Δt would result in Courant number divergence, and any coarser mesh for the given Δt would result in lower computed drag value, this

ensures that the computed drag values were grid independent for the given Δt. Our current computational approach was validated by comparing the non-dimensional frictional coefficient, c_f/c_{f_0} against the air injection rates, $\dot{m}$ at various water stream velocities, V_∞ against the experimental results of [12] and a good agreement was observed between them.

3 Results and Discussion

The contours of instantaneous pressure for the side view and top view ($y = -0.004$ m-plane) together with the instantaneous velocity vectors are shown for $V_\infty = 20$ m/s, $\dot{m} = 0.051970140$ kg/s for the circular vent geometry in Fig. 1a, b at an instance in time after a steady state in drag is reached. Pressure is observed to be maximum at the leading edge of the flat plate due to the presence of a stagnation point and minimum at the trailing edge of the flat plate as observed by the contours in Fig. 1a–b for the circular vent geometry. Pressure drops immediately downstream of the stagnation point on the flat plate owing to expansion. The velocity vectors around the flat plate indicate the magnitude of velocity by their length and colour values in Fig. 1a, b. The velocity vectors close to the air injection vents indicate the air injection velocity magnitude and direction clearly in the side view Fig. 1a for the circular vent geometry. The colour bar on the left corresponds to pressure magnitude, and the velocity vector magnitude is indicated by the colour bar on the right hand side in Fig. 1a. The colour bar on the left hand side corresponds to pressure and the colour bar on the right hand side corresponds to velocity magnitude in Fig. 1b. A similar pressure distribution is also observed for the four vents, six vents and eight vents geometry with the large pressure found at the stagnation point of the flat plate at the leading edge at various air flow rates and free-stream velocities.

The contours of velocity for the side view and top view ($y = -0.004$ m) together with the velocity vectors are shown for $V_\infty = 20$ m/s, $\dot{m} = 0.051970140$ kg/s for the eight vents geometry in Fig. 2a, b. It is to be noted that the magnitude of velocity is close to minimum magnitude near the surface of the flat plate, where there is a presence of boundary layer and in the wake region downstream of the flat plate as indicated by the contour colour values of velocity for the eight vents geometry for $V_\infty = 20$ m/s, $\dot{m} = 0.051970140$ kg/s, as shown in Fig. 2a, b. The colour bar on the left correspond to pressure magnitude and the velocity vector magnitude is indicated by the colour bar on the right hand side in Fig. 2a. The magnitude of velocity farther away from the flat plate is close to the maximum magnitude on the colour bar of velocity for all the eight vents geometries for $V_\infty = 20$ m/s, $\dot{m} = 0.051970140$ kg/s, as shown in Fig. 2 (a,b). The colour bar on the left hand side corresponds to pressure and the colour bar on the right hand side corresponds to velocity magnitude in Fig. 2b. The velocity vectors around the flat plate indicate the magnitude of the velocity by their length and colour values for the eight vents geometry for $V_\infty = 20$ m/s, $\dot{m} = 0.051970140$ kg/s, as shown in Fig. 2a, b. A similar velocity distribution is also observed for the circular vent, four vents and six vents geometry with the lower
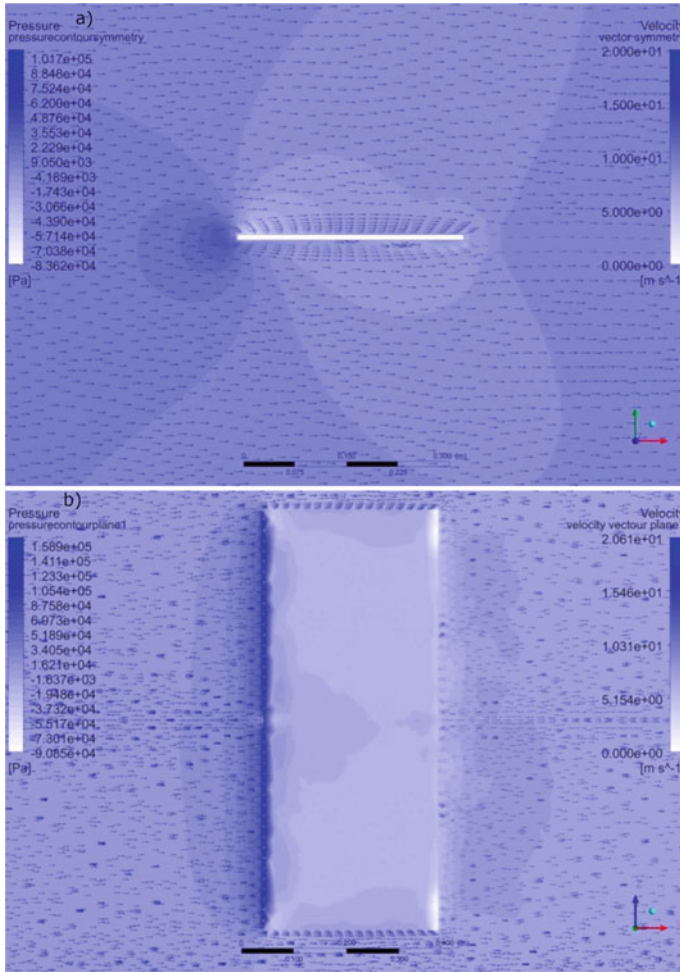
Fig. 1 $V_\infty = 20$ m/s, $\dot{m} = 0.051970140$ kg/s: **a** the pressure contours for the side view in the symmetry plane for the circular vent geometry together with the velocity vectors. **b** The pressure contours together with the velocity vectors in $y = -0.004$ m-plane of the flat plate for the circular vent geometry together with the velocity vectors

magnitudes of velocity in the boundary layer regions and the wake of the flat plate at various air flow rates and free-stream velocities.

The contours of volume fraction of air for the side view on the symmetry plane are shown in Fig. 3a for the four vents geometry together with the velocity vectors for $V_\infty = 20$ m/s, $\dot{m} = 0.051970140$ kg/s. The colour bar on the left hand side corresponds to the volume fraction of air while that on the right hand side corresponds to the magnitude of the velocity in Fig. 3a, b. It is to be noted that the regions of air-water mixture in the bubbly flow is visible in the regions near the flat plate and the regions
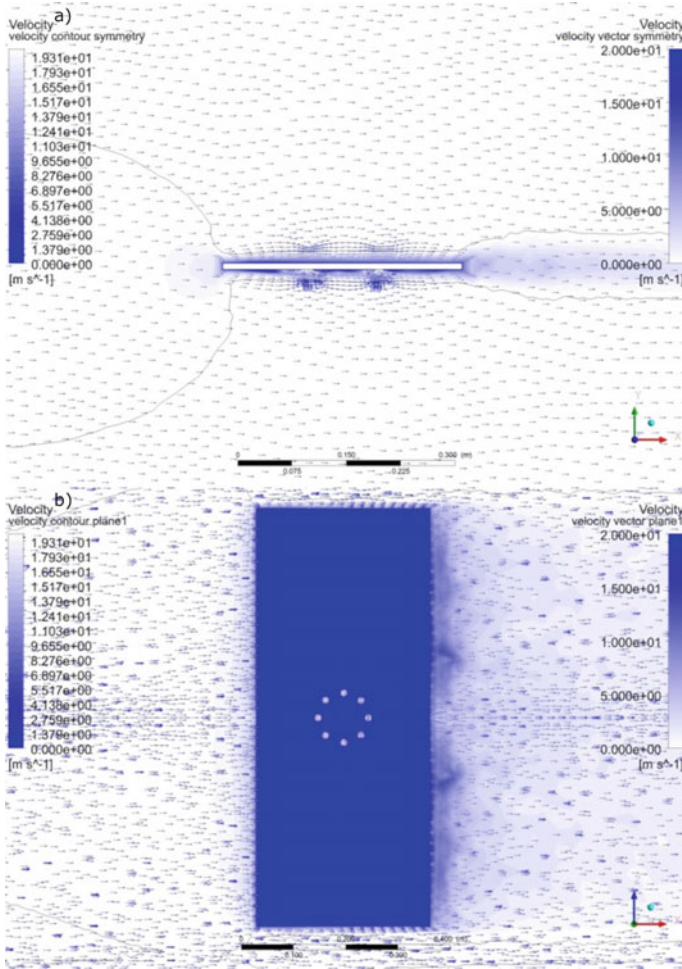
Fig. 2 $V = 20$ m/s, $\dot{m} = 0.051970140$ kg/s: **a** the velocity contours for the side view in the symmetry plane for eight vents geometry together with the velocity vectors. **b** The pressure contours together with the velocity vectors in $y = -0.004$ m-plane of the flat plate for the eight vents geometry together with the velocity vector

where there is pure water is indicated by white values in the volume fraction of air. The injected air that gets advected downstream of the flat plate in the streamwise direction as seen by finite magnitude of volume fraction of air in the leeward side of the flat plate. The boundary layer around the flat plate is also evident from the velocity vectors near the flat plate. The air injection velocity vectors are visible near the air injection vents near flat plate. The contours of volume fraction of air are shown in Fig. 3b for the four vents geometry, together with the velocity vectors for $V_\infty = 20$ m/s, $\dot{m} = 0.051970140$ kg/s on $y = -0.004$ m plane together with the

velocity vectors. The injected air is indicated by the colour value in the contour being close to unity, while the white regions in the contour indicate the water filled regions. The injected air that gets advected downstream of the flat plate as observed by the blue regions in $y = -0.004$ m plane in Fig. 3. It is to be noted that the injected air not only gets advected downstream along with the water stream, but also spreads in the lateral direction underneath the flat plate, being subject to buoyant force. A similar spatial distribution of volume fraction of the injected air is observed for circular vent, six vents and eight vents geometries at other free-stream velocities and air injection rates.
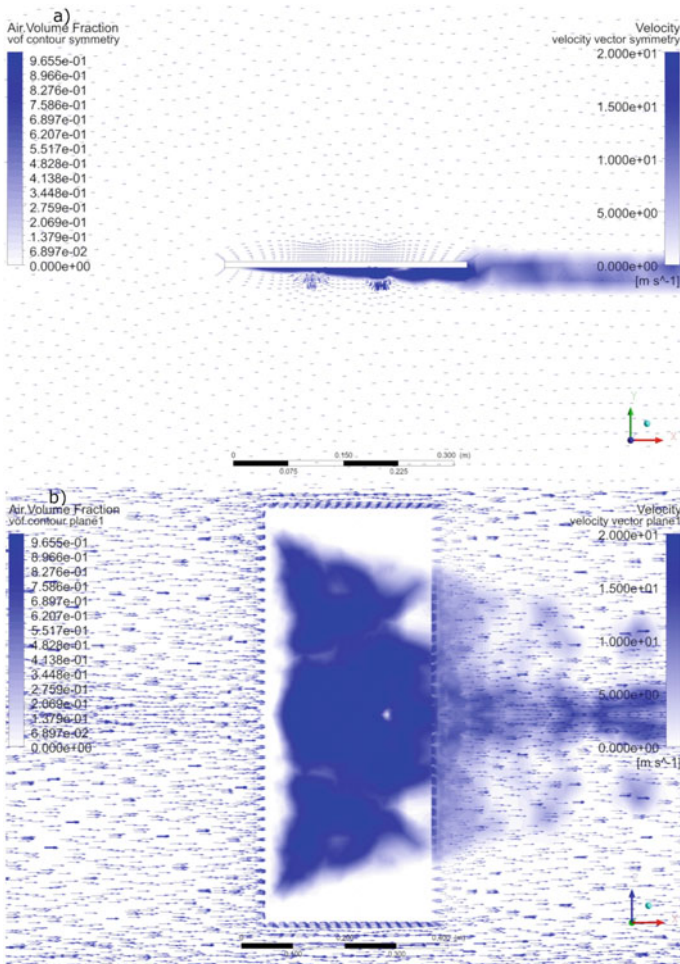
Fig. 3 $V_\infty = 20$ m/s, $\dot{m} = 0.051970140$ kg/s: **a** the volume fraction of air contours for the side view in the symmetry plane for the four vents geometry together with the velocity vectors. **b** The pressure contours with the velocity vectors in $y = -0.004$ m-plane of the flat plate for the four vents geometry together with the velocity vectors

The non-dimensional parameters that determine the dynamics of such a two-phase flow of air injection through a flat plate fully immersed in a steady water stream are $Re = \rho V_\infty \, l/\mu$, and $m^* = \rho A_d V_\infty/\dot{m}$, where V_∞ is the free-stream velocity of water, l is the length of the flat plate, μ is the dynamic viscosity of water, g is the acceleration due to gravity, d is the diameter of the air injection vent, A_d is the area of the rectangular domain and $\dot{m}$ is the mass flow rate of the injected air.

$$c_d = D/(0.5 \times \rho V_\infty^2 (2lb)),$$

where D is the drag force on the flat plate, b is the width of the flat plate. The variation of the drag coefficient, c_d against the coefficient of mass, m^* at various Reynolds number, Re for four vents, six vents, eight vents and circular vent are shown in Fig. 4a–d, respectively. The drag coefficient is observed to decrease with the decrease in mass coefficient, m^* for air injection at various Reynolds numbers, $Re \sim \mathcal{O}(10^6)$ for the air injection through four vents, six vents, eight vents and circular vent configurations in Fig. 4a–d, respectively. It is observed that the magnitude of the drag coefficient at various coefficient of mass and Reynolds number for all the four vents, six vents, eight vents and circular vent configurations is almost of the same magnitude, suggesting that the geometry of the air injection vents placed on a guide diameter of 95 mm does not have a role in determining the magnitude of the calculated drag coefficient. Based on the observed data of drag coefficient, varying as a function of Reynolds number and coefficient of mass in Fig. 4a–d, we arrive at a power-law model for the drag coefficient based on general linear least squares method for the four vents, six vents, eight vents and the circular vent cases in the form of Eqs. 1–4.

$$c_d = 0.4391 \times m^{*-0.29} \times Re^{0.023} - 0.2, \tag{1}$$

$$c_d = 0.4344 \times m^{*-0.291} \times Re^{0.024} - 0.197, \tag{2}$$

$$c_d = 0.4447 \times m^{*-0.29} \times Re^{0.025} - 0.203, \tag{3}$$

$$c_d = 0.4485 \times m^{*-0.291} \times Re^{0.018} - 0.2. \tag{4}$$

A good linear fit is obtained between the model predictions from Eqs. 1–4 and the calculated values of the drag coefficient, as observed by the values of the coefficient of determination values, R^2 being equal to unity for all these cases in Fig. 5a–d for the four vents, six vents, eight vents and circular vent geometries respectively. In Fig. 5a–d respectively for the four vents, six vents, eight vents and circular vent geometries, the horizontal axis is the non-dimensional function, f of the coefficient of mass and the Reynolds number, while the vertical axis is the coefficient of drag. The relation between the coefficient of drag, c_d and the non-dimensional function of independent variables, f is showing within the for the four vents, six vents, eight
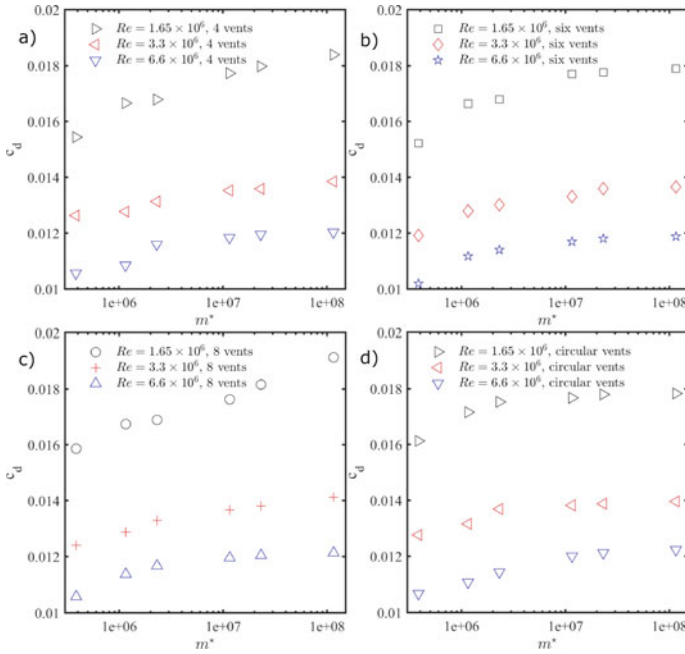
Fig. 4 Drag coefficient variation with the change in the mass coefficient at various Reynolds number: **a** four vents **b** six vents **c** eight vents **d** circular vent

vents and circular vent geometries are shown within the plot region in Fig. 5a–d, respectively.

4 Conclusions

Air injection through vents underneath a flat plate in a steady free-stream of water was studied using Volume of Fluid method in ANSYS Fluent. The effect of the vent geometries, namely, four vents, six vents, eight vents and circular vent on the drag coefficient of the flat plate was studied. It was observed that the drag coefficient decreased with the increase in the air injection rate at all Reynolds numbers for all the vent geometries considered in the studies. We also obtain a power-law relation for the drag coefficient in terms of the non-dimensional coefficient of mass and Reynolds number and find a good agreement between the model findings and the computational data. The drag reduction benefit is attributed to the mean of the area weighted average of air volume fraction observed underneath the flat plate surface.
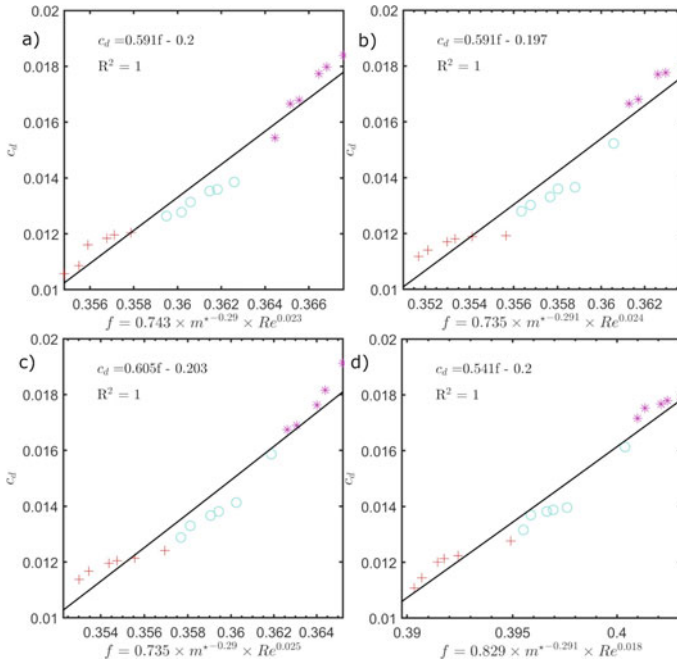
Fig. 5 Linear fit between the computed drag coefficient, c_d and the function of mass coefficient, m^* and Reynolds number, Re: **a** four vents **b** six vents **c** eight vents **d** circular vents. Reynolds number, Re = 1.65×10^6, Re = 3.3×10^6 and Re = 6.6×10^6 are shown by red, cyan and pink markers

References

1. Ceccio SL (2010) Friction drag reduction of external flows with bubble and gas injection. Annu Rev Fluid Mech 42:183–203
2. Ma¨kiharju SA, Lee I-HR, Filip GP, Maki KJ, Ceccio SL (2017) The topology of gas jets injected beneath a surface and subject to liquid cross-flow. J Fluid Mech 818:141–183
3. Nagarathinam D, Kim K, Ahn B-K, Park C, Kim G-D, Yim G-T (2021) Experimental investigation of bubbly flow by air injection on an inclined hydrofoil. Phys Fluids 33(4):043309
4. Kim D-Y, Ha J-Y, Paik K-J (2020) Numerical study on the extrapolation method for predicting the full-scale resistance of a ship with an air lubrication system. J Ocean Eng Technol 34(6):387–393
5. Hao WU, Yongpeng OU, Qing YE (2019) Experimental study of air layer drag reduction on a flat plate and bottom hull of a ship with cavity. Ocean Eng 183:236–248
6. Kim H-T, Kim H-T, Kim J-J, Lee D-Y (2019) Study on the skin-friction drag reduction by air injection using computational fluid dynamics-based simulations. In: Practical design of ships and other floating structures. Springer, Berlin, pp 205–226

7. Zhang J, Yang S, Liu J (2020) Numerical investigation of frictional drag reduction with an air layer concept on the hull of a ship. J Hydrodyn 32(3):591–604
8. Montazeri MH, Alishahi MM (2019) An efficient method for numerical modeling of thin air layer drag reduction on flat plate and prediction of flow instabilities. Ocean Eng 179:22–37
9. Park SH, Lee I (2018) Optimization of drag reduction effect of air lubrication for a tanker model. Int J Naval Architect Ocean Eng 10(4):427–438
10. Elbing BR, Winkel ES, Lay KA, Ceccio SL, Dowling DR, Perlin M (2008) Bubble-induced skin-friction drag reduction and the abrupt transition to air-layer drag reduction. J Fluid Mech 612:201–236
11. Hoang CL, Toda Y, Sanada Y (2009) Full scale experiment for frictional resistance reduction using air lubrication method. In: The nineteenth international offshore and polar engineering conference. OnePetro, pp 812–817
12. Qin S, Chu N, Yao Y, Liu J, Huang B, Wu D (2017) Stream-wise distribution of skin-friction drag reduction on a flat plate with bubble injection. Phys Fluids 29(3):037103

Effect of Wave and Current Interaction on Flow Hydrodynamics Around a Pier

Gaurav Misuriya and T. I. Eldho

Nomenclature

f	Frequency of wave $[\text{s}^{-1}]$
h	Flow depth [m]
H	Wave height [m]
Lw	Length of wave [m]
d_p	Seeding particle diameter $[\mu\text{m}]$
ρ_p	Density of seeding particles $[\text{g/cm}^3]$
d	Diameter of pier [m]
Re	Reynolds number $-$
Fr	Froude number $-$

1 Introduction

The presence of wave along with the current is a prevailing condition in the coastal area and governs many physical processes in practical application such as local scour around the bridges in coastal areas. Local scour around the foundation of the bridge, which leads to its exposure, is one of the main causes of the failure of bridges. Interaction of surface waves with the current is known to modify the turbulent characteristics and the velocity distribution which results the change in momentum transfer and shear stress and particle transport characteristics of the flow.

The accurate estimation of velocity distribution and the bottom shear stress under the combination of wave and current is very important for the study of sediment

G. Misuriya · T. I. Eldho (✉)

Department of Civil Engineering, IIT Bombay, Mumbai 400076, India

e-mail: eldho@civil.iitb.ac.in

transport leading to local scour. Furthermore, study the interaction of combined and current around the bridge pier on a flat rigid bed gives an idea about the flow circulation and variation of other turbulent parameters which will be helpful in identifying the critical zones and in optimal and economical design of pier in coastal environment.

Several efforts have been made by the researchers [1–4] in the last three decades to investigate the change in the mean flow velocity when a surface wave of particular frequency superimposed with the current. However, most of these studies have emphasis on examining the mean flow velocity and its deviation from the universal logarithmic law observed in current only condition. Van Hoften and Karaki [5] measured the velocity field using the laser Doppler anemometer (LDA) for the surface wave traveling along the direction of flow and observed an increase in the mean velocity near the bed up to a certain distance from the bed. Further, Klopman [2] experimentally studied the flow filed for the wave traveling opposite to the direction of flow and observed reduction in the mean flow velocity. Further, a significant effect of the direction of the superimposed wave with respect to the current on the Reynolds stress was observed by Umeyama [3]. Further, he also observed the variation in the wave form due to interaction of wave and current; however, the attenuation of surface wave was not affected by the direction of current. Mazumder and Ojha [6] investigated the shallow water wave following the current direction. In continuation with it, Umeyama [7] studied the effect of wave height on the turbulent intensity and Reynolds shear stress. Singh and Debnath [8] also investigated the effect of superimposed wave frequency on the various turbulent flow parameters such as turbulent intensity and the Reynolds shear stress. A modulation in the eddy length scales due to superimposed wave in the direction of current is highlighted by Roy et al. [9].

It is clear from the literature presented that the superposition of surface wave with current (in direction or opposite) changed the turbulent flow field which is very well addressed in the literature. However, the effect of coexistence of wave and current on the hydrodynamics around the pier is not very well explored in the literature. Therefore, this study experimentally investigated the effect of superposition wave in the direction of current on the various turbulent characteristics around a bridge pier mounted on a flat rigid bed.

2 Experimental Setup

The experiments were conducted in a 15-m-long rectangular flume. Width and height of the flume were 0.5 m and 0.9 m, respectively. The pier of 0.03 m diameter was placed at the test section located 9 m from the flume inlet. The flow in the flume was maintained by the centrifugal pump, which was precisely controlled by variable frequency device (VFD). The required flow depth in the flume was maintained by adjusting the tail gate height. A schematic diagram of the flume is shown in Fig. 1.

The discharge in the flume was measured with an accuracy of ± 0.01 cm^3/s using ultrasonic flow meter (UFM) attached with the inlet pipe. A plunger type wave maker

Fig. 1 Schematic diagram of experimental flume
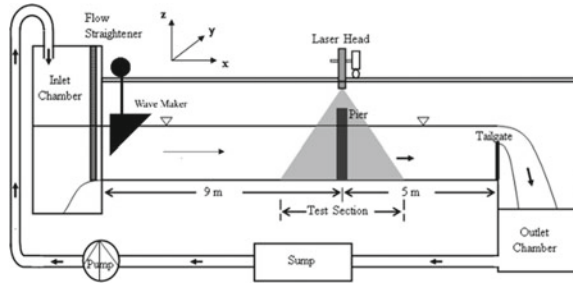
Table 1 Wave characteristics

Parameters	Values
Time period, T (s)	2
Frequency, f (Hz)	0.5
Flow depth, h (cm)	16
Height of wave, H (cm)	4
Length of wave, Lw (cm)	92
Wave length to water depth ratio, Lw/h	5.75
Wave amplitude	2
Wave steepness	0.022

with slope of plunger $-15/11$ was used for the generation of waves. Initially, a steady current of constant flow depth of 0.16 m and velocity 0.56 m/s was allowed to run in the flume for a duration of 1 h. The Reynolds number (Re) and the Froude number (*Fr*) for only current condition were 89,600 and 0.45, respectively. After that, wave with frequency of 0.5 Hz was superimposed in the direction of current. The wave characteristics were calculated by averaging the water profiles calculated from 10 different photographs. The characteristics of waves are summarized in Table 1.

A typical wave steepness observed in nature is observed less than 0.05 [10]; therefore, all the experiments were performed in this range. Further, L_w/H ratio in the natural waves is prevalent in the range of 4–56 [11] which is also satisfied in this study.

2.1 PIV Setup

The PIV system consisted of a double pulsed Nd-Yag laser, and one camera was used to measure 2D flow field. The per pulse energy of the laser was 200 mJ, and the pulse duration was 4 ns. The camera was able to capture eight images per second in double frame mode. The camera was placed on a traverse system which precisely

Table 2 Summary of various parameters of PIV setup

Parameters	Values
Thickness of the light sheet	0.002 m
Pixels per mm	8.2 (approx.)
Time between pulses	2932 μs
Interrogation area size	16 × 16 pixel
Camera object distance	0.93 m
Seeding particle diameter	10 μm
Particle response time (t_p)	0.000066 s
Stokes number (S)	0.0023
Average uncertainty due to sub-pixel analysis	1.2%
Operational frequency	8 Hz (in double frame mode)

control the movement. In addition, a timer was also used to synchronize the camera shutter timing with the laser pulse time.

A calibration sheet having equidistant (11 mm) black marker on it was used to set up a calibration function to convert the pixel distance into SI units. The hollow spherical borosilicate particles were used as seeding particles in the flow. The diameter (d_p) and density (ρ_p) of the seeding particles were 10 μm and 1.03–1.05 g/cm^3. The density of the particles was almost equal to the water which ensured that particles followed the flow. Further, the stokes number which is defined as the ratio of the particle response time and the largest scale eddy turnover time was also calculated as 0.0023, significantly less than 1 also ensured the particles followed the flow closely [12]. A summary of various PIV parameters is presented in Table 2.

3 Results and Discussion

The effect of superposition of wave on various turbulent parameters is discussed in this section. The results are presented for the only current condition as well as for coexisting wave and current condition.

3.1 Mean Velocity

The mean streamwise velocity contours are shown in Fig. 2 for the interaction with wave and current condition (Fig. 2a) and for only current condition (Fig. 2b). On the superposition of wave, the velocity plot showed the deviation from the universal logarithmic profile on far upstream of pier. The mean flow velocity increased near

Fig. 2 Contour plot for stream wise velocity **a** wave and current **b** only current condition
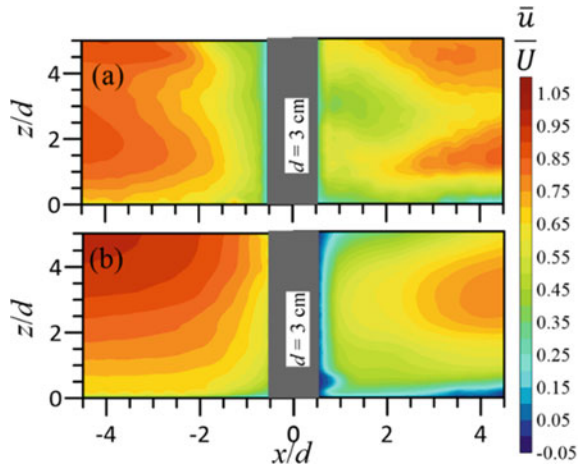
the bed and decreased toward the surface till up to a certain depth and then increased again. The mean velocity decreased near the pier in current and wave condition.

Further, on the downstream, with the superposition of wave, the magnitude of stream wise velocity decreased near the pier and increased near the bed and the water surface.

3.2 Intermittency Factor (IF)

Time averaged streamwise velocity can only represent the region with permanent flow reversal, whereas the reverse flow of less magnitude or for smaller time duration cannot be captured by the time averaged mean velocity profiles [13]. Therefore, intermittency factor (IF) defined the percentage time of occurrence of reverse flow denoted by negative streamwise velocity is calculated. The variation of IF around the pier under the wave and current condition and only current condition is shown in Fig. 3.

The variation of IF showed that the probability of occurrence of reverse flow is more on the downstream of the pier than that of upstream in both the cases. However, frequency of occurrence of reverse flow increased with the superposition of wave on both upstream as well as downstream of the pier. It was observed that the percentage time of occurrence of reverse flow increased by more than 100% on the superposition of wave with 0.5 Hz frequency. Similarly, on the upstream it increased by more than 200%.

Fig. 3 Contour plot for IF **a** wave and current **b** only current condition
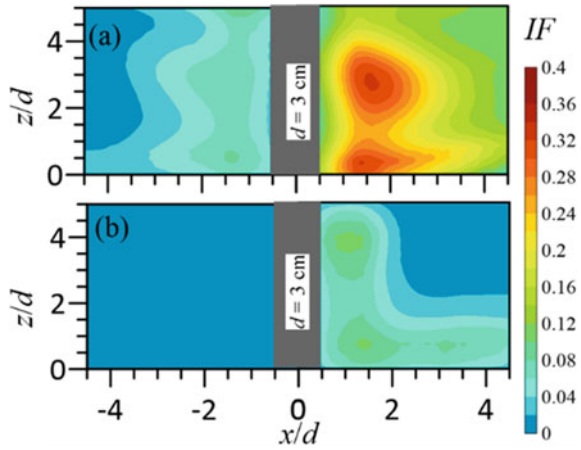
3.3 Turbulent Kinetic Energy (TKE)

Turbulent kinetic energy (TKE) is extracted by the eddies from the mean flow energy. The time average TKE over a time period gives a clear picture about overall variation of turbulence strength in the flow. Figure 4 shows the variation of TKE around the pier for only current condition and for coexisting wave and current condition.

Similar to the flow circulation, TKE increased with 50% on the downstream of pier on the superposition of wave. However, effect of wave on the TKE is not significant on the upstream of the pier. The maximum TKE zone is limited to near bed region on the downstream of the pier for current only condition, whereas it spread over the depth for the current and wave condition. Similarly, on the upstream, the region of high TKE increased with superposition of wave.

Fig. 4 Contour plot for TKE **a** wave and current **b** only current condition
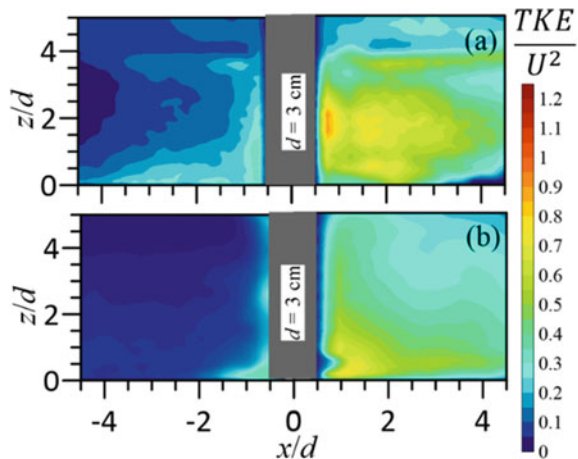
Fig. 5 Contour plot for
$-\overline{u'w'}$ **a** wave and current
b only current condition
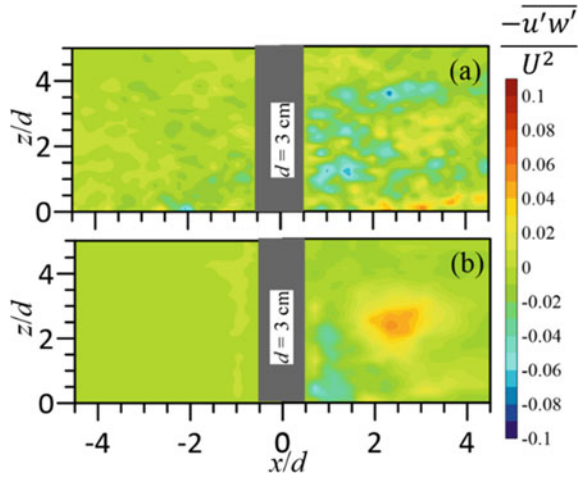
3.4 Reynolds Shear Stress (RSS)

The Reynolds shear stress gives idea about the transfer of momentum flux. The velocity data was recorded using only one camera; the velocity field only on xz plane was recorded. Therefore, only $-\overline{u'w'}$ component of RSS was calculated. The variation of RSS around the pier on wave and only current condition is shown in Fig. 5.

The maximum value of $-\overline{u'w'}$ was observed maximum on the downstream of the pier. Near the pier changes its sign from positive to negative for both the cases signifying that the basic characteristics of RSS near the pier does not affected by the wave superposition. However, further, on the downstream the positive RSS increased in the mid depth for only current conditions, whereas it increased near the bed for the wave and current conditions.

4 Conclusions

This study experimentally investigated the effect of superposition of wave in the direction of current on various turbulent characteristics. Some important conclusions from the study are as follows.

- Superposition of wave increased the turbulent strength on both upstream and downstream of the pier.
- The velocity distribution deviates from universal law and an increase in mean velocity was observed near the bed on wave superposition.

- Flow circulation on the downstream increased by 100% on the downstream and 200% on the upstream of the pier.
- TKE increased by 50%, whereas no significant effect of the wave was observed on the RSS.

References

1. Brevik I, Bjørn A (1979) Flume experiment on waves and currents. I. Rippled bed. Coast Eng 3:149–177
2. Klopman G (1994) Vertical structure of the flow due to waves and currents-laser-doppler flow measurements for waves following or opposing a current.WL report H840-30, part II, for Rijkswaterstaat
3. Umeyama M (2005) Reynolds stresses and velocity distributions in a wave-current coexisting environment. J Waterw Port Coast Ocean Eng 131(5):203–212
4. Singh SK, Raushan PK, Debnath K (2018) Combined effect of wave and current in rough bed free surface flow. Ocean Eng 160:20–32
5. Van Hoften JDA, Karaki S (1976) Interaction of waves and a turbulent current. Proc Int Conf Coast Eng 1976 04–422
6. Mazumder BS, Ojha SP (2007) Turbulence statistics of flow due to wave–current interaction. Flow Meas Instrum 18(3–4):129–138
7. Umeyama M (2009) Changes in turbulent flow structure under combined wave-current motions. J Waterw Port Coast Ocean Eng 135(5):213–227
8. Singh SK, Debnath K (2016) Combined effects of wave and current in free surface turbulent flow. Ocean Eng 127:170–189
9. Roy S, Debnath K, Mazumder BS (2017) Distribution of eddy scales for wave current combined flow. Appl Ocean Res 63:170–183
10. Banerjee T, Muste M, Katul G (2015) Flume experiments on wind induced flow in static water bodies in the presence of protruding vegetation. Adv Water Resour 76:11–28
11. Goda Y (2000) Random seas and design of maritime structures (vol. 33). World Scientific Publishing Company
12. Raffel M, Willert CE, Scarano F, Kähler CJ, Wereley ST, Kompenhans JJ (2018) Particle image velocimetry: a practical guide. Springer, New York City, USA
13. Misuriya G, Eldho TI, Mazumder BS (2021) Higher order turbulence around different circular cylinders using particle image velocimetry. ASME J Fluids Eng 143(9)

Influence of Axial Wall Slip on Swirl Velocity in a Laminar Microtube Flow

Dhananjay Kumar and Pranab Kumar Mondal

Nomenclature

L	Characteristic length [m]
R	Pipe radius [m]
r	Dimensionless radius –
θ	Circumferential coordinate –
ρ	Density of fluid [kg/m^3]
μ	Dynamic viscosity [kg/m/s]
u_{av}	Average axial velocity [m/s]
r_t	Dimensionless transition radius –
Z	Dimensionless axial coordinate –
U	Dimensionless axial velocity –
W	Dimensionless swirl velocity –
Re	Reynolds number –
S	Swirl number –

1 Introduction

The development of numerous practical devices and systems depends critically on our understanding of the transport phenomena of liquids in small spaces. The addition of the swirl [1–3] is one of the conventional ways to improve transport characteristics in micro-pipes. Uses for swirling flows in pipes include swirl atomizers, cyclone separators, and swirl combustors to separation of solid, liquid, and gas [4], in addition

D. Kumar (✉) · P. K. Mondal
Department of Mechanical Engineering, IIT Guwahati, Guwahati 781039, India
e-mail: dhananjay1993@iitg.ac.in

to improving transport qualities and enhancement of heat and mass transfer. It is worth mentioning that swirling flow in the pipe/channel is commonly introduced by either twisted tape arrangements or by swirl generators, which signifies the presence of tangential velocity along the axial flow direction. As a result, the literature has extensively explored and researched these movements. Twisted tapes have been used frequently to start swirling flows, and sometimes swirl generators have also been used based on applications. It is crucial to understand how a pipe's whirling flow degrades along the flow direction. For instance, it's crucial to know how much straight pipe is necessary to reduce a designated upstream swirl to a certain allowable amount of swirl since swirl can result in convincing flow measurement errors. Therefore, it is crucial for the design of these devices to comprehend and manage the swirl transport in a pipe.

2   Literature Review and Objective

Consequently, to study the decay of swirl in pipe, perhaps one of the first attempts on laminar flow was theoretically and experimentally reported by Talbot [5] in the cylindrical duct; the experimental swirl decay rates agreed well with the theoretical rates. Further, experimental studies on swirl decay were investigated by Kreith and Sonju [6] in the fully developed turbulent flow regime, where they established a correlation for the swirl decay as a function of Reynolds number and axial length moved by the fluid. Buoyancy-driven Swirling laminar flow was investigated by Taub et al. [7] using analytical methods and obtained similar kind of solutions and validated using numerical techniques. Kiya et al. [8] numerically solved laminar swirl flow by considering the entrance region employing finite difference method and depicted the significance of swirl effects and pressure drop. Kitoh [9] experimentally investigated the turbulent swirl flow in straight pipe and also determined that swirl decay along with the downstream as a result of wall friction and finally flow approached fully developed condition after the decay of swirl.

A generalized swirl decay equation for laminar flow in the pipe was obtained by Ayinde [10] using the curve fitting technique. Yao and Feng [11] obtained analytical expression of swirl decay in laminar flow pipe with swirl being superimposed over parabolic axial flow, slug flow, and slug flow. The obtained analytical expression of the velocity of swirl profile is found to be a function of Reynolds number, pipe axial distance, and swirl intensity. Kaushik et al. [2] numerically solved decay of swirl in microtubes by considering the wall slip boundary conditions and quantified it using swirl number (swirl intensity) at different sections along the downstream. Pati et al. [12] numerically investigated, the influence of thermodynamic irreversibility on the transport of thermal energy in microscale swirling flows pertaining to slip conditions. Therefore, in recent work, we determine the analytical solution for decay of swirl while accounting for wall slip. A good match for the validation considering without slip at the wall is obtained by comparing with existing result of Yao and Feng [11]. Furthermore, parametric quantitative variations are shown to analyse the effect of

variables intricated on the swirl decay. Furthermore, path travelled during swirl–slip versus no-slip interaction is carried out qualitatively in the present study.

3 Mathematical Formulation

In the present work, we consider a small cylindrical micro-pipe with radius 'R' and length 'L' as mentioned in Fig. 1. For this study, cylindrical coordinate system is considered with 'r' is along the tube's radius, 'Z' is along its axis, and 'θ' is along azimuthal (or tangential) direction as shown in Fig. 1.

To simplify the governing equation, the flow is presumed to be steady, axis-symmetric, and fully developed in the axial direction. The simplified governing equations for incompressible and laminar flow are

Continuity equation:

$$\frac{1}{r}\frac{\partial(\rho r u_r)}{\partial r} = 0, \tag{1}$$

r-momentum equation:

$$\frac{u_\theta^2}{r} = \frac{1}{\rho}\frac{\partial p}{\partial r}, \tag{2}$$

θ-momentum equation:

$$u_z\frac{\partial u_\theta}{\partial z} = \frac{\mu}{\rho}\left[\frac{1}{r}\frac{\partial}{\partial r}\left(r\frac{\partial u_\theta}{\partial r}\right) - \frac{u_\theta}{r} + \frac{\partial^2 u_\theta}{\partial z^2}\right], \tag{3}$$

z-momentum equation:

Fig. 1 Diagrammatic representation of flow domain with inlet swirl
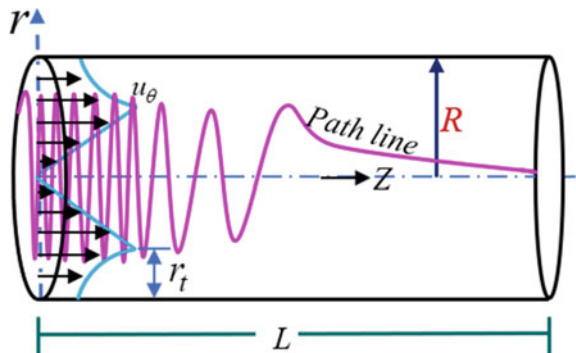
$$\frac{1}{\rho}\frac{\partial p}{\partial z} = \frac{\mu}{\rho}\left[\frac{1}{r}\frac{\partial}{\partial r}\left(r\frac{\partial u_z}{\partial r}\right)\right], \tag{4}$$

where u_r, u_θ, and u_z are the velocity components along the r, θ, and z directions respectively. 'μ' is the fluid dynamic viscosity, 'p' is the fluid pressure, 'ρ' is the density of the fluid.

Dimensionless variables for the further analysis to obtain the component of tangential (swirl) velocity component considering with wall slip (l_s) are defined as follows:

$$r \to \frac{r}{R}, \; Z \to \frac{z}{R}, \; W(z, r) \to \frac{u_\theta}{u_{av}}, U(r) \to \frac{u_z}{u_{av}},$$

$$\mathrm{Re} \to \frac{\rho u_{av} R}{\mu}, \; r_t \to \frac{r_t}{R}, \; l_s \to \frac{l_s}{R}.$$

Using the above mentioned all assumption with considering slug flow with uniform axial velocity at the inlet in dimensionless form, the dimensionless form of 'θ' momentum equation given as

$$Re\left[U\frac{\partial W}{\partial Z}\right] = \left[\frac{1}{r}\frac{\partial}{\partial r}\left(r\frac{\partial W}{\partial r}\right) - \frac{W}{r^2}\right] \tag{5}$$

This term's '$\partial^2 W/\partial Z^2$' absence may be justified by the fact that it is less significant in the equation than other terms due to the smaller magnitudes of the swirl velocity and also the long micro-pipe axial length scale compared to radius ($R \ll L$).

3.1 Boundary Condition with Slip at the Wall

To find out the solution of Eq. (5), the non-dimensional form of boundary condition with slip (l_s) at the wall with superimposing the inlet swirl velocity profile as Rankine vortex is given in the dimensionless format as:

$$W(Z, 0) = 0, \; W(Z, 1) = l_s\big|\partial W/\partial r\big|_{R=1}$$

$$W(0, r) = \begin{cases} \frac{u_{\theta,i,\max}}{u_{av}}\frac{r}{r_t}, & r \le r_t \\ \frac{u_{\theta,i,\max}}{u_{av}}\frac{r_t(1-r)}{r(1-r_t)}, & r \ge r_t \end{cases}. \tag{6}$$

Here transition radius (r_t) is fixed between a forced and free vortex used to obtain the inlet's full Rankine vortex profile.

The analytical solution of swirl velocity '$W(Z, r)$' with above boundary conditions considering with slug flow uniform axial velocity say $U(r) = 1$ is given as

$$W(Z, r) = \sum_{n=1}^{\infty} C_n e^{\left(-\frac{\lambda_n^2 Z}{Re}\right)} \text{Bessel} J(1, \lambda_n r), \tag{7}$$

where 'Bessel$J(a, r)$' is called the generalized Bessel function of first kind and 'λ_n'' is the Eigen value. Using the boundary conditions $W(Z, 1) = 0$, the Eigen values (λ_n) are calculated using equation Bessel$J(1, \lambda_n) = 0$ and the first five of which are listed in Table 1 for different value of slip length.

At this junction, the swirl number '$S(Z)$' [13] is used to explain the relationship between the axial flux of angular momentum and the axial flux of axial momentum. Mathematically, it is defined as

$$S(Z) = \left(\int_0^R u_z u_\theta r^2 \mathrm{d}r \right) \Big/ \left(R \int_0^R u_z^2 r \mathrm{d}r \right). \tag{8}$$

The quantification of swirl intensity in this case in relation to axial flow intensity is called the swirl number. At the intake, it is assumed that the swirl number is one, meaning that the momentum fluxes are equal.

Further, to comprehend the decay of swirl velocity, an attempt is also made to differentiate the intensity of swirl at any axial position with the input intensity of swirl using Eqs. (6–8), given by the below expression as

$$\frac{S(Z)}{S(0)} = \frac{\sum_{n=1}^{\infty} C_n e^{\left(-\frac{\lambda_n^2 Z}{Re}\right)} \int_0^1 \text{Bessel} J(1, \lambda_n r) r^2 \mathrm{d}r}{\int_0^1 W(0, r) r^2 \mathrm{d}r}. \tag{9}$$

In Sect. 4, the aforementioned results are first verified against results from the literature. Results obtained with the help of the present solution are also mentioned.

Table 1 First five Eigen values (λ_n) for the generalized Bessel function of first kind with four different value of slip length given as

n	$\lambda_n(l_s = 0.1)$	$l_s = 0.01$	$l_s = 0.001$	$\lambda_n(l_s = 0)$
1	3.4798	3.7936	3.8279	3.8317
2	6.4201	6.9459	7.0086	7.0156
3	9.3926	10.0726	10.1633	10.1735
4	12.4054	13.1919	13.3104	13.3237
5	15.4502	16.3082	16.4542	16.4706

4 Results and Discussion

In order to compare our analytical results with those found in the literature [11] for a laminar swirl flow without slip boundary condition at the wall, we first benchmark our analytical results of the current analysis.

As the swirl velocity profile is a function of Reynolds number 'Re', transition radius, slip length and axial length. It is indeed to vary the parameters to study its individual influence on swirl velocity profile. Therefore, throughout our study, we vary the Reynolds number between 10^0 and 10^3, dimensionless slip length between 0 and 0.1 (for tube diameter ranging between 10 and 100 μm) [14] and transition radius between 0.5 and 0.9. In the following discussion, the obtained velocity profile and intensity of swirl decay are in exact match with the research work of Yao and Fang [11] with no-slip at transition radius, '$r'_t = 0.9$ shown in Figs. 2 and 3, respectively. This is further supported by the perfect agreement between the eigenvalues described by Yao and Fang [11] with no-slip ('$l'_s = 0$) and displayed in Table 1. In order to attain the results, the eigenvalues for the different dimensionless slip lengths were also calculated and given in Table 1.

First, the impact of non-dimensional slip length ($l_s = 0 \sim 0.1$) on swirl decay for Re = 10 and 100 at $r_t = 0.8$ is shown in Figs. 4 and 5, respectively. On comparing the above-mentioned figures, that increasing the slip length and Reynolds number, decay of swirl intensity '$S(Z)\big/ S(0)$' is decreasing significant along the downstream. The cause of this can be attributed to the fact that there is not a complete transfer of momentum from the immobile walls to the bulk fluid with increase in slip length and decrease in wall shear stress. Observing the Table 1, it clear that there is no sufficient increase in Eigen values when comparing $l_s = 0$ and $l_s = 0.001$, which is also shown in inset of Fig. 4 as no significant change in swirl decay.

The variation of Reynolds number (1 ~ 100) on the decay of swirl intensity at transition radius 0.8 is shown in Figs. 6 and 7 with dimensionless slip length 0.01 and 0.1, respectively. Reynolds number play a significant role in decay of swirl velocity along the downstream. The average axial velocity is used to define Reynolds number

Fig. 2 Validation of tangential (swirl) velocity profile along the radial position at Re = 1000 with no-slip [11]
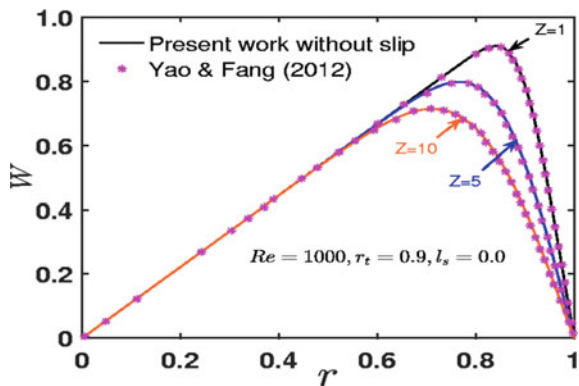
Fig. 3 Validation of swirl decay profile along the axial position at Re = 1, 10 with no-slip [11]
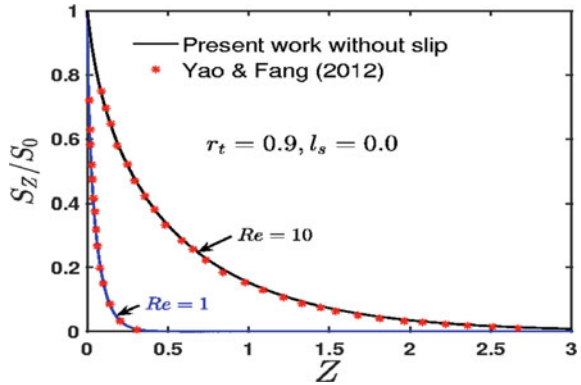
Fig. 4 Intensity of swirl decay by varying the slip lengths at Re = 10 and $r_t = 0.8$
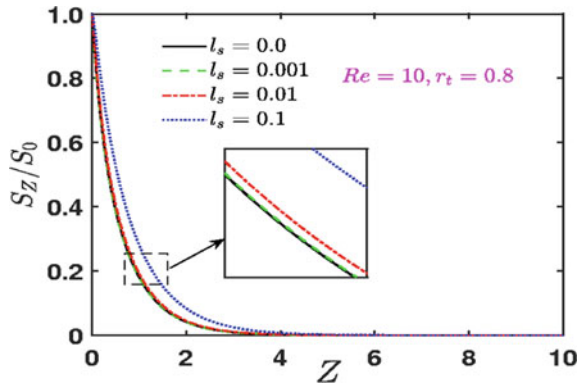
Fig. 5 Intensity of swirl decay by varying the slip lengths at Re = 100 and $r_t = 0.8$
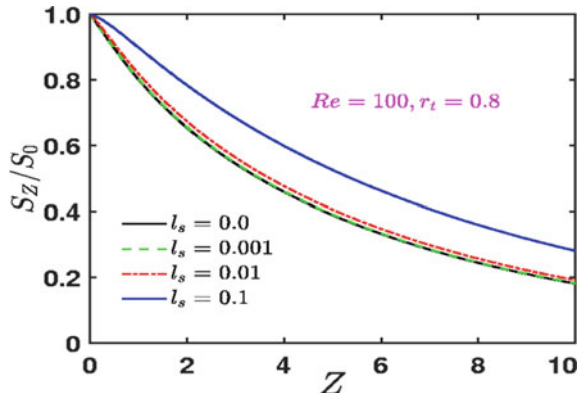
Fig. 6 Intensity of swirl decay for different Reynolds number with slip length ($l_s = 0.01$) at $r_t = 0.8$
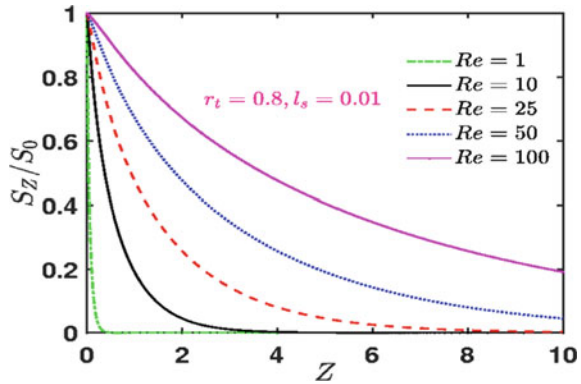
Fig. 7 Intensity of swirl decay for different Reynolds number with slip length ($l_s = 0.1$) at $r_t = 0.8$
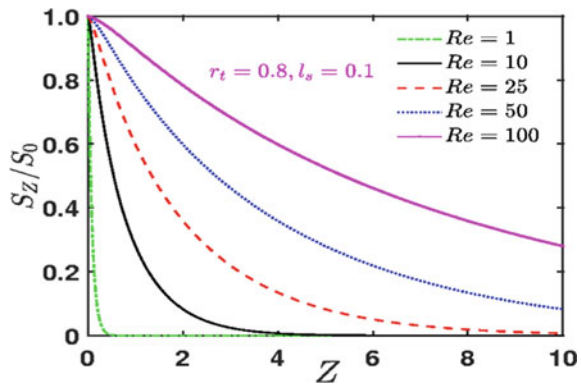
in this study; as a result, the greater axial flow velocity induces swirl momentum advection farther into the pipe which delay swirl decay.

Therefore, it is evident that increasing 'Re' at a specific axial length from the inlet, the swirl decay rate is significantly lower. No matter what other criteria are considered, this trend still holds true. Increasing the Reynolds number and the non-dimensional wall slip is found to be a useful strategy to reduce the swirl degradation.

The variation of Reynolds number ($10^0 \sim 10^2$) for swirl velocity profile is shown in Fig. 8 for an axial location $Z = 1$, $r_t = 0.8$ and slip length $l_s = 0.1$. At this instant, the wall shear stress diminishes as the slip length rises, preventing a complete transfer of momentum from the immobile walls to bulk fluid. It can be observed from Fig. 8, for particular slip length that increasing the Reynolds number up to certain value sufficiently maintains the momentum at the wall. For Re = 50 and 100, there is no significant rise in swirl momentum is observed. In the aspect of understanding the swirl decay through swirl velocity profile, we intended to plot the swirl velocity profile at axial length $Z = 10$ for higher Reynolds number in Fig. 9.

Fig. 8 Swirl velocity profile for different Reynolds number at $Z = 1$ with $r_t = 0.8$ and $l_s = 0.1$ along the radial coordinate
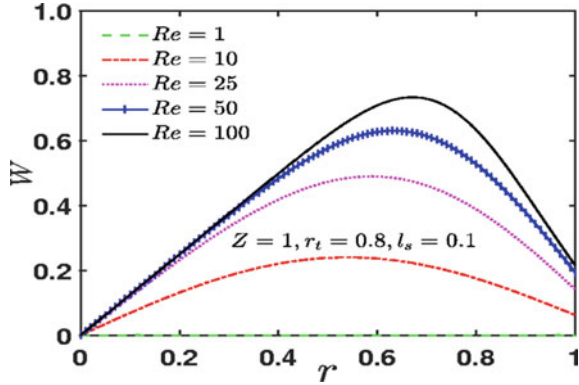
Fig. 9 Swirl velocity profile for different Reynolds number at $Z = 10$ with $r_t = 0.8$ and $l_s = 0.1$ along the radial coordinate
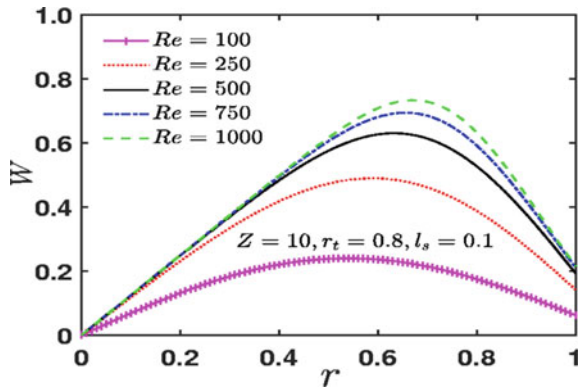
As the Reynolds number rises, advection is facilitated by an increase in axial velocity, which significantly raises the magnitude of swirl velocity and also, because of considering the wall slip, the swirl velocity is higher at the wall.

Variation of dimensionless transition radius (0.5 ~ 0.9) on intensity of swirl decay at particular Reynolds number 100 for slip length 0.01 and 0.1 is shown in Figs. 10 and 11, respectively. Figures show that the peak of the tangential velocity is closer to the axis of micro-pipe at the lower value of transition radius. Figures show with smaller transition radii, the wall effects on the swirl velocities is diminished, which validates are argument we made above. Increasing the Reynolds number and the non-dimensional slip length while lowering the non-dimensional transition radius is found to be an effective strategy for reducing swirl decay.

Additionally, to comprehend how non-dimensional transition radius affects the profile of swirl velocity, we plotted Fig. 12 for Reynolds number 100, slip length 0.1 at an axial location 0.1. It is critical to infer that, for same slip length, the swirl velocity at the wall is more pronounced for higher transition radius.

Fig. 10 Intensity of swirl decay by varying the transition radius at Reynolds number 100 and slip length 0.01
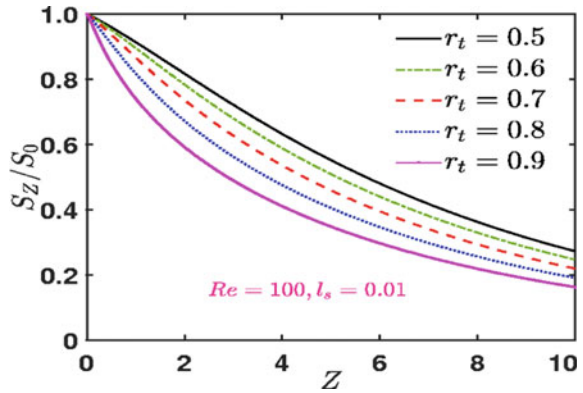
Fig. 11 Intensity of swirl decay by varying the transition radius at Reynolds number 100 and slip length 0.1
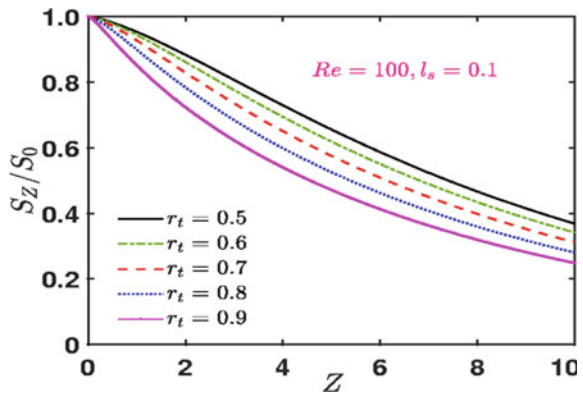
Fig. 12 Swirl velocity profile by varying the transition radius at $Z = 0.1$ with $Re = 100$ and $l_s = 0.1$
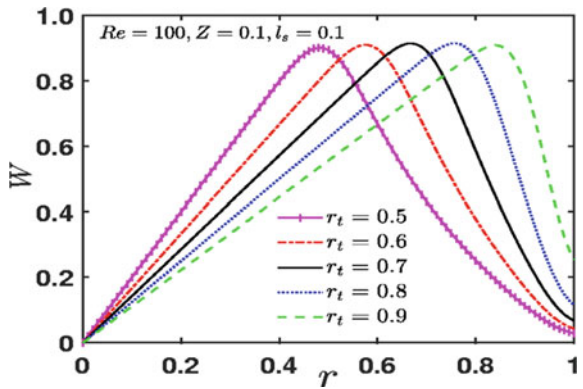
Fig. 13 Swirl velocity profile for different axial position at Re = 1000 with $r_t = 0.8$ and $l_s = 0.1$
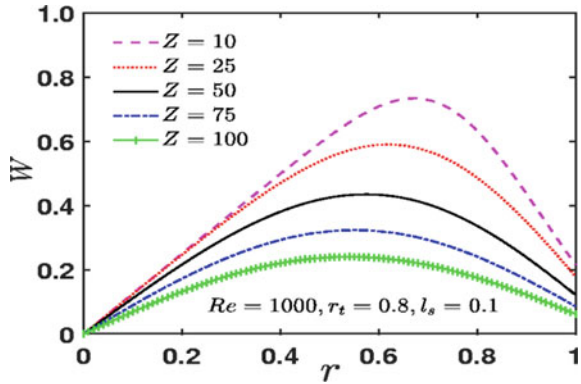
Wall drag effect on swirl velocity profile is shown in Fig. 13 for Reynolds number 1000 with $r_t = 0.8$ and $l_s = 0.1$ at different axial position. It clearly shows at downstream, swirl velocity is decreasing due to friction between the layers of fluid and wall, which can be observed as reduced in magnitude.

Further, three-dimensional path line of two fluid particles at two different non-dimensional slip length $l_s = 0.01$ and 0.1 is compared with no-slip $l_s = 0$ in Figs. 14 and 15, respectively for Reynolds number 1000 and transition radius 0.9. As seen in figures, the fluid particle's swirl momentum disappears earlier axially for the no-slip case than it does for the slip case. Additionally, it demonstrates that average distance travelled by particles in the swirling flow having slip case is larger compared to without slip. This results from slower swirl momentum depletion as length of slip increases.

Fig. 14 Path way of two hypothetical fluid particles proceeding inside the microtubes with no-slip $l_s = 0$ and slip $l_s = 0.01$. Here considered Reynolds number 1000, transition radius 0.9, and the radial location is $r = 0.7$
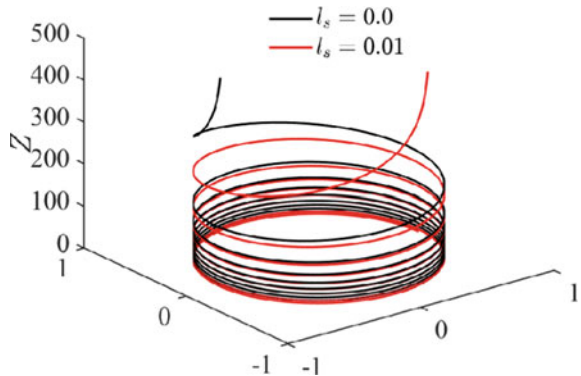
Fig. 15 Path way of two hypothetical fluid particles proceeding inside the microtubes with no-slip $l_s = 0$ and slip $l_s = 0.1$. Here considered Reynolds number 1000, transition radius 0.9, and the radial location is $r = 0.7$
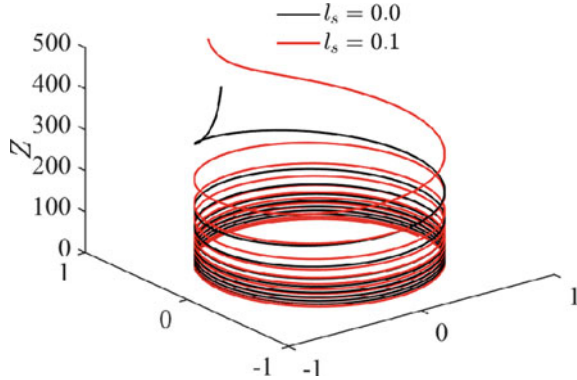
5   Conclusions

In the present work, with wall slip boundary conditions, the governing partial differential equations are solved analytically to examine laminar decay of swirl in a straight pipe. The analytical solution is compared to the literature-based solution for the no-slip wall condition. Later, we have explored the influence of various parameters such as Reynolds numbers, transition radius, wall slip on swirl velocity distribution, and swirl decay along the downstream of the microtube. According to the results, increasing Reynolds number causes slower swirl decay velocity and intensity. Due to wall drag, an inlet swirl profile with a high transition radius decay more quickly. The outcomes also imply that longer slip lengths result in higher velocity and a slower decay of the swirl compared to no-slip. The present result has major implications for microtubes investigations where it is desired to improve transportation characteristics.

References

1. Dewan A, Mahanta P, Raju KS, Kumar PS (2004) Review of passive heat transfer augmentation techniques. Proc Inst Mech Eng Part A J Power Energy 218:509
2. Kaushik P, Pati S, Som SK, Chakraborty S (2012) Hydrodynamic and thermal transport characteristics of swirling flows through microchannels with interfacial slip. Int J Heat Mass Transf 55:4359
3. Sheikholeslami M, Gorji-Bandpy M, Ganji DD (2015) Review of heat transfer enhancement methods: focus on passive methods using swirl flow devices. Renew Sustain Energy Rev 49:444
4. Lefebvre A (1988) Atomization and Sprays, Taylor Fr

5. Talbot L (1954) Laminar swirling pipe flow. J Appl Mech 21:1
6. Kreith F, Sonju OK (1965) The decay of a turbulent swirl in a pipe. J Fluid Mech 22:257
7. Taub GN, Lee H, Balachandar S, Sherif SA (2011) A study of similarity solutions for laminar swirling axisymmetric flows with both buoyancy and initial momentum flux. Phys Fluids 23:113601
8. Kiya M, Fukusako S, Arif M (1971) Laminar swirling flow in the entrance region of a circular pipe. Bull JSME 14:659
9. Kitoh O (1991) Experimental study of turbulent swirling flow in a straight pipe. J Fluid Mech 225:445
10. Ayinde TF (2010) A generalized relationship for swirl decay in laminar pipe flow. Sadhana 35:129
11. Yao S, Fang T (2012) Analytical solutions of laminar swirl decay in a straight pipe. Commun Nonlinear Sci Numer Simul 17:3235
12. Pati S, Som SK, Chakraborty S (2013) Thermodynamic performance of microscale swirling flows with interfacial slip. Int J Heat Mass Transf 57:397
13. Reader-Harris MJ (1994) The decay of swirl in a pipe. Int J Heat Fluid Flow 15:212
14. Tretheway DC, Meinhart CD (2006) Erratum: A generating mechanism for apparent fluid slip in hydrophobic microchannels. [Phys Fluids 16:1509 (2004)], Phys Fluids 18:109901 (2006)

Numerical Comparison of Turbulence-Chemistry Interactions Models with Radiation Effect for Non-premixed Flames: Sandia-E and DLR-B

Naveen Kumar, Ram Kumar, and Ankit Bansal

1 Introduction

Combustion is an exothermic chemical reaction that occurs between a combustible substance and an oxidizer. Combustion is vital in industrial burners, detonation, internal combustion engines, and power plants [1, 2]. In commercial and industrial applications, three types of combustion have commonly been observed: premixed, non-premixed (or diffusion), and partially premixed. Petrol engines and household burners [3] are good examples of premixed and partially premixed combustions, respectively. The diesel engine, candles, and matches come under non-premixed combustion.

Most combustion systems produce non-premixed flames in the presence of turbulence and chemical kinetics. Moreover, the chemical and turbulent time scales involved are of the same order and hence comparable. Therefore, turbulence-chemistry interactions (TCI) modeling of turbulent non-premixed flames (TNF) plays a significant role in designing a better and safer combustion device [4]. However, TCI modeling is more challenging in computational fluid dynamics (CFD) due to the strong coupling between turbulence and finite rate chemistry.

N. Kumar (✉) · R. Kumar · A. Bansal
Department of Mechanical and Industrial Engineering, IIT Roorkee, Roorkee 247667, India
e-mail: nkumar@me.iitr.ac.in

2 Literature Review and Objective

For turbulent reactive flows [4, 5], the eddy dissipation concept (EDC) [6], the partially stirred reactor (PaSR) model [7], the flamelet models [8], the conditional moment closure (CMC) model [9], and the probability density function (PDF) [10] methods are powerful TCI models extensively used to capture the interactions between turbulence and chemistry. The EDC and PaSR were developed to consider all the elementary chemical reactions. A detailed reaction mechanism [GRI-Mech 3.0 (36 species and 218 reactions)] was designed for the combustion of methane-air [11] and showed its potential with the EDC and PaSR. The reduced chemical kinetics [Tabulation of Dynamic Adaptive Chemistry (TDAC) method] was preferred for beta-pdf due to the high computational cost and time associated with the detailed chemical mechanisms [12].

Large-eddy simulation (LES) is preferred for complex and real engineering problems as it demands more computer resources and simulation time. The Reynolds-Averaged Navier Stokes (RANS) method has been extensively used for low-speed turbulent reacting flows, and it provides promising results at a relatively lower computational cost. The k-epsilon RANS model neatly captures the turbulence in flames and fires [5, 13].

Radiation is a significant physical phenomenon intricately related to combustion [13–16]. Radiative properties of the medium and boundaries and maybe the turbulence-radiation interactions need to be considered for computing the radiation effects. The radiative source term is included in the energy equation to account for absorption and emission. Many more precise techniques have been developed to solve the radiative transfer equation (RTE). Nonetheless, the spherical harmonics (P_1) and discrete ordinates (DO) methods demonstrated their great potential for radiative transfer problems due to their ease of implementation and convergence [17]. For gray medium, the gas absorption coefficients are assumed to be constant across the entire spectrum and independent of the wavelength.

CFD technologies like AnsysFluent (AF) and OpenFOAM (OF) have been widely employed to simulate turbulent reacting flows [5]. The geometry of a piloted and simple jet flame is straightforward; the turbulence and chemical reactions exhibit strong coupling with each other [18, 19]. Thus, it is frequently considered for the validation of TCI models. In the literature on TNF, it was noticed that only a few investigators had compared the TCI models using the different CFD packages. However, there are still research gaps, including the radiation effects on turbulence and chemistry. Sandia-E (Re = 33,600) and DLR-B (Re = 22,800) are highly turbulent flames compared to Sandia-D (Re = 22,400) and DLR-A (Re = 15,200).

Thus, the primary aim of this paper is to simulate the two types of turbulent diffusion jet flames (Sandia-E and DLR-B [18]) in OpenFOAM (OF) and AnsysFluent (AF), and check the precision of these two CFD software. The secondary aim is to compare the flow-field properties calculated using the three TCI models (EDC, PaSR, and beta-PDF) along with two radiation methods (P_1 and DO). The influence of turbulence on the flame temperature and species concentrations along the axial

and radial directions is investigated and compared with the published experimental data of the TNF workshop [19].

3 Materials and Methods

The fluid motion around the flame is assumed to be a low-speed turbulent reactive flow. The flow and chemistry of fires, flames, and burners are governed by the following species transport, mass, momentum, and energy conservation equations [3]:

$$\frac{\partial}{\partial t}(\rho Y_k) + \frac{\partial}{\partial x_j}(\rho Y_k u_j) = \frac{\partial}{\partial x_j}\left(\rho D_k \frac{\partial Y_k}{\partial x_j}\right) + R_k \tag{1}$$

$$\frac{\partial \rho}{\partial t} + \frac{\partial}{\partial x_j}(\rho u_j) = 0 \tag{2}$$

$$\frac{\partial}{\partial t}(\rho u_i) + \frac{\partial}{\partial x_j}(\rho u_i u_j) = -\frac{\partial p}{\partial x_i} + \frac{\partial \tau_{ij}}{\partial x_j} + \rho f_i \tag{3}$$

$$\frac{\partial}{\partial t}(\rho h_s) + \frac{\partial}{\partial x_j}(\rho h_s u_j) = \frac{\partial}{\partial x_j}\left(\rho \alpha \frac{\partial h_s}{\partial x_j}\right) + S_h \tag{4}$$

where p, ρ, h, α, u_j, and f represent the pressure, density, enthalpy, thermal diffusivity, velocity vector in the x_j spatial co-ordinate, and body force. D_k and Y_k represent the diffusion coefficient and mass fraction of kth species, respectively. R_k and S_h denote the chemical and energy source terms, respectively. The viscous stress for an isotropic fluid can be defined in the following form:

$$\tau_{ij} = \mu\left(\frac{\partial u_j}{\partial x_i} + \frac{\partial u_i}{\partial x_j} - \frac{2}{3}\frac{\partial u_k}{\partial x_k}\delta_{ij}\right) \tag{5}$$

where μ and δ_{ij} are the dynamic viscosity and Kronecker delta, respectively. The gas state equation is written as follows:

$$p = \rho RT \sum_{k=1}^{N} \frac{Y_k}{M_k} \tag{6}$$

where R and M_k denote the universal gas constant and molar mass of kth species, respectively. The governing equations from (1) to (4) are recast using the Reynolds decompositions and Favre averaging.

3.1 Turbulence Model

Two equation standard k-ε model was employed for the closure of the turbulent eddy viscosity. The governing equations for generation of turbulent kinetic energy (k) and its dissipation (ε) are written as [20]:

$$\frac{\partial(\rho k)}{\partial t} + \frac{\partial(\rho u k_i)}{\partial x_i} = \frac{\partial}{\partial x_j}\left[\left(\mu + \frac{\mu_t}{\sigma_k}\right)\frac{\partial k}{\partial x_j}\right] + G_k + G_b - \rho\varepsilon \tag{7}$$

$$\frac{\partial(\rho\varepsilon)}{\partial t} + \frac{\partial(\rho u \varepsilon_i)}{\partial x_i} = \frac{\partial}{\partial x_j}\left[\left(\mu + \frac{\mu_t}{\sigma_\varepsilon}\right)\frac{\partial\varepsilon}{\partial x_j}\right] - C_{\varepsilon 1}\frac{\varepsilon}{k}G_k - C_{\varepsilon 2}\rho\frac{\varepsilon^2}{k} \tag{8}$$

where the generation values of k caused by mean velocity gradients and buoyancy are G_k and G_b. The model constants $C_{\varepsilon 1}$, $C_{\varepsilon 2}$, σ_k, and, σ_ε have values of 1.44, 1.92, 1.0, and 1.3, respectively. The turbulent eddy viscosity is given by:

$$\mu_t = \rho C_\mu \frac{k^2}{\varepsilon} \tag{9}$$

where $C_\mu = 0.09$ is a model constant. The study of flames, which makes use of a modified value of $C_{\varepsilon 1} = 1.60$, yields superior results and strengthens the iterative process' robustness [21, 22]. As a result, in the current work, the model constant of 1.60 is used with beta-PDF to solve the turbulence equation.

3.2 Turbulence-Chemistry Interactions (TCI) Models

Three different TCI models have been used to simulate the jet flames and are discussed in the following subsections: 3.2.1, 3.2.2, and 3.2.3.

3.2.1 Eddy Dissipation Concept (EDC)

The EDC extends the eddy dissipation model to incorporate the detailed chemistry of turbulent flow. Each grid cell is split into reacting (fine structures) and non-reacting (surroundings) zones. It attempts to incorporate the importance of fine structures into turbulent reacting flows where combustion is significant. The turbulence parameters (k and ε) have been used to determine the scale of fine structures from macroscopic to Kolmogorov length scales. The mean chemical reaction rate of the kth species is written as [6]:

$$\overline{R}_k = \frac{\overline{\rho}}{\tau^*}\frac{\gamma_L{}^2\chi}{1 - \gamma_L{}^2\chi}\left(\overline{Y}_k - Y_k{}^*\right) \tag{10}$$

where $\overline{\rho}$ and γ_L are the mean density and length fraction; τ^*, and χ are the residence time and volume fraction of the fine structure, respectively. The $Y_k{}^*$ and $\overline{Y}_k$ represent the reacting and mean mass fraction of the kth species, respectively.

3.2.2 Partially Stirred Reactor (PaSR)

This model separates the reacting and mixing zones within each grid cell. The uniform composition of a reacting zone makes it possible to treat it as a reactor that has been perfectly stirred. The reacting zones only transfer mass within the mixing zones. The chemical and mixing time scales affect the reacting fluid fraction $(\mathcal{F})$. The relation between average reaction rate $(\overline{R}_k)$ and reacting fluid fraction $(\mathcal{F}_k)$ is given as [7]:

$$\overline{R}_k = \mathcal{F}_k R_k \tag{11}$$

3.2.3 Presumed Probability Density Function (Beta-PDF)

Presumed PDF is a commonly used technique for the closure of turbulence-chemistry interactions. This model can be easily applied to those systems that have sufficiently fast and irreversible reactions. The mixture fraction (ξ) is assumed in such a manner that $Y_k(\xi = 0)$ is oxidizer and $Y_k(\xi = 1)$ is fuel. The average mass fraction of kth species is given as

$$\overline{\rho}\tilde{Y}_k = \int_0^1 Y_k(\xi)\rho(\xi)p(\xi)d\xi \tag{12}$$

The mean $(\tilde{\xi})$ and variance $(\widetilde{\xi''^2})$ of the mixture fraction are the presumed parameters for the probability density function $p(\xi)$. Then, rather than solving transport equations for all species, only the functions of $\tilde{\xi}$ and $\widetilde{\xi''^2}$ are computed.

3.3 Radiation Models

The energy is transported as electromagnetic waves in radiative heat transfer. Gases' radiative properties may change as they travel across a medium. The general radiative transfer equation (RTE) can be written in the following form [17]:

$$\frac{1}{c}\frac{\partial I_\lambda}{\partial t} + \frac{\partial I_\lambda}{\partial s} = \kappa_\lambda(I_{b\lambda} - I_\lambda) - \sigma_{s\lambda}I_\lambda + \frac{\sigma_{s\lambda}}{4\pi}\int_{4\pi} I_\lambda(\hat{\mathbf{s}}_i)\phi_\lambda(\hat{\mathbf{s}}_i, \hat{\mathbf{s}})d\Omega_i \tag{13}$$

where c, κ, σ, λ, s, Ω, and $\hat{s}$ are the speed of light, absorption coefficient, scattering coefficient, wavelength, path length, solid angle, and unit vector, respectively. The radiation intensity (I) is calculated using the integro-differential RTE solution, approximated using discrete ordinate and spherical harmonics methods as discussed in the subsections: 3.3.1 and 3.3.2.

3.3.1 Spherical Harmonics Method (P$_1$)

This method is easy to implement in finite volume codes. In the P$_1$ approximation, the radiative intensity is represented as a series of spherical harmonic functions. The P$_1$ equation is expressed as [17]:

$$\nabla_\tau^2 G = -(1 - \omega)(3 - A_1\omega)(4\pi I_b + G) \tag{14}$$

where G, ω, I_b, $A_1\omega$, and τ stand for the incident radiation, single albedo constant, black body radiative intensity, a constant, and optical thickness.

3.3.2 Discrete Ordinates (DO) Method

The DO method uses the discrete representation of radiation intensity over a solid angle of 4π, which is approximated using numerical quadrature techniques. In terms of quadrature weightage (w_i), the radiative flux and incident radiation are calculated using the following relations [17]:

$$q(\mathbf{r}) = \int_{4\pi} I(\mathbf{r}, \hat{s})\hat{s}d\Omega \simeq \sum_{i=0}^{n} w_i I_i(\mathbf{r})\hat{s}_i \tag{15}$$

$$G(\mathbf{r}) = \int_{4\pi} I(\mathbf{r}, \hat{s})d\Omega \simeq \sum_{i=0}^{n} w_i I_i(\mathbf{r}) \tag{16}$$

3.4 Computational Domain and Boundary Conditions

Figures 1 and 2 and Tables 1 and 2 show the computation domains and inlet conditions for Sandia-E and DLR-B flames.

Fig. 1 Computational domain of Sandia-E flame
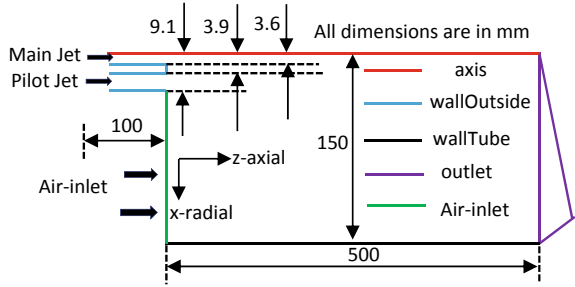
Fig. 2 Computational domain of DLR-B flame
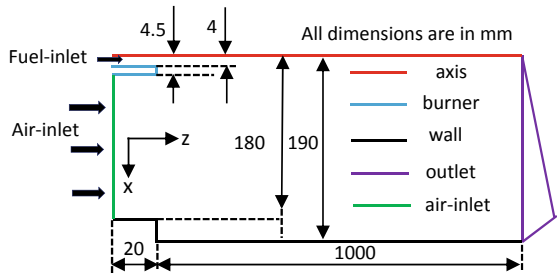
Table 1 Inlet conditions of Sandia-E flame

		Main jet	Pilot jet	Airflow
Temperature		294 K	1880 K	291 K
Velocity		74.4 m/s	17.1 m/s	0.9 m/s
Species mass fractions	CH_4	0.1561	0	0
	O_2	0.1966	0.054000	0.23
	CO_2	0	0.109800	0
	H_2O	0	0.094200	0
	N_2	0.6473	0.734200	0.77
	CO	0	0.004070	0
	H	0	0.000025	0
	H_2	0	0.000129	0
	O	0	0.000747	0
	OH	0	0.002800	0

3.4.1 Sandia-E Flame

The Sandia-E flame is a fuel mixture of methane and air. On a volume basis, the main jet supplies a mixture of methane (25%) and air (75%) into the computational domain. The main jet (diameter = 7.2 mm) is surrounded by a pilot jet (diameter = 18.2 mm), whereas an air-coflow surrounds the pilot. The pilot supplies around 6%

Table 2 Inlet conditions of DLR-B flame

	Species	Fuel inlet	Air inlet
Temperature		292 K	292 K
Velocity		63.2 m/s	0.3 m/s
Species mass fraction	CH_4	0.211770	0
	H_2	0.039985	0
	H_2O	0	0.005008
	N_2	0.748245	0.763149
	O_2	0	0.231843

of energy to the main jet, which helps in combustion. Using the main jet diameter and fuel velocity (74.4 m/s), the calculated Reynolds number for the Sandia-E flame is 33,600. Pre-inlet pipes were added to achieve a fully developed turbulent flow for both the jets. The computational domain is expanded to 69.5D and 20.83D in z- and x-directions. After conducting the mesh independence test, an axis-symmetric mesh with 5080 hexahedral cells and 90 prismatic cells has been adopted for the simulation in AF and OF. A *zeroGradient* boundary conditions are specified for pressure and temperature at all the boundaries except for the pressure at the outlet, which is fixed at 100,000 N/m^2. The boundary conditions for velocity; *noSlip*, *zeroGradient*, and *pressureInletOutletVelocity* is specified at the wallTube, wall, and outlet, respectively.

3.4.2 DLR-B Flame

The DLR flame comprises 22.1% CH_4, 33.2% H_2, and 44.7% N_2 by volume. The diluted CH_4 burns in the presence of H_2 and N_2. Adding hydrogen and nitrogen to methane stabilizes the flame, reduces radiation, and enhances measurement quality. The fuel is surrounded by a low-velocity (0.3 m/s) airflow, and a nozzle (diameter = 140 mm) supplies the air. Based on fuel pipe diameter (D = 8 mm) and fuel velocity (63.2 m/s), the Reynolds number of the DLR-B flame is 22,800.

The computational domain is extended to 127.5D and 23.75D in the axial (z) and radial (x) directions. After satisfying the grid convergence criteria, an axis-symmetric mesh with 3372 hexahedral and 94 prismatic cells was used in AF and OF simulations. Excluding the outlet, *zeroGradient* conditions were applied to other boundaries for the pressure. The *zeroGradient* and *fixed* boundary conditions were applied to the burner and wall for the temperature and velocity. At the outlet, a *fixed-Value*, *inletOutlet*, and *inletOutletVelocity* conditions have been applied for pressure, temperature, and velocity.

4 Results and Discussion

Two turbulent diffusion jet flames (Sandia-E and DLR-B) of different Reynolds numbers have been simulated in OpenFOAM (OF) and AnsysFluent (AF). The standard $k - \varepsilon$ model is used for turbulence closure. The EDC, PaSR, and beta-PDF methods were employed individually to account for TCI. The EDC and PaSR simulations were carried out in OF with *reactingFoam* solver, while beta-PDF in AF. The detailed (36 species) and reduced (20 species PDF table) chemical kinetics were incorporated with the EDC and PaSR models, and the beta-PDF method, respectively.

During AF simulation of the Sandia-E flame with beta-PDF, due to the nature of the two separate jets consisting of fuel and pilot, the mean mixture fraction for fuel is assumed to be unity while the secondary mixture fraction of the pilot is set to be one. However, for the DLR-B flame, the mean mixture fraction of the fuel is assumed to be one and zero for the fuel and air, respectively

The temperature and velocity contours of flames are shown in Figs. 3 and 4, respectively. The peak temperatures attained by the flames are 2017 K and 1870 K for Sandia-E and DLR-B, respectively

The flame temperatures and species concentrations of methane with individual schemes along the axial and radial directions are compared with available experimental results from the TNF workshop, as shown in Figs. 5, 6 and 7. All the results predicted by the P_1 and DO methods are in very close agreement whenever the same TCI model is applied. The beta-PDF models the experimental results better when $C_{\varepsilon 1}$ changed from 1.44 to 1.6.

Overall, the axial temperature distribution with all the TCI models follows a similar trend for both the flames, as shown in Fig. 5. However, for PaSR and EDC, the results of axial peak temperature in the upstream regions are the same, with a significant deviation in the downstream. There is a slight upward movement and a downstream shift in the peak temperature with PaSR. The beta-PDF and EDC give the best results for Sandia-E and DLR-B flames, respectively.

Fig. 3 a, b Temperature (K) contour of flames
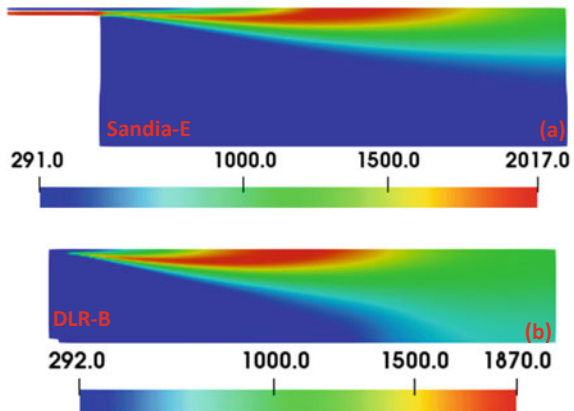
Fig. 4 a, b Velocity (m/s)
contour of flames
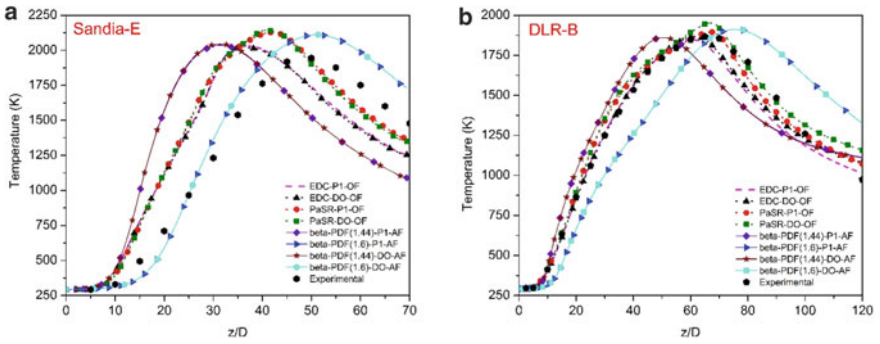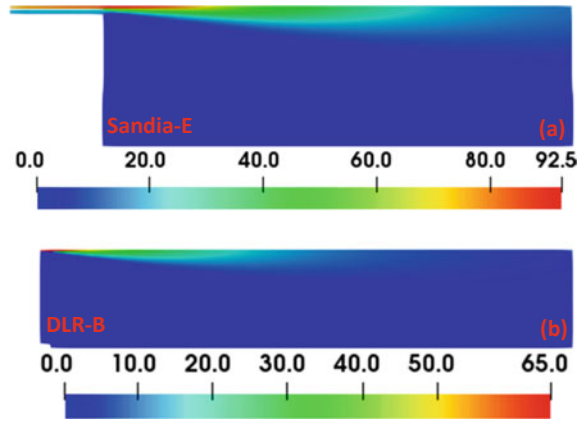
Fig. 5 a Comparison of axial flame temperature. **b** Comparison of axial flame temperature
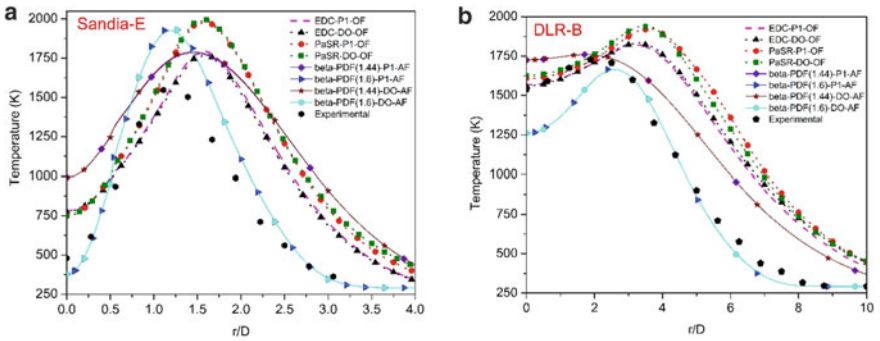
Fig. 6 a Comparison of radial flame temperature. **b** Comparison of radial flame temperature
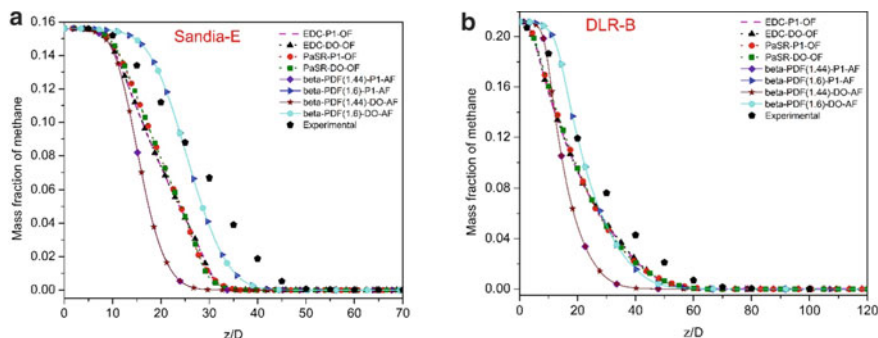
Fig. 7 a Comparison of mass fraction of CH_4 in the axial direction. **b** Comparison of mass fraction of CH_4 in the axial direction

The radial temperature distribution of both flames shows similar behavior to all the TCI models, with minor differences. The peak radial temperatures are slightly higher in the PaSR than with other models. The radial temperature obtained with beta-PDF is very close to experimental results for both the flames, as shown in Fig. 6.

The axial distribution of methane shows a pretty similar picture with EDC and PaSR, while a slight variation was observed with beta-PDF. Figure 7 shows that, once again, the beta-PDF best fits the experimental data.

5 Conclusions

The Sandia-E and DLR-B flames are simulated with three different TCI models to examine the effects of turbulence on the chemical kinetics. The radiative properties of gray-gas mixtures were modeled using the P_1 and discrete ordinates methods. The results show that using the same TCI with standard turbulence and radiation models predicts nearly identical results within the same CFD codes. The P_1 and DO models show their potential to simulate the diffusion jet flames with great precision. The modification in the constant ($C_{\varepsilon 1}$) of the standard turbulence model from 1.44 to 1.6 significantly impacts the results. Overall, the beta-PDF has proven to be a suitable TCI model among others for both the flames. However, with DLR-B, the EDC seems to be the best fit only for the axial temperature.

References

1. Haworth DC (2010) Progress in probability density function methods for turbulent reacting flows. Prog Energy Combust Sci 36(2):168–259
2. Kumar N, Dilawari V, Bansal A (2020) Chemical equilibrium analysis of energetic materials using particle swarm optimization. Fluid Phase Equilib 522:112738

3. Kumar N, Suktel P, Bansal A (2019) Combustion analysis of premixed laminar burner flame in OpenFoam, Paper No. IHMTC2019–768, 25th National and 3rd International ISHMT-ASTFE Heat and Mass Transfer Conference, December 28–31, 2019, IIT Roorkee, Uttarakhand, India, pp. 937–940

4. Wang H, Chen Y (2010) PDF modelling of non-premixed combustion with detailed chemistry. Prog Energy Combust Sci 59(16):3477–3490

5. Lewandowski MT, Pozorski J (2016) Assessment of turbulence-chemistry interaction models computation of turbulent non-premixed flame. J Phys Conf Ser 760(1):01215

6. Magnussen BF (1981) On the structure of turbulence and a generalized eddy dissipation concept for chemical reaction in turbulent flow, 19th aerospace science meeting, 12–15 January 1981, St. Louis, MO, USA

7. Berglund M, Fedina E, Fureby C, Tegner J, Sabel'nikov V (2010) Finite rate chemistry large-eddy simulation of self-ignition in supersonic combustion ramjet. AIAA J 48(3):540–550

8. Peters N (1984) Laminar diffusion flamelet models in non-premixed turbulent combustion. Prog Energy Combust Sci 10(3):319–339

9. Klimenko AY (1990) Multicomponent diffusion of various admixtures in turbulent flow. Fluid Dyn 25(3):327–334

10. Pope SB (1985) PDF methods for turbulent reactive flows. Prog Energy Combust Sci 11(2):119–192

11. GRI-Mech website. http://combustion.berkeley.edu/gri-mech/

12. Lucchini T, D'Errico G, Contino F, Jangi M (2014) Towards the use of eulerian field PDF methods for combustion modeling in IC engines. SAE Int J Engines 7(1):286–296

13. Kumar N, Bansal A (2022) Combustion and radiation modeling of non-premixed turbulent DLR-A flame, Paper No. ICFTES-2022–TS-145. In: 1ts International conference in fluid, thermal and engineering systems, 9–11 June 2022, NIT Calicut, India

14. Kumar N, Bansal A (2022) Radiation modeling on methanol whirling flame, pp. 253–261, Paper No. TFEC-2022–41140. In: 7th thermal and fluid engineering conference, 15–18 May 2022, Las Vegas, NV, USA

15. Kumar N, Bansal A (2022) Non-gray radiation modeling of methanol swirling flame, Paper No. CONV-22–A61. In: 5th international symposium on convective heat and mass transfer, 5–10 June 2022, İzmir, Turkey, pp 563–570

16. Tien CL, Lee SC (1982) Flame radiation. Prog Energy Combust Sci 8(1):41–59

17. Modest MF (2003) Radiative heat transfer. Academic Press, California

18. Barlow RS, Frank JH (1998) Effects of turbulence on species mass fractions in methane/Air jet flames. Symp (Int) Combust 27(1):1087–1095

19. TNF Workshop (1998) Third international workshop on measurement and computation of turbulent non-premixed flames, Colorado, USA. http://www.ca.sandia.gov/TNF/abstract.html

20. Yang X, He Z, Dong S, Tan H (2017) Combustion characteristics of bluff-body turbulent swirling flames with coaxial air microjet. Energy Fuels 31(12):14306–14319

21. Dally BB, Karpetis AN, Barlow RS (2002) Structure of turbulent non-premixed jet flames in a diluted hot coflow. Proc Combust Inst 29(1):1147–1154

22. Pope SB (1978) An explanation of the turbulent round-jet/plane-jet anomaly. AIAA J 16(3):279–281

Effects of Nanoparticle Shapes on SiO_2-engine Oil Nanofluid Flow and Heat Transfer Over a Stretchable Rotating Disk

Amit Kumar Pandey and Abhijit Das

Nomenclature

F	Radial velocity
G	Tangential velocity
H	Axial velocity
θ	Temperature
ϕ	Volume fraction parameter
S	Stretching parameter
Nu	Nusselt number
Cf	Skin friction coefficient
Pr	Prandtl number
m	Shape factor.

1 Introduction

The flow and heat transfer caused by a rotating disk is a classical problem in fluid mechanics due to its practical applications in engineering and industrial fields like thermal power generating systems, rotating machinery, food processing, medical equipment, etc. In 1921, von Kármán [1] performed the first study on the steady flow of an incompressible, viscous fluid due to an infinite rotating disk. He introduced his well-known similarity transformations, in order to convert the physically modeled partial differential equations into simple ordinary differential equations. After von Kármán's pioneer work, numerous theoretical/experimental studies have been done

A. K. Pandey (✉) · A. Das
Department of Mathematics, NIT-Tiruchirappalli, Tiruchirappalli, Tamil Nadu 620015, India
e-mail: amitpandey754703@gmail.com

by many researchers on flows induced by rotating disk [2, 3]. In a recent work, the boundary-layer flow caused by a rotating disk was studied by Griffiths [4] for various generalized Newtonian fluid models. Fang [5] was the first to extend the von Kármán flow for a rotating disk which was stretchable. The flow as a result of stretchable rotating disk is investigated by numerous researchers due to its major applications in various industrial processes, including the production and drawing of plastic and rubber sheets, extrusion of metals and polymers, paper production etc. [6, 7]. The recent articles [8, 9] produced analytical solutions and discussed the effects of surface stretching on some rotating disk flow problems. Nanofluids, a novel classification of heat transfer fluids, are engineered colloids made of base fluid and nanoparticles (particles < 100 nm in diameter). Choi [10] coined the term "nanofluids" and had shown that suspending nanoparticles in conventional fluids increases the thermal conductivity which directly makes such fluid applicable to thermal management systems. Oxides like silica, alumina, titania, etc., and metals like copper, silver, and gold are often used as nanoparticles. And for base fluids, water and organic fluids such as ethanol are popularly used [11]. Nanofluids are found to have abnormally high thermal conductivity, viscosity, and single-phase convective heat transfer coefficient relative to the base fluid [12, 13]. These properties make nanofluids useful in a broad range of engineering applications such as cooling engines in transportation, as well as in the production and fabrication industries in order to cool down the welding equipment. It is also used to enhance the thermal transport of lubricants and coolants. A comprehensive review on the mechanism of heat transport in nanofluids can be found in [14]. Due to the aforementioned applications, many researchers [15, 16] have been working extensively in this area to inspect the flow as well as the heat transfer properties of nanofluids. Recently, Yin et al. [17] considered three categories of nanoparticles, viz. Cu, Al_2O_3, and CuO with water-based nanofluid to study the effects of radial stretching on the flow and heat transfer of nanofluids as a result of rotating disk. Many researchers have noted that, except for nanoparticle categorization, dimension, agglomeration, and concentration, thermophysical properties of the nanofluids are significantly affected by the nanoparticle structure [18, 19]. The effect of various shapes of nanoparticles on the SiO_2 nanofluid flow along with the heat transfer in a liquid film over a stretching sheet was investigated by Sobia et al. [20]. Recently, Saranya et al. [21] studied the effect of various shapes on Al_2O_3-silicon oil nanofluid flow on a radially stretching rotating disk. More recently, the performance of SiC and SiO_2 nano-powders in the engine oil base flow on a rotating disk with thermal jump constraints was investigated by Iqbal et al. [22]. Given its strong propensity to be evenly dispersed in nanofluids and nanolubricants, SiO_2 has a leading position among all nanoparticles. According to [23], SiO_2 nanoparticles are known to have low toxicity, good thermal stability, and can be synthesized easily. Besides, its particle size, crystallinity, porosity, and shape can be precisely manipulated. Hence, among all nanomaterials, SiO_2 is a better choice due to its low cost, easy availability, and excellent thermophysical property. Due to aforementioned properties silicate-based nanomaterials have drawn more research attention. Applications for it can be found across a wide range of industries, including industrial engineering, thin film substrates, thermal insulators,

catalytic pigments, and humidity sensors [22, 24]. The present work deals with the traditional rotating disk flow, with the exception that the disk is stretchable and the flow is made of silicon dioxide suspended in engine oil base fluid. To find the best- performing solution, the flow and heat transfer parameters are affected by the presence of five different shaped SiO_2 nanoparticles namely, sphere, brick, cylinder, platelet, and blade. It is assumed that all differently shaped nanoparticles are of equivalent spherical diameter $dp = 45$ nm. The effects of stretching and volume fraction parameters on the velocity and temperature profiles are also analyzed. In addition, the effect of different shapes and stretching parameter on the Nusselt number and skin friction are carefully investigated.

2 Methodology

Consider the flow of an axially symmetric, incompressible nanofluid on a rotating disk, which rotates about its axis with an angular velocity, Ω and positioned at $z = 0$. The disk is expanding farther in the radial direction r with a constant rate s. Revising the nanofluid model put out by Tiwari and Das [12], the governing equations for nanofluid flow and pressure, in a rotating frame of reference, can be written as

$$u_r + \frac{u}{r} + w_z = 0, \tag{1}$$

$$uu_r + wu_z - \frac{(v + r\Omega)^2}{r} = \frac{1}{\rho_{nf}} p_r + \frac{\mu_{nf}}{\rho_{nf}} \left(u_{rr} + \frac{1}{r}u_r - \frac{u}{r^2} + u_{zz} \right), \tag{2}$$

$$2u\Omega + uv_r + wv_z + \frac{uv}{r} = \frac{\mu_{nf}}{\rho_{nf}} \left(v_{rr} + \frac{1}{r}v_r - \frac{v}{r^2} + v_{zz} \right), \tag{3}$$

$$uw_r + ww_z = -\frac{1}{\rho_{nf}} p_z + \frac{\mu_{nf}}{\rho_{nf}} \left(w_{rr} + \frac{1}{r}w_r + w_{zz} \right), \tag{4}$$

$$uT_r + wT_z = \alpha_{nf} \left(T_{rr} + \frac{1}{r}T_r + T_{zz} \right), \tag{5}$$

with corresponding boundary conditions:

$$u(0) = sr, \ v(0) = \Omega r, \ w(0) = 0, \ T(0) = T_w,$$
$$u \to 0, \ v \to 0, \ T \to T_\infty \ as \ z \to \infty. \tag{6}$$

The velocity components are given by its constituent parts, (u, v, w) in the direction of rising (r, θ, z), respectively. The pressure term is denoted by p, T is temperature with T_w and T_∞ standing for the conditions at the wall and the ambient environment, respectively.

The thermophysical properties of SiO$_2$ and engine oil are given in Table 1. The viscosity and shape factor of the nanoparticles are given in Table 2. In (7), the nanofluid's density, dynamic viscosity, and thermal diffusivity are denoted by the letters ρ_{nf}, μ_{nf}, and α_{nf} respectively, and nanofluid's heat capacitance, effective thermal conductivity are given by $(\rho C_p)_{nf}$, k_{nf}, respectively. Here, ϕ represents the nanoparticle volume fraction parameter, μ_f stands for fluid fraction viscosity, and ρ_s, ρ_f denotes the solid fractions and density of the fluid, respectively [16].

$$\rho_{nf} = \rho_s \phi + \rho_f (1 - \phi),$$
$$\mu_{nf} = \mu_f \left(1 + A_1 \phi + A_2 \phi^2\right),$$
$$\alpha_{nf} = \frac{k_{nf}}{(\rho C_p)_{nf}},$$
$$(\rho C_p)_{nf} = (1 - \phi)(\rho C_p)_f + \phi(\rho C_p)_s,$$
$$\frac{k_{nf}}{k_f} = \frac{k_s + (m-1)k_f - (m-1)(k_f - k_s)\phi}{k_s + (m-1)k_f + (k_f - k_s)\phi}. \tag{7}$$

Using the similarity variables given by von Kármán [1],

$$\eta = z\left(\Omega/v_f\right)^{1/2}$$
$$(u, v, w) = \left(r\Omega F(\eta), r\Omega G(\eta), \left(\Omega/v_f\right)^{1/2} H(\eta)\right),$$
$$(p, T) = \left(2\Omega \mu_f P(\eta), T_\infty + \theta(T_w - T_\infty)\right), \tag{8}$$

the Systems (1)–(5) are converted to the following ordinary differential equations:

$$H' + 2F = 0$$

Table 1 Experimental results on thermophysical properties for engine oil and SiO_2 [22]

Nanoparticle/Base fluid	Density ρ (kg/m^3)	Specific heat C_p (J/ kg K)	Thermal conductivity k (W/m K)
Engine-oil	884	1910	0.144
SiO_2	2200	703	1.2

Table 2 Experimental results on viscosity constants and shape factor for different nanoparticles [20]

Nanoparticles/Parameters	Sphere	Brick	Cylinder	Platelet	Blade
A_1	2.5	1.9	13.5	37.1	14.6
A_2	6.2	471.4	904.4	612.6	123.3
m	3.0	3.72	4.82	5.72	8.26

$$C_\phi F'' - F^2 + (G+1)^2 - H F' = 0$$
$$C_\phi G'' - 2F(G+1) - H G' = 0$$
$$\frac{\nu_{nf}}{\nu_f} H'' - H H' - 2\frac{\rho_f}{\rho_{nf}} P' = 0$$
$$\frac{C_\theta}{P_r}\theta'' - H\theta' = 0 \tag{9}$$

In (9), the Prandtl number Pr is given by $\mu_f C_{pf}/k_f$, and prime represents the derivative with respect to η. Physical parameters C_ϕ and C_θ are given as

$$C_\phi = \frac{1 + A_1\phi + A_2\phi^2}{(\rho_s/\rho_f)\phi + 1 - \phi}$$
$$C_\theta = \frac{k_{nf}/k_f}{(\rho C_p)_{nf}/(\rho C_p)_f} \tag{10}$$

The boundary conditions (6) are transformed into

$$F(0) = s/\Omega = S, \, G(0) = 0, \, \theta(0) = 1,$$
$$F \to 0, \, G \to -1, \, \theta \to 0, \quad as \ z \to \infty \tag{11}$$

The nanofluid pressure term can be simply integrated from the 3rd momentum equation because it is separated from the flow field, which is why it is not described here.

The tangential shear stress τ_θ and the radial shear stress τ_r are determined by using the Newtonian formulas once the mean flow quantities have been solved and are given by

$$\tau_\theta = \mu_{nf}(v_z)|_{z=0} = \frac{\Omega^{3/2} r\mu_f}{\nu_f^{1/2}}\left(1 + A_1\phi + A_2\phi^2\right)G'(0),$$

$$\tau_r = \mu_{nf}(u)|_{z=0} = \frac{\Omega^{3/2} r\mu_f}{\nu_f^{1/2}}\left(1 + A_1\phi + A_2\phi^2\right)F'(0),$$

which both results in the skin friction coefficient

$$C_f = \frac{\sqrt{\tau_r^2 + \tau_\theta^2}}{\rho_f(\Omega r)^2} = \left(\frac{\Omega r^2}{\nu_f}\right)^{-1/2}\left(1 + A_1\phi + A_2\phi^2\right)\left(F'(0)^2 + G'(0)^2\right).$$

Next, the Fourier's law is used to determine the rate of heat transfer

$$q = -k_{nf} T_z|_{z=0},$$

and the scaled (by the factor $\left(\Omega r^2/\nu_f\right)^{-1/2}$) Nusselt number can be calculated from

$$N_u = -\frac{k_{nf}}{k_f}\theta'(0).$$

A. Validation

A convenient BVP4C scheme is opted to solve the ordinary differential Equations (9)–(11). The BVP4C technique can be interpreted as a continuous extension of the implicit Runge-Kutta formula or as collocation with a C^1 piece-wise cubic polynomial (interpolant). The fundamental approach of BVP4C is a widely used Simpson's method. The suggested BVP4C technique is well-liked in the research community because of its key advantages, which include faster convergence with less error, direct acceptance of both two-point and multi-point BVPs with improved accuracy [25, 26]. To apply BVP4C technique, Equations (9)–(11) are reduced into system of equations by substituting:

$H = y_1,\ F = y_2,\ F' = y_3,\ G = y_4,\ G' = y_5,\ \theta = y_6,\ and\ \theta' = y_7$. A first order system of equations is given by

$$y_1' = -2y_2,$$
$$y_2' = y_3,$$
$$y_3' = \frac{y_2^2 - (y_4 + 1)^2 + y_1 y_3}{C_\phi},$$
$$y_4' = y_5,$$
$$y_5' = \frac{2y_2(y_4 + 1) + y_1 y_5}{C_\phi},$$
$$y_6' = y_7,$$
$$y_7' = \frac{y_1 y_7 Pr}{C_\theta}, \tag{12}$$

with the boundary conditions:

$$y_1 = 0,\ y_2 = S,\ y_4 = 0,\ y_6 = 1,\ \text{at } z = 0,$$
$$y_2 \to 0,\ y_4 \to -1,\ y_6 \to 0,\ \text{as } z \to \infty. \tag{13}$$

Numerical results are calculated by keeping the error tolerance $\epsilon = 10^{-9}$ and $Pr = 6.2$. These numerical results are verified with those obtained by spectral local linearization (SLLM) method. The spectral method [27] is used with 30 collocation points. Additionally, these solutions are compared with the existing literature. Table 3 shows that these comparisons are in absolute agreement.

Table 3 Comparison of BVP4C with numerical solutions at $\phi = 0$, S $= 0$ and Pr $= 6.2$

	M. Turkyilmazoglu [16]	BVP4C	SLLM
$F^{'}(0)$	0.51023262	0.510214	0.510214
$-G^{'}(0)$	0.61592210	0.615910	0.615910
$-H(\infty)$	0.88447411	0.881359	0.882296
$-\theta^{'}(0)$	0.93387794	0.933848	0.933847

3 Results and Discussion

The velocity and temperature distributions of different shapes of SiO_2 nanoparticles are investigated and graphically presented for a selected value of $Pr = 6.4$. These results are obtained by solving the systems (12)–(13) by the BVP4C technique within 10^{-9} absolute and relative error tolerance. It is observed that for each shape of nanoparticles considered in this study, the radial velocity component attains its maximum near the disk and decays to zero as one drift away from the disk. This means that the fluid closure to the disk is thrown outward radially as a consequence of centrifugal forces and stretching. The component of axial velocity, $H(\eta)$, is found negative for all η, which means that the radially outward flow is compensated via axial inward flow which is toward the disk. The component of tangential velocity, $G(\eta)$, is decaying exponentially in a monotonic nature with η. These observations are in line with previously published results [28].

Figure 1 shows the effects of stretching parameter, S, on velocity components in the radial $F(\eta)$, tangential $G(\eta)$ and the negative axial $H(\eta)$ directions for differently shaped SiO_2 nanoparticles. It is noticed that an increase in the value of the stretching parameter leads to an increase in the radial and negative axial velocity, whereas it decreases the tangential velocity component. It is also noted that the platelet-shaped nanoparticle has a greater impact on the stretching parameter, whereas spherical nanoparticles have the least. The effects of volume fraction ϕ on the velocity profiles are depicted in Fig. 2. It is observed that with an increase in nanoparticle volume fraction parameter, there is a decrease in the radial velocity component near the disk until a point of crossover after which it shows an opposite behavior. This behavior of the radial velocity component is compensated by the component of the axial velocity $H(\eta)$ as expected. Contrary to the effect of stretching parameter, the tangential velocity component $G(\eta)$ increases for the increasing value of ϕ.

Furthermore, we noticed that the platelet shape and cylinder shape nanoparticles demonstrate almost similar growth on velocity components but more than bricked shape nanoparticle followed by blade shape nanoparticles with the least effects shown by the spherical nanoparticle.

Figure 3 shows impact of the stretching parameter S on temperature profile for different nanoparticles. The temperature profile is plotted for a selective value of $\phi = 0.050$ and Prandtl number $Pr = 6.4$. For all the shapes considered here, the temperature is found to gradually decrease from its starting value to the limiting value with η and is observed to decrease with increasing value of stretching parameter S. The
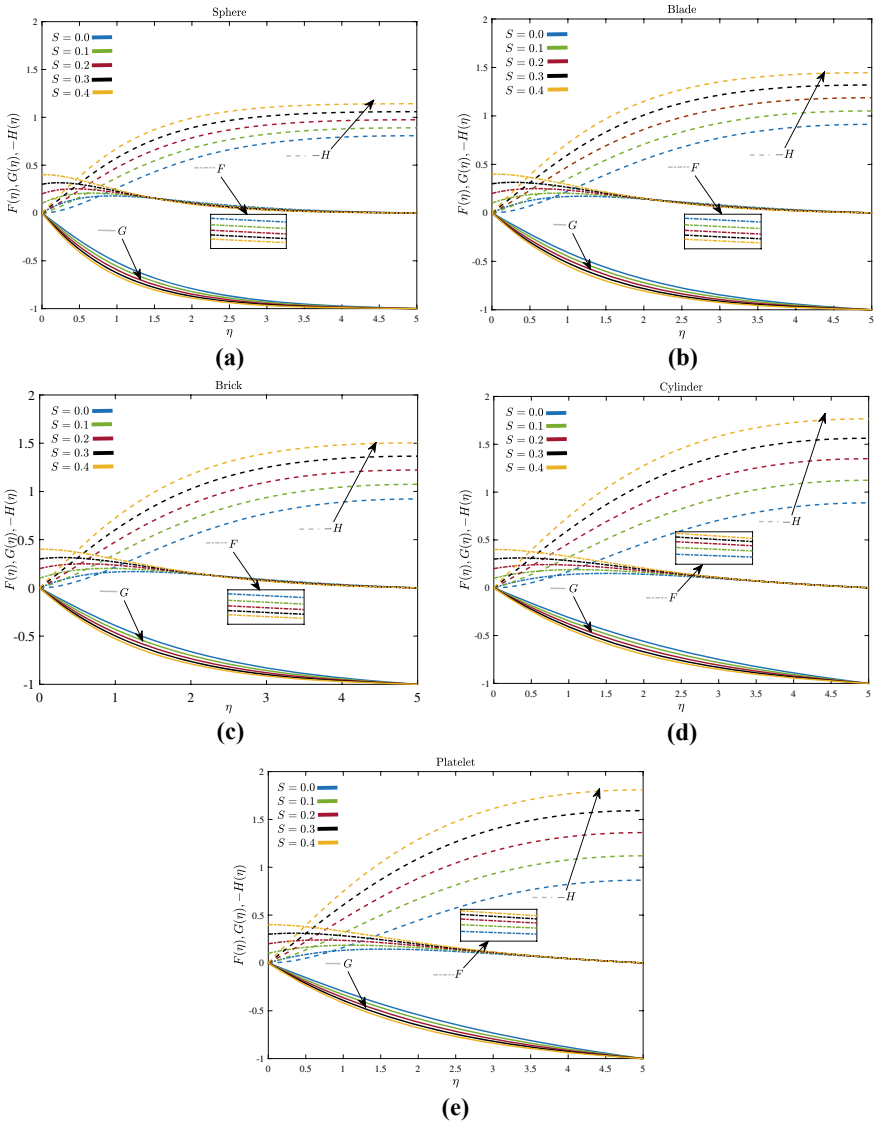
Fig. 1 Velocity profiles for varying stretching parameter S

platelet shape has a greater physical impact on the temperature profile than others to compare the shape effect. Figure 4 shows the physical impact of the nanoparticle volume fraction parameter, ϕ. The temperature profile is plotted for a selective value of $S = 0.1$ and $Pr = 6.4$. It is observed that as the weight percentage of nanoparticles in the base fluid increases, the temperature of the nanofluid also increases for all the shapes. This is because thermal conductivity is an increasing function of nanoparticle
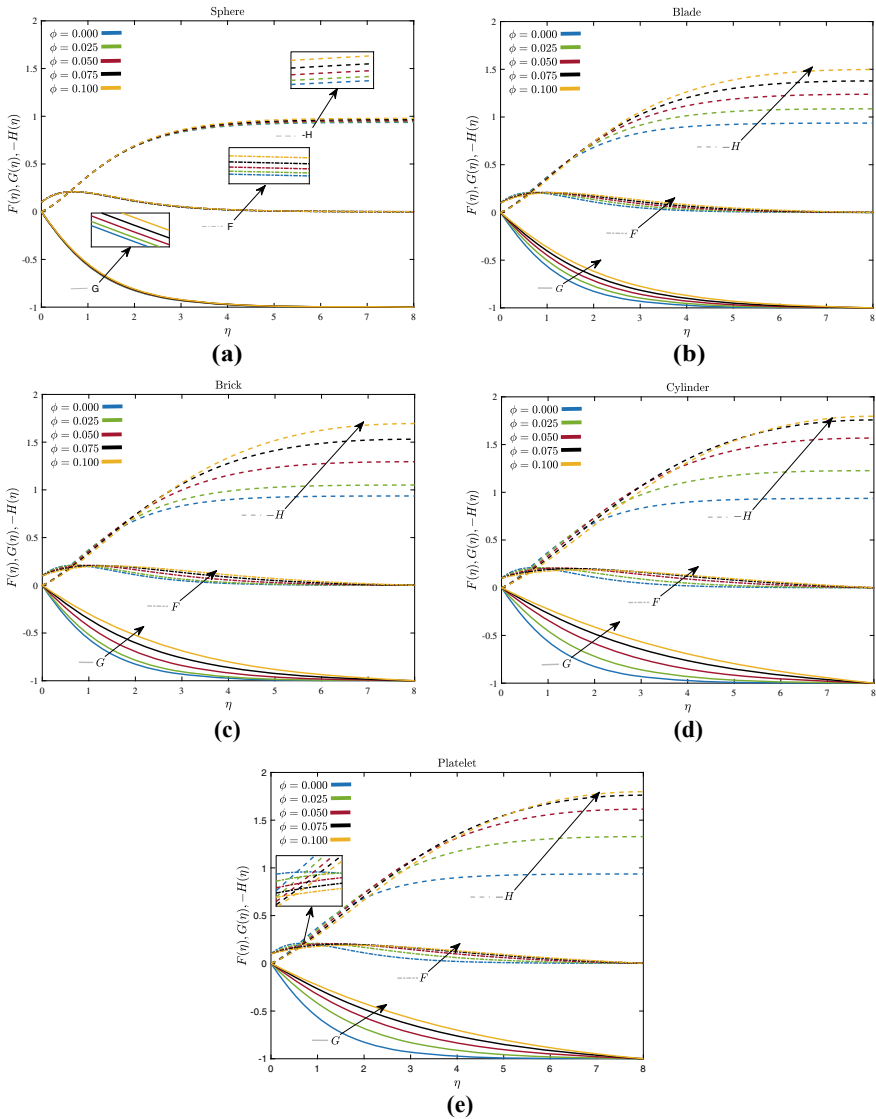
Fig. 2 Velocity profiles for varying volume fraction ϕ

volume fraction ϕ. The impact of stretching parameter S on the skin friction coefficient C_f and local Nusselt number Nu, for five different shaped SiO_2 nanoparticles, is shown in Figs. 5 and 6, respectively. It is observed that these parameters increase almost linearly with the nanoparticle volume fraction. Also, they increase along with the value of the stretching parameter, S.
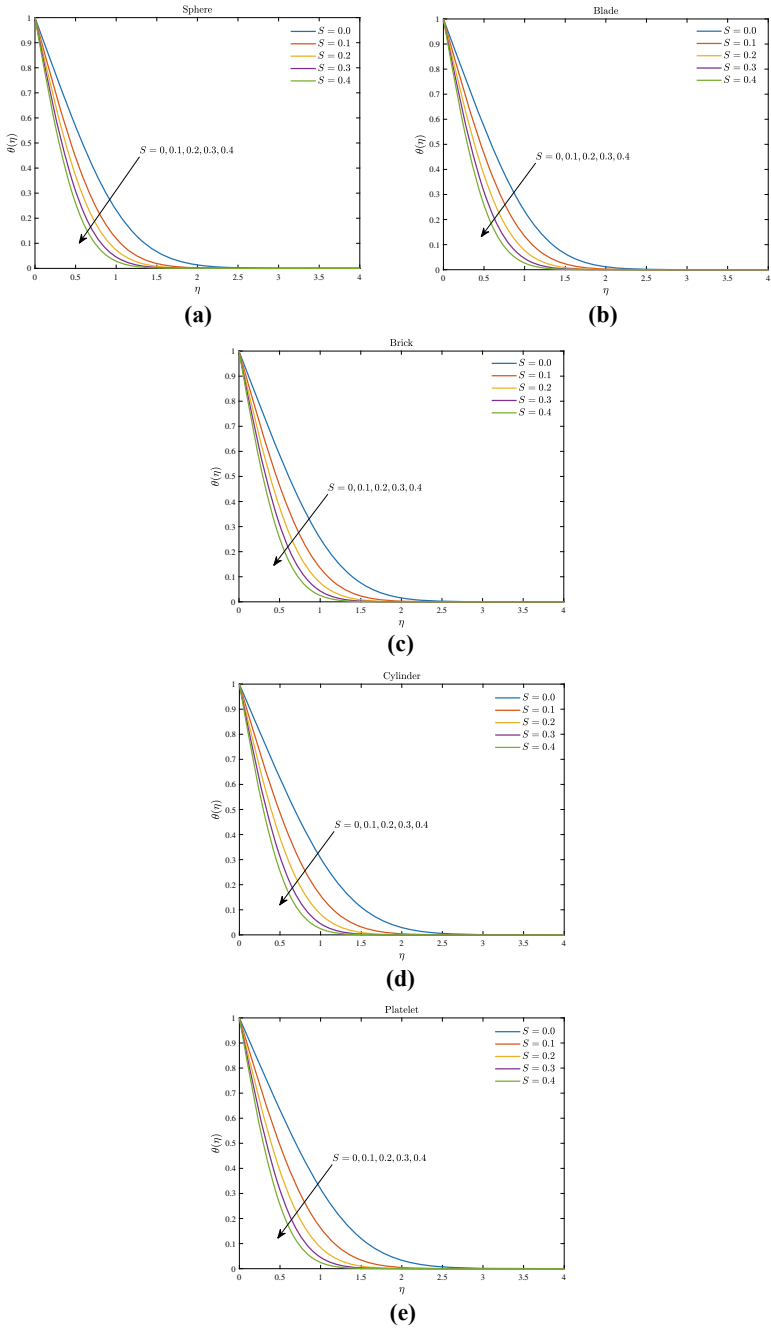
Fig. 3 Temperature profile for varying stretching parameter S
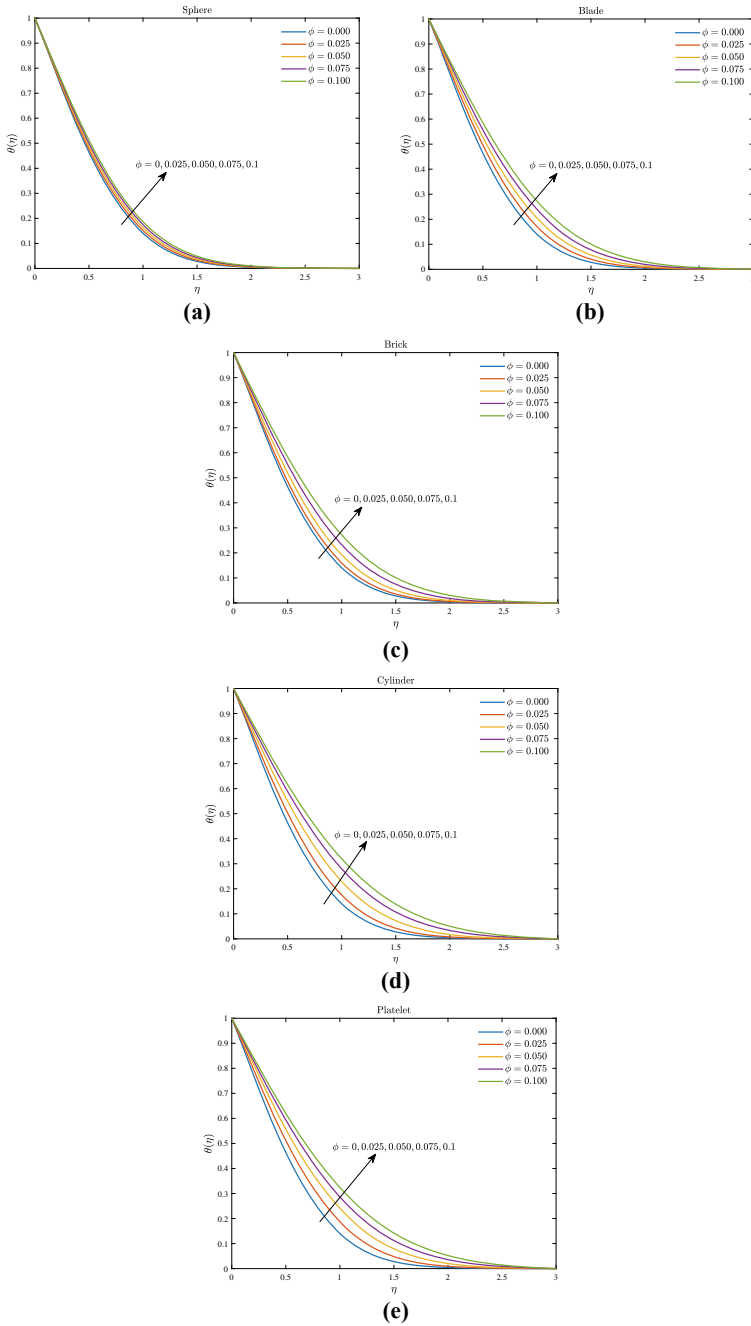
Fig. 4 Temperature profile for varying volume fraction ϕ

Fig. 5 Variation of skin
friction versus ϕ
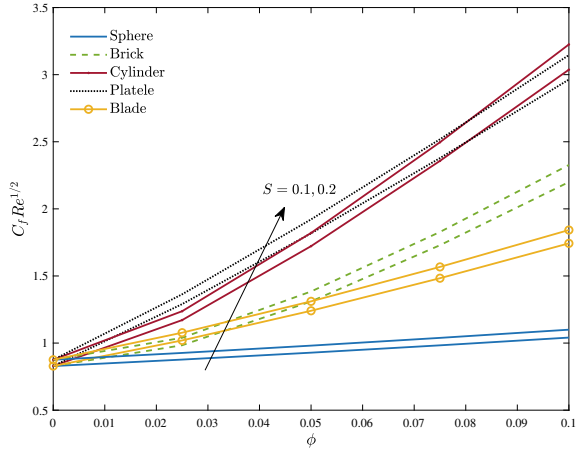
Fig. 6 Variation of Nusselt
number versus ϕ
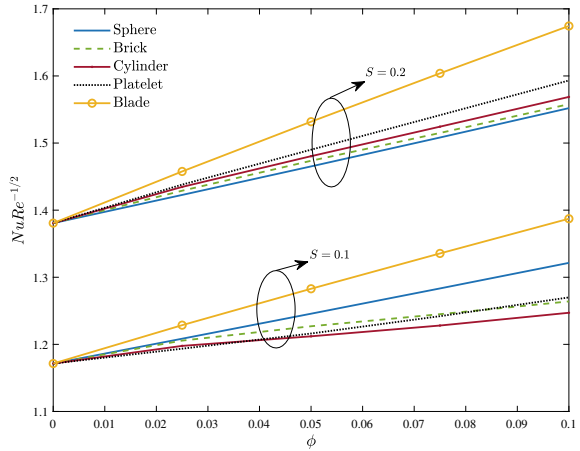
4 Conclusions

The effect of stretching and volume fraction parameters on the velocity as well as
temperature profiles are investigated and represented graphically for five different
shaped SiO_2 nanoparticles. It is noteworthy that platelet-shaped nanoparticle has
more effects on physical profiles with the sphere shaped having least. Below
discussed are some significant results of the ongoing study.

- The velocity profiles of SiO_2 nanoparticle attain its maximum for platelet shape
  followed by cylinder shape nanoparticle and its minimum for sphere shape.
- An increase in the value of volume fraction parameter causes an increase to the
  temperature profile, whereas it decreases with the stretching parameter for all the
  shapes.

- Skin friction coefficient and Nusselt number increase almost linearly along with the nanoparticle volume fraction as well as stretching parameter.

References

1. Ka´rma´n T, Laminare U, Reibung T (1921) ZAMM-J Appl Math Mech/Zeitschrift fu¨r Angew Math Mechanik 1(4):233–252
2. Benton ER (1966) On the flow due to a rotating disk. J Fluid Mech 24(4):781–800
3. Lingwood RJ (2013) An experimental study of absolute instability of the rotating-disk boundary-layer flow. J Fluid Mech 314:373–405.
4. Griffiths PT (2015) Flow of a generalised newtonian fluid due to a rotating disk. J Non-Newton Fluid Mech 221:9–17
5. Fang T (2007) Flow over a stretchable disk. Phys Fluids 19(12), 128105
6. Altan T, Oh S-I, Gegel G (1983) Metal forming fundamentals and applications. Am Soc Met (1983):353
7. Fisher EG (1976) Extrusion of plastics
8. Das A, Sahoo B (2018) Flow and heat transfer of a second grade fluid between two stretchable rotating disks. Bull Braz Math Soc New Ser 49(3):531–547
9. Das A, Sarkar S (2020) Flow analysis of reiner–rivlin fluid between two stretchable rotating disks. In: Recent trends in wave mechanics and vibrations. Springer, Berlin, pp 61–70
10. Choi SUS, Eastman JA (1995) Enhancing thermal conductivity of fluids with nanoparticles. Tech. report, Argonne National Lab.(ANL), Argonne, IL (United States)
11. Buongiorno J (2006) Convective transport in nanofluids
12. Tiwari RK, Das MK (2007) Heat transfer augmentation in a two-sided lid-driven differentially heated square cavityutilizing nanofluids. Int J Heat Mass Transf **50**(9–10):2002–2018
13. Pak BC, Cho YI (1998) Hydrodynamic and heat transfer study of dispersed fluids with submicron metallic oxide particles. Exp Heat Transf Int J 11(2):151–170
14. Chandrasekar M, Suresh S (2009) A review on the mechanisms of heat transport in nanofluids. Heat Transfer Eng 30(14):1136–1150
15. Roy G,Nguyen CT, Lajoie P-R (2004) Numerical investigation of laminar flow and heat transfer in a radial flow cooling system with the use of nanofluids. Superlattices Microstruct 35(3–6):497–511
16. Turkyilmazoglu M (2014) Nanofluid flow and heat transfer due to a rotating disk. Comput Fluids 94:139–146
17. Yin C, Zheng L, Zhang C, Zhang X (2017) Flow and heat transfer of nanofluids over a rotating disk with uniform stretching rate in the radial direction. Propul Power Res 6(1):25–30
18. Sobamowo G (2019) Free convection flow and heat transfer of nanofluids of different shapes of nano-sized particles over a vertical plate at low and high prandtl numbers. J Appl Comput Mech 5(1):13–39
19. Timofeeva EV, Routbort JL, Singh D (2009) Particle shape effects on thermophysical properties of alumina nanofluids. J Appl Phys 106(1):014304
20. Bibi S, Elahi Z, Shahzad A (2020) Impacts of different shapes of nanoparticles on Sio_2 nanofluid flow and heat transfer in a liquid film over a stretching sheet. Phys Scr 95(11):115217
21. Saranya S, Al-Mdallal QM (2021) Computational study on nanoparticle shape effects of Al_2O_3-silicon oil nanofluid flow over a radially stretching rotating disk. Case Stud Therm Eng 25:100943

22. Iqbal Z, Azhar E, Maraj EN (2021) Performance of nano- powders sio2 and sic in the flow of engine oil over a rotating disk influenced by thermal jump conditions. Phys A Stat Mech Appl 565:125570
23. Bahari NM, Hussein SNCM, Othman NH (2021) Synthesis of al_2o_3–sio_2/water hybrid nanofluids and effects of surfactant toward dispersion and stability, Part Sci Technol 39(7):844–858
24. Zhang L, Zhang A, Jing Y, Qu P, Wu Z (2021) Effect of particle size on the heat transfer performance of sio2– water nanofluids. J Phys Chem C 125(24):13590–13600
25. Shampine LF, Kierzenka J, Reichelt MW et al (2000) Solving boundary value problems for ordinary differential equations in matlab with bvp4c. Tutorial Notes 2000:1–27
26. Kierzenka J, Shampine LF (2001) A bvp solver based on residual control and the maltab pse. ACM Trans Math Softw (TOMS) 27(3):299–316
27. Motsa SS (2013) A new spectral local linearization method for nonlinear boundary layer flow problems. J Appl Math
28. DasA, Bhuyan SK (2018) Application of ham to the von ka´rma´n swirling flow with heat transfer over a rough rotating disk. Int J Appl Comput Math **4**(5):1–15

Influence of Geometric Parameters on Power Generation from a Thermoelectric Module

Dakesh Sahu, Keyur Kansara, and Shobhana Singh

Nomenclature

α_p, α_n	P- And n-type leg Seebeck coefficient [V/K]
ρ_p, ρ_n	P- And n-type leg resistivity [Ω m]
k_p, k_n	P- And n-type leg thermal conductivity[W/mK]
R	Total electrical resistance [Ω]
K	Total thermal conductance [W/mK]
L_p, L_n	P- And n-type leg length [m]
A_p, A_n	P- And n-type leg cross-section area [m^2]
Q_h, Q_c	Heat supplied, Heat rejected [W]
R_l	Load resistance [Ω]
ρ	Density [Kg/m^3]
C_p	Specific heat [J/KgK]
Q	Heat source [W/m^3]
Q_{ted}	Thermoelastic effects [Pa/s]
Q_j	Current source [A/m^2]
q	Heat flux in conduction [W/m^2]
T	Absolute temperature [K]
P	Peltier coefficient [J/Couloumb]
J	Induced electric current [A/m^2]
J_e	External current source [A/m^2]
E	Electrical field [V/m]
V	Electric potential [V]
α	Seebeck coefficient [V/K]

D. Sahu · K. Kansara · S. Singh (✉)
Department of Mechanical Engineering, IIT Jodhpur, Jodhpur 342037, India
e-mail: shobhana@iitj.ac.in

σ Electrical conductivity [$1/\Omega$ m]
I Electric current [A]
n Number of TE element pairs

1   Introduction

The increasing demand for energy requirement by the human population leads to an imbalance in environmental energy resources. Conventional energy resources fulfill the needs for energy demand, but due to excessive use of traditional energy sources, they are degrading very fast. Using conventional energy resources leads to global warming and greenhouse emission of gases. Energy crises and environmental pollution lead researchers to investigate alternative means of energy resources to cope with the present situation. Thermoelectric devices are one of the best-suited solutions for energy crises. It is a solid-state device through which direct energy conversion of heat energy into electrical energy is possible. Thermoelectric devices work similarly to heat engine devices. It operates between two reservoirs. One of the reservoir acts as a heat source and the other as a heat sink. In a thermoelectric device, no moving parts are present, so an appliance's life is longer, the operation is noiseless, and it is also lightweight. In the working of the thermoelectric device, there is no requirement for any working fluid, so it helps to remove the problem of environmentally harmful gas emissions [1].

The thermoelectric effect works on the principle of Seebeck effect, according to which a circuit is made up of two dissimilar wires; when one of the junctures is hot compared to another juncture, potential difference is produced from the circuit. The thermoelectric device has a great potential for harvesting waste heat from power plants and automobiles. Despite all that salient features, thermoelectric devices are still not used for large-scale applications because of their low-level conversion performance. There are two methods for enhancing the performance of thermoelectric device conversion efficiency. The first is to create highly desirable thermoelectric functional materials, and the second is to develop a more suitable structure for thermoelectric devices [2]. The research work for thermoelectric functional materials is underway. Fan et al. [3] create a mathematical model to find the optimum leg cross-section area and leg length for thermoelectric units and study the effect of leg length and cross-section area of thermoelectric legs on the conversion efficiency, output power, and power density using different thermal boundary conditions. Jia and Guo [2] developed a more realistic structure for thermoelectric devices; thus, the form of instruments becomes a crucial strategy to increase thermoelectric conversion performance. Analyzed the thermoelectric model more practically and studied the model's performance by using time-changing thermal environments. Rezania et al. [4] investigated thermoelectric unicouple to achieve maximum power, the conversion efficiency with the best cost performance with the optimum ratio between the n-type and p-type leg of unicouple over a wide range of n-type and p-type leg ratios and found

that the ratio between cross-section area of the n-type leg to p-type leg is less than 1 to generate maximum power output. Khalil et al. [5] performed numerical study for optimal thermoelectric design. The author evaluated and compared the performance of the thermoelectric device by choosing legs of the same volume and numerous designs. Effects of the cross-section area of leg and leg length on the internal resistance, output power, and thermal conductance of multiple designs of thermoelectric unicouple were calculated and compared. Acquired results show that the rectangular design of the thermoelectric leg provides the best performance compared to other designs. Li et al. [6] studied three dissimilar copper pad thicknesses on the power production of the thermoelectric device and found that variation in thickness of copper pad does not affect the device's power output. Mu et al. [7] developed a three-dimensional finite model of the Mg_2Si-based thermoelectric unicouple for harvesting automobile exhaust surplus heat. Thermoelectric unicouple was studied for varying geometric dimensions. Results were obtained for thermal stress distribution, output power, and power conversion efficiency with varying geometric sizes. He et al. [8] constructed an enhanced mathematical model of thermoelectric generator which considers the impact of change in temperature in the flow direction is presented in the study and discovered that maximum power output in ideal module area was significantly influenced exhaust gas flow rate. Gou et al. [9] developed a waste heat thermoelectric generator model to harvest energy for low-temperature regions and found that increasing electrical serial connection and thermoelectric element improve the system's performance.

The cited works of literature present several mathematical and statistical models created, and numerous design modifications were suggested to improve the performance of thermoelectric devices. However, it is essential to optimize the thermoelectric unicouple structure and for that coverage of all possible factors which affect the performance of the thermoelectric unicouple. In a thermoelectric device, due to the temperature difference on both sides of the module so the charge carriers on the hotter side, both in the n-type and p-type leg, vibrate with more energy net effect of this is the migration of charge carriers from the hot side to cold side due to which potential difference is generated. The flow of charge carriers faces internal resistance in the n-type and p-type legs. Internal resistance depends upon the device's geometric dimensions, like the leg's length and width, which affect the internal resistance. Draw the current from the thermoelectric device through the electrical circuit; external resistance also comes into play, called load resistance, which affects the current flow.

The present study develops a mathematical model to analyze the effect of leg length, the width of the leg, load resistance, and temperatures on the hot side of the thermoelectric unicouple. Leg length is in the range of 1–15 mm, and width of leg range is 0.4–1.2 mm reason behind those ranges is to study the thermoelectric unicouple for commercial purposes which available in the market and for a compact design of thermoelectric modules to use in remote areas, in that ranges both the goals is fulfilling. The range of load resistance is 0.005Ω to 0.1Ω. These load resistance ranges go above and below the temperature-dependent electrical resistance offered by thermoelectric legs. The temperature of the hot side varied from 300 to 500 K.

Automobile exhaust gas temperature falls under that range, so during harvesting waste heat energy from automobiles, the performance of the thermoelectric device is studied. Moreover, the output power and efficiency at different parameters are study and provide instructions for the logical structure optimization design of the thermoelectric unicouple.

2 Calculation Model and Method

2.1 *Physical Model and Assumptions*

A single unit of a thermoelectric module shown in Fig. 1 is called a thermoelectric unicouple or thermoelectric element. Thermoelectric elements comprised insulation substrates, conductor pads, and thermoelectric element legs. Thermoelectric legs in the device in a vertical arrangement made up of *n*-type and *p*-type thermoelectric functional material properties. The whole setup is placed between the insulation substrates, making a thermally parallel connection. The effect of leg length and width of leg is studied in the paper for geometrical effect. For a fundamental unit structure to make calculation simple, some assumptions taken are listed below [2]:

(1) Properties of thermoelectric materials are isotropic.
(2) Resistance due to the contact being neglected.
(3) Losses of heat due to radiation and convection from the wall of the thermoelectric elements are neglected.
(4) Steady-state heat transfer and current flow.

Materials used for *p*-type and *n*-type legs are bismuth telluride (Bi_2Te_3) because bismuth telluride performs well in the selected temperature range and also has good
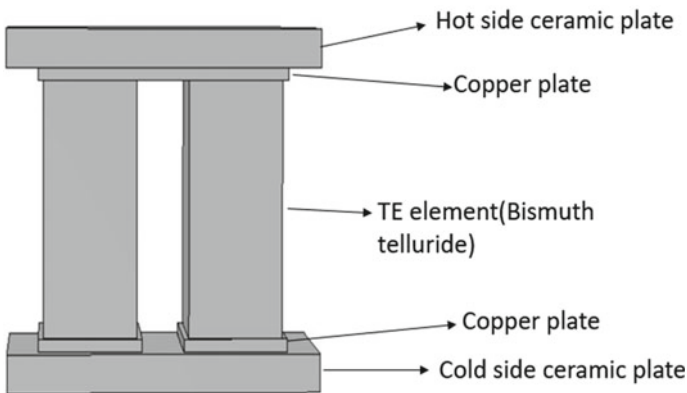
Fig. 1 Schematic diagram of thermoelectric unicouple

Table 1 Geometry sizes (reference sizes)

Materials	L_x (mm)	L_y (mm)	L_z (mm)
n-type element	0.9	2	1.1
p-type element	0.9	2	1.1
Copper (Hot side)	2.4	0.1	1.2
Copper (Cold side)	1	0.1	1.2
Ceramic	3	0.1	1.5

Table 2 Material properties

Properties	n-type	Units
Seebeck coefficient $\alpha(T)$	$(0.00153073*T^2 - 1.08058874*T - 28.338095)*10^{-6}$	(V/K)
Electrical conductivity $\sigma(T)$	$(0.01057143*T^2 - 10.16048*T + 3113.714229)*10^2$	(S/m)
Thermal conductivity $k(T)$	$0.0000334545*T^2 - 0.023350303*T + 5.606333$	(W/m.K)
Properties	p-type	Units
Seebeck coefficient $\alpha(T)$	$(-0.003638095*T^2 - 0.023350303*T - 296.214286)*10^{-6}$	(V/K)
Electrical conductivity $\sigma(T)$	$(0.015601732*T^2 - 15.708052*T + 4466.38095)*10^2$	(S/m)
Thermal conductivity $k(T)$	$0.0000361558*T^2 - 0.026351342*T + 6.22162$	(W/m.K)

electrical conductivity, low thermal conductivity, high figure of merit, and economical cost, making it the best material [2]. Dimensions of unicouple are shown Table 1. Temperature-dependent properties of bismuth telluride follow a polynomial function, as given in Table 2.

2.2 Governing Equations

The underlying governing equations in the computational domain are described in this section [10]. In COMSOL Multiphysics, the 'Heat Transfer in Solids' interface is utilized to simulate the heat transfer in solids through conduction. The generalized equation for the temperature in the differential form and the heat flux following the Fourier's law are expressed as.

$$\rho C_p u.\nabla T + \nabla.q = Q + Q_{\text{ted}}, \tag{1}$$

$$q = -k\nabla T. \tag{2}$$

The 'Electric Current' interface is used to solve the physics of the current conservation equation by Ohm's law. This interface computes potential distribution in conducting media, electric field, and electric current.

$$\nabla J = Q_j, \tag{3}$$

$$J = \sigma E + J_e, \tag{4}$$

$$E = -\nabla V. \tag{5}$$

The 'Thermoelectric Effect' interface coupled the heat transfer in solids and current equations for modeling Seebeck effect in the present model.

$$q = PJ, \tag{6}$$

$$P = ST, \tag{7}$$

$$J_e = -\sigma S \nabla T. \tag{8}$$

2.3 Performance of Thermoelectric Generator

A thermoelectric generator generates electrical power, which depends on key parameters like thermal resistance, Seebeck coefficient, and electrical resistance. Equations for analyzing the performance of the thermoelectric device are discussed in this section. Hot side temperature T_h where the heat absorbed is expressed as

$$\dot{Q}_h = n[\alpha T_h I - 0.5 \dot{I}^2 R + K(T_h - T_c)]. \tag{9}$$

where

$$\alpha = \alpha_p - \alpha_n, \tag{10}$$

$$R = \frac{\rho_p L_p}{A_p} + \frac{\rho_n L_n}{A_n}, \tag{11}$$

$$K = \frac{k_p A_p}{L_p} + \frac{k_n A_n}{L_n}. \tag{12}$$

The assumption used in this study is that both n-type and p-type materials are the same, we have that $R = \rho L / A$ and $= kA/L$, where $\rho = \rho_p + \rho_n$ and $k = k_p + k_n$. From cold side, the rate of heat liberated is

$$Q_c = n[\alpha T_c I + 0.5 \dot{I}^2 R + K(T_h - T_c)]. \tag{13}$$

The first law of thermodynamics for the thermoelectric module is $W_n = Q_h - Q_c$. Total power output from the thermoelectric device is

$$W_n = n\left[\alpha I (T_h - T_c) - I^2 R\right]. \tag{14}$$

Total power output in terms of external load resistance can be defined as

$$W_n = n I^2 R_l. \tag{15}$$

Equating Eqs. (14) and (15) with $W_n = I V_n$ gives the total voltage as

$$V_n = n I R_l = n[\alpha (T_h - T_c) - I R]. \tag{16}$$

The electric current for the thermoelectric device from Eq. (16)

$$I = \frac{\alpha (T_h - T_c)}{R_l + R}. \tag{17}$$

From the current expression, we can conclude that it is independent of the number of thermocouples. For voltage across the module, inserting Eq. (17) into (16)

$$V_n = \frac{n\alpha (T_h - T_c)}{\frac{R_l}{R} + 1} \left(\frac{R_l}{R}\right). \tag{18}$$

Using Eq. (17) into (15) gives the power output for the device

$$W_n = \frac{n\alpha^2 (T_h - T_c)^2}{R} \frac{\frac{R_l}{R}}{\left(1 + \frac{R_l}{R}\right)^2}. \tag{19}$$

The figure of merit is the term by which the performance of the thermoelectric device is measured. ZT is a dimensionless term, and T is the absolute temperature.

$$Z = \frac{\alpha^2}{\rho k} = \frac{\alpha^2 \sigma}{k}. \tag{20}$$

For higher conversion efficiency, the material value of ZT needs to be higher. Seebeck coefficient α and electrical conductivity σ must be large, and thermal conductivity k needs to be minimum. This type of interconnectedness among the physical properties makes it challenging to develop solution techniques for improving the material's ZT.

The ratio of the power output over heat absorbed at the hot junction gives the efficiency of the thermoelectric device.

$$\eta = \frac{W_n}{Q_h}. \tag{21}$$

Inserting Eqs. (9) and (19) into Eq. (21) for the efficiency

$$\eta = \frac{\left(\frac{T_c}{T_h}\right)\frac{R_l}{R}}{\left(1 - \frac{R_l}{R}\right) - 0.5\left(1 - \frac{T_c}{T_h}\right) + \frac{1}{2Z\overline{T}}\left(1 - \frac{R_l}{R}\right)^2\left(1 + \frac{T_c}{T_h}\right)}, \tag{22}$$

where $\overline{T} = \frac{T_h + T_c}{2}$.

2.4 Numerical Model

The present numerical model is validated with the study reported by Fan et al. [3]. The author also used thermoelectric unicouple and develop mathematical model to find the optimum leg length and cross-section area of leg. For validation of this study, same geometry is built by using COMSOL Multiphysics software based on finite element method, following the similar boundary conditions, which is a constant surface temperature boundary conditions. Temperature on hot side is 500 K and at cold side, it is 400 K with same geometric dimensions but with different leg length. The power output is calculated and compared with results from Fan et al. [3] in Fig. 2. From the graph, maximum discrepancy found is 5%, which is below the standard discrepancy of 5%, which support the validity of present prediction.
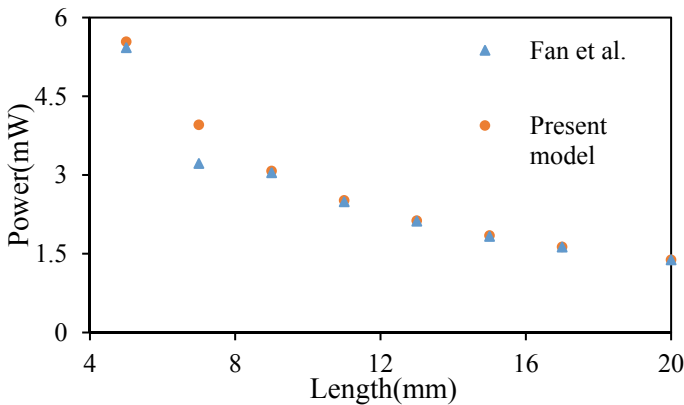
Fig. 2 Validation of present model with previous study [3]

3 Results and Discussions

This section presents the results obtained from simulation for varied parameters of thermoelectric unicouple. The parameters studied are leg height, width, load resistance, and temperature on the hot side.

3.1 Effect of Leg Length

The outturn of leg height on internal resistance, power output, and efficiency is studied. Leg length varied from 1 to 15 mm, and the leg's thickness was 1.1 mm. The effect of leg length on internal resistance is shown in Fig. 3a. It is seen that the internal resistance of leg material is linearly dependent on the leg length. This behavior can be described by when leg length increases, the volume of leg increases, which supports the obstruction for the flow of current means increasing the internal resistance. When the variation of leg length is the same and increasing the width of the leg, it is seen that as the width increases, the slope of the line decreases. The trend for increasing internal resistance after the width of 0.8 mm effect is insignificant. This internal resistance variation explains Fig. 3b and c, which is the variation of power output and efficiency of thermoelectric unicouple with varying leg lengths.

As leg length increases, internal resistance increases, so the current generation is reduced, and the performance power output and efficiency decrease as leg length increase. The figure shows that change in power and efficiency is significant when leg length is below 5 mm. After that, the difference in control and efficiency is insignificant. A combination of the width of 1.2 mm and leg length of 1 mm showed maximum performance of thermoelectric unicouple. Significant performance drop can be seen between 1 and 2 mm leg length. When the width of the leg decreases, performance curve is also shifted downward.

3.2 Effect of Leg Width

In addition to the leg length, the leg width is also an essential geometric dimension that affects the performance of thermoelectric unicouple. Thus, this paper studies the effect of leg width on the internal resistance of leg material, power output, and efficiency of thermoelectric unicouple. It is seen in.

In Fig. 3d, that internal resistance showed a decreasing trend with an increase in the width of the leg. When leg width increases cross-section area of the leg increases, which leads to a decrease in internal resistance. A significant drop in internal resistance happens near smaller values of leg width; for the same variation of width, when leg length decreases curve shifts toward a downward leg length of 15 mm, and a leg width of 0.4 mm shows the maximum value of internal resistance. These trends of

Fig. 3 a Variation of internal resistance with length of TE unicouple for different width(mm) conditions, **b** Variation of power with length of TE unicouple for different width(mm) conditions, **c** Variation of efficiency with length of TE unicouple for different width(mm) conditions, **d** Variation of internal resistance with leg width of TE unicouple for different leg length (mm) conditions, **e** Variation of efficiency with leg width of TE unicouple for different leg length(mm) conditions, **f** Variation of power with leg width of TE unicouple for different leg length(mm) conditions, **g** Variation of power with load resistance for different leg width(mm) conditions, **h** Variation of efficiency and power with temperature on the hot side.
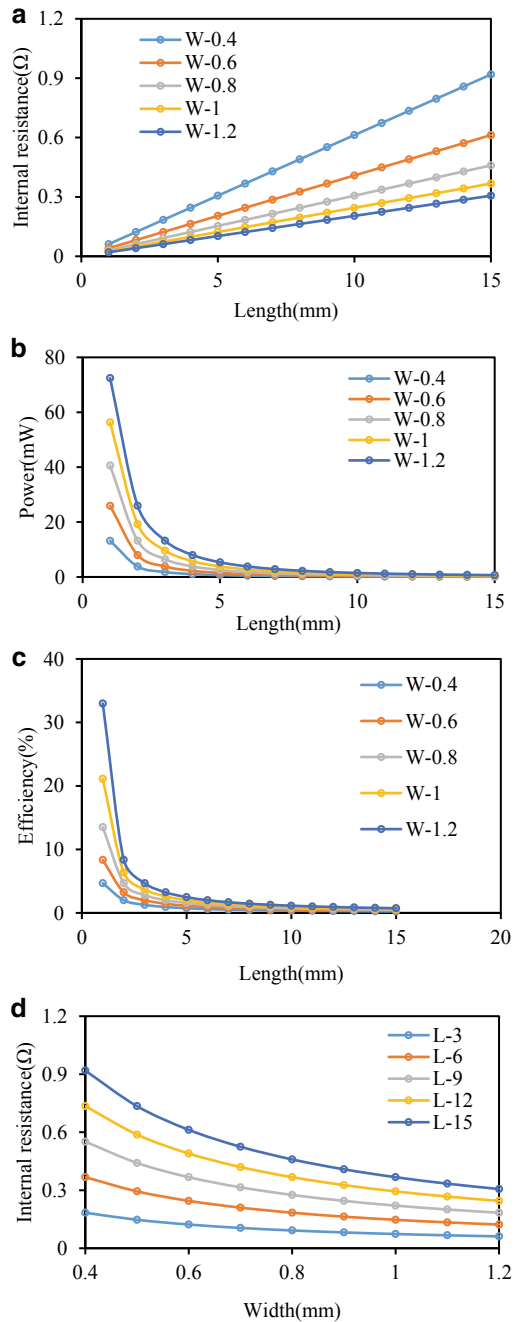
Fig. 3 (continued)
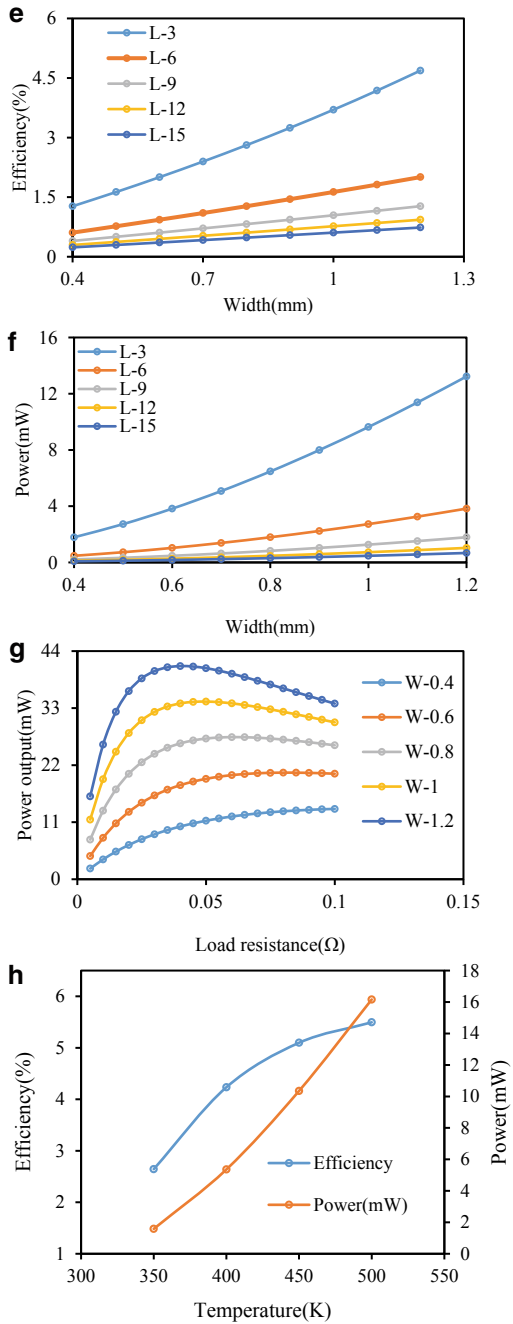
internal resistance can explain Fig. 3e and f, which shows the trends for power output and efficiency of thermoelectric unicouple.

It is seen that power output and efficiency show an increasing trend as leg width increases and internal resistance of leg material decreases which means electric current flow increases from the unicouple, which leads to an increase in the performance of the thermoelectric unicouple. From the graphs, it can be concluded that maximum deviation in power output and efficiency is for smaller leg lengths and larger leg width after leg length of 9 mm change with width on the performance of unicouple is very small.

3.3 Effect of Load Resistance

Load resistance is provided by the circuit through a thermoelectric unicouple from which current is drawn. Load resistance is a vital parameter that needs to be considered for analyzing the performance of unicouple. The variable parameter is the width, and the leg length is 2 mm from the Fig. 3g; as the load resistance increases, power output first increases, then it follows a decreasing trend. From the graph, maximum power output was obtained at a width 1.2 mm, leg length of 2 mm, and load resistance of 0.04 Ω.

3.4 Effect of Temperature on Hot Side

The optimum performance of a thermoelectric unicouple at hot side temperature is simulated to compare the performance of the unicouple at different temperatures. In this manner, range of parameters of thermoelectric unicouple could be generated. In this manner, it is practicable to depict the performance of the unicouple for different operating conditions. Coverage of hot side temperature from 300 to 500 K satisfies the material chosen in this study and applies to waste exhaust heat from automobiles. Cold side temperature is fixed at 300 K, leg length 2 mm, leg width 0.9 mm, and leg thickness 1.1 mm. As seen in Fig. 3h, with increasing the temperature on the hot side, the power and efficiency of the unicouple show an increasing trend.

Charge carriers can explain this behavior as the temperature increases; charge carriers vibrate with more energy on the hot side of unicouple high energy charge carriers net effect is the migration of charge carriers from the hot side to the cold side increases as temperature increases this increases current flow in the unicouple and lead to increase in performance of thermoelectric unicouple.

4 Conclusions

The effects on performance of thermoelectric unicouple due to the various parameters like leg length, leg width, load resistance and different temperatures on the hot side of thermoelectric unicouple.

- Shorter TE leg lengths gives high efficiency and power. Highest performance given by 1 mm length it is difficult from manufacturing point of view it is too tiny besides it has highest efficiency. On increasing the width of the leg in thermoelectric unicouple efficiency and power increases linearly.
- On increasing the load resistance power of thermoelectric unicouple first increases and after achieving optimum level, it starts decreasing with increases load resistance. In this model, maximum power output is achieved at leg length 2 mm, leg width 1.2 mm, and load resistance 0.04 Ω where external load resistance becomes equal to the internal resistance.
- On increasing the temperature on hot side, the efficiency and power shows an increasing trend. Increases the temperature on side of unicouple provide charge carriers higher energy to vibrate and net effect of that is more migration of charge carriers from hot side to cold side which gives higher current flow and increase the performance of thermoelectric unicouple.

References

1. Lamba R, Kaushik SC (2017) Thermodynamic analysis of thermoelectric generator including influence of Thomson effect and leg geometry configuration. Energy Convers Manag 144:388–398. https://doi.org/10.1016/j.enconman.2017.04.069
2. Jia X, Guo Q (2020) Design study of Bismuth-Telluride-based thermoelectric generators based on thermoelectric and mechanical performance. Energy 190:116226. https://doi.org/10.1016/j.energy.2019.116226
3. Fan L, Zhang G, Wang R, Jiao K (2016) A comprehensive and time-efficient model for determination of thermoelectric generator length and cross-section area. Energy Convers Manag 122:85–94. https://doi.org/10.1016/j.enconman.2016.05.064
4. Rezania A, Rosendahl LA, Yin H (2014) Parametric optimization of thermoelectric elements footprint for maximum power generation. J Power Sources 255:151–156. https://doi.org/10.1016/j.jpowsour.2014.01.002
5. Khalil AL, Elhassnaoui A, Yadir S, Abdellatif O, Errami Y, Sahnoun S (2021) Performance comparison of TEGs for diverse variable leg geometry with the same leg volume. Energy 224:119967. https://doi.org/10.1016/j.energy.2021.119967
6. Li S, Liu C, Hsu C, Hsieh M, Dai M, Wu S (2010) Thermo-mechanical analysis of thermoelectric modules, pp 18–21
7. Mu Y, Chen G, Yu R, Li G, Zhai P, Li P (2014) Effect of geometric dimensions on thermoelectric and mechanical performance for Mg2Si-based thermoelectric unicouple. Mater Sci Semicond Process 17:21–26. https://doi.org/10.1016/j.mssp.2013.08.009

8. He W, Wang S, Zhang X, Li Y, Lu C (2015) Optimization design method of thermoelectric generator based on exhaust gas parameters for recovery of engine waste heat. Energy 91:1–9. https://doi.org/10.1016/j.energy.2015.08.022

9. Gou X, Xiao H, Yang S (2010) Modeling, experimental study and optimization on low-temperature waste heat thermoelectric generator system. Appl Energy 87(10):3131–3136. https://doi.org/10.1016/j.apenergy.2010.02.013

10. Prasad A, Thiagarajan RCN (2018) Multiphysics modeling and multilevel optimization of thermoelectric generator for waste heat recovery. (September):560066, 201

Experimental Investigation of Chimney Plume Dispersion Characteristics

Abhishek Pednekar and Shailesh R. Nikam

Nomenclature

V_W Wind velocity [m/s]
V_p Plume velocity [m/s]

1 Introduction

In many industries, flue gas plume is exhausted to the atmosphere through tall chimney (stack). Once plume leaves chimney, it comes in contact with atmospheric air. While plume mix with the atmospheric air, it travels in specific direction. Thus, dilution of plume due to mixing with atmospheric air reduces the concentration of pollutant. Mixing of jet plume with atmospheric air and its motion is governed by atmospheric condition like wind velocity, wind direction, atmospheric boundary layer, and vertical temperature gradient at given place. To maintain air quality and minimize the undesirable effect of pollutant coming out with plume, concentration of this pollutant should be as low as possible which depends on rate of mixing of plume with atmospheric air. Importance of the subject motivated many researchers to investigate flow physics of chimney gas plume.

A. Pednekar · S. R. Nikam (✉)
Somaiya Vidyavihar University, K J Somaiya College of Engineering, Mumbai, India
e-mail: shailesh.n@somaiya.edu

2   Literature Review and Objective

Though initial work started in this area since 1940s [1], plume development remains a topic of investigation till now [2]. Various researchers adopted theoretical, computational as well as experimental methodology by doing experiment in wind tunnel for their investigation. Sherlock and Lesher [3] reported various factors which influence jet plume. They have explained that if the gases emitted by chimney come in contact with the turbulence generated by chimney or surrounding building, the gases may be brought down which is called as downwash of plume. Under this situation, concentration of pollutant reaching to the ground close to the plant will be very high. They have also explained effect of terrain (hills or valleys) on the plume. Robins [4] in his experimental investigation explained about wind tunnel experimental technique and model scaling criteria while investigating chimney plume dispersion. Advantages and limitations of wind tunnel for this study are discussed.

Said et al. [5] through experimental and numerical methodology investigated effect of wind velocity, height of chimney, and wake region of chimney on plume development. Particle image velocimetry (PIV) is used for measurement in wind tunnel. Experiments are conducted with scaled model of chimney as 0.1 m in height and 10 mm internal diameter at exit. Experiments are conducted at wind velocities ranging from 0 to 16 m/s and plume velocity 11 m/s. It is confirmed from their study that flow field of a chimney plume in crosswind is influenced by plume wake, chimney wake, downwash effect, and plume to wind velocity ratio. Sang and Seouk [6] numerically investigated the plume dispersions for various altitudinal temperature variations. The normal atmosphere has a temperature decrease of -0.6 °C/ 100 m; however, the real atmosphere has various altitudinal temperature profiles (-1.5 to 1.0 °C/100 m) according to meteorological factors. Air can occasionally make very strong upward/downward wind current or flow fluctuation due to buoyancy force. In this study, the results of the plume dispersion are discussed along the altitudinal temperature variation. The developing processes of the plume after being discharged from a chimney and the ground level concentrations at various positions are compared under various altitudinal temperature conditions. Changes in altitudinal temperature difference beyond -1 °C/100 m increases ground concentration. Kozarev et al. [7] numerically investigated the effect of meteorological situations on plume development. The influence of the emission and stack parameters, the ground level air temperature, the temperature gradient of the atmosphere, and the surface wind velocity in the range from 0.0 to 1.0 m/s is investigated.

Yang and Zang [8] investigated power plant plumes using CFD. They defined the plume jet-dominated region (JDR) which is characterized by a high momentum jet flow of flue gas and the ambient-dominated region (ADR), driven by atmospheric boundary layer turbulence.

Velamati et al. [9] numerically investigated dispersion characteristics of buoyant plumes of the pollutant released from a multi-flue vertical stack into a variable temperature gradient atmosphere in a constant-velocity crosswind using inline and parallel stack configurations. They reported that the plume rises higher and disperses

over a larger area with the inline configuration due to better mixing and shielding effect. Sivanandan et al. [10] numerically investigated effect of negative atmospheric temperature gradient and the plume stack orientation of two individual equal-height stacks on the vertical rise and dispersion of the plume. Thought most of the work is carried out using experimental work is carried out in India in the subject. Present experimental work is focused on investigation of effect of velocity ratio (plume velocity to wind velocity) on chimney plume development and associated downwash characteristics.

3 Materials and Methods

Cylindrical chimney model of PVC material is used in present study. Internal diameter of model is 32 mm (d) with thickness 3 mm and length 200 mm. Model is placed at 100 mm from wind tunnel exit at the center. Exit plane of the chimney is at a height of 200 mm from base, which lies exactly at the center of tunnel. Measurements are taken using Pitot probe along the centerline of the plume from the chimney exit in y direction and in the wake of chimney at different x location in the y direction. Flow visualization is carried out for qualitative flow field study. To get plume gas flow through chimney (at atmospheric temperature), the model is connected from below with air source. Air compressor along with smoke generator and smoke mixing arrangement with compressed air is used. To get required wind velocity, wind tunnel velocity is varied, whereas plume velocity is obtained by varying compressed air discharge. Photograph of experimental setup and measuring arrangement is shown in Fig. 1. Table 1 gives various combinations of wind and plume velocity studied in present investigation. Figure 2 represents coordinate system followed in the present study.

Fig. 1 Schematic diagram of experimental setup and measuring arrangement
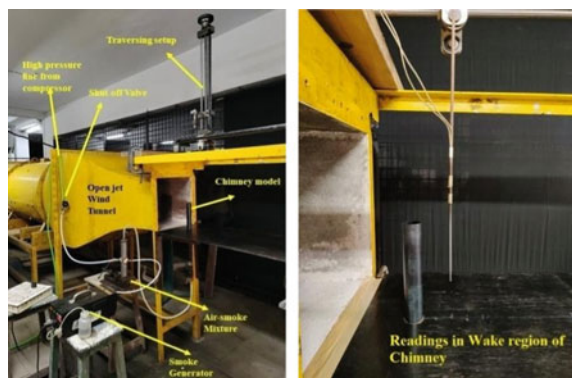
Table 1 Plume velocity and wind velocity conditions

V_w (m/s)	0	2	4	6	10
V_p/V_w for $V_p = 4$ (m/s)	0	2	1	0.6	0.4
V_p/V_w for $V_p = 6$ (m/s)	0	3	1.5	1	0.6

Fig. 2 Basic layout and coordinate system
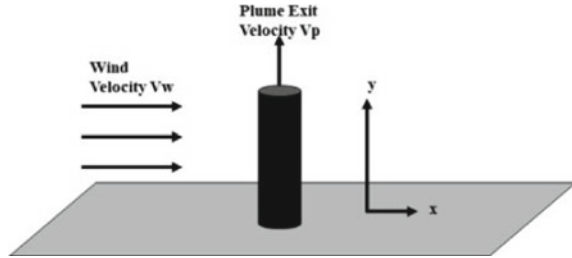
4   Results and Discussion

4.1   Flow Visualization

Flow visualization is carried out for qualitative analysis of flow field for different combination of plume and wind velocity. Results obtained are shown in Fig. 3.

At no wind condition ($V_p = 4$ m/s and $V_w = 0$ m/s), plume is developing in upward direction due to buoyancy effect and momentum of plume imparted at the exit of chimney. Plume travels in vertical direction. As it travels upward, mixing of atmospheric air takes place due to which plume growth takes place. Further when wind velocity is increased to 2 m/s, (cross flow condition) jet plume bends in the direction of wind flow. However, plume continues to grow. Further with increase in wind velocity (4 m/s), plume bends with higher angle which indicates dominance of cross flow at higher wind velocity. At wind velocity 6 m/s, plume bends further. At this wind velocity, it is observed that plume interacts with flow in the wake of the chimney which results into downwash characteristics of plume. At higher wind velocity, 10 m/s, this effect further increases. This higher wind velocity results into downwash which increases chances of pollutants reaching to ground over smaller distance from chimney.

In Fig. 4, at ($V_p = 6$ m/s and $V_w = 0$ m/s) plume rises due to buoyancy effect and momentum imparted at plume exit. The plume rise takes place in vertical direction as seen in earlier case for $V_p = 4$ m/s. Further when wind velocity increases to 2 m/s, it is observed that the plume bends, but the bending is less as observed for the $V_p = 4$m/s. Thus, the plume dominates the flow. However for wind velocity of 4 m/s, there is increase in angle of bend along with plume growth is seen. With increase in wind speed to 6 m/s, the plume interacts with the turbulent region in the wake of chimney

Fig. 3 Chimney plume growth for different wind velocity at constant plume velocity of 4 m/s
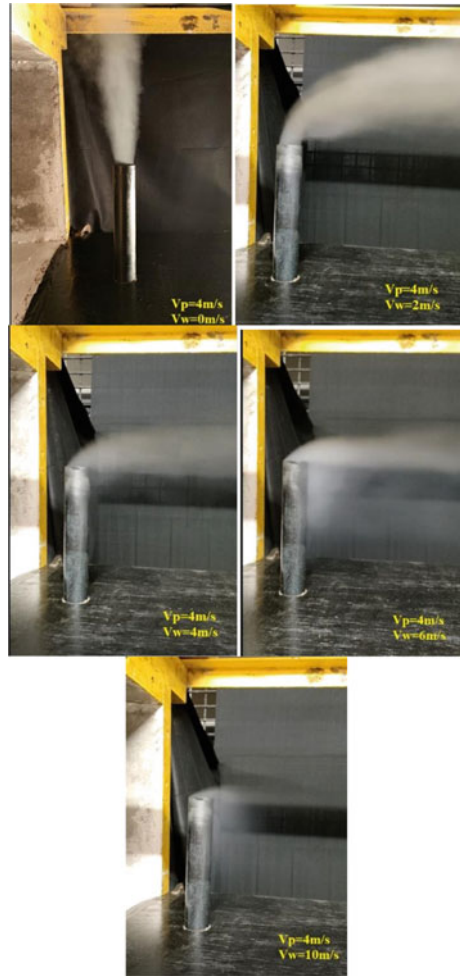
and downwash is seen. Further, increase in wind velocity increases downwash, and wind dominates the flow in cross flow between plume and wind.

For higher plume velocity, bending of plume takes place at relatively higher wind velocity.

4.2 Velocity Distribution

Plume centerline velocity is obtained in Y direction from chimney exit using Pitot measurements for $Vp = 6$ m/s and at different wind velocity. Figure 5 shows this velocity distribution against Y/d for different velocity ratio. Plume velocity decreases

Fig. 4 Chimney plume growth for different wind velocity at constant plume velocity of 6 m/s
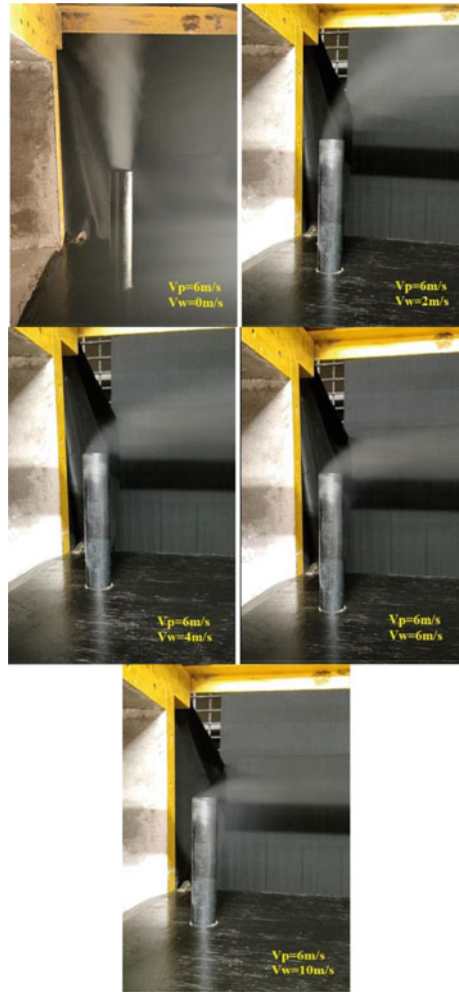
with decrease in velocity ratio. These measurements are compared with the flow visualization results which prove that with decrease in velocity ratio there is increase in plume bending. The decay of centerline velocity at higher wind velocity shows that the plume interacts chimney wake and the cross flow dominates and results in downwash.

Figure 6 shows wake velocity distribution for wind velocity 2 m/s and plume velocity of 4 m/s. Wake region of the chimney shows that the velocity is nearly constant to the height of chimney (about 6.5 d), but as the distance increases (y/d) above the chimney height, the wake region of plume is dominant for low speed wind flow (2 m/s). Similar results are reported for longitudinal velocity earlier by Said et al. [5]. The boundary layer upstream the cylinder undergoes a three-dimensional separation. The boundary layer may separate if the pressure gradient is strong enough. The
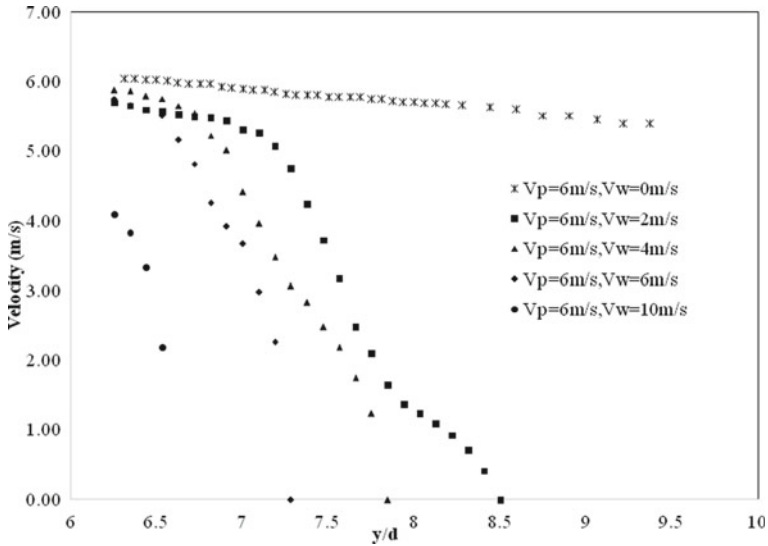
Fig. 5 Centerline Velocity distribution for different wind velocity at constant plume velocity of 6 m/s

flow behind the chimney is less encountered as it comes close to the separation region. As distance is increased velocity in the wake of chimney remains nearly constant but in the plane at $x/d = 2$, there is region of recirculation zone which leads to zero-velocity. With increase in x/d, further there is growth of the plume seen as there is mass of wind entrained which can be verified by both flow visualization and by experimental results. At furthest distance $x/d = 10$, the velocity profile is constant for both plume and chimney wake which represents complete mixing of plume with wind and flows with wind velocity.

5 Conclusions

From present experimental study, following key findings are obtained

- Chimney plume growth is dominated by relative velocity between plume and wind.
- Bending angle of plume reduces with increase in plume velocity in cross flow.
- With increase in wind velocity, plume bends and shows downwash characteristics.
- A downwash characteristic is seen at velocity ratio of 0.6.
- Wake region closer to the chimney is dominated by interaction between plume and vortices in the base of chimney.
- Far away from chimney ($x/d = 10$) similarity is obtained, i.e., plume is fully mixed with wind.
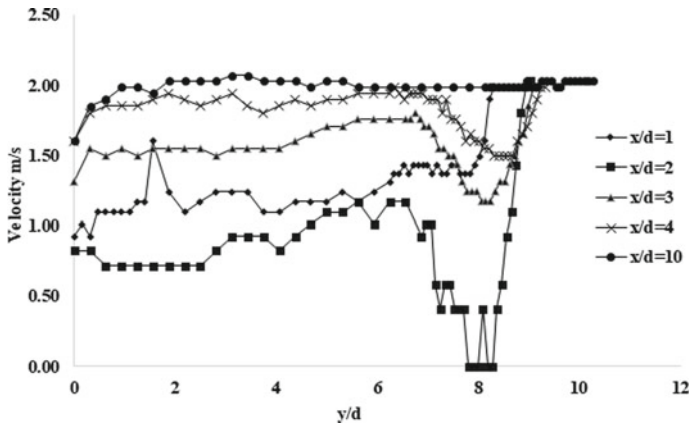
Fig. 6 Wake velocity distribution for wind velocity 2 m/s and plume velocity of 4 m/s

References

1. Sherlock RH, Stalker AE (1947) A study of flow phenomenon in the wake of smokestacks. Eng Res Bull 29, Mar 1941
2. Monbureau EM, Heist DK, Perry SG, Tang W (2020) Modeling lateral plume deflection in the wake of an elongated building. Atmos Environ 234:117608, 1 Aug 2020 https://doi.org/10.1016/j.atmosenv.2020.117608
3. Sherlock RH, Lesher EJ (1955) Role of chimney design in dispersion of waste gases. Air Repair 4(2):13–23. https://doi.org/10.1080/00966665.1954.10467643
4. Robins A (1975) Experimental model techniques for the investigation of the dispersion of chimney plumes. Proc Inst Mech Eng 189:44
5. Said NM, Mhiri H, Palec GL, Bournot P (2005) Experimental and numerical analysis of pollutant dispersion from a chimney. Atmos Environ 39:1727–1738
6. Wee S-K, Park IS (2009) Plume dispersion characteristics in various ambient air temperature gradient conditions, numerical heat transfer. Part A: Appl 56(10):807–826. https://doi.org/10.1080/10407780903463318
7. Kozarev N, Ilieva N, Sokolovski E (2014) Full scale plume rise modeling in calm and low wind velocity conditions. Clean Technol Environ Policy 16:637–645. https://doi.org/10.1007/s10098-013-0650-2
8. Yang B, Zhang KM (2017) CFD-based turbulent reactive flow simulations of power plant plumes. Atmos Environ 150:77–86, Feb 2017
9. Velamati RK, Vivek M, Goutham K et al (2015) Numerical study of a buoyant plume from a multi-flue stack into a variable temperature gradient atmosphere. Environ Sci Pollut Res 22:16814–16829. https://doi.org/10.1007/s11356-015-4877-9
10. Sivanandan H, Ratna Kishore V, Goel M, Asthana A (2020) A study on plume dispersion characteristics of two discrete plume stacks for negative temperature gradient conditions. Enviro Model Assess. https://doi.org/10.1007/s10666-020-09747-1

Performance Characteristics of Journal Bearings with Vertical Shaft

Mohanish Goel, S. Aravindan, K. V. Sreedharan, and U. Parthasarathy

Nomenclature

C	Radial clearance [m]
e	Eccentricity [m]
ε	Eccentricity ratio –
ϕ	Attitude angle (°)
μ	Fluid viscosity [Ns/m^2]
ω	Rotor rotational speed [rad/s]
h_o	Steady state film thickness [m]
W	Radial load [N]
S	Sommerfeld number –
$K_{xx}, K_{xy}, K_{yx}, K_{yy},$	Film stiffness coefficients [N/m]
$B_{xx}, B_{xy}, B_{yx}, B_{yy}$	Film damping coefficients [Ns/m]
$K_{xx}^*, K_{xy}^*, K_{yx}^*, K_{yy}^*$	Non-dimensionalized stiffness coefficients –
$B_{xx}^*, B_{xy}^*, B_{yx}^*, B_{yy}^*$	Non-dimensionalized damping coefficients –

1 Introduction

The journal bearing lubrication problem has been a matter of study for more than five decades. The dynamic behavior of journal bearing plays a vital role in estimating the response of a rotor due to unbalanced forces. In the literature, the stability of rotor during pump operation has been studied by numerically calculating the rotor

M. Goel (✉) · S. Aravindan · K. V. Sreedharan · U. Parthasarathy
Sodium Heat Transport Division, Reactor Design and Technology Group, IGCAR,
Kalpakkam 603102, India
e-mail: mohanish@igcar.gov.in

dynamic coefficients of the bearing (stiffness and damping) for journal bearings [1–3]. In order to study the dynamic characteristics of rotors with vertical shafts, exact computation of rotordynamic parameters is essential.

The characteristic of the bearing is governed by Reynolds' equation. Applying small perturbation on the journal, the governing differential equations are derived for obtaining oil film pressure (static characteristics) and stiffness and damping coefficients (dynamic characteristics). The equations are discretized using finite difference method (FDM). Further, using iterative method of Successive Over Relaxation (SOR), the discretized equations are solved over a rectangular grid of the fluid film domain.

In the present work, the methodology of estimating the rotor dynamic coefficients of a typical hydrodynamic journal bearing supporting horizontal shaft is validated against literature [4]. Further, the formulation is extended to journal bearings with vertical shafts, and the load capacity and stiffness coefficients are computed. The results will be useful to estimate the journal stability in vertical shaft bearings. The orbit plots provided can be used to determine position of the shaft corresponding to any bearing load, while the stiffness plots can be used to obtain the rigidity of bearing corresponding to different shaft positions.

2   Literature Review and Objective

Several theoretical and experimental investigation studies have been conducted in the field of performance characteristics of journal bearing in the past. The present study is classified into the following sections:

1. Solution of Reynolds' equation
2. Calculation procedure of performance characteristics
3. Validation study with horizontal shaft bearing
4. Study of journal bearings with vertical shafts.

2.1   Solution of Reynolds' Equation

The governing equation for the pressure distribution in the bearing fluid film is Reynolds' equation [5], which is represented in the polar coordinate system as

$$\frac{\partial}{\partial z}\left(h^3\frac{\partial P}{\partial z}\right) + \frac{1}{R^2}\frac{\partial}{\partial \theta}\left(h^3\frac{\partial P}{\partial \theta}\right) = 6\mu\omega\frac{\partial h}{\partial \theta} + 12\mu\dot{h}, \tag{1}$$

where $P = P(\theta, z, t)$ is the oil film hydrodynamic gauge pressure, $h = h(\theta, z, t)$ is the lubricant film thickness, μ is the dynamic viscosity of the fluid, and $\omega = 2\pi N/60$ is the angular speed in rad/s. The generalized schematic of typical radial journal bearing is shown in Fig. 1.
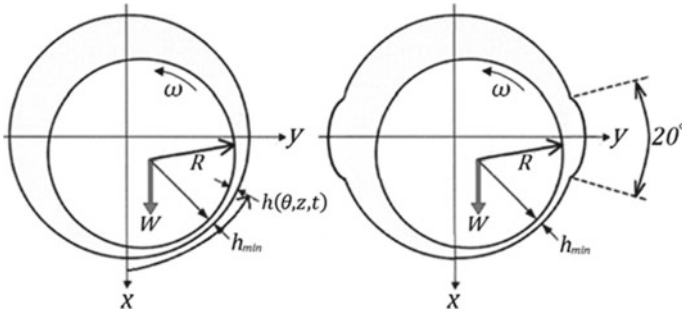
Fig. 1 Radial journal bearing without and with groove

A linear perturbation approach gives the expression for film thickness and its derivative w.r.t. time as

$$h = h_o - \Delta x \cos \theta - \Delta y \sin \theta, \tag{2}$$

$$\dot{h} = \dot{h}_o - \Delta \dot{x} \cos \theta - \Delta \dot{y} \sin \theta, \tag{3}$$

where Δx and Δy are small perturbations in film thickness about the equilibrium position, and h_o is the steady state film thickness, characterized by the position of the rotor, given by (x_o, y_o). Neglecting higher order terms, the value of h^3 would approximately be equal to

$$h^3 \approx h_o^3 - 3h_o^2 (\Delta x \cos \theta + \Delta y \sin \theta). \tag{4}$$

Applying Taylor Series expansion and neglecting higher order terms, the pressure profile can be expressed as

$$P = P_o + \frac{\partial P}{\partial x} \Delta x + \frac{\partial P}{\partial y} \Delta y + \frac{\partial P}{\partial \dot{x}} \Delta \dot{x} + \frac{\partial P}{\partial \dot{y}} \Delta \dot{y}. \tag{5}$$

From the bearing geometry, the steady state film thickness can be written as

$$h_o = C(1 - \epsilon \cos(\theta - \phi)), \tag{6}$$

where C is the radial clearance, $\epsilon = e/C$ is the eccentricity ratio of the bearing and ϕ is the attitude angle of the bearing.

Substituting Expressions (2) to (5) in the governing Eq. (1), we get the following operator form:

$$L_o(P_o) + L_o\left(\frac{\partial P}{\partial x} \Delta x\right) + L_o\left(\frac{\partial P}{\partial y} \Delta y\right) + L_o\left(\frac{\partial P}{\partial \dot{x}} \Delta \dot{x}\right) + L_o\left(\frac{\partial P}{\partial \dot{y}} \Delta \dot{y}\right)$$

$$+ L_x(P_o) + L_y(P_o) = 6\mu\omega\frac{\partial h_o}{\partial \theta} - 6\mu\omega\frac{\partial(\Delta x \cos\theta)}{\partial \theta} - 6\mu\omega\frac{\partial(\Delta y \sin\theta)}{\partial \theta}$$

$$+ 12\mu(\dot{h}_o) - 12\mu(\Delta\dot{x}\cos\theta) - 12\mu(\Delta\dot{y}\sin\theta), \tag{7}$$

where

$$L_o() = \frac{\partial}{\partial z}\left(h_o^3\frac{\partial}{\partial z}()\right) + \frac{1}{R^2}\frac{\partial}{\partial\theta}\left(h_o^3\frac{\partial}{\partial\theta}()\right)$$

$$\begin{Bmatrix} L_x() \\ L_y() \end{Bmatrix} = -\frac{\partial}{\partial z}\left(3h_o^2\begin{Bmatrix}\Delta x\cos\theta \\ \Delta y\sin\theta\end{Bmatrix}\frac{\partial}{\partial z}()\right)$$

$$-\frac{1}{R^2}\frac{\partial}{\partial\theta}\left(3h_o^2\begin{Bmatrix}\Delta x\cos\theta \\ \Delta y\sin\theta\end{Bmatrix}\frac{\partial}{\partial\theta}()\right).$$

Equation (7) contains coefficients of Δx, Δy, $\Delta\dot{x}$, and $\Delta\dot{y}$; hence, separation of variables leads to a system of five linear differential equations, as shown below

$$L_o(P_o) = 6\mu\omega\frac{\partial h_o}{\partial\theta}, \tag{8}$$

$$L_o\left(\frac{\partial P}{\partial x}\Delta x\right) = 6\mu\omega\Delta x\sin\theta + L_x(P_o), \tag{9}$$

$$L_o\left(\frac{\partial P}{\partial y}\Delta y\right) = -6\mu\omega\Delta y\cos\theta + L_y(P_o), \tag{10}$$

$$L_o\left(\frac{\partial P}{\partial\dot{y}}\Delta\dot{x}\right) = -12\mu\Delta\dot{x}\cos\theta. \tag{11}$$

$$L_o\left(\frac{\partial P}{\partial\dot{y}}\Delta\dot{y}\right) = -12\mu\Delta\dot{y}\sin\theta. \tag{12}$$

The schematic of node representation is shown in Fig. 2.
The finite difference approximations of terms given in Eq. (8) are

$$\frac{\partial}{\partial z}\left(h_o^3\frac{\partial}{\partial z}P_o\right) = \frac{\left(h^3\frac{\partial P_o}{\partial z}\right)_{i,j+\frac{1}{2}} - \left(h^3\frac{\partial P_o}{\partial z}\right)_{i,j-\frac{1}{2}}}{\Delta z}$$

$$= \frac{\left(\frac{h_{i,j+1}+h_{i,j}}{2}\right)^3\left(\frac{P_{i,j+1}-P_{i,j}}{\Delta z}\right) - \left(\frac{h_{i,j}+h_{i,j-1}}{2}\right)^3\left(\frac{P_{i,j}-P_{i,j-1}}{\Delta z}\right)}{\Delta z}, \tag{13}$$

$$\frac{1}{R^2}\frac{\partial}{\partial\theta}\left(h_o^3\frac{\partial}{\partial\theta}P_o\right) = \frac{1}{R^2}\frac{\left(h^3\frac{\partial P_o}{\partial\theta}\right)_{i+\frac{1}{2},j} - \left(h^3\frac{\partial P_o}{\partial\theta}\right)_{i-\frac{1}{2},j}}{\Delta\theta}$$

Fig. 2 Schematic of node representation
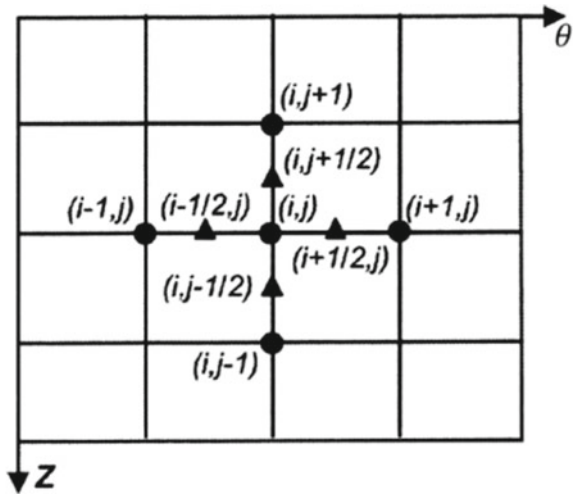
$$= \frac{\left(\frac{h_{i+1,j}+h_{i,j}}{2}\right)^3 \left(\frac{P_{i+1,j}-P_{i,j}}{\Delta\theta}\right) - \left(\frac{h_{i,j}+h_{i-1,j}}{2}\right)^3 \left(\frac{P_{i,j}-P_{i-1,j}}{\Delta\theta}\right)}{R^2 \Delta\theta}, \quad (14)$$

$$6\mu\omega\frac{\partial h_o}{\partial\theta} = 6\mu\omega\left(\frac{h_{i+1,j} - h_{i-1,j}}{2\Delta\theta}\right). \quad (15)$$

Substituting (13), (14), and (15) in Eq. (8), and applying successive over relaxation (SOR) algorithm, with over-relaxation parameter β, we get the expression for the pressure at any (i, j) node as

$$P_{i,j} = \beta\frac{a P_{i+1,j} + b P_{i-1,j} + c P_{i,j+1} + d P_{i,j-1} - F_{i,j}}{a + b + c + d} + (1 - \beta)P_{i,j}, \quad (16)$$

where

$$a = \frac{1}{R^2\Delta\theta^2}\left(\frac{h_{i,j} + h_{i+1,j}}{2}\right)^3,$$

$$b = \frac{1}{R^2\Delta\theta^2}\left(\frac{h_{i,j} + h_{i-1,j}}{2}\right)^3,$$

$$c = \frac{1}{(\Delta z)^2}\left(\frac{h_{i,j} + h_{i,j+1}}{2}\right)^3,$$

$$d = \frac{1}{(\Delta z)^2}\left(\frac{h_{i,j} + h_{i,j-1}}{2}\right)^3,$$

$$F_{i,j} = 6\mu\omega\left(\frac{h_{i+1,j} - h_{i-1,j}}{2\Delta\theta}\right).$$

The convergence criteria is that after kth iteration, if the pressure at a general node i, j is $P_{i,j}^k$, the error at the node is computed as

$$e_{i,j}^k = \left(P_{i,j}^k - P_{i,j}^{k-1} \right) / P_{i,j}^{k-1},$$

and the net error for the kth iteration is computed as

$$e^k = \max\left(\left| e_{i,j}^k \right| \right).$$

The iterations are performed successively, until the condition $e^k \leq 10^{-6}$ is satisfied, and the solution is said to be converged [6].

Similarly, Eqs. (9) to (12) can be discretized as in the Eq. (8), with $F_{i,j}$ being replaced by $F_{x|i,j}$, $F_{y|i,j}$, $F_{\dot{x}|i,j}$ and $F_{\dot{y}|i,j}$, as mentioned below.

$$F_{x|i,j} = 6\mu\omega(\sin\theta)_{i,j} + \frac{\left(3h^2 \cos\theta \frac{\partial P}{\partial \theta} \right)_{i+\frac{1}{2},j} - \left(3h^2 \cos\theta \frac{\partial P}{\partial \theta} \right)_{i-\frac{1}{2},j}}{R^2 \Delta\theta}$$
$$+ \frac{\left(3h^2 \cos\theta \frac{\partial P}{\partial z} \right)_{i,j+\frac{1}{2}} - \left(3h^2 \cos\theta \frac{\partial P}{\partial z} \right)_{i,j-\frac{1}{2}}}{\Delta z},$$

$$F_{y|i,j} = -6\mu\omega(\cos\theta)_{i,j} + \frac{\left(3h^2 \sin\theta \frac{\partial P}{\partial \theta} \right)_{i+\frac{1}{2},j} - \left(3h^2 \sin\theta \frac{\partial P}{\partial \theta} \right)_{i-\frac{1}{2},j}}{R^2 \Delta\theta}$$
$$+ \frac{\left(3h^2 \sin\theta \frac{\partial P}{\partial z} \right)_{i,j+\frac{1}{2}} - \left(3h^2 \sin\theta \frac{\partial P}{\partial z} \right)_{i,j-\frac{1}{2}}}{\Delta z},$$

$$F_{\dot{x}|i,j} = -12\mu(\cos\theta)_{i,j},$$
$$F_{\dot{y}|i,j} = -12\mu(\sin\theta)_{i,j}.$$

2.2 Calculation Procedure of Performance Characteristics

The loads along the x-axis and y-axis (refer Fig. 1) are W_x and W_y, respectively, which can be evaluated by integrating pressure over the entire area.

$$W_x = \int_0^{2\pi} \int_0^L PR \cos\theta \mathrm{d}z \, \mathrm{d}\theta,$$

$$W_y = \int_0^{2\pi} \int_0^L PR \sin\theta \mathrm{d}z \, \mathrm{d}\theta.$$

Hence, the resultant load is

$$W = \sqrt{W_x^2 + W_y^2}. \tag{17}$$

The Sommerfeld number S is defined as

$$S = \mu \frac{\omega}{2\pi} \frac{LD}{W} \left(\frac{R}{C}\right)^2. \tag{18}$$

The stiffness coefficients K_{xx}, K_{xy}, K_{yx}, and K_{yy} can be evaluated by integrating pressure gradients over the entire area.

$$K_{xx} = \int_0^{2\pi} \int_0^L \left(\frac{\partial P}{\partial x}\right) R \cos\theta \, dz \, d\theta, \tag{19}$$

$$K_{xy} = \int_0^{2\pi} \int_0^L \left(\frac{\partial P}{\partial x}\right) R \sin\theta \, dz \, d\theta, \tag{20}$$

$$K_{yx} = \int_0^{2\pi} \int_0^L \left(\frac{\partial P}{\partial y}\right) R \cos\theta \, dz \, d\theta, \tag{21}$$

$$K_{yy} = \int_0^{2\pi} \int_0^L \left(\frac{\partial P}{\partial y}\right) R \sin\theta \, dz \, d\theta. \tag{22}$$

Similarly, the damping coefficients B_{xx}, B_{yx}, B_{xy}, and B_{yy} can be obtained by integrating the pressure derivatives with respect to $\dot{x}$ and $\dot{y}$. The stiffness and damping coefficients are non-dimensionalized as

$$K^* = \frac{Kc}{W}, \quad B^* = \frac{B\omega c}{W}.$$

2.3   Validation Study with Horizontal Shaft Bearing

To validate the calculation methodology, the performance characteristics of journal bearing with horizontal shaft are evaluated and compared against Lund and Thomsen [4]. The bearing has two axial grooves (groove angle = 20°), which are located at 90° and 270° with respect to the load direction, as shown in Fig. 1. The length to diameter ratio of the bearing (L/D) is 0.5.

The fluid film is discretized over a uniform rectangular grid, as shown in Fig. 3. The pressure at the grooves and bearing ends is taken same as the ambient pressure. The Reynolds' boundary condition is applied throughout the fluid film domain, giving a zero pressure gradient at the point wherever the film pressure falls to the same level as the ambient pressure.
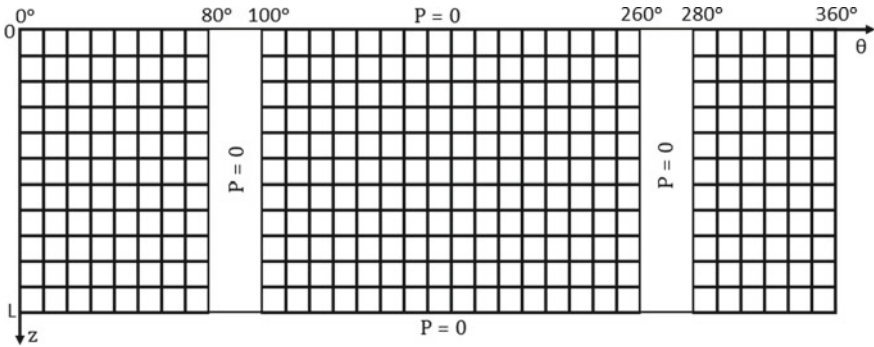
Fig. 3 Two-groove journal bearing developed view

2.4 Study of Journal Bearings with Vertical Shafts

For the pumps operating with vertical shafts, the net radial load comprises multiple factors, viz. mechanical imbalance, eccentricity in journal, gyroscopic effect, etc. Therefore, the direction of net radial load with respect to the grooves can be in any radial direction. The journal bearing considered in this study consists of two diametrically opposite grooves (groove angle $= 8°$), with two pockets each. The length and diameter of the bearing is 95 mm and 364 mm respectively ($L/D = 0.26$). The bearing is assumed to be completely submerged in oil at a known pressure $P_1 = 0.14$ MPa, and the shaft is rotating at 200 rpm. The lubricant used is oil with viscosity grade ISO VG 32. The developed view of the bearing is shown in Fig. 4.

For a particular load magnitude, since the load direction w.r.t. grooves is variable, the equilibrium position of the shaft changes. The angle between load vector and the first groove (α) varies from 0 to 360 deg during the shaft rotation corresponding to
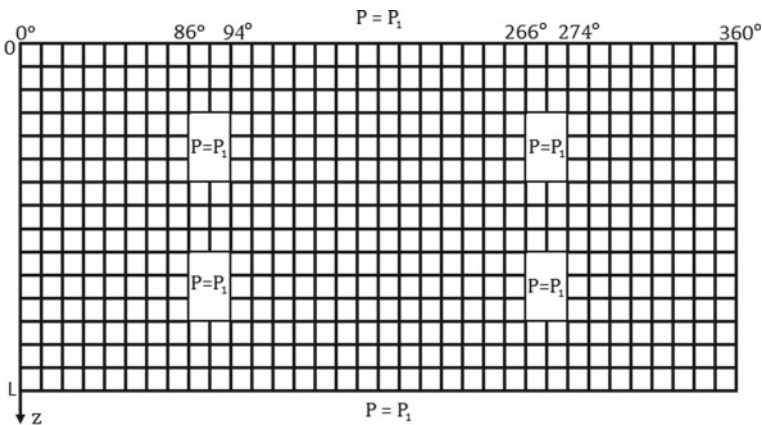
Fig. 4 Developed view of journal bearing with vertical shaft

different load values. Hence, the equilibrium position of the bearing is estimated at each orientation of load direction and eccentricity. From these equilibrium positions, the orbit plots for various load values are obtained. The corresponding stiffness of the bearing is also estimated at each orientation of load direction and eccentricity.

3 Results and Discussion

3.1 Validation Results for Horizontal Shaft Bearing

For the radial bearing on a horizontal shaft, the load-bearing capacity of the bearing is estimated. Sommerfeld number is also estimated as per Eq. (18). The plot for the Sommerfeld number S at various eccentricity ratios is shown in Fig. 5. The estimated load-bearing capacity is compared well with the results available in the literature [4].

It can be observed that at large Sommerfeld numbers (S) (small W, large ω, large viscosity μ), the bearing operates nearly at center, i.e., $\varepsilon \to 0.0$, , while at small Sommerfeld numbers (large W, small ω, low viscosity μ), the bearing operates at high eccentricities, i.e., $\varepsilon \to 1.0$.

The plots for the stiffness coefficients K_{xx}, K_{xy}, K_{yx} and K_{yy} at various eccentricity ratios are shown in Fig. 6.

It can be observed that as the journal center approaches the bearing center ($\varepsilon \to 0$), the bearing offers no direct stiffness (K_{xx}^*) but offers only cross-coupled support (K_{xy}^* and K_{yx}^*). A small disturbance on the bearing in orthogonal (y) direction would lead to a significant resistance along that direction ($K_{yy}^* \neq 0$). However, the effect of the orthogonal stiffness (K_{yy}^*) relative to the direct stiffness (K_{xx}^*) diminishes as the journal becomes eccentric. This is because, as noted in the plot for Sommerfeld number, the load-bearing capacity rises with a rise in eccentricity ratio.

The plots for the damping coefficients at various eccentricity ratios are shown in Fig. 7.

Fig. 5 Variation of Sommerfeld number S with eccentricity ratio
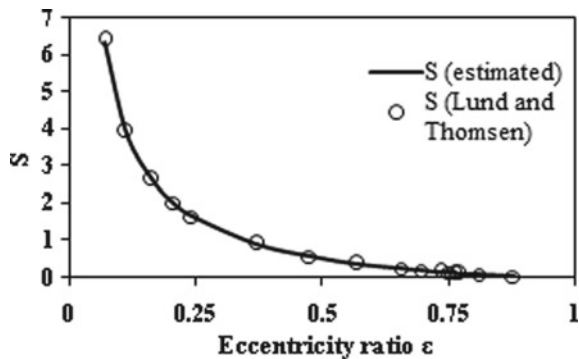
Fig. 6 Variation of
non-dimensionalized
stiffness coefficients with
eccentricity ratio
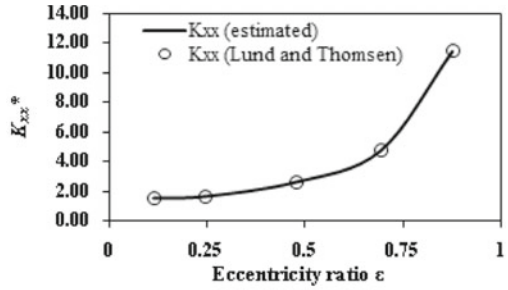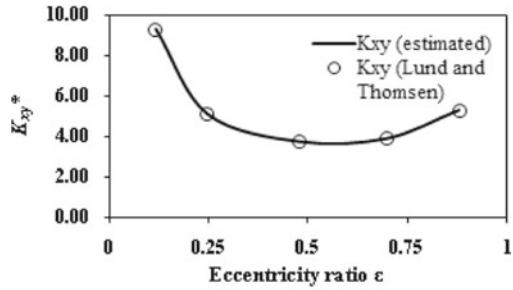
(a) Non-dimensionalised stiffness coefficient K_{xx}

(b) Non-dimensionalised stiffness coefficient K_{xy}
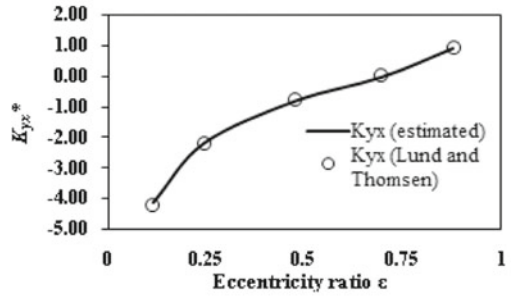
(c) Non-dimensionalised stiffness coefficient K_{yx}
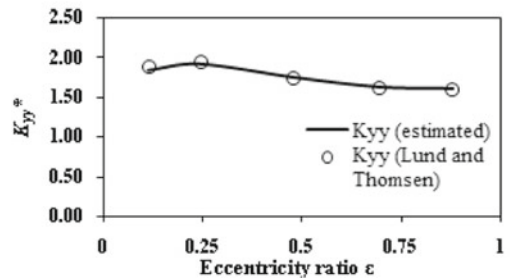
(d) Non-dimensionalised stiffness coefficient K_{yy}

Fig. 7 Variation of non-dimensionalized damping coefficients with eccentricity ratio
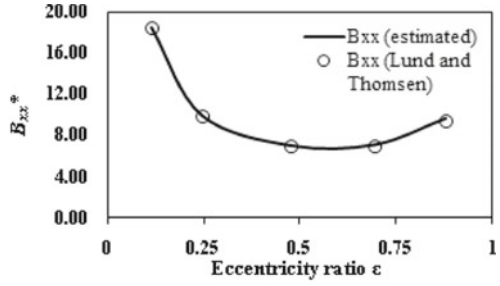
(a) Non-dimensionalised damping coefficient B_{xx}
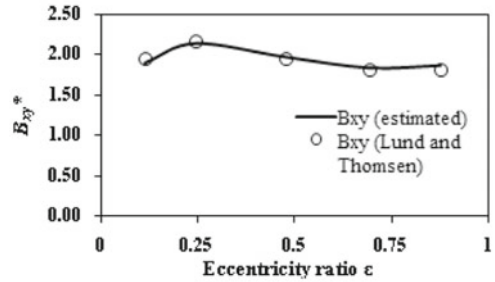
(b) Non-dimensionalised damping coefficient B_{xy}
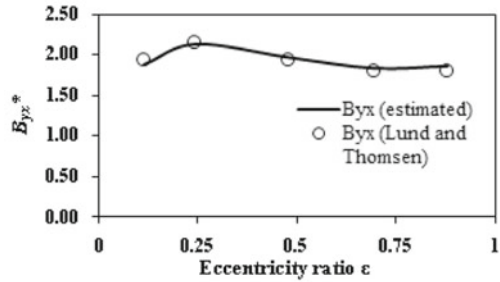
(c) Non-dimensionalised damping coefficient B_{yx}
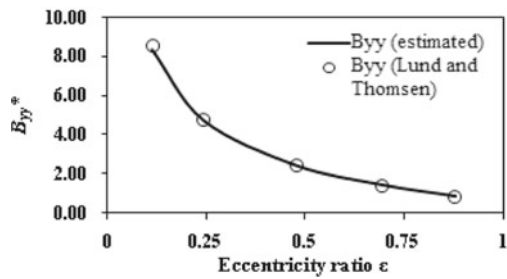
(d) Non-dimensionalised damping coefficient B_{yy}

It can be observed that the cross-coupled damping coefficients (B^*_{xy} and B^*_{yx}) are equal at any value of eccentricity. The direct damping (B^*_{xy}) decreases with eccentricity, reaches a minimum at mid-range eccentricity value, and then again increases. The orthogonal stiffness (B^*_{xy}), however, decreases with increase in eccentricity ratio.

As shown in Figs. 5, 6 and 7, it is observed that a good agreement exists between the present analysis and Lund and Thomsen [4] over the entire eccentricity range.

3.2 Results for Journal Bearings with Vertical Shafts

The load capacity is estimated by varying the shaft orientation angle α and eccentricity. The orbit plots formed for different loads are shown in Figs. 8 and 9.

From the above plots, it can be observed that the orbit size increases with the increase in the load experienced by the shaft. Also, the shaft traces a nearly circular orbit at mid-range load values (between 500 and 2000 N).

The plots for the stiffness coefficients for various eccentricity ratios and different orientation with respect to the first groove are shown in Fig. 10.

From the above plots, it can be observed that the stiffness coefficients increase with an increase in the eccentricity ratio. The direct stiffness coefficient is negative at low eccentricity, which is likely due to the lower load-bearing capacity of the bearing and lower speed of the bearing.

Fig. 8 Orbit plots for load ranging from 100 to 1000N
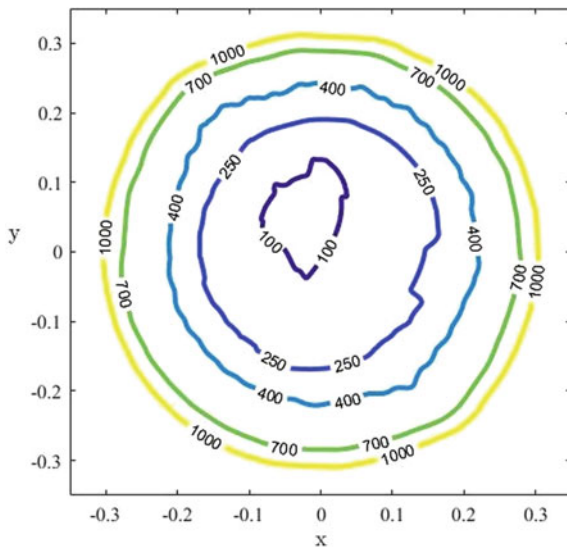
Fig. 9 Orbit plots for load ranging from 1000 to 10000N
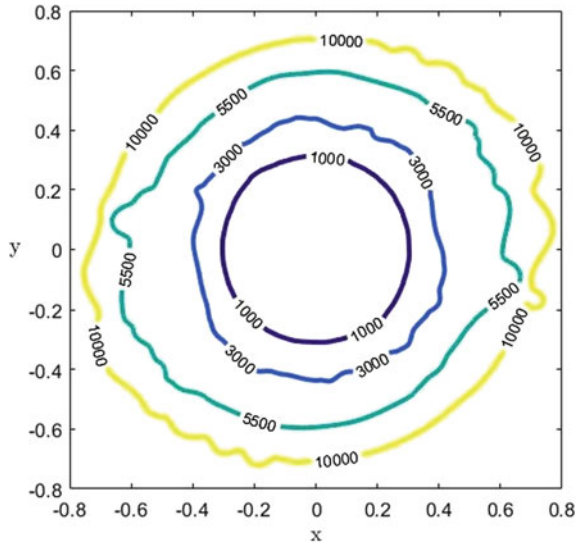
4   Conclusions

The present study is carried out to estimate the rotor dynamic coefficients of hydrodynamic journal bearing in pumps having a vertical shaft. Using finite difference method (FDM), the governing equation is solved. The fluid film pressure, stiffness coefficients, and damping coefficients are evaluated for various bearing configurations using Successive Over Relaxation (SOR) method.

Following are the findings from this study:

- The results from Lund and Thomsen for performance characteristics of horizontal shaft bearing compare well with the computed results.
- For vertical shafts, the shaft orbit becomes larger as the load increases. The shaft traces a nearly circular orbit at mid-range load values (between 500 and 2000 N).
- For vertical shafts, the stiffness coefficients increase with an increase in the eccentricity ratio.

Fig. 10 Orbit plots for stiffness coefficients K_{xx}, K_{xy}, K_{yx} and K_{yy}
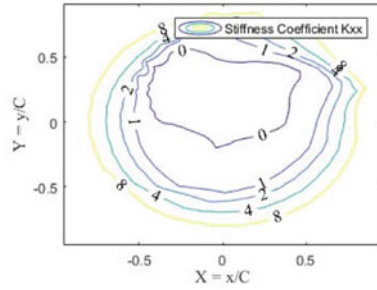
(a) Non-dimensionalised stiffness coefficient K_{xx}
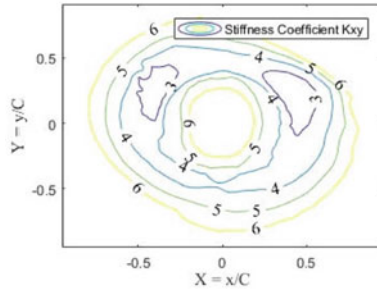
(b) Non-dimensionalised stiffness coefficient K_{xy}
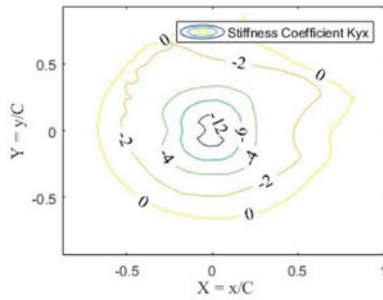
(c) Non-dimensionalised stiffness coefficient K_{yx}
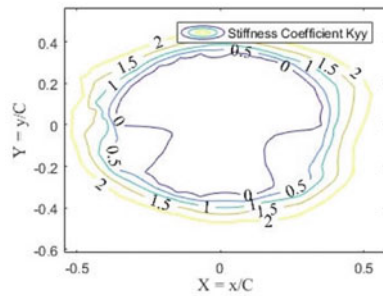
(d) Non-dimensionalised stiffness coefficient K_{yy}

References

1. Raimondi AA, Boyd J (1958) A solution for the finite journal bearing and its application to analysis and design. I, A S L E Trans 1(1):159–174
2. Raimondi AA, Boyd J (1958) A solution for the finite journal bearing and its application to analysis and design: II. A S L E Trans 1(1):175–193
3. Raimondi AA, Boyd J (1958) A solution for the finite journal bearing and its application to analysis and design: III. A S L E Trans 1(1):194–209
4. Lund JW, Thomsen KK (1978) Calculation method and data for the dynamic coefficients of oil-lubricated journal bearings, topics in fluid film bearing and rotor bearing system design and optimization, ASME New York
5. Dowson D (1962) A generalized Reynolds equation for fluid-film lubrication. Int J Mech Sci 4(2):159–170
6. Song Y, Gu C (2015) Development and validation of a three-dimensional computational fluid dynamics analysis for journal bearings considering cavitation and conjugate heat transfer, ASME. J Eng Gas Turbines Power

Asymmetry Analysis of the MHD Flow in Sudden Expansion

Rupesh Baroniya, Manoj Arya, and N. L. Gajbhiye

Nomenclature

B	Applied magnetic field [kg·s^{-2}·A^{-1}]
L_1	Length of the inlet part [m]
L_2	Length of the expanded part [m]
d_1	Height of inlet section [m]
d_2	Height of expanded section [m]
Ha	Hartmann number –
Re	Reynolds number -
j	Electric current density [A·m^{-2}]
ρ	Density [Kg.m^{-3}]
P	Pressure [N·m^{-2}]
N	Stuart number –
X & Y	Cartesian co-ordinates [m]
U	Velocity of fluid [m·s^{-1}]
v	Vertical velocity component [m·s^{-1}]
σ	Fluid electrical conductivity [s^3·A^2·m^{-3}·kg^{-1}]
ϕ	Electric potential [m^2·kg·s^{-3}·A^{-1}]
μ	Dynamic viscosity [kg m^{-1} s^{-1}]
τ	Non-dimensional time component [s]

R. Baroniya (✉) · M. Arya · N. L. Gajbhiye
Department of Mechanical Engineering, Maulana Azad National Institute of Technology Bhopal, Bhopal 462003, India
e-mail: rupeshbaroniya19@gmail.com

1   Introduction

When a fluid flow passes through a suddenly expanded channel it may produce either symmetric or asymmetric flow, which depends upon the expansion ratio and the velocity of the flow. A fluid flow in a 2D symmetric channel with a suddenly expanded section is a basic flow configuration that can be classified by symmetry breaking bifurcation. It has been seen that the bifurcations of this simple class of flows at not-so-large values of Re can reveal the unexpected structure and the rich details of the fluid flow based on the Navier–Stokes equations [1].

This intriguing flow physics and its importance in engineering applications have drawn a lot of attention to magnetohydrodynamics liquid metal flows as it can provide a more sophisticated method to understand the flow asymmetry in the existence of the magnetic field.

2   Literature Review and Objective

Vast research has been carried out in the case of sudden expansion for a magneto-hydrodynamics fluid flow. Mastrangelo et al. [2] carried out an MHD flow simulation for sudden expansion in a rectangular channel. They considered the Hartmann number (Ha) up to 250 and the Reynolds number (Re) up to 25. The calculations were done considering conducting walls in the direction of flow. Buhler et al. [3] also did an experimental study for MHD flow in a rectangular channel considering conducting walls in the direction of the magnetic field. They studied the effect of Hartmann number up to 1250 and Re in the order of 10,000. The flow behavior is observed for different expansion ratios. Praveen et al. [4] carried out two-dimensional MHD simulations for sudden expansion considering the Reynolds number up to 100 and identified the change in flow symmetry. They reported results for interaction parameters in the range of 1–100. Singh et al. [5] performed a two-dimensional natural flow analysis for sudden expansion in a cavity. They studied the effect of Hartmann number ranging from 0 to 500 for a cavity in which walls are exposed to different temperatures. Kumamaru et al. [6] simulated magnetohydrodynamics flow in a sudden expansion rectangular channel. The authors reported results for the magnetic field when it is applied in the direction of the fluid flow in one case and orthogonal to the direction of the fluid flow in another case. They considered Hartmann number of Ha = 100 and Reynolds number ranging from 500 to 1000. The results suggest that when a magnetic field was applied orthogonal to the direction of fluid flow, the loss coefficient is negligible. On the other hand, when the magnetic field was applied at an inclination to the direction of fluid flow the loss coefficient become considerably large. Aleksandrova and Molokov [7] performed a numerical study for 2D magnetohydrodynamic flow for sudden contraction and expansion in a duct for a high Hartmann number and a magnetic field was applied in the transverse direction. Branover et al. [8] experimentally calculated the total inertia

force for insulated sudden expansion for MHD flow. Drikakis et al. [9] carried out a numerical analysis of laminar flow in a channel with sudden expansion. They considered various expansion ratio and Reynolds number. The result suggests that the flow asymmetry depends on Re and the expansion ratio. The higher asymmetry was found to be associated with a higher Re. In Durst et al. [10], a similar study was carried out for asymmetry analysis in MHD flow for sudden expansion at low Re and a higher aspect ratio. Xiao et al. [11] performed a three-dimensional numerical study for MHD flow for sudden contraction and gradual contraction. The results show a small vortex generation close to the leading edge in sudden contraction and smooth streamlines generation in the gradual contraction. Mandal et al. [12] carried out the numerical analysis in a suddenly expanded channel with a fence considered as a diffuser for Re in the range of 20–100 and the fence subtended angle was in the range of 10°–30° for an aspect ratio of 2. The results suggest that the fence subtended angle does not affect the stagnation pressure drop.

3 Materials and Methods

3.1 Calculation Models

The schematic diagram of the channel studied in the present study is shown in Fig. 1. The length and height of the inlet part are represented by L_1 and d_1, respectively. Here, length L_1 is considered as two and a half times height d_1. The length and height of the expanded part are represented by L_2 and d_2, respectively. The length of the expanded part L_2 is taken as 50 times the height d_1. The expansion ratio is 4, which is the ratio of inlet height d_1 and expanded height d_2. The origin of the $X–Y$ coordinate is considered at a point in the centerline joining inlet and expanded part. It is assumed that flow is incompressible and two-dimensional. For the magnetohydrodynamics case, it is assumed that the fluid is electrically conductive. A magnetic field is considered in the direction of fluid flow. A fully developed flow is considered to enter the inlet with the velocity U.

Fig. 1 Schematic diagram of 2D geometry

3.2   Calculation Methods

The non–dimensional governing equations for MHD flow are as follows:

$$\nabla.\vec{u} = 0, \tag{1}$$

$$\frac{\partial u}{\partial \tau} + (\vec{u}.\nabla)\vec{u} = -\nabla p + \frac{1}{\text{Re}}\nabla^2\vec{u} + N\vec{j} \times \vec{B}, \tag{2}$$

$$\vec{j} = -\nabla\varphi + \vec{u} \times \vec{B}. \tag{3}$$

Above non-dimensional equations are obtained by scaling variables as follows:

$$u = \frac{u_x}{U},$$
$$v = \frac{u_y}{U},$$
$$X = \frac{x}{d_1},$$
$$Y = \frac{y}{d_1},$$
$$\tau = \frac{t.d_1}{U},$$

where U, u_x, u_y, and τ are average inlet velocity, x-component of velocity, y-component of velocity and non-dimensional time, respectively.

The variables $\vec{u}$, $\vec{j}$, and $\vec{B}$ represent non-dimensional velocity vector field, current density, and the magnetic field, respectively.

In the above equation various non-dimensional numbers appear as follows:

$$\text{Re} = \frac{\rho U d_1}{\mu}, \text{Ha} = B_x d_1\sqrt{\frac{\sigma}{\mu}}, N = \frac{H_x^2}{\text{Re}} = \frac{\sigma d_1 B_x^2}{\rho U},$$

where Re is Reynolds number, Ha is Hartmann number, and N is the interaction parameter which is also known as Stuart number.

3.3   Validation

The current numerical analysis is compared with the results of Praveen et al. [4] at Reynolds number of Re $=$ 70 is shown in Fig. 2. The present numerical results matched well with the reference results.
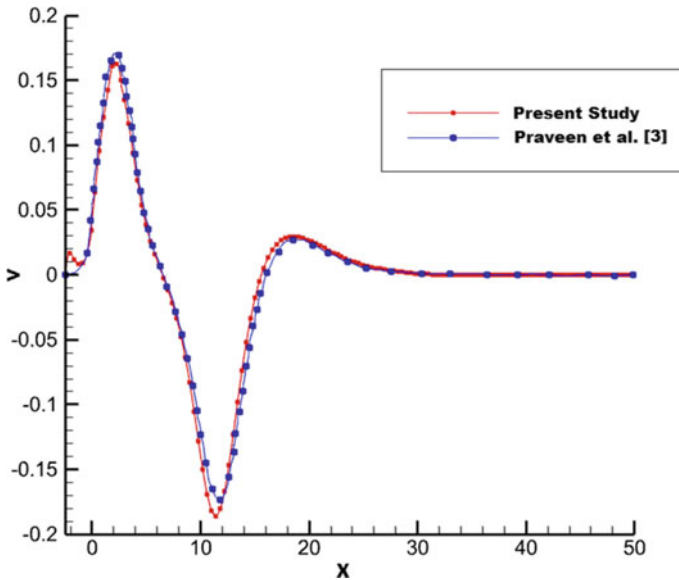
Fig. 2 Comparison of the vertical velocity component at Reynolds number = 70

Re used for the base calculation is 70. The Hartmann number (Ha) used for the base calculation is zero.

4 Results and Discussion

A magnetic field on a liquid metal magnetohydrodynamics flow is applied and studied for sudden expansion (ER = 4) at a fixed value of Re and different value of Ha in the present study. The asymmetry of flow is represented by the change occurring in the vertical velocity component. To observe the effect of the varying Hartmann number (Ha) on flow asymmetry, a magnetic field is applied in the direction of the fluid flow. The strength of the magnetic field on fluid flow is measured by Hartmann number which defines as the ratio of Lorentz force and viscous force. Figure 3 represents the variation in the centerline vertical velocity at Re = 60 and different value of Ha. It has been observed that increasing Hartmann number reduces the flow asymmetry because magnetic field stretches the circulation along the direction of the flow.

The effect of a fixed Hartmann number with varying Reynolds number is also reported. Figure 4 represents the variation in the centerline vertical velocity at Ha = 1 and Re ranging from 40 to 80.

Figure 4 reveals that increasing the value of Re, also increases the flow asymmetry. The velocity streamlines at Hartmann number = 1 and various Reynolds number is shown in Fig. 5.
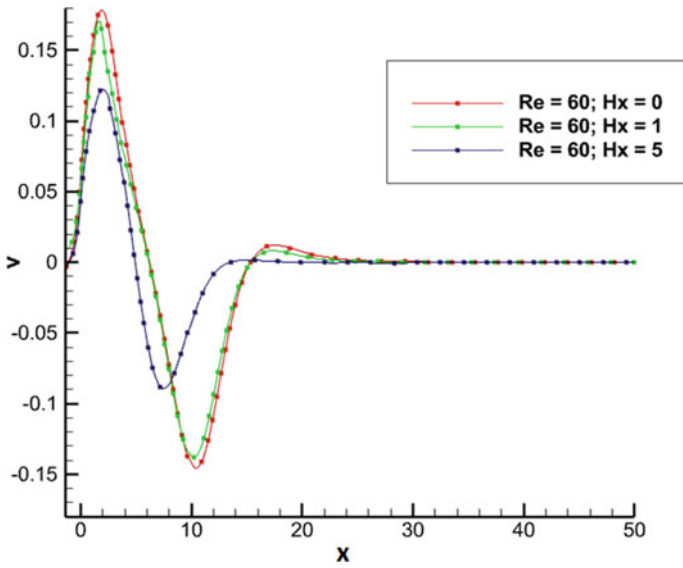
Fig. 3 Variation on the vertical velocity component at different values of Hx for Re = 60
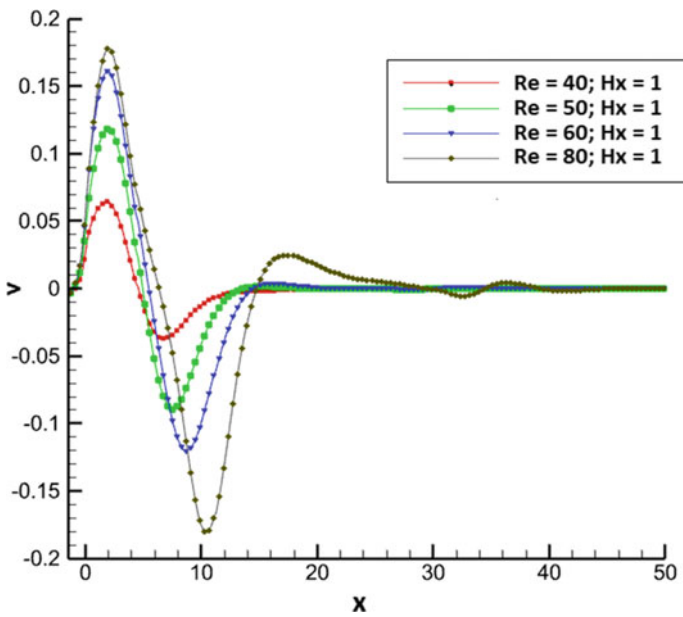
Fig. 4 Variation on the vertical velocity component at different Reynolds number for Hx = 1
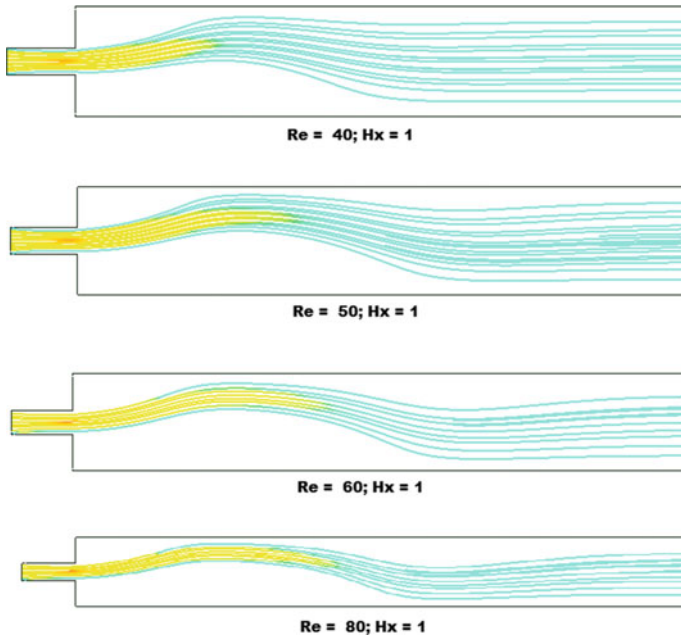
Fig. 5 Velocity streamlines at different Reynolds numbers and Hx = 1

The present study clears that both Hartmann number and Reynolds number affect the asymmetry of the flow and varying Re and Ha can make the flow symmetrical. In previous studies, it has been seen that the fluid flow in the presence of the Hartmann number of Ha = 2 becomes completely symmetrical at the Reynolds number of Re = 40 [4].

In the current study, the effect of fluid flow asymmetry is observed at fixed Hartmann number Ha = 5 for various Reynolds number. Figure 6 depicts the variation on the vertical velocity at a fixed Hartmann number and different Reynolds number.

It can be understood from Fig. 6 that the flow becomes completely symmetrical at Reynolds number 55. As the magnetic field in the direction of the flow stretches the streamlines along its direction. A magnetic field with a high Hartmann number can make high turbulent flow symmetrical.

Figure 7 shows that the velocity streamlines become completely symmetrical at Ha = 5 and Re = 55.
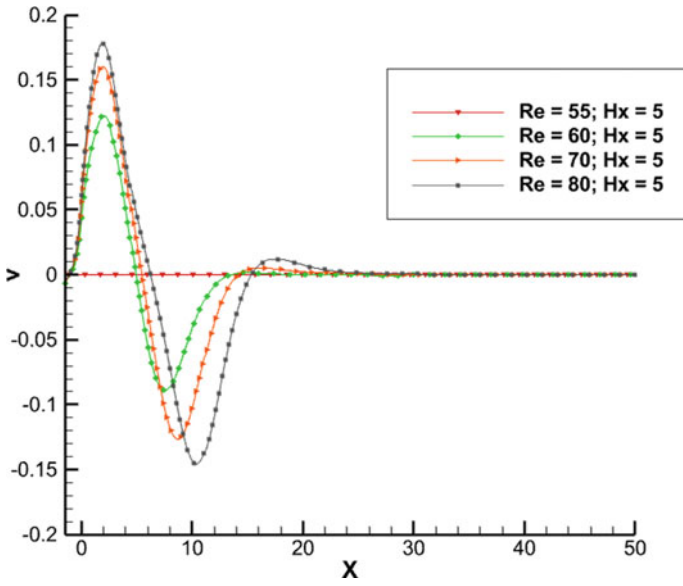
Fig. 6 Variation on the vertical velocity component at different Reynolds number and Hx = 5
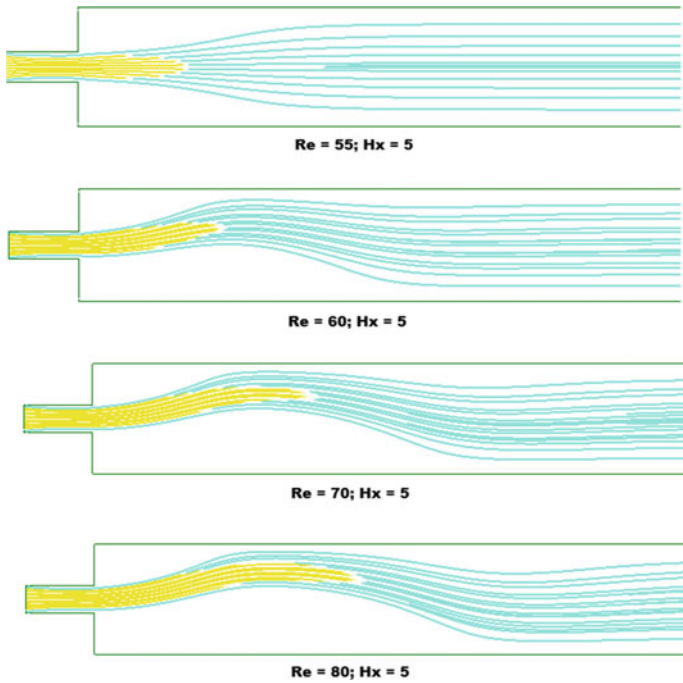
Fig. 7 Velocity streamlines at different Reynolds numbers and Hx = 5

5 Conclusions

A numerical study has been done on the liquid metal magnetohydrodynamics flow with an expansion ratio of 4. In the magnetic field, different values of the Hartmann are applied in the direction of the liquid metal flow and the effect on flow asymmetry is observed. Based on the numerical calculations performed, it is seen that the flow asymmetry depends on both the Reynolds number and Hartmann number. With increasing the Reynolds number, the flow asymmetry increases, while it reduces on increasing Hartmann number. By increasing the value of the Hartmann number flow can be made completely symmetrical.

It is also observed that when the Hartmann number of Ha = 5 is fixed in the direction of the fluid flow, it becomes completely symmetric at Re = 55.

References

1. Fearn RM et al (1990) Nonlinear flow phenomena in a symmetric sudden expansion. J Fluid Mech 211:595–608
2. Mistrangelo C (2006) Three-dimensional MHD flow in sudden expansions, Ph.D. Thesis, FZK
3. Bühler L (2003) Inertialess magnetohydrodynamic flows in expansions and contractions, FZKA 6904, Kernforschungszentrum Karlsruhe
4. Praveen T, Eswaran V (2017) Transition to asymmetric flow in a symmetric sudden expansion: Hydrodynamics and MHD cases. Comput Fluids 148:103–120
5. Singh RJ, Gohil TB (2020) Numerical analysis of unsteady natural convection flow and heat transfer in the existence of lorentz force in suddenly expanded cavity using open FOAM. J Therm Sci 29(6):1513–1530
6. Kumamaru H (2017) Numerical analyses on liquid-metal magnetohydrodynamic flow in sudden channel expansion. J Nucl Sci Technol 54(2):242–252
7. Aleksandrova S, Molokov S (2012) The structure of parallel layers in steady twodimensional magnetohydrodynamic flows in sudden duct expansions and contractions. Theor Comput Fluid Dyn. 26:29–35
8. Branover GG, Vasil'ev AS, Gel'fgat YM (1967) Effect of a transverse magnetic field on the flow in a duct at a sudden cross section enlargement. Magnetohydrodynamics 3(3):61–65
9. Drikakis D (1997) Bifurcation phenomena in incompressible sudden expansion flows. Phys Fluids 9(1):76–87
10. Durst F, Melling A, Whitelaw JH (1974) Low Reynolds number flow over a plane symmetric sudden expansion. J Fluid Mech 64(1):111–128
11. Xiao X, Kim CN (2020) Numerical simulations of MHD flows in a conduit that contracts in the magnetic field direction. Fusion Eng Des 160:111990
12. Mandal DK, Bandyopadhyay S, Chakrabarti S (2011) A numerical study on the flow through a plane symmetric sudden expansion with a fence viewed as a diffuser. Int J Eng Sci Technol 3(8):210–233

Non-isothermal, Incompressible Flow of a Viscoelastic Fluid Inside a Square Cavity at High Weissenberg Number

Deepak Talan and Shyam Sunder Yadav

Nomenclature

$\vec{u}$	Non-dimensional Velocity vector [–]
T	Non-dimensional Temperature [–]
p	Non-dimensional Pressure [–]
c	Non-dimensional Conformation tensor
ψ	Non-dimensional Logarithm of c
τ_s	Non-dimensional Solvent stresses [–]
τ_p	Non-dimensional Polymer stresses [–]
λ	Relaxation time [s]
$\alpha_T(T)$	Shift factor [–]

1 Introduction

Natural convection heat transfer by a fluid have wide range of engineering applications involving chemical refineries, metallurgical industries, electricity generation with thermal and nuclear power plants, building thermal management, solar-thermal heat collectors, heat extraction from the battery pack of electric vehicles and many more. The natural convection heat transfer with viscoelastic fluids is encountered in polymer industries, food manufacturing and packaging industries. The natural convection phenomenon is also relevant to geophysical flows and the behaviour of molten rocks in the earth's mantle. A review on the natural convection with viscoelastic fluids can be found in Demir and Akyıldız [1], Demir [2].

D. Talan · S. S. Yadav (✉)

Department of Mechanical Engineering, BITS Pilani, Pilani, Rajasthan 333031, India
e-mail: ss.yadav@pilani.bits-pilani.ac.in

One of the problems with the simulation of viscoelastic flows is the divergence of the numerical setup at Weissenberg numbers higher than a certain value which is around one in most of the cases. For tackling this problem, Fattal and Kupferman [3] proposed the log conformation approach in which the exponential variation of viscoelastic stresses is changed to algebraic variation by introducing the logarithm of the conformation tensor. The log-conformation approach was used by Habla et al. [4] for simulating two-phase viscoelastic flows with OpenFOAM [5] which is an open source flow solver. They simulated two-phase flow cases like the rod climbing effect, die swell effect, drop deformation in planar elongating and shearing flows etc. The three dimensional lid driven cavity flow of a viscoelastic fluid was investigated by Habla et al. [6]. A Navier–Stokes solver based on the stream function–vorticity and log conformation approach was developed by Comminal et al. [7] for simulating viscoelastic flows. Two-phase viscoelastic flows were studied by Figueiredo et al. [8] by using the kernel conformation transformation technique and Volume-of-Fluid method. For capturing the interface in two-phase viscoelastic flows, López-Herrera et al. [9] implemented the log-conformation approach in a Volume of-fluid method based two-phase flow solver. In spite of the fundamental work on the constitutive modelling for non-isothermal viscoelastic flows by Marrucci [10], Gupta and Metzner [11], Peters and Baaijens [12], very few works are dedicated to the numerical simulation of non-isothermal viscoelastic flows. Zhang et al. [13] used the non-isothermal constitutive equations based on FENE, Hooke and FENE-P models for the non-isothermal flow of a polymer inside a rectangular channel and a planar contraction geometry.

From the above literature review, it can be noted that the log conformation approach has proven itself for handling viscoelastic flows at high Weissenberg number. Also, compared to the literature on isothermal viscoelastic flows, far lesser numerical works exist on the non-isothermal viscoelastic flows. In this paper, we study the non-isothermal flow of a viscoelastic fluid inside a square cavity where the left and right wall are kept at different temperatures. We study the distribution of temperature, flow velocity and the viscoelastic stresses in the domain under steady state conditions. This paper is organized as follows: In Sect. 2, we present the governing equations and the details on numerical implementation, in Sect. 3 we present and discuss the various results obtained by the numerical simulations, and finally, in Sect. 4, we conclude the current work.

2 Methodlogy

The non-dimensional mass, momentum, and energy conservation equations for an incompressible, non-isothermal flow of a viscoelastic fluid are as follows:

$$\nabla . \vec{u} = 0,$$

$$\frac{\partial \vec{u}}{\partial t} + \nabla.(\vec{u}\vec{u}) = -\nabla p + \nabla.\left(Pr\,Ra^{-0.5}\nabla\vec{u}\right)$$
$$+ \nabla.\tau_p + Pr\,T\hat{e}_y,$$

and finally,

$$\frac{\partial T}{\partial t} + \nabla.\vec{u}T = \nabla.\left(Ra^{-0.5}\nabla T\right).$$

In the above equations, $\vec{u}$ denotes the non-dimensional velocity vector, p denotes the non-dimensional pressure, τ_p are non-dimensional polymer stresses, T is the non-dimensional temperature, $Ra = \frac{g\beta\Delta T H^3}{\kappa\vartheta}$ is the Rayleigh number, and $Pr = \frac{\vartheta}{\kappa}$ is the Prandtl number. Because of the low velocities expected under natural convection, the dissipation of mechanical energy to thermal energy is not considered in the energy equation written above. The above equations are derived from the respective dimensional forms using the following characteristics scales: for mass $[M] = \rho H^3$, for length $[L] = H$, for temperature $[T] = \Delta T_{\text{Dim.}}$, and finally, for velocity $[U] = \frac{k}{H}\sqrt{\frac{g\beta\Delta T H^3}{\kappa\vartheta}}$.

The viscoelastic behavior of the fluid is captured with the help of Oldroyd-B model, the non-dimensional constitutive equation for which is given by

$$\tau_p + Wi\,\overset{\nabla}{\tau p} = 2\frac{(1-\beta)}{\text{Re}}\mathbf{D}.$$

In the above equation, β is the ratio of the solvent viscosity to the total viscosity, τ_p denotes the non-dimensional $\overset{\nabla}{\tau p}$ is the upper convected derivative of the polymer stresses, and finally, $Wi = \frac{\lambda U}{H}$ is the Weissenberg number, and $\text{Re} = \frac{\rho U H}{H}$ is the Reynolds number. On solving the above equation in terms of τ_p, there are high chances of divergence of the numerical solution procedure and this phenomenon is termed as the 'High Weissenberg number problem.' Therefore, τ_p is calculated in terms of the conformation tensor $\mathbf{c}$ which is related to the polymeric stresses as $\tau_p = \frac{\mu_p}{\lambda_R}(\mathbf{c} - \mathbf{I})$. The evolution equation for the conformation tensor is given by

$$\frac{\partial \mathbf{c}}{\partial t} + \vec{v}.\nabla\mathbf{c} - \mathbf{c}.\nabla\vec{v} - \nabla\vec{v}^T.\mathbf{c} = -\frac{(\mathbf{c} - \mathbf{I})}{\lambda_R}.$$

Under the log-conformation approach, the logarithm of the conformation tensor $\psi = \log\mathbf{c}$ is actually used in the calculation procedure and the evolution equation for which is

$$\frac{\partial \psi}{\partial t} + u.\nabla\psi = \mathbf{\Omega}.\psi - \psi.\mathbf{\Omega} + 2\mathbf{B} + \frac{\left(\mathbf{I} - e^\psi\right)}{\lambda_R}.$$

The tensors **B** and **Ω** are obtained from the decomposition of the transpose of velocity gradient tensor as follows:

$$\nabla \vec{v}^T = \mathbf{\Omega} + \mathbf{B} + \mathrm{N}c^{-1}.$$

The material properties, namely the polymer viscosity μ_p, the solvent viscosity μ_s, and the relaxation time λ are considered functions of temperature as follows:

$$\frac{\mu_s(T)}{\mu_s(T_0)} = \frac{\mu_p(T)}{\mu_p(T_0)} = \frac{\lambda(T)}{\lambda(T_0)} = \alpha_T(T).$$

William et al. [14] gave the following equation for calculating the shift factor α_T:

$$\alpha_T(T) = \exp\left(\frac{-c_1(T - T_0)}{c_2 + T - T_0}\right).$$

A square cavity of unit side length is taken as the computational domain as shown in Fig. 1. Dirichlet boundary condition is given to the left and right walls where non-dimensional temperature equal to -0.5 is applied to right wall. Zero temperature gradient is forced to the top and bottom walls. No-slip boundary condition is enforced to all the walls for the flow velocity. $\tau_{p,xx}$ values are enforced to zero on the left and right walls, while $\tau_{p,yy}$ values are fixed to zero on the top and bottom walls. Rayleigh number is taken as 1000, and Prandtl number is taken as 0.71 for the current problem. The ratio of the solvent viscosity to the total viscosity, β, is taken as 0.5, and Weissenberg number is taken as 10. The initial condition for the temperature is the linear distribution starting from zero at the left boundary and one at the right boundary. This is done so that steady state condition can be achieve with least possible computational effort. The steady state condition is confirmed by observing the variation of different physical quantities over various time steps. The initial condition for velocity is set to zero value everywhere in the domain.

3 Results and Discussion

In this section, we discuss the different results obtained by us based on the current simulations. Figure 2 shows the velocity distribution inside the cavity under steady state conditions. It can be noted that the velocity is almost zero at the corners, near the walls and at the center of the cavity. Higher values of the velocity lie at four locations inside the cavity which are approximately located at symmetric locations inside cavity.

Further information on the velocity distribution can be drawn from Figs. 3 and 4 which respectively show the x and y components of the velocity. There is anticlockwise motion of the fluid inside the cavity under natural convection (temperature on the right wall is higher than that at the left wall). As can be seen in Fig. 3, the x

Fig. 1 Computational domain for the non-isothermal, incompressible viscoelastic flow of a viscoelastic fluid in a square cavity
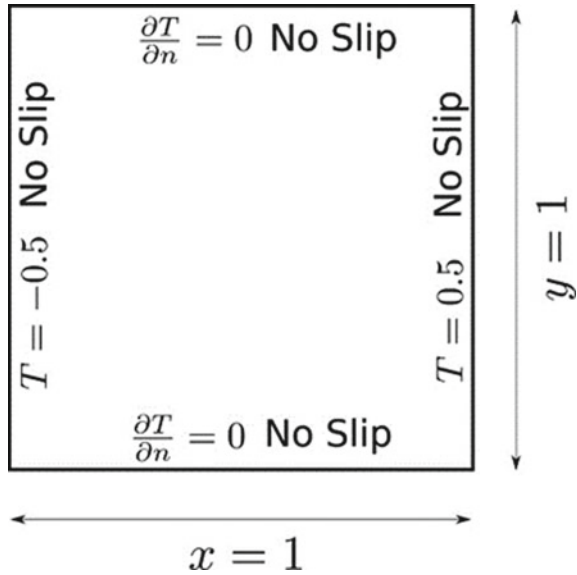
Fig. 2 Distribution of non-dimensional velocity in the cavity
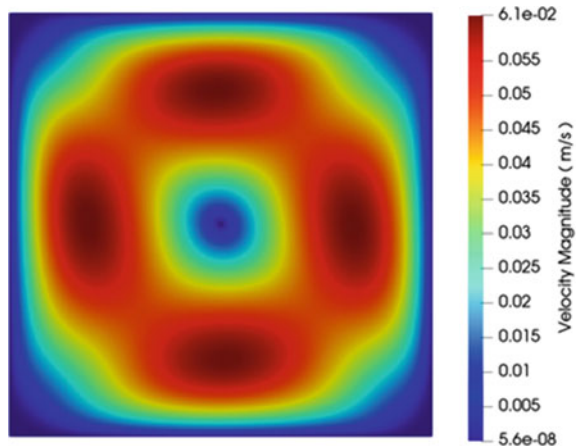
velocity is negative with a higher value in the upper half of the domain while it is positive with a higher value in the lower half of the domain. Similarly, the y velocity is negative with a higher value in left half of the domain while it is positive with a higher value in the right half of the domain as can be seen in Fig. 4. The net results are the four lobed distribution as shown Fig. 2.

The distribution of the non-dimensional temperature inside of the cavity is shown in Fig. 5. Although the left side and the right side of the domain are approximately at the respective wall temperatures, there is a wavy pattern of temperature around the

Fig. 3 Distribution of
x component of
non-dimensional velocity in
the cavity
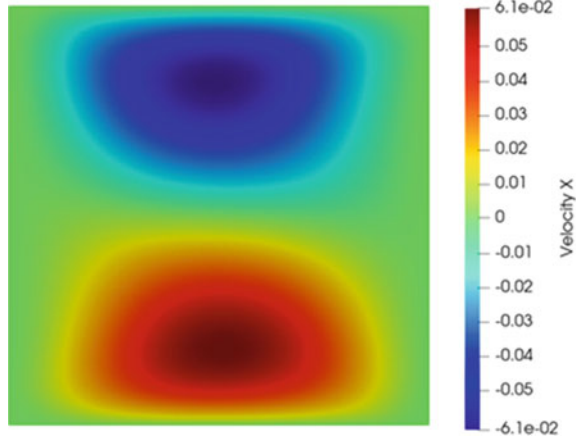
Fig. 4 Distribution of
y component of
non-dimensional velocity in
the cavity
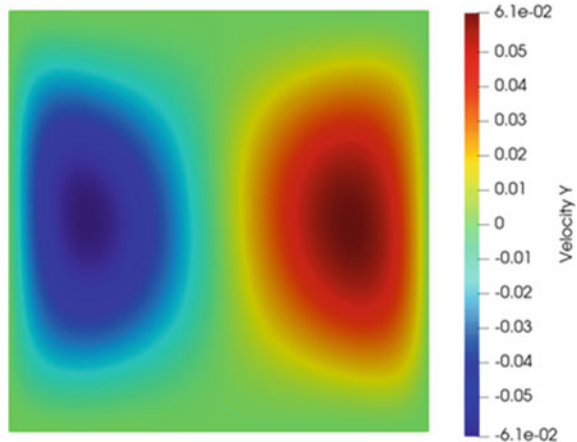
middle plane of the cavity. This is due to the slow rotation of the viscoelastic fluid inside the cavity under natural convection.

Figure 6 shows the distribution of $\tau_{p,xx}$ component of the polymeric stresses inside the domain. The $\tau_{p,xx}$ component is the stress on a plane perpendicular to the *x*-axis and along the *x* direction. It is maximum on the top and bottom walls, and almost negligible around the center of the cavity and on the left and the right walls.

Figure 7 shows the beautiful distribution of the shear component $\tau_{p,yx}$ of polymeric stresses inside the cavity. It can be noted from the figure that shear stress component is negative around the top of right wall and bottom of left wall where the flow deaccelerates while it is positive near the bottom of the right wall and top of the left wall where the flow accelerates. The acceleration and deacceleration of the flow change the sign of the shear stress. Finally, the distribution of the normal stress component $\tau_{p,yy}$ is shown in Fig. 8. This normal stress component is maximum on

Fig. 5 Distribution of non-dimensional temperature in the cavity
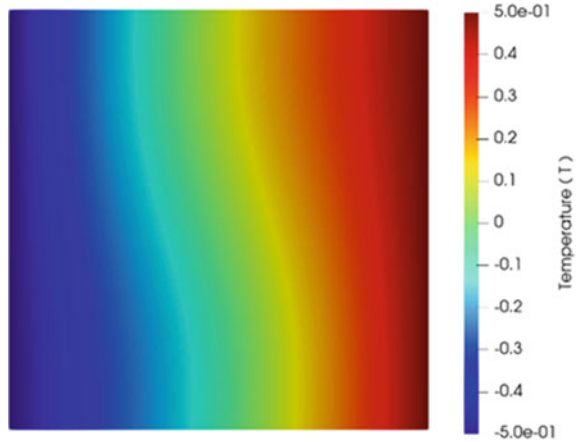
Fig. 6 Distribution of non-dimensional, normal stress component $\tau_{p,xx}$ in the cavity
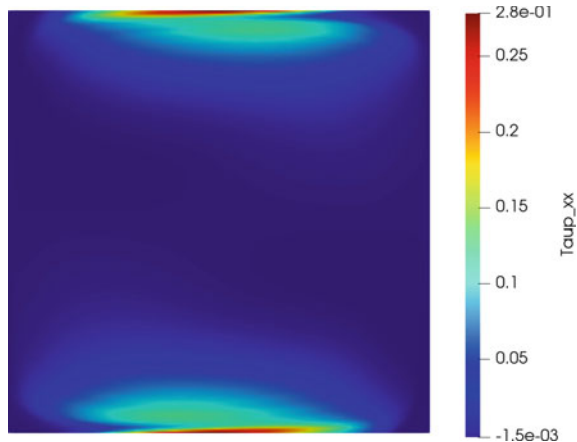
the left and right walls and negligible around the center of the cavity and on the top and bottom walls. In the next section, we conclude the current work.

4   Conclusions

The natural convection process of a viscoelastic, incompressible fluid inside a cavity is numerically investigated. Based on the simulation results, following conclusion can be drawn. Due to natural convection, the viscoelastic fluid starts to move upward when it comes in contact with the right, hotter wall while it moves downward at the left, cooler wall. A four lobed velocity profile is observed inside the cavity with a wavy temperature profile around the mid plane due to the convection of the fluid.

Fig. 7 Distribution of
non-dimensional, shear
stress component $\tau_{p,yx}$ in the
cavity
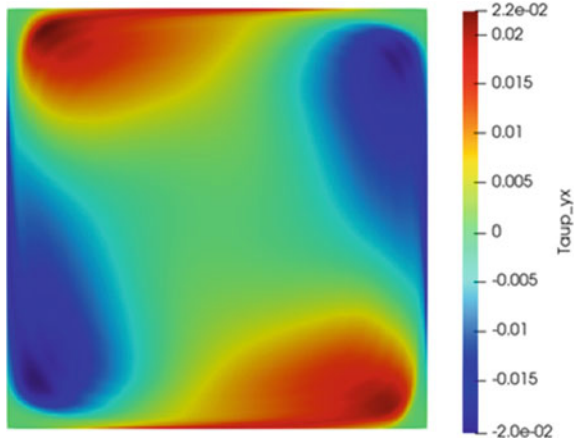
Fig. 8 Distribution of
non-dimensional, normal
stress component $\tau_{p,yy}$ in the
cavity
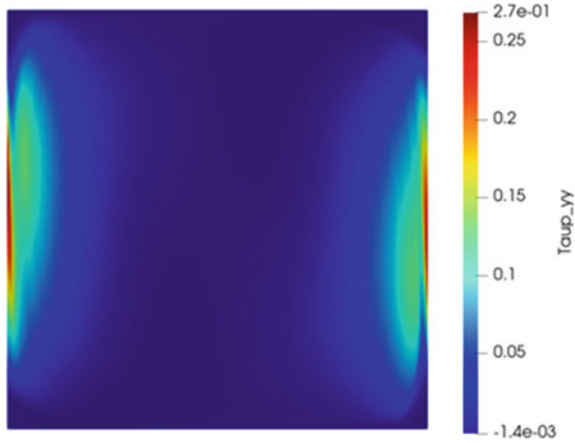
There is a stretching of the viscoelastic fluid observed along the x direction at the
top and the bottom walls resulting in a higher value of the $\tau_{p,xx}$ component of the
polymer stresses. Similarly, there is a stretching of the fluid along the y direction at
the left and the right walls resulting in a higher value of $\tau_{p,yy}$ component. The shear
component of the polymeric stresses, $\tau_{p,yx}$ displays a beautiful pattern inside the
cavity with negative values in the regions of fluid deacceleration and positive values
in the regions of fluid acceleration. The current work helps one to visualize the stress
pattern created in a viscoelastic fluid under natural convection.

References

1. Demir H, Akyıldız FT (2000) Unsteady thermal convection of a non-newtonian fluid. Int J Eng Sci 38(17):1923–1938
2. Demir H (2003) Rayleigh–benard convection of viscoelastic fluid. Appl Math Comput 136(2–3):251–267
3. Fattal R, Kupferman R (2005) Time-dependent simulation of viscoelastic flows at high weissenberg number using the log-conformation representation. J Nonnewton Fluid Mech 126(1):23–37
4. Habla F, Marschall H, Hinrichsen O, Dietsche L, Jasak H, Favero JL (2011) Numerical simulation of viscoelastic two-phase flows using openfoam®. Chem Eng Sci 66(22):5487–5496
5. Weller HG, Tabor G, Jasak H, Fureby C (1998) A tensorial approach to computational continuum mechanics using object-oriented techniques. Comput Phys 12(6):620–631
6. Habla F, Tan MW, Haßlberger J, Hinrichsen O Numerical simulation of the viscoelastic flow in a three-dimensional lid-driven cavity using the log-conformation reformulation in OpenFOAM®. J Non-Newtonian Fluid Mech 212:47–62
7. Comminal R, Spangenberg J, Hattel JH (2015) Robust simulations of viscoelastic flows at high Weissenberg numbers with the streamfunction/log-conformation formulation. J Non-Newtonian Fluid Mech 223:37–61
8. Figueiredo RA, Oishi CM, Afonso AM, Tasso IVM, Cuminato JA (2016) A two-phase solver for complex fluids: studies of the Weissenberg effect. Int J Multiphase Flow 84:98–115
9. López-Herrera JM, Popinet S, Castrejón-Pita AA (2019) An adaptive solver for viscoelastic incompressible two-phase problems applied to the study of the splashing of weakly viscoelastic droplets. J Non-Newtonian Fluid Mech 264:144–158
10. Marrucci G (1972) The free energy constitutive equation for polymer solutions from the dumbbell model. Trans Soc Rheol 16(2):321–330
11. Gupta RK, Metzner AB (1997) Modeling of non-isothermal polymer process. J Rheol 68(2–3):205–224
12. Peters GWM, Baaijens FPT (1997) Modelling of non-isothermal viscoelastic flows. J Nonnewton Fluid Mech 68(2–3):205–224
13. Zhang H, Ouyang J, Ruan C (2011) Constitutive equations of non-isothermal polymer melt. Appl Math Model 35(4):2024–2040
14. Williams ML, Landel RF, Ferry JD (1955) The temperature dependence of relaxation mechanisms in amorphous polymers and other glass-forming liquids. J Am Chem Soc 77(14):3701–3707

Study of Pocket Pressure and Load Bearing Capacity in Pocket Type Hydrostatic Bearing Under Rotation

S. Aravindan, K. V. Sreedharan, U. Partha Sarathy, and A. John Arul

1 Introduction

Pocket type hydrostatic bearing (HSB) supports the shaft of sodium pumps of sodium cooled fast breeder reactors. A typical four pocket hydrostatic bearing is shown in Fig. 1, and the developed view of the pocket type bearing is shown in Fig. 2. The bearing consists of four pockets P1, P2, P3 and P4. Each pocket will be surrounded by low clearance region called land, which offers significant resistance for the flow from leaving the pocket. The flow in the land region is governed by Reynolds equation.

In a typical journal bearing without pockets, due to rotation of the journal, pressure in the bearing film land will increase, which supports the load of the shaft. In a hydrostatic bearing, when there is rotation of the journal, the pressure developed due to dynamic action of the rotor will be small.

Precise estimation of load bearing capacity of the bearing is very crucial, especially in sodium pumps as the bearings are supplied with sodium flow from pump itself. Thus, the load capacity of the bearings has to be estimated considering the pressure developed due to the dynamic action of the rotor, which is obtained on solving the Reynolds equation for the land region of bearing along with the appropriate boundary conditions. Upon the integration of the pressure, load bearing capacity of bearing is estimated. The developed pressure due to dynamic action will also affect the pocket pressure in the hydrostatic bearing. The effect of rotation on the pocket pressure is also studied.

In this study, 2D code is developed for generating grid points in land region of the bearing, solving Reynolds equation, identifying correct pocket pressures and

S. Aravindan (✉) · K. V. Sreedharan · U. Partha Sarathy
Indira Gandhi Centre for Atomic Research, Kalpakkam, Tamilnadu 603102, India
e-mail: aravinds@igcar.gov.in

S. Aravindan · A. John Arul
Training School Complex, Homi Bhabha National Institute, Anushaktinagar, Mumbai 400094, India
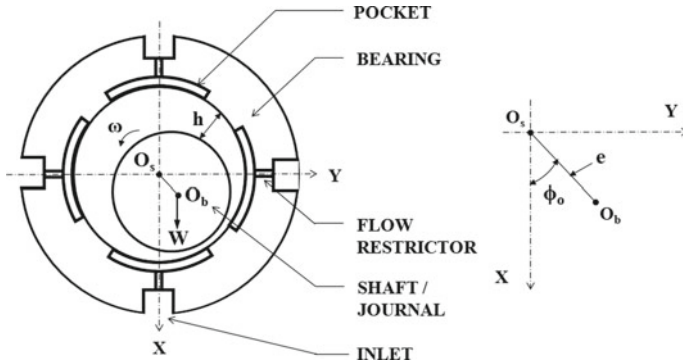
Fig. 1 Sectional view of pocket type hydrostatic bearing
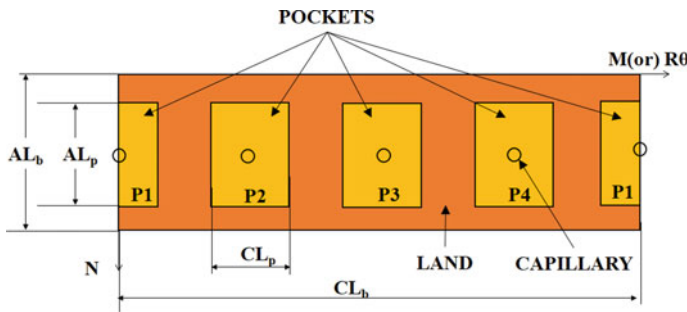
Fig. 2 Developed view of pocket type hydrostatic bearing

estimating load capacity. The pocket pressure and the load bearing capacity of the bearing under non-rotating and rotating conditions are estimated. The results obtained were compared with the literature results and validated.

2 Literature Review and Objective

Pocket type hydrostatic bearings under static condition was studied by Metman et al. [1], where the pocket pressure for a given bearing geometry is measured under static condition at various eccentricity. The bearing geometry along with the capillary dimensions defines the characteristic number of a bearing (β), which is defined as the ratio of pocket pressure to the supply pressure, when the bearing is in concentric condition. Metman indicated that the bearing studied has ($\beta = 0.555$).

The load capacity of the pocket type bearings was estimated by Ghosh et al. [2]. The effect of variation of capillary dimensions and eccentricity on the load capacity

of the bearing is estimated under stationary condition. The effect of rotation of the HSB on the load capacity and attitude angle of the bearing is studied.

The objective of the study is to develop code towards the estimation of pocket pressure in hydrostatic bearing and validate the results with the literature. The effect of attitude angle and eccentricity on the pressure distribution of HSB under static condition is studied. The effect of rotation on the pocket pressure and load bearing capacity is also studied.

3　Methodology

3.1　Governing Equation and Solving Methodology

The pressure in the fluid film of bearing is given by Reynolds equation, which in $m - n$ coordinate system (as shown in Fig. 2) is given by [3]

$$\frac{\partial}{\partial m}\left(h^3\frac{\partial P}{\partial m}\right) + \frac{\partial}{\partial n}\left(h^3\frac{\partial P}{\partial n}\right) = 6\mu\omega\frac{\partial h}{\partial m} + 12\mu\dot{h} \tag{1}$$

where $P = P(m, n, t)$ is the oil film pressure, $h = h(m, n, t)$ is the lubricant film thickness, μ is the dynamic viscosity of the fluid, and $\omega = 2\pi N/60$ is the angular speed in rad/s.

HSB is supplied with the lubricant at a specified supply pressure (P_S). A flow restrictor such as capillary tube or orifice is provided between the supply plenum and the pocket of HSB (as shown in Fig. 1). Hence, the pressure reduces from supply pressure (P_S) to pocket pressure (P_{Ri}) when the flow enters the ith pocket through the flow restrictor. In a pocket, the pressure in pocket (P_{Ri}) is assumed to be constant in the entire region of the ith pocket. The top and bottom ends of the bearing are open to atmosphere. Hence, the pressure is considered as 0 at the nodes along the top and bottom edges.

For a given eccentric position of the rotor, all the pocket pressures (P_{Ri}) are initialized to an initial value (say $0.5 \times P_S$). Hence, the nodes in pocket are assigned with the initial pressure. From the finite difference approximation of Reynolds equation, pressure at node (i, j) is given by [4]

$$P_{i,j} = \frac{a_1 P_{i+1,j} + a_2 P_{i-1,j} + a_3 P_{i,j+1} + a_4 P_{i,j-1} - F_{i,j}}{a_1 + a_2 + a_3 + a_4} \tag{2}$$

where $a_1 = \frac{1}{R^2\Delta\theta^2}\left(\frac{h_{i,j}+h_{i+1,j}}{2}\right)^3$, $a_2 = \frac{1}{R^2\Delta\theta^2}\left(\frac{h_{i,j}+h_{i-1,j}}{2}\right)^3$, $a_3 = \frac{1}{(\Delta y)^2}\left(\frac{h_{i,j}+h_{i,j+1}}{2}\right)^3$, $a_4 = \frac{1}{(\Delta y)^2}\left(\frac{h_{i,j}+h_{i,j-1}}{2}\right)^3$ and $F_{i,j} = 6\mu\omega\left(\frac{h_{i+1,j}-h_{i-1,j}}{2\Delta\theta}\right)$.

Applying successive over-relaxation (SOR) algorithm, with over-relaxation parameter α, the pressure is obtained as

$$P_{i,j} = \beta \frac{a_1 P_{i+1,j} + a_2 P_{i-1,j} + a_3 P_{i,j+1} + a_4 P_{i,j-1} - F_{i,j}}{a_1 + a_2 + a_3 + a_4} + (1 - \alpha) P_{i,j} \quad (3)$$

The above equation is solved at all grid points until the convergence criteria for pressure is satisfied at all nodes in land $\left(\left| \frac{P_{i,j}^{n-1} - P_{i,j}^{n}}{P_{i,j}^{n-1}} \right| < 10^{-6} \right)$, where n is the number of iteration. Though the pressure distribution obtained here is a converged solution, it does not represent the true pressure distribution in HSB as the pocket pressure is an assumed value.

3.2 Convergence of Mass

To verify the correctness of the pocket pressures, mass continuity is estimated between flow entering the pocket and flow leaving the pocket. The mass flow rate through the restrictor (capillary tube) entering the pocket is given by

$$Q_{\text{in-Ri}} = \frac{\pi d_c^4 \rho}{128 \mu l_c} (P_s - P_{\text{Ri}}) \quad (4)$$

The net mass flow rate entering/leaving the pocket is due to combination of Poiseuille flow (due to pressure in pocket) and Couette flow (rotation of rotor). The total mass flow rate is estimated by integrating the pressure gradient along the edges of the pocket along with the Couette flow at appropriate edges. The net mass flow rate leaving the pocket is given by

$$Q_{\text{out-Ri}} = \oint \left(\frac{\rho h U}{2} - \frac{\rho h^3}{12 \times \mu} \nabla P \right) \cdot I \, dl \quad (5)$$

where U is the tangential velocity ($U = \pi D N / 60$), I is the unit vector normal to the element considered, ∇P is the pressure gradient at the edges of pocket. $\frac{\rho h U}{2}$ represents the flow entering/leaving the pocket due to Couette flow, and $\frac{\rho h^3}{12 \times \mu} \nabla P$ represents the flow entering/leaving the pocket due to Poiseuille flow.

Based on the difference between $Q_{\text{in-Ri}}$ and $Q_{\text{out-Ri}}$ for ith pocket, the pocket pressure P_{Ri} is corrected. The general constraint applied for such correction is that the maximum value of P_{Ri} cannot be more than P_s and the minimum value of P_{Ri} cannot be less than 0.

All the pocket pressures are corrected accordingly and solved again, until the flow continuity is attained in all pocket $\left(\left| \frac{Q_{\text{out-Ri}} - Q_{\text{in-Ri}}}{Q_{\text{in-Ri}}} \right| < 10^{-4} \right)$. The result gives the pressure distribution of HSB, for given eccentricity and supply pressure.

The components of pressure along X and Y are integrated to get load capacity along X and Y directions.

$$W_x = \int_0^{2\pi} \int_0^L P R \cos\theta \, dz \, d\theta$$

$$W_y = \int_0^{2\pi} \int_0^L P R \sin\theta \, dz \, d\theta \tag{6}$$

Hence, the total load is given by

$$W = \sqrt{W_x^2 + W_y^2} \tag{7}$$

The methodology for obtaining load bearing capacity of hydrostatic bearing is shown in Fig. 3.

Fig. 3 Flow chart on procedure for solving and obtaining load bearing capacity of HSB
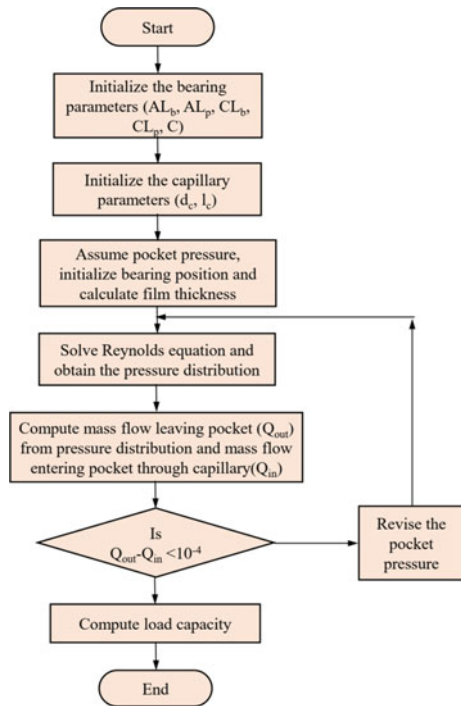
4 Results and Discussion

4.1 Effect of Eccentricity on Pressure Distribution

HSB is initially assumed to be in concentric position and the pressure distribution in land as well as at pocket is estimated. A typical plot of pressure ratio (P/P_s) in the developed view of the bearing is shown in Fig. 4. The ratio of pocket pressure to supply pressure when the bearing is in concentric condition is a characteristic feature of a bearing, which is defined as concentric pressure ratio ($\beta = P_{\text{Ri-concentric}}/P_s$). The concentric pressure ratio (β) can be varied by changing bearing and pocket geometry, clearance and capillary dimensions.

The pressure along the circumferential direction at axial midsection ($y = \text{AL}_b/2$) and along the axial direction at the cross-section (at $x = 0°$) is shown in Fig. 5. The pressure variation along the circumferential direction is non-linear between lands and constant along the pocket region. The pressure variation along the axial direction is nearly linear at top and bottom lands.

When the shaft is moved along X-direction (shown in Fig. 1), it results in eccentric position of the journal (say, $\epsilon = 0.5$). The pressure distribution in eccentric condition is estimated and shown in Fig. 6. As the shaft moves along $+X$ direction (attitude angle $\phi = 0°$), the clearance at land around pocket 1 reduces and the clearance at land increases at other pockets. Hence, the pocket pressure increases in pocket 1 (P1) and decreases drastically in pocket 3 (P3) and reduces moderately in pocket pressure in pockets 2 and 4 as shown in Fig. 6.

The attitude angle (ϕ) is also significantly affecting the pressure distribution. The pressure distribution with ($\epsilon = 0.5$ and $\phi = 90°$) is shown in Fig. 6. This has resulted
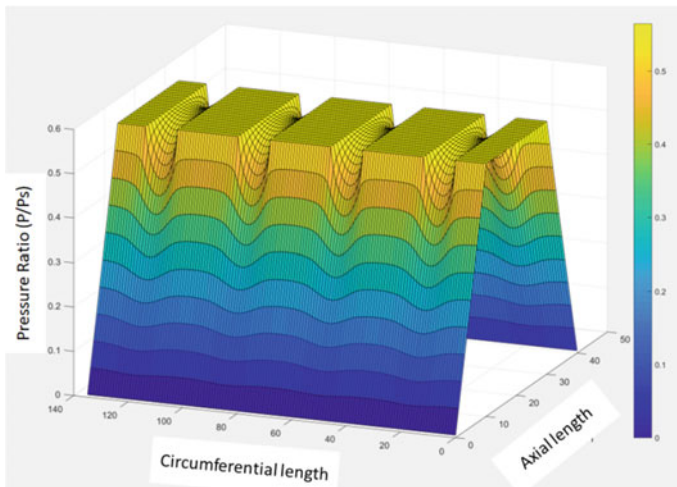
Fig. 4 Pressure distribution in HSB when the bearing is concentric
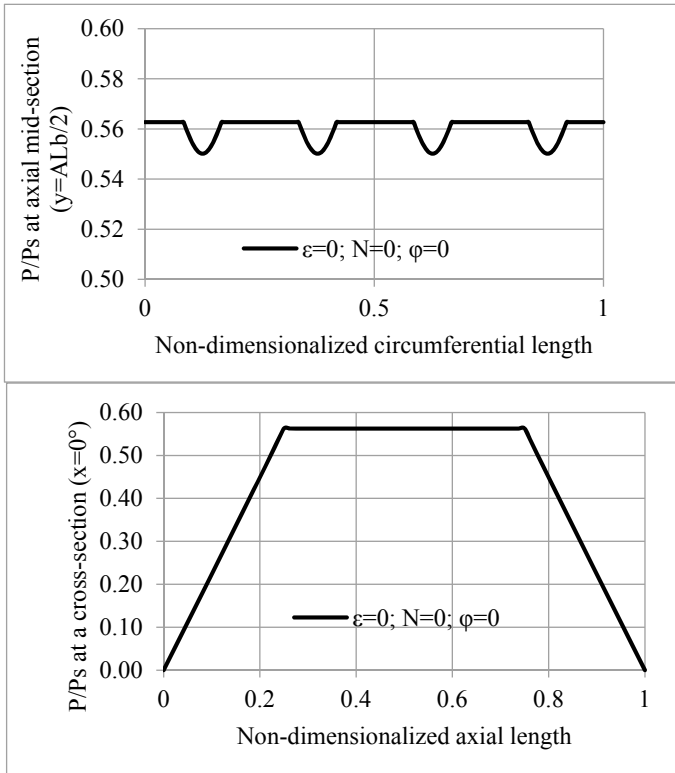
Fig. 5 Pressure distribution along the circumferential and axial direction in HSB
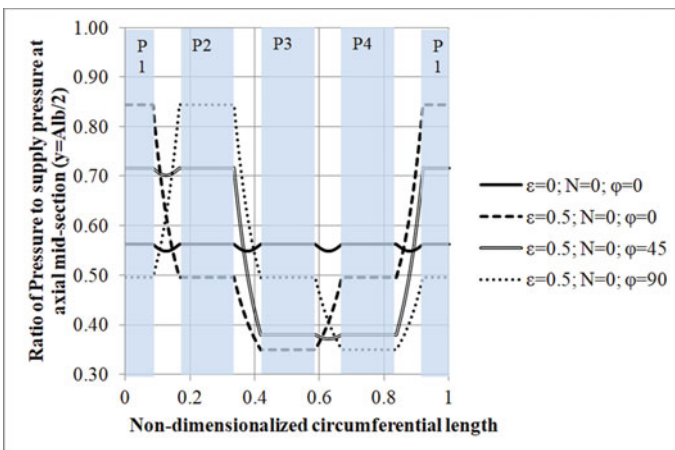
Fig. 6 Comparison of pressure distribution along circumference under eccentric condition
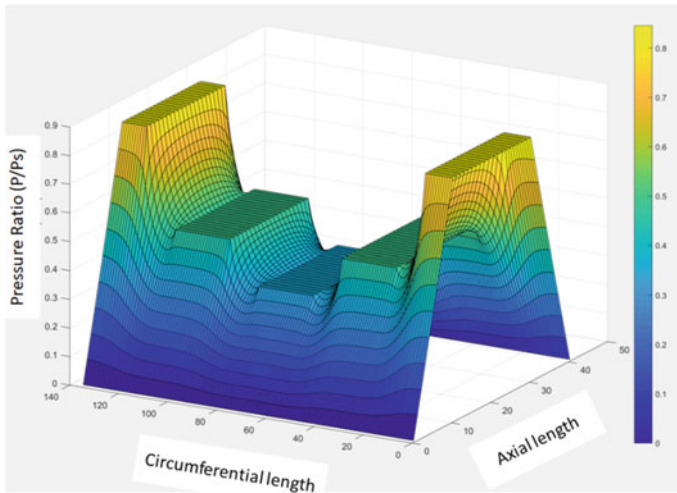
Fig. 7 3D plot of pressure distribution in HSB under eccentric condition ($\epsilon = 0.5$ and $\phi = 0°$)

in phase shift in pressure distribution by 90°. Similarly, when the attitude angle is 45°, the movement of shaft is between P1 and P2. Hence, the pockets P1 and P2 will have same pressure and pockets P3 and P4 will have same pressure as shown in Fig. 6. A 3D plot of pressure distribution in HSB under eccentric condition ($\epsilon = 0.5$ and $\phi = 0°$) is shown in Fig. 7.

4.2 Validation of Pocket Pressure

Towards verifying the estimation of pocket pressure at various eccentricities, a validation study is carried out. An experimental estimation of pocket pressure at each pocket in a four pocket HSB for concentric and eccentric cases was carried out by Metman et al. [1]. The bearing and pocket dimensions are selected as given in Table 1.

Table 1 Range of R/C and L/C ratio of wear rings to be studied

Parameter	Ratio	Metman et al.	Ghosh et al.
g1—axial length to diameter ratio of bearing	$\frac{\text{AL}_b}{D}$	1	1
g2—axial length of pocket to bearing ratio	$\frac{\text{AL}_p}{\text{AL}_b}$	0.5	0.5
g3—circumferential length of all pocket to total circumference	$\frac{\text{CL}_p \times \text{NR}}{\text{CL}_b}$	0.67	0.5
g4—number of pockets	NR	4	4
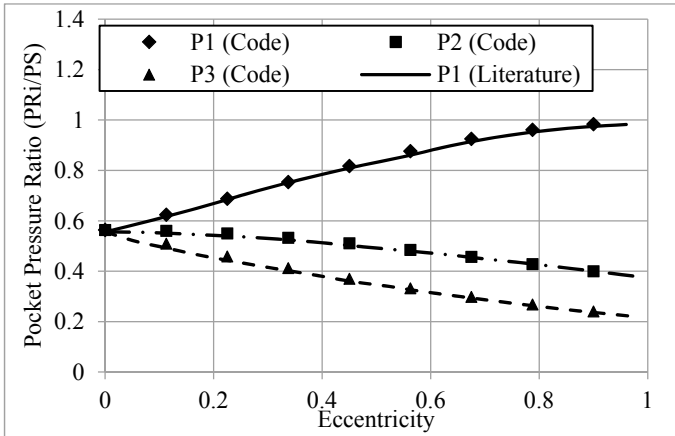
Fig. 8 Pressure ratio of pocket pressure to pocket pressure for a four pocket HSB

The concentric pressure ratio chosen by the authors was $\beta = 0.555$. Hence, the capillary dimensions are adjusted in this study such that the above pressure ratio is achieved in concentric condition.

The eccentricity of the shaft is increased in steps from 0 to 0.9, and the ratio of pocket pressure to supply pressure (P_{Ri}/P_S) is estimated for all pockets for each eccentricity case. The results obtained are plotted in Fig. 8. From the plot, it can be observed that the pocket pressure estimated in the present code matches well with the literature results. As the eccentricity increases, the pressure in pocket 1 increases due to reduction in land clearance around pocket 1. As the eccentricity becomes close to 1, the land clearance around pocket 1 will become negligible, and hence, flow leaving/entering pocket will be negligible due to very high resistance. Hence, the pressure in pocket 1 will approach supply pressure (P_S). On the other hand, the pressure in pocket 3 reduces significantly (as shown in Fig. 8) due to very high clearance in land area around pocket 3. Similarly in pockets 2 and 4, land clearance will increase resulting in lower pocket pressure at higher eccentricities. Since the pressure in pocket 2 and pocket 4 are equal due to symmetric nature of bearing, pocket 2 alone is plotted in Fig. 8.

4.3 Effect of Rotation on Pressure Distribution

When the rotation of the journal is considered, the pressure distribution in the bearing will be a combination of hydrostatic effect (due to pressurized pockets) and hydro-dynamic effect (due to rotation of journal). The rotation of the journal will affect $6\mu\omega\frac{\partial h}{\partial \theta}$ term in Eq. (1) and hence $F_{i,j}$ term in Eq. (2).

The pressure distribution along the circumference of the bearing at the axial midsection is studied for two cases ($\epsilon = 0$, $N = 100$ and $\epsilon = 0.5$, $N = 100$) and
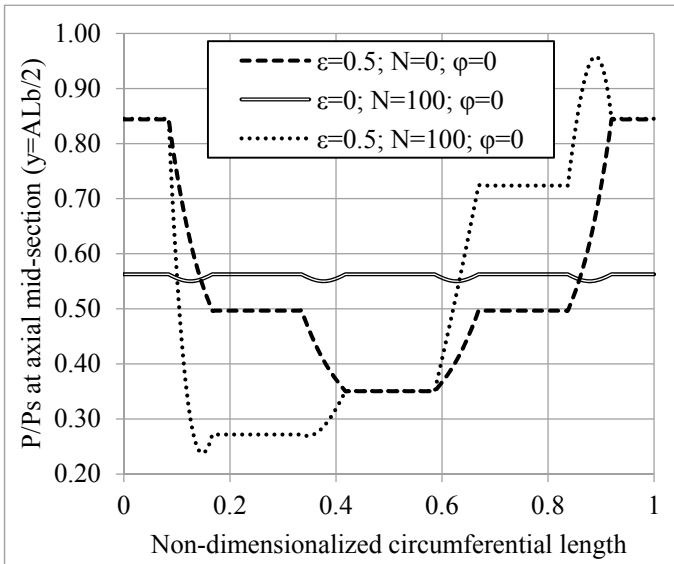
Fig. 9 Comparison of pressure distribution along circumference under rotation of journal

compared with the reference case on concentric stationary journal ($\epsilon = 0, N = 0$) as shown in Fig. 9 When the journal is concentric, hydrodynamic action is not possible. Hence, it resulted in same pressure distribution as ($\epsilon = 0, N = 0$) case. When the journal is eccentric and rotating ($\epsilon = 0.5, N = 100$), the pressure distribution observed is plotted in Fig. 9. The pressure distribution in stationary and eccentric case ($\epsilon = 0.5, N = 0$) given in Fig. 6 is replotted in Fig. 9.

It is noted that when the journal is eccentric and under rotation, the peak pressure observed is 20–30° behind the attitude angle. A similar observation is noted in Fig. 9, where the peak pressure is observed between P4 and P1. The rotation also results in increase in pocket pressure P4, however results in a decrease in pocket pressure P2.

Since the peak pressure observed is about 30° behind the attitude angle, the pressure distribution in case of attitude angle ($\phi = 45°$) with rotation of journal is studied as shown in Fig. 10. It results in drastic increase in pocket pressure P1, due to hydrodynamic effect. Another observation is, when the speed is increased to ~ 200 rpm, the pocket pressure P1 increases beyond supply pressure (P_s). However, since the pocket pressure is assumed to lie between supply pressure and zero (as explained in Sect. 3.2), the constraint on the upper limit has to be relaxed when the journal is under rotation.
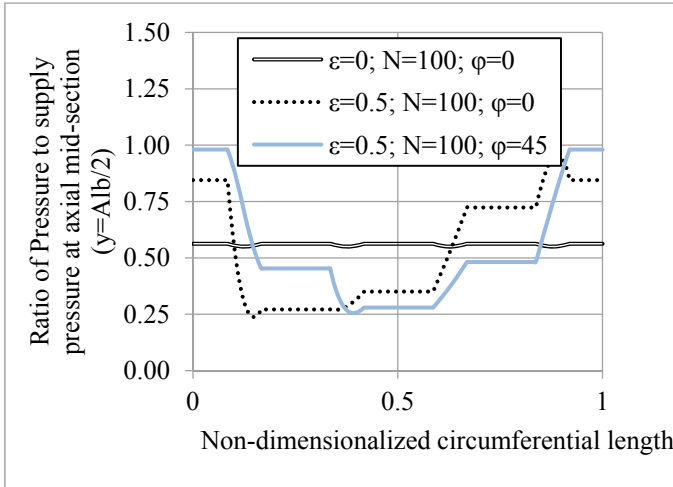
Fig. 10 Effect of attitude angle on pocket pressure and pressure distribution along circumference under rotation of journal in HSB

4.4 Effect of Rotation on Load Bearing Capacity

The load capacity of the bearing is estimated when the journal is under rotation. The rotation of the bearing is given by a bearing parameter (ψ), which is given by

$$\psi = \frac{6\mu\omega}{P_s(C/R)^2} \qquad (8)$$

The load capacity and attitude angle of bearing under rotation is shown in Figs. 11 and 12, respectively. For a given bearing number and eccentricity, the attitude angle is estimated where the ratio of W_y/W_x attains minimum. The results are comparing well with the results from the literature [5]. The non-dimensionalized load capacity $\left(W^* = W/(P_s R^2)\right)$ and attitude angle is observed to increase with increase in speed due to hydrodynamic effect of the bearing.

Thus, it was observed that even at the lower speeds, the pocket pressure in the bearings can be significantly altered by the pressure developed due to dynamic action of the rotor, resulting in enhanced load bearing capacity of the HSB.
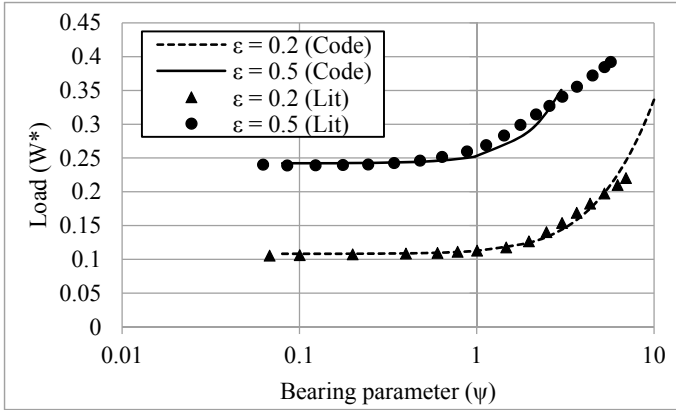
Fig. 11 Load capacity as a function of bearing parameter
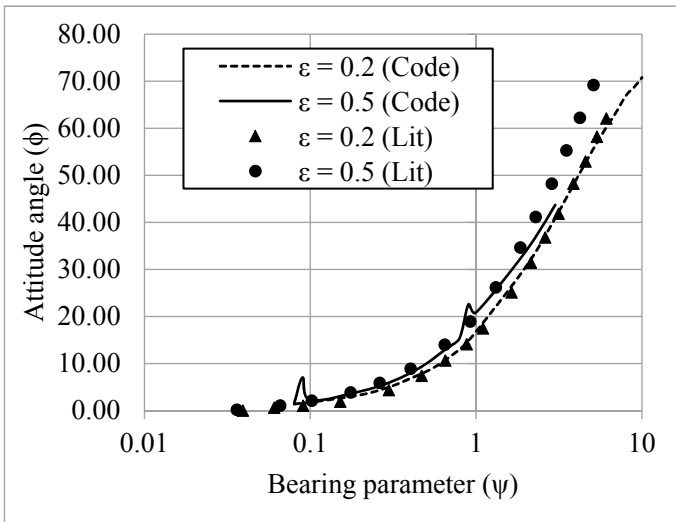
Fig. 12 Attitude angle as a function of bearing parameter

5 Conclusions

A general 2D code is developed for solving Reynolds equations to obtain the pressure distribution in the hydrostatic bearing. The Reynolds equation is solved along with mass continuity equation in the bearing pockets. The conclusions from the study are the following:

- With increase in the eccentricity of the HSB, the pocket pressure increases in one pocket and decreases in other three pockets. When there is no rotation, the pocket pressure is symmetric.
- When there is rotation of the journal in eccentric condition, the pressure developed due to the dynamic action of the bearing alters the symmetric pressure distribution. When the attitude angle is 0°, the distortion in the symmetric pressure distribution is significant, whereas when the attitude angle is at 45°, the pressure distribution remains nearly symmetrical in four pocket hydrostatic bearing.
- Due to the rotation of the journal, the load capacity of the bearing increases with increase in speed. The increase in speed also results in increase in pocket pressure at 20–30° behind the attitude angle, where the pressure exceeds the supply pressure of the bearing, resulting in flow reversal in the capillary.

Nomenclature

P	Oil film pressure (Pa)
h	Film thickness of bearing (m)
ω	Speed (rad/s)
μ	Dynamic viscosity (Ns/m^2)
P_s	Supply pressure (Pa)
P_{Ri}	Pocket pressure (Pa)
α	Over-relaxation parameter (–)
d_c	Diameter of capillary (m)
l_c	Length of capillary (m)
$Q_{\text{in - Ri}}$	Mass flow entering the pocket (kg/(m^2 s))
$Q_{\text{out - Ri}}$	Mass flow leaving the pocket (kg/(m^2 s))
U	Tangential velocity of rotor (m/s)
W	Load bearing capacity of bearing (N)
β	Concentric pressure ratio (–)
ϕ	Attitude angle (–)
AL$_b$	Axial length of bearing (m)
AL$_p$	Axial length of pocket (m)
D	Diameter of bearing (m)
CL$_p$	Circumferential length of pocket (m)
CL_b	Circumferential length of bearing (m)
NR	Number of pockets (–)
ψ	Bearing parameter

References

1. Metman KJ, Muijderman EA, van Heijningen GJJ, Halemane DM (1986) Load capacity of multi-recess hydrostatic journal bearings at high eccentricities. Tribol Int 19(1):29–34
2. Ghosh MK, Majumdar BC (1980) Design of multirecess hydrostatic oil journal bearings. Tribol Int 13(2):73–78
3. Du J, Liang G (2019) Performance comparative analysis of hydrostatic bearings lubricated with low-viscosity cryogenic fluids. Tribol Int 137:139–151
4. Ebrat O, Mourelatos ZP, Vlahopoulos N, Vaidyanathan K (2004) Calculation of journal bearing dynamic characteristics including journal misalignment and bearing structural deformation. Tribol Trans 47(1):94–102
5. Ghosh MK, Majumdar BC, Rao JS (1979) Steady-state and dynamic behaviour of multi-recess hybrid oil journal bearings. J Mech Eng Sci 21(5):345–351

Discrepancy in Predicted Head Loss of Non-Newtonian Aqueous Suspension of Fly Ash with Two Different Yield Stress Values Obtained from Rheological Data

Check for updates

Sambit Senapati, Vighnesh Prasad, Anil Dubey, and Alangar Sathyabhama

1 Introduction

Thermal power plants based in India generate huge quantities of coal ash (fly ash + bottom ash) to a tune of around 200 million tons per annum. The efficient disposal of these huge wastes still remains a concern from an environmental point of view. By adopting the wet disposal method, by making a slurry form of these solid wastes, they may be transported through pipelines at higher solids concentrations to save the precious water. According to a report notification on November 3, 2009, from the Ministry of Environment and Forests (MoEF) and climate change (CC), there was an urge for 100% disposal of fly ash in dry form for a gainful utilization that was to come to effect within 5 years, but as per the record available in a report from 2020, 83% utilization has been effected so far [1]. In the context of slurry pipeline transportation, the correct estimation of head loss of ash-water suspension is quite important to negotiate the pumping pressure for commercial disposal of these solid wastes through ash slurry pipelines economically. The prediction of head loss for a non-Newtonian suspension may be carried out either by evaluating the head loss of the suspension using non-Newtonian head loss models from rheological data or by using scale-up methods proposed by Thomas [2]. It is indicated that pipe loop tests may be conducted in smaller pipe sizes (50–150 NB) for accurate prediction of head loss of aqueous suspension of the industrial wastes. The experimental pipe loops generally consist of 3 or 4 different diameters with the largest often being around 150 mm. However, the scale-up prediction of head loss requires the availability

S. Senapati (✉) · A. Sathyabhama
Department of Mechanical Engineering, NIT Surathkal, Surathkal, India
e-mail: sambitpropulsion23@gmail.com

V. Prasad · A. Dubey
Design and Project Engineering Department, CSIR-IMMT, Bhubaneswar, India

of appropriate experimental pipe loop test facilities, huge quantity of samples for the experimental campaign, and moreover it is time-consuming. In this situation, the prediction of head loss from rheological data may be considered as a suitable proposition.

The rheological flow characteristics of ash-water suspension at high solids concentration have been investigated by many researchers [3–11]. The investigators have characterized the suspension behavior using non-Newtonian rheological models such as Bingham plastic model, power-law model and yield-pseudoplastic model. The yield stress parameter in a rheological measurement for high concentration suspensions is quite vital, and accurate determination of this value may help for disposal system design and operating conditions predicting head loss of mineral slurry [12]. The yield stress is the minimum stress that must be applied to a sample in order to induce flow. This is quite important to pump start-up conditions. Mostly, two techniques are employed to determine the yield stress by direct measurement using a rotational rheometer. They are termed as stress–growth and creep-recovery. In the present study, the stress–growth method has been adopted to measure the yield stress at a very slow constant shear rate (0.01 s^{-1}), and the resulting stress has been measured as a function of time. The yield stress parameter obtained from this method has been considered to predict the pressure drop using a non-Newtonian head loss model. Further, the yield stress value obtained from the linear fit of the shear stress–shear rate data was considered for predicting the head loss. The Bingham viscosity value obtained from linear plot of shear stress–shear rate data at a specified concentration has been also used for head loss prediction in both cases. The discrepancy in predicted values of the head loss with two different yield stress values at different weight concentration of ash-water suspension has been analyzed and discussed.

2 Materials and Methods

2.1 Characterization Studies

2.1.1 Particle Size Distribution (PSD)

For the present analysis, the ash samples were collected from an Indian Thermal Power Plant. Their particle size distribution (PSD) was determined using a Laser Scattering Particle Size Distribution Analyzer named HORIBA LA-960. The data on PSD of the samples are plotted in Fig. 1. The median particle size (d_{50}) of the ESP fly ash samples (mixed from all fields) was found to be 20.77 μm with d_{90} as 148.2 μm and top size having 344.2 μm.
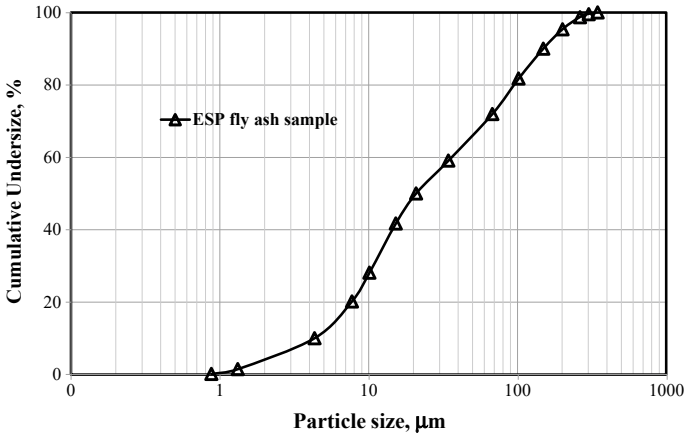
Fig. 1 Particle size distribution of representative fly ash samples

2.1.2 Determination of Material Density

The particle density or mass per unit volume of any solid particles which is insoluble and heavier than water was determined by water displacement method using a specific gravity bottle or pycnometer. This density bottle is a narrow mouth glass bottle having a capillary stopper. A precision electronic balance having three decimal reading was used for accuracy with distilled water at a temperature around 25 °C. The ash samples of particle size with less than 75 μm was oven-dried for the determination of material density. First the empty weight (A) of a 50 ml capacity clean and dry density bottle with its capillary stopper was measured. Then, sample was poured into the bottle using a funnel approximately up to 1/3rd by bottle volume, and the weight of the bottle along with distilled water (B) was taken. After pouring distilled water into the bottle up to half of its volume, the bottle was swirled for a few minutes to ensure the removal of the entrapped air within the solid–water mixture. Then, more water was added up to the neck of the bottle and swirled again and again to ensure complete removal of air bubbles from the bottle. The bottle was then completely filled with water, and the suspended fine particles were allowed to settle down till the supernatant liquid became clear. Then, the stopper was slowly closed, and the excess water was allowed to escape through the capillary. The wetted portion of the bottle at the outer surface of the bottle was wiped properly with tissue paper and the weight (C) was noted down. Then, the bottle was emptied completely by throwing out the sample and was filled with water completely and the weight was taken (D).

The material density (ρ_s) of the fly ash samples was then determined by using the following formula:

$$\rho_s = \frac{B - A}{(D - A) - (C - B)} \tag{1}$$

Table 1 Chemical analysis of the fly ash samples

Element's name	%
SiO_2	56.01
Al_2O_3	28.07
Fe_2O_3	6.38
CaO	2.19
TiO_2	2.09
K_2O	2.33
MgO	0.92
P_2O_5	0.66
SO_3	0.61
$SiO_2 + Al_2O_3 + Fe_2O_3$	90.46

where A is the weight of empty bottle in grams, B is the weight of bottle + solids in grams, C is the weight of bottle + solids + enough water to fill the bottle in grams, D is the weight of empty bottle + water in grams, $B - A$ is the weight of the sample in grams, and $(D - A) - (C - B)$ is the weight of water displaced by the immersed solids in grams, which is equal to volume of water displaced in cc, since water density is 1 g/cc. The repeatability of density value was checked by taking three density bottles at a time, and the average of three density values was taken for all computations. The material density of the ash samples was determined to be 2089.73 kg/m^3.

2.1.3   Chemical Composition

Malvern Analytical WDXRF Zetium 4.0 kW by fusion method was used to obtain the chemical analysis of the ash sample, and the data on the elemental compounds present in the samples are given in Table 1.

2.1.4   Maximum Static Settled Concentration (Sedimentation) Tests

The maximum static settled concentration (C_{W-max}) tests for the ESP fly ash samples were carried out to ascertain at which exact concentration the slurry starts to flow, thereby indicating the limiting maximum concentration beyond which the flowability of the ash slurry stops to occur. Initially, slurries were prepared at concentrations of 55%, 60, 65, 70, 75 and 80 by weight for determining the C_{W-max} values of the ESP ash samples.

The slurry at a specific concentration was allowed to settle in a standard graduated cylinder for a long time (> 48 h) until the equilibrium condition was reached. The data obtained on C_{W-max} values for the sample prepared are plotted in Fig. 2.
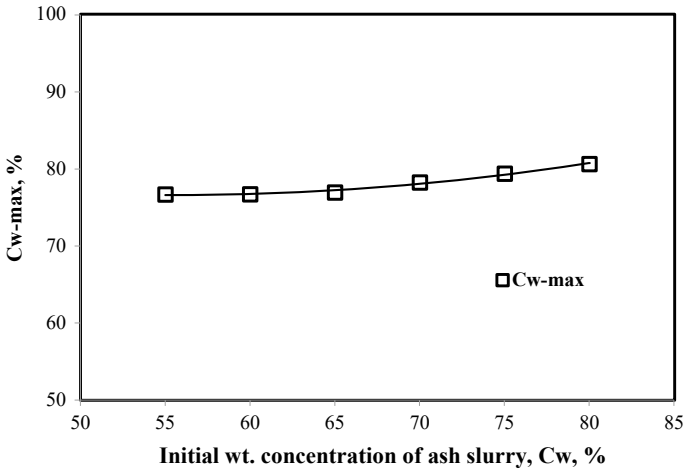
Fig. 2 $C_{W\text{-max}}$ values of ash samples with initial slurry concentrations (Cw)

It was indicated from Fig. 2 that the values of $C_{W\text{-max}}$ increased with increase in initial concentrations of the suspension for the fly ash sample and reached a maximum value of 80.6% by weight. This indicated that the mixed fly ash samples of ESP fields may be transported relatively at higher solids concentration of 70–75% by weight.

2.1.5 pH of Ash-Water Suspension Samples

Ash suspension samples were prepared in distilled water medium at a solids weight concentration of 70%. The pH of the suspension was measured using a ORION STAR A211 bench top pH meter (Thermo Fisher Scientific Water Analysis Instruments, USA) fitted with ROSS combination electrode specifically designed for mineral slurries. Prior to the measurement, the instrument was calibrated with standard buffer solution of values 4.01, 7.0 and 10.01 provided by the manufacturer. The calibration slope of the instrument was recorded which was found to be 95%, which is acceptable for accuracy of pH measurement.

Then, the pH values of the sample were measured and recorded on hourly basis for a period of 5 h. The data on pH values with mixing time are presented in Fig. 3. It was observed that the instantaneous and final pH of the ash suspension sample were found to be 4.37 and 5.62, respectively.
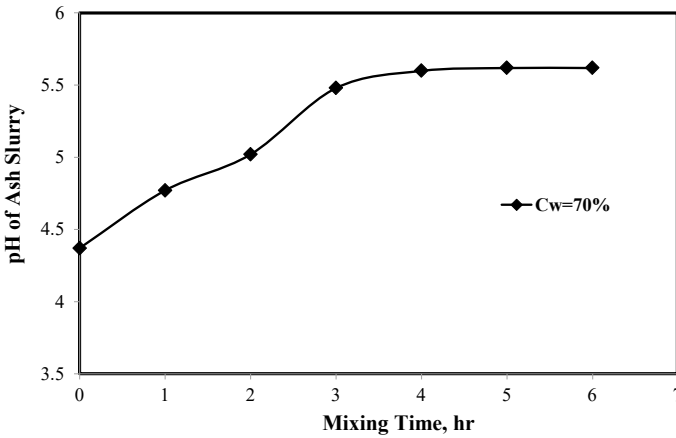
Fig. 3 pH variation of fly ash slurry sample with mixing time, Cw = 70%

3 Rheological Studies

The rheology for the ash suspension samples were conducted using a HAAKE Rotational Rheometer (Model: Rheostress 1, Thermo Fisher Scientific) at solids concentration range of 60–70% by weight. The rheometer consisting of a cylindrical sensor system Z with a collapsible beaker Z-43 and a rotor Z-41 was used for the rheological studies. Ash slurry samples were prepared in distilled water medium to obtain the required concentration (Cw). Each time, about 100 ml of slurry was prepared for the experimental studies. A high precision electronic balance was used so as to weigh the ash samples more accurately. In order to eliminate any possible attrition of the ash particles, the slurry samples were mixed slowly by a glass rod. Then, the cup was installed in the Rheometer and the ash suspension was poured into the cup. The shear rate was fixed in the range of 0–300 s^{-1} in the RheoWin 1 software, and gradually the shear rate was slowly increased from 0 to the desired shear rate for 2 min. The rheological parameters such as viscosity and shear stress were measured under a controlled rate. The rheological experiments were carried out at room temperature of 30 °C which was maintained throughout the measurements. The variation in temperature was ± 0.1 °C through a constant circular bath connected to rheometer. The operation of the rheometer was carried out by a software HAAKE RheoWin 1. The rheological data for the ash slurry samples at various solids weight concentration were obtained in a computer screen which was recorded for analysis.

3.1 Measurement of Yield Stress by Stress–Growth Method

The direct measurement of yield stress of the ash slurry samples in concentration range of 60–75% by weight was carried out by stress–growth method. A vane tool geometry was used for the measurement as it barely disturbs the samples at all upon insertion prior to testing and eliminates slippage as well. A very slow constant shear rate (0.01 s^{-1}) was applied to the vane dipped in the aqueous suspension of the ash sample, and the final stress was measured as a function of time. The gradual building-up of the stress within the suspension was observed. At a certain critical yield stress value, the applied stress surpasses the internal resistance within the sample and the suspension starts flowing. The yield stress was then evaluated as the maximum stress under the stress–time profile curve.

4 Results and Discussion

4.1 Rheological Behavior of Ash-Water Suspension

The flow characteristics of the ash-water suspension sample indicated Bingham plastic behavior in the studied range of concentration (60–70% by weight). The shear stress (τ)–shear rate $(\dot{\gamma})$ data obtained for the fly ash samples in suspension concentration range of 60–70% by weight are plotted and are presented in Fig. 4.

The flow behavior was non-Newtonian in the studied range of slurry concentrations and was fitted to the well-known Bingham Plastic model:
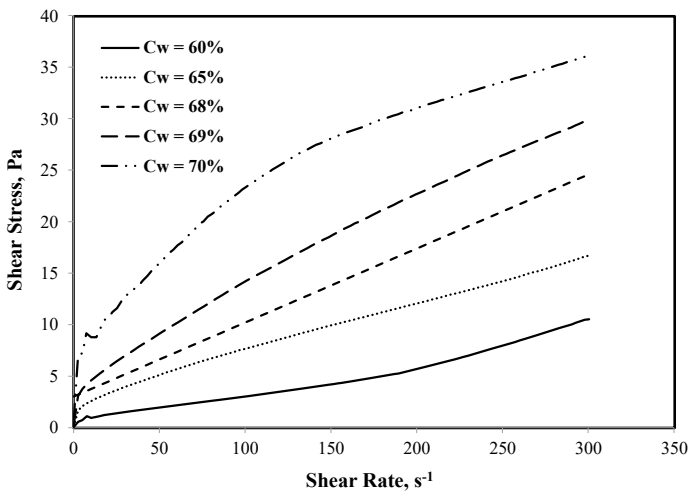
Fig. 4 Rheogram of ESP fly ash slurry sample at different weight concentrations

$$\tau = \tau_0 + \eta_p \dot{\gamma} \tag{2}$$

where τ is the shear stress (Pa), η_p is the coefficient of rigidity or plastic viscosity (Pa s), $\dot{\gamma}$ is the shear rate (s^{-1}), and τ_0 is the yield stress (Pa). It was seen from Fig. 4 that with increase in suspension concentration, the shear stress increases monotonically in the investigated range of shear rates. Thus, it is inferred that higher pumping pressure will be required to transport the ash suspension at higher solids concentration. The variation of stress measured as a function of time for the aqueous suspension of fly ash suspension in solids weight concentration of 60–75% are presented in Fig. 5a and b.
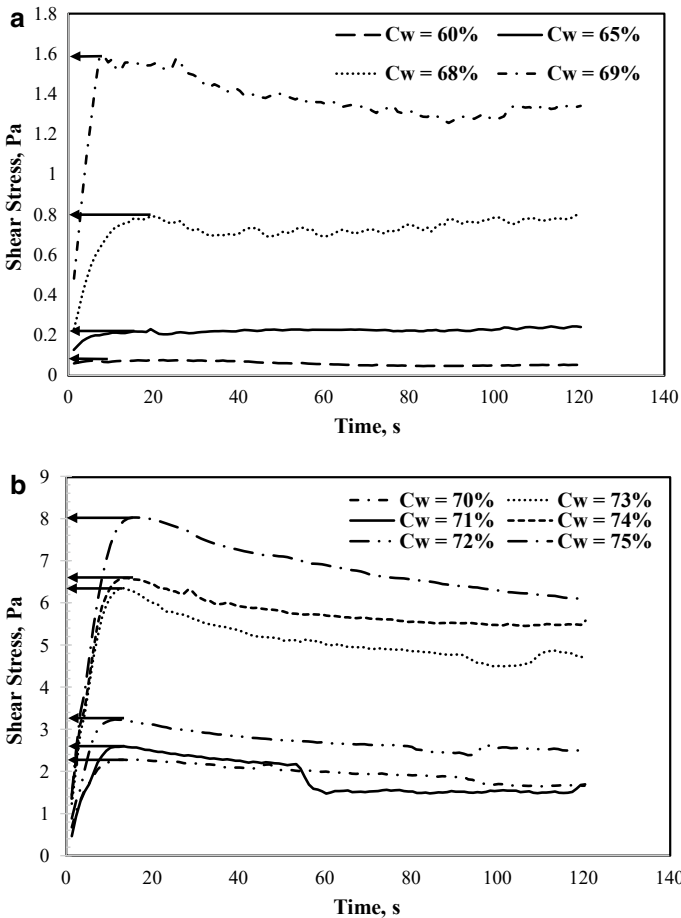
Fig. 5 a Direct measurement of yield stress by stress–growth method (Cw = 60–69%). **b** Direct measurement of yield stress by stress–growth method (Cw = 70–75%)

Table 2 Rheological parameters obtained from rheological measurements

Weight concentration (Cw%)	τ_0 (Pa)	τ_{0sg} (Pa)	η_p (Pa s)
60	0.097	0.076	0.031
65	2.64	0.23	0.047
68	3.03	0.8	0.072
69	4.81	1.6	0.088
70	11.87	2.28	0.092

It was observed from Fig. 5a and b that the build-up stress within the sample gradually increased with time, and at a critical yield stress, the applied stress overcomes the inherent resistance within the sample and the suspension starts flowing at a specified concentration. Besides, with increase in concentration of the suspension, the yield stress value increased and the yield stress value (τ_{0sg}) has been determined as the maximum stress in the stress–time profile curve as indicated by an arrow in Fig. 5a and b. Thus, it can be concluded that a certain amount of stress is required to break the flock structure in the ash-water suspension so as to induce flow. The rheological parameters such as τ_0, τ_{0sg} and η_p obtained for the ash suspension at different weight concentrations are presented in Table 2.

4.2   Prediction of Head Loss

The computation of frictional losses for aqueous suspension of fly ash in concentration range of 60–70% by weight in a 400 mm NB mild steel pipe was carried out by applying a non-Newtonian head loss model. The frictional losses of suspension in m of water per meter length of pipe (*i*) were computed by using Fanning equation given as

$$i = \frac{2\rho_m f V^2}{g D_i \rho_w} \tag{3}$$

where *i* is the head loss gradient of suspension (m of water per meter length of pipe), ρ_m is density of the ash suspension (kg/m^3), ρ_w is the density of water (kg/m^3), *V* is the flow velocity (m/s), D_i is the internal diameter of the pipe (m), *g* is the acceleration due to gravity (m/s^2), and *f* is the combined laminar–turbulent fanning friction factor. In order to compute the value of *f*, the following equation proposed by Darby et al. [12] was used.

$$f = (f_L^m + f_T^m)^{1/m} \tag{4}$$

where f_L is the laminar friction factor and f_T is the turbulent friction factor and *m* = 1.7 + 40,000/Re$_B$. The head loss of ash suspension in the investigated range of concentration with slurry velocity range of 1.0–2.0 m/s was computed by using the

rheological parameters as indicated in Table 2. The plot of head loss versus pipe flow velocity at different weight concentrations of the ash-water suspension in a 400 mm nominal bore pipeline considering the two different yield stress values is presented in Fig. 6a and b.

It was observed from Fig. 6a and b that the head loss of ash suspension increased with increase in slurry concentration irrespective of the two different yield stress values considered for predicting the head loss. Due to very high value of yield stress evaluated from linear fit of shear stress–shear rate data, the head loss increased substantially at concentration of 70% by weight as indicated in Fig. 6a.

The comparison of predicted head loss of aqueous suspension of fly ash at different pipe flow velocity with two different yield stresses are presented in Fig. 7a and b. It is indicated from the figure that there is a discrepancy in predicted head loss values when two different yield stresses have been considered during the evaluation of frictional losses of ash-water suspension. The difference in frictional loss values is quite prominent at higher solids concentration of 70% than 65% for the suspension.

Fig. 6 **a** Head loss of aqueous suspension of fly ash (yield stress value taken from linear fit of τ–$\dot{\gamma}$ plot). **b** Head loss of aqueous suspension of fly ash (yield stress value taken from stress–growth method)
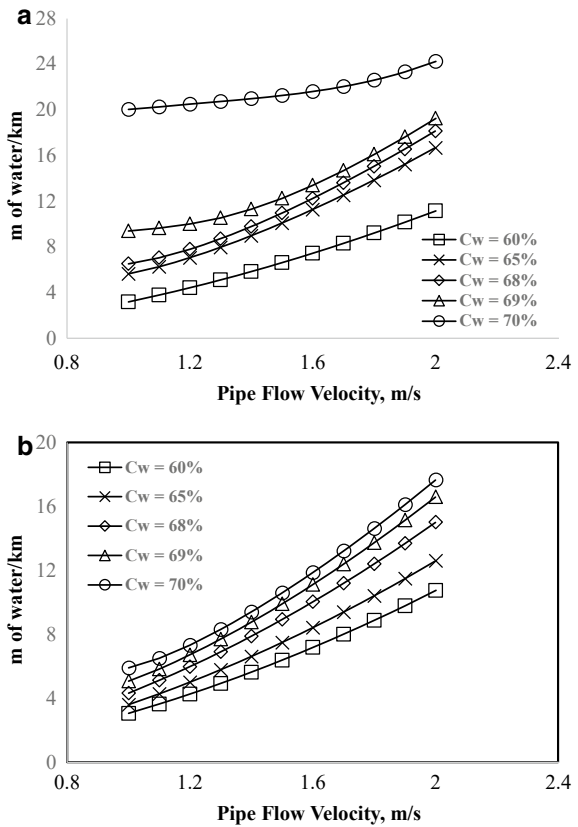
Fig. 7 **a** Comparison of predicted head loss of aqueous suspension of fly ash using two different yield stresses values (Cw = 65%). **b** Comparison of predicted head loss of aqueous suspension of fly ash using two different yield stresses values (Cw = 70%)
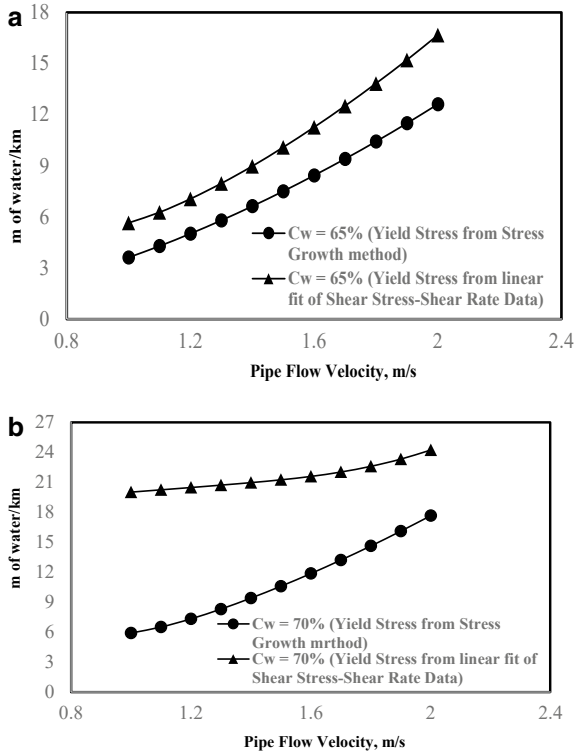
It was found that the percentage reduction in the predicted head loss values were in the range of 24–73% at higher solids concentration of 65 and 70% while computing the head loss of ash suspension using the yield stress value from stress–growth method.

5　Conclusion

The rheological characteristics of the aqueous suspension of ash was fitted well by Bingham plastic model at high solids concentration in the range of 60–70% by weight. The head loss predicted for the suspension was very much influenced by two different yield stress values obtained from rheological measurements. There is a considerable reduction in the predicted head loss of the ash suspension when the yield stress value obtained by stress–growth method was used. The low values of head loss predicted by using τ_{0sg} values from stress–growth method may be economical for designing ash slurry pipelines, whereas by using the τ_0 values obtained from shear stress–shear rate data overestimated the head loss of ash suspensions which may lead to overdesign of the slurry pump incurring higher capital expenditure. Thus, the

discrepancy in the predicted head loss values may put a pipeline designer in dilemma to select appropriate slurry pump for efficient disposal of ash-water suspension at high solids concentration.

Nomenclature

τ	Shear stress (Pa)
η_p	Coefficient of rigidity or plastic viscosity (Pa s)
$\dot{\gamma}$	Shear rate (s^{-1})
τ_0	Yield stress (value from linear fit of $\tau-\dot{\gamma}$ data) (Pa)
τ_{0sg}	Yield stress (value taken from stress–growth method) (Pa)
i	Head loss gradient of slurry (m H_2O/m)
ρ_m	Density of the ash suspension (kg/m^3)
ρ_w	Density of water (kg/m^3)
V	Flow velocity (m/s)
D_i	Internal diameter of the pipe (m)
g	Acceleration due to gravity (m/s^2)
f	Combined laminar–turbulent fanning friction factor (–)
f_L	Laminar friction factor (–)
f_T	Turbulent friction factor (–)
Re_B	Bingham Reynold's number (–)

References

1. Senapati S, Mohanty A (2022) Studies on parameters affecting flow behaviour of high-concentration ash slurry: effect of a natural drag reducing agent on pumping power during pipeline transportation. J Inst Eng India Ser C. https://doi.org/10.1007/s40032-022-00822-y
2. Thomas AD (1976) Scale-up methods for pipeline transport of slurries. Int J Miner Process 3:51–69
3. D. Kaushal, N. Kumar, 2013. Optimum design of high concentration fly ash slurry disposal pipeline. EJPAU, 16(4). Available online: http://www.ejpau.media.pl/volume16/issue4/art-03.html
4. Bunn TF, Chamber AJ (1993) Experience with dense phase hydraulic conveying of Vales Point fly ash. Powder Handling and Processing 5(1):35–44
5. N. I. Heywood, K. B. Mehta, D. Poplar, 1993. Assessment of pipe flow properties of pulverized fuel ash slurries at high concentration. In: Proceedings of 12th international conference on slurry handling and pipeline transport: Hydrotransport 12, Brugge, Belgium.
6. B. Singh, W. Foley, 1998. HCSD Technology: Concept, Scope and experience. In: Proceedings of 1st international conference—fly ash disposal and utilization, CBIP, New Delhi, pp. 35–44.
7. Das D, Pattanaik S, Parhi PK, Mohapatra RK, Jyothi RK, Lee JY, Kim HI (2019) Stabilization and rheological behavior of fly ash–water slurry using a natural dispersant in pipeline transportation. ACS Omega 4(25):21604–21611
8. Assefa KM, Kaushal DR (2015) Experimental study on the rheological behaviour of coal ash slurries. J. Hydrol. Hydromech. 63(4):303–310

9. Lee JY, Ko J, Kim YS (2017) Rheology of fly ash mixed tailings slurries and applicability of prediction models. Minerals 7(9):165. https://doi.org/10.3390/min7090165
10. Kumar S, Singh G, Mohapatra SK (2016) An assessment of the physical, mineral, and rheological properties of fly ash for stowing in coal mines. Energy Sources, Part A: Recovery, Utilization, and Environmental Effects 38(20):2955–2962
11. Zhao Y, Taheri A, Karakus M, Chen Z, Deng A (2020) Effects of water content, water type and temperature on the rheological behaviour of slag-cement and fly ash-cement paste backfill. Int J Min Sci Technol 30:271–278
12. Dzuy NQ, Boger DV (1983) Yield stress measurement for concentrated suspensions. J Rheol 27:321
13. Darby R, Mun R, Borger DV (1992) Predict friction loss in slurry pipes. Chem Eng 9:116

Numerical Study of Plate-Fin Heat Exchanger for Cryogenic Application

Margam Ramprasad and Manoj Kumar Moharana

1 Introduction

Plate-fin heat exchangers are one kind of compact heat exchangers which outperform in terms of heat transfer density compared to conventional heat exchangers. The compactness in design provides a large heat transfer area as its heat transfer surface area to total volume ratio is much higher than conventional heat exchangers. Compact surfaces help to gain desired heat exchanger performance (ratio of heat transfer to true mean temperature difference) for very low mass and volume. Plate-fin heat exchangers are widely used in cryogenic air separation, bigger refrigeration and air-conditioning systems, natural gas liquefaction, etc.

The constructional details of an offset-strip fin heat exchanger are shown in Fig. 1. The heat exchanger consists of parallel parting plates or sheets, called primary surface, connected to each side by different geometry shapes of fins, also called secondary surface. The connection can be made by the dip brazing process or vacuum brazing process. Comparatively, thick sidebars are used to close the flow path on both sides of the fins along the flow direction. Fins not only act as a heat transfer medium but also give structural rigidity to the entire rig of the heat exchanger matrix.

The secondary surface transfers heat from the primary surface to the fluid stream. As fins connect two adjacent cover plates, conduction through the wall of fins happens in a parallel direction and the structure of the fin can generate the boundary layer and develops the local convective heat transfer. The herringbone type plate-fin heat exchangers, like offset-strip fin and wavy fin heat exchangers, give growth of boundary layer during the flow.

Plate-fin heat exchangers are categorized as plain and straight fins, which involves plane, triangular and rectangular fins; herringbone fins which include wavy and

M. Ramprasad · M. K. Moharana (✉)
Thermal Systems Laboratory, Department of Mechanical Engineering, National Institute of Technology Rourkela, Rourkela, India
e-mail: mkmoharana@gmail.com

Fig. 1 Constructional
details of PFHE
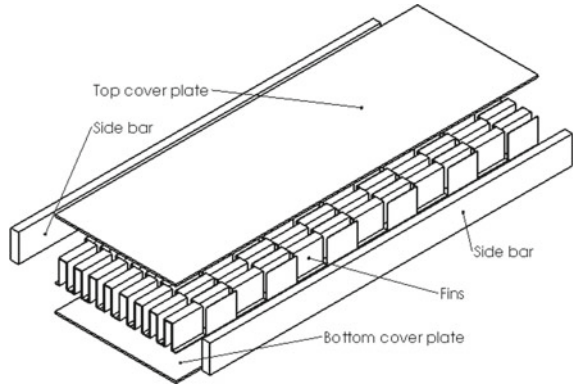
obstructive type structure in the primary fluid flow direction, which improves convection heat transfer part; and serrated and perforated type which involves cuts and perforation in the fin wall itself.

2 Literature Review and Objective

Plate-fin heat exchangers are being produced since 1910 in the auto industry (copper fin brass tubes). In the 1940s, aerospace industries used aluminum. In the 1950s, aluminum is used in liquefaction applications for better mechanical characteristics at low temperatures. Kays and London [1] played the main role in developing compact heat exchangers. They developed different geometries of fins to reduce the size and weight of the plate-fin heat exchangers.

An experimental analysis has been done by Wieting [2] for 22 rectangular offset-strip fin heat exchangers for the characteristics of heat transfer and pressure drop, and proposed correlations for j factor and f factor. Mochizuki et al. [3] proposed correlations for j and f factors for interrupted fin surfaces and concluded that the offset-strip fin heat exchanger is more advantageous than slotted and plain straight fins. Manglik and Bergles [4] developed thermo-hydraulic tools for 18 offset-strip fin surfaces along with the correlations. Chennu et al. [5] proposed correlations for j and f factor of the offset-strip fin heat exchanger, which involves geometric parameters, and Reynolds number. Kim et al. [6] studied the blockage ratio in offset-strip fin heat exchangers and proposed a new correlation with a blockage ratio greater than 20%. Cao et al. [7] experimentally studied thermal performance of plate-fin heat exchanger using mixed refrigerants for a single stage cryogenic cycle. They made comparison of their experimental date with existing correlations. Kuchhadiya and Rathod [8] worked on the experimental investigation on crossflow plate-fin heat exchanger with offset-strip fins, they compared the result with different correlations as well. An experimental study has been done by Gupta et al. [9] to predict the effectiveness and performance of plate-fin heat exchangers at low-temperature ranges with variation

in mass flow rate of liquid nitrogen to cool the high-pressure gas. Jiang et al. [10] experimentally studied pressure drop and heat transfer in different types of plate-fin heat exchangers (having perforated and offset-strip fins) using gaseous helium. They considered wide parametric variations.

Jiang et al. [11] worked on the thermo-hydraulic characteristics of offset-strip fin heat exchangers for large-sized helium liquefiers or refrigerators by experiment and numerical simulation. It involves the parametric comparison of the Colburn factor, friction factor with different input parameters like inlet fluid temperature, Reynolds number, fin spacing, and fin thickness. Different correlations from CFD models have been included and compared. Jiang et al. [12] also proposed improvements in existing correlations for offset-strip fin heat exchangers using helium for different cryogenic applications based on their numerical and experimental study. They compared the same with the past correlations.

Recently Gupta et al. [13] conducted systematic experimental study on cryogenic plate-fin heat exchangers. They believed that there are so many correlations available for cryogenic heat exchangers but doing experimental work need to study them practically. However, the advantages of the numerical method can be appreciated as it reduces time, cost, and material usage by compromising the accuracy of results within the permissible limits.

From all the proposed and studied topics, and methods on plate-fin heat exchangers for cryogenic applications, it can be concluded that experimental analysis is needed to study the new fin types practically. However, there is a need for improvement in parameters like heat transfer and pressure drop, and taking care of effects like longitudinal heat conduction, flow maldistribution, heat leakage, and fluid property variation concerning temperature. The parametric analysis is more beneficial by using numerical methods than experimental methods as we can easily change the geometrical structure, flow conditions, and temperature ranges in numerical approach by compromising accuracy level. Considering all effects, an improved and comparative numerical solution of plate-fin heat exchangers for cryogenic applications has been proposed.

3 Methodology

3.1 Geometry

The fin geometry considered herein can be described by the following parameters: fin height (h), fin space (s), fin wall thickness (t), fin length (l), and parting plate thickness (b). An offset-strip fin heat exchanger as described in Yang et al. [14] has been considered for this study. The non-dimensional geometry parameters are as follows:

$$\alpha = s/h; \quad \gamma = t/s; \quad \delta = t/l \tag{1}$$
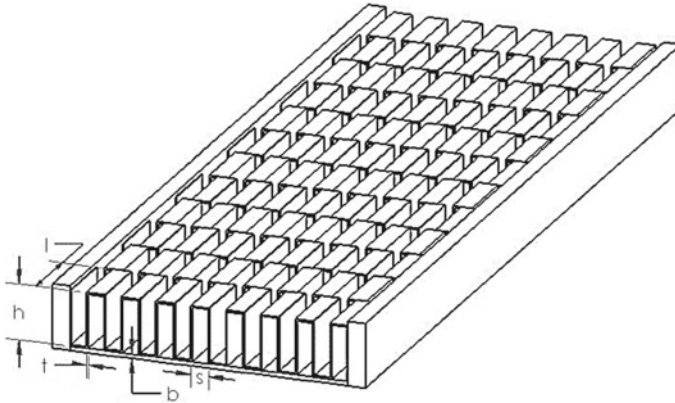
Fig. 2 Offset-strip fin heat exchanger

The adopted values of geometry parameters according to the non-dimensional parameters are $\alpha = 0.3149$; $\gamma = 0.1$; $\beta = 0.025$, $h = 6.35$ mm; $s = 2$ mm; $t = 0.2$ mm; $l = 8$ mm. The hydraulic diameter D_h is defined as (Fig. 2):

$$D_h = \frac{4l(h-t)(s-t)}{2(l(h-t)+l(s-t)+t(h-t))+t(s-2t)} \qquad (2)$$

Considering the existence of periodicity in the geometry, the computational domain is considered as shown in Fig. 3. Different fin materials such as copper, Al 1100, Al 3003F, brass, and stainless steel 304 is used in the numerical simulation. Nitrogen (gaseous as will in liquid form) is used as the working fluid. The thermos-physical properties of nitrogen as given in Leachman et al. [15] is considered in the numerical simulation, which is shown in Table 1 and Fig. 4.

3.2 Mathematical Model

Numerical simulation has been carried out using ANSYS Fluent® with the following assumptions: (i) fluid flow and heat transfer in steady-state, (ii) there is no phase transformation, (iii) interfacial thermal resistance between fluid and solid is negligible, (iv) heat loss by thermal radiation and natural convection are negligible, and (v) flow maldistribution is negligible.

Governing equations:

The governing differential equations considered in the numerical simulation are the following:

Continuity equation
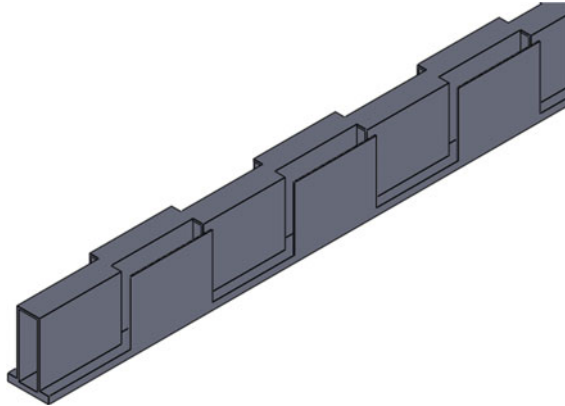
Fig. 3 Computational domain

Table 1 Properties of working fluid

Property	Liquid nitrogen (LN1)	Liquid nitrogen (LN2)	Gaseous nitrogen (GN)
T_{ref} ($T_{in} \sim T_w$)	65.5 K (65–66 K)	77.5 K (77–78 K)	77.5 K (77–78 K)
P_{ref} (MPa)	0.3	0.3	0.05
ρ (kg/m^3)	858.03	805.93	2.2196
C_p (J/kg K)	2002.6	2040	1077.15
k_f (W/m K)	0.16879	0.14478	0.0071205
μ (Pa s)	0.00027598	0.00016031	5.4132E−06
Pr	3.2749	2.2586	0.8189

Fig. 4 Thermal conductivity of fin material varying with operating temperature
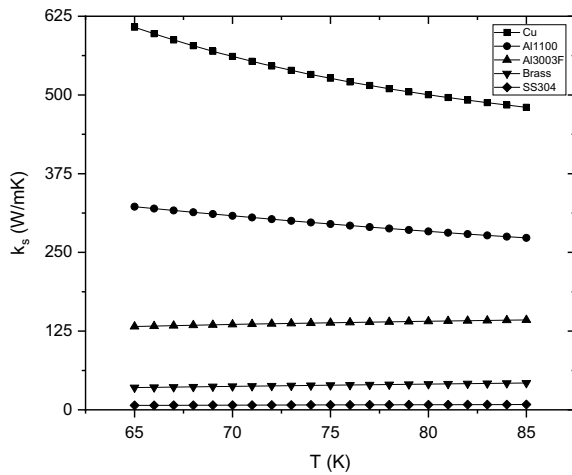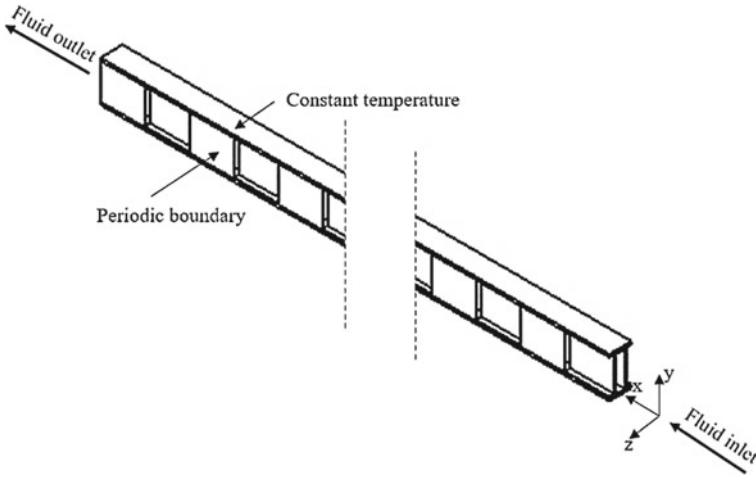
Fig. 5 Schematic representation of boundary conditions used in the computational domain

$$\frac{\partial u_i}{\partial x_i} = 0 \tag{3}$$

Momentum equation

$$\frac{\partial}{\partial x_i}(\rho u_i u_i) = \frac{\partial}{\partial x_i}\left(\mu \frac{\partial \phi}{\partial x_i}\right) - \frac{\partial p}{\partial x_i} \tag{4}$$

Energy equation

$$\frac{\partial}{\partial x_i}(\rho u_i T) = \frac{\partial}{\partial x_i}\left(\frac{\mu}{\mathrm{Pr}} \frac{\partial \phi}{\partial x_i}\right) \tag{5}$$

Boundary conditions: Constant temperature boundary condition is considered over the parting plate. Velocity inlet and outflow conditions are considered at the inlet and outlet, respectively. The periodic boundary condition is considered on both sides of the solid and fluid surfaces. The temperature difference between cover plate and fluid is not more than 1 K (Fig. 5).

3.3 Data Reduction

The study's outcomes are observed in terms of outlet temperature, total heat transfer rate, average velocity at the outlet, and pressure drop. To analyze heat transfer and pressure drop behavior, j and f factors have been considered. The following mathematical relations are used for data reduction. The logarithmic mean temperature

difference between the cover plate and the fluid domain is

$$\Delta T_{\text{LMTD}} = \frac{\left(T_{\text{base}} - T_{\text{bulk,in}}\right) - \left(T_{\text{base}} - T_{\text{bulk,out}}\right)}{\ln\left(\frac{T_{\text{base}} - T_{\text{bulk,in}}}{T_{\text{base}} - T_{\text{bulk,out}}}\right)} \tag{6}$$

The overall heat transfer coefficient is given by:

$$U = \frac{Q}{A\,\Delta T_{\text{LMTD}}} \tag{7}$$

The fin efficiency is expressed as:

$$\eta_f = \frac{\tanh(mh/2)}{mh/2} \tag{8}$$

where $m = \sqrt{2h_c/k_s t}$. The surface fin efficiency η_o for the fin channel is

$$\eta_o = 1 - \frac{A_{\text{sec}}}{A}\left(1 - \eta_f\right) \tag{9}$$

Average heat transfer coefficient h_c is

$$h_c = \frac{1}{\eta}\left[\frac{1}{U} - \frac{b}{k_s}\frac{A}{2A_{w,\text{cp}}}\right]^{-1} \tag{10}$$

The Nusselt number, Reynolds number, and Prandtl number are given by

$$\text{Nu} = \frac{h_c D_h}{k_f} \tag{11}$$

$$\text{Re} = \frac{G D_h}{\mu} \tag{12}$$

$$\text{Pr} = \frac{\mu C_p}{k_f} \tag{13}$$

The f factor and j factor are given by

$$f = \frac{\Delta P D_h}{2\rho L v_{\text{avg}}^2} \tag{14}$$

$$j = \frac{\text{Nu}}{\text{Re}\,\text{Pr}^{1/3}} \tag{15}$$
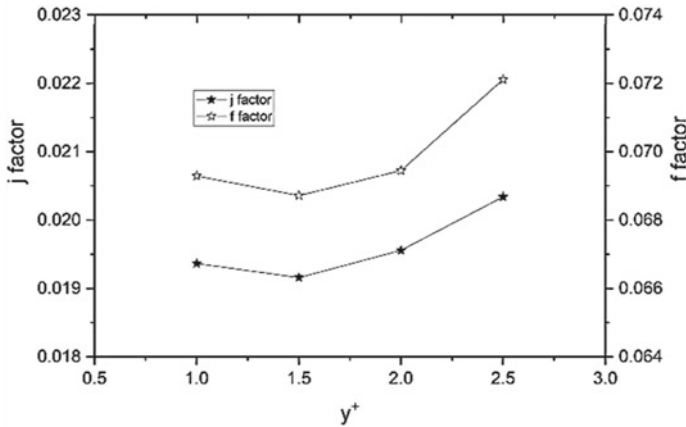
Fig. 6 Grid-independent test

3.4 Meshing

Standard grid independence test procedure is adopted for finalizing the optimum grid size for every geometry under consideration in this study. A grid-independent test has been conducted by considering face size as 0.18 mm for different $y+$ values concerning the j and f factor. The grid-independent test was carried out for aluminum 99% with liquid nitrogen as working fluid, and the values of f and j factors with varying $y+$ are presented in Fig. 6. The percentage error for j and f factors at $y+ = $ 1.5 are 2.0437 and 1.0494, respectively while at $y+ = 1.0$ are 0.0693 and 1.0494, respectively. Based on this, $y+ = 1.5$ has been considered.

3.5 Setup and Model Validation

For the pressure velocity coupling, the SIMPLE method has been adopted. In controls, relaxation factors have been changed by trial-and-error method to converge the solution. For momentum and energy, second-order upwind method was chosen. The convergence criteria considered for continuity and momentum equations is less than 10^{-6} and for energy equation it is less than 10^{-8}. The present model has been validated with five correlations of j and f factor as shown in Figs. 6 and 7. Upon validation, the maximum and minimum percentage of errors are 11.82% and 0.01%, respectively.
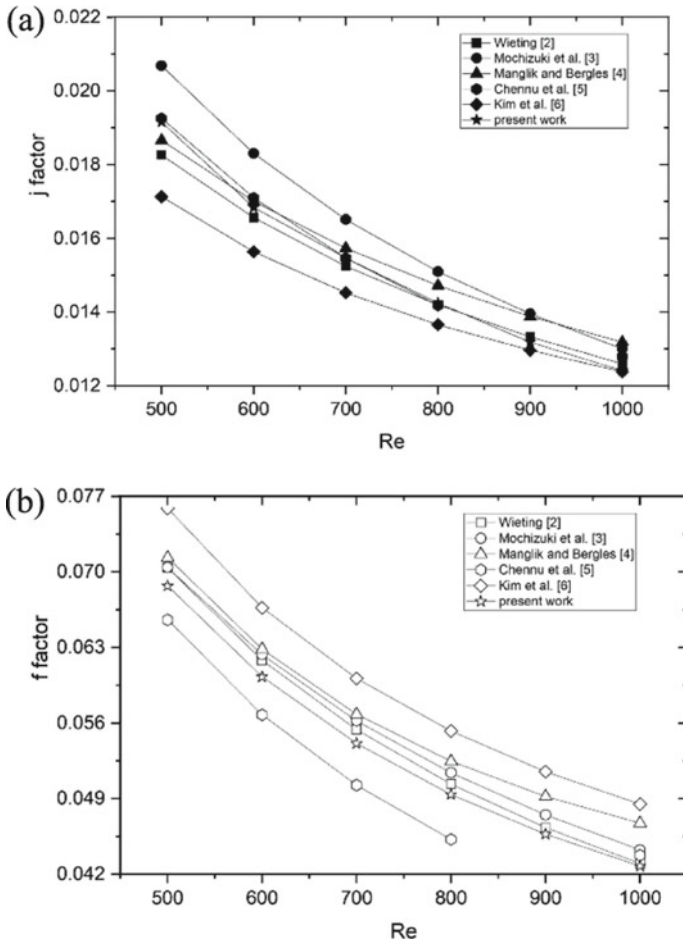
Fig. 7 Model validation for **a** j factor **b** f factor

4   Results and Discussion

Three-dimensional numerical conjugate heat transfer analysis of plate-fin heat exchanger is carried out consisting of offset-strip fin channels. The fin material conductivity is varied by considering five different solid materials: SS304, Al1100, Al3003F, Brass, and copper. The flow Re is varied in the range of 50–1000. The variation of f and the j factor along with average Nusselt number and overall efficiency with varying solid material conductivity, flow Re for nitrogen as the working fluid at three states is numerically simulated using commercially available Ansys Fluent®.

4.1   Model Validation

The value of j and f factor for varying Re in the range of Re $= 500$–1000 is numerically evaluated and compared with existing correlations as shown in Fig. 7a and b, respectively. As can be seen in Fig. 7a and b that the present numerical prediction for both j and f are in good agreement with existing correlation.

4.2   Effect of Fin Material Conductivity

It is observed that Nusselt number is increasing with increasing fin material conductivity as can be seen in Fig. 8a. However, the rate of increase in Nu with fin material conductivity is decreasing with increasing fin conductivity. The increase in Nu with fin material conductivity is higher for liquid nitrogen (LN1) and lower for gaseous nitrogen (GN). The change in Nusselt number with respect to fin thermal conductivity for gaseous nitrogen is comparatively low than liquid nitrogen (LN1, LN2). At lower fin material conductivity, gaseous nitrogen (GN) yields higher Nu compared to liquid nitrogen (LN1 and LN2). However, at higher fin material conductivity, the LN1 yield highest Nu followed by LN2 and GN, i.e., $Nu_{LN1} > Nu_{LN2} < Nu_{GN}$.

Overall efficiency of gaseous nitrogen is found to be higher compared to liquid nitrogen (LN1, LN2). Secondly, the overall efficiency is found to be increasing with fin material conductivity for both gaseous and liquid nitrogen (GN, LN1, and LN2). However, the curve getting flattened with increasing fin material conductivity (Fig. 9).

4.3   Effect of Prandtl Number Under Varying Flow Re

The effect of Prandtl number on Nusselt number, overall efficiency and j factor for varying flow Re is presented in Figs. 10, 11, and 12 respectively, by considering LN1, LN2, and GN as the working fluid corresponding to Prandtl number value of 3.274, 2.259, and 0.819, respectively. It is found that Nusselt number is increasing while overall efficiency and j factor is decreasing with increasing flow Re. However, the rate of decrease in overall efficiency with flow Re for GN is very small, which can be observed in Fig. 13.

Next, it is observed that Nusselt number at any flow Re is increasing as Prandtl number is decreasing. Secondly, the rate of increase in Nu with Re is higher for LN1 and lower for GN. Again, overall efficiency of gaseous nitrogen is higher compared to liquid nitrogen (LN1, LN2). j factor increases as Pr increases, and j factor decreases with increase in Re.
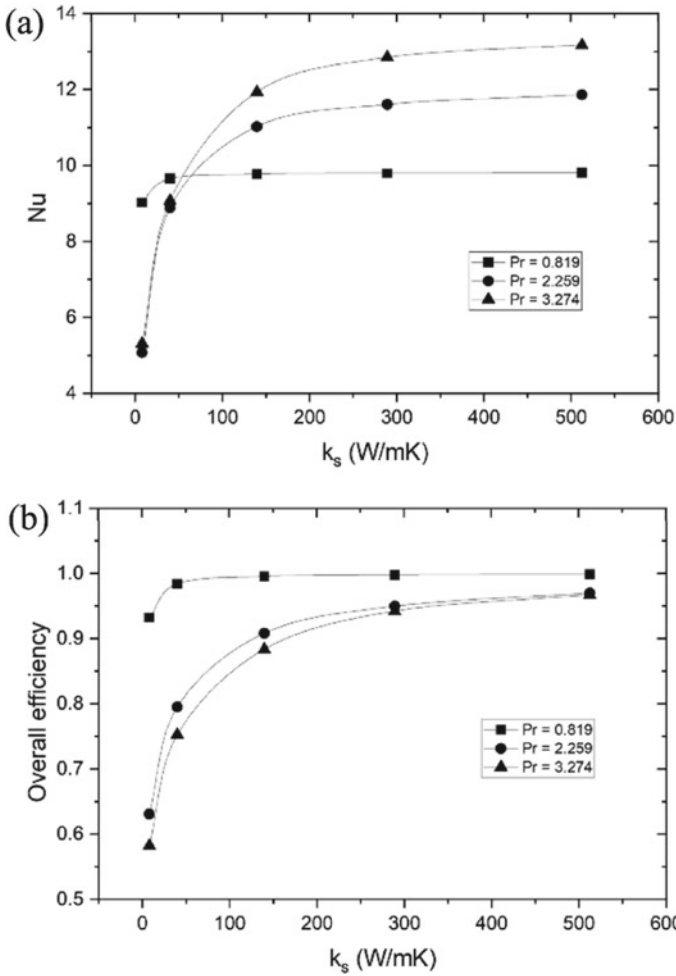
Fig. 8 Variation of **a** Nusselt number **b** overall efficiency with thermal conductivity of solid

4.4 *Effect of Flow Re on* **j** *and* **f** *Factor for Different Fin Material*

It has been observed that *f* factor is not affected by the fin material, but may be affected by the temperature-dependent properties of fin material. *j* factor is increasing as thermal conductivity of fin material increasing.

Fig. 9 Variation of
a j factor **b** f factor with
thermal conductivity of solid
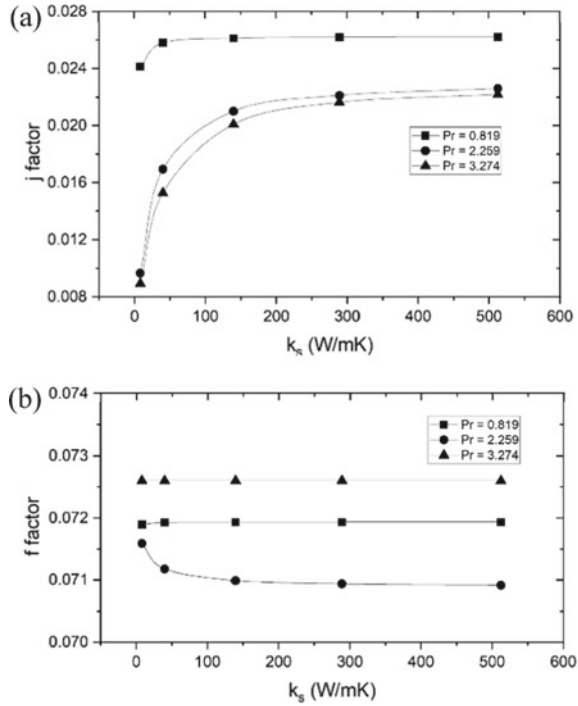
Fig. 10 Variation of Nusselt
number with flow Re for
different Pr
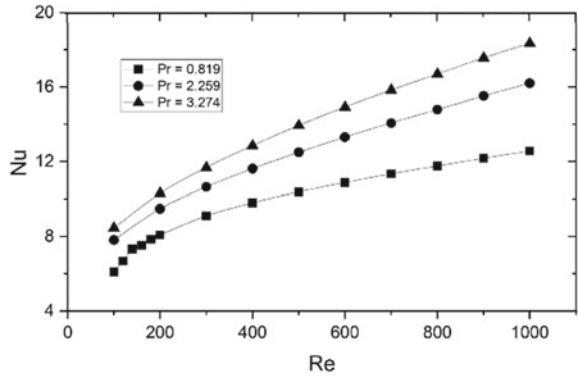
5 Conclusions

In this work, an offset-strip plate-fin heat exchanger has been adopted with five different fin materials and three different states of Nitrogen as the working fluid. The simulations are done for Re = 50 to 1000 with varying temperature ranges of primary fin cover plate.

Fig. 11 Variation of overall
efficiency with flow Re for
different Pr
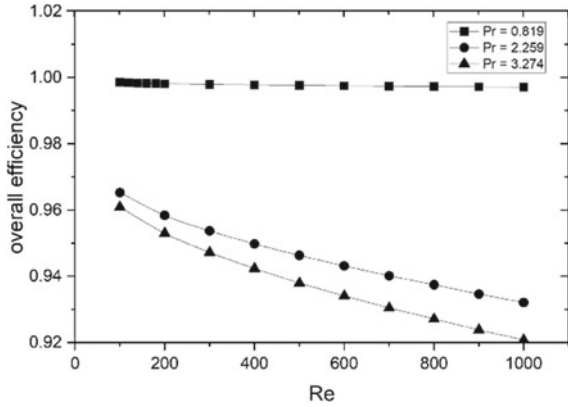
Fig. 12 Variation of j factor
with Re for different Pr
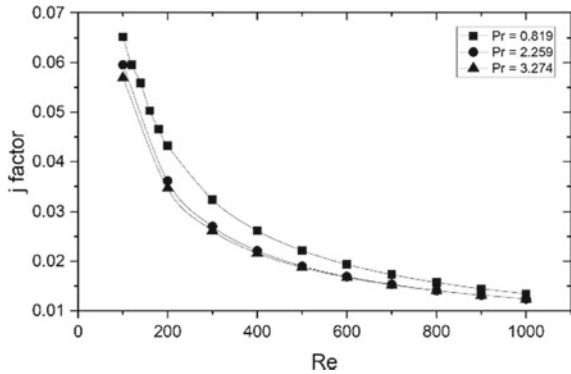
1. From the study of considering temperature-dependent fluid properties with three different temperature ranges (i.e., 1, 2, and 3 K), it has been concluded that there is no significant variation in overall efficiency, and j factor. However, there is small decrease in Nu and f factor as temperature difference increasing.
2. For Pr $<$ 1, considered output parameters like Nu, overall efficiency, f factor, and j factor are almost constant as thermal conductivity of fin material changes except at the thermal conductivity ranges below 50 W/m K.
3. As thermal conductivity increases the Nu, overall efficiency, and j factor are increasing rapidly for Pr $>$ 1, but the increment is comparatively very small for Pr $<$ 1.
4. At a particular Re, as Pr increases Nu increases, but as thermal conductivity of fin material decreases below certain values with respect to Pr, the same phenomenon will be inverted. For remaining parameters there is no such behavior.
5. Overall efficiency with Pr $<$ 1 is almost independent of Re, whereas with Pr $>$ 1 it decreases as Re increases.
6. The f factor is independent of the thermal conductivity of fin material and the Prandtl number of working fluids.

Fig. 13 Variation of
a f factor **b** j factor with flow
Re
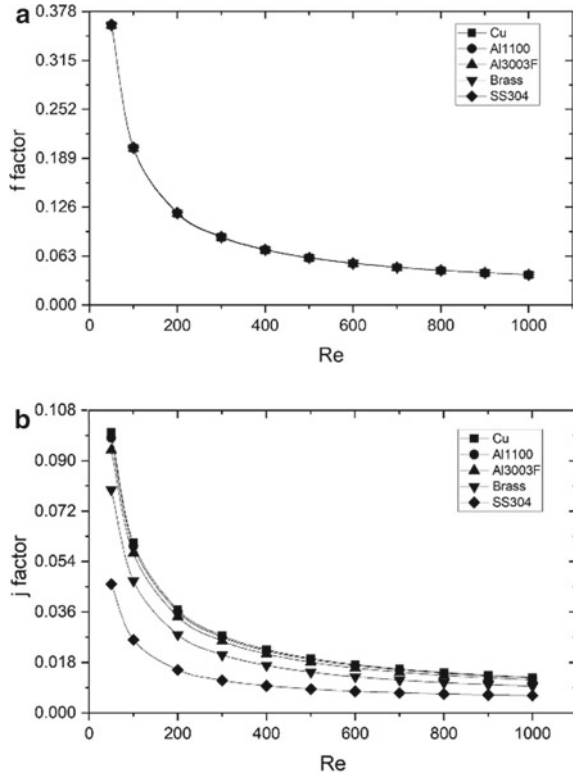
7. For j factor, it increases as thermal conductivity increases and Prandtl number decreases.
8. From the results and observations, it can be concluded that the offset-strip fin heat exchanger is having high overall efficiency, low pumping power requirement, the high-temperature difference from outlet to inlet, and high heat transfer per unit mass flow, at low Re, and having high heat transfer rate, and high pumping power requirement, at high Re.

Nomenclature

A	Total heat transfer area (m²)
$A_{w,\,cp}$	Cover plate area (m²)
A_{sec}	Secondary surface fin area (m²)
C_p	Specific heat at constant pressure (J/kg K)
G	Mass flux (kg/m² K)
h_c	Mean heat transfer coefficient (W/m² K)

K Turbulent kinetic energy (m^2/s^2)
k_f Thermal conductivity of fluid (W/m K)
k_s Thermal conductivity of solid (W/m K)
T_{bulk} Bulk temperature of fluid (K)
T_{base} Base temperature (K)
ε Dissipation rate of k (m^2/s^3)
ϕ General-dependent variable (–)

References

1. Kays WM, London AL (1984) Compact heat exchangers. McGraw-Hill, New York
2. Wieting AR (1975) Empirical correlations for heat transfer and flow friction characteristics of rectangular offset-fin plate-fin heat exchangers. J Heat Transfer 97(3):488–490
3. Mochizuki S, Yagi Y, Yang WJ (1987) Transport phenomena in stacks of interrupted parallel-plate surfaces. Exp Heat Transf 1(2):127–140
4. Manglik RM, Bergles AE (1995) Heat transfer and pressure drop correlations for the rectangular offset-strip fin compact heat exchanger. Exp Thermal Fluid Sci 10(2):171–180
5. Chennu R, Paturu P (2011) Development of heat transfer coefficient and friction factor correlations for offset fins using CFD. Int J Numer Meth Heat Fluid Flow 21(8):935–951
6. Kim MS, Lee J, Yook SJ, Lee KS (2011) Correlations and optimization of a heat exchanger with offset-strip fins. Int J Heat Mass Transf 54(9–10):2073–2079
7. Cao L, Liu J, Li R, Huang S, Zhang F, Xu X (2016) Experimental study on the mixed refrigerant heat transfer performance in a plate-fin heat exchanger during a single-stage cryogenic cycle. Appl Therm Eng 93:1074–1090
8. Kuchhadiya BB, Rathod PP (2016) Experimental investigation of thermal behaviour of cross flow plate-fin heat exchanger with offset strip fin. Procedia Technol 23:423–430
9. Gupta AK, Kumar M, Panda D, Sahoo RK (2018) Experimental analysis to predict the performance of a plate-fin heat exchanger at cryogenics temperature. Instrumentation Mesure Metrologie 17(2):315–329
10. Jiang Q, Zhuang M, Zhang Q, Zhu Z, Geng M, Sheng L, Zhu P (2018) Experimental study on the thermal hydraulic performance of plate-fin heat exchangers for cryogenic applications. Cryogenics 91:58–67
11. Jiang Q, Zhuang M, Zhu Z, Shen J (2019) Thermal hydraulic characteristics of cryogenic offset-strip fin heat exchangers. Appl Therm Eng 150:88–98
12. Jiang Q, Pan C, Chen Y, Zhang Q, Tang Y, Gu J, Aleksandr P (2021) Improved heat transfer and friction correlations of aluminum offset-strip fin heat exchangers for helium cryogenic applications. Appl Therm Eng 192:116892
13. Gupta AK, Kumar M, Sahoo RK, Sarangi SK (2021) Analytical and experimental investigation of a plate-fin heat exchanger at cryogenics temperature. Int J Heat Technol 39(4):1225–1235
14. Yang Y, Li Y, Si B, Zheng J (2017) Heat transfer performances of cryogenic fluids in offset strip fin-channels considering the effect of fin efficiency. Int J Heat Mass Transf 114:1114–1125
15. Leachman JW, Jacobsen RT, Lemmon EW, Penoncello SG, Van Sciver SW, Jeong S (2017) Thermodynamic properties of cryogenic fluids. Springer, New York

Instantaneous RUL Prediction of a Two-Stage Force Feedback Electro-hydraulic Servo Valve (EHSV)

Pratik Punj and Md Adil

1 Introduction

Electro-hydraulic servo valve (EHSV) is one of the most powerful control devices as an outcome of the coupling between electronics and hydraulic power system. They are used to control almost all the hydraulic parameters such as the pressure, pressure difference, angular speeds, etc., with very high precision and speedy responses which makes them highly useful in aviation control system and other sophisticated system which requires high precision and reliability. The most hydraulic fluid used in EHSV can be classified into jet fuel (fuel oil), hydraulic oil and phosphate ester hydraulic oil.

The life span and reliability of EHSV is very vulnerable to the external factors like contamination of hydraulic fluid which leads to the erosion and abrasive wear of the components [1]. Particle erosion wear is ubiquitous while EHSV is operating and is the leading cause of failures [2]. From technical research in this field, it was found that due to the presence of impurities in the circulating hydraulic fluid, the sharp edges of the valve components are washed out, resulting in increased internal leakage flow, input current hysteresis and null leakage, as well as a decrease in input current threshold, pressure gain and gain linearity [3]. Much research has been done qualitatively by analysing the erosive wear (and manufactured geometric error) for the degraded performance of sliding spool [4–6]. Xin Fang established a set of physics-of-failure models for particle erosion wear of EHSV [7], which can help to design an EHSV with high reliability and long life. Ashok K. Singhal created the mathematical basis of the full cavitation model, which showed the effect of cavitation on the service life of hydraulic machines [8]. Yuanbo Chu proposes a

P. Punj (✉)

Department of Mining Machinery Engineering, IIT (ISM) Dhanbad, Dhanbad, India
e-mail: pratik26punj@gmail.com

M. Adil
Department of Mechanical Engineering, Jadavpur University, Kolkata, India

dynamic erosion wear characteristics analysis and service life prediction method in which the structural feature and working principle of the nozzle flapper pressure valve are analysed using the brake cavity as the load blind cavity [9]. Wallace MS demonstrated the ability of computational fluid dynamics techniques to study and predict the rate of solid particle erosion in industrially relevant geometries using an Eulerian–Lagrange model of flow in combination with empirically developed mass removal equations to study erosion in valve components in aqueous slurry flows [10]. Paolo Tamburrano et al. 2019 in his paper discussed the operating principle and the analytical models to study EHSV and reported the performance levels using CFD analysis along with the use of smart materials, which aim to improve performance and reduce cost were also analysed in detail [12].

This paper is focused on determining the remaining useful life (RUL) of the EHSV due to erosion wear by studying the nature of the volume flow rate collected through return oil port and then using a machine learning algorithm to determine the RUL of any new similar EHSV at any instant. The volume of return oil is a contribution from three sources: discharge through flapper nozzle assembly, discharge through radial clearance between spool and valve casing and due to the fillet at spool lands and casing ports.

2 Methodology

The mathematical model helps to analyse the effect of erosion wear on the components geometrical structure and how this change effects the overall performance of the valve, so that the degradation of performance can be linked to its life cycle. Figure 1 shows the schematic diagram of a two-stage force feedback EHSV. It consists of two parts namely a pre-amplifier stage that consists of moving-iron torque motor and double nozzle-flapper valve, and a slide valve power amplifier stage.

The armature is supported by spring and is evenly spaced between the upper and lower permanent magnets. The flapper is evenly spaced between the two nozzles. The main spool of the EHSV, which is in the neutral position, has no output.

When Δi is supplied as the electrical input control current to the armature coil, the armature assembly deflects out of position and the flapper moves out of its centre position, blocking flow from one of the nozzles, and due to flow accumulation in the corresponding nozzle, there is a generation of a pressure differential across the spool ends will cause the spool to move from its zero or zero position, opening the EHSV and outputting the appropriate pressure and flow [11]. Reversing the direction of flow correspondingly reverses the direction of flow pressure since valve output magnitude and armature deflection angle are proportional to electric current. In Fig. 1, the i_1, i_2 are the input control currents; P_1, P_2 are the respective pressures at the spool ends; P_s is the supply oil pressure; P_A, P_B are the respective load pressures at ports A and B; P_o is the pressure of the return oil port.

As discussed above, the main contributor in the volume collected at the return oil port are as follows:
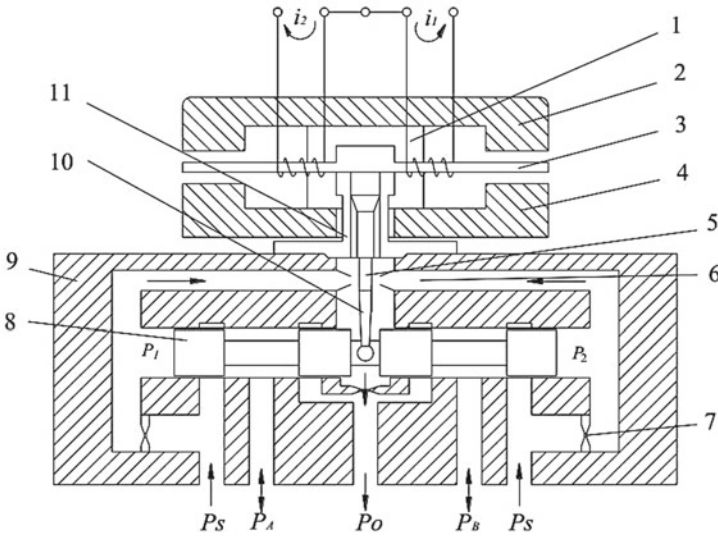
1. control coil; 2. upper permanent magnet; 3. armature; 4. lower permanent magnet; 5. flapper; 6. nozzle; 7. fixed restrictor; 8. main spool; 9. valve sleeve; 10. feedback bar; 11. spring tube

Fig. 1 Schematic diagram of a two-stage electro-hydraulic servo valve [11]

- Leakage flow through nozzle jets
- Leakage flow due to the clearance between spool and sleeve
- Leakage flow due to increase in fillet radius at spool lands and valve ports.

The mathematical models of each of these are discussed below.

2.1 Flow Through Nozzle Jet

From Fig. 2, it is clear that the maximum leakage flow through nozzle exists at the zero position also called as the null position of the flapper. The flow loss and power loss decrease with the change of flapper position.

In Fig. 2, Q_a, Q_b are flow through restrictor a and b, respectively; Q_s be the supply flow into the valve; Q_1, Q_2 be the respective flow through the nozzles 1 and 2, respectively; A is the axial area of the spool land, and U is the velocity with which spool moves. Then

$$Q_s = Q_a + Q_b \tag{1}$$

$$Q_a = Q_1 + AU \tag{2}$$
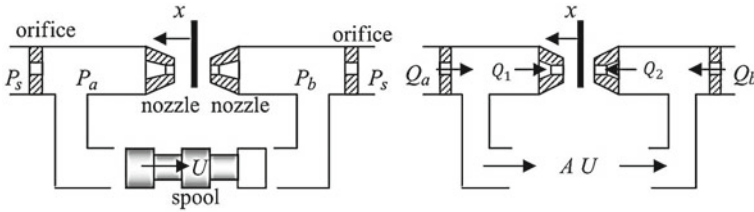
Fig. 2 Flapper nozzle amplifier used to move spool [11]

$$Q_b = Q_2 - AU \qquad (3)$$

Since restrictor a and b are orifices, then the flow through them (Q_a, Q_b) are as follows:

$$Q_a = C_{do} \cdot A_o \sqrt{\frac{2(P_s - P_a)}{\rho}}, \quad Q_a = C_{do} \cdot A_o \sqrt{\frac{2(P_s - P_b)}{\rho}} \qquad (4)$$

and flow through nozzles 1 and 2 (Q_1, Q_2) are as follows:

$$Q_1 = C_{dn} \cdot A_{n1} \sqrt{\frac{2P_a}{\rho}}, \quad Q_2 = C_{dn} \cdot A_{n2} \sqrt{\frac{2P_b}{\rho}} \qquad (5)$$

as shown in Fig. 3,

$$A_o = \frac{\pi}{4} d_o^2 \qquad (6)$$

$$A_{n1} = \pi d_n (x_o - x) \qquad (7)$$

$$A_{n2} = \pi d_n (x_o + x) \qquad (8)$$

x_o = nozzle flapper clearance at null position,
d_o = diameter of restrictor orifice,
d_n = diameter of nozzle.

While in operation the movement of spool is very small and slow so, we can neglect its effect, i.e. taking $AU = 0$, then $Q_a = Q_1 = Q_2 = Q_b$. This leads to

$$\overline{P_a} = \frac{1}{1 + z(1 - \overline{x})^2} \quad \text{and} \quad \overline{P_b} = \frac{1}{1 + z(1 + \overline{x})^2} \qquad (9)$$

Fig. 3 Flapper nozzle schematic
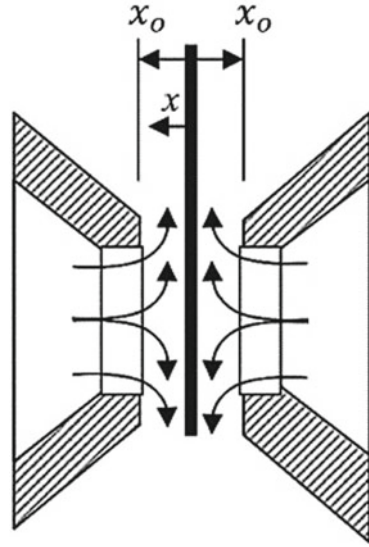
where $\overline{P_a} = \frac{P_a}{P_s}$; $\overline{P_b} = \frac{P_b}{P_s}$; $\overline{x} = \frac{x}{x_o}$; $z = 16\left(\frac{C_{qn}}{C_{qo}}\right)^2\left(\frac{d_n}{d_o}\right)^2\left(\frac{x_o}{d_o}\right)^2$.

So, the pressure differential is

$$\Delta\overline{P} = \overline{P_a} - \overline{P_b} = \frac{4z\overline{x}}{\left[1 + z(1 - \overline{x})^2\right]\left[1 + z(1 + \overline{x})^2\right]}$$

and the total flow loss through the two nozzles are as follows:

$$\overline{Q_l} = \frac{(1 - \overline{x})}{\sqrt{1 + z(1 - \overline{x})^2}} + \frac{(1 + \overline{x})}{\sqrt{1 + z(1 + \overline{x})^2}} \tag{10}$$

At null position, i.e. $\overline{x} = 0$, $\Delta\overline{P} = 0$, then $\overline{P_a} = \overline{P_b} = \frac{1}{(1+z)}$ and the null pressure gain $= \frac{d\Delta\overline{P}}{d\overline{x}} = \frac{4z}{(1+z)^2}$.

The maximum null gain is obtained at $z = 1$ which suggest that at null pressures $P_a = P_b = \frac{P_s}{2}$ and $\overline{Q_l} = \sqrt{2} = 1.414$. The total leakage flow due to the flapper–nozzle assembly is

$$Q_{ln} = \overline{Q_l} \cdot k_n \tag{11}$$

where

$$k_n = C_{dn} \cdot \pi d_n x_o \sqrt{\frac{2P_s}{\rho}}. \tag{12}$$

From the earlier research works, it is reasonable to select the nozzle flow coefficient (C_{dn}) to be 0.62 and the orifice flow coefficient (C_{do}) to be of value 0.79. The orifice diameter generally varies between 0.15 and 0.4 mm, nozzle diameter varies between 0.45 and 0.7 mm, and the flapper clearance varies very little around 0.03 mm.

2.2 Flow Through Radial Clearance of Spool Valves

Due to the sliding of spool, the erosion wear occurs and the radial clearance between spool and sleeve increases with time resulting in the increase of leakage flow through the return port. Considering the valve set are ideal and there only a radial clearance exist as shown in Fig. 4 and when the load flow is zero, the maximum leakage flow can be expressed by a mean flow, which is laminar when the flow is through the sharp-edged orifices.

So, the leakage flow through the radial clearance can be expressed as

$$Q_c = \frac{\pi W c^2}{32\mu} \cdot \Delta P \tag{13}$$

where $W = nw$ = total port area gradient, w is the single port area gradient, μ is the dynamic viscosity of the hydraulic fluid, ΔP is pressure between the spool, c is the radial clearance.

At null position flow through each orifice is $\frac{Q_s}{2}$ and pressure drop is $\frac{P_s}{2}$. Then

$$Q_c = \frac{\pi W c^2}{32\mu} \cdot P_s \tag{14}$$

Fig. 4 Spool with radial clearance only
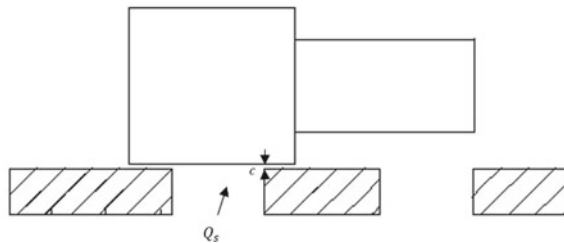
2.3   Leakage Flow Due to Spool Valve Fillet

Due to the manufacturing limitations, even a new spool valve has a rounded corner or fillet at its edges and cannot go below 0.5 μm of fillet radius. Due to the flow recirculation, cavitation and erosion wear due to contaminated fluid, these sharp edges wear out and the fillet radius increases with time. Considering only rounded corners of equal radius and zero radial clearance as shown in Fig. 5, the orifice length (l_f)

$$l_f = \sqrt{(2r)^2 + (2r)^2} - (2r) \tag{15}$$

And the leakage flow through them is as follows:

$$Q_f = \frac{\pi W l_f^2}{32\mu} \cdot P_s \tag{16}$$

The leakage flow through the combination of both clearances as well as valve fillets is the following:

$$Q_{fc} = \frac{\pi W l^2}{32\mu} \cdot P_s \tag{17}$$

where $l = \sqrt{(2r + c)^2 + (2r)^2} - (2r)$ as shown in Fig. 6. So, the total flow rate through the return oil port is given by: $Q_r = Q_{ln} + Q_{fc}$.

3   Using ML Model for Instantaneous RUL Prediction

Using the above relations, a data sheet is created that contains the values that varies with time. Then, this data sheet if fed to a ML algorithm which is then used to calculate the instantaneous RUL. The predictors are return oil flow rate, supply pressure, fluid density and viscosity while the response is the time. This predicted time is used to calculate the RUL by subtracting it from the time of failure at that supply pressure, density and viscosity. The algorithm of the ML model is explained in Fig. 7.

From the data sheet created the predictor and response is selected and is split into training and testing dataset. Training data is fed to KNN Regressor with 1 neighbour and then training and testing RMSE is calculated. If the $RMSE_{Test} < RMSE_{Training}$, then the model can be used for making prediction on new sample and if $RMSE_{Test} > RMSE_{Training}$ then the number of neighbours is increased until $RMSE_{Test} < RMSE_{Training}$. Now, this final ML model is used to calculate the instantaneous RUL with the new sample in the same sequence as that of predictor.

Fig. 7 KNN regression model for prediction RUL
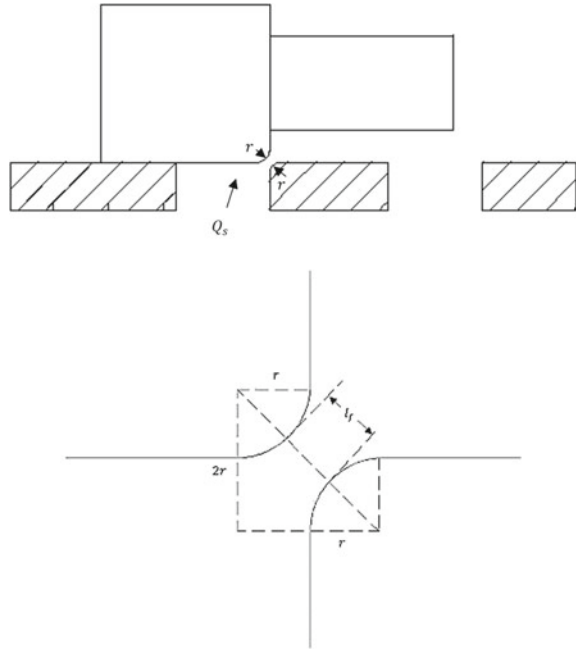
Fig. 6 Spool with both radial clearance and worn orifice
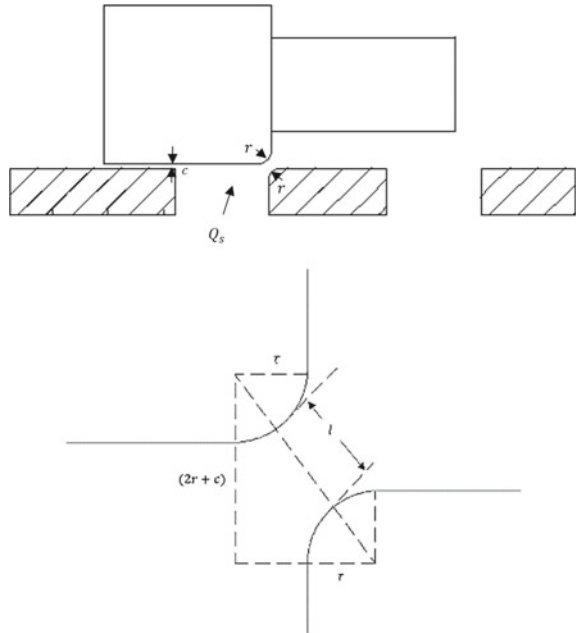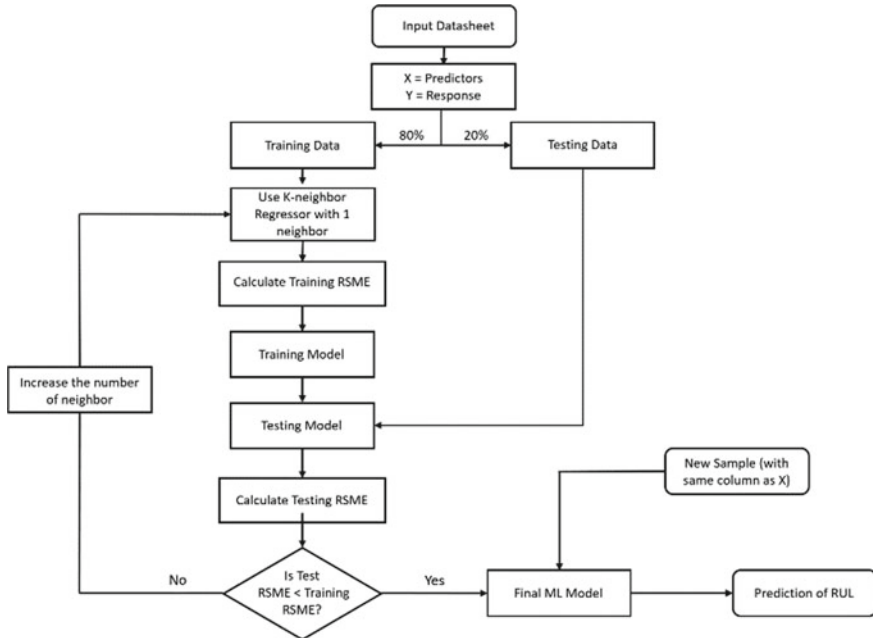
Fig. 5 Spool with worn orifice only

4 Simulation and Results

To proceed with the simulation and finding the variation and dependency of fillet radius, radial clearance as well as the failure time of the valve, the parameters are obtained with reference to the research article [7]. The data are as follows:

Parameter	Marks	Value
Discharge coefficient of nozzle	C_{dn}	0.62
Supply pressure	P_s	100–210 bar
Hydraulic fluid density	ρ	850 kg/m^3
Dynamic viscosity of hydraulic fluid	μ	0.01257 kg/m s
Slot orifice length	w	2.641 mm
Total slots length	W	10.564 mm
Nozzle inner diameter	d_n	0.5 mm
Radial clearance of spool and sleeve	c	2.2 mm
Clearance between nozzle and flapper	x_o	0.03125 mm
Threshold value of internal leakage flow	Q'_r	2.5 lpm

Initial fillet radius is increased by the reverse flow and the presence of cavitation which results in the contamination of hydraulic fluid and there is rapid increase

of the fillet radius due to the fluid contamination. So, a quadratic relation between fillet radius and time is assumed according to the data from research article [7]. The relationship is as follows:

$$r(t) = 1.75 \times 10^{-6}t^2 + 0.001t + 0.604$$

With the increase in fillet radius and fluid contamination, the radial clearance also increases. For this assuming a linear relationship with the increase in fillet radius:

$$c = 0.477r + 1.9136$$

Due to the fluid contamination, the nozzle diameter also increases (although very small). Considering the linear relationship of increase in nozzle diameter with time as:

$$d_n = 3.513 \times 10^{-5}t + 0.5$$

Putting the above three equations, the final return oil flow rate for different supply pressures is as shown in Fig. 7. The plot shows the quadratic relationship with time for the return oil flow collected form return oil port, although the nature is not accurate as that of the actual data collected from the return oil port which shows the linear dependency of return oil flow with time. The comparison is shown in Fig. 8 at 210 bar supply pressure. Although a lot of variation is present in middle portion at the threshold value of 2.5 lpm (as per the design), the MM (Mathematical model) reached the threshold before the actual with RMSE of 0.41.

Using the above data, a database (shown in Fig. 10) is created with time, return oil flow rate, supply pressure, density of fluid, dynamic viscosity of fluid, and with the use of machine learning tool KNN regression, with return oil flow rate, supply

Fig. 8 Comparison of return oil flow at different supply pressures as per mathematical model
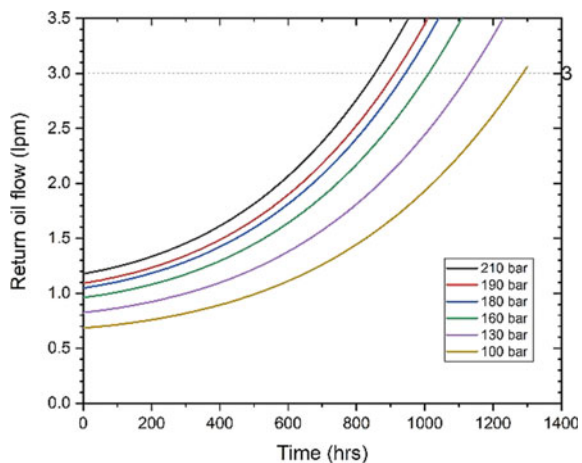
pressure, fluid density, dynamic viscosity, as predictors and time as response, the instantaneous RUL can be calculated taking in account the time required to reach the threshold return oil flow volume (3.0 lpm) for the particular supply pressure. The R^2 score of the KNN regression with 2 neighbours is 0.999448297.

5   Conclusions

Using the nonlinear variation of wear with time, a mathematical model is created above to estimate the contribution of different sources in the return oil flow rate collected from the port in EHSV. Although the plot from Fig. 9 shows that the flow rate calculated by MM varies quadratically with time, the actual flow rate is showing a linear relationship but still both showed the same failure time. A database is created using the data from MM at different supply pressures, and a ML model is used to predict the instantaneous RUL by using the required data from the new EHSV (Fig. 10).
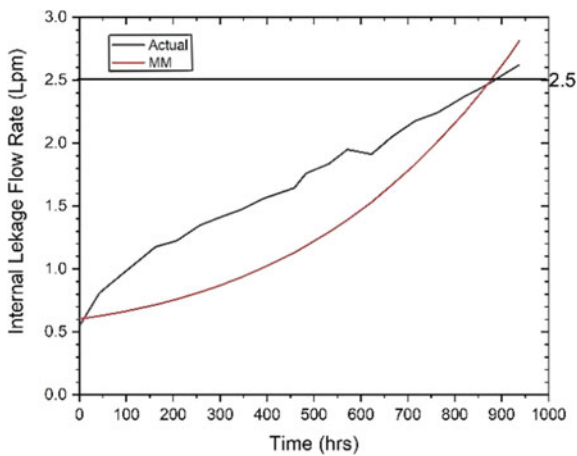
Fig. 9   Comparison between actual and predicted with mathematical model

	Time	radius	clearance	Internal_Leakage	Nozzle_leakage	Total	Pressure	Density	viscosity
0	0.000000	0.604000	2.201708	0.603491	0.573954	1.177446	210	850	0.01257
1	8.686869	0.612819	2.205915	0.607935	0.574305	1.182240	210	850	0.01257
2	17.373737	0.621902	2.210247	0.612541	0.574655	1.187197	210	850	0.01257
3	26.060606	0.631249	2.214706	0.617313	0.575005	1.192318	210	850	0.01257
4	34.747475	0.640860	2.219290	0.622252	0.575356	1.197608	210	850	0.01257

Fig. 10   Datasheet for ML modelling

```
# put sample data in order [Total Leakage Volume, Supply Pressure, Density of Hydraulic Fluid, Dynamic Viscosity of fluid]
x_t = np.array([[1.7,210,850,0.01257]])

for i in range(len(T_f[0,:])):
    if x_t[0,1] == T_f[0,i]:
        break

t_f = T_f[1,i]
y_t = knn.predict(x_t)
RUL = t_f - y_t
print('Current used time is',y_t,'and the avg. failure time for',x_t[0,1],'bar pressure is',t_f,'. RUL is',RUL)
```

Current used time is [[447.37373737]] and the avg. failure time for 210.0 bar pressure is 859 . RUL is [[411.62626263]]

Fig. 11 Instantaneous prediction of RUL using ML model in python

A robust model can be created by collecting experimental return oil flow data at different supply pressure, density of working fluid, dynamic viscosity of fluid and then creating the database using the ML prediction on those data and then with the help of another ML model predicting the instantaneous RUL (Fig. 11).

Nomenclature

Q_S	Supply flow into valve (lpm)
Q_a, Q_b	Flow through restrictor (lpm)
A	Axial area of spool (mm^2)
A_o	Area of orifice (mm^2)
A_n	Area of nozzle (mm^2)
U	Spool velocity (mm/s)
w	Single port area gradient (mm)
d_o	Diameter of restrictor orifice (m)

References

1. Nystad BH, Gola G, Hulsund JE, Roverso D (2010) Technical condition assessment and remaining useful life estimation of choke valves subject to erosion. In: Annual conference of the PHM Society, vol 2
2. Fitch EC, Ing T (2004) Hydraulic system design for service assurance. BarDyne, Incorporated
3. Zhang K, Yao J, Jiang T (2014) Degradation assessment and life prediction of electro-hydraulic servo valve under erosion wear. Eng Fail Anal 36:284–300
4. Vaughan ND, Pomeroy PE, Tilley DG (1998) The contribution of erosive wear to the performance degradation of sliding spool servovalves. Proc Inst Mech Eng Part J: J Eng Tribol 212(6):437–451
5. Xin Bi H, Yong Yao J, Li Y (2011) Research to the wear and geometric error relations of electro hydraulic servo valve. Procedia Eng 15:891–896
6. Fang X, Yao J, Yin X, Chen X, Zhang C (2013) Physics of-failure models of erosion wear in electrohydraulic servovalve, and erosion wear life prediction method. Mechatronics (Oxf) 23(8):1202–1214
7. Zhang L, Luo J, Yuan RB, He M (2012) The CFD analysis of twin flapper-nozzle valve in pure water hydraulic. Procedia Eng 31:220–227

8. Singhal AK, Athavale MM, Li H, Jiang Y (2002) Mathematical basis and validation of the full cavitation model. J Fluids Eng 124(3):617–624
9. Zhang H, Xiong SB, Liang YW, Xiong X (2008) Analyses of erosion wear characteristic and structure research on hydraulic valve. J China Coal Soc 33(2):214–217
10. Wallace MS, Dempster WM, Scanlon T, Peters J, McCulloch S (2004) Prediction of impact erosion in valve geometries. Wear 256(9–10):927–936
11. Watton J (2014) Fundamentals of fluid power control. Cambridge University Press, Cambridge, England
12. Tamburrano P, Plummer AR, Distaso E, Amirante R (2019) A review of electro-hydraulic servovalve research and development. Int J Fluid Power 20(1)

Inter-Code Comparison Exercise for Predicting Transient Helium Distribution in a Scale Down Containment Facility, CSF

B. Gera, Nandan Saha, Aditya Karanam, P. K. Sharma, I. Thangamani, Shubham Mishra, P. Goyal, A. Dutta, V. Verma, and J. Chattopadhyay

1 Introduction

In case of severe accident in water-cooled nuclear power reactors, hydrogen may get released into the nuclear containment due to metal–water reaction. This hydrogen may form combustible mixture and pockets in some local zones. Hydrogen is combustible above 4% v/v in dry air. Steam which create inert atmosphere is also present in the containment but due to operation of sprays or containment coolers, the steam may get condensed and in certain zone, flammable mixture may be formed. Passive autocatalytic recombiners are being deployed in the containment of Indian reactors to manage the released hydrogen. In order to find the suitable locations and required numbers of recombiners, the detailed three-dimensional (3D) local distribution of hydrogen must be known. This requires the use of CFD codes. However, the CFD code should be validated before doing such exercises.

Hence, there is a need to have experimental data on hydrogen distribution behaviour in multi-compartment geometry. It is practically impossible to conduct experiments at actual rector containment scale. Various containment facilities, ranging from small to medium scale, have been commissioned worldwide to conduct containment safety-related experiments. Some of the important facilities are PANDA [1], MISTRA [2] and THAI [3], etc. One multiple compartment scaled containment facility (Containment Studies facility (CSF)) has been commissioned at BARC, Trombay to conduct containment thermal hydraulic and safety-related experiments.

B. Gera (✉) · N. Saha · A. Karanam · P. K. Sharma · I. Thangamani · S. Mishra · P. Goyal · A. Dutta · V. Verma · J. Chattopadhyay
Reactor Safety Division, Bhabha Atomic Research Centre, Mumbai 400085, India
e-mail: bgera@barc.gov.in

In this facility, helium (in place of hydrogen due to safety reason) distribution experiments have been conducted. Before conducting the experiments, blind CFD simulation exercise has been carried out. Results of this blind exercise are presented in this paper.

Various 3D transient CFD simulations of hydrogen distribution for containment scale geometry with or without validation are available in the literature [4–7]. Efforts are being made all over the world for developing and use of sophisticated containment codes with 3D capabilities for simulation of hydrogen behaviour, i.e. hydrogen distribution, recombination and combustion [8, 9].

In the present work, four different CFD codes have been utilised for performing simulation for helium distribution in the CSF geometry. The details of the CSF, experiments and details of various parameters used by different participants, their predictions and differences in results are explained in the present paper.

2 Problem Description and Modelling

Containment Studies Facility (CSF) [10] is approximately 1:250 volumetrically scaled down model of a standard 220 MWe Indian Pressurized Heavy Water Reactor (PHWR) containment system. CSF consists of three levels above ground representing V1 region and a basement. The basement, which is a single compartment represents the V2 volume of Indian PHWR. This V2 volume are connected to the ground floor of V1 volume through several vent pipes. In this present study, only V1 volume is considered due to non-participation of V2 volume in the hydrogen distribution during accident condition. Schematic view of the V1 volume considered for the analysis is shown in Fig. 1. Since hydrogen is released in fuelling machine vault, the CSF volume above the floor of injection room is considered for helium distribution experiments. The entire V1 volume consists of ten compartments as shown in Fig. 2. These compartments in total represent the scaled down V1 volume of Indian PHWR.

CSF is a multi-compartment containment structure having internal diameter of 5.7 m and height of 7.15 m as shown in Fig. 2. It has two compartments (R1 and R2) with a height of 2.5 m in half cylindrical shape at the ground floor representing fuelling machine vaults with another annular compartment R10 surrounding them. There are two compartments at first floor, directly above R1 and R2 and these quarter cylindrical rooms R3 and R4 represents steam generator vaults and pump rooms. Above second floor, the entire dome shape area is representing containment dome (R7). The height of each floor with other relevant dimensions is shown in Fig. 2. Different compartments of CSF are interconnected through several openings as shown in Fig. 1. Openings between R1 and R2 are closed in all the simulations as the fuelling machine vaults are isolated in actual case so that helium can only escape through top horizontal opening between R1 and R3. All the vent pipe openings (connecting V1 to V2) are closed. R1 and R2 are connected to R3 and R4, respectively with individual openings. The R3 and R4 compartments are connected to the dome and also to the compartment R5 and R6 (situated between R3 and R4 with dome at the top) via three

Fig. 1 3D geometry of CSF
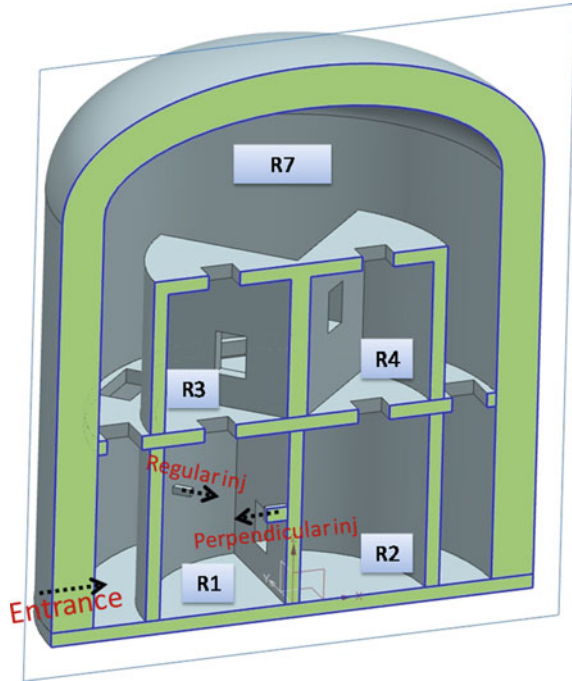
openings each. The annulus behind R3 and R4 are termed as R8 and R9, respectively. The total internal volume of the V1 region of CSF is approximately 150 m^3

In this present study, two cases of helium distribution in CSF are simulated with different CFD codes and their predictions are compared among them. The details of helium injection for the simulated cases are presented in Table 1. The helium is injected in the R1 compartment with regular injection position (elevation 1170 mm) as depicted in Fig. 1. The injector size is 0.2 m × 0.2 m. In both the cases, the total helium injected is equivalent to the homogeneous concentration of 8% v/v of the entire V1 volume. Simulations have been carried out for a sufficiently long time after injection to study the mixing in diffusion phase also. The results of helium concentrations are compared at different locations. Only selected important location data have been presented and compared here. The coordinates of the monitoring points are provided in Table 2.

For inter-code comparison exercise, fast and slow injection cases have been simulated and compared with different codes results. CFD codes used are, i.e. FLUIDYN, CFD-ACE+, FDS (Fire Dynamics Simulator) and OPEN-FOAM by various participants. In all the cases, complete 3D simulations are carried out in the computational domain as shown in Fig. 1. All the participants have used different meshing, time step, numerical models and solution methods as per their understanding of the problem. The details are provided in Tables 3 and 4, respectively.

Fig. 2 **a** Elevation of CSF.
b Sectional view of CSF
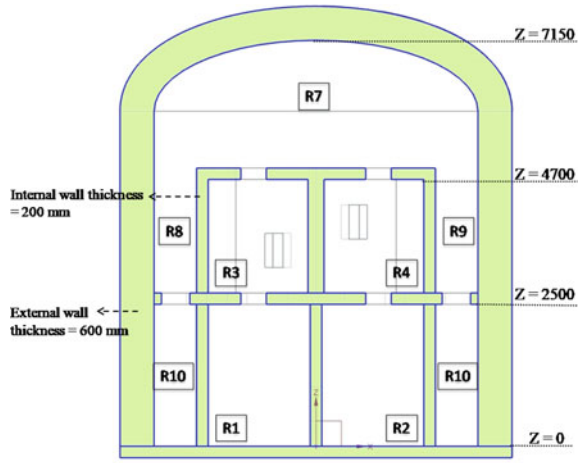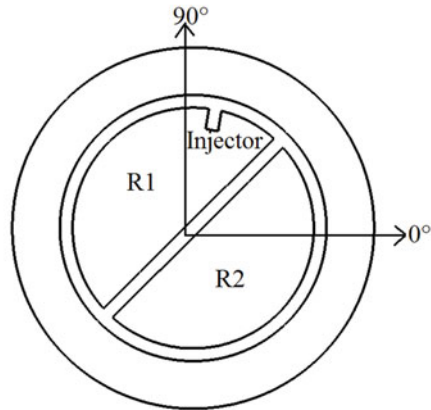
Table 1 Case details

Case	Injection area (m^2)	Injection rate (SLPM)	Injection duration (min)
Fast	0.2 × 0.2	600	20
Slow	0.2 × 0.2	100	120

Helium distribution in a multi-compartment geometry like CSF involves solution of transient mass, momentum and species transport equation in 3D computational domain. It also requires appropriate turbulence model to correctly predict the turbulent diffusion and modelling. As buoyancy plays an important role in diffusion and mixing, capability of individual CFD solver to handle buoyancy driven flow becomes very important in predicting the correct result. In this work, simulations are carried

Table 2 Monitor location

Sl. No.	Location	R (m)	θ	Z (m)
1	R1	0.856	173.3	1.95
2	R2	1.2	315	1.45
3	Dome	0	0	6.9
4	Annulus ground floor	2.46	90	0.950
5	Annulus 1st floor	2.47	337.6	3.4
6	Hor. opening b/w R1 and R3	1.1	135	2.7
7	Vert. opening b/w R4 and R6	0.955	6	3.95

Table 3 Summary of mesh and time step

Codes	Mesh size	Mesh type	Time step (s)
FLUIDYN	7.4 lacs	Unstructured	0.25
CFD_ACE+_1	5 lacs	Unstructured	0.5, 0.01 adaptive
FDS	2.21 lacs	Structured	0.5, 0.05 adaptive
OPEN-FOAM	5.62 lacs	Structured with predominantly hexahedron	Adaptive, courant number < 5
CFD-ACE+_2	8.5 lacs	Unstructured	0.02

Table 4 Summary of numerical models and solution methods

Codes	Discretisation	Turbulence	Schmidt No.
FLUIDYN	2nd order upwind, Euler 1st order implicit	Standard $k–\varepsilon$	0.7
CFD_ACE+_1	1st order upwind, Euler 1st order implicit		0.7
FDS	TVD with explicit	LES	0.5
OPEN-FOAM	1st order upwind, Euler 1st order implicit	Standard $k–\varepsilon$	0.85
CFD-ACE+_2			0.9

out for two helium injection cases as mentioned in Table 1 and results were compared. In all the simulations, it is considered that the air inside the CSF before injection is in quiescent conditions. Hence, all the velocity component and turbulence level are initialised with zero value. Initial pressure and initial temperature are set to 101,325 Pa and 303 K, respectively. Density is calculated from ideal gas law, and mass Diffusivity is considered constant. Appropriate mixing laws has been used for calculating mixture properties available in the respective software.

3   Results and Discussion

In this section, the results of simulation have been presented and compared. Detail understanding is required to model the buoyancy-driven/dominated flow in confined domain such as in present case; the density field is varying significantly across the domain. Moreover, the turbulence modelling plays an important role in capturing the buoyant jet/plume behaviour at the injection location and also across the openings. The refinement of mesh at appropriate location like near the injection and near the openings (especially vertical openings) is also crucial. In the subsequent section, these aspects will be considered while discussing and comparing the simulation results of different CFD tools.

In case of fast injection, higher level of stratification and higher localised concentration is expected as the large amount of helium is being injected in a very short time. On the other hand, slow injection will result in less localised helium concentration peaks as there is sufficient time for mixing due to larger injection time. This two extreme cases are considered here so that an overall view can be presented to the readers. In Fig. 3, the helium concentration at the injection room ceiling has been presented for fast injection case. It can be seen that the results of OPEN-FOAM slightly under predict the peak concentration, FDS under predict in comparison with other three results. This is may be due to the fact that FDS uses very less mesh and more refinement is required in the injection room. Also the turbulent Schmidt number value in FDS case is 0.5 which may result in more turbulent mixing of helium than the other code results. Figure 4 shows the variation of helium concentration at the monitor location for slow injection in injection room. As expected, higher peak concentration is seen in a very short time span, for fast injection in comparison with the slow injection. Here, also the OPEN-FOAM and FDS results under predict the peak concentration. It may be due to the fact that in both these codes, mesh refinement is not carried out near the injection location. The post-injection diffusion phase is captured by all the software almost in similar way except the FLUIDYN code for slow injection. FLUIDYN under predicts the diffusion in slow injection.

Helium concentration at dome centre location (250 mm below the top most point) has been shown in Figs. 5 and 6, respectively, for fast and slow injection. In both the cases, the peak concentration in the dome reaches almost to the same value for all the software. In all the cases, peak concentration is reached at the end of injection phase. In diffusion phase, the helium concentration in the dome area remains almost constant for FDS and OPEN-FOAM predictions. However for others, it decreases slowly over time. Hence, OPEN-FOAM and FDS predict stable stratification while other software does not. In this case, the modelling of species mass diffusion coefficient in gas mixture plays the important role and difference in concentration gradient in diffusion phase may be attributed to this.

In Fig. 7, the helium concentration for fast injection has been shown at ground floor annulus location (R10). It can be seen that for CFD-ACE_2 and OPEN-FOAM, the concentration continue to rise rapidly even after end of injection while in case of FDS and CFD-ACE_1, the peak concentration reaches at the end of injection.

Fig. 3 Variation of Helium Conc. in injection room (R1) for fast injection case
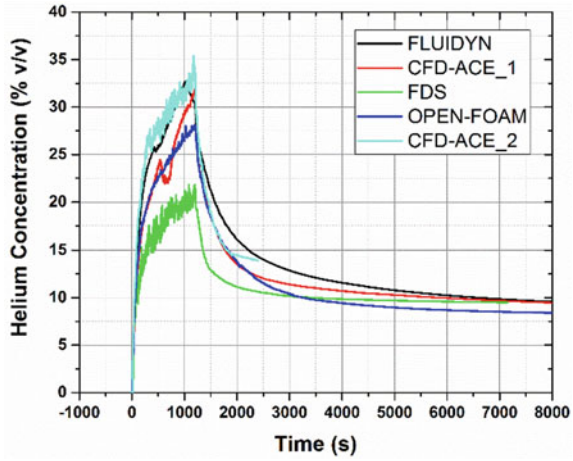
Fig. 4 Variation of Helium Conc. in injection room (R1) for slow injection case
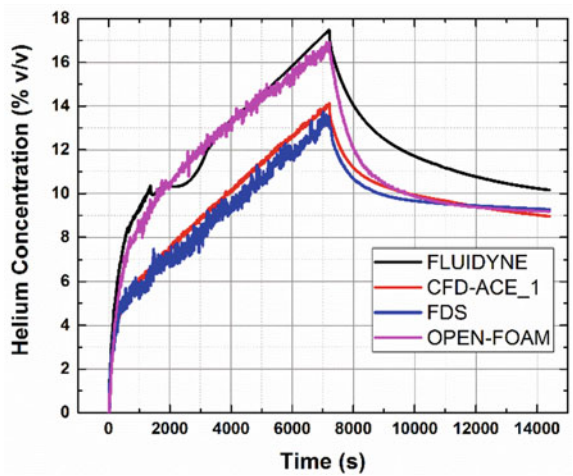
FLUIDYN predicts a totally different profile. It can be concluded here that due to the mesh refinement near the annulus opening, the convective flux across the first and ground floor is better predicted by CFD-ACE_2 and OPEN-FOAM. In case of FLUIDYN, further localised mesh refinement near the annulus opening is required. The same trend is observed in Fig. 8 where the helium concentration at ground floor annulus has been presented for slow injection. On the other hand, all the software predicted similar helium concentration transients at the first floor annulus (R8) as shown in Fig. 9. However, again the FDS result shows very less concentration gradient in the diffusion phase compared to the other simulation results. Comparison of helium concentration data for ground floor annulus and first floor annulus leads

Fig. 5 Helium Conc. in dome for fast injection
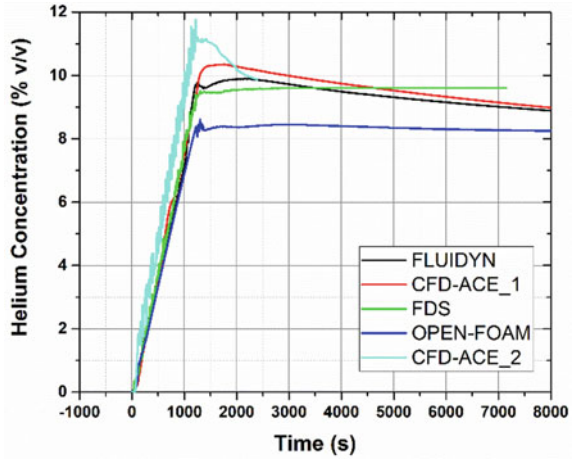
Fig. 6 Helium Conc. in dome for slow injection
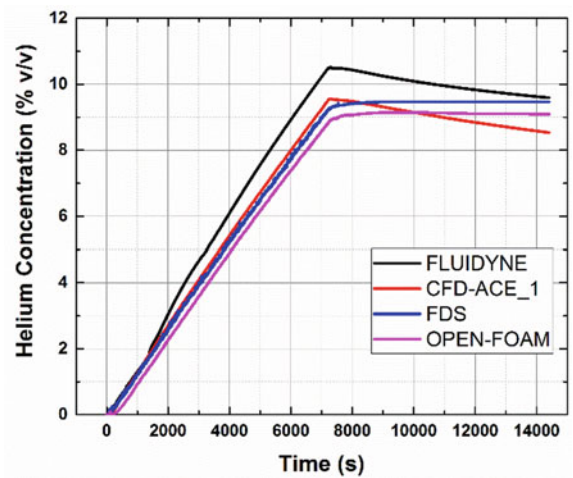
to an important observation that mesh refinement near the openings is very crucial for capturing correct convective flux across the openings.

In Fig. 10, the helium concentration at R2 location has been presented. Helium could reach R2 compartment only when it passes through multiple openings, as opening between R1 and R2 is kept closed in all the simulation. CFD-ACE+_2 and OPEN-FOAM which uses higher mesh refinement near the opening predict a different transient than the simulation with others (CFD-ACE+_1, FDS, FLUIDYN). Here also the helium concentration remains almost same in diffusion phase for FDS simulation and further study in diffusion modelling is required in case of FDS simulations.

To further establish, the importance of capturing accurate convective flux across the openings in multi-compartment buoyancy-driven flow, helium concentration in

Fig. 7 Helium Conc. in ground floor annulus (R10) for fast injection
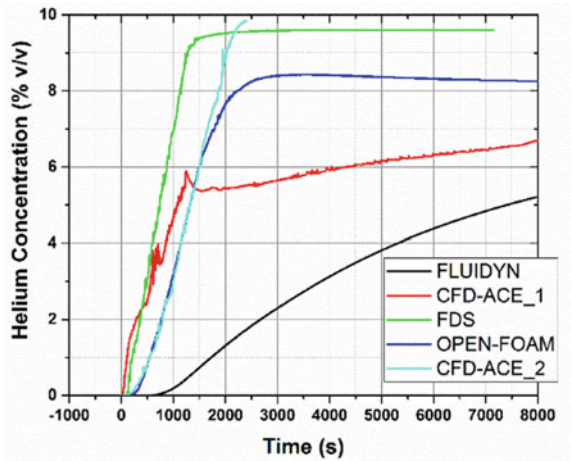
Fig. 8 Helium Conc. in ground floor annulus (R10) for slow injection
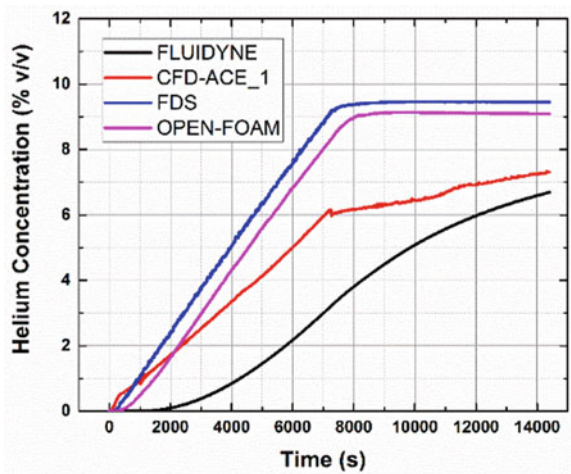
the vertical and horizontal opening have been shown in Fig. 11. It can be clearly seen that in the horizontal opening (opening at injection room ceiling), there is a large fluctuations in helium concentration which manifest the classic buoyant ceiling jet behaviour. However, in vertical wall opening at R4 wall leading to R6 room, no such fluctuations have been found. In the vertical openings, the buoyant flow behaves like a plume instead of buoyant jet as significant amount of momentum is lost while the flow exists through the vertical opening.

In Figs. 12, 13 and 14, contours of helium concentration have been shown for fast injection at 600 s (half way in injection), 1200 s (end of injection) and at 8400 s (long time after injection). It can be seen that the hydrogen concentration varies greatly at any point of time in different compartment of this multi-compartment
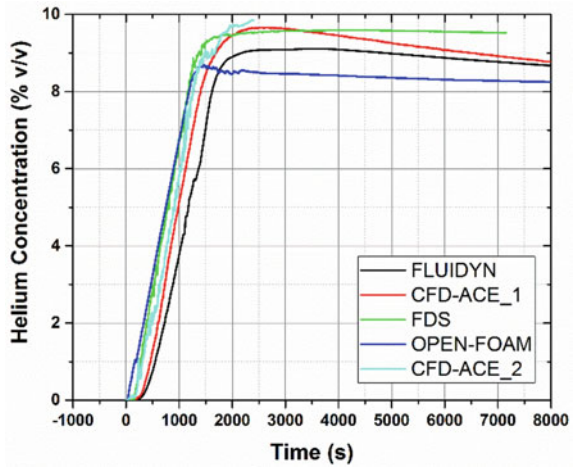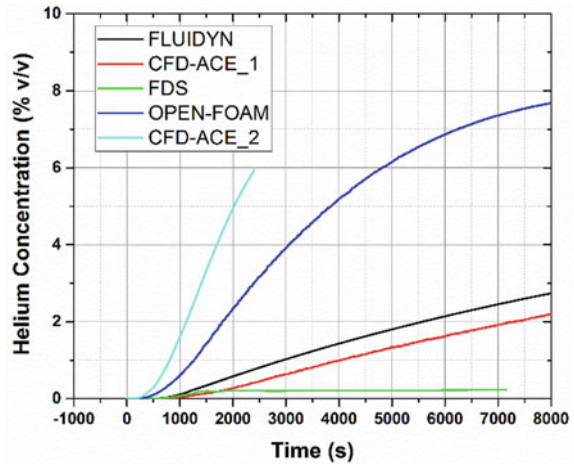
geometry. In post-injection diffusion phase, the helium concentration at different location tends to the homogeneous concentration value of 8% v/v correspondence to the total helium injected. However, it takes a significantly long time to homogenise the helium concentration in the diffusion phase due to multi-compartment nature of this geometry.

It can be concluded here that this kind of lighter gas distribution studies in large multi-compartment scaled down geometry are very much important to gain experience before performing actual reactor calculations. Several important characteristics of lighter gas distribution in multi-compartment geometry are presented and discussed here. Characteristics difference between the simulation results of different software are highlighted and probable cause are also discussed. Based on present

Fig. 11 Helium Conc. in openings for fast injection
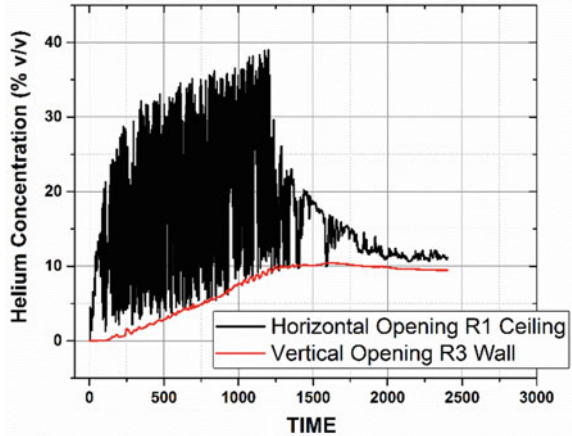
Fig. 12 Contour of Helium Conc. on injection plane at 600 s (Fluidyn fast injection)
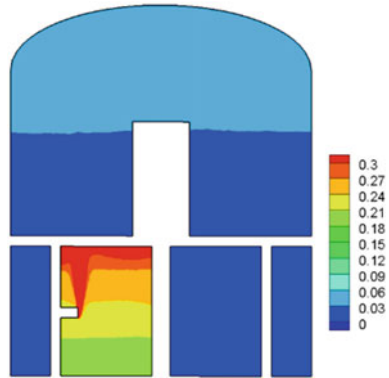
Fig. 13 Contour of Helium Conc. on injection plane at 1200 s (Fluidyn fast injection)
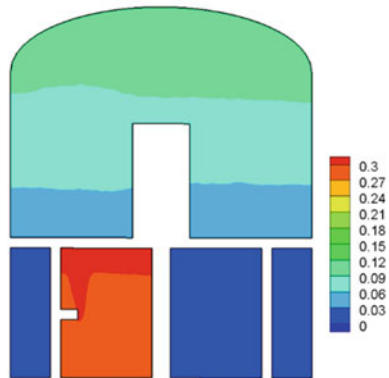
Fig. 14 Contour of Helium
Conc. on injection plane at
8400 s (Fluidyn fast
injection)
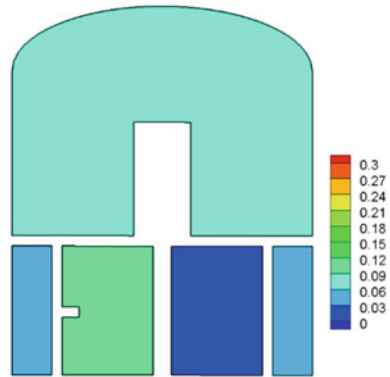
finding, simulations can be carried out again in future to reduce the scatter in predicted
results by different software/participants.

4 Conclusions

CFD inter-code comparison exercise has been carried out under blind bench-
marking exercise. CFD simulations have been carried out with four different codes
(FLUIDYN, CFD-ACE+, FDS and OPEN-FOAM) and compared for CSF experi-
mental test conditions. Code exercise was carried out for fast and slow injection of
helium (simulant of hydrogen) in CSF.

It was found that

(i)   Maximum helium concentration is predicted in injection room by all codes for
      fast and slow injection.
(ii) Fast injection creates more inhomogeneity rapidly compares to the slow one.
(iii) Localised mesh refinement near the buoyant jet and openings, convergence
      criteria, suitable time step are very crucial to achieve an intended mass balance.
(iv) The flow across the ceiling openings depicts classical oscillating ceiling jet
      behaviour.
(v)   Standard k–ε turbulence model, its buoyant variant and LES were found
      adequate to capture the helium distribution in injection room. However, scatter
      among the prediction was observed in annulus and dome regions, which will
      be addresses in future studies.

References

1. Kljenak I, Andreani M (2012) OECD, OECD/SETH-2 Project PANDA and MISTRA Experiments Final Summary Report, Paris, France
2. Studer E, Magnaud JP, Dabbene F, Tkatschenko I (2007) International standard problem on containment thermal hydraulics ISP47: step 1—results from the MISTRA exercise. Nucl Eng Des 237:536–551
3. Sonnenkalb, Poss G (2009) The International Test Programme in the THAI facility and its use for code validation. In: EUROSAFE Forum, Brussels, Belgium
4. Royl P, Rochholz H, Breitung W, Travis JR, Necker G (2000) Analysis of steam and hydrogen distributions with PAR mitigation in NPP containments. Nucl Eng Des 202:231–248
5. Choi YS, Lee UJ, Park GC (2001) Study on local hydrogen behaviours in a sub compartment of the NPP containment. Nucl Eng Des 208:99–116
6. Prabhudharwadkar DM, Iyer KN, Mohan N, Bajaj SS, Markandeya SG (2011) Simulation of hydrogen distribution in an Indian Nuclear Reactor Containment. Nucl Eng Des 241:832–842
7. Visser DC, Houkema M, Siccama NB, Komen EMJ (2012) Validation of a FLUENT CFD model for hydrogen distribution in containment. Nucl Eng Des 245:161–171
8. Visser DC, Siccama NB, Jayaraju ST, Komen EMJ (2014) Application of a CFD based containment model to different large-scale hydrogen distribution experiments. Nucl Eng Des 278:491–502
9. Kudriakov S, Dabbene F, Studer E, Beccantini A, Magnaud JP, Paillère H, Bentaib A, Bleyer A, Malet J, Porcheron E, Carol C (2008) The TONUS CFD code for hydrogen risk analysis: physical models, numerical schemes and validation matrix. Nucl Eng Des 238:551–565
10. Thangamani I, Gera B, Verma V, Chattopadhyay J (2019) Design basis report on CSF. RSD Report, RSD/CSS/016/12/2019

Retrieving Energy from an Inline Hydro Turbine of Irrigation-Dependent Hydropower Plant Under Part Flow Conditions

Maya Kurulekar, Krishnaswamy Kumar, and Shardul Joshi

1   Introduction

enlargethispage36ptIndia is an irrigation-dependent country, around 70% of the population depends on farming. So more water is required and used for the purpose of agriculture. NITI Aayog 2018 has mentioned that India uses 85 per cent of water for agriculture. Considering yield from a particular crop and allied benefits, the production of water-consuming crops has increased creating the water crisis. The unpredictable nature of monsoons, increased urbanization, diminishing groundwater resources and demand of consumers for water supply necessitate sensible use of water resources exclusively for dry regions. Expected growth of Indian population is from 410 million in 2014 to 814 million in 2050, and along with agriculture, demand of power generation is also increasing exponentially. Also there is a still scope to connect many consumers to national grid. The different states of India are facing water crisis. In summer season, most of the areas experiencing water shortage for daily requirement even. In such cases, mandatory releases from impoundment like water supply, irrigation, etc. and power generation need to address simultaneously. Hydropower plant is not only a renewable and green resource but also has higher ramp rate and

Present Address:

M. Kurulekar
Department of Civil Engineering, Vishwakarma Institute of Information Technology and Vishwakarma University, Pune 411048, India
e-mail: maya.kurulekar@vupune.ac.in

K. Kumar (✉)
Central Water and Power Research Station, Pune 411024, India
e-mail: krishnaswamy_kumar@yahoo.co.in

S. Joshi
Department of Civil Engineering, Vishwakarma Institute of Information Technology, Pune 411048, India
e-mail: shardul.joshi@viit.ac.in

advantage of satisfying varying demand unlike to other non-renewable power generating resources. So, there is a need to target existing hydropower plant for renovation, modernization and uprating than suggesting new hydropower plant which is challenging to execute. Existing hydropower plant has various limitations of mandatory discharge requirements towards water supply, irrigation, flora and fauna, capacity restrictions on storing water and power generating units, operational restrictions of turbine under low discharge, type of turbines, etc.; due to which power generation may be taken as secondary objective. So it is now important to target all possible locations to generate electricity in addition to existing plant capacity. Agricultural-dependent hydropower plant restricts the power generation in both cases of high and low irrigation releases due to capacity of hydro turbine and minimum discharge requirements, respectively. So finding the innovative way of generating power after discharging for irrigation requirements was identified as area of interest. This paper presents the study of retrieving energy from an inline hydro turbine of irrigation-dependent hydropower plant under part flow conditions.

2 Literature Review and Objective

Sanchez et al. [1] observed that pump as a turbine can be thought for pressurized and open channel flow. It showed that payback period is less than 2 years with 5–500 kW energy generation. Water wheels were suggested for water treatment plant. Volume of water consumed by irrigation calls for the modernization of irrigation sustainable infrastructure. Author has commented that in case of installing energy recovery system, flow distribution should be known.

Energy converters will help to reduce energy footprints. Energy recovery through irrigation network was suggested by author which helps to reduce the cost of other systems and carbon foot print of crops. Such solution may help to increase the competitiveness in energy production through existing HPP or unsaid solutions may be proposed by innovators. Marillo et al. [2] have suggested energy-saving measures in pipe network for irrigation. Power generation has been suggested in water hammer as well by tapping excessive head. Additional power can satisfy need in failure of power units or non-availability of grid power. Rechargeable battery can be additionally made. Potential site for power units for irrigation network and diversion structure has been suggested by Sari et al. [3]. Modernization practices is an important factor in recovery of energy potential. Quaranta et al. [4] have been suggested the practices based on discharge, head, efficiency and time period. These practices were examined to relate them in additional power generation and installed power. These practices are reliable, secure and green, mentioned the scope for outages.

In flooded events, capacity restriction on power unit has been observed. Thus, excess water handled by drains, jumps and safety structures was suggested as source for hydropower generation. Hydropower potential of spilled water over weir was used by Predin et al. [5] to achieve 40% benefits with steffturbine. Muhammad et al. (2020) have mentioned that there is an urgent need of alternate source of

power generation for developing countries considering insufficient power generation and ineffective distribution. Energy dissipating points can be converted to energy harvesting spots. Diversion structure can be provided with reaction turbines. In this work, hydrokinetic machines were suggested. The review paper is presented by Kishore [6] showing study of small hydropower plant. Suggestions of immovable guide vanes in turbine were given, and also scope for harnessing energy in low head falls of irrigation systems is mentioned. Thakur [7] have studied the effect of providing different types of opening in the gate such as circular, rectangular and elliptical. When the water is subjected to hydrostatic and hydrodynamic forces, how maximum stress and maximum deformation takes place in each shape of opening. Circular opening is found with minimum stress and deformation relative to other shapes. This paper has emphasized on design of circular opening in the irrigation gate to accommodate further modification for power generation.

3   Problem Statement

The untapped energy recovery potential of existing hydropower plant is necessary to address to satisfy the need of increasing population. The water in the impoundment used for irrigation is a function of changes in water availability and thus shows variation in availability of head as well [8]. Hence, in case of agricultural-dependent hydropower plant, it is very important to select the proper type of turbine for power generation even at the low discharge of irrigation. Existing hydropower plant has various limitations: (1) mandatory discharge requirements towards water supply, irrigation, flora and fauna, (2) capacity restrictions on storing water and power generating units, (3) operational restrictions of turbine under low discharge, (4) type of turbines, (5) suction height, (6) efficiency, (7) cavitation, etc. Characteristic curves are being used for selection of hydro turbine. Behaviour of hydro turbine as efficiency versus discharge is used to decide the hydro unit for any application, site condition, head and discharge. Figure 1 shows that Francis, Full Kaplan and Pelton wheel perform better than crossflow and fixed propeller. Whereas in case of reaction turbine, Kaplan is performing better than that of Francis. Improvement in the working of turbine at both high and low discharge conditions has been the area of research since long. Hence, this work addresses the energy recovery solution under part flow in irrigation channel of existing agricultural-dependent hydropower plant.

Typical case of Dhom irrigation-dependent hydro power station of capacity 2 × 1 MW at Vyahali dam at Wai of Satara in Maharashtra is considered.

3.1   Characteristics of Dhom Hydropower Plant

Dhom hydro power station of capacity 2 × 1 MW has been erected at Vyahali dam at Wai of Satara in Maharashtra. Right bank of river Krishna has the reservoir along with
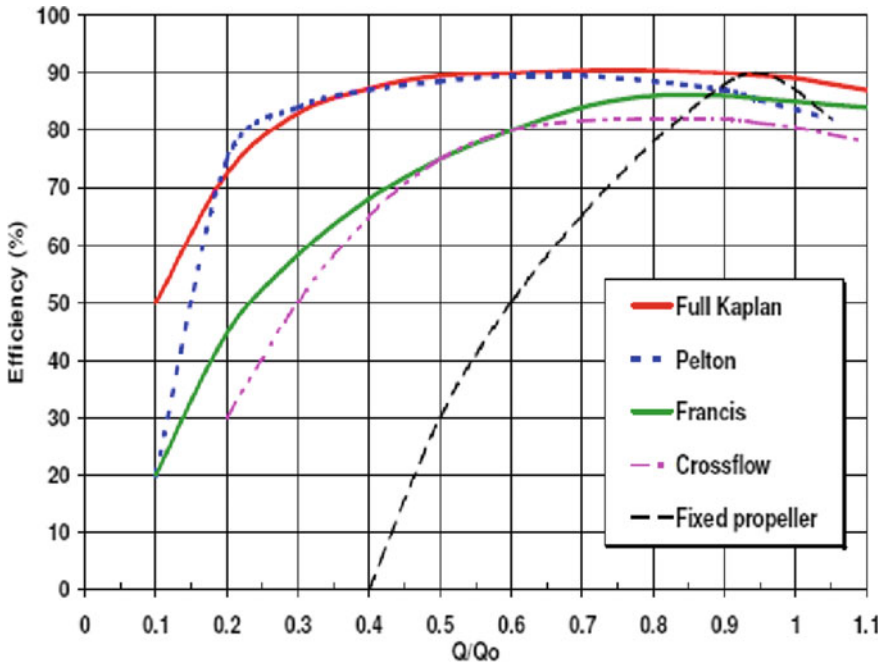
Fig. 1 Behaviour of different turbine under low discharge [13]

two distinct passages; (1) for irrigation discharge (ID) and (2) for energy generation. Left bank canal of Dhom splits from right bank canal on downstream side as shown in Fig. 1.

The important landscapes of power plants are,

Installed capacity	2×1 MW
Annual design energy generation	10.56 MU
Average rainfall	1500–6250 mm
Average inflow of water	423.91 MM^3
Gross dam storage	382 MM^3
Live storage	331 MM^3
Minimum ID level	733.08 m
Design head	18 m
Design discharge	14 m^3/s
Diameter of penstock	2.5 m

3.2 Performance of Hydropower Station

For agricultural-dependent power plant, the power generation is a function of irrigation release. The power generation depends on precipitation of the area as well. The Dhom Dam receives an average rainfall of 970 mm. In case of maximum rainfall of 1725 mm and minimum rainfall of 580 mm, the reservoir has released water towards irrigation without power generation, which was 108.73 MM^3 and 24.78 MM^3, respectively. So, if the untapped irrigation release (loss) is converted into an opportunity of power generation, the capacity factor for the power plant would definitely increase. Table 1 shows the irrigation release in (Million cubic meter) MM^3 and corresponding water loss in (Million units) MU [10]. Layout of Dhom canal system is showing the release of water for irrigation purpose after power generation in Fig. 2.

$$\text{Average irrigation release} = \frac{77.40 * 10^6}{12 * 30 * 24 * 3600} = 2.47 \text{ m}^3/\text{s} \tag{1}$$

$$\text{Power generated} = \frac{1000 * 9.81 * 14 * 2.47}{10^6} = 0.339 \text{ MW} \tag{2}$$

The irrigation water released from one gate is 2.47 m^3/s, and power generated from this water will be 340 kW. Dam has two such irrigation gates, and this implies that total additional power of 680 kW will be generated apart from existing 2 MW.

Table 1 Status of irrigation discharge and water loss

Year	Irrigation discharge MCM (Million Cubic Meter)	Water loss in MU (Million Units)	Year	Irrigation discharge MCM (Million Cubic Meter)	Water loss in MU (Million Units)
91–92	98.543	3.425	2005–06	30.324	0.968
92–93	54.346	1.864	2006–07	57.345	2.156
93–94	58.241	2.432	2007–08	27.85	0.96
94–95	37.421	1.296	2008–09	154.24	4.671
95–96	92.357	3.361	2009–10	29.8367	0.887
96–97	61.437	2.683	2010–11	52.2128	1.165
97–98	165.291	5.373	2011–12	90.8709	3.246
98–99	88.541	3.186	2012–13	58.5124	1.783
99–2000	27.651	0.87	2013–14	161.318	6.973
2000–01	59.563	2.453	2014–15	58.7621	2.286
2001–02	86.461	3.215	2015–16	58.898	0.96
2002–03	163.435	5.427	2016–17	165.391	4.237
2003–04	56.347	2.543	2017–18	46.237	2.538
2004–05	48.475	1.641	Avg	77.40 MCM/year	

DHOM HYDRO POWER STATION
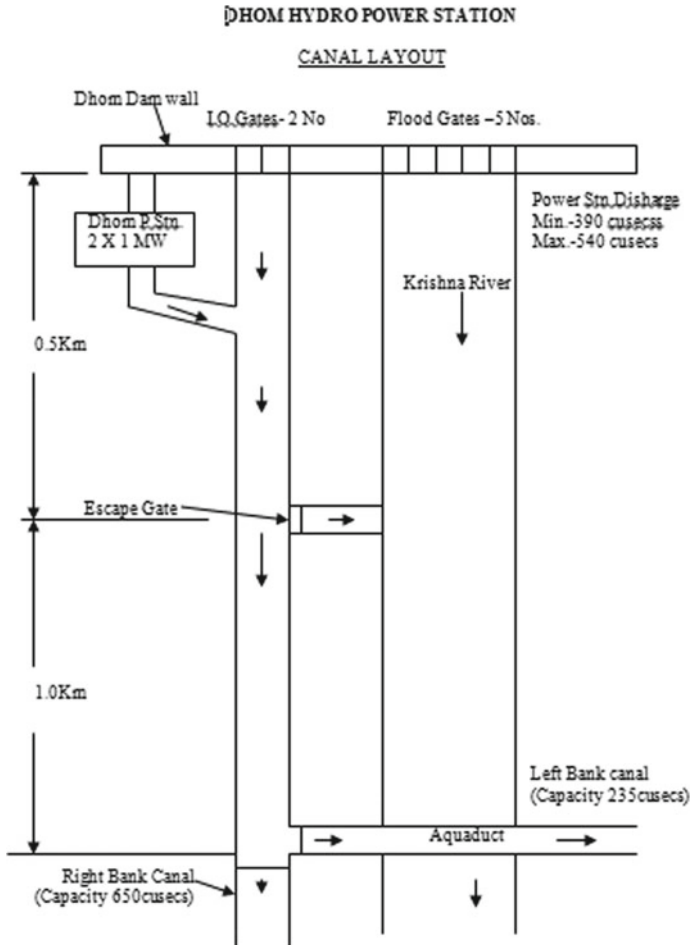
CANAL LAYOUT

Fig. 2 Layout of Dhom canal system

For this additional power generation, modernization of existing irrigation channel is proposed in the form of new irrigation gate along with sliding gate conveying water to the inline axial turbine. The methodology of the proposed modification is explained in next section.

4 Methodology

Flow regulating structures help in managing the flow. The conditions of unsteady flow, varying discharge due to climatic changes demand concrete solution. Therefore, the modified form of irrigation gate along with existing gate opens the door for flow

regulation and additional power generation through pressurized hydraulic system having inline turbine. Also at part flow conditions, the proposed arrangement of hydraulic system would work well.

4.1 Modernization—Irrigation Gate with Sliding Mechanism

The modification in the water regulating structure depends on releases for the irrigation in case of agricultural-dependent hydropower plant. The stochastic nature of releases creates two conditions; high rainfall, low irrigation releases could not generate power due to functional restriction of reaction turbine and low rainfall, high irrigation releases could not generate power due to capacity restrictions. Therefore, to accommodate the discharge during both high and low release, modification is proposed after the existing irrigation gate. Figure 3 shows the modification concept for effective energy recovery, and Fig. 4 shows sliding gate with an opening [10].

$$P_2/\rho g + V_2^2/2g + h_2 = P_3/\rho g + V_3^2/2g + h_4 \tag{3}$$

$$P_2/\rho g = P_3/\rho g - (h_2 - h_4) - \left((V_2^2 - V_3^2)/2g\right) \tag{4}$$

$$P_3/\rho g = P_a/\rho g + h_3 \tag{5}$$

$$P_2/\rho g = P_a/\rho g - (h_2 - h_3 - h_4) - \left((V_2^2 - V_3^2)/2g\right) \tag{6}$$

$$h_2 - h_3 - h_4 = H_s \tag{7}$$
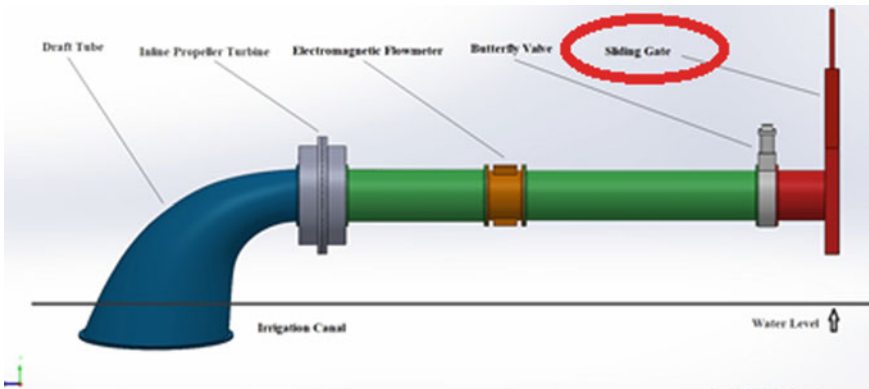
Fig. 3 Modified energy recovery arrangement [10]
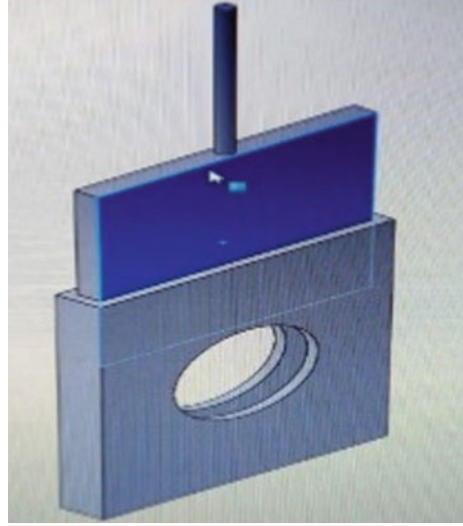
H_s = static suction head

$$P_2/\rho g = P_a/\rho g - \left(H_s + (V_2^2 - V_3^2)/2g\right) \qquad (8)$$

$$((V_2^2 - V_3^2)/2g) = \text{dynamic suction head} \qquad (9)$$

Frictional loss in the draft tube is h_f.

$$P_2/\rho g = P_a/\rho g - \left(H_s + (V_2^2 - V_3^2)/2g + h_f\right) \qquad (10)$$

The pressure head $(P_2/\rho g) < (P_a/\rho g)$, So $P_2 < P_a$ where P_2 is pressure at runner outlet, P_a is pressure at tail race and P_3 is pressure at draft tube end.

Figure 5 shows the draft tube after the inline turbine. The pressure head section 2-2 is less than the atmospheric pressure. So the net head on the turbine with the draft tube increases. The draft tube helps in converting the kinetic energy $V_2^2/2g$ rejected at the outlet of the turbine into useful pressure energy. Therefore, total increase in net head improving the marginal efficiency of the reaction type hydraulic turbine shows the huge saving of water utilized by the hydraulic turbine. In practical conditions, the turbine operated under variable load and the flow causes the change in the tail water level. For this, the gate was suggested after the energy generation from hydro turbine to accommodate even the low discharge. The same hydraulic system can be used after energy recovery from inline turbine in proposed modification [9, 11]. Performance analysis of any turbine for selection or prediction of its behaviour can be studied based on computational fluid dynamics [12].
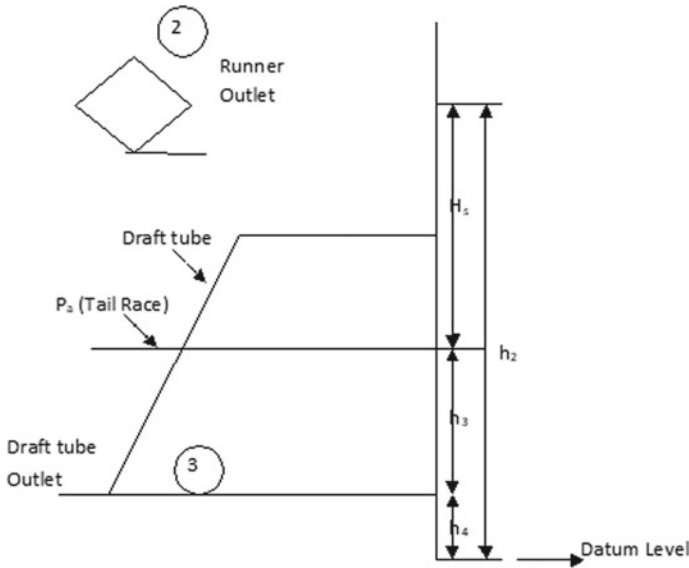
Fig. 5 Draft tube after inline turbine [11]. h_2 = height of runner from datum level. H_s = suction height. V_2, V_3 = velocity of fluid at inlet and outlet section of draft tube. h_4 = height of outlet of the draft tube from datum level. h_3 = height of outlet section of draft tube from tail race. Applying the Bernoulli's theorem between (2) inlet and (3) outlet of the draft tube

5   Results and Discussion

The proposed solution for addressing energy recovery and improving pressure conditions at draft tube head would impact the overall hydraulic system. The stochastic nature of irrigation-de pendent hydropower plant of high rainfall and low irrigation releases restrict the power generation due to operational limitations, and low rainfall and high irrigation releases restrict the power generation due to capacity limitations. Only providing first part of hydraulic system having sliding gate and penstock with inline turbine able to generate the power at high releases. From even the small amount of water, energy recovery is possible by putting gate next to the draft tube improving the pressure conditions [11]. For any irrigation-dependent power plant, canal falls, etc., this approach would stand useful in long term because 1. erecting new hydropower plant is difficult and 2. also environmental concerns demand green solution for satisfying electricity requirements of increasing population along with agricultural need. The net head improvement and related benefit of energy generation have been observed at Kanher Dam of Maharashtra [9]. Experimenting gate immediately after draft tube shows improvement in net head, and corresponding additional energy generation has been observed as 11.491MU per year for 2021–22 against designed power generation of 8MU per year for the Kanher hydropower plant. Table 2 shows the benefits from the modification suggested at Kanher Dam. This indicates that additional 2.5MU of power has been generated. Thus, the similar

Table 2 Units generated after implementation of gate [9]

S. No.	Unit load (MegaWatt)	Discharge cusecs (cubic feet per second)	Generation (MUs)
Generation for the financial year 2018–19			
1	2	262	1.79
2	1.67	237	0.21
3	2.125	270	0.1
4	1.6	257	0.11
5	1.2	249	0.11
Total generation for the year			2.32 MUs
Generation for the financial year 2019–20			
1	1	185	0.234
2	1.1	215	0.288
3	0.85	270	0.0354
4	1.1	170	0.0116
5	2.1	270	0.1272
6	1.4	225	0.0678
7	0.8	185	0.2886
8	0.7	201	0.0474
Total generation for the year			1.10 MUs
Generation for the financial year 2020–21			
1	0.9	190	0.015
2	0.9	200	0.081
3	1.1	215	0.45
Total generation till to date			0.546 MUs

solution can be accommodated at Dhom Dam after modified recovery arrangement, and this gate will serve under part flow conditions even to add in energy recovery.

6　Conclusions

1. Dhom, a typical irrigation-dependent dam having two irrigation gates, releases the discharge around 2.47 m^3/s has potential to generate additional power under stochastic nature of water availability.
2. This release would additionally generate around 0.339 MW of power from irrigation channel if proposed solution is incorporated.
3. This additional power would serve the purpose of local power and auxiliary system of hydropower plant.
4. The gate after the draft tube of inline turbine would help to use the inline reaction turbine even at the part flow conditions.

5. The irrigation requirement is based on conventional approach of farming, rainfall received by the area, condition of soil, modern irrigation practices followed and cropping pattern adopted by the farmer. The demand and supply required for irrigation-dependent hydropower plant is helpful to estimate the additional power generation.
6. Experimenting gate immediately after draft tube shows improvement in net head. Additional energy generation has been observed as 11.491 MU per year for 2021–22 against designed power generation of 8 MU per year for the Kanher hydropower plant. This indicates that additional 2.5 MU (30%) of power has been generated.
7. The solution of additional gate next to the draft tube will be definitely useful at the Dhom Dam under part flow conditions to generate energy in addition to 0.339MW. This suggested modification is the scope for future work.

References

1. Pérez-Sánchez M, Sánchez-Romero FJ, Ramos HM, Amparo L-J (2017) Energy recovery in existing water networks: towards greater sustainability. Water 9:97
2. Morillo JG, Rodríguez Díaz JA, Crespo M, McNabola A (2018) Energy saving measures in pressurized irrigation networks: a new challenge for power generation. Proceedings 2:1440
3. Saria MA, Badruzzamana M, Cherchia C, Swindleb M, Ajamic N, Jacangelo JG (2018) Recent innovations and trends in in-conduit hydropower technologies and their applications in water distribution systems. J Environ Manag 416–428
4. Quaranta E, Aggidis G, Boes RM, Comoglio C, De Michele C, Patro ER, Georgievskaia E, Harby A, Kougiasi I, Muntean S, Pérez-Díaz J, Romero-Gomez P, Rosa-Clot M, Schleiss AJ, Vagnoni E, Wirth M, Pistocchi A (2021) Assessing the energy potential of modernizing the European hydropower fleet. Energy Convers Manag 246:114655
5. Predin A, Fike M, Pezdevšek M, Hren G (2021) Lost energy of water spilled over hydropower dams. Sustainability 13:9119
6. Kishore TS, Patro ER, Harish VSKV, Haghighi AT (2021) A comprehensive study on the recent progress and trends in development of small hydropower projects. Energies 14:2882
7. Thakur A (2018) Design analysis of water control gate for diversion dams. Int J Curr Eng Technol 8(3)
8. Krueger RE (1976) Selecting hydraulic reaction turbines. Office of Design and Construction, Engineering and Research Center
9. Kurulekar M, Kumar K, Joshi S, Kurulekar M (2021) Optimizing the operation of reaction turbines under part flow conditions. IEEE, Bombay
10. Kurulekar M, Kumar K, Joshi SG, Kurulekar M, Kongaonkar P (2022) A system and method for retrieving energy potential through irrigation gate of an agricultural dependent hydro power plant. In: International conference on recent advances in fluid mechanics (ICRAFM-2022)
11. Kumar K (2021) Improved operation of a reaction turbine method for the same. Indian patent, 358415
12. Tiwari G, Kumar J, Prasad V, Patel VK (2020) Utility of CFD in the design and performance analysis of hydraulic turbines—a review. Energy Rep 2410–2429
13. Sinagra M, Sammartano V, Aricò C, Collura A, Tucciarelli T (2014) Cross-flow turbine design for variable operating conditions. Procedia Eng 70:1539–1548

Predicting the Flight Behaviour of a Guided Projectile Through a Six Degrees of Freedom Trajectory Model

Sourabh Khambra, Chandan Kumar, Dipankar Chatterjee, and Bittagopal Mondal

1 Introduction

Mechanically guided projectiles are muzzle loaded weapons used in the battle field in order to aid the combat unit as direct and indirect fire support. Ballistic is the field of mechanics that deals with the launching, flight behaviour and the impact of guided projectile at the target. Exterior ballistic deals with the motion of the projectile in air, i.e. the flight behaviour. Precisely, the modern exterior ballistic may be viewed as the dynamics of the rigid body moving under the influence of gravitation and other forces acting on it. Exterior ballistic encompasses the period when the projectile leaves the muzzle until it impacts on the target. Several methods have so far been proposed to track the trajectory and flight behaviour of the projectile: Out of those, the 6-DOF model initially suggested by Fowler et al. [1] found to be very precise. Later, many researchers updated this model by making it more rigorous [2, 3]. In 6-DOF model, each degrees of freedom (pitch, yaw, rolling) is tied to a coordinate necessary to completely define the position of the body. Once a projectile leaves the muzzle, many forces act on it such as aerodynamic drag, lift, Magnus force and moment, pitch damping force and moment, spin damping moment and rolling moment. 6-DOF model takes into account all of these forces to precisely describe the trajectory of the projectile. Gkritzapis and Panagiotopoulos [4, 5] developed a 6-DOF model for spin stabilized projectiles to follow flight trajectories. This model has a limitation of having multiple coordinate systems whilst performing simulation at larger angle of attack which makes the computation complex. Du [6] performed a standard comparative study for a 6-DOF model and point-mass model, and his work was an approach to study the variation in trajectories of spinning projectiles. Gorecki [7] did some major work in studying 6-DOF for ballistics as he developed a generic

S. Khambra · C. Kumar · D. Chatterjee (✉) · B. Mondal
Academy of Scientific and Innovative Research, Ghaziabad 201002, India
e-mail: d_chatterjee@cmeri.res.in

CSIR—Central Mechanical Engineering Research Institute, Durgapur 713209, India

Table 1 Technical description of 120-mm mortar [8]	120-mm mortar projectile consists of
	• HE, M934
	• Illuminating M930
	• Smoke, M929 rounds

6-DOF model for missile. Major contribution of his work was towards simplifying the dynamics equations used to develop the model. However, the developed 6-DOF models are not capable enough to accurately predict the trajectory of guided projectile system due to its complicated geometry. The present work develops a full-scale 6-DOF model for the projectile flight dynamics analysis in order to predict accurate trajectory of 120-mm mortar (technical specifications depicted in Table 1). HE, M934 round is a fin-stabilized, naturally fragmented round which is intended to launch from muzzle-loaded mortar. 120-mm mortar also consists of illuminating M930 cartridge which is used for illuminating a desired point of area. Smoke, M929 rounds present in mortar cartridge which contains white phosphorous (WP) impregnated felt payload to provide obscuration screening on impact. Mortars are used to provide indirect fire support to the ground artillery. It is semifixed ammunition which uses adjustable increment charges to adjust desired range.

2 Mathematical Flight Models

A 6-DOF model considers projectile to be a rigid body which has three rotations and three translations. Developed code solves pitching and yaw motion of the projectile in terms of the direction cosines of the projectile axis. This gives an advantage when angle of attack is large as it does not require additional coordinate system and it is valid for all angles of attack. We have adopted right-handed rectangular coordinate system where the origin is located at the end of the bore, i.e. muzzle of the gun. The coordinate axis notation is named to 1, 2, 3, whereas (x, y, z) notations are used to denote other entities in the 6-DOF equations. Our defined coordinate system 1–3 plane lies tangent to the earth surface. The mathematical formulation is based on Newton's law of motion, which is rate of change of momentum must be equal to the sum of all the forces and moments applied externally. 6-DOF model includes the equation of motion that is suitable for rockets and as well as conventional projectiles [6] (Fig. 1).

$$m \frac{\mathrm{d}\vec{V}}{\mathrm{d}t} = \sum \vec{F} + m\vec{g} + m\vec{\Lambda} + \text{Rocket Thrust Force} \qquad (1)$$

$$\frac{\mathrm{d}\vec{H}}{\mathrm{d}t} = \sum \vec{M} + \text{Rocket Thrust Moments} \qquad (2)$$

A denotes the total vector of the projectile angular velocity about any perpendicular axis, the second component of angular velocity is *B*, and the total vector of the projectile angular momentum is $\overrightarrow{H}$.

$$A = \left(\vec{x} \times \frac{\mathrm{d}\vec{x}}{\mathrm{d}t} \right),$$

$$B = I_y \left(\vec{x} \times \frac{\mathrm{d}\vec{x}}{\mathrm{d}t} \right), \tag{3}$$

$$\overrightarrow{H} = I_x p \vec{x} + I_y \left(\vec{x} \times \frac{\mathrm{d}\vec{x}}{\mathrm{d}t} \right)$$

Equation (4) describes all the significant aerodynamics forces and moments acting on a rigid symmetric projectile in vector differential form. In addition, the forces and moments due to effect of earth rotation (Coriolis forces), wind, gravity, spin torque, rocket thrust and jet damping are also taken into consideration for developing 6-DOF model.

$$\begin{aligned}
\frac{\mathrm{d}\overrightarrow{V}}{\mathrm{d}t} = &-\frac{\rho v S C_D}{2m} \vec{v} + \frac{\rho S C_{L_\alpha}}{2m} \left[v^2 \vec{x} - (\vec{v} \cdot \vec{x}) \vec{v} \right] \\
&- \frac{\rho S d C_{N_{p\alpha}}}{2m} \left(\frac{I_y}{I_x} \right) (\vec{h} \cdot \vec{x})(\vec{x} \times \vec{v}) \\
&+ \frac{\rho v S d (C_{N_q} + C_{N_\alpha})}{2m} (\vec{h} \times \vec{x}) + \vec{g} \\
&+ \vec{\Lambda} + \frac{gT}{m} \vec{x} + \left(\frac{I_y}{mr_1} - \frac{\dot{m}r_e}{m} \right) (\vec{h} \times \vec{x})
\end{aligned} \tag{4}$$

The vector differential equation of motion describing the spin, pitch and yaw motion about its centre of mass is given in the equation below:

$$\begin{aligned}
\frac{\mathrm{d}\overrightarrow{h}}{\mathrm{d}t} = &\frac{\rho v S d^2 C_{l_p}}{2I_x} (\vec{h} \cdot \vec{x}) \vec{x} + \frac{\rho v^2 S d^2 C_{l_\delta}}{2I_y} \vec{x} \\
&+ \frac{\rho v S d C_{M_\alpha}}{2I_y} (\vec{v} \times \vec{x}) + \frac{\rho S d^2 C_{M_{p\alpha}}}{2I_x} (\vec{h} \cdot \vec{x}) \left[\vec{v} - (\vec{v} \cdot \vec{x}) \vec{x} \right] \\
&+ \frac{\rho v S d^2 (C_{M_q} + C_{M_\alpha})}{2I_y} \left[\vec{h} - (\vec{h} \cdot \vec{x}) \vec{x} \right] \\
&+ \frac{gT_s}{I_y} \vec{x} - \left(\frac{\dot{I}_y - \dot{m}r_e r_t}{I_y} \right) \left[\vec{h} - (\vec{h} \cdot \vec{x}) \vec{x} \right]
\end{aligned} \tag{5}$$

Above equations also take account of jet dumping and rocket thrust. For non-rocket projectiles, the last two terms of the equation will be neglected.

Components of Coriolis effect,
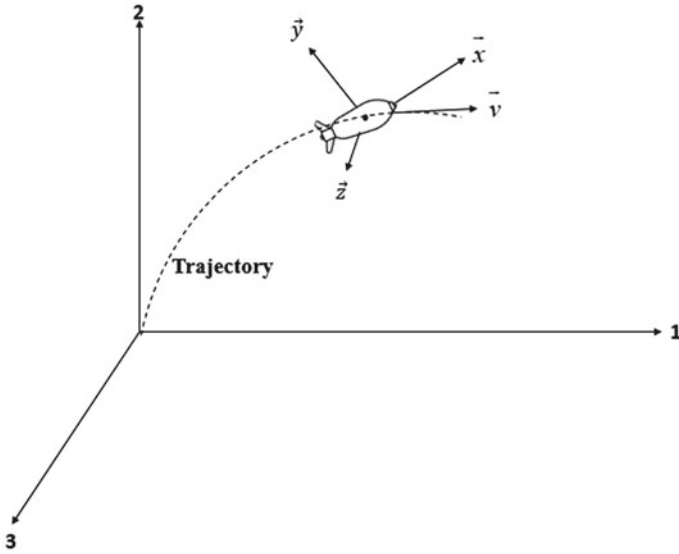
Fig. 1 Coordinate system

$$\vec{\Lambda} = \begin{bmatrix} \Lambda_1 = 2\Omega(-V_2 \cos L \sin AZ - V_3 \sin L) \\ \Lambda_2 = 2\Omega(V_1 \cos L \sin AZ - V_3 \cos L \sin AZ) \\ \Lambda_3 = 2\Omega(V_1 \sin L - V_2 \cos L \cos AZ) \end{bmatrix} \tag{6}$$

Initial Condition of the 6-DOF Trajectory

In order to solve the 6-DOF equations correctly, proper specification of the initial condition is important.

$$\vec{V_0} = \begin{bmatrix} V_{1_0} \\ V_{2_0} \\ V_{3_0} \end{bmatrix} = V_0 \begin{bmatrix} \cos \phi_0 \cos \theta_0 \\ \sin \phi_0 \cos \theta_0 \\ \sin \theta_0 \end{bmatrix} \tag{7}$$

$$\vec{v_0} = \begin{bmatrix} v_{1_0} \\ v_{2_0} \\ v_{3_0} \end{bmatrix} = \begin{bmatrix} V_{1_0} - W_{1_0} \\ V_{2_0} - W_{2_0} \\ V_{3_0} - W_{3_0} \end{bmatrix} \tag{8}$$

Unit vectors of all three initial components are listed below,

$$\vec{x_0} = \begin{bmatrix} x_{1_0} \\ x_{2_0} \\ x_{3_0} \end{bmatrix} = \begin{bmatrix} \cos(\phi_0 + \alpha_0) \cos(\theta_0 + \beta_0) \\ \sin(\phi_0 + \alpha_0) \cos(\theta_0 + \beta_0) \\ sin(\theta_0 + \beta_0) \end{bmatrix} \tag{9}$$

$$\vec{y}_0 = \begin{bmatrix} y_{1_0} \\ y_{2_0} \\ y_{3_0} \end{bmatrix} = -\frac{1}{\sqrt{Q}} \begin{bmatrix} -\cos^2(\theta_0 + \beta_0)\sin(\phi_0 + \alpha_0) \\ \cos(\phi_0 + \alpha_0) \\ \cos^2(\theta_0 + \beta_0)\cos^2(\phi_0 + \alpha_0) \\ +\sin^2(\theta_0 + \beta_0) \\ -\sin(\theta_0 + \beta_0)\cos(\theta_0 + \beta_0) \\ \sin(\phi_0 + \alpha_0) \end{bmatrix} \tag{10}$$

$$\vec{z}_0 = \begin{bmatrix} z_{1_0} \\ z_{2_0} \\ z_{3_0} \end{bmatrix} = -\frac{1}{\sqrt{Q}} \begin{bmatrix} -\sin(\theta_0 + \beta_0) \\ o \\ \cos(\theta_0 + \beta_0)\cos(\phi_0 + \alpha_0) \end{bmatrix} \tag{11}$$

$$Q = \sin^2(\theta_0 + \beta_0) + \cos^2(\theta_0 + \beta_0)\cos^2(\phi_0 + \alpha_0) \tag{12}$$

The vector $\frac{d\vec{x}_0}{dt}$ is given by:

$$d\vec{x}_0/dt = \vec{\omega} \times \vec{x}_0 = (\vec{\omega}_0 \cdot \vec{z}_0)\vec{y}_0 - (\vec{\omega}_0 \cdot \vec{y}_0)\vec{z}_0 \tag{13}$$

where the components of the column vector $\vec{\omega}_0$ are $(\vec{\omega}_1, \vec{\omega}_2, \vec{\omega}_3)$ and $\omega_{z_0} = \vec{\omega}_0 \cdot \vec{z}_0$ and $\omega_{y_0} = \vec{\omega}_0 \cdot \vec{y}_0$, then $d\vec{x}_0/dt$ is given by:

$$\frac{d\vec{x}_0}{dt} = \left[\omega_{z_0}\vec{y}_0 - \omega_{y_0}\vec{z}_0\right] = \begin{bmatrix} \dot{x}_{1_0} \\ \dot{x}_{2_0} \\ \dot{x}_{3_0} \end{bmatrix} = \begin{bmatrix} \omega_{z_0} y_{1_0} - \omega_{y_0} z_{1_0} \\ \omega_{z_0} y_{2_0} - \omega_{y_0} z_{2_0} \\ \omega_{z_0} y_{3_0} - \omega_{y_0} z_{3_0} \end{bmatrix} \tag{14}$$

The initial velocity, i.e. velocity at muzzle of h-vector, is denoted by $\vec{h}_0$ and is described in equation below:

$$\vec{h}_0 = \begin{bmatrix} h_{1_0} \\ h_{2_0} \\ h_{3_0} \end{bmatrix} = \begin{bmatrix} \frac{I_x p_0}{I_y} x_{1_0} + x_{2_0}\dot{x}_{3_0} - x_{3_0}\dot{x}_{2_0} \\ \frac{I_x p_0}{I_y} x_{2_0} + x_{1_0}\dot{x}_{3_0} - x_{3_0}\dot{x}_{1_0} \\ \frac{I_x p_0}{I_y} x_{3_0} + x_{1_0}\dot{x}_{2_0} - x_{2_0}\dot{x}_{1_0} \end{bmatrix} \tag{15}$$

where $p_0 = \frac{2\pi V_0}{nd}$, n and d are the axial spin rate and rifling twist rate at the gun muzzle, respectively.

$\frac{d\vec{x}}{dt}$ can also be written as:

$$\frac{d\vec{x}}{dt} = \left(\vec{h} \times \vec{x}\right) = \begin{bmatrix} \dot{x}_1 \\ \dot{x}_2 \\ \dot{x}_3 \end{bmatrix} = \begin{bmatrix} h_2 x_3 - h_3 x_2 \\ h_3 x_1 - h_1 x_3 \\ h_1 x_2 - h_2 x_1 \end{bmatrix} \tag{16}$$

Point-Mass Model

A numerical code for the point-mass model is also developed in order to understand and compare the impact of the forces considered in the 6-DOF model. In the point-mass model, the projectile mass is assumed to be concentrated at a point which reduces the complexity of the problem. Uniform air drag is considered over the surface area of the projectile. Coriolis's acceleration is neglected in the model. The equation of motion in consideration of the air resistance is solved to get the desired trajectory of the projectile. The total drag coefficient (F_D) acting on the projectile is given as,

$$F_D = \rho S C_d / 2m \tag{17}$$

Acceleration components are given by:

$$a_x = -\left(\frac{F_D}{m}\right) v v_x, a_y = -g - \left(\frac{F_D}{m}\right) v v_y \tag{18}$$

v_x and v_y are the velocity components, given as

$$v_x = v_{xi} + a_x \Delta t$$
$$v_y = v_{yi} + a_y \Delta t \tag{19}$$

x_f and y_f represent the position of the projectile.

$$x_f = x_i + v_x \Delta t + \frac{1}{2} a_x (\Delta t)^2$$
$$y_f = y_i + v_y \Delta t + \frac{1}{2} a_y (\Delta t)^2 \tag{20}$$

3 Computational Simulation

The computer code for the point-mass model and the 6-DOF flight dynamic model are developed by using Fortran 90 programming language. Developed 6-DOF code consists of several coupled differential equations (1–16) which are solved simultaneously. The experimental aerodynamic coefficients used in this model are given in Tables 3a, 3b, 3c. However, Eqs. (17)–(20) are used to solve the point-mass model. Technical data and physical characteristics of 120-mm mortar are listed in Table 2.

Table 2 Physical data of 120-mm mortar [8]

Reference diameter	119.56 mm
Projectile total length	704.9 mm
Projectile weight	13.585 kg
Axial moment of inertia	0.02355 kg m^3
Transverse moment of inertia	0.23187 kg m^3
Centre of gravity	42.29 cm from the base

Table 3a Trajectory parameters of the projectile with variable coefficients [8]

Mach No.	$C_{D_{\vartheta 2}}$	Mach No.	$C_{D_{\vartheta 2}}$
0	0.119	0	2.32
0.7	0.119	0.4	2.44
0.85	0.120	0.6	2.66
0.87	0.122	0.7	2.87
0.90	0.126	0.75	3.01
0.93	0.148	0.85	3.55
0.95	0.182	0.90	4.03
–	–	0.95	5.20

Table 3b Trajectory parameters of the projectile with variable coefficients [8]

Mach No.	$C_{L_{\alpha 0}}$	Mach No.	$C_{L_{\alpha 2}}$	Mach No.	$C_{M_{\alpha 0}}$	Mach No.	$C_{M_{\alpha 2}}$
0	1.75	0	14.8	0	− 0.2	0	− 15.1
0.6	1.95	0.5	14.8	0.4	− 1.02	0.45	− 15.1
0.8	2.02	0.6	4.5	0.6	− 1.62	0.6	− 12.7
0.9	2.06	0.63	1.4	0.8	− 2.41	0.7	− 8.5
0.95	2.08	0.7	0.4	0.9	− 2.72	0.75	− 4.5
–	–	0.8	8.8	0.92	− 2.75	0.8	1.5
–	–	0.9	28.3	0.95	− 2.71	0.85	13.9
–	–	0.95	40	–	–	0.90	30.2
–	–	–	–	–	–	0.95	59.9

Table 3c Trajectory parameters of the projectile with variable coefficients [8]

Mach No.	$(C_{M_q} + C_{M_\alpha})_2$	Mach No.	$(C_{M_q} + C_{M_\alpha})_2$
0	− 22.0	0	+ 48
0.8	− 21.1	0.5	− 46
0.85	− 21.9	0.6	− 86
0.9	− 24.2	0.7	− 144
0.92	− 26.8	0.8	− 259
0.95	− 31.5	0.85	− 357
–	–	0.9	− 468
–	–	0.95	− 745

4 Results and Discussion

The present study aims to investigate the flight trajectories of a guided projectile system (120-mm mortar) using a 6-DOF model. Five different velocities in the range of $V_M = 102$–318 m/s are considered for this study. The minimum and maximum velocities are corresponding to increment charge zero and increment charge 4 [8]. Three other intermediate velocities are taken into account in order to get copious data for a detailed understanding of the trajectories. The flight data and trajectories at three different initial pitch angles (which are also known as quadrant elevation angles, QE $= 45°$, 55° and 65°) for the above-mentioned velocity range are evaluated.

For the verification of simulation results, the range and altitude of 120-mm mortar at velocities 102 m/s and 318 m/s for the quadrant elevation angle are evaluated and compared with the results of McCoy's atmospheric flight model (as shown in Fig. 2). It is observed that the present code shows strong agreement with McCoy's flight dynamics model [8]. The range achieved for $V_M = 102$ m/s at QE $= 45°$ has a difference of 11.8 m between the developed code and McCoy's data, whilst the altitude from the developed code is observed 9.81 m higher than McCoy's data. For $V_M = 318$ m/s, the trend of the trajectory is similar and the difference between range and altitude with McCoy's data is 16.61 m and 7.48 m, respectively. Figures 3, 4, 5, 6 and 7 show the range and altitude achieved during the flight of the projectile at different muzzle velocities and various quadrant elevation angles. It is evident from the figures that the range and height achieved during the flight are the functions of muzzle velocity and QE angle. If muzzle velocity is constant, altitude increases with increasing QE, whereas the range decreases. At the constant QE, the range and the altitude increase with increasing muzzle velocity. Table 4 shows the range chart of 6-DOF model and also compares with the McCoy's Data [8]. At low muzzle velocity, the difference between present results and the McCoy's data is small, whereas difference is increasing with velocity (maximum difference within 5%). The 6-DOF model considers the various forces acting on the projectile during flight; therefore, these results can help in achieving the target accurately and also designing a guided projectile system to perform specific missions.

To understand the impact of all the aerodynamic forces acting on the projectile, a point-mass model is also developed and compared with the 6-DOF model. In the point-mass model, uniform air drag with $C_d = 0.25$ [6] is considered and the flight trajectories are obtained at muzzle velocities of 102 and 318 m/s. Figure 8 demonstrates the flight trajectory of the projectile using the point-mass model where only gravity and air resistance are considered as the external forces. Table 5 compares the range chart for the projectile, evaluated using the point-mass model and the 6-DOF model. The maximum height and the maximum range are obtained at muzzle velocities 102 m/s and 318 m/s at various QE.

A significant difference can be seen in the results of the point-mass model and the 6-DOF model. The maximum range achieved during flight is higher in the point-mass model, whereas the maximum altitude obtained in 6-DOF is higher for respective muzzle velocity and QE. The difference in results is due to the influence of lift and
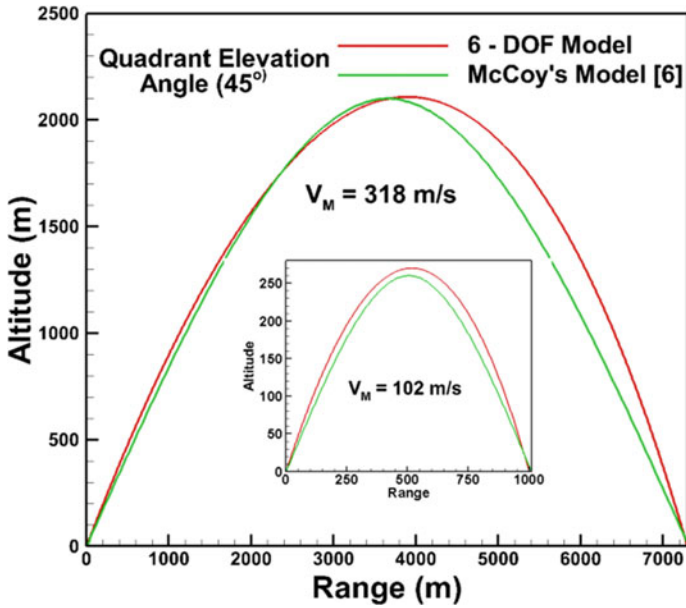
Fig. 2 Altitude and range of the projectile at $V_M = 102$ m/s and 318 m/s at QE $= 45°$
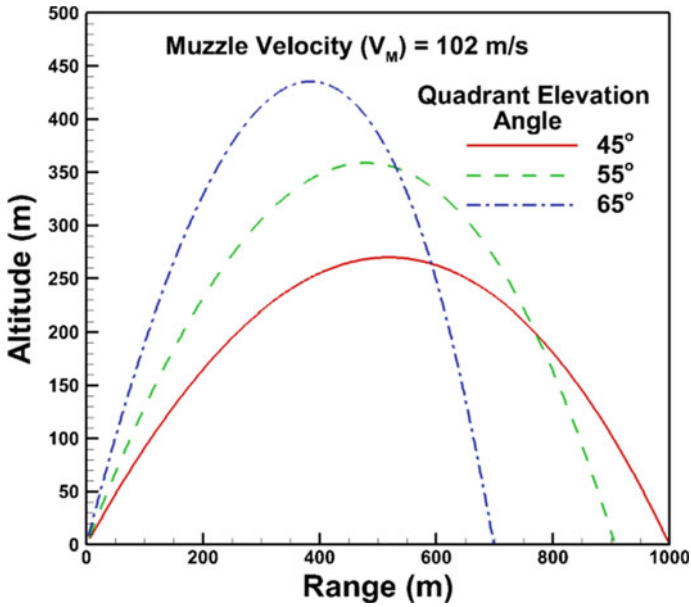
Fig. 3 Altitude and range of projectile for $V_M = 102$ m/s at various QE
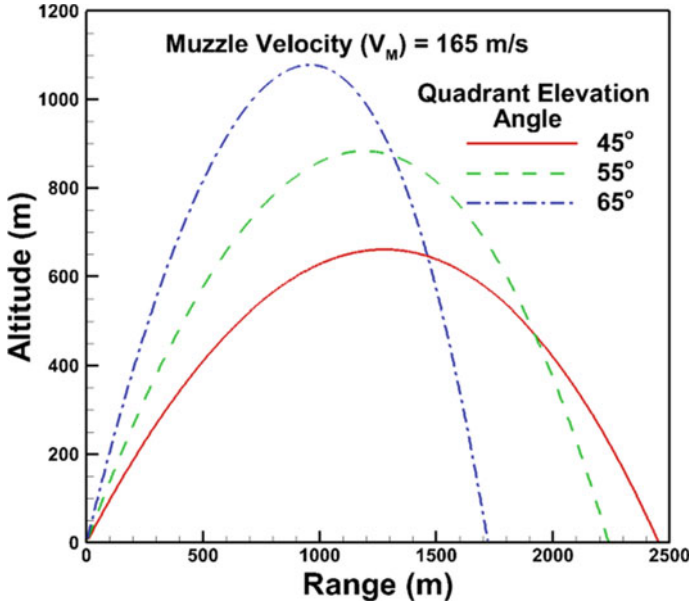
Fig. 4 Altitude and range of projectile for $V_M = 165$ m/s at various QE
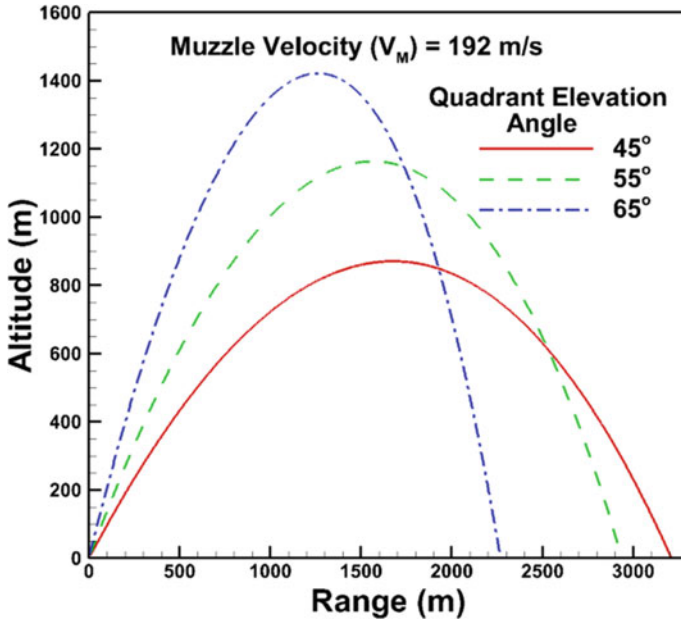
Fig. 5 Altitude and range of projectile for $V_M = 192$ m/s at various QE
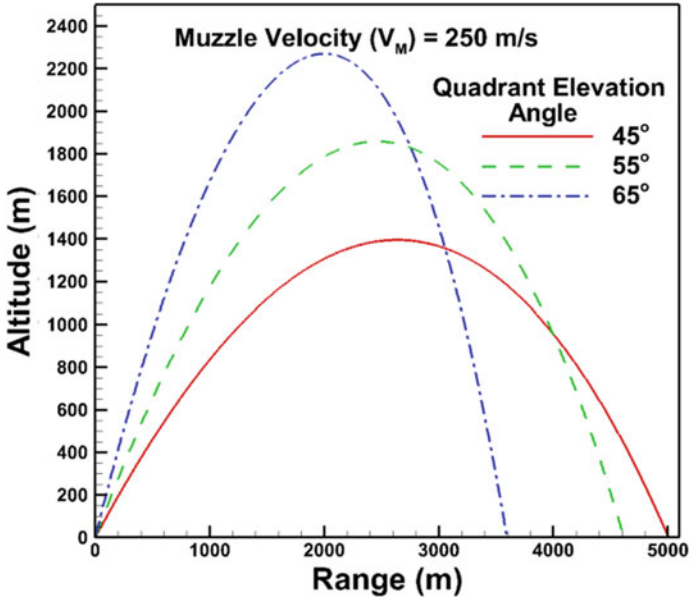
Fig. 6 Altitude and range of projectile for $V_M = 250$ m/s at various QE
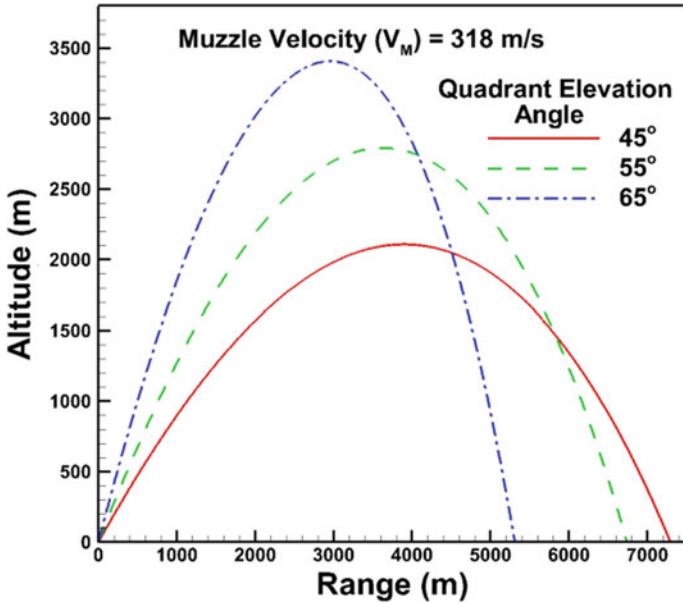
Fig. 7 Altitude and range of projectile for $V_M = 318$ m/s at various QE

Table 4 Range chart of 6-DOF

Developed 6-DOF code				McCoy's data [8]	
V_M (m/s)	QE (deg)	R (m)	H (m)	R (m)	H (m)
102	45	998.21	269.812	1010	260
	55	904.83	358.75	–	–
	65	698.30	435.43	770	420
165	45	2451.81	660.85	–	–
	55	2237.65	883.35	–	–
	65	1720.69	1077.87	–	–
192	45	3209.10	870.52	–	–
	55	2939.03	1163.40	–	–
	65	2267.60	1421.52	–	–
250	45	5007.36	1395.21	–	–
	55	4615.87	1857.74	–	–
	65	3593.53	2270.18	–	–
318	45	7298.39	2107.48	7315	2100
	55	6743.78	2791.50	–	–
	65	5310.76	3406.28	5570	3380
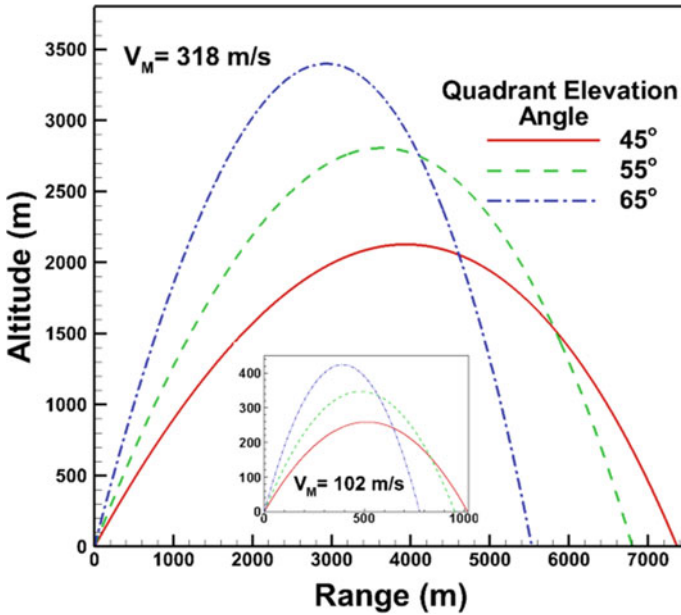
Fig. 8 Altitude and range for $V_M = 102$ m/s and 318 m/s at various QE using point-mass model

Table 5 Range chart from the point-mass model

V_M (m/s)	QE (°)	Point-mass model		6-DOF model	
		R (m)	H (m)	R (m)	H (m)
102	45	1016	259	998.21	269.812
	55	952.36	346.78	904.83	358.75
	65	776.31	423.94	698.30	435.43
318	45	7371	212.6.7	7298.39	2107.48
	55	6804.3	2804.7	6743.78	2791.50
	65	5534	3398.8	5310.76	3406.28

normal forces along with overturning moments and other physical factors which influence the trajectory of a projectile in a real course of action. Lift and normal forces deviate the projectile from its desired path, and due to this, the 6-DOF model tends to achieve a higher altitude and lesser range with respect to the point-mass model.

Therefore, the developed 6-DOF model is proven to be a robust and accurate model for predicting flight trajectories as compared to the point-mass model. This model also has a potential to predict the range and altitude of other guided projectiles by changing the physical parameters.

5 Conclusions

The developed six degrees of freedom (6-DOF) flight dynamics model predicts the trajectories accurately. Several aerodynamic considerations are taken into account like Mach number, total angle of attack, variable and constant aerodynamic coefficients, etc. The flight trajectory is evaluated for the range of velocity 102–318 m/s at the range of quadrant elevation angle 45–65°. Initially, the results are compared, and it is found that the computational results are in good agreement with the available technical data of flight dynamics model. The developed 6-DOF model will help to predict the flight trajectories of the guided projectile system with precise accuracy. The results associated with 120-mm mortar are encouraging to predict the range and altitude of the projectile, and this model can be applied for other guided projectiles for future study.

Nomenclature

$\vec{\Lambda}$	Coriolis acceleration due to earth rotation (rad/s)
C_d	Coefficient of drag
$\sum \vec{F}$	Vector sum of all aerodynamic forces (N)
$\vec{g}$	Acceleration due to gravity (m/s)
$\vec{H}$	Total vector angular momentum of the projectile (kg m^2/s)
$\dot{I}_y$	Rate of change of the rocket projectile's transverse moment of inertia (kg m^3)
m	Mass of projectile (kg)
$\dot{m}$	Rate of change of the rocket projectile's mass (kg/s)
$\sum \vec{M}$	Vector sum of all aerodynamic moments (Nm)
r_t	Distance from projectile centre of mass to the throat of the rocket nozzle (positive if throat is *aft* of the centre of mass) (m)
S	Impact area of the projectile (m^2)
t	Time (s)
T	Rocket thrust force (N)
T_s	Rolling moment due to rocket spin torque (Nm)
$\vec{V}$	Velocity vector with respect to the ground fixed coordinate axes (m/s)
$\vec{V_0}$	Muzzle velocity vector (m/s)
V_0	$\sqrt{V_{1_0}^2 + V_{2_0}^2 + V_{3_0}^2}$ (M/s)
$\vec{v_0}$	Initial velocity vector with respect to air $\left[v_0 = \vec{V}_0 - \vec{W}_0 \right]$ (m/s)
V_M	Muzzle velocity (m/s)
ϕ_0	Vertical angle of departure, positive upward (°)
θ_0	Horizontal angle of departure relative to the 1–2 plane, positive to the right when looking downrange (°)
α_0	Initial pitch angle at the gun muzzle (°)
β_0	Initial yaw angle at the gun muzzle (°)
ρ	Density of air (kg/m^3)

References

1. Fowler R, Gallop E, Lock C, Richmond H (1920) The aerodynamics of spinning shell. Philos Trans Roy Soc Lond Ser A: Math Phys Sci 221:199–205
2. Cooper G (2001) Influence of yaw cards on the yaw growth of spin stabilized projectiles. J Aircr 38(2):266–270
3. Guidos B, Cooper G (2000) Closed form solution of finned projectile motion subjected to a simple in-flight lateral impulse. AIAA Paper 2000-0767
4. Gkritzapis D, Panagiotopoulos E (2009) Accurate computation of the trajectory of the spin and fin-stabilized projectiles. Int J Math Comput Simul 3(2):73–80
5. Gkritzapis D, Panagiotopoulos E, Margaris D, Papanikas D (2007) A six degree of freedom trajectory analysis of spin-stabilized projectiles. AIP Conf Proc 963:1187

6. Du A (2021) A comparative study between 6 degree-of-freedom trajectory model and modified point mass trajectory model of spinning projectiles. PhD Dissertations and Master's Theses, p 594
7. Gorecki R (2003) A baseline 6 degree of freedom (DOF) mathematical model of a generic missile. DSTO Systems Sciences Laboratory, Australia
8. McCoy R (1999) Modern exterior ballistics. Schiffer, Attlen, PA

IoT-Based Smart Vaporizer

Samyak Jain, Minal Gaydhane, Rutuj Saraf, Omkar Koli, Gayatri Mhaske, and Manisha Mhetre

1 Introduction

Whilst not particularly novel, a smart vaporizer is similar to a standard vape that is already on the market. The key distinction is that we have given it some unique characteristics, such as the ability to detect the water level in the container using water level sensors [1]. Additionally, we have the ability to regulate the water's temperature so that we may regulate the temperature of the steam [2]. Therefore, it will be convenient for all types of users, including young and old. A vaporizer warms water and releases steam into the atmosphere. It uses internal heating technology to boil the water before dispersing it as steam and warm mist into the air. It is made to lessen pain, including skin dryness and nasal or throat dryness. Additionally, this gadget might improve breathing difficulties and reduce nasal congestion. In essence, a vaporizer is a boiler that does not produce pressure. Liquid LPG enters the vaporizer and leaves as gas. Vaporizers are a crucial part of many LPG and propane systems and can be used for a wide range of purposes. Vaporizers do not create more pressure; instead, they guard against pressure loss and icing caused by refrigeration. Humans and animals alike can contract illnesses from coronaviruses.

First, collect all the required components. After collecting the components, code is written in Arduino IDE and connections are performed and implemented as per code written in Arduino IDE. In this, we have used Water Level Depth Detection Sensor Module (EC-3190) and Wire Temperature Sensor (DS18B200) [3]. After compiling the code, code is dumped into Arduino UNO R3 board. Then, the required system is ready.

The main motto to use these sensors here is that by using water level sensor, it will help in detecting where the tank of vaporizer is full or not. On the other hand, the temperature sensor will detect the temperature of the water.

S. Jain · M. Gaydhane · R. Saraf · O. Koli · G. Mhaske · M. Mhetre (✉)
Department of Instrumentation and Control Engineering, VIT Pune, Pune 411037, India
e-mail: manisha.mhetre@vit.edu

So, in this model, we are using Arduino; temperature level sensor, water level sensor, and relay are connected to Arduino. As a result, temperature level of water can be controlled automatically: Heater system can be operated by the relay, and if the water level gets low, then we get an indication according to that and we can pour the required water to the container. So, it will continue its working up to our necessity.

2 Literature Review

Yunus Tjandi proposed a system where they are able to control rice cookers, electronic TVs, lights, fans, and much more using relay logic and Arduino [4]. From this, we are able to understand how we can use relay board and logic with Arduino and adapt to our system. Anil Bezawada proposed another system to have water level indication and control using Arduino, relay boards, and ultrasonic sensors [3]. Sabar Sabar also proposed another system to detect the water level in a given container using the water level sensor and Arduino [1]. Rifqi Firmansyah proposed a system to measure temperature using PI controller. They have used wire temperature sensor DS18B20, and Nodemcu (ESP8266) [2].

3 Materials and Methods

3.1 Block Diagram

See Fig. 1.
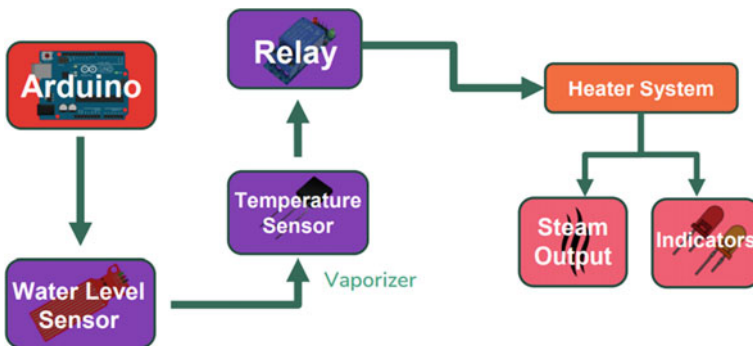
Fig. 1 Block diagram
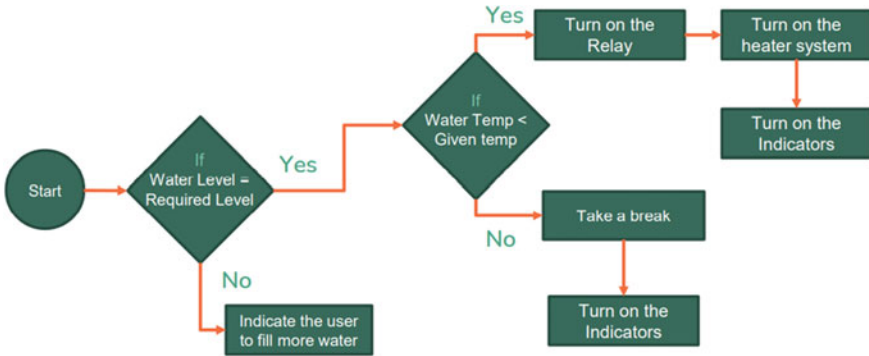
Fig. 2 Process flow

3.2 Process Flow

See Fig. 2.

This is the whole process flow of our system. First, the water level will be checked. And if the water level is the equal to the set point that we have set, then it will go to the further process, otherwise it will ask the user to fill more water. Once that is done, then it will check the water temperature with the help of the wire temperature sensor (its water proof). According to the temperature, it will again compare with the set point. In our case, we have set that set point to 50 °C. If the water temperature is below the set point, then it will trigger the relay to turn on the heater system [4]. And if the temperature is above the set point, then it will indicate the user to take a break (Fig. 3).

The heater system is made by using two copper strips kept together with a small gap in between. When current is passed to the system, the copper strips get heated which in turn heat the surrounding water as well. The current given to the copper strips is controlled by the relay. So, only when the relay receives a signal from the Arduino board, then only it will turn on the supply for the current to the copper strips.

3.3 Components

Arduino UNO R3—ATMEGA 328 PIN IC. It has 14 digital input/output pins. It has 6 analogue input pins. The operating voltage of IC is 5 V [4] (Fig. 4).

Relay—It works on the principle of an electromagnetic attraction. The supply voltage of the relay module is 3.75–6 V. They have three high voltage terminals and VCC and ground that connect to the device you want to control which are as follows (Fig. 5):

COM common terminal
NC normally closed

Fig. 3 Heater system
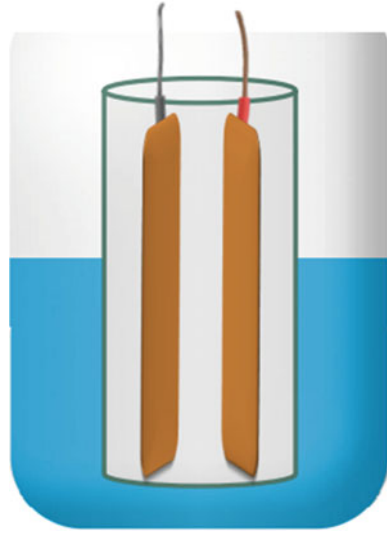
Fig. 4 Arduino UNO R3

NO   normally opened
VCC   power
GND   ground.

Water Level Depth Detection Sensor Module (EC-3190):

The working voltage of this sensor is 3–5 dc volt. This sensor is an analogue-type sensor. The detection area of this sensor is 40 mm * 60 mm [1] (Fig. 6).

Wire Temperature Sensor (DS18B200):

The supply voltage of this sensor is 3–5.5 V. The temperature range is − 55 to 125 °C. Detection area of this sensor is 40 mm * 60 mm (Fig. 7).

Fig. 5 Relay
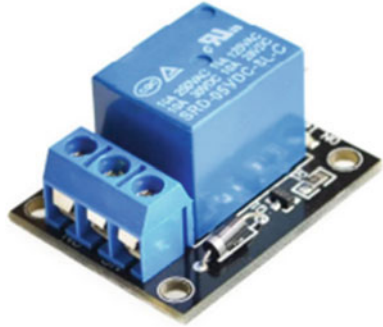
Fig. 6 Water level sensor

Fig. 7 Wire temperature sensor (DS18B200)
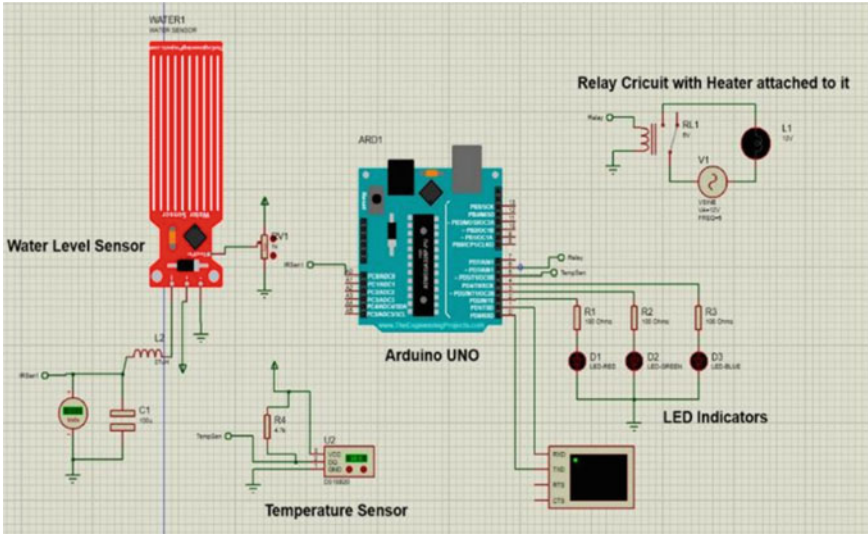
Fig. 8 Simulating circuit in proteus

4 Results and Discussion

4.1 Simulation of Circuit

In this circuit, Arduino UNO IC is used. It has 14 digital input/output pins [3]. It has 6 analogue input pins. Pin no 2 of Arduino IC is connected to red LED, pin no 3 of Arduino IC is connected to green LED, and pin no 4 of Arduino IC is connected to blue LED. Then, there is a temperature sensor which is connected to pin no 5 of Arduino IC. In this temperature sensor, GND pin is connected to the ground, the VCC pin is connected to power, and pin no 2 is connected to Arduino. The temperature sensor is used for measuring the temperature of the water. Pin no 6 of Arduino IC is connected to relay module: There is a relay circuit with heater system, and relay circuit is used to on and off the heater [3]. Then, on the left side, there is a water level sensor, pin no 3 is connected to the ground, pin no 2 is connected to VCC, and the first pin is connected to A0 which is the analogue pin of Arduino IC. A water level sensor is used to check the level of water in that container. If water is filled in the container, the green LED will be on and the red LED is for indicating the user to take a breaks (Fig. 8).

4.2 Prototyping the Circuit

See Figs. 9 and 10.
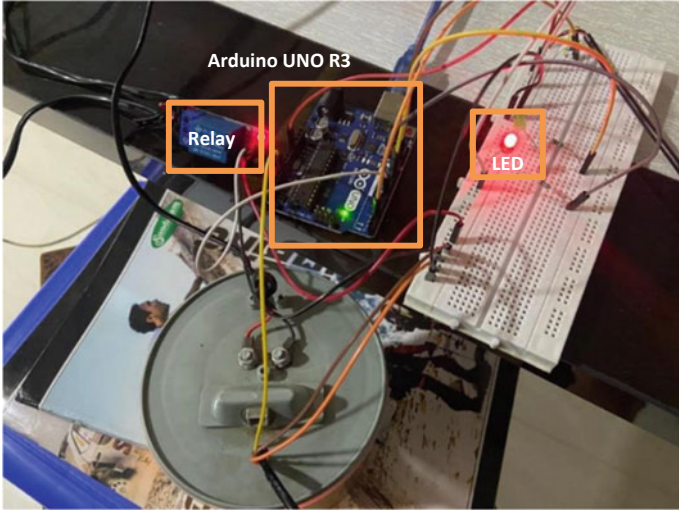
Fig. 9 Circuit build on breadboard
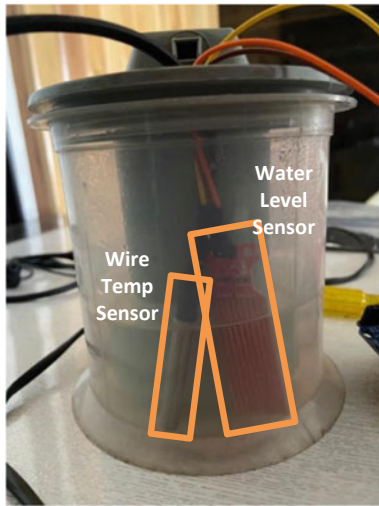
Fig. 10 Container with water level sensor and wire temperature sensor

4.3 Features of Our System

1. Works as an advanced version of vaporizer found in homes.
2. Can be connected with Google Home.
3. Can be used with various home assistants as well (Google Assistant).
4. Control the temperature of the water.

5. Red and blue LED for the timing of steam.
6. Helps relieve nasal congestion.

5 Conclusions

IOT-based smart vaporizer device is functioning properly. This project has been prepared for helping people to provide quick relief from common cold, cough, and throat irritation. This paper was planning to execute detection of water level in the container using water level sensors. By adding an Arduino and Raspberry pi circuit, temperature detection is also been possible and because of the LEDs, safety from the heater is also increased. The entire framework works consequently. So, it does not require any master individual to function it. We tried to plan this model in such a way that its components will be effortlessly connected together and give a clear vaporized steam.

It is not at all exceptionally costly. The smart vaporizer can used as the advanced version of vaporizer appears in home. Also, the vaporizer will help people relieve nasal congestion and enjoy healthy glowing skin.

References

1. Sabar S, Anjani D, Wijaya S (2021) Water level detection system based on Arduino and LabVIEW for flood monitors using virtual instrumentation. Al-Fiziya J Mater Sci Geophys Instr Theor Phys 4:29–35. https://doi.org/10.15408/fiziya.v4i1.19808
2. Firmansyah R, Yusuf M, Surya Saputra PP, Prasetyo ME, Mochtar FM, Kurniawan FA (2020) IoT based temperature control system using node MCU ESP 8266. In: Proceedings of the international joint conference on science and engineering (IJCSE 2020). https://doi.org/10.2991/aer.k.201124.072
3. Eshwar IVS, Bezawada A, Babu MD (2021) Relay based water level indicating and controlling system using Arduino. Int Res J Eng Technol (IRJET)
4. Tjandi Y, Kasim S (2019) Electric control equipment based on Arduino relay. J Phys Conf Ser 1244:012028. https://doi.org/10.1088/1742-6596/1244/1/012028

Effect of Size Ratio on Permeability and Local Packing Fraction of the Binary Packed Bed

Pratyush Kumar, Sandip K. Saha, and Atul Sharma

1 Introduction

The breeding blanket (BB) concept is an important module for the demonstration power reactor (DEMO). The breeding blanket concepts such as water-cooled ceramic breeder (WWCB) of Japan [1], helium-cooled ceramic breeder (HCCB) of China [2], helium-cooled pebble bed (HCPB) of EU [3], helium-cooled solid breeder (HCSB) of India [4], and helium-cooled ceramic reflector (HCCR) of Korea [5] use Beryllium (Be) pebbles as multipliers and Li_2TiO_3 or Li_4SiO_4 pebbles as a breeder. Generally, these breeder blankets acting as binary packed beds have particle size ratio (SR) in the range of 1–10. In packed beds, the permeation of fluid is an essential factor in understanding the overall flow behaviour of the system. Moreover, it is also required to determine the equivalent hydraulic permeability to use the Eulerian porous media approach [6]. Various models are stated in the literature to approximate the equivalent permeability of the packed bed filled with mono-sized particles [7–9]. However, the studies on the packed bed filled with binary particles are relatively low [7, 8, 10–13].

It is reported that the volumetric packing fraction of the bed depends on the size and the blending ratio of the two particles of the binary packed bed [7, 13]. In a binary packed bed, one type of void is filled by small particles and another kind of void by large particles, which increases the packing density compared to a packed bed with mono-sized particles. This effect also increases the hydraulic permeability of the packed bed. It was also found that permeability of the packed bed is strongly dependent on the characteristics of the particle (e.g. particle size and shape, porosity, and packing arrangement) [14, 15]. Many studies reported the correlations of fluid permeability of binary packed beds [10, 11]. Thies-Weesie et al. [10] presented a scaled relation of Kozeny–Carmen's equation for binary packed bed, whose values differ from the experimental results. Abe et al. [13] presented two

P. Kumar (✉) · S. K. Saha · A. Sharma
Department of Mechanical and Industrial Engineering, IIT Bombay, Mumbai 400076, India
e-mail: pratbharat@iitb.ac.in

models to determine the liquid permeability of a binary packed bed. Their models were based on the particle characteristics, i.e. surface factor, porosity, size ratio, and packing density. Furthermore, Lee et al. [7] studied the effect of particle size distribution. They presented different models based on average diameter, total force, and tortuosity effect to determine the permeability of the packed bed with $1 < SR < 2.5$.

In this paper, we have presented a CFD–DEM methodology to simulate the flow through binary packed bed. The present study focuses on determining the permeability of binary packed beds for different SR in the range of 1–10. In this work, the effect of size ratio ($1 \leq SR \leq 10$) on the local packing fraction and the permeability of the packed bed is studied. We adopted open-source software LIGGGHTS for DEM and OpenFOAM for CFD simulations. The work also focuses on the packing arrangement of binary packed beds at VFL ~ 40%. Further, we have evaluated the permeability analytically using the different models from the literature, and the analytical results are compared with DEM–CFD results to study the effects of different size ratios.

2 Permeability Models

The average packing fraction of a binary packed bed is greater than the mono-sized packed bed at maximum packing fraction. The reason is that small particles occupy the void amongst the large particles. It is found that the permeability of the packed bed is affected by the packing fraction. Many authors have given different correlations for the permeability of binary packed beds. In the present work, we focus on the models given in [7, 13, 16]. These models are as follows.

2.1 Deterministic Model [16]

$$K(\emptyset) = \frac{D_{p_2}^2 \emptyset^3}{180(1 - \emptyset)^3},$$ (1)

where $\emptyset$ is the average porosity and

$$D_{p_2} = \int\limits_0^\infty D_p^3 h(D_p) dD_p \Big/ \int\limits_0^\infty D_p^2 h(D_p) dD_p$$ (2)

with $h(D_p)$ is the density function of the diameters (D_p) for distribution of the different sizes of the particles.

M Model [13]: In this model, it is assumed that both particles of the packed bed are mixed very well. The permeability can be written as,

$$K = \frac{\emptyset_{av}^3}{180(1 - \emptyset_{av})^2} \left(\frac{X_v}{\in_{c1} d_l} + \frac{1 - X_v}{\in_{c2} d_s} \right)^{-2},$$ (3)

where $\emptyset_{av}$ is the average porosity of the packed bed, d_l and d_s are the size of large and small particles, respectively, $\in_{c1}$ and $\in_{c2}$ are the surface factors of the large particles and small particles, respectively, and X_v is the volume fraction of large particles.

Equation (2), for binary particles D_{p_2} can be written as [7],

$$D_{p_2} = \left(\frac{X_v}{d_l} + \frac{1 - X_v}{d_s} \right)^{-1}$$ (4)

Therefore, it is observed from Eqs. (1) and (3) that the M model of Abe et al. [13] and the deterministic model of Bejan [16] give the same result for the binary packed bed filled with the spherical particles.

S Model [13]: This model assumes that small particles fill the interstices between large particles due to segregation. As a result, the binary packed bed consists of two parts: One is the mixture of the two particles, and the second part is the packed bed with large particles. Using the S model, the permeability can be written as,

$$K = \frac{1}{180(1 - \phi_{av})} \left(\frac{\dfrac{1 - \phi_{avt}}{\{1 - X_v(1 - \gamma)\phi_{avt}^3\}}}{\left(\dfrac{X_v \gamma}{\in_{c1} d_l} + \dfrac{1 - X_v}{\in_{c1} d_s} \right)^2 + \dfrac{1 - \phi_1}{\phi_1^3} \dfrac{X_v(1 - \gamma)}{\in_{c1}^2 d_l^2}} \right),$$ (5)

where γ can be defined as,

$$\gamma = \left\{ \frac{\dfrac{X_{vt}(1 - \phi_{avt})(1 - \phi_1)}{X_c(1 - \phi_{av})\{(1 - \phi_1) - X_{vt}(1 - \phi_{avt})\}}}{\dfrac{X_{vt}(1 - \varphi_{avt})}{(1 - \phi_1) - X_{vt}(1 - \phi_{avt})}} - \right\},$$ (6)

where X_{vt} is the volume fraction of large particles, X_{vt} is the X_v, which gives the minimum porosity of packed bed, $\emptyset_{avt}$ is the average porosity of the packed bed at X_{vt}, and $\emptyset_1$ and $\emptyset_2$ are the porosity of packed bed with large particles and small particles alone, respectively. The term $\emptyset_1$ and $\emptyset_2$ are calculated using the formula recommended by Fenech [17] and Achenbach [18],

$$\emptyset_{bed} = \frac{0.78}{\left(D/d_p \right)^2} + 0.375$$ (7)

Summation of Force [7]: In this model, the expression of permeability is derived by summing the average forces on the particles. The expression can be written as,

$$K = \frac{1}{18\varepsilon K(\varepsilon)} \left[\frac{(d_s d_l)^2 \varepsilon}{d_s^2 \varepsilon_l + d_l^2 \varepsilon_s} \right], \tag{8}$$

where ε, ε_s, ε_l are the average packing density of packed bed, the packing density of small particles, and the packing density of large particles, respectively. The term $K(\varepsilon)$ is defined as,

$$K(\varepsilon) = \frac{10\varepsilon}{(1-\varepsilon)^3} \tag{9}$$

Tortuosity Model [7, 19]: Mota et al. [20] derived an expression for permeability by considering the tortuosity factor. The expression of which can be written as,

$$K = \frac{1}{18\varepsilon K(\varepsilon)} \left(\frac{3(1-\varepsilon)^{0.8}}{2\varepsilon} \right) \left[\frac{d_s d_l \varepsilon}{d_l \varepsilon_s + d_s \varepsilon_l} \right]^2 \tag{10}$$

2.2 Discrete Element Method (DEM)

In the present work, the discrete element method (DEM), first introduced by Cundall [21] is used to model the binary packed bed under gravity. For each particle, the particle–particle interactions and the particle with cylinder wall interactions are modelled using force–displacement relations. The nature of their interactions is collisions and sliding. The contact force between the particles is calculated using the Hertz–Mindlin theory [21, 22]. The resulting contact forces determine the location of each particle due to the particle motion governed by Newton's second law of motion. The simulation runs until the steady-state condition is achieved or up to a specified number of iterations. Here, steady state implies that each particle has virtually zero velocity, i.e. when the velocity of the particles is below 10^{-3}.

2.3 DEM–CFD Methodology

Figure 1 shows the modelling approach used in the present work. The pebble bed is created using the LIGGGHTS software, which is based on the discrete element method (DEM) [22]. The script is written to fill the packed bed with pebbles falling under gravity. The simulation input parameters are taken from [23], and the dimensions used in this study are given in Table 1. A filling simulation is run for sufficient

time to ensure the complete filling of the packed bed. Once the pebbles are settled, the corresponding values (velocity, angular velocity, and position of the pebbles) are exported using ParaView software. Further, a python macro is written in an open-source-based 3D computer-aided design (CAD) modeller, i.e. FreeCAD to create the geometry using the positions and the size of the particles from the exported file. Finally, the meshing is generated with hexahedral cut-cell-based tool, i.e. snappy-HexMesh of OpenFOAM. It should be noted here that in order to avoid the meshing problems near the contact points, the pebble diameters are reduced to 0.98 of the original diameters [24]. Due to this treatment, the average porosity of packed bed will increase. Therefore, the updated porosity values are considered to calculate the permeability analytically using different models (Eqs. 1–10). Further, to avoid the effect of boundary conditions of inlet and outlet, an extrusion method is adopted from Eppinger et al. [25]. Similar to [25], in the present study, there is an inlet extrusion of $3d$ and outlet extrusion of $10d$, where $d = d_1$ (d_1 = diameter of the large particle).

Figure 2 shows the schematic representation of the packed bed reactor and CFD simulation set-up. Finite volume-based open-source software, i.e. OpenFOAM, is

Fig. 1 Illustration of modelling approach
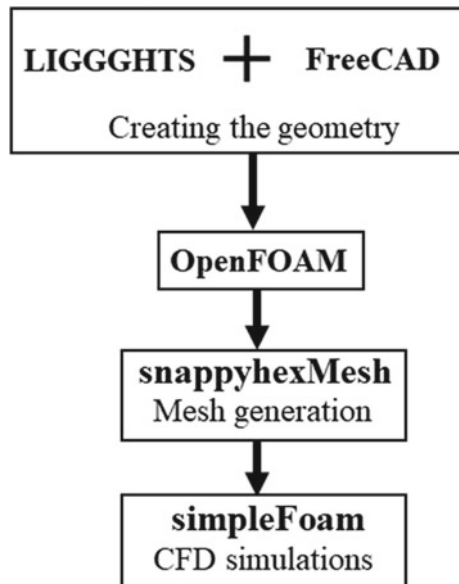
Table 1 DEM simulation parameters

Property	Pebbles [23]	Wall [23]
Materials	Li_2TiO_3	IN-RAFMS steel
Diameter of small particles (mm)	2	–
Diameter of large particles (mm)	2, 6, 10, 14	–
Outer diameter (mm)	–	50

used. The flow is assumed to be incompressible and isothermal. The physical properties of air are considered at 20 °C. The particle Reynolds numbers for different SR are calculated as,

$$\text{Re}_p = \frac{\rho v_0 D_{p_2}}{\mu},$$ (11)

where D_{p_2} is given by Eq. (4) for binary packed bed, ρ is the density, v_0 is the inlet velocity, and μ is the dynamic viscosity. All the simulations are done in the steady laminar flow regime ($\text{Re}_p < 40$). The standard solver, i.e. simpleFoam of OpenFOAM, which is based on SIMPLE algorithm, is used for CFD simulations.

$$\nabla.(\vec{v}) = 0$$ (12)

$$\nabla.(v\vec{v}) = -\nabla P + \nabla.(\tau),$$ (13)

where $\vec{v}$ is the velocity vector, P is the kinematic pressure, and τ is the stress tensor.

Fig. 2 Schematic view of CFD set-up used in simulations
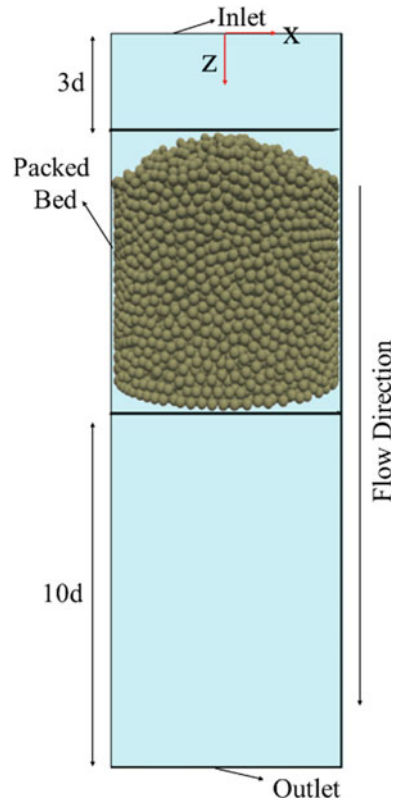
After the DEM–CFD simulation, Darcy's permeability is calculated using the overall pressure drop and superficial/inlet velocity.

3   Results and Discussions

Figure 3 shows the results of DEM simulations for different size ratios. In the present study, the packing is done at VFL (volume fraction of large particle) ~ 40%. The corresponding values of the number of pebbles for SR1 are 12,162 with a diameter of 2 mm; SR3 has 4852 pebbles with a diameter of 2 mm and 319 pebbles of diameter 6 mm; SR5 has 5899 pebbles of diameter 2 mm and 69 pebbles of diameter 10 mm; and SR7 has 6553 pebbles of diameter 2 mm and 25 pebbles of diameter 14 mm.

Validation of DEM Model: Figure 4 shows the average packing fraction of the fixed bed for different size ratios at VFL of ~ 40%. There are no experimental results available for the packing fraction for VFL ~ 40% in the literature as per the best of
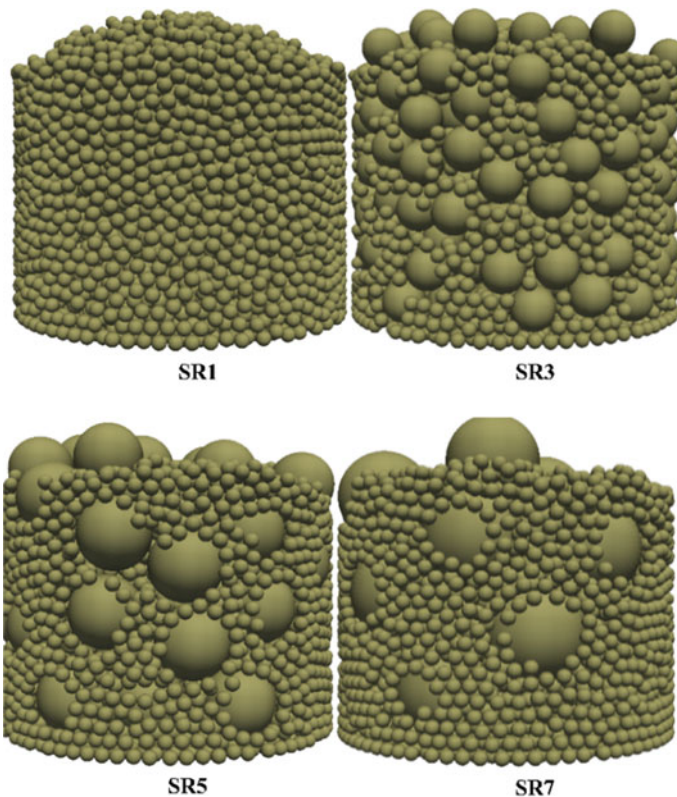
Fig. 3 Packing of binary packed bed for different size ratios (SRs)
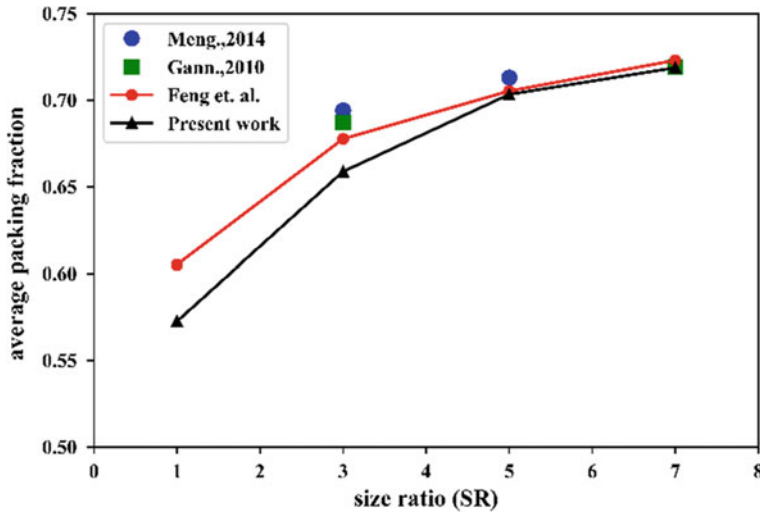
Fig. 4 Average packing fraction of binary packed bed for different size ratios compared with the literature results (Meng et al. [27], Feng et al. [26], and Gan et al. [28])

the authors' knowledge. Therefore, the result of the present work is validated by the work of Feng et al. [26], Meng et al. [27], and Gann et al. [28] on binary packed beds. There is a relative error of a maximum of 5.67% for SR1 with the result of Feng et al. [26] for VFL = 41%. It is observed from the figure that at lower SR, our methodology underpredicts the average packing fraction. The reason could be that segregation effects dominate the wall effect at higher SR.

Local Packing Distribution: Figure 5 compares the local packing fraction of a mono-sized packed bed, i.e. SR = 1 with $d_1 = d_s = 2$ mm with de Klerk correlation [29]. It is found that the variation of local packing fraction of present DEM simulation for mono-sized packed bed (SR1) agrees with de Klerk correlation with a relative error of a maximum of 11.02%. There is no correlation available for binary packed beds. However, Fig. 6 shows the radial porosity distribution of binary packed bed for the different size ratios. It is observed that in case of binary packed bed, the variation in local packing fraction is mainly due to large size particle and partially due to small size particles. Furthermore, with increase in the size ratio of the packed bed, the local packing fraction increases.

Permeability: Figure 7 shows the variation of permeability with respect to different particle size ratios (*SRs*) using different models. The calculated results are compared with the result of the present methodology of DEM–CFD. The numerical result compares the different models stated in the literature for predicting the permeability very well for the size ratio in the range of 1–10. The tortuosity model approximates the permeability very well for all size ratios. Further, the M model, deterministic
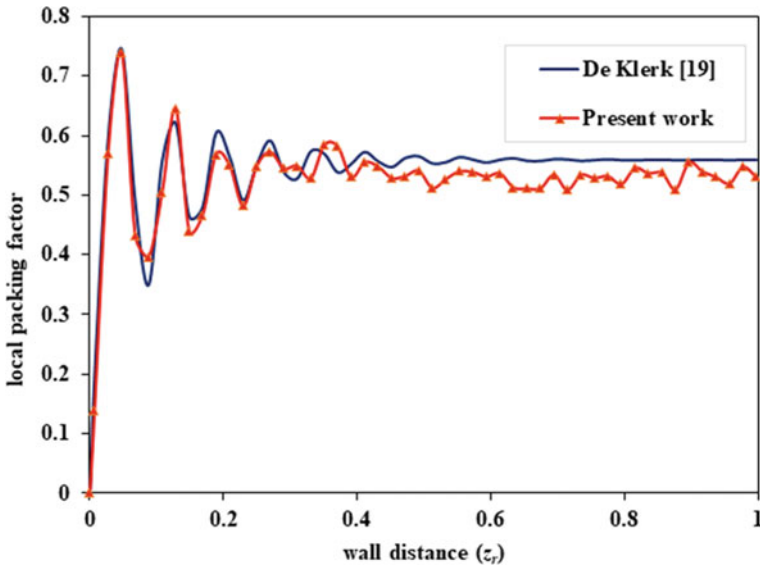
Fig. 5 Validation of DEM model with De Klerk [29] correlations for mono-sized packed bed
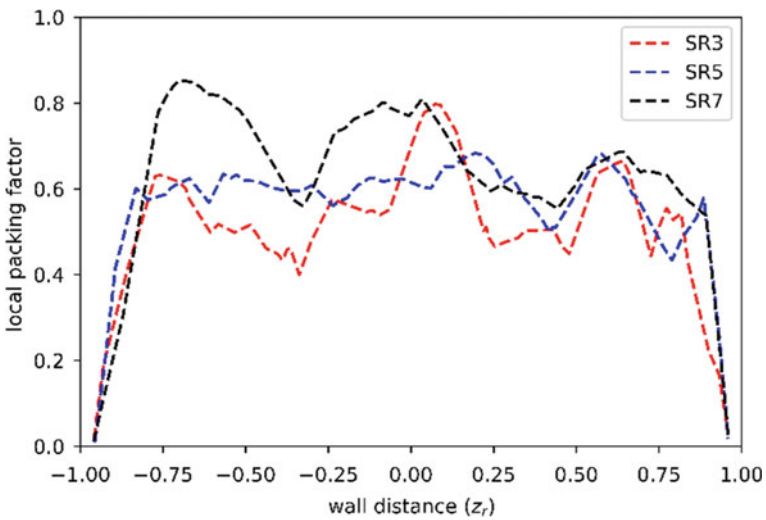
Fig. 6 Effect of size ratio on overall packing fraction at VFL ~ 40%

model, and force model also approximate the permeability with a maximum relative deviation of 29.37%. As pointed out earlier that the deterministic model and m model give the same result for binary packed beds. The S model overestimates the permeability at a higher size ratio. This is because the S model relies on the fact that
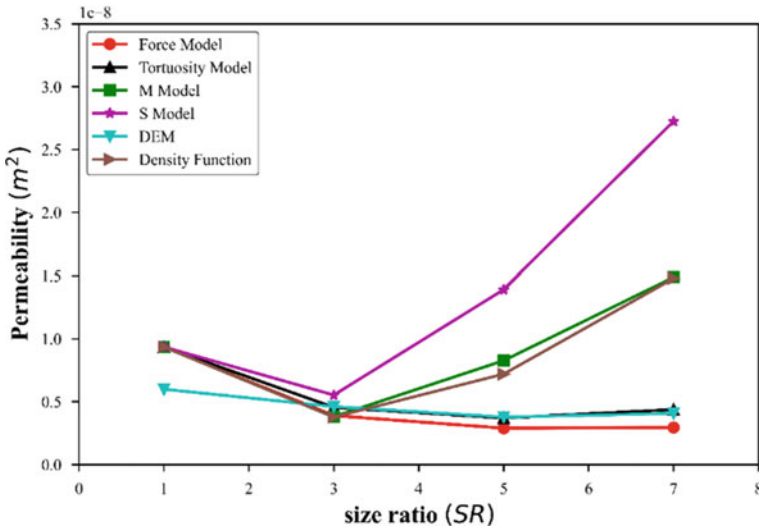
Fig. 7 Comparison amongst different models of permeability and the effect of size ratio on permeability

small particles segregate in the large particles' interstices. The extent of the segregation effect is great at VFL, close to 60% [13]; however, our study mainly focuses on VFL ~ 40%. Further, it is observed that permeability decreased with increasing the size ratio due to the decrease in porosity (i.e. pore volume).This behaviour shows that with increase in the size ratio, packing density increases which increases the permeability of the packed bed.

4   Conclusion

In this paper, the effect of the size ratio on the permeability and the local packing fraction of the binary packed bed is studied numerically using the DEM–CFD approach. The DEM simulation is performed using open-source software, i.e. LIGGGHTS. After the DEM simulations, the open-source 3D computer-aided design (CAD) modeller, i.e. FreeCAD, is used to create the solid geometry. Further, the meshing is generated using the snappyHexMesh utility of OpenFOAM. The OpenFOAM standard solver 'simpleFoam' is simulated for the CFD study.

The result of packing distribution shows that the variation of local packing fraction for binary packed bed at VFL ~ 40% is mainly due to large size particles and partially due to small size particles. Further, it is observed that the overall packing of the packed bed increases with an increasing size ratio. Different models for permeability are compared with the result of the present DEM–CFD result. It is observed that the

permeability of the binary packed bed decreased with increasing the size ratio due to a decrease in porosity. Studying the effect of size ratios on the velocity and pressure distribution is still an outstanding topic for future work.

Nomenclature

d_l	Particle diameter of large particle [mm]
d_p	Particle diameter [mm]
d_s	Particle diameter of small particle [mm]
$h(D_p)$	Density function of the diameters (D_p) [–]
$K(\emptyset)$	Dimensionless drag coefficient [–]
K	Permeability [m^2]
P	Pressure [Pa]
Re_p	Particle Reynolds number [–]
v_0	Superficial/inlet velocity [m/s]
$\overrightarrow{v}$	Velocity vector [m/s]
X	Cartesian axis direction [–]
X_v	Volume fraction of large particles [–]
X_{vt}	X_V which gives maximum packing fraction [–]
Y	Cartesian axis direction [–]
Z	Cartesian axis direction [–]
z_r	Wall distance $(^r/_R)$ [–]
ϕ	Porosity
ϕ_1	Porosity of packed bed at large particle alone
ϕ_{av}	Average porosity of the packed bed
ϕ_{avt}	Porosity at X_{vt}
$\in_{c1}$	Surface factor of large particle
$\in_{c2}$	Surface factor of large particle
ε	Average packing density
ε_s	Packing density of small particles
ε_l	Packing density of large particles
ρ	Density
μ	Dynamic viscosity
τ	Shear stress
DEM	Discrete element method
CFD	Computational fluid dynamics
SR	Size ratio

References

1. Tanigawa H (2018) Cylindrical breeding blankets for fusion reactors. Fusion Eng Des 136:1221–1225
2. Wang XY, Feng KM, Chen YJ, Zhang L, Wu XH, Liao HB, Ye XF, Zhao FC, Cao QX (2019) Current design and R&D progress of the Chinese helium cooled ceramic breeder test blanket system. Nucl Fusion 59:076019
3. Zmitko M, Vladimirov P, Knitter R, Kolb M, Leys O, Heuser J, Schneider HC, Rolli R, Chakin V, Pupeschi S, Magielsem L, Fedorov A, Poitevin Y (2018) Development and qualification of functional materials for the European HCPB TBM. Fus Eng Des 136:1376–1385
4. Chaudhuri P, Danani C, Chaudhari V, Kumar ER (2013) Overview of design and thermal–hydraulic analysis of Indian solid breeder blanket concept. Fus Eng Des 88:209–215
5. Cho S, Ahn M, Choi J, Chun Y, In K, Jin HG, Kim CS, Kim D, Kim SK, Ku DY, Lee CW, Lee DW, Lee EH, Lee Y, Park SD, Park SC, Park Y, Yoon JS (2018) Investigation of technical gaps between DEMO blanket and HCCR TBM. Fus Eng Des 136, Part A:190–198
6. Kumar P, Thakur A, Saha SK, Sharma A, Sharma D, Chaudhuri P (2021) CFD investigation of helium gas flow in sphere packed (pebble bed) in a rectangular canister using OpenFOAM. Fus Eng Des 172:112858
7. Lee H, Koo S (2014) Liquid permeability of packed bed with binary mixture of particles. J Ind Eng Chem 20:1397–1401
8. Dias RP, Fernandes CS, Mota M, Teixera JA, Yelshin A (2007) Permeability and effective thermal conductivity of bisized porous media. 50:1295–1301
9. Kumar P, Saha SK, Sharma A (2022) Entropy generation minimization-based heat transfer and mass transfer study of rectangular packed-bed filled with spherical particles. Eng Des 184:113295
10. Thies-Weesie DME, Philipse AP (1994) Liquid permeation of bidisperse colloidal hard-sphere packings and the Kozeny-Carman scaling relation. 162:470–480
11. Mota M, Teixeira JA, Bowen WR, Yelshin A (2001) Binary spherical particle mixed beds: porosity and permeability relationship measurement, pp 101–106
12. Sohn H, Koo S (2012) Permeability of viscous flow through packed bed of bidisperse hard spheres. Korean Chem Eng Res 50:66–71
13. Abe E, Hirosue H, Yokota A (1978) Pressure drop through a packed bed of binary mixture. J Chem Eng Jpn: 302–306
14. Amiri L, Ghoreishi-Madiseh SA, Hassani FP, Sasmito AP (2019) Estimating pressure drop and Ergun/Forchheimer parameters of flow through packed bed of spheres with large particle diameters. Powder Technol 356:310–324
15. Rahman A (2013) Gas dynamics and heat transfer in a packed pebble-bed reactor for the 4th generation nuclear energy, Doctoral Dissertations, Department of Chemical and Biochemical Engineering (2013)
16. Nield DA, Bejan A (2017) Convection in porous media, 5th edn. Springer, Berlin
17. Fenech H (1981) Heat transfer and fluid flow in nuclear systems, 1st edn. Pergamon Press, New York, USA
18. Achenbach E (1995) Heat and flow characteristics of packed beds. Exp Therm Fluid Sci 10:17–27
19. Achenbach E (1982) Heat transfer and pressure drop of pebble beds up to high Reynolds number. In: 7th international heat transfer conference, pp 3–8
20. Mota M, Teixeira JA, Bowen WR, Yelshin A (2001) Trans Filtr Soc 1(4):101
21. Cundall P et al (1979) A discrete numerical model for granular assemblies. Géotechnique 29:47–65
22. LIGGGHTS, (R)-Public Documentation, Version 3.X. Available online http://www.liggghts.com
23. Eisfeld B, Schnitzlein K (2001) The influence of confining walls on the pressure drop in packed beds. Chem Eng Sci 56:4321–4329

24. Sharma A, Thakur A, Saha SK, Sharma A, Sharma D, Chaudhuri P (2020) Thermal-hydraulic characteristics of purge gas in rectangular packed pebble bed of a fusion reactor using DEM-CFD and porous-medium analyses. Fusion Eng Des 160:111848
25. Eppinger T, Seidler K, Kraume M (2011) DEM-CFD simulations of fixed bed reactors with small tube to particle diameter ratios. Chem Eng J 166:324–331
26. Feng Y, Gong B, Cheng H, Luo X, Wang L, Wang X (2021) Effects of bed dimension, friction coefficient and pebble size distribution on the packing structures of the pebble bed for solid tritium breeder blanket. Fusion Eng Des 163:112156
27. Feng Y, Gong B, Cheng H, Wang L, Wang X (2021) Effects of fixed wall and pebble size ratio on packing properties and contact force distribution in binary-sized pebble mixed beds at the maximum packing efficiency state. Powder Technol 390:504–520
28. Meng L, Lu P, Li S (2014) Packing properties of binary mixtures in disordered sphere systems. Particuology 16:155–166
29. de Klerk A (2003) Voidage variation in packed beds at small column to particle diameter ratio. AIChE J 49:2022–2029

Numerical Study of Cryogenic Transfer Line Under Conjugate Conditions

Kamala Kannan Vijesh and Manoj Kumar Moharana

1 Introduction

The cryogenic end uses require specialized storage and transport systems due to their low boiling point and latent heat of vaporization because of low-temperature characteristics of fluid (below the temperature of 123 K is known as cryogenic fluid). To prevent evaporation losses and to promote maximal fluid collection during the transfer of the cryogens, it is crucial to adopt insulated cryogenic transfer lines. The cryogenic transfer system is used at a workplace, whether it be a research facility, a contemporary location, or as an instrumentation gadget. It is more common in industries like those in the food, car, gadget, drug, etc. In 1980, the first vacuum-insulated transfer line (4-tube design for LHe/GHe) was delivered to CERN. From 1980 to 2011, several transfer line systems for industrial applications and research facilities were designed, produced, and delivered on a global scale.

The thermodynamic conditions of the atoms in cryogenic liquids determine their significance; thus, transferring them should not result in significant changes to those parameters. It suggests that the temperature increase or the fluid-related vapour quality and pressure changes should be minimally significant. The most important considerations include the geometrical constraints (total distance, potential routings, and available space), for the required mass flow rate and its time characteristic, the minimum and maximum temperature, the minimum and maximum pressure, the thermodynamic properties of the chosen cryogenic fluid, and the mechanical properties of the preferred pipe materials.

K. K. Vijesh · M. K. Moharana (✉)
Thermal Systems Laboratory, Department of Mechanical Engineering, National Institute of Technology Rourkela, Rourkela, India
e-mail: mkmoharana@gmail.com

Cryogenic transfer lines are designed to be constructed from a certain number of modules to facilitate their construction, shipment, and installation. As opposed to rigid transfer lines that assist in the presentation of the stream peculiarities of cryogenic fluids, recent work on flexible transfer lines is simple to handle and dealt with variations in the statures between the capacity and destination storage tank.

2 Literature Review and Objective

To design such pipelines, it is essential to understand the usual flow patterns, pressure drops, and heat transfer characteristics during cryogenic flow. For the transport of liquid helium, the strength analysis [1] of the transfer line is majorly considered, where the terrestrial gravity condition is not ignored [2]. Due to the effects of axial wall conduction in a conjugate heat transfer, the average Nusselt number (Nu) is increased for such a value of k_{sf} [3], for the case of circular microtubes. The transient process of pipe cooling by the internal flow of cryogenic fluid is usually carried out to extend the quenching database with liquid oxygen to predict the cryogenic line chill down process [4, 5], for the observations in the mixing and flow processes of cryogenic liquids that are encountered in liquid propellant rocket engines. The pressure, temperature, and density of the flowing cryogen have certain impacts on walls of the process line. The higher the pressure and density, the thicker the pipe walls and the stronger the supports. The material to the pipeline is very important. The usage of a horizontal copper transfer line shows better results, with reduction of 50% in critical heat flux [6], and thermal mass function reduction by a factor of 100, when copper transfer lines are used instead of stainless steel. Sometimes it is also observed that the inclination of chilling line [7] on temperature profile gives the results that suggested the existence of an optimum upward line inclination minimizing the chill down time. The lengths and states of modules of the transfer line rely mostly on cryogenic line routings, transportation strategies, and fixed help areas.

The most frequently used are straight and elbow modules. The Zed module is used where the cryogenic line routing has a significantly small step, whilst the Tee module is dedicated to distributing the cryogenic fluids. Hu et al. [8] used the Pyrex glass tube as the test section as straight module with the vacuum insulation, and with foams like polyurethane foam insulation [9], is used for chill down process. In the solid–fluid interface, the parameters are governed carefully in the heated microtubes as there is some constant heat flux at the tube's outer layer due to ambient temperature conditions [10], where the same phenomena occur in the force convective heat transfer [11] of the microchannel.

When a horizontal tube is vacuum-insulated using a vacuum pump, the heat transfer on the bottom wall is essential whilst the upper wall is cooled by forced convection [12] with the superheated vapour of fluid. The effect of gravitational acceleration plays a key role on the relation between the flow and thermal behaviour, where it was observed that as the heat transfer increases under microgravity conditions [13]. The performance evaluation criteria [14] analyse the effect of the Reynolds

number and thermo-hydraulic function, which are involved in the surface relative roughness research [15] including variations in Nusselt number in the low Reynolds number region and close to the transition region.

A literature review indicates that there are only a few investigations on the thermal performance of cryogenic transfer lines using foam-insulating materials. In this context, a three-dimensional numerical study is conducted utilizing the commercial ANSYS Fluent® software. The inlet temperature of the transfer line was set at 77 K, with the intent of achieving the acceptable cryogenic temperature at the outlet using a few kinds of foam insulation. The objectives of this study are to assess the effectiveness of thermal stability, and to comprehend and emphasise the impact of the inner wall to working fluid conductivity ratio (k_{sf}), fluid, and wall temperatures at various axial points of the model to monitor the chill down process with flow Re on the axial wall conduction in transfer line when it is subjected to constant heat flux boundary condition along length. The next section provides a thorough explanation of the numerical procedure.

3   Materials and Methods

In this work, an insulated pipe has been used to complete a three-dimensional numerical simulation. This investigation considers a pipe with an insulating layer thickness of 0.6 m around a circular tube.

Depending on the case, the input fluid's Reynolds number and velocity are varied, where single-phase laminar flow is considered with fluid as incompressible. It is also assumed as the heat loss by natural convection and radiation is negligible. The liquid nitrogen, working fluid, enters through the inlet section of the fluid domain, which has a hydraulic diameter of 0.01 m and a length of 2 m along the z-axis which is shown in Fig. 1.
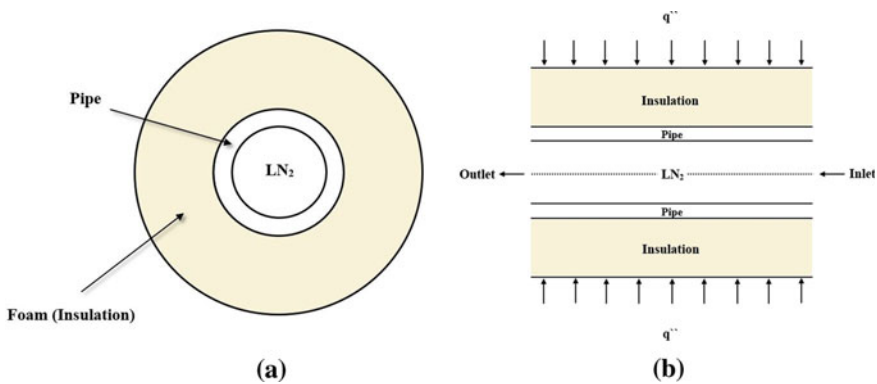
Fig. 1 Details of simulated domain. **a** Cross-sectional view, **b** transverse section (Y–Z) plane

3.1 Model Simulation

This simulation is carried out in ANSYS Fluent® commercial v18.1 software. The geometry comprises of two domains: a fluid domain for the liquid nitrogen and solid domains for the pipe and insulation in 3D. For the best results in both fluid and solid surfaces, Boolean surfaces are carefully chosen. The diameter for the liquid nitrogen domain was set to 0.1 m, and for the pipe domain, the inner diameter was set to 0.1 m, and the outer diameter was set to 0.15 m. Similarly, the inner and outer diameters of the insulating domain were adjusted to 0.15 m and 1.2 m, respectively.

The cylindrical domain was meshed using an o-grid structured mesh for the model. It is easy to exclude severely skewed cells from circular cylinders by using the sort of meshing technique that is frequently used in the CFD of the cylindrical domain. The different mesh domains utilized to analyse simulation data for a grid independence study are shown in Fig. 2.

This method involves inflating the divisions along the radial length of a circular cylinder. The bias type approach is used with a bias factor of 2.5 in inflation for each domain, with 100 divisions along the length and at the circumferential boundaries of the domain where 30, 45, and 60 divisions were set. It exhibits a very low parameter value error of 0.3%, a model with a higher number of elements, fine meshing with 4,787,501 nodes, and 4,680,000 elements is chosen for the simulation.
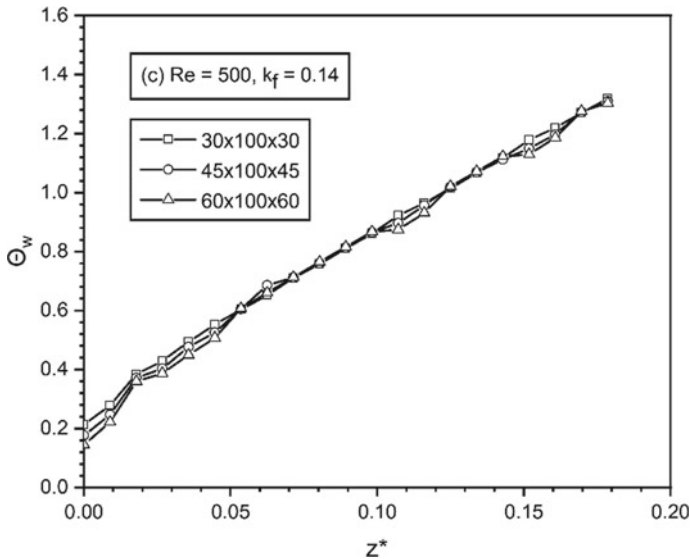
Fig. 2 Axial variation of non-dimensional wall temperature at Re = 500 for stainless steel 316L pipe with PUF insulation

3.2 Numerical Validation of the Model

The model for the axial change in the non-dimensional heat flux in the single-phase laminar flow in the microchannel from Moharana et al. [3] is numerically validated, as shown in Fig. 3a, where it exhibits a very low error of 2.46% in the simulated domain.

Similar to this, the conjugate analysis in partially heated microtubes from Tiwari and Moharana [10], where the shape of the domain is same which is cylindrical, is followed to validate the results as shown in Fig. 3b. The axial variation in Nusselt number using the three-dimensional model from Lee and Garimella [11], where the laminar convective heat transfer phenomena occur, is shown in Fig. 3b. It illustrates a small error in the axial variation of the local Nusselt number results from both references of 5.12% and 3.22%, respectively.

3.3 Set-Up and Solution

The simulation of the model of domain was set up for steady-state model for laminar flow in the flow channel, used the standard continuity and momentum conservation equation. Liquid nitrogen is used as the working fluid in the material section, and air is used for the ambient conditions.

The thermo-physical characteristics of pipes and insulations [16] were acquired for the solids and implemented to the simulation. As the fluid flows into the channel with an inlet temperature of 77 K, the thickness ratio between the overall thickness and the thickness of the fluid which is $t = 11.5$ was adjusted. Additionally, a constant heat flux of 5 W/m^2 was applied to the outer wall surface of the insulation. The outlet was configured to the pressure outlet. The pressure in the solution was treated as "body force weighted", and the momentum and energy are maintained at "first order upwind". For the convergence criterion, continuity was set at 10^{-6}, whilst energy was set at 10^{-9} for residuals. The computation is executed for 500 iterations after the inlet initialization. The inbuilt CFD post is used for data processing post-simulation on Ansys Fluent® platform.

4 Results and Discussion

The pipe material conductivity and insulation material are varied. The values of wall temperature and wall flux at the wall–fluid interface and bulk fluid temperature are analysed to determine their impact on the overall performance of cryogenic transfer lines. The comparison of simulation results for different pipe materials and insulations are presented using non-dimensional parameters as defined below.

(a)

(b)
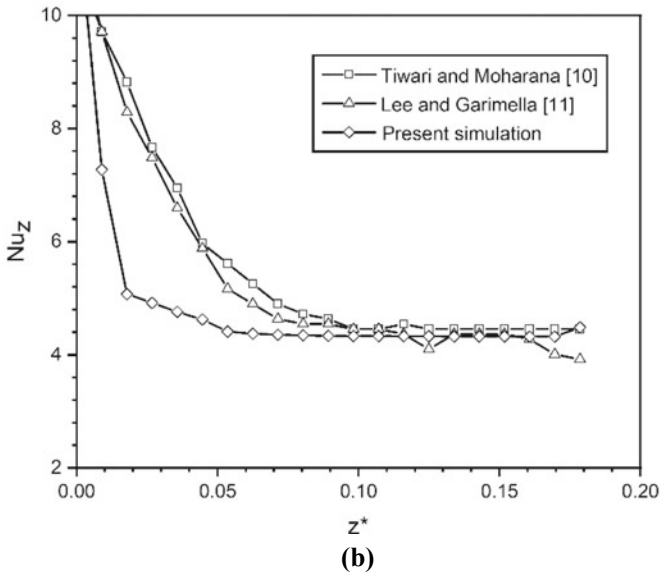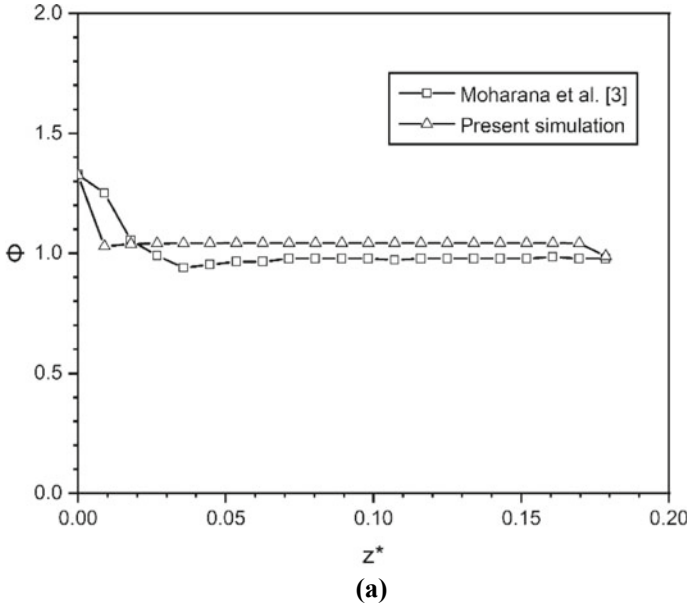
Fig. 3 **a** Numerical validation of the model with microchannel. **b** Numerical validation of the model with microtubes

The characteristic length, average, and local Nusselt number across the pipe length are given by:

$$z^* = \frac{z}{Re \times Pr \times D_h} \tag{1}$$

$$Nu = \frac{1}{L} \int_0^L Nu_z dz, \quad Nu_z = \frac{h_z \times D_h}{k_f}. \tag{2}$$

The thickness ratio of the flow channel is given by:

$$t = \frac{t_o}{t_f} = \frac{t_f + t_{ins}}{t_f} = 1 + \frac{t_{ins}}{t_f} \tag{3}$$

The dimensionless heat flux at the solid–fluid interface and local heat transfer coefficient is given by:

$$\Phi = \frac{q''_{int}}{q''(1+t)} \tag{4}$$

$$h_z = \frac{q''_{int}}{(T_w - T_f)} \tag{5}$$

The inner wall of pipe (solid–fluid interface) temperature and bulk fluid temperature are given by:

$$\Theta_w = \frac{T_{wz} - T_{fi}}{T_{fo} - T_{fi}} \tag{6}$$

$$\Theta_f = \frac{T_{fz} - T_{fi}}{T_{fo} - T_{fi}} \tag{7}$$

The solid-to-fluid conductivity ratio k_{sf} is altered by considering different pipe materials such as steel, aluminium, and copper. The thickness ratio between the overall thickness and the fluid thickness, $t = 11.5$, is fixed. As a result, the parametric changes employed in the study are $k_{sf} = 88.75 - 2722.72$, with the fluid velocity also varied to modulate the flow Re. When the fluid is moving through the pipe, the phenomenon of temperature changes was seen using an area-weighted average in the inner walls. The same observation was made using a mass-weighted average for the bulk fluid's temperature (Figs. 4, 5 and 6).

For stainless steel 316L, the value of $Nu_{avg} \sim 5.01$ is shown for $Re = 200\text{–}500$ with polyurethane foam with some discrete values in the middle of the simulation results, and at $Re = 1000$, as it approaches the higher Reynolds number, the value of $Nu_{avg} \sim 5.52$ is shown (Fig. 7).
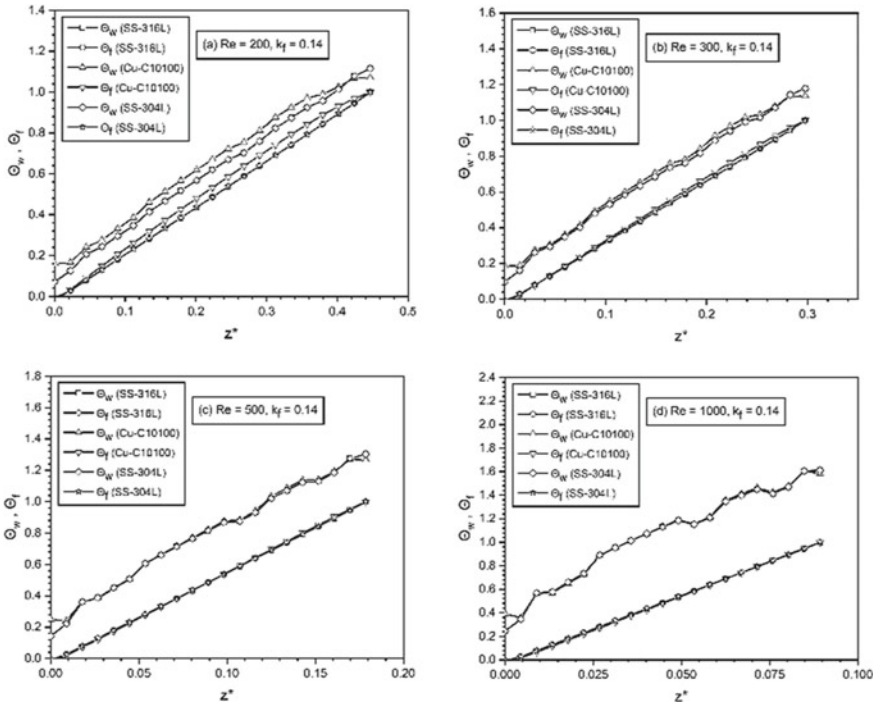
Fig. 4 Axial variation in the wall and the fluid temperature with polyurethane foam at Re = 200–1000

The same is observed as the Nusselt number demonstrates the same downward trend in the simulation results of the model with extruded polystyrene foam, and the value is $Nu_{avg} \sim 5.23$, which is only slightly more than the value of the polyurethane foam insulation used. Additionally, the Nu_{avg} value at Re = 1000 is 5.85. This insulating material also has a major impact on the regulation of maintaining the fluid's temperature throughout the channel.

The constant heat flux that is applied to the insulating outer wall has a significant impact on the simulation model. In order to maintain the fluid's temperature along the channel whilst applying insulation, a small presence of heat flux is created at the pipe's outer wall interfaces. Thermal performance deteriorates as a result of the difference between the heat flux applied to the outer surface and the heat flux experienced at the solid–fluid interface. The results were shown for the observation where it maintains $\Phi \sim 1$ value throughout the channel length (Figs. 8 and 9).

When the Reynolds number in extruded polystyrene foam is changed from 300 to 1000, as shown in the temperature distribution plots, the temperature at outlet changes between 78 and 84 K (Fig. 10).

The same thing happens when polyurethane foam is used, illustrating that it significantly impacts the transfer line when it comes to sustaining the cryogenic temperature of bulk fluid at the outlet.
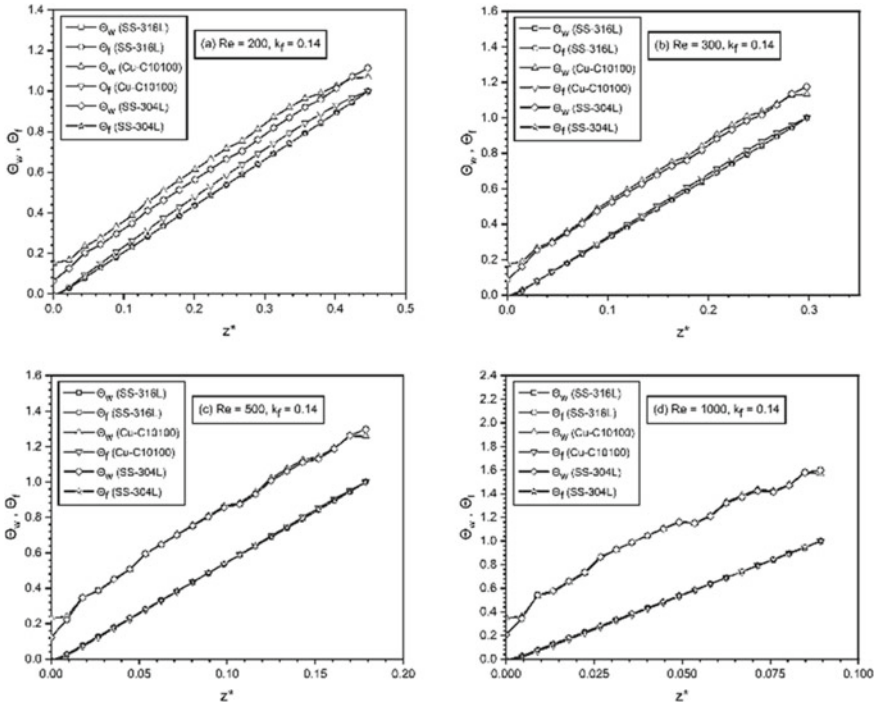
Fig. 5 **a**, **b** Axial variation in the wall and the fluid temperature with and extruded polystyrene foam at Re = 200–1000

5 Conclusions

The model is set up under constant heat flux at the insulation's outer wall and boundary conditions when various cases of Reynolds number were given at the fluid's inlet, with various types of pipes and insulations, and the model is validated using references. According to the research, the ideal cryogenic flow requires either a pipe with sufficient foam insulation (especially cold insulation materials) or a pipe that is totally vacuum-insulated, depending on the characteristics of the specific cryogenic fluid. The model was seen to have attained the thermal stability of maintaining the desired temperature at the transfer line outlet when pipe materials like stainless steel 316L or Copper (C10100) with extruded polystyrene foam were utilized. These approaches gave some substantial and improved results. Given the high-demand modified cryogenic transfer lines in the refrigeration industry, the results of the numerical simulation of model with new materials will help improve the designs used in industrial applications and can be used for the experimental purpose. In order to identify the necessary adjustments to the transfer line and include innovative thinking into this project, a study into the interactions between fluid temperature and wall temperature was accomplished.
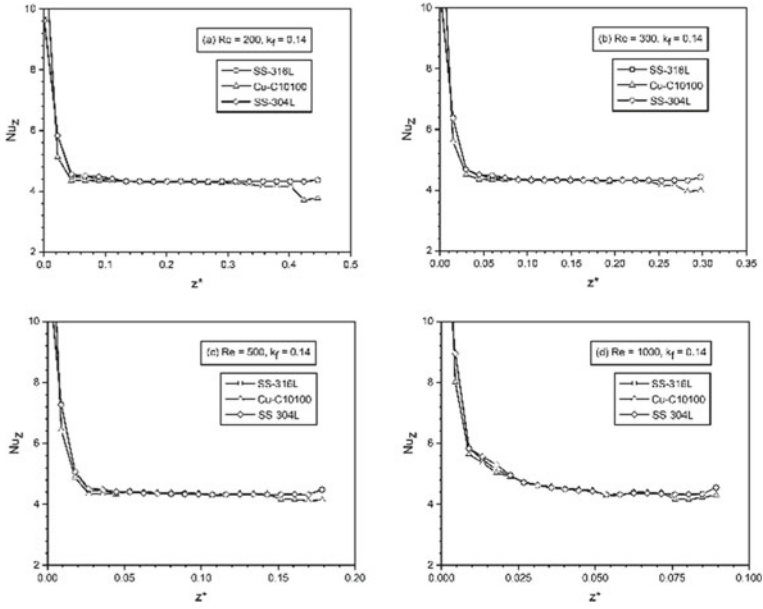
Fig. 6 Axial variation in the Nusselt number with polyurethane foam at Re = 200–1000
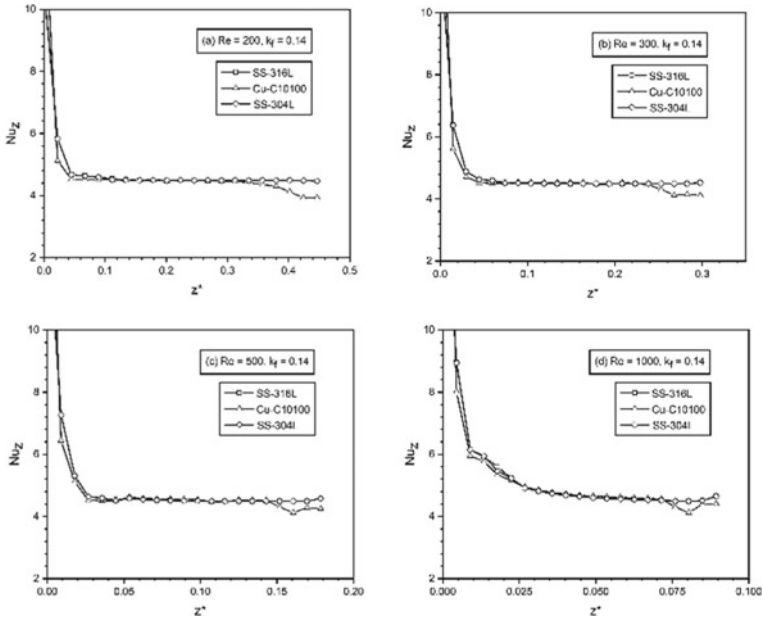
Fig. 7 **a**, **b** axial variation in the Nusselt number with extruded polystyrene foam at Re = 200–1000
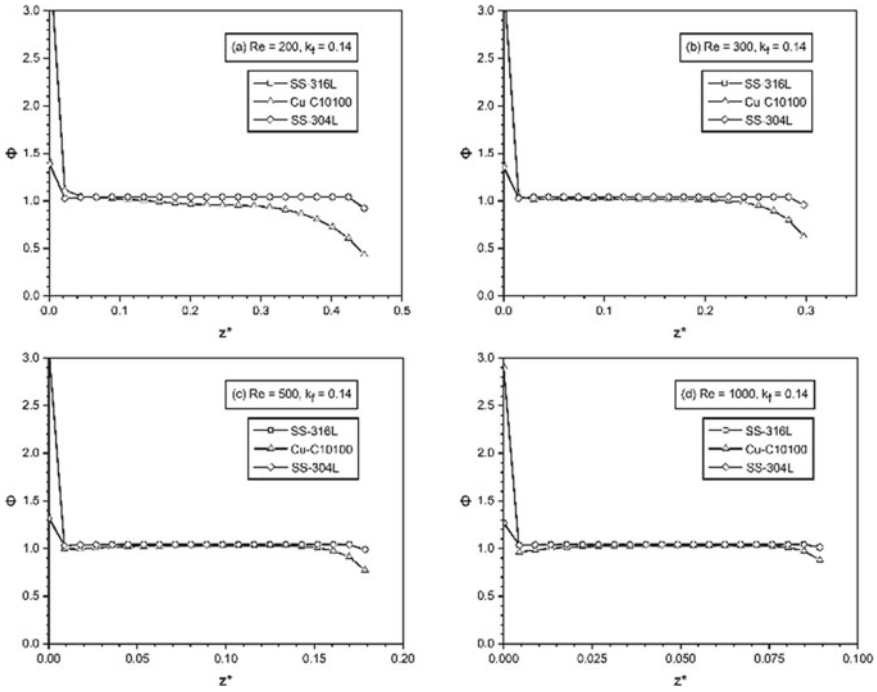
Fig. 8 a, b Axial variation in the heat flux with extruded polystyrene foam at Re = 200–1000
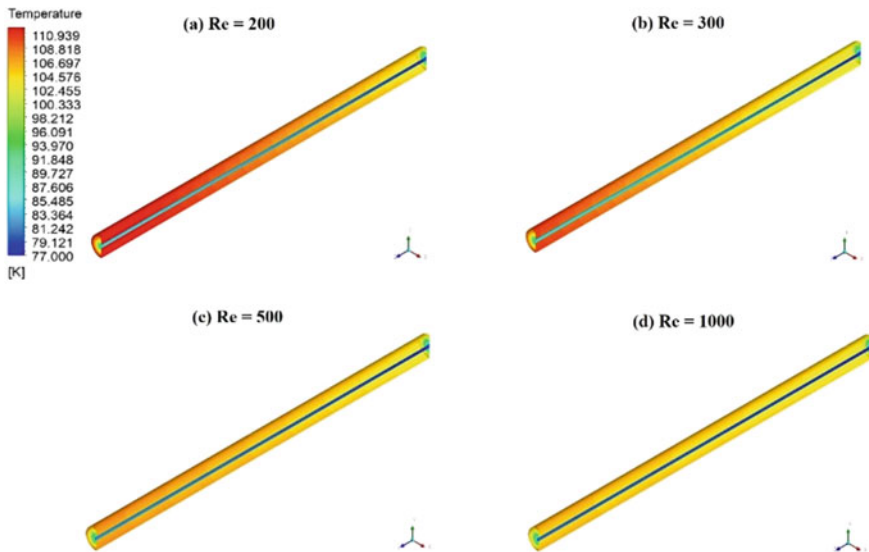
Fig. 9 Temperature distribution in stainless steel 316L with polyurethane foam insulation
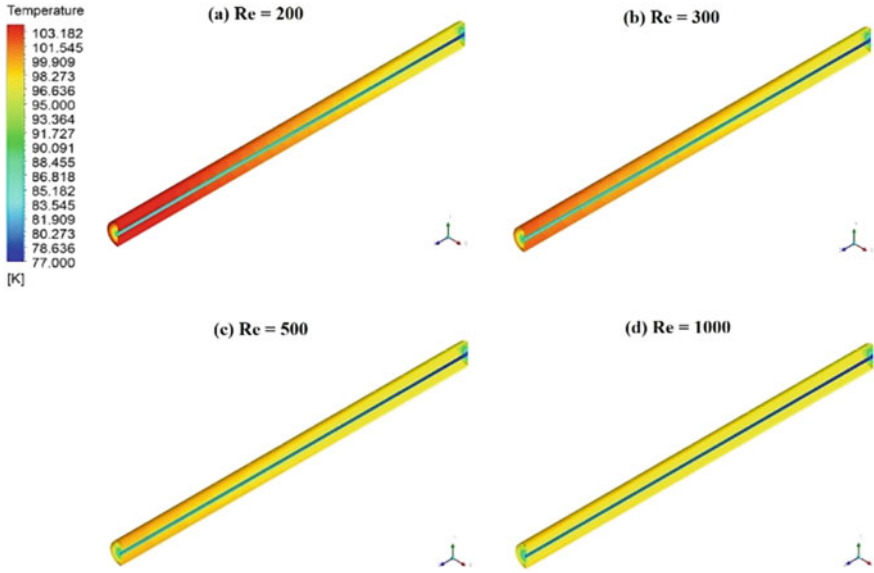
Fig. 10 Temperature distribution in stainless steel 316L with extruded polystyrene foam insulation

Nomenclature

D_h	Hydraulic diameter of the pipe [m]
h_z	Local heat transfer coefficient [W/m^{2}K]
k_s	Thermal conductivity of the pipe [W/mK]
k_f	Thermal conductivity of the working fluid [W/mK]
k_{sf}	Ratio of thermal conductivity of the pipe and thermal conductivity of the working fluid [W/mK]
L	Length of the pipe [m]
Nu_z	Local Nusselt number [–]
Nu_{avg}	Average Nusselt number over the pipe length [–]
Pr	Prandtl number [–]
q''	Heat flux applied at the outer wall surface of the insulation [W/m^2]
q''_{int}	Heat flux at the interface of the pipe [W/m^2]
Re	Reynolds number [–]
T	Temperature [K]
T_o	Ambient temperature [K]
t_f	Thickness of the fluid [m]

t_{ins}	Thickness of the insulation [m]
t	Ratio of total thickness to the thickness of the fluid (t_o/t_f) [–]
v	Average fluid velocity at inlet of the pipe [m/s]
z	Axial length along the length of the pipe [mm]
z^*	Non-dimensional axial distance along the pipe length [–]
ρ	Density [kg/m^3]
μ	Dynamic viscosity [Ns/m^2]
Φ	Non-dimensional heat flux [–]
Θ	Non-dimensional temperature [–]
f	Fluid [–]
i	Inlet conditions, inner [–]
int	Interface [–]
o	Outlet conditions, outer [–]
s	Solid [–]
w	Inner wall surface [–]

References

1. Rusinski E, Chorowsm M, Iluk A, Fydrych J, Malcher K (2014) Selected aspects related to the calculations and design of a cryogenic transfer line. Arch Civ Mech Eng 14:231–241
2. Darr SR, Hu H, Glikin NG, Hartwig JW, Majumdar AK, Leclair AC, Chung JN (2016) An experimental study on terrestrial cryogenic transfer line chill down. Effect of mass flux, equilibrium quality, and inlet sub cooling. Int J Heat Mass Transf 103:1225–1245
3. Moharana MK, Singh PK, Khandekar S (2012) Optimum Nusselt number for simultaneously developing internal flow under conjugate conditions in a square microchannel. J Heat Transf 134(7):071703, 01–10
4. Jin L, Lee J, Jeong S (2020) Investigation on heat transfer in line chill-down process with various cryogenic fluids. Int J Heat Mass Transf 150:119–204
5. Kim T, Kim Y, Kim SK (2011) Numerical study of cryogenic liquid nitrogen jets at supercritical pressures. J Supercrit Fluids 56:152–163
6. Mohammed J, Mohizin A, Roy KER (2020) Experimental investigations on transient cryogenic chill down of a short horizontal copper transfer line. Sadhana 45(12):01–10
7. Johnson J, Shine SR (2015) Transient cryogenic chill down process in horizontal and inclined pipes. Cryogenics 71:07–17
8. Hu H, Chung JN, Amber SH (2012) An experimental study on flow patterns and heat transfer characteristics during cryogenic chill down in a vertical pipe. Cryogenics 52:268–277
9. Mohammed J, Mohizin A, Sasikumar S, Kafle S, Shameer M, Roy KER (2018) Experimental investigations on helical and straight cryogenic transfer lines under different mass flux. Int J Sci Eng Res 9(5):698–703
10. Tiwari N, Moharana MK (2021) Effect of conjugate heat transfer in single-phase laminar flow through partially heated microtubes. Sadhana 46(28):01–12
11. Lee PS, Garimella SV (2006) Thermally developing flow and heat transfer in rectangular microchannels of different aspect ratios. Int J Heat Mass Transf 49:3060–3067
12. Bai X, Yi Y, Liu C, Zhang W, Nakayama A (2021) A simple conjugate analysis and its comparison with experiment for heat transfer problems associated with hot gas flows in a partially transpiration-cooled channel. Int J Heat Mass Transf 165(120729):01–09

13. Li Z, He YL, Tang GH, Tao WQ (2007) Experimental and numerical studies of liquid flow and heat transfer in microtubes. Int J Heat Mass Transf 50:3447–3460
14. Al-Ajlan SA (2006) Measurements of thermal properties of insulations materials by using transient plane source technique. Appl Therm Eng 26:2184–2191
15. Kim CS (1975) Thermophysical properties of stainless steel. Argonne National Laboratory, National Technical Information Service, United States Department of Commerce, Illinois, USA
16. Weisend JG, Flynn TM (2016) Cryostat design: case studies, principles and engineering. Springer International Publishing, Cham, Switzerland

Initial Flow Behavior in Laminar Line Source Twin Plumes of Equal Strength

Ujjwal Chetan, Prabir Kumar Kar, Toshan Lal Sahu, Saurabh Dhopeshwar, and Rajaram Lakkaraju

1 Introduction

Thermal plumes are nothing but convection patterns popping up as a result of localized heating in a fluid system, such as deep-sea hydrothermal vents, incense smoke, and chimney smoke. Its initial morphology consists of three basic components: mushroom cap, stem, and boundary layer. It has been observed by [17, 20, 22, 23, 30] that mostly laminar plumes are the initial main constituent structures, which subsequently gives rise to large-scale circulations in moderate to high Rayleigh number ($\sim 10^9$), where Rayleigh number is a dimensionless number associated with buoyancy-driven flows to characterize the flow regime as laminar, transition, or turbulent. As an instance, [27] showed, based on the experimental study on Rayleigh Benard Convection (RBC), how (i) the interactions among plumes via large-scale vortices and (ii) the interaction of plume with large-scale vortices, generated by plume itself, results in large-scale horizontal motion and steady-state circulations. Therefore, studying the interactions of the laminar thermal plumes is quite relevant.

For the plumes manifesting at the atmospheric level, some notable works have been done by [3, 4, 12, 24–26]. Apart from that, there are few works on laminar plumes that can be closely observed on a heated plate, ice formation, room heater, etc. In this regard, extending the analytical work of [1, 13] explained the constant head rise velocity of the plume cap using Rankine fairing, i.e., a combination of a uniform flow, a source, and a sink, in the potential flow. They also explained that the expansion of the plume head is because of thermal diffusion. The shape of the

U. Chetan (✉) · S. Dhopeshwar · R. Lakkaraju
Department of Mechanical Engineering, IIT Kharagpur, Kharagpur 721302, India
e-mail: ujjwalchetan00001@gmail.com

T. L. Sahu
Advanced Technology Development Centre, IIT Kharagpur, Kharagpur 721302, India

P. K. Kar
School of Energy Science and Engineering, IIT Kharagpur, Kharagpur 721302, India

cap is unaffected at the far field by the shape of the heater. They came up with some empirical correlations for boundary layer thickness at the point source heater, cap-tip rise velocity, and the average temperature at the heat source for different Rayleigh numbers. Kaminski and Jaupart [9] explained that plume rise velocity has insignificant dependence on Prandtl number (σ), though it increases with σ. After initial instability up to approximately five times the heater diameter, the plume attains a constant terminal rise velocity, again supporting what was reported by [13]. Furthermore, [21] experimentally reported that for Richardson number (Ri, which is the ratio of buoyancy and inertia force) greater than unity, a stable vortex ring with retained mushroom shape is observed as the plume develops. But, for $Ri < 1$, plume heads are unconfined due to the flow feeding the vortex ring failing to close.

Regarding the plume interactions, some literature is also noteworthy. The bending effect of a pair of point and line source plumes of different strengths is experimentally studied by [19]. The plume stems bend toward each other, as a result of the constricted flow of entrained fluid, between them. Based on the different strengths of the sources and their separations, they correlated the bend angle of the plume stem. Later, [6] developed the mathematical model for the entrainment mechanism for two unequal strength laminar plumes placed side by side. Moses et al. [14] explained the merging phenomenon of twin plume caps when placed side by side, using a potential flow model consisting of a uniform flow, a source, and a sink per plume. The criterion for merging the two laminar point source plumes was developed by [13] in terms of source separations. A theoretical model for explaining the merging height, flow rate after merging, and virtual origin of the merged turbulent plume was developed by [11]. Although it overestimated the merging height, it explained well the other plume interaction features. An experiment to explain the heat distribution in a closed chamber due to the merging of two laminar plumes was conducted by [7], and they found that with the increase in source separation, the mean Nusselt number of the top wall increases. Durve et al. [2] propounded that mixing is more prominent and efficient for three jets as compared to two jets for the same governing parameters. Based on the inclination of the enclosure, aspect ratio (1, 5, 10), source separations, and Rayleigh number ($10^3 - 10^6$), twin point source plume interaction was studied, and they found that the maximum heat transfer takes place at an inclination of $60°$ while at $180°$, the effect of Ra is insignificant. Moreover, the Nusselt number (Nu) gets reduced by 15% by decreasing the source separations. When two thermal plumes interact in a ventilated chamber, thermal stratification takes place in the chamber's environment over time. In this line, for a pair of turbulent plumes, [5] reported the height of the thermal stratification decreases with an increase in source separation, and beyond a threshold value, it is unaffected by the source separations. As most large-scale circulations are initiated by laminar plume interactions only, [29] studied the interaction of three buoyant plumes placed equidistant, at the same height, in light of large-scale circulations. They found that based on local instabilities near the heater, there are three types of plume interactions (left slanting, right slanting, and axisymmetric) that result in totally different large-scale flow patterns in all three cases. For $10^8 \leq \text{Ra} \leq 10^{10}$, the touching height of two turbulent plumes was found

to be increasing non-linearly, with an increase in source separations as reported by [28].

As most of the works are related to turbulent plume interactions or within a closed or ventilated chamber, in this article, we have studied the initial flow structures of the laminar plume interactions, with constant heat flux being supplied at line sources, in an ambient open environment. The Rayleigh number, thus defined in terms of heat flux, is termed as the Rayleigh flux number [13]. Keeping the effective Rayleigh flux number ($Ra_f = 1 \times 10^6$), we have varied the source separations and studied its effect on flow structures and heat transfer in the near field. Here, effective Ra_f is calculated considering the twin plume sources as one effective source, whose surface area and power supply are the summed-up surface area and power supply of the individual heaters, respectively.

2 Mathematical Modeling

In the present work, we are trying to understand the initial flow features when the two equal strength laminar plumes interact in a quiescent environment. For this, we have carried out direct numerical two-dimensional simulations, for effective $Ra_f = 1 \times 10^6$ and $\sigma = 7$, for different test cases, based on source separations (i) $2D$, (ii) $3D$, (iii) $4D$, (iv) $5D$, (v) $6D$, and (vi) equivalent single plume, where D is the diameter of cylindrical heat source. A constant power P (W) is supplied at each heat source in the domain. Based on the observations, the merged height of two infant plumes, at the largest separation ($6D$), is $\sim 60D$, suggesting to consider the domain size larger than that so that the behavior of the merged plume can be studied properly. Also, the two infant plumes, after merging, eject side masses, which travel in lateral directions. Therefore, to accommodate all these flow features, we have chosen the domain size as $200D \times 205D$, with the two cylindrical heat sources of diameter D, placed side by side, at equal height, symmetrically in the domain, at an offset of $5D$ from the bottom boundary, so that the boundary effect can be minimized (Fig. 1). Since our interest is only limited to the initial flow features in the near field, we can expect the plume to behave as laminar in the Ra_f range up to $= 1 \times 10^9$ [27].

The main governing equations are continuity (1), momentum (2), and energy Eq. (3), with Boussinesq approximations for modeling the density of the fluid, as the temperature variations are insignificant for laminar flows.

$$\nabla \cdot \mathbf{u} = 0, \tag{1}$$

$$(\partial_t + \mathbf{u} \cdot \nabla)\mathbf{u} = -\frac{1}{\rho}\nabla p + \nu\nabla^2\mathbf{u} + g\alpha(T - T_m), \tag{2}$$

$$(\partial_t + \mathbf{u} \cdot \nabla)T = \kappa\nabla^2 T \tag{3}$$
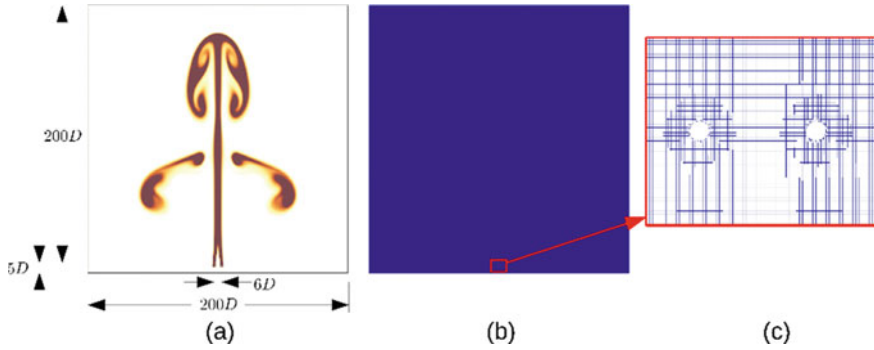
Fig. 1 Schematic diagram of twin plume system: **a** domain dimensions expressed in terms of heater's diameter (D) with a sample temperature contour for $Ra_f = 1 \times 10^6$, $\sigma = 7$ and $t/\tau = 39.67$, **b** mesh distribution ($n_x \times n_y \equiv 1200 \times 1230$), **c** enlarged view of the mesh refinements, near the heat sources

Here, $\mathbf{u} = (u, v)$ is the velocity vector field, p is the dynamic pressure field (hydrostatic component subtracted), T is the temperature field, κ is the thermal diffusivity of fluid, ρ, ν, α being the density, kinematic viscosity, and thermal expansion coefficient of the fluid under consideration, respectively. T_m is the mean temperature of the domain. For non-dimensionalisation of the governing Eqs. (1, 2, 3), R, R^2/κ and $P/R\kappa\rho C_p$ are length, time (τ) and temperature (χ) scales in order, which gives rise to following set of non-dimensionalised equations:

$$\nabla \cdot \mathbf{u} = 0, \tag{4}$$

$$(\partial_t + \mathbf{u} \cdot \nabla)\mathbf{u} = -\nabla p + \sigma \nabla^2 \mathbf{u} + Ra_f(T - T_m)\hat{y}, \tag{5}$$

$$(\partial_t + \mathbf{u} \cdot \nabla)T = \nabla^2 T \tag{6}$$

Thus, we get some relevant non-dimensional parameters like Prandtl number ($\sigma = \nu/\kappa$), which is the ratio of momentum diffusivity to thermal diffusivity, and Rayleigh flux number ($Ra_f = g\alpha P R^2/\kappa^3 \rho C_p$) which is Rayleigh number defined in terms of heat flux, injected at the source of the heater.

Outer boundaries are open, i.e., for outflow (velocity vector pointing outward of the domain), $\nabla p = 0$, $\nabla T = 0$, and $\nabla u_\perp = 0$, while for inflow (velocity vector pointing inward of the domain), we considered $p = 0$, $T = 0$ and $\nabla u_\perp = 0$. At the heater surface, the no-slip boundary condition for velocity, the zero-gradient boundary condition for pressure, and the fixed gradient temperature condition ($\nabla T = P/2\pi Rl\kappa\rho C_p$) are applied as we are considering constant heat flux at the source. Here, l and R are unit length and heater's radius, respectively.

The governing Eqs. 4, 5, and 6 are solved using OpenFOAM finite volume solver [8] whose numerical code has been validated by [10, 15, 16, 18], extensively.

Spatial discretizations are done using Gauss linear scheme, while temporal terms are discretized using the Euler scheme. Equations 4 and 5 are solved using the PISO algorithm (pressure implicit with splitting of operator), which involves one predictor step and two corrector steps. This algorithm is well suited for pressure–velocity coupled equations. A uniform structured mesh with mesh size 1200 in horizontal direction (n_x) and 1230 in vertical direction (n_y) has been used for all source separations. These refined meshes are carefully chosen after thoroughly conducting grid independence tests to ensure the physics is independent of the grid size. Moreover, local refinements are performed in the vicinity of the heater so that the thermal and viscous boundary layers can be captured properly (Fig. 1).

3   Results and Discussion

As the constant heat flux is injected at the heater, the boundary layer develops in the vicinity of the heater. Sooner, due to Rayleigh–Taylor instability at the boundary layer, a lump of hot fluid rises up against the quiescent cold fluid environment. As a result of the continuous injection of rising hot fluid, having an upward velocity, against the stationary ambient fluid, the hotter fluid starts accumulating at the plume front and then onwards, rolls up sideways due to the shear action of the surrounding fluid. This results in a mushroom cap like plume head, which subsequently grows in size and moves upward because of buoyancy (see Fig. 2a). In the case of twin plumes of equal strength, placed at different source separations (d), the two infant plumes at first grow by themselves and then, due to constriction in the entrained fluid in between, bend toward each other and start merging [14, 19]. Sooner, the two infant plume heads pinch off sideways in the form of mass ejections, and the central stem rises up with the merged plume head in the downstream direction. It can be seen from Fig. 2b–f that in the case of two sources, the amount of ejected mass increases with an increase in source separations. Also, for the same instant of time, the rise height decreases with an increase in d. With more mass ejected subsequently, the mushroom cap size also decreases for larger d.

From Fig. 2, it can be seen that provided the equal time to plume growth, the horizontal spread of the hotter buoyant fluid is more in case of larger source separations. A vertical line of length $190D$ at an offset of $6D$ from the origin (the midpoint joining the line of the centers of the two cylindrical heaters) is drawn to quantify the same. Then, the total heat crossing it from time $(t/\tau)_i = t_i^* = 0$ to $(t/\tau)_o = t_o^* = 34.0$ has been calculated using the relation:

$$Q = \int_{t_i^*}^{t_o^*} \overline{q_x} dt^*, \tag{7}$$
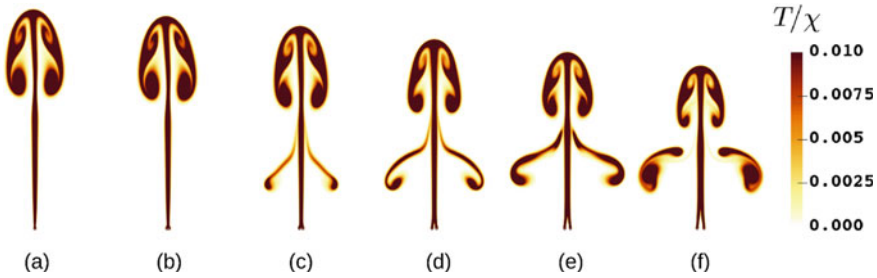
Fig. 2 Snapshot of the plume development in the twin plume system for $Ra_f = 1 \times 10^6$ at $t/\tau = 34.59$ for **a** equivalent single plume and at source separations, **b** 2*D*, **c** 3*D*, **d** 4*D*, **e** 5*D*, **f** 6*D*. Here, the equivalent single plume is a plume system with same effective Ra_f, but there is only one heater of radius *R*. Temperature fields are normalized by the steady-state average temperature of the heat source, for single plume system, corresponding to $Ra_f = 1 \times 10^6$

where,

$$\overline{q_x} = \frac{1}{L} \int_0^L u(T - T_0)\mathrm{d}l \tag{8}$$

Here, u is the x-component of velocity, T_0 is the initial temperature field at $t/\tau = 0$, and $\overline{q_x}$ is the heat flux in x-direction, averaged over the vertical line from $l = 0$ to $l = L$, where $L = 190D$. As per Fig. 3, the total heat transfer increases with an increase in source separations in a quadratic fashion, which supports the observations of Fig. 2. This behavior can be explained as follows. With the increase in the source separations, the plume takes a longer time to merge as it has to travel more distance in the horizontal direction to reach each other. This longer merging time generates a bigger accumulation of hot fluids at the merge point, which are ejected sideways. As most of the hot fluid is ejected sideways, the final mushroom cap also reduces in size for larger source separations. So, this ejected mass sideways mostly contributes to increased heat transfer in the horizontal direction as far as initial flow dynamics are concerned.

As the plume merges and rises, it involves entrainment of the ambient fluid into the mainstream, and recirculation currents develop too. Moreover, the merging phenomenon must involve some mixing of the streams coming from the two plumes. All these flow dynamics may disturb the stability of the vertical plume rising. To understand this, root mean square of y-component of velocity fluctuations has been calculated for the whole domain, for time range $t/\tau = 0$ to $t/\tau = 41.66$, as shown in Fig. 4. It can be observed from the contour that most of the fluctuations in vertical velocity are concentrated along the vertical axis of the flow passing through the origin. As the separation increases, the v'_{rms} spreads horizontally more, resulting in less concentration along the centerline. To understand it further, we plotted the v'_{rms}
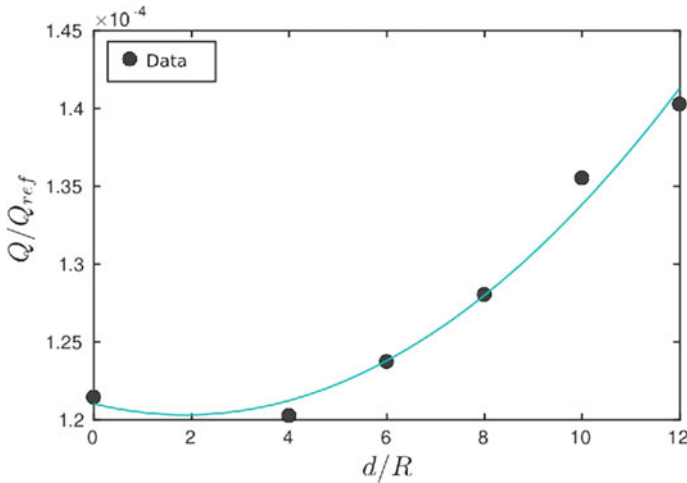
Fig. 3 Total heat crossing a vertical line of height 190D at an offset of 6D offset of the origin (the midpoint of the line connecting the two heat sources) from $t/\tau = 0$ to $t/\tau = 34.04$ in the horizontal direction. The line is carefully chosen to neglect the boundary effect (10D offset from the top and 5D offset from the bottom). Here, $Q_{\text{ref}} = R\chi$

along the centerline for different d (refer Fig. 5a). It can be observed that up to $y/R \sim 180$ (which is a height sufficient to ensure completion of merging of the two plumes for all the 6 cases), the lowest separation had the highest v'_{rms}, while just after it, the case is the opposite. After sideways mass ejection, a lesser amount of hot fluid will be retained along the centerline, so they will rise with lesser velocity giving rise to lesser v'_{rms}. But the peak value of v'_{rms} is observed largest, for the equivalent single Plume, and this $\left(v'_{\text{rms}}\right)_{\text{max}}$ has been plotted against source separations d (refer Fig. 5b). It decreases with an increase in source separations following a fitting curve given by:

$$\frac{\left(v'_{\text{rms}}\right)_{\text{max}} R}{\kappa} = a\left(\frac{d}{R}\right)^2 + b\left(\frac{d}{R}\right) + c \tag{9}$$

where $a = -0.06$, $b = -0.07$, and $c = 28.70$. The higher value of v'_{max} can cause instability in the central laminar stem. It can be concluded that with the increase in source separations, the merged plume will rise in a more stable way as compared to smaller separations. This also assures a larger height of rise in the far field before deflecting sideways or starting the swaying motion.

(a)   (b)
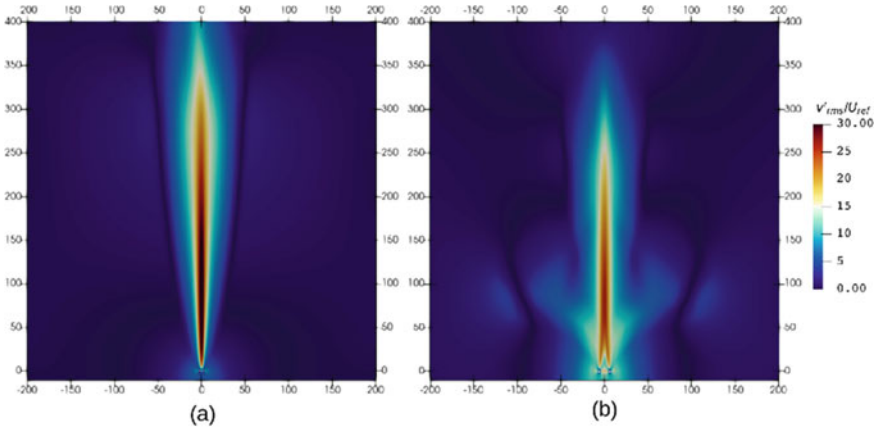
Fig. 4 $v'_{\mathbf{rms}}/U_{\mathbf{ref}}$ plotted for the whole domain for **a** $d = 2D$ and **b** $d = 6D$. Here, $U_{\mathrm{ref}} = \kappa/R$, $v'_{\mathbf{rms}}$ is the root mean square of the fluctuation in the vertical component of the fluid velocity, given by

$$v'_{\mathbf{rms}} = \sqrt{\frac{1}{(t_o-t_i)}\int_{t_i}^{t_o}(v-\overline{v})^2 dt},$$ where t_i is the initial time and t_o is the final time, $\overline{v}$ is the temporal mean vertical velocity at a cell

(a)   (b)
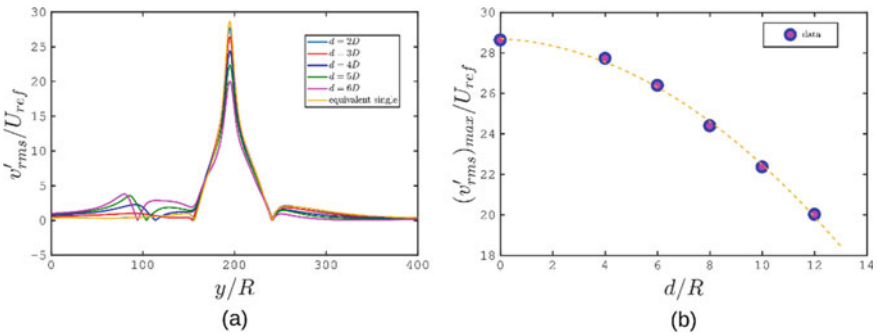
Fig. 5 **a** v_{rms} plot along the centerline for different source separations and **b** maximum v_{rms} with different source separations. Here, $U_{\mathrm{ref}} = \kappa/R$, and the dashed yellow line is just for guiding the eye

4 Conclusion

Twin line source laminar plumes, placed side by side in an open, quiescent ambient, have been studied for a range of source separations and a fixed effective Rayleigh flux number (1×10^6) in light of near-field flow characteristics. It has been observed that each of the infant plumes rises with the development of mushroom-like plume heads, which attract each other due to congested entrained fluid in between, leading to merging. This merging phenomenon is accompanied by side mass ejections and an emergence of a single merged plume out of the two infants. The side mass ejections

are found to be increasing with source separations, and also, the cap size of the merged plume decreases as most of the masses are drained off sideways, with larger separations of the sources. These mass ejections contribute to an enhanced lateral heat transfer with larger source separations, and the trend is quadratic in nature. We further noticed that the fluctuations in downstream velocities are distributed away from the centerline with larger source separations. This is because of the draining away of the hotter fluid from the center line in the form of side mass ejections after merging. Moreover, the maximum v'_{rms} has been found to decrease with an increase in source separations, suggesting a more stable plume rise with lesser chances of swaying off or deflections sideways in the near field.

Nomenclature

d	Source separation [m]
g	Gravitational acceleration [m/s^2]
p	Dynamic pressure [kg/ms^2]
P	Power supplied at source [W]
$\overline{q_x}$	Mean heat flux in x-direction [W/m^2]
Q	Total heat transfer [J]
Q_{ref}	Reference total heat transfer [J]
R	Radius of the cylindrical heater [m]
Ra_f	Rayleigh flux number
t	Time [s]
T	Temperature field [K]
T_m	Mean temperature [K]
u	X-Component of velocity field [m/s]
v	Y-Component of velocity field [m/s]
$\mathbf{u}$	Velocity field vector [m/s]
U_{ref}	Reference velocity [m/s]
v'_{rms}	Root mean square of vertical velocity fluctuation [m/s]
σ	Prandtl number [–]
ν	Kinematic viscosity [m^2/s]
α	Thermal expansion coefficient [1/K]
κ	Thermal diffusivity [m^2/s]
ρ	Fluid density [kg/m^3]
τ	Reference time [s]
χ	Reference temperature [K]

References

1. Batchelor GK (1954) Heat convection and buoyancy effects in fluids. Q J R Meteorol Soc 80(345):339–358
2. Durve A, Patwardhan AW, Banarjee I, Padmakumar G, Vaidyanathan G (2012) Numerical investigation of mixing in parallel jets. Nucl Eng Des 242:78–90
3. Fay JA (1973) Buoyant plumes and wakes. Annu Rev Fluid Mech 5(1):151–160
4. French SW, Romanowicz B (2015) Broad plumes rooted at the base of the earth's mantle beneath major hotspots. Nature 525(7567):95–99
5. Gao X, Li A, Yang C (2018) Study on thermal stratification of an enclosure containing two interacting turbulent buoyant plumes of equal strength. Build Environ 141:236–246
6. Gebhart B, Shaukatullah H, Pera L (1976) The interaction of unequal laminar plane plumes. Int J Heat Mass Transf 19(7):751–756
7. Ichimiya K, Saiki H (2005) Behavior of thermal plumes from two-heat sources in an enclosure. Int J Heat Mass Transf 48(16):3461–3468
8. Jasak H, Jemcov A, Tukovic Z et al (2007) Openfoam: a C++ library for complex physics simulations. In: International workshop on coupled methods in numerical dynamics, vol 1000. IUC Dubrovnik Croatia, pp 1–20
9. Kaminski E, Jaupart C (2003) Laminar starting plumes in high-Prandtl-number fluids. J Fluid Mech 478:287–298
10. Kar PK, Kumar YN, Das PK, Lakkaraju R (2020) Thermal convection in octagonal-shaped enclosures. Phys Rev Fluids 5(10):103501
11. Kaye NB, Linden P (2004) Coalescing axisymmetric turbulent plumes. J Fluid Mech 502:41–63
12. List EJ (1982) Turbulent jets and plumes. Annu Rev Fluid Mech 14(1):189–212
13. Moses E, Zocchi G, Libchaberii A (1993) An experimental study of laminar plumes. J Fluid Mech 251:581–601
14. Moses E, Zocchi G, Procaccia I, Libchaber A (1991) The dynamics and interaction of laminar thermal plumes. EPL (Europhys Lett) 14(1):55
15. Nandukumar Y, Chakraborty S, Verma MK, Lakkaraju R (2019) On heat transport and energy partition in thermal convection with mixed boundary conditions. Phys Fluids 31(6):066601
16. Pandey A, Kumar A, Chatterjee AG, Verma MK (2016) Dynamics of large-scale quantities in Rayleigh-Bénard convection. Phys Rev E 94(5):053106
17. Pandey A, Scheel JD, Schumacher J (2018) Turbulent super-structures in Rayleigh-Bénard convection. Nat Commun 9(1):1–11
18. Pandey A, Verma MK (2016) Scaling of large-scale quantities in Rayleigh-Bénard convection. Phys Fluids 28(9):095105
19. Pera L, Gebhart B (1975) Laminar plume interactions. J Fluid Mech 68(2):259–271
20. Poel EPVD, Verzicco R, Grossmann S, Lohse D (2015) Plume emission statistics in turbulent Rayleigh-Bénard convection. J Fluid Mech 772:5
21. Rogers MC, Morris SW (2009) Natural versus forced convection in laminar starting plumes. Phys Fluids 21(8):083601
22. Solomon TH, Gollub JP (1990) Sheared boundary layers in turbulent Rayleigh-Bénard convection. Phys Rev Lett 64(20):2382
23. Sparrow EM, Husar RB, Goldstein RJ (1970) Observations and other characteristics of thermals. J Fluid Mech 41(4):793–800
24. Turner JS (1969) Buoyant plumes and thermals. Annu Rev Fluid Mech 1(1):29–44
25. Woods AW (2010) Turbulent plumes in nature. Annu Rev Fluid Mech 42:391–412
26. Worster G, Moffatt K, Batchelor G (2000) Perspectives in fluid dynamics: a collective introduction to current research. Cambridge University Press, Cambridge, UK
27. Xi HD, Lam S, Xia KQ (2004) From laminar plumes to organized flows: the onset of large-scale circulation in turbulent thermal convection. J Fluid Mech 503:47–56
28. Yang C, Li A, Gao X, Ren T (2020) Interaction of the thermal plumes generated from two heat sources of equal strength in a naturally ventilated space. J Wind Eng Ind Aerodyn 198:104085

29. Yin S, Li Y, Fan Y, Sandberg M (2018) Unsteady large-scale flow patterns and dynamic vortex movement in near-field triple buoyant plumes. Build Environ 142:288–300
30. Zocchi G, Moses E, Libchaber A (1990) Coherent structures in turbulent convection, an experimental study. Physica A 166(3):387–407

Influence of Liquid Discharge Rate on the Genesis of Bathtub Vortices with Air-Entrained Structures During Draining of a Water Pool Through Multiple Outlets

Rahul Kumar Mondal and Parmod Kumar

1 Introduction

There are several applications for free surface vortices in both natural and industrial environments. At the inception, the free surface appeared as a shallow dip on the gas–liquid interface, and its further propagation led to the formation of a spiral-shaped hollow air core within the liquid. These types of situations usually occur when liquids flow from a larger container to a very small pipe outlet. Frequently encountered free surface vortices occur when emptying bathtubs [1–4] or sinks [5], in hydropower stations, during pumping, in turbine intakes, and when air is trapped in hydraulic jumps [6]. It is the presence of velocity within the free surface vortex that distinguishes it from other vortices [5]. The presence of swirling flow associated with free surface vortices causes a decrease in the efficiency of hydraulic machines. At fully developed conditions, free surface vortices pull air–liquid combinations and different floating materials in the intakes which are harmful to the rotating part of the hydraulic machinery. Since the free surface vortex observed to reveal its presence in a diverse place in nature and human applications, it is important to understand its physical behavior. A lot of experimental and computational analysis is done in the past by scientists, physicists, and engineers to understand the behavior of air-entrained vortex and still getting new insights of the phenomenon through sophisticated techniques, so that it can be used to harness our interests. Rankine et al. [7] provided a theoretical description of the circular flow associated with free surface vortices. In the Rankine vortex model, the core of the vortex is considered identical to the solid-body rotation, and the region away from the core is formulated as vorticity

R. K. Mondal · P. Kumar (✉)

School of Mechanical and Materials Engineering, Indian Institute of Technology Mandi, Kamand, Himachal Pradesh 175075, India

e-mail: parmod@iitmandi.ac.in

free, where velocity is inversely proportional to the distance in the radial direction. This model includes a simple mathematical relation of tangential velocity for both the regions to demonstrate the associated fluid flow dynamics. The Rankine vortex model is significant for a non-viscous fluid. Burgers [8], Rott [9], and Sullivan [10] also introduced a mathematical model for free surface vortex. In their formulation, the profile of tangential velocity is more realistic as the presence of eddy viscosity is considered. Ahmed et al. [1] have studied the generation of a plughole vortex and its consequences in a drainpipe during drainage of water from a stationary rectangular tank by using experimental and numerical analysis. Their numerical investigations used the volume of fluids multiphase model, which was earlier developed by Hirt and Nichols [11]. The analysis used three different methods for estimating the critical height, namely, measurement of critical height using drain flow rate, estimation of critical height from flow visualization, and calculation of critical height from Lubin and Springer [LS] correlation [12]. Studies reveal the generation of plughole vortex as soon as the free surface reaches the critical height. In the initial stage, the plughole vortex looks like a shallow dip, and further in time, it grows to an inverted cone shape. As the vortex tip reaches the inlet of the out pipe, the droplet-shaped air bubble is detached from the tip of the vortex. These bubbles are driven by the flowing water in the outlet pipe, which is further converted into a donut-shaped bubble ring. The flow becomes bubbly in the outlet pipe which is further converted into slug flow and finally becomes an annular flow. Experimental and numerical studies were performed by Rathaur and Ghosh [13–15] to determine the influence of liquid properties and outlet pipe location on square tank drainage behavior. There are four types of liquids used in this process: 60% glycerine, water, 20% glycerine, and kerosene. Three different positions are used to connect the drainpipe with an inner diameter of 9 mm. Bubbles, slugs, churns, extended slugs, and annular flows are observed within the drain port. There is a proposed empirical correlation indicating that discharge time varies with the kinematic viscosity of the liquid due to the eccentricity of the connection. In the reservoir, the liquid height changes quadratically as time passes.

The previous experimental studies were only limited to observing the genesis of the plughole vortex and subsequent air entrainment when liquid is draining out from a single outlet.

In the present study, we investigated the genesis of vortex formation when liquid is discharged through multiple outlets from a rectangular tank. The spacing between two outlets and ratio of their liquid discharge rates are considered the controlling parameters in the present experiments. Symmetric and asymmetric vortex profiles are obtained for equal and unequal discharge rates between the two outlets. The critical water level at which vortex formation starts is obtained using visualization of the free surface. The paper is organized as follows: Sect. 2 introduces the experimental setup and the procedure used in the present experiments. Section 3 discusses the results obtained from the present experiments. Lastly, Sect. 4 concludes the key findings of the experimental investigations.

2   Experimental Setup and Procedure

Experimental studies have been conducted to understand different fluidic structures under varying conditions when water is draining due to pure gravity under stationary and steady-state conditions. A schematic diagram of the experimental setup for multiple outlets drainage is shown in Fig. 1. The stationary tank measures 0.68 m × 0.53 m × 0.40 m in size and is made from an acrylic sheet with a thickness of 0.01 m. This tank is located at a height of 1.14 m off the ground and is mounted on a metallic structure. The bottom of the tank has two holes for accommodating transparent drainpipes of 44 mm diameter. This study defines pitch (P) as the central distance between outlet pipes. Experiments were conducted at $P = 1.35d$, and $P = 5d$ where d is the internal diameter of the drainpipe. The length of the drainpipes is considered 400 mm. The inlet of the drainpipes has been raised 100 mm above the bottom of the tank so that the plughole vortex can be clearly seen into both drainpipes. Every drainpipe outlet is equipped with two shutoff valves. Water is held in a tank by the first valve while the second valve is used to control the drainage rate. The six equi-spaced angular positions are used to obtain the variable flow rates. A pair of collectors is placed just below the drainpipe outlets to receive the water during the draining process. The drain times of individual drainpipes were measured using two stopwatches for all experiments. During experiments, the initial water height has always been 113 mm above the inlet of the drainpipe. All experiments are designed to avoid the initial denting of free surfaces by choosing the right level of water. Each experiment begins with a 30-min waiting period to achieve stagnant conditions throughout the water pool. A high-speed camera measures the transition from the free surface to a plughole vortex within a tank, as well as the transition from a droplet-shaped bubble to an annular air core fluidic structure, at a rate of 50–125 frames per second. There are two DC light sources of 50 W placed just behind the tank, and a translucent sheet is used as a diffuser. To measure the initial level of water within the tank, two metallic scales have been pasted on the front wall of the tank. All experiments are conducted with water as the working fluid. Each experiment was repeated five times for confirmation of the repeatability of the results. Under atmosphere pressure and temperature, all experiments are performed. Water properties are taken as density (ρ) of 998.4 kg/m^3; dynamic viscosity (μ) of 1.0266×10^{-3} Pa s. The surface tension between air and water is considered 0.072 N/m, and the density of air is 1.2 kg/m^3.
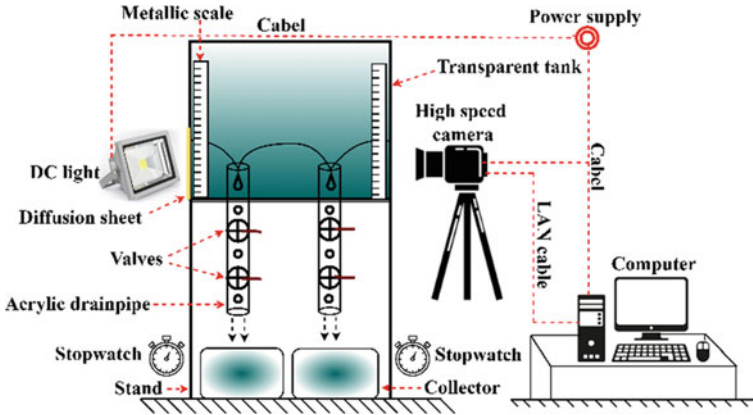
Fig. 1 Schematic diagram of the experimental setup

3   Results and Discussion

3.1   *Effect of Pitch*

Above both the outlets, the free surface appears perfectly flat at the beginning of draining process. A multiple point outlet with $P = 5d$ generates two surface dips above the outlet pipes ($t = 0$ s in Fig. 2b), whereas a multiple point outlet with $P = 1.35d$ has a single surface dip in the center of outlets ($t = 0$ s in Fig. 2a). The surface dips have grown continuously and eventually reached the outlet pipe. In multiple point outlets with $P = 5d$, two separate surface dips, each expanding into their corresponding outlet pipe, but in multiple outlets with $P = 1.35d$, originate from a single center surface dip and extend into both outlet pipes (Fig. 2a). In addition, pendent-drop-shaped bubbles are pinched off from the tip of the cone-shaped free surface when surface dip entered the outlet pipe (Figs. 2 and 3). One important observation is noted that the tip of the inverted cone surface dip entered toward the inner wall of the drainpipe at $P = 1.35d$, and under this condition, shapes of the entered tip are asymmetric, while surface tip entered in the center of the drainpipe at $P = 5d$ and is completely symmetric. Figure 3 shows the temporal evolution of the plughole vortex and air-entrained structures from droplet-shaped bubbles to annular air core in water drainage for $P = 1.35d$. Initially, small-sized bubbles are pinched off from the surface tip when the water level is high. After passing some time with the draining process, the size of the bubbles is increased.

Decreasing water level decreases hydrostatic pressure which allows for expansion in bubble sizes. The generation of larger size bubbles is responsible for eventually causing slug flow in the drainpipe. At the end of slug flow, bubbles are merged with each other and form an annular flow. The draining process is completed with the annular flow, and the drain rate of water is minimum in this condition because the
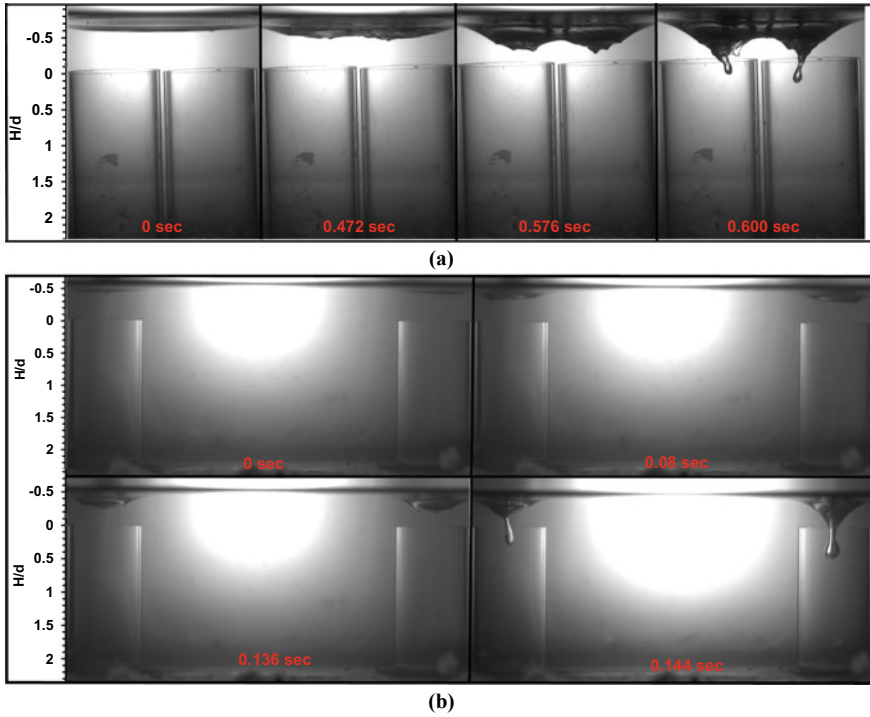
Fig. 2 Investigation of pitch effect on the initial generation of the surface dip formation in plughole vortex using multiple outlets for 44-mm drainpipe at **a** $P = 1.35d$ and **b** $P = 5d$

maximum pipe volume is covered with air. To locate the critical spacing between the outlets at which transition from single and vortex to two non-intracting vortices, more experiments need to be performed for a wide range of pitches.

We have also performed several experiments to examine the influence of different discharge rates between the two outlets. These differences in discharge rates are maintained by varying the opening position of the valves. The experimental findings are presented in terms of ratio of discharge rate between right and the left outlets, and it is termed the liquid discharge ratio in the present study. The effect the liquid discharge ratio on the genesis of the surface dip in the tank and air-entrained structures within the drainpipe is shown in Fig. 4 at $P = 1.35d$. We have achieved six different flow volumetric ratios by keeping one valve completely open while the second valve is fixed at 6 different opening positions during the draining process. From Fig. 4, it is seen that the inverted cone-shaped free surface is simultaneously entered into the drainpipe and droplet-shaped bubbles are also simultaneously pinched off from the tip at $Q_R/Q_L = 1$. Due to the symmetry generation of fluidic structures, they look like a mirror image of each other. Due to variation of flow rates in the drainpipe, vortex formation and occurrence of air entrainment phenomenon occurred early in the left drainpipe and delayed in the right drainpipe. At $Q_R/Q_L = 0.81$, bubbly flow
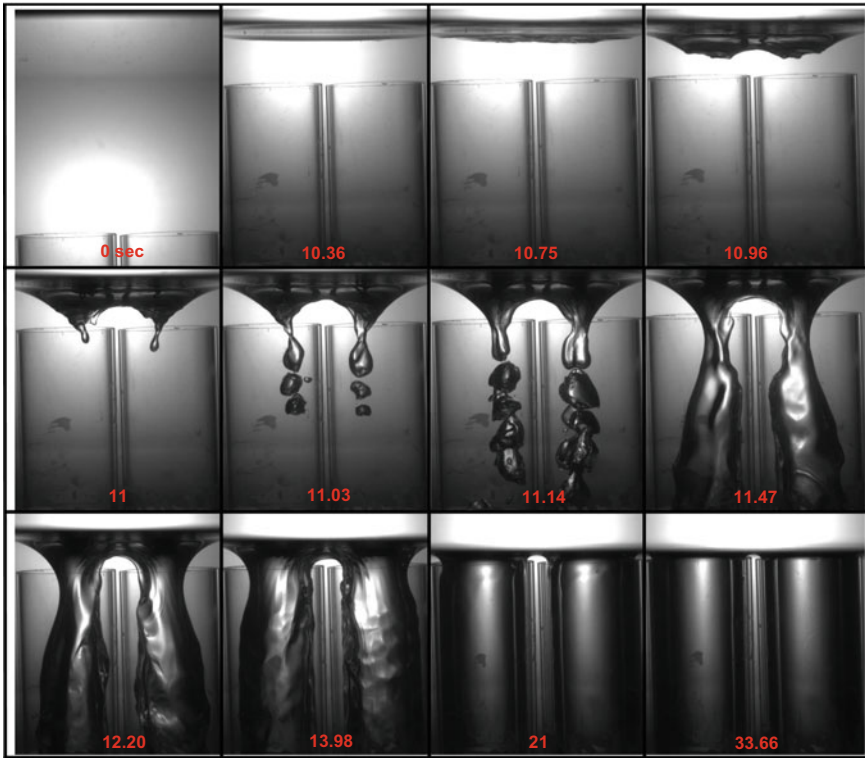
Fig. 3 Temporal evolution of surface dip to annular core within 44-mm drainpipe at $P = 1.35d$ and $Q_R/Q_L = 1$

is observed in the right pipe, whereas the initial stage of annular flow is observed in left drainpipe. The tip of the surface dip has just reached the inlet of right drainpipe where at that moment annular air core has partially developed within the left drainpipe by passing bubbly and slug flow at $Q_R/Q_L = 0.53$. The left drainpipe experienced vortex formation and air entrainment phenomenon early while the right drainpipe experienced it late.
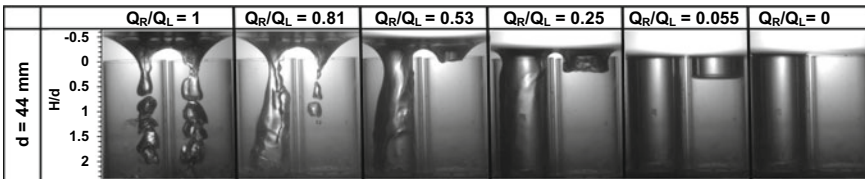
Fig. 4 Comparison of asymmetry fluidic structures at variable liquid discharge ratio within 44-mm drainpipe at $P = 1.35d$

Fig. 5 Obtained possible symmetry fluidic structures at $P = 5d$ for the different average liquid discharge rates

3.2 Effect of Liquid Discharge Ratio

An interesting result is observed in the right drainpipe from $Q_R/Q_L = 0.25$ to 0. At $Q_R/Q_L = 0.25$, a developed annular air core is observed in the left drainpipe after passing bubbly, slug, and partially developed annular air core phenomena. At that moment, a blunt surface dip enters into the right drainpipe at a lower water depth. Neither droplet-shaped bubbles pinched off from tip of blunt surface dip nor bubbly, and slug flows are observed within drainpipe. Blunt surface dip directly entered into the drainpipe in the form of annular air core with some perturbations at its tip. Similar results of $Q_R/Q_L = 0.25$ are also seen for the left drainpipe when we maintained $Q_R/Q_L = 0.055$. A negligible amount of water has passed between the outer surface of the cylindrical air core and the inner wall of the drainpipe. In $Q_R/Q_L = 0$ conditions, a fully developed annular air core is observed in the left drainpipe after passing bubbly, slug, and partially developed annular air core phenomena. This vortex appeared almost identical to that of vortex formation in single outlet system.

Figure 5 shows the experimental photographs to depict interfacial profiles at $P = 5d$ and different liquid discharge rates. It is to highlight that the entrained structures are almost the mirror images of each other in the two outlets and appears as observed in case of single outlet systems. This shows that at this spacing between the outlets, the two vortices are non-interacting.

The height of the free surface above the inlet of the drainpipe is measured using image analysis and plotted as function of time in Fig. 6. The height of the free surface has varied in a linearly with time indicating the constant liquid discharge rate, and after reaching the critical height, it varied non-linearly. This is the point where a dimple appeared in the free surface and further elongated with time. Transient Bernoulli's equation is also used to derive the variation of free surface height with time, and the final expressions are given in Eqs. (1) and (2) for single and two outlets, respectively.

$$H_f = \left(\sqrt{H_i} - \frac{t A_P C_d}{A_t} \sqrt{\frac{g}{2}} \right)^2 \tag{1}$$

$$H_f = \left(\sqrt{H_i} - \frac{2t A_P C_d}{A_t} \sqrt{\frac{g}{2}} \right)^2 \tag{2}$$

Fig. 6 Comparison of
experimental and theoretical
water depth variation for two
equal drainpipes diameters
of 44 mm at **a** $Q_R/Q_L = 0$
and **b** $Q_R/Q_L = 1$
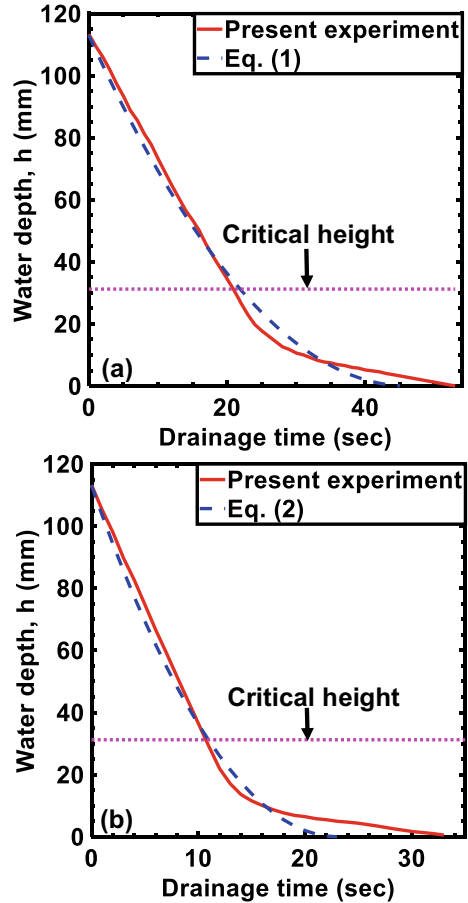
When these equations are plotted in Fig. 6 for two cases of single and two outlets, these show a close agreement with present experiments up to the critical height. The deviation between experimental and theoretical data is observed when the water height reached the critical height, indicated by a horizontal dotted line. With time, a surface dip develops, which eventually enters the drainpipe inlet after reaching critical height. Air entrainment was initiated by the entry of surface dip in the forms of bubbles, slugs, and annular flows. By entraining air into the tank, the water drains more slowly and takes longer to empty. During this time, the theoretical drain has remained the same. Plughole vortex and associated air entrainment phenomena during emptying water tanks are not included in the theoretical calculation of water depth variation with time.

4 Conclusions

This study investigates the effect of liquid discharge ratios on the genesis of bathtub vortices in multiple outlet drainage systems. This study revealed the following key findings:

1. There is good agreement between the experimental and theoretical drain flow rates for $Q_R/Q_L = 0$ and $Q_R/Q_L = 1$.
2. For multiple outlets at $P = 5d$, two separate surface dips occur and expand into respective outlets.
3. It is quite evident that for $P = 1.35d$, a single surface breaks into two surface dips very close to outlets and enters the respective outlet pipes after splitting into two.
4. Asymmetric free surface profiles and corresponding entrained air structures are observed when $Q_R/Q_L \neq 1$.
5. The transition from drop-shaped bubbles to annular air core takes place in drainpipe through bubbly and slug flows at high liquid discharge rates, and direct annular flow pattern is observed at low liquid discharge rates.
6. The critical height of the free surface can be decreased by decreasing the liquid discharge rate; however, it increases the total drainage time. Therefore, multipoint outlets can serve the purpose of mitigating vortex formation and improving the drainage time.

Nomenclature

Q_R	Average drain rate of the right pipe [m³/s]
Q_L	Average drain rate of the left pipe [m³/s]
H_c	Critical height [m]
r	Radius of drainpipe [m]
g	Acceleration due to gravity [m/s²]
H_i	Initial water height [m]
H_f	Final water height [m]
C_d	Coefficient of discharge [–]
A_t	Area of rectangular tank [m²]
A_p	Cross-sectional area of pipe [m²]

References

1. Ahmed R, Lim H (2017) Study of air-core vertical flow structure induced by a plughole vortex. J Fluid Mech 823:787–818
2. Andersen A, Bohr T, Stenum B, Rasmussen JJ, Lautrup B (2006) The bathtub vortex in a rotating container. J Fluid Mech 556:121–146
3. Andersen A, Bohr T, Stenum B, Rasmussen JJ, Lautrup B (2003) Anatomy of a bathtub vortex. Phys Rev Lett 91(10):104502
4. Sibulkin M (1962) A note on the bathtub vortex. J Fluid Mech 14(1):21–24
5. Cristofano L, Nobili M, Caruso G (2014) Experimental study on unstable free surface vortices and gas entrainment onset conditions. Exp Thermal Fluid Sci 52:221–229
6. Kumar P, Prajapati M, Das AK, Mitra SK (2018) Vortex formation and subsequent air entrainment inside a liquid pool. Ind Eng Chem Res 57(18):6538–6552
7. Rankine WJM (1858) Manual of applied mechanics. Griffin, London
8. Burgers JM (1948) A mathematical model illustrating the theory of turbulence. Adv Appl Mech 1:171–199
9. Rott N (1958) On the viscous core of a line vortex. Zeitschrift für angewandte Mathematik und Physik ZAMP 9(5):543–553
10. Sullivan RD (1959) A two-cell vortex solution of the Navier-Stokes equations. J Aerosp Sci 26(11):767–768
11. Hirt CW, Nichols BD (1981) Volume of fluid (VOF) method for the dynamics of free boundaries. J Comput Phys 39(1):201–225
12. Lubin BT, Springer GS (1967) The formation of a dip on the surface of a liquid draining from a tank. J Fluid Mech 29(2):385–390
13. Rathaur R, Ghosh S (2021) Interfacial dynamics of air–liquid flow in eccentric drainpipe while draining from a square tank. Exp Thermal Fluid Sci 124:110370
14. Rathaur R, Ghosh S (2022) An experimental study of interfacial dynamics during stratified oil-water draining from storage tank. Exp Thermal Fluid Sci 132:110547
15. Rathaur R, Ghosh S (2022) Numerical investigation of water draining and oil-water draining from a square tank—a comparison. Int J Multiph Flow 150:104001

Design and Numerical Analysis of a High Head Inducer for a Rocket Pump

T. V. Sanand, Nitin Rathee, K. Harikumar, P. Unnikrishnan Nair, N. Jayan, and G. Nageswaran

1 Introduction

The need of high thrust levels for future space transportation systems results in high combustion chamber pressures in liquid rocket engines. Rocket propellant fed turbopumps have inducers in order to avoid cavitation, improve the suction performance and reduce the propellant tank pressure and weight. The main task of the inducer is to provide a modest increase in pressure upstream of the main pump, typically a radial impeller, which in turns prevents cavitation and allows sufficiently reasonable operating conditions in the main pump. The optimum design, therefore, is a compromise that provides adequate suction performance while maintaining good overall efficiency under all operating conditions.

A broad outline of the various types of pumps and the typical expected performance vs specific speed is shown in Fig. 1. Inducers are axial flow pumps with high value of specific speeds (Ns > 2500 U.S. units). They are classified according to head rise capability and also according to the shape of the meridional flow path. According to [1], inducers in general fall into two categories, low head type with head coefficient, $\psi < 0.15$ and high head type, with $\psi > 0.15$. The high head designs are usually more efficient also.

A basic comparison of a low head and high head inducers is given in Fig. 2. High head inducers are typically distinguished by smoothly profiled hub contour and a high hub to tip diameter at the outlet to achieve a higher head coefficient. Earlier low head inducers were essentially axial flow impellers with constant-pitch helical blading and nearly uniform mean radius, mostly relying on the change in relative velocity for raising the fluid pressure. Instead, today's high head inducers are mixed-flow machines with tapered hubs, nearly cylindrical casings and variable-pitch blades, where a significant portion of the pressure rise is generated due to

T. V. Sanand · N. Rathee (✉) · K. Harikumar · P. Unnikrishnan Nair · N. Jayan · G. Nageswaran
LPSC, ISRO, Thiruvananthapuram, Kerala, India
e-mail: nitinrathee05@gmail.com
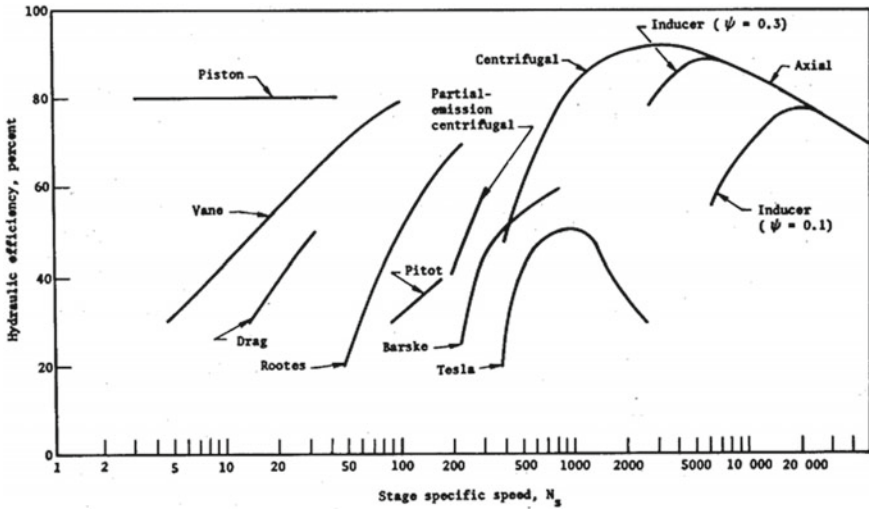
Fig. 1 Eff. versus specific speed for various pumps [1]

the higher peripheral velocity at the inducer exit. Compared to centrifugal pump impellers, inducers have fewer blades (usually 3 or 4) with smaller angles of attack to improve suction performance. The resulting configuration leads to relatively low values of the hydraulic efficiency due to the higher viscous and turbulent losses in the blade passages.

The inducer design is usually optimized with respect to system considerations. Suction specific speed S'_s and suction specific diameter D'_s are the characteristic parameters that describe the inducer suction performance in terms of shaft rotative speed N, flowrate Q, inducer inlet tip diameter D_{tip}, and critical or required net positive suction head NPSH. Details of selection of various parameters are given in the respective sections.

Low head   High head
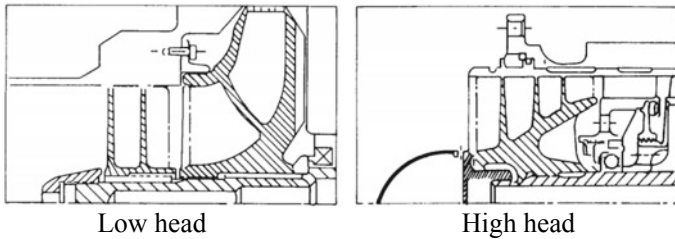
Fig. 2 Low and high head inducer configuration [1]

2 Literature Review

A very good overview on the various design aspects of inducers for liquid rocket engines are given in [1–3]. The state-of-the-art design practices and typical design and geometric parameters for selected rocket engine pump designs are given there. A detailed overview on the design considerations for modern industrial rocket turbopump inducers is given in [4]. Acosta [5], Bakir [6], and Cervone [7] made some efforts to understand the influence of the leading-edge sweep on the performance in cavitating regimes, whereas Lulu and Li [8] published results on the impact of the number of blades on the cavitation behaviour of inducers. The effect of tip clearance on inducer performance has been investigated by Hong and Kim [9]. A detailed study of flow phenomena inside rocket pump inducers has been conducted by Lakshminarayana [10], however operating medium for the inducer was air for the experimental studies. A good numerical investigation with an aim to analyse the influence of the incidence angle on the performance of the inducer was done in [10]. Among various high head inducer designs from the literature, the Space Shuttle Main Engine (SSME) Low-Pressure Oxidizer Turbopump (LPOTP) inducer is reported to have a head coefficient of 0.366 and inlet tip flow coefficient of 0.076 in [11]. The current paper also focuses on a typical high head inducer design similar to SSME LPOTP.

3 Preliminary Design and Selection of Major Parameters

The inducer inlet tip diameter shall be derived from mathematical consideration of optimum flow conditions for maximum suction performance. According to [1], a major design parameter which considerably influences the inducer geometry is the inlet tip flow coefficient, φ. Lower values of φ results in larger tip diameters and hence lower NPSH requirements (and vice versa.) due to lower values of meridional velocity at inducer inlet. However, too low a value can lead to larger re-circulation losses at inlet there by adversely affecting suction performance. An optimum value of φ can be determined by using Brum field criteria [1], which relates optimum value of flow coefficient φ_{opt} to the blade tip cavitation number K. The choice if K is mainly driven by experience gained by previous designs. A smaller value of K results in lower value of NPSH and vice versa.

$$\varphi_{opt} = \sqrt{\frac{K}{2(1+K)}}$$

According to [1] from a given value of φ or K, the optimum tip diameter can be determined from Fig. 3. The dotted line in the middle shows the optimum choice based on Brumfield criteria. For the present case, a value of 0.076 is chosen considering the SSME LPOP design. Accordingly, value of blade tip cavitation number works out
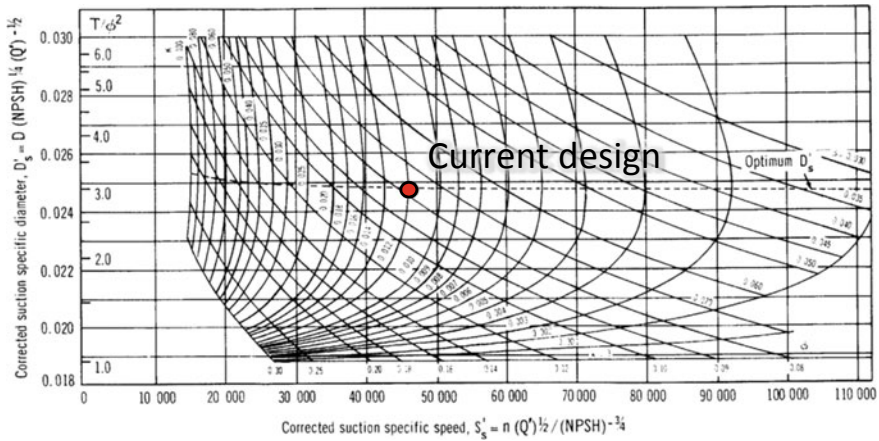
Fig. 3 Specific diameter versus suction specific speed [1]

to be 0.012. The corrected suction specific diameter and suction specific speed are estimated as 0.0248 and 46,653, respectively, which are in the recommended range for a typical rocket engine pump 20,000–50,000 as per [3].

The total head rise, flow rate, and operating speed are selected to have the specific speed within the usual recommendation for high head inducers as shown in Fig. 1. The limitation imposed by the in house test facility is also considered for the selection of these parameters. For high head inducers, the specific speeds are generally on the lower side as compared to low head inducers. A value of 2544 (U.S. units) is selected for the specific speed, which is expected to give a good overall efficiency as well.

The hub-to-tip ratio at the inlet is generally selected within 0.2–0.4, which is a compromise between suction performance and mechanical design considerations. A mean value of 0.3 is chosen for the current design. The hub-to-tip ratio at the outlet is selected to meet the hear rise requirements for a targeted head coefficient $\psi > 0.35$, at the same time limiting the blade angle at the inducer exit within acceptable limits. The mean line design is done in an iterative manner and the final results of the same are tabulated in Table 1. Based on the methodology given in [1], an estimate of the cavitation coefficient is made for the inducer design. An assessment on the expected efficiency was also made based on empirical correlations.

Based on the mean line design calculations, a model for the high head inducer was generated. A 3D view of the same is shown in Fig. 4. Other design parameters like wrap angle, tip clearance, number of blades, etc., were finalized based on sensitivity studies through 3D CFD analysis, details of the same are given in the subsequent sections.

Table 1 Major design parameters for high head inducer

Parameter	Value	Unit
Specific speed	2544	US units
Inducer inlet tip flow coefficient	0.076	–
Inducer head coefficient	0.398	–
Mean blade angle at inducer inlet	10.2	°
Mean blade angle at inducer exit	50.7	°
Hub-to-tip ratio at inlet	0.3	–
Hub-to-tip ratio at outlet	0.75	–
Efficiency	70%	%
Cavitation coefficient, σ	0.017	

Fig. 4 3D model view of the high head inducer
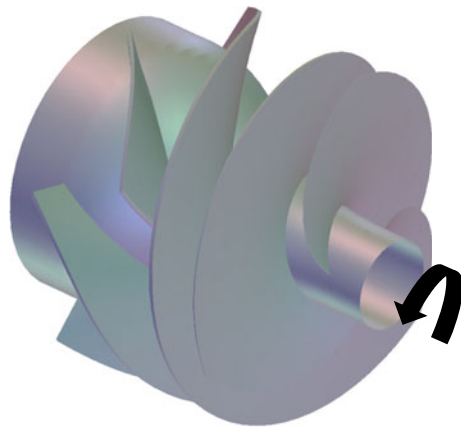
4 Numerical Analysis and Sensitivity Studies

A series of CFD simulations were done to evaluate the performance of the initial design of the high head inducer based on guidelines of [1]. Commercial CFD solver ANSYS CFX was used for numerical studies. The computational method solves the Reynolds-averaged Navier–Stokes (RANS) equations with the two-equation k–ω shear-stress transport (SST) turbulence model by Menter, with the default parameters provided by the ANSYS CFX formulation. Water was used as medium and steady state simulations were run until overall residuals were $< 1 \times 10^{-5.}$

ANSYS Turbogrid was used for structured grid generation. To reduce the computational demand, a single blade passage only was modelled. The computation domain for a typical case is shown in Fig. 5.

A baseline mesh is constructed following best practices for turbomachinery computational fluid dynamics, and the results of the calculations are compared against those obtained with a coarse mesh and two levels of mesh refinement. The details of the mesh generated are given in Table 2.

Fig. 5 Computation domain
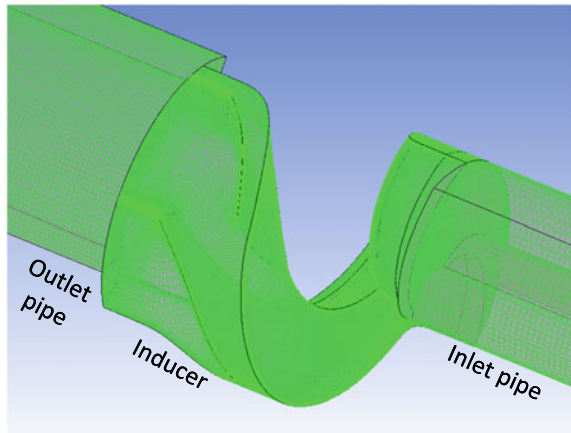
Table 2 Details of the computational grid

Grid	No. of nodes	No. of elements
Mesh#1 (coarse)	1,061,736	979,912
Mesh#2 (medium)	1,703,748	1,594,347
Mesh#3 (fine)	2,487,150	2,349,424

The meshes include the tip clearance, with 12–14 nodes between the blade and the casing. The inlet of the computational domain is extended upstream of the inducer leading edge, and the outlet downstream of the blade trailing edge to avoid any effect of boundary conditions in the solution. The total pressure is specified at the inlet, whereas the mass flow is defined at the outlet. No-slip walls are used for the blades, the hub, and the shroud. No appreciable difference in the pressure rise, efficiency, and velocity profiles could be observed of the baseline, first, and second refinements. A comparison of the pressure rise along the meridional direction is shown in Fig. 6 for the three grids.

The difference between pressure profile for Mesh#2 and 3 was < 0.05% only. Based on the results, Mesh#2 (Medium) grid was used for further studies as a compromise between accuracy and computational efforts.

In order to further fine tune, the mean line design A series of CFD analysis were carried out. Table 3 gives the parameters varied for CFD analysis and the respective range studied. The effect of each of the above parameters is discussed below.

The effect of blade wrap angle on the head rise and efficiency of the inducer is shown in Fig. 7. It is seen that the overall efficiency increases with increasing value of wrap angle, however there is no appreciable rise expected beyond 360°. The hear rise is almost constant for the cases studied. The value of 360° is recommended based on the analysis.

The effect of blade tip clearance on the head rise and efficiency of the inducer is shown in Fig. 8. It is seen that the overall efficiency and head rise decreases
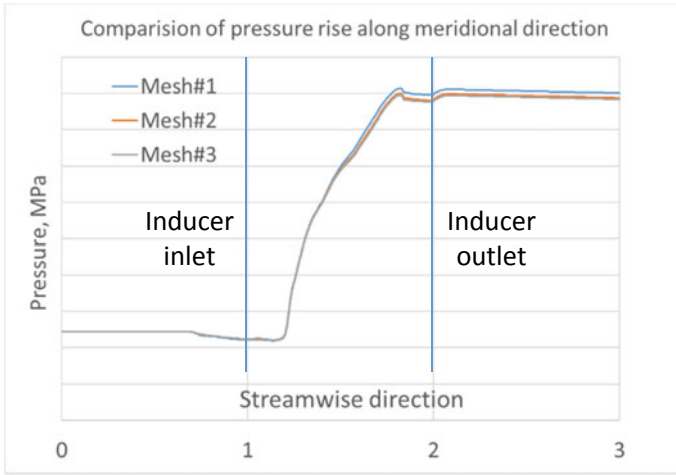
Fig. 6 Comparison of pressure rise for Mesh#1, 2, and 3

Table 3 Parameters for sensitivity studies

Parameter	Usual recommendation [1]	Cases analysed
Blade wrap angle, °	To achieve solidity (C/S) in the range 2–2.5	360 325 290 270
Tip clearance (% of D_{tip})	0.2–0.3%	0.22 0.27 0.325
Number of blades	2–4	3 main blades 3 main + 3 splitter 4 main blades

Fig. 7 Effect of blade wrap angle
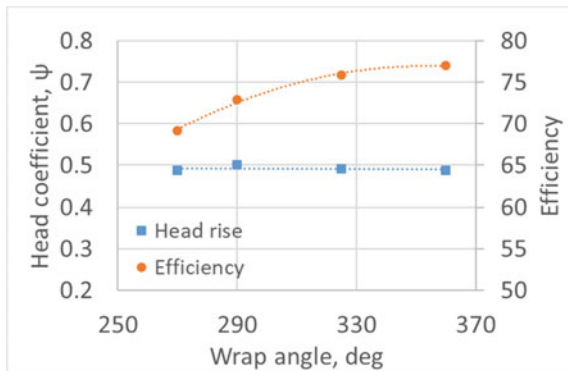
Fig. 8 Effect of blade tip clearance
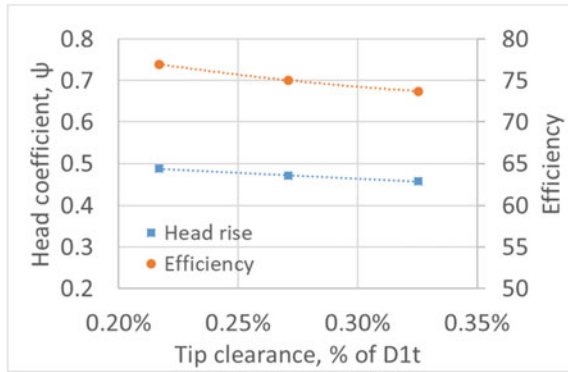
with increasing value of tip clearance. This is due to the higher leakage of fluid through the tip clearance. Considering this, it is recommended to go for min. value of the clearance (0.22%) which is within the recommended range of 0.2–0.3% of tip diameter as per [1].

The effect of number of blades on the head rise and efficiency of the inducer is shown in Fig. 9. The case with 3 main and splitter blades is designated as 3.5. It is seen that the overall efficiency is almost same for 3 bladed case and 3 + 3 case, however there is a marginal improvement (+ 4.2%) in the head rise for 3 main and 3 splitter bade case. As the number of blade increases, better guidance is available to the flow as it flows through inducer and a better performance is expected. However, too many blades can adversely affect the performance due to excessive blockage and can increase the NPSH requirement as well. Considering this, it is recommended to go for 3 main + 3 splitter blade configuration which is within the recommended range of 2–4 as per [1].

Based on the above, the model with finalized design parameters for the inducer was analysed for determination of head rise and efficiency characteristics for a range of flow rates from 70 to 130% of the design flow rate. A plot of the same is shown in

Fig. 9 Effect of number of blades

Fig. 10. Values obtained for all the 3 grids are plotted for comparison. The achieved head coefficient from CFD is meeting the design requirement; in fact, it is higher by 22%. However, this type of inducer will require a flow straightener at the exit for reducing swirl losses in the downstream pipe line and some extra margin is preferable to take care of the losses in the same. Moreover, the surface roughness effects are not modelled here, some losses are expected as a result of that too when the actual hardware is tested. The achieved efficiency is also meeting the mean line design estimated based on empirical correlations. The achieved efficiency is ~ 10% higher based on CFD studies. A plot of the steam lines at mid span (50%) is shown in which there are no major re-circulation zones in the flow passage from inlet to outlet. A plot of the pressure distribution at mid span is also shown there for comparison (Fig. 11).

The required NPSH was also estimated using the Rayleigh–Plesset cavitation model in CFX. A series of steady state isothermal simulations were carried out with different values of inlet pressures and constant flow rate through the pump. A plot of the head coefficient ψ versus cavitation coefficient σ is shown in Fig. 12. Typically for inducer designs, the cavitation coefficient corresponding to 10% drop in head rise
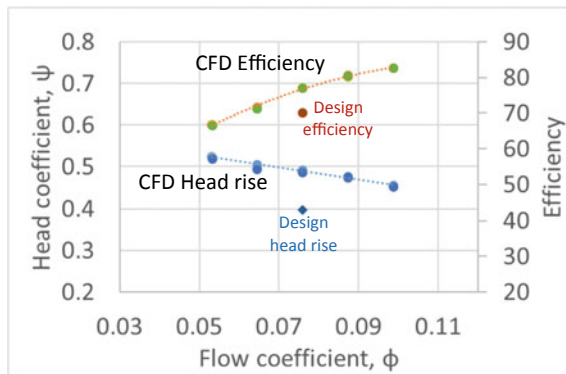
Fig. 10 Head rise and eff characteristics of finalized configuration
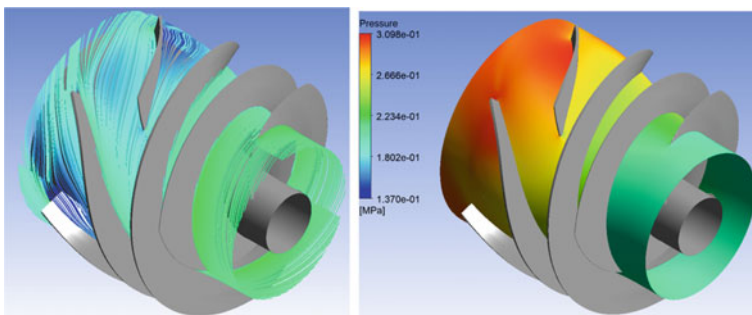
Fig. 11 Streamline and pressure plots at mid span for design flow

Fig. 12 Head coefficient ψ versus cavitation coefficient σ
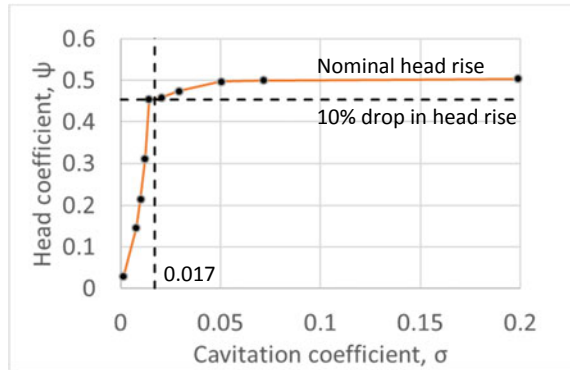
is determined as critical cavitation number. The achieved value from CFD for 10% hear rise drop is in the range 0.014–0.021 (average value 0.0175) and very close to the estimated value of 0.017 as per [1].

For cavitation coefficients below the critical value, the head rise abruptly drop as the pump undergoes a vapour blockage at inducer inlet. A plot of the zones with vapour volume fraction $= 0.5$, for different values of cavitation coefficients are shown in Fig. 13 to show the extend of build-up of vapour volume at inducer inlet. Below the value of 0.014 for cavitation coefficient, almost the entire inlet area is blocked by vapour and it is expected that a drastic drop in head rise will happen for values of cavitation coefficient below that.

5 Conclusions

Mean line design of a high head coefficient inducer ($\psi > 0.35$) has been carried out based on the recommended criteria as per published literature. The mean line design was further analysed through steady state 3D CFD simulations using ANSYS CFX and geometrical parameters were finalized to maximize the performance in terms of head rise and efficiency. The performance characteristics of the finalized geometry in terms of head rise and efficiency were generated through CFD analysis for a wide range of flow coefficients. The suction performance of the inducer was also analysed through CFD using Rayleigh–Plesset model available in ANSYS CFX. Results of the numerical analysis show that the design meets the requirements in terms of head rise, efficiency, and suction performance. Based on the confidence from the numerical analysis, hardware can be realized and tested to validate the same, which is planned in the next phase.

Fig. 13 Zones of vapour volume fraction $= 0.5$

$\sigma = 0.623$ $\sigma = 0.05$

$\sigma = 0.021$ $\sigma = 0.014$

$\sigma = 0.012$ $\sigma = 0.008$
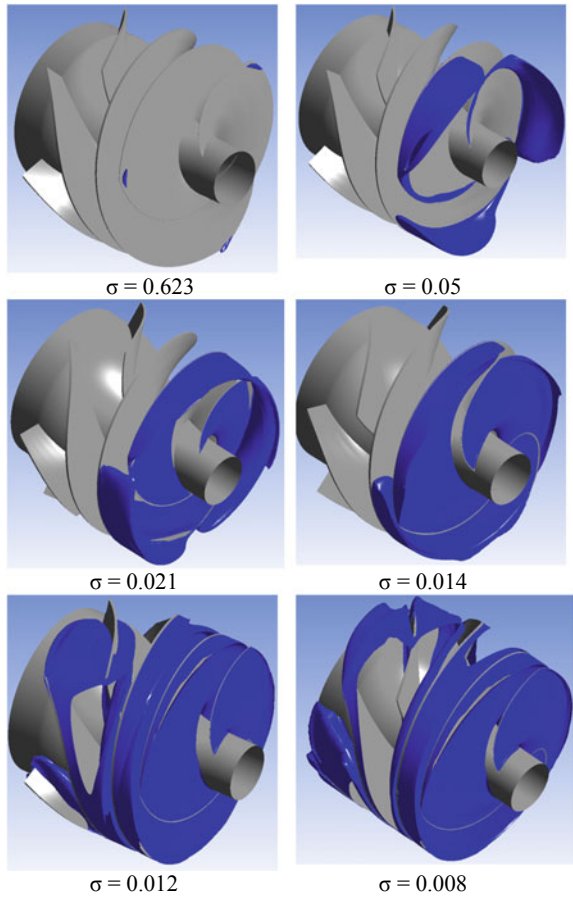
Nomenclature

ψ	Head coefficient $= gH/U_{tip}^2$
H	Total head rise, m
Q	Volume flow rate, m^3/s
U_{tip}	Tip speed at inlet $= \pi D_{tip} N/60$, m/s
D_{tip}	Tip diameter at inducer inlet, m
N	Operating speed, rpm
φ	Inlet tip flow coefficient $= C_m/U_{tip}$
C_m	Meridional velocity at inducer inlet, m/s
K	Blade tip cavitation number
NPSH	Net Positive Suction Head, m
Ns*	Specific speed, $NQ^{1/2}/H^{3/4}$

(continued)

(continued)

$S_s'^*$	Suction specific speed $= NQ^{1/2}/NPSH^{3/4}$
$D_s'^*$	Suction specific diameter $= D_{tip}\, NPSH^{1/4}/Q^{1/2}$
σ	Cavitation coefficient $= (P_{in} - P_v)/(0.5\rho\, U_{tip}^2)$
P_{in}	Inlet pressure, MPa
P_v	Vapour pressure, MPa

* In U.S. units

References

1. Keller RB, Jakobsen JK (1971) Liquid rocket engine turbopump inducers. Series on NASA space vehicle design criteria, NASA SP-8052
2. Sobin AJ, Bissell WR (1974) Turbopump systems for liquid rocket engines (NASA SP-8107). Lewis Research Center, NASA (Design Criteria Office), Cleveland, Ohio
3. Huzel DK, Huang DH. Design of liquid rocket propellant engines. NASA SP-125
4. Japikse D (2001) Overview of industrial and rocket turbopump inducer design. CAV2001: session B7.001
5. Acosta AJ, Tsujimoto Y, Yoshida Y, Azuma S, Cooper P (2001) Effects of leading-edge sweep on the cavitating characteristics of inducer pumps. Int J Rotating Mach 7(6):397–404
6. Bakir F, Kouidri S, Noguera R, Rey R (2003) Experimental analysis of an axial inducer influence of the shape of the blade leading edge on the performances in cavitating regime. J Fluids Eng 125(2):293–301
7. Cervone A, Pace G, Torre L, Pasini A, Bartolini S, Agnesi L, D'Agostino L (2012) Effects of the leading-edge shape on the performance of an axial three bladed inducer. In: 14th international symposium on transport phenomena and dynamics of rotating machinery (ISROMAC-14), Honolulu, HI
8. Zhai L, Li Y, Cui B, Guo J, Li X, Zhu Z (2021) Studies of cavitation characteristics of inducers with different blade numbers. AIP Adv 11:085216. https://doi.org/10.1063/5.0054057
9. Hong S, Kim J, Choi C, Kim J (2006) Effect of tip clearance on the cavitation performance of a turbopump inducer. J Propulsion Power 22(1):174–179
10. Lakshminarayana B (1981) Analytical and experimental study of flow phenomena in non-cavitating rocket pump inducers. NASA Contractor Report 3471, Oct 1981
11. Veggi L, Pauw JD, Wagner B, Haidn O (2017) A study on the design of LOx turbopump inducers. In: 17th international symposium on transport phenomena and dynamics of rotating machinery (ISROMAC2017), Dec 2017, Maui, United States

The Effect of Reynolds Number on Mass Suction and Outlet Temperature in IRS Device

Maheswar Rout, Jnana Ranjan Senapati, and Suman Ghosh

1 Introduction

The infrared suppression sys, known as IRS devices, are regularly used in defense helicopters and naval warships. It is used to lower the temperature of the turbine exhaust gases of naval warships and helicopters. If we eject the turbine exhaust without reducing the temperature of the flue gases in this machinery, it might be a source for radar to detect the ship or helicopters. Therefore, it is essential to bring down the temperature of the turbine exhaust before allowing it into the atmosphere. The IRS device reduces the temperature of the turbine exhaust gases of naval warships and helicopters. So IRS devices have broad applications. This encourages several researchers to work in this area and develop correct computational schemes to predict these devices' fluid flow and heat transfer within an affordable computational cost.

2 Literature Review and Objective

In the last three decades, much research being carried out on IRS devices [1–4]. Birk and Vandam [5] conducted a 1/4th parametric survey of the Infrared Signature Suffield (IRSS) ball Defense Research Establishment (DRES) system and compared result to a full-scale naval model. Thompson et al. [6] discuss the prime causes of infrared signature in ships and also various techniques to eliminate the signature. Im and Song [7] experimentally investigated air entrainment and mixing and found that using a short circular ejector makes a compact design and improves the overall performance. Barik et al. [8] performed the experimental analysis of a laboratory scale IRS device using cylindrical funnels of different dimensions one after the other,

M. Rout (✉) · J. R. Senapati · S. Ghosh
Department of Mechanical Engineering, NIT Rourkela, Rourkela 769008, India
e-mail: 522me6010@nitrkl.ac.in

founding that maximum air entrainment is achieved in zero overlapping funnels. Mukharjee et al. [9] carried out numerical simulations in a full-scale IRS device using conical funnels with three different types of walls: adiabatic, conducting, and both conducting and radiating, and found that the mass entrainment is more in the case of conducting and radiating wall. Chandrakar et al. [10] discuss the fluid flow and heat transfer characteristic of a real-scale IRS device using cylindrical funnels and concludes that the mass suction increase. At the same time, the outlet plume temperature decreases with an increase in inlet velocity and plume temperature. As mentioned above, researchers have proposed various models to form an IRS device to maximize mass suction rate and reduce turbine exhaust temperature.

3   Materials and Methods

3.1   Physical Description of the Model

The present numerical computation considers a conical full-scale IRS device with a computational domain. The computational domain is shown in Fig. 1. The conical IRS device consists of two conical funnels first funnel has an initial diameter of 2.0 m and an outlet diameter of 1.6 m. The second funnel was considered to have an initial diameter of 1.8 m and an outlet diameter of 2.0 m. The length of each funnel was taken as 2.5 m. An axial gap of 0.2 m was considered for easy mass suction. Also, a radial gap of 0.1 m was considered between the first funnel's outlet diameter and the second funnel's inlet diameter to increase the mass suction rate. The funnel walls are considered adiabatic walls. The nozzle diameter of 0.8 m is considered. The IRS system length to nozzle diameter length is taken as 6.5. Hot air enters the nozzle with an initial velocity of U_{nz} and temperature T_{nz}. The fresh air is sucked into the IRS device, and also the temperature of the hot flue gases decreases. The dimension was taken from various worldwide used ships and frigates [11–13]. A cylindrical computational domain of equal diameter and height is considered for the computation. The ratio of computational domain diameter to nozzle diameter is taken as 25.

3.2   Turbulent Transport Equation

The Reynold time-averaged mass, momentum, and energy in the inertial reference frame can be expressed in terms.
   Continuity equation:

$$\frac{\partial \overline{u}_i}{\partial x_i} = 0 \tag{1}$$
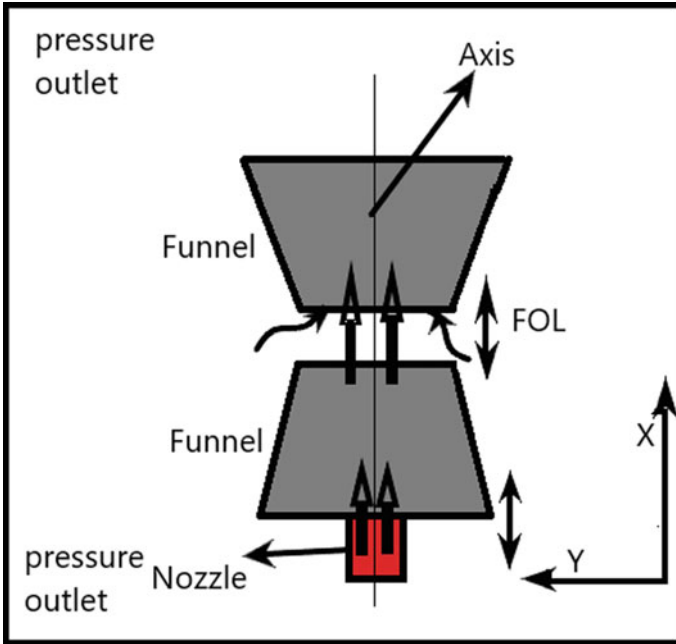
Fig. 1 Computational domain with boundary condition

Momentum equation:

$$\rho \bar{u}_j \frac{\partial \bar{u}_i}{\partial x_i} = -\frac{\partial \bar{p}}{\partial x_i} + \frac{\partial}{\partial x_j}\left(2\mu \bar{S}_{ij} - \mu \overline{u'_i u'_j}\right) \tag{2}$$

Energy equation:

$$\rho \bar{u}_j \frac{\partial \bar{T}}{\partial x_j} = \frac{\partial}{\partial x_j}\left(\frac{\lambda}{c_p}\frac{\partial \bar{T}}{\partial x_i} - \rho \overline{u_i T'}\right) \tag{3}$$

The transport equations for k and ω [14] are

$$\frac{\partial}{\partial x_i}(\rho k u_i) = \frac{\partial}{\partial x_j}\left[\left(\mu + \frac{\mu_t}{\sigma_k}\right)\frac{\partial k}{\partial x_j}\right] + \min\left(p_k 10\rho\beta^* k\omega\right) - \rho\beta^* k\omega \tag{4}$$

$$\frac{\partial}{\partial x_j}(\rho\omega u_i) = \frac{\partial}{\partial x_j}\left[\left(\mu + \frac{\mu_t}{\sigma_\omega}\right)\frac{\partial\omega}{\partial x_j}\alpha\frac{\omega}{k}P_k\right] - \rho\beta\omega^2 + 2(1 - F_1)\frac{\rho\sigma_{\omega 2}}{\omega}\frac{\partial k}{\partial x_j}\frac{\partial\omega}{\partial x_j} \tag{5}$$

3.3 Boundary Condition

The pressure outlet boundary condition is implemented on the computational domain's top, bottom, and outlet boundary temperature at the inlet of the nozzle ranging from 400 to 700 K.

At the solid walls

$$v_x = v_y = v_z = 0 \tag{6}$$

At the top, bottom and outlet boundary

$$P = P_\infty, T = T_\infty \tag{7}$$

At the nozzle exit

$$v_x = u_{nz}, v_y = v_z = 0, T_x = T_{nz} \tag{8}$$

3.4 Numerical Solution Procedure

Integrating the mass, momentum, energy balance equations, turbulent kinetic energy, and their dissipation through the control volume in a finite volume technique yields a set of algebraic equations. The jet impingement heat transfer is estimated using an SST K-ω model. Utilizing a central difference technique, the diffusion term in the momentum and energy equations is discretized. The second-ordered scheme represents the convective term in momentum and turbulence equations. The pressure correction equation for pressure velocity coupling was solved using the SIMPLE algorithm.

3.5 Validation of Numerical Scheme

The numerical scheme is validated with verified experimental data from Barik et al. [8] published in the literature. Experimental results validate the current numerical scheme. A series of the cylindrical funnel of the laboratory scale is taken one above the other to form the IRS device. The corresponding dimensions, such as funnel diameter, funnel height, funnel overlap, and nozzle overlap, are taken per the experimental setup. This specific problem is considered with the present boundary condition for validation. The variations are shown in Fig. 2.
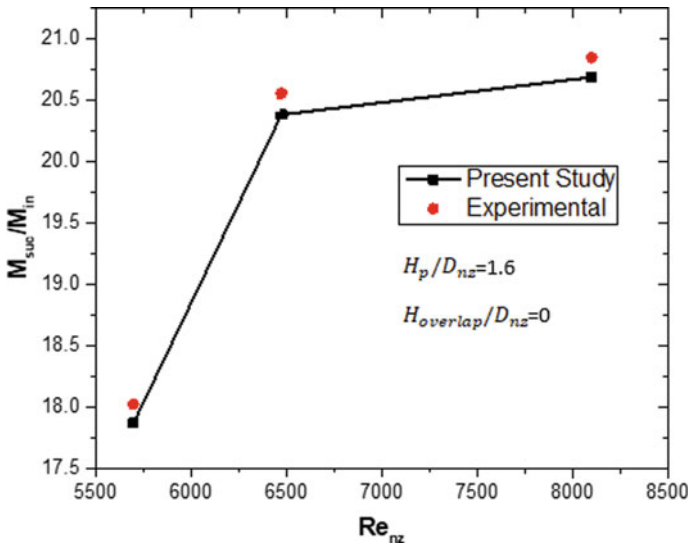
Fig. 2 Comparison between the present CFD study and experimental results of Barik et al. [8]

3.6 Grid and Domain Sensitivity Test

Figure 3 shows the grid sensitivity test for the current numerical computation for nozzle overlap length of − 25% and funnel overlap of − 25%. Initially, a small number of grids are taken, and the mass entrainment ratio concerning this particular number of grids is calculated. As the number of grids gradually increases, the mass entrainment ratio gradually decreases. We got that the mass entrainment does not change very much with an increasing number of grids over 81,881. So a domain of 81,881 grids is considered.

4 Results and Discussion

4.1 Comparison of Mass Entrainment Ratio and Outlet Temperature Ratio with Re_{nz} at Various Inlet Nozzle Temperatures

Figure 4 illustrates how the mass entrainment ratio varies with the Reynolds number for various nozzle input temperatures. The graphic shows that the mass entrainment ratio rises as the Reynolds number rises. This happens due to viscous drag because as the velocity increases, the viscous drag increases. At a relatively low inlet temperature, nominal changes in the mass entrainment ratio occur. It can be seen from
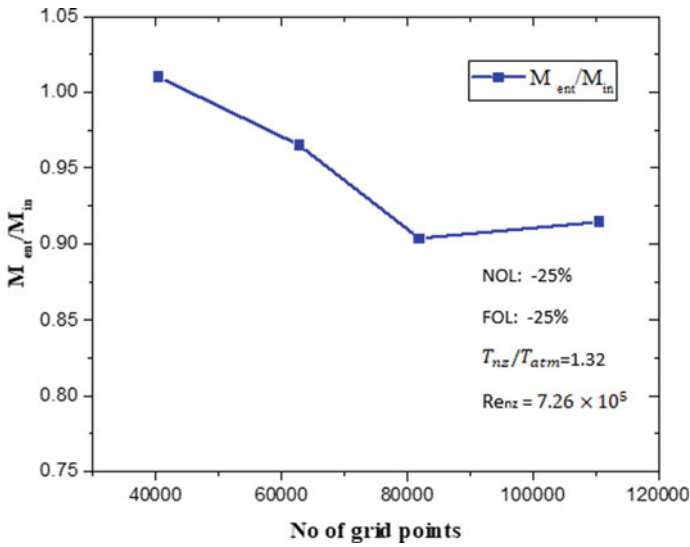
Fig. 3 Variation of mass entrainment ratio with the number of grids

the figure. It can be observed from Fig. 5 that a higher inlet nozzle temperature for a certain Reynolds number has more mass entrainment ratio than a lower one. As shown in Fig. 5, for temperature 600K, the mass entrainment ratio increases by 1.13% when the Reynolds number rises from 6.65×10^5 to 9.08×10^5.
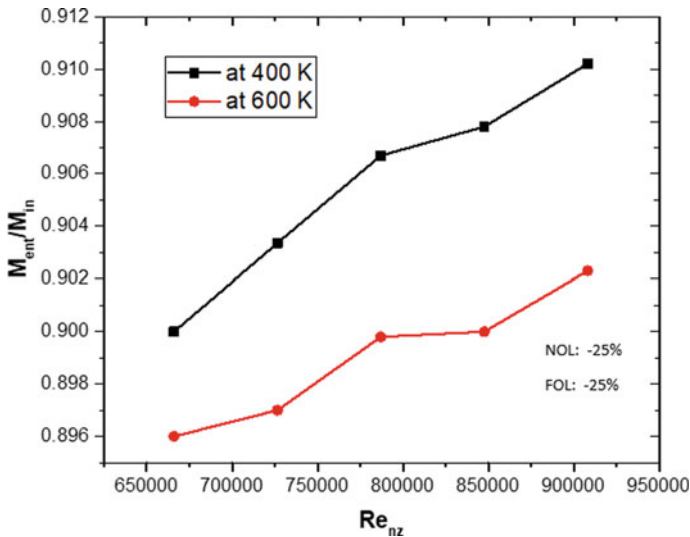
Fig. 4 Comparison of mass suction ratio with Re_{nz}
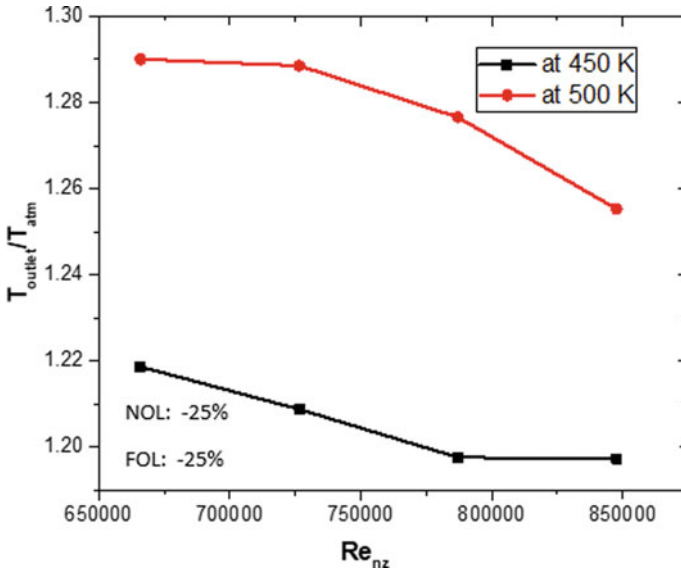
Fig. 5 Comparison of outlet temperature ratio with Re_{nz}

The ratio of exit air temperature from the funnel to the atmospheric air temperature was calculated at different inlet Reynolds numbers, and the comparison is shown Fig. 5. The temperature ratio decreases as the Reynolds number increases because the mass suction also increases. The temperature ratio at different inlet temperatures is plotted. It can be observed that the variation is more at a higher inlet temperature.

5   Conclusions

From the numerical simulation, it is observed that with the rise in Reynolds number, the mass suction ratio increases, and the outlet temperature of air decreases. When high-velocity and high-temperature air from the nozzle exhaust are passed through the IRS device, a low-pressure zone is set up inside the system. That means the pressure inside the device becomes lower than the atmospheric pressure. Therefore, surrounding fresh air from the surrounding entrains the device through inter-funnel gaps or through the bottom part of the lower funnel. This fresh air mixes with the hot air and moves upward, resulting in a lower temperature at the device outlet.

Nomenclature

IRS	Infrared Suppression System
NOL	Nozzle overlap [m]
FOL	Funnel overlap [m]
M_{suc}	Mass entrainment into IRS device [kg/s]
Min	Mass inlet into IRS device [kg/s]
ρ	Density of air [kg/m^3]
ω	Specific dissipation rate [s^{-1}]
ε	Rate of dissipation of turbulent dissipation rate [m^{2}s^{-3}]
μ	Dynamic viscosity [Pa-s]

References

1. Werle M, Presz W, Paterson R (1987) Flow structure in a periodic axial vortex array
2. Birk A, Davis W (1989) Supressing the infrared signatures of marine gas turbines. J Eng Gas Turbines Power 111:123–129
3. Wang S, Li L (2006) Investigation of flows in a new infrared suppressor. Appl Therm Eng
4. Bettini C, Cravero C, Cogliandro S (2007) Multidisciplinary analysis of a complete infrared suppression system. ASME Turbo Expo: 1365–1370
5. Birk A, VanDam D (1994) Infrared signature suppression for marine gas turbines: comparison of sea trial and model test results for the DRES ball IRSS system. J Eng Gas Turbines Power 116:75–81
6. Thompson J, Vaitekunas D (1998) IR signature suppression of modern naval ships. In: ASNE 21st century combat technology symposium, pp 1–9
7. Im J, Song S (2015) Mixing and entrainment characteristics in circular short ejectors. J Fluids Eng Trans ASME
8. Barik A, Dash S, Guha A (2015) Experimental and numerical investigation of air entrainment into an infrared suppression device. Appl Therm Eng 75:33–44
9. Mukharjee A, Chandrakar V, Senapati J (2021) Flow and conjugate heat transfer with surface radiation characteristics of a real-scale infrared suppression device with conical funnels. Int Commun Heat Mass Transf 123
10. Chandrakar V, Senapati J (2020) Numerical investigation of flow and heat transfer characteristics of a full-scale infrared suppression device with cylindrical funnels. Int J Thermal Sci 153
11. Shaorong Z, Zhaohui D, Hanping C, Fangyuan Z (2000) Numerical and experimental study on the suppression for the infrared signatures of a marine gas turbine exhaust system. ASME Turbo Expo
12. Mahulikar S, Sane S, Gaitonde U, Marathe A (2001) Numerical studies of infrared signature levels of complete aircraft. Aeronaut J 105:185–192
13. Mishra D, Dash S (2010) Prediction of entrance length and mass suction rate for a cylindrical sucking funnel. Int J Numer Methods Fluids
14. Menter F (1994) Two-equation eddy viscosity turbulence models for engineering applications. AIAA J

Discrete Element Modeling of Discharge of Granular Matter from a Silo at Different Eccentric Opening

Abhinesh Kumar and Prasanta Kumar Das

1   Introduction

Granular matters widely exist in nature and are also used in food processing, mining, pharma industries, etc. Natural flows like debris flow, landslides, etc., are very hazardous, and to prevent these kinds of hazards, researchers are trying to study the flow behavior and physics behind them. Many researchers have proposed theories to explain flow physics, but no well-accepted theory can still explain all flow behaviors involved. Safely storing granular materials are also a very challenging task, as the complex physics of granular matter is still not well explored.

Silo is an essential part of industries for storing granular matter. Predicting the actual discharge is very important in many industrial processes. The complex flow characteristics lead to difficulty in predicting the discharge rate. During a silo discharge, the motion of the grains is complex. It may lead to stress on the silo walls. Due to these stresses, the silo may fail or break. The flow patterns which emerge due to the flow depend upon many factors like particle–particle friction coefficient, particle shape, particle size, and silo geometry [1, 2]. Mainly two regions are observed during granular discharge from the silo: the dynamic and stationary regions. Flow patterns like mass flow, funnel flow, and mixed flow exist during the discharge based on the motion of the particles and particle properties [3, 4].

A. Kumar (✉) · P. K. Das
Department of Mechanical Engineering, IIT Kharagpur, Kharagpur 721302, India
e-mail: abhineshkumariitg@gmail.com

2   Literature Review and Objective

The flow of granular media inside the silo has been investigated by various researchers across the world. Anshu Anand et al. have numerically investigated the discharge rate of granular matter through a hopper [5]. The experimental analysis of flow through different eccentric openings of the silo has been investigated by Maity et al. [3]. Various experimental and numerical instigations have been done by varying the particle shape, particle size, effect of material properties, and different eccentricity by researchers in the past [6–8] to study the discharge dynamics and flow pattern. Our objective is to investigate the discharge dynamics and flow pattern when there are two eccentric openings at the bottom of the silo using discrete element modeling with the help of LIGGGHTS-PUBLIC-3.8.0, which has not yet been done, to our knowledge.

3   Materials and Methods

The numerical investigation has been done using the discrete element method (DEM). The displacement and dynamic forces that a particle experiences when interacting with other particles are calculated using DEM. Generally, the soft particle approach is the most widely used in the dense granular flow. In the soft particle approach, the two particles contacting each other can penetrate with an infinitesimally small distance [9]. There are various soft particle contact models, one of which is Hertz-Mindlin no-slip contact. This model is the spring-dashpot model, as the elastic force is represented by spring, and the penetration is modeled by dashpot. The slip at the contact point is neglected for our numerical investigation. Figure 1 shows the schematic of the spring-dashpot model [10]. We have used the no-slip Hertz-Midlin contact model for our simulation.

The following formula gives the forces between the two particles *i* and *j* in the normal and tangential direction [11]:

Fig. 1 Schematic of the spring-dashpot contact model
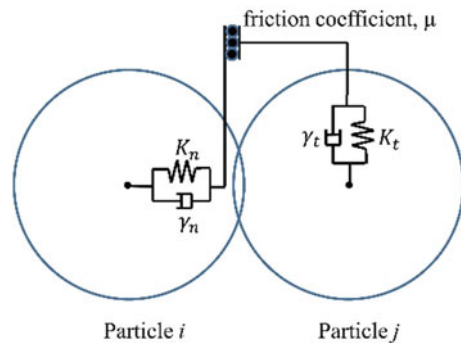
$$F_n = K_n \delta_n + \gamma_n \Delta U_n \tag{1}$$

$$F_t = \min \left\{ \left| K_t \int_{T_c,0}^{T} \Delta U_t \mathrm{d}T + \gamma_t \Delta U_t \right|, \mu F_n \right\} \tag{2}$$

where ΔU_n and ΔU_t are the normal and tangential relative velocity of the particles, K_n is normal and K_t is the tangential spring coefficient, γ_n is normal and γ_t is the tangential dashpot coefficients, and δ_n is the infinitesimally small normal penetration.

The simulation domain used for our numerical simulation is shown in Fig. 2a, b rectangular silo of dimension $200 \times 400 \times 10$ mm^3 ($L \times H \times Y$) has been used. We varied the bottom opening position from the center of the silo and studied the flow dynamics; we also used the same domain for the two openings with different eccentricities.

Table 1 gives the values of the variables used for our numerical simulation. The modulus of elasticity is taken lower than the actual modulus of elasticity of the particle to reduce the simulation cost and time without affecting the end result [12].
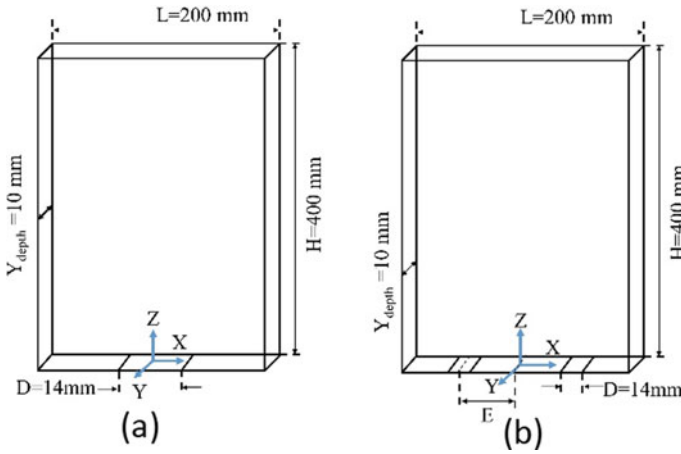

Fig. 2 Geometry of the silo used for the simulation

Table 1 Parameters for the simulation for our numerical investigation

Variables	Value
Modulus of elasticity, Y (MPa)	5.5
Poisson coefficient, ν	0.25
Restitution coefficient, e	0.45
Friction coefficient, μ	0.3
DEM time step, Δt (s)	3e-5
Density of particles, ρ (kg/m^3)	2500
Radius of particles, r (m)	0.0006 and 0.0012

4 Results and Discussion

4.1 Flow Pattern of the Discharge

The flow behavior of the granular bed in the silo with one concentric opening has been studied using discrete element modeling. Figure 3 shows the flow pattern of the granular bed at different times. We have used granular matter of diameter $d = 2.4$ mm for this flow pattern behavior study. We have also done the numerical study for the granular matter of diameter $d = 1.2$ mm, but here we have only shown the flow pattern for the eccentricity, $E = 0.0$, because of a similar flow pattern and better visualization. Initially, the bed near the orifice is only eroded, but as time progresses, the erosion propagates toward the upper layers and reaches up to the free surface. We did numerical simulation for the eccentric openings $E = 0.5$ and $E = 0.93$. We found that the granular bed flow patterns at different times are similar, but we observed quicker discharge than the eccentric opening. The reason is discussed in Sect. 4.2.

4.2 Temporal Velocity Variation and Flow Analysis for One Eccentric Opening

Further, we did a series of numerical simulations for three different eccentric openings at the bottom of the silo for the granular matter of particle size, $d = 0.0012$ mm, which is half of the previous simulation of Sect. 4.1. Our first aim was to validate our numerical results with the theoretically obtained velocity plot. For that, we used our numerical results to validate the theoretical results of Ritwik et al. [13] at $z = 10$ mm height from the base of the silo. We found that the numerical outcomes demonstrate good agreement with the theory proposed by Ritwik et al. Figure 4 shows the same plot for concentric opening, and Fig. 5 shows the plot for eccentric opening $E = 0.93$.

We can see from Figs. 4 and 5 that our numerical results demonstrate good concordance with the theoretical findings. In Fig. 7, the numerical non-dimensional velocity
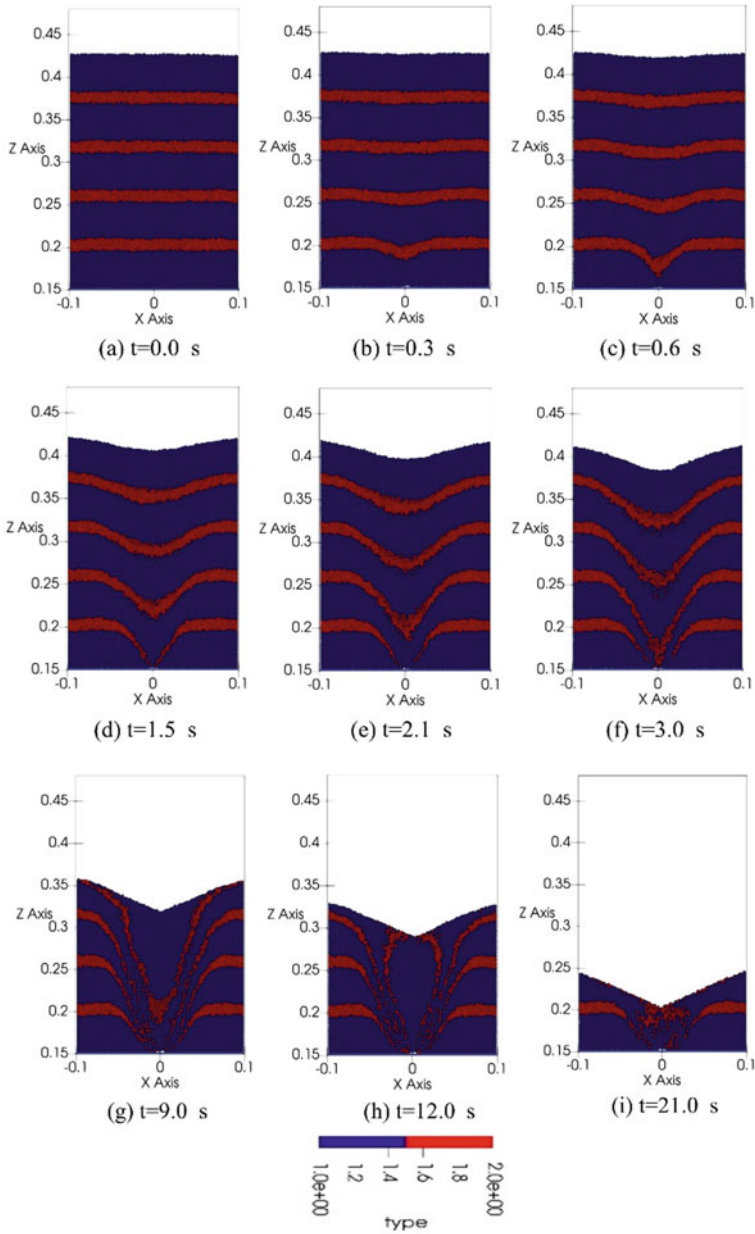
Fig. 3 Flow pattern of the granular bed for concentric discharge with particle diameter $d = 2.4$ mm

Fig. 4 Plot of comparison of theoretical and numerical non-dimensional velocity with the non-dimensional silo width at $z = 10$ mm for concentric opening
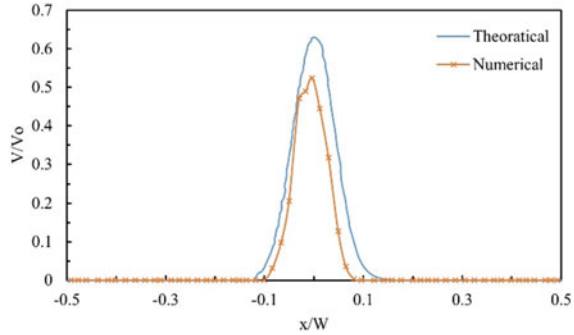
Fig. 5 Plot of comparison of theoretical and numerical non-dimensional velocity with the non-dimensional silo width at $z = 10$ mm for $E = 0.93$
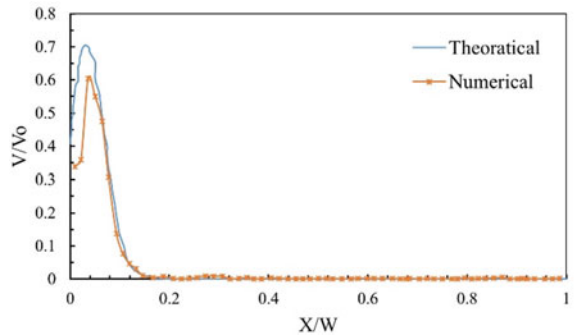
near the wall is lower than the theoretical one due to the no-slip boundary condition taken by us during the numerical simulation. Also, we have considered lowering the modulus of elasticity to the actual so that we can reduce the simulation time and cost without sacrificing much with the final results.

4.2.1 Temporal Velocity Profile

We further post-processed the results of the numerical simulation and plotted the velocity contour snapshots at different time steps throughout the discharge of granular matter for $E = 0.0$ (Fig. 6), $E = 0.5$ (Fig. 7), and $E = 0.93$ (Fig. 8). We can see that in the case of $E = 0.0$, the moving zone can broaden up on either side of the orifice without any obstruction, but in the case of $E = 0.93$, the moving zone can widen up in the one side only because the wall restricts the other side. Similar is the case with $E = 0.5$ (Fig. 7), where one side widens more, and the other side is less. Due to this, the discharge dynamics are different, and the discharge rate is also different for these three openings.

Fig. 6 Plot of velocity contour during discharge process at a different time for eccentric opening $E = 0.0$

(a) t=0 s

(b) t=0.03 s

(c) t=0.30 s

(d) t=1.5 s

(e) t=3 s

(f) t=4.5 s

(g) t=7.50 s

(h) t=12 s

v Magnitude (m/s)
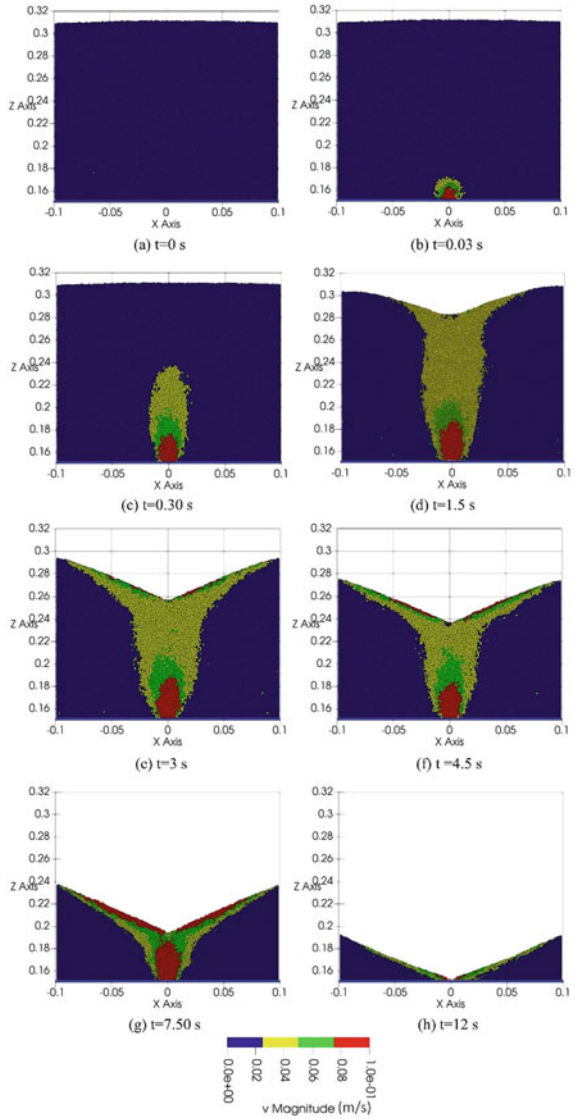
Figure 9 shows the vertical velocity plot along the silo width at different heights of the silo from the bottom surface for the concentric opening at the concentric opening ($E = 0.0$). Figures 10 and 11 are the vertical velocity plot for the eccentricity $E = 0.5$ and 0.93, respectively. From the plot, we can see that the velocity is maximum at the centerline of the opening.

Fig. 7 Plot of velocity contour during discharge process at a different time for eccentric opening $E = 0.50$

(a) t=0 s

(b) t=0.03 s

(c) t =0.30 s

(d) t =1.5 s

(e) t =3 s

(f) t =4.5 s

(g) t =7.50 s

(h) t =12 s

v Magnitude (m/s)
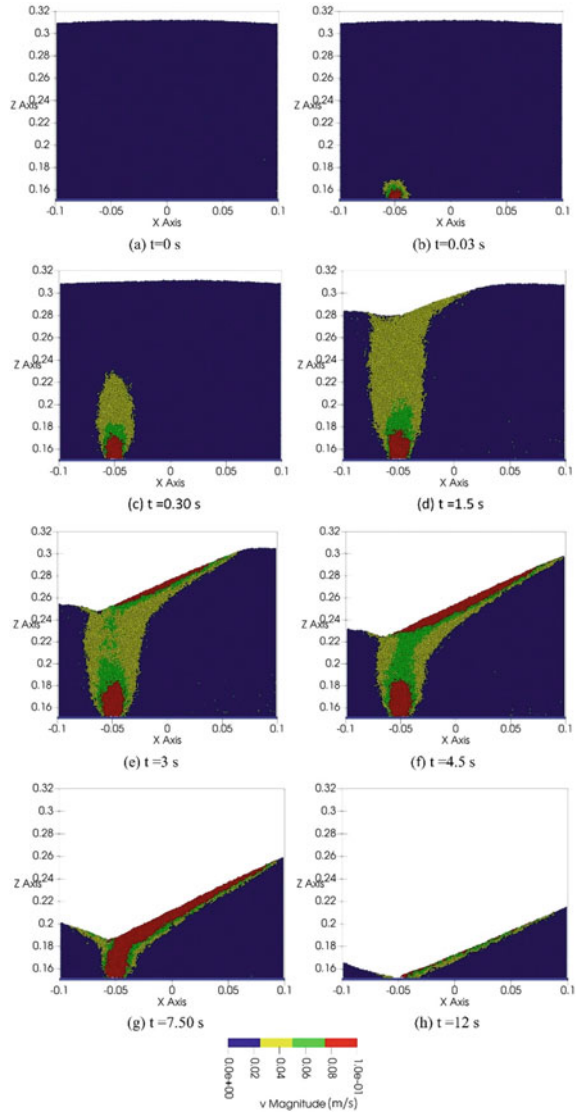
4.3 Temporal Velocity Variation and Flow Analysis for Two Eccentric Opening

We further extended our numerical investigation for two eccentric openings. The velocity contour at different time steps for two eccentric openings (at $E = 0.5$ and 0.93) is shown Figs 12 and 13. Unlike one opening, the two eccentric openings possess more discharge and less widening space for the moving zone. At $t = 0.09$ s,

Fig. 8 Plot of velocity contour during discharge process at a different time for eccentric opening $E = 0.93$
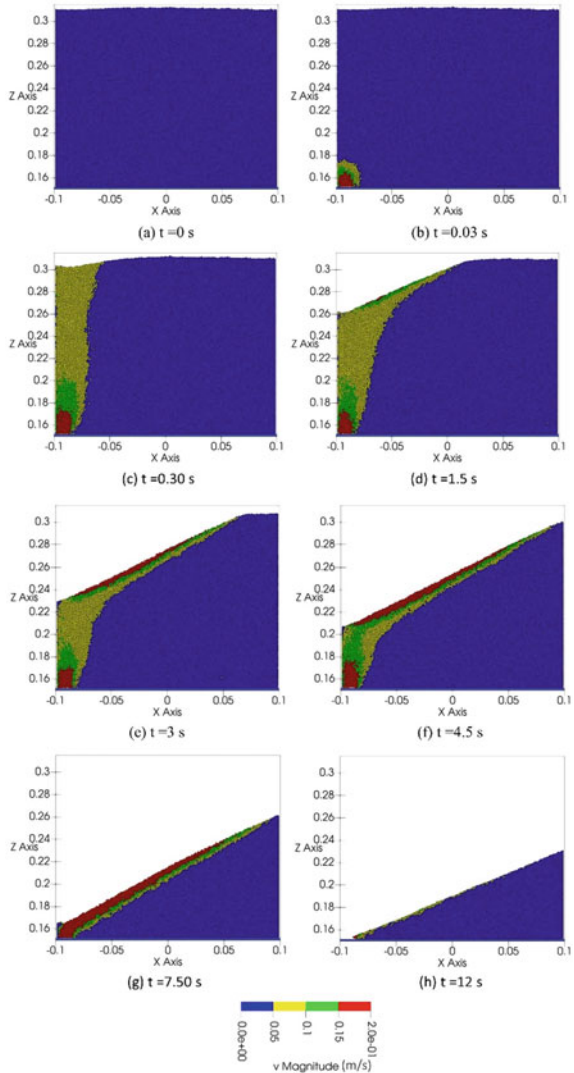
we can see that the free surface of the granular bed was undisturbed up to this time step in both Figs. 12 and 13, and only some regions are getting eroded near the openings. But, at $t = 0.30$ s, the bed at $E = 0.5$ is not yet disturbed, whereas, at $E = 0.93$, the free surface of the bed is disturbed. From the different time step contours of both figures, we can clearly conclude that the discharge rate is higher at $E = 0.93$.

Fig. 9 Plot of *z*-direction velocity with respect to silo width at a different height from the bottom of the silo for $E = 0.0$
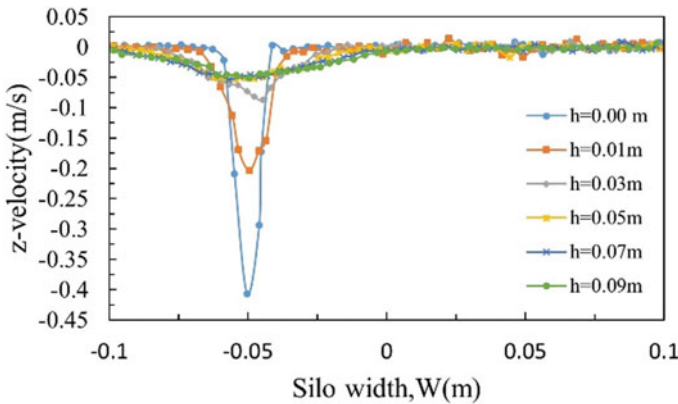
Fig. 10 Plot of *z*-direction velocity with respect to silo width at a different height from the bottom of the silo for $E = 0.5$

Figures 14 and 15 are the plot of vertical velocity over the width of the silo at a different height from the bottom of the silo. Compared with the single opening, two eccentric openings have a more expanded moving zone in the upward direction from the bottom of the silo. We can also see that the velocity magnitude plot is symmetric about the center of the silo geometry.
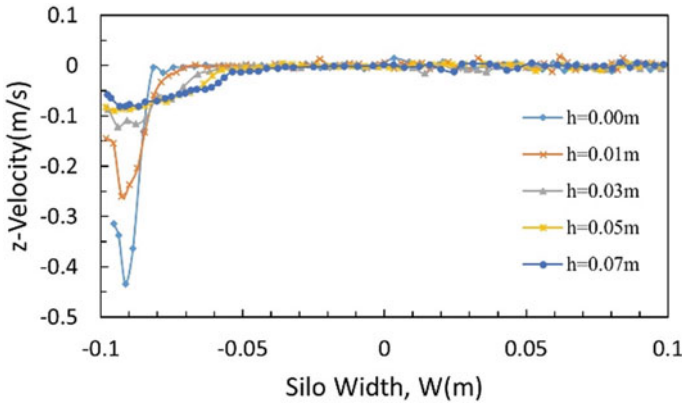
Fig. 11 Plot of *z*-direction velocity with respect to silo width at a different height from the bottom of the silo for $E = 0.93$

5 Conclusions

We numerically analyzed the dynamics of discharge flow in a silo having eccentric openings at the bottom by discrete element modeling. We aimed to validate the results of an eccentric and concentric opening numerically, and then we further extended our numerical investigation for two symmetric eccentric openings. Firstly, we compared the proposed theoretical result by Ritwik et al. [3] of the concentric and eccentric opening with the obtained numerical results, showing a good match. Then we extend our numerical investigation for two eccentric openings at the eccentricity, $E = 0.5$ and 0.93, and we found that the flow patterns of the two eccentric openings are similar to the one flat-bottomed opening. As expected, the discharge rate is higher in the case of two eccentric openings because of more erosion and a wider velocity zone than the one eccentric opening. Two differentiable regimes are observed from velocity contour plots. The first one is the stationary regime, and the second one is the moving region. Maximum velocity is along the centerline of the opening, and lowest velocity is near the walls left and right wall of the silo. The flow characteristics change as the eccentricity changes, and the discharge rate is also affected by this.

Fig. 12 Velocity contour plot for $E = 0.5$ at different time
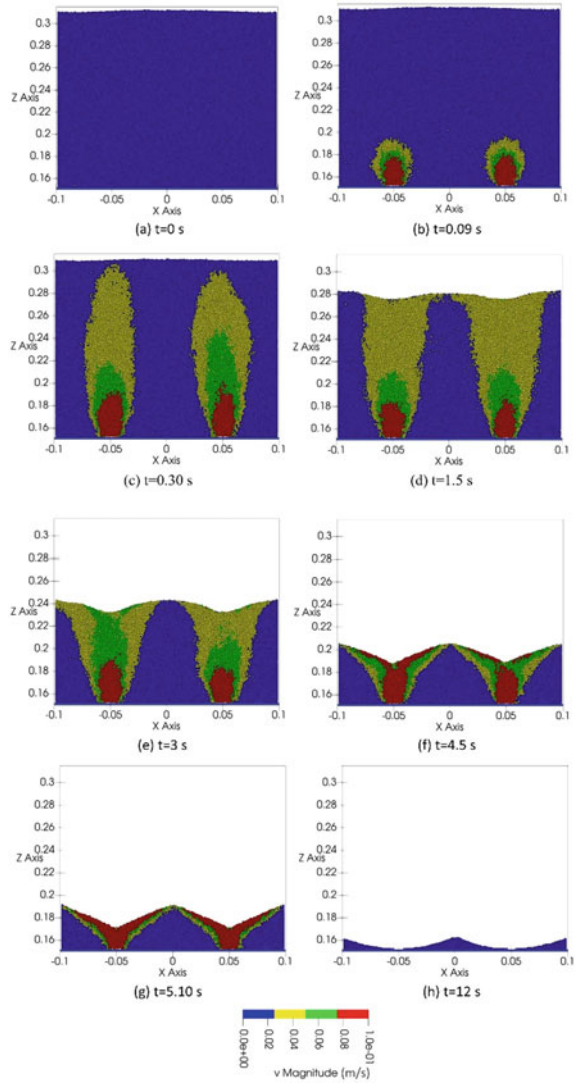
Fig. 13 Velocity contour plot for $E = 0.93$ at different time

(a) t=0 s

(b) t=0.09 s

(c) t=0.30 s

(d) t=1.5 s

(e) t=3 s

(f) t=4.5 s

(g) t=7.50 sec
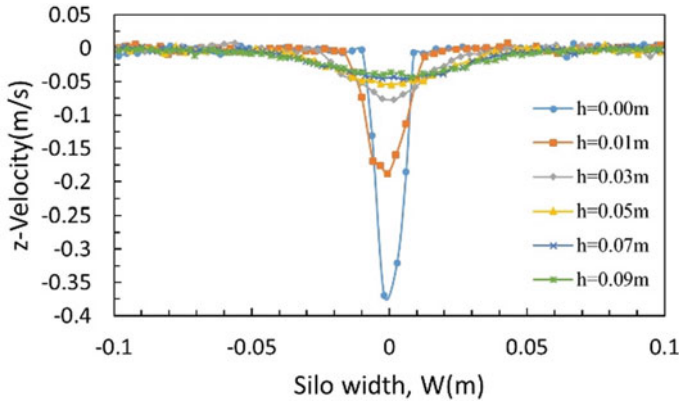
(h) t=12 sec

v Magnitude (m/s)
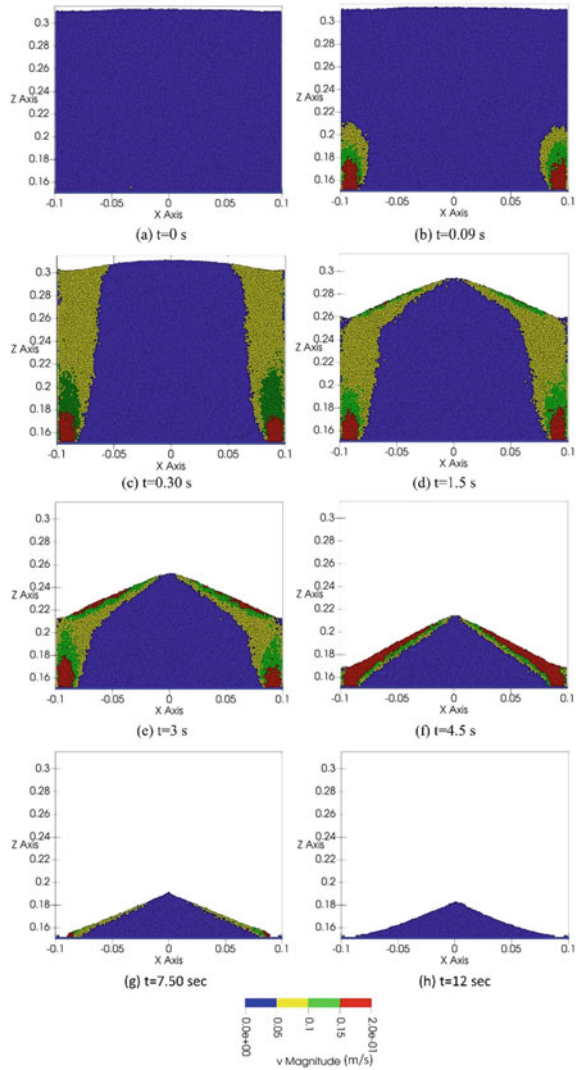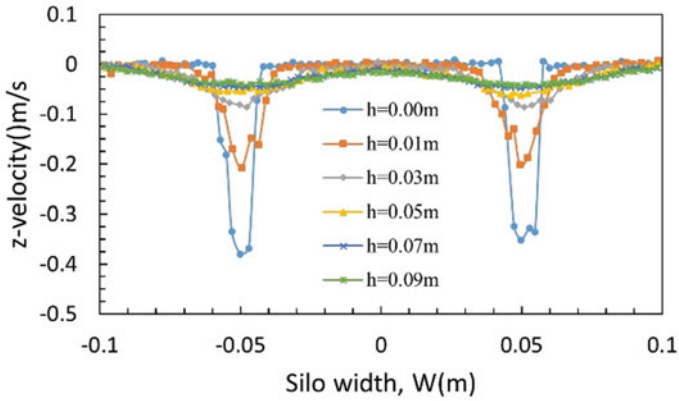
Fig. 14 Plot of *z*-direction velocity with respect to silo width at a different height from the bottom of the silo for $E = 0.5$
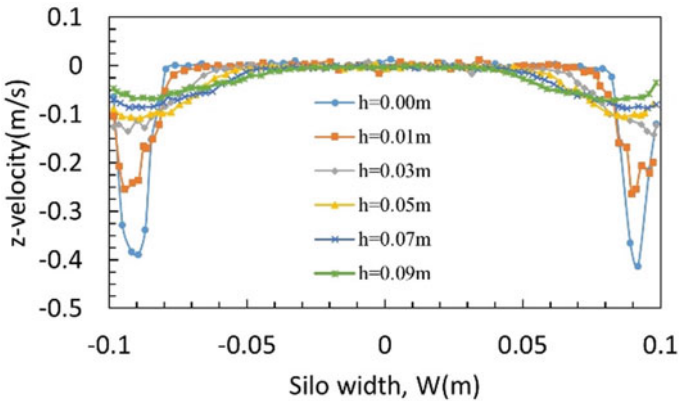
Fig. 15 Plot of *z*-direction velocity with respect to silo width at a different height from the bottom of the silo for $E = 0.93$

References

1. Zhang D, Dong S, Guo H, Yang X, Cui L, Liu X (2022) Flow behavior of granular material during funnel and mixed flow discharges: a comparative analysis. Powder Technol 396:127–138. https://doi.org/10.1016/j.powtec.2021.10.047
2. Wang Y, Lu Y, Ooi JY (2013) Numerical modelling of dynamic pressure and flow in hopper discharge using the Arbitrary Lagrangian-Eulerian formulation. Eng Struct 56:1308–1320. https://doi.org/10.1016/j.engstruct.2013.07.006
3. Maiti R, Das G, Das PK (2017) Granular drainage from a quasi-2D rectangular silo through two orifices symmetrically and asymmetrically placed at the bottom. Phys Fluids 29. https://doi.org/10.1063/1.4996262

4. Wang Y, Jia F, Zhang J, Han Y, Chen P, Li A, Fei J, Feng W, Hao X, Shen S (2022) Model construction method of discharge rate of eccentric silo. Powder Technol 405:117555. https://doi.org/10.1016/j.powtec.2022.117555

5. Anand A, Curtis JS, Wassgren CR, Hancock BC, Ketterhagen WR (2008) Predicting discharge dynamics from a rectangular hopper using the discrete element method (DEM). Chem Eng Sci 63:5821–5830. https://doi.org/10.1016/j.ces.2008.08.015

6. Cheng X, Zhang Q, Shi C, Yan X (2017) Model for the prediction of grain density and pressure distribution in hopper-bottom silos. Biosyst Eng 163:159–166. https://doi.org/10.1016/j.biosystemseng.2017.09.006

7. Daviet G, Bertails-Descoubes F (2016) A semi-implicit material point method for the continuum simulation of granular materials. ACM Trans Graph 35. https://doi.org/10.1145/2897824.2925877

8. Xu Y, Kafui KD, Thornton C, Lian G (2002) Effects of material properties on granular flow in a silo using DEM simulation. Part Sci Technol 20:109–124. https://doi.org/10.1080/02726350215338

9. Burman BC, Cundall PA, Strack ODL (1980) A discrete numerical model for granular assemblies. Geotechnique 30:331–336. https://doi.org/10.1680/geot.1980.30.3.331

10. Kloss C, Goniva C (2011) LIGGGHTS—open source discrete element simulations of granular materials based on LAAMPS. Suppl Proc Mater Fabr Prop Charact Model 2:781–788. https://doi.org/10.1002/9781118062142.ch94

11. Kloss C, Goniva C, Hager A, Amberger S, Pirker S (2012) Models, algorithms and validation for opensource DEM and CFD-DEM. Prog Comput Fluid Dyn 12:140–152. https://doi.org/10.1504/PCFD.2012.047457

12. Lacaze L, Phillips JC, Kerswell RR (2008) Planar collapse of a granular column: experiments and discrete element simulations. Phys Fluids 20. https://doi.org/10.1063/1.2929375

13. Das Ritwik Maiti PK, Meena S (2012) Flow field during eccentric discharge from quasi-two-dimensional silos–extension of the kinematic model with validation. AIChE J 59:215–228. https://doi.org/10.1002/aic.15149

Numerical Study of the Plane, Slotted and Holed Disc Magnetorheological Brakes: A Computational Fluid Dynamics Approach

Manish K. Thakur, Chiranjit Sarkar, Shubham Chouksey, and Rathod Srinivas

Nomenclature

T Transmittable torque (N m)
h MR gap (m)
η Viscosity (Pa s)
B Magnetic flux density (T)
ρ Density (kg/m^3)
ω Rotor rotational speed (rad/s)

1 Introduction

The conventional brakes' performance reduces with time due to wearing out of the brake pads and hence deteriorates the braking performance. The brake dust (iron, carbon, and other metallic particles) becomes air born from the grinding of the brake pad and rotor [1]. Conventional hydraulic brakes use pneumatic pumps and pipes to transfer air pressure to the brake actuators. But when the "x by wire" was introduced in the tech field, the use of electromechanical brakes (EMB) system appeared in the industry [2, 3]. So the conventional brakes are replaced by the EMB system. One example of EMB is the drum brake system [4]. In this research work, an EMB based on MR fluids is presented. MR fluid is well known colloidal suspension which consists of magnetic particles, base fluid, and some additives [5].

M. K. Thakur · C. Sarkar (✉) · S. Chouksey · R. Srinivas
Department of Mechanical Engineering, IIT Patna, Bihta, Bihar 801103, India
e-mail: csarkar@iitp.ac.in

In the MR brake, shear friction is generated due to the controlled characteristics of MR fluid which is situated between the stator and the rotor [6]. MR fluids are prepared by adding micron-sized of approx. 1–10 μm diameter carbonyl-iron (CI) particles to an appropriate carrier fluid, e.g., silicone oil or mineral oil [7]. In the absence of a magnetic field, their rheological behavior is almost the same as that of carrier fluid. When they are subjected to the magnetic field, the particles of iron acquire a dipole moment supported by the applied magnetic field to form a linear chain-like formation parallel to the field. This leads to the changes in liquid to semi-solid and hence its yield strength, which is directly proportional to the magnitude of the magnetic field applied.

2 Literature Review and Objective

Shio and Kantipudi [8] studied experimentally and numerically an MR brake with high-density torque characteristics with dual disc construction. Nguyen et al. [9] presented a novel MR brake with electromagnetic coils placed on side housings directly using a thin wall. The MR fluid is kept in between the parallel disc of the MR brake which is enclosed by an electromagnet. The performance of the MR brake depends on retaining MR fluid inside the gap between the two parallel brake discs. Jianwei et al. [10] did their experiments on a leak-proof MR device to improve its performance. Kuzhir et al. [11] studied theoretically and experimentally the MR fluid flow through various porous media. While Recebli and Kurt [12] have investigated steady two-phase fluid flows under the effects of magnetic and electrical fields in circular pipes.

The main idea in this research work to represent the MR fluid braking torque obtained by Sarkar and Hirani [13] by the simulation tool. In the MR brake, the MR fluid flows which contains iron micro-particles in a carrier liquid is studied numerically by using a COMSOL Multiphysics module based on magnetic induction, CFD, and multi-phase flow equation solver method. The combined numerical study of magnetic field distribution, the CFD and multi-phase simulation have been used further to obtain the maximum braking torque for MR brake consists of three different types of braking discs. The results obtained from simulation provide the velocity of MR fluid flow and particle migration with time and then the maximum braking torque for each type of MR brake disc.

3   Materials and Methods

3.1   MR Brake with Different Rotor Design

The MR brake designing process includes several steps such as the material selection, magnetic circuit design, and sealing. The MR brake consists of an enclosed electromagnet and multiple rotating disks immersed in an MR fluid. MR fluid solidifies when current is applied to the electromagnetic coil. This controlled yield stress produces on the disks which are rotating with some omega value, generates the torque. In MR brake, the MR fluid particles entrapped between the disc and the housing plates act as a friction material. Generally, the material of the disc and the housing plates is made of mild steel (MS), while seals and bearings are made of rubber and stainless steel (SS), respectively. The suggested MR brake is of a single disc type with a rotating rotor plate and stationary armature housing plates which covers the central electromagnet. MR fluid is kept in the annular space along the periphery as well as at both sides of the MS rotor which is mounted on the SS shaft. The wiper seals around the shaft are used to seal the MR fluid and allow sliding in the direction of attractive force by the stator when the magnetic field is applied in the side electromagnet. A detailed illustration of the MR brake is shown in Fig. 1a and the prototype of the MR brake is in Fig. 1b.

In the compression mechanism, a side electromagnet is used. During the compression, the carrier fluid passes through the compression to the expansion zone via small holes in the case of holed disc or slots in the case of a slotted disc. Due to this the iron particle percentage increases in the compression zone and reduces the iron percentage in the expansion zone. This MR brake has an inner radius of the disc $r_1 = 10$ mm, an outer radius of the disc $r_2 = 45$ mm, and an initial MR fluid gap $h = 1$ mm in consideration of the 1:5 scale of a Volvo disc brake. The proposed design of the modified MR brake with changes in rotor design is a plane disc, slotted disc, and holed disc as shown in Fig. 2. The schematic consists of three equal size slots with an inner and outer radius of 17 mm and 23 mm, respectively, with an angle of 75 °C making with the center.

During compression, the carrier fluid passes through the compression to the expansion zone via small holes in the case of the holed disc. Due to the compression mechanism in holed disc MR brake, the iron weight percentage 50 or MRF50 fluid can be used effectively in driving condition. The proposed holed disc with schematic is shown in Fig. 2c. The schematic shows the total number of holes of 2, 3, and 4 mm which are 11, 20, and 30.

3.2   Mathematical Modeling of MR Brake

The viscosity of MR fluid rapidly increases by applying a magnetic field. While in the absence of a magnetic field, it is a freely flowing fluid. Equation (1) represents
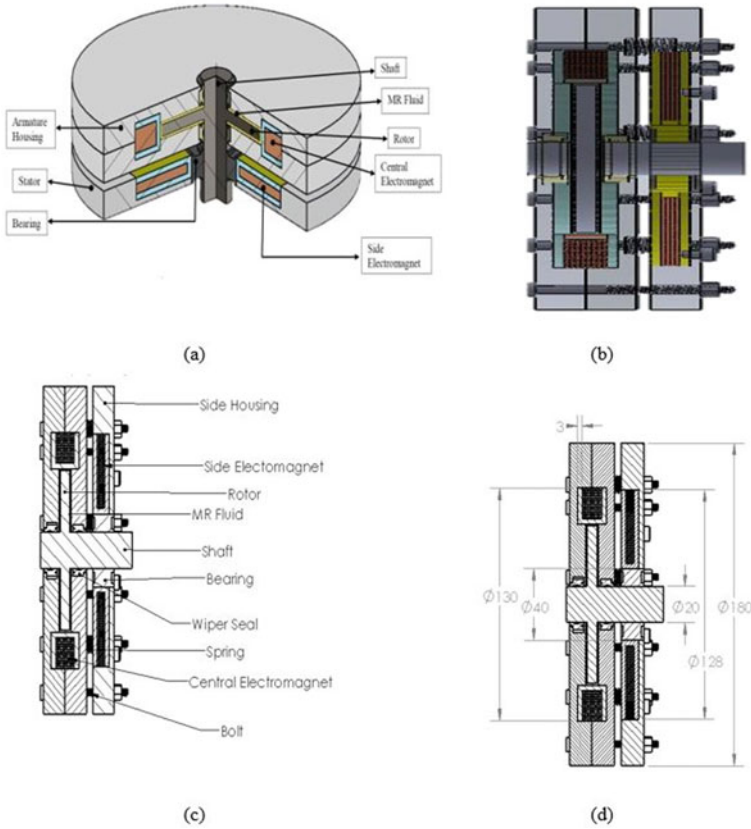
Fig. 1 **a** Isometric view, **b** section view of MR brake, **c** schematic and **d** detailed illustrative of MR brake

the MR fluid characteristic expressed by Bingham rheological model [13].

$$\tau = \tau_{yd}(B) + \eta_0\dot{\gamma} \tag{1}$$

where τ_{yd} is the field-dependent shear stress, where B is the magnetic field intensity, $\dot{\gamma}$ is the shear rate, and η_0 is the base fluid viscosity. On further simplification of Eq. (1), we obtain Eq. (2), where η_d is the dynamic viscosity which is field-dependent.

$$\eta_d = \frac{\tau_{yd}(B)}{\dot{\gamma}} + \eta_0 \tag{2}$$

The rheological characteristic of MR fluid is drawn at various magnetic fields and found that the shear stress increases with increasing magnetic flux density which is predicted in Eqs. (1) and (2). The Bingham shear stress model is used for MR fluid kept in an MR brake with an inner and outer radius of 10 mm and 45 mm

Fig. 2 Isometric view of
a plane disc rotor with
b detailed illustrative of
plane disc rotor, isometric
view of **c** holed disc rotor
with **d** detailed illustrative of
holed disc rotor, isometric
view of **e** slotted disc rotor
with **f** detailed illustrative of
the slotted disc rotor
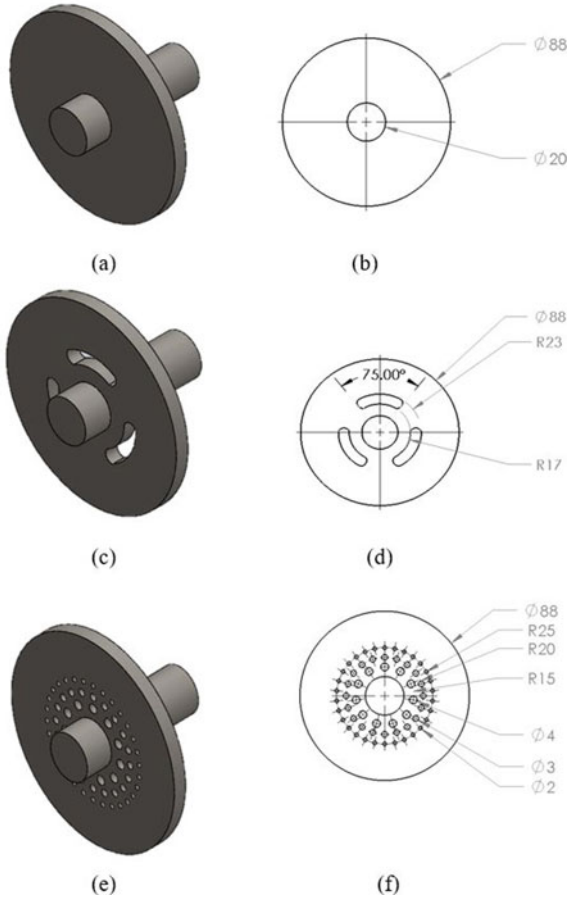
respectively and MR fluid gap of $h = 1$ mm. For MR brake, the maximum resistance
of the transmittable torque is thus a function of (B) and $\dot{\gamma}$. $\dot{\gamma}$ is a function of angular
velocity, distance from the rotational axis (r), and the MR fluid gap (h).

$$T_t = \pi r^3 \eta_d \dot{\gamma} \tag{3}$$

$$\dot{\gamma} = \frac{r\omega}{h} \tag{4}$$

On combining Eqs. (3) and (4)

$$T_t = \pi r^3 \left(\eta_0 + \frac{\tau_{yd}(B)h}{r\omega} \right) \left(\frac{r\omega}{h} \right) \tag{5}$$
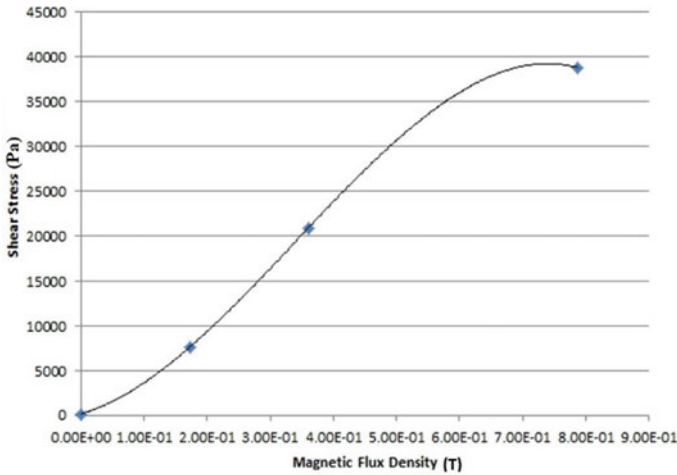
Fig. 3 Graph of magnetic flux density versus shear stress of the MR fluid

Equation (5) is used to find the braking torque using CFD. The graph, shown in Fig. 3, presents magnetic flux density versus shear stress at a constant shear rate of 100 1/s. The polynomial model that best fits the variation of magnetic field and yield shear stress is expressed in Eq. (6).

$$\tau_{yd} = 102676B^5 - 327698B^4 + 330047B^3 - 62023B^2 + 19164B + 145.33 \quad (6)$$

3.3 Numerical Simulation Study

To simulate the magnetic field distribution, a magnetic field (mf) interface in the AC/DC module of COMSOL Multiphysics software has been used. It has been used for finding the yield stress dependency to solve the torque equation Eq. (3). Magnetic field interface is used to find the induced current distribution and the magnetic field in and around the coil, magnets, and conductors. This module solves Maxwell's equations which are formulated using the scalar electric potential and magnetic vector potential as the dependent variable. To calculate the field intensity (H) across the shear surfaces, the line and area integrations available in the postprocessor of the AC/DC module are utilized. The geometry of MR Brake is drawn in SolidWorks software and then imported into COMSOL Multiphysics.

To implement the Amperes' Law, the component of the MR Brake is selected as separate domains. The material properties of each domain are listed in Tables 1 and 2. All domains are selected to solve Amperes' Law. An initial value of zero

Table 1 Material description for various components used in MR brake simulation

S. No	Component	Material
1	Shaft, roller bearing, fasteners, rotor, armature housing	Low carbon steel (1002)
2	Wiper seal	NR (polyisoprene)
3	Central core	Aluminum
4	Current carrying coil	Copper

Table 2 MR fluid properties

S. No	Material property	Values
1	Relative permeability	10
2	Electrical conductivity (S/m)	10
3	Relative permittivity	200,000

magnetic vector potential has been used in the simulation. A homogenized multi-turn conductor model for the circular coil in the MR brake is implemented with 300 turns as shown in Fig. 4. The wire has a conductivity of 0.6 μS/m, and a cross-section area of $4.1 \times 10 - 7$ m^2. Mesh size is selected using the COMSOL's automatic mesh generator with the "Extra fine" element option.

CFD analysis is used to find the magnitude of the MR fluid velocity field and the streamlined velocity of the MR fluid in MR brakes. The Laminar Flow interface of COMSOL Multiphysics has been used to solve the velocity and pressure flow field for a single phase MR fluid of density 3860 kg/m^3 and dynamic viscosity as 0.150 Pa s. The applied material to each domain is shown in Fig. 5. The variation of
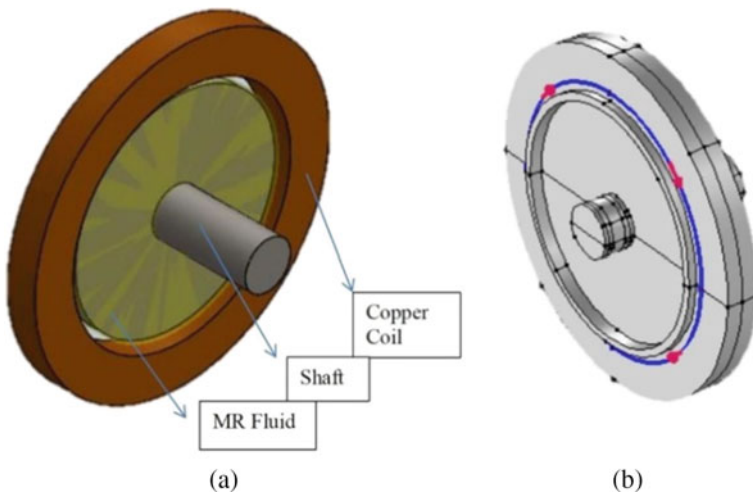

(a)   (b)

Fig. 4 a Applied boundary conditions with domains given and **b** coil geometry and current direction applied in COMSOL Multiphysics

dynamic viscosity is given by Eq. (2), where η_0 has a numerical value of 0.15 Pa s and the yield shear stress is given by Eq. (6).

The rotating wall boundary condition is used for the rotating shaft (yellow lines in Fig. 5c and no-slip, i.e., static boundary conditions to the outer wall represented in blue lines). At $r = 0$ or about the z-axis (represented by red color in Fig. 5b), the geometry is symmetric. A pressure point constraint of 0 Pa is given to the vertex of the fixed wall (represented as a red dot in Fig. 5c). An axisymmetric boundary condition is applied along the shaft rotating axis. To solve MR fluid flow at low and moderate Reynolds number of liquid containing a dispersed phase, a mixture model laminar flow interface of COMSOL has been used. The iron particle of MR fluid (i.e., the dispersed phase) volume fraction variation with time in MR Brake has been computed. The dispersed phase is assumed to always travel with a terminal velocity. This module interface solves one set of Navier–Stokes equations for the momentum of the mixture. The slip model describes the velocity of the dispersed phase and pressure distribution is calculated from the average continuity equation. The flow of complex fluid-like grease is predicted by Eq. (7), which relates the velocity and the radial distance (r) [14].

$$u(r) = U_S e^{\alpha(r-r_i)} \left[\frac{\frac{r_0}{r} - \frac{r}{r_0}}{\frac{r_0}{r_i} - \frac{r_i}{r_0}} \right] \tag{7}$$

where U_s is the shaft rotating speed, r_i and r_0 are the inner radius and outer radius of the MR Brake, and α is the fitting parameter (constant) which is evaluated experimentally. The axisymmetric boundary condition is applied along the axis of the rotating shaft. The rotating walls were selected as the inlet walls as shown in Fig. 6. In the MR Fluid domain, the volumetric force is applied and is given by Eq. (8) [14].

$$F_{\text{vol}} = \frac{4a^3 U_S^2 (\rho_d - \rho_{cp})}{3rw (r_{d0}^2 - r_{di}^2)} \tag{8}$$

where U_s is the rotational speed of the shaft, r_{di} and r_{d0} are the inner and the outer radius of the MR Fluid domain and w is the width of the domain.

4 Results and Discussion

To find the solution of the magnetic field distribution, a parametric sweep of current comprising 0, 0.5, 1, and 1.5 A has been done. The result on various planes and MR fluid plane is plotted. A plane passing through the center of the rotor is used which is referred to as MR fluid plane. The surface magnetic flux density (T) in the XZ plane for the plane disc (b) holed disc (c) slotted disc with both (central and side) active coils is shown in Fig. 7. Figure 7a represents the surface magnetic flux density when both coils have current flowing through them. The parameter of current is given
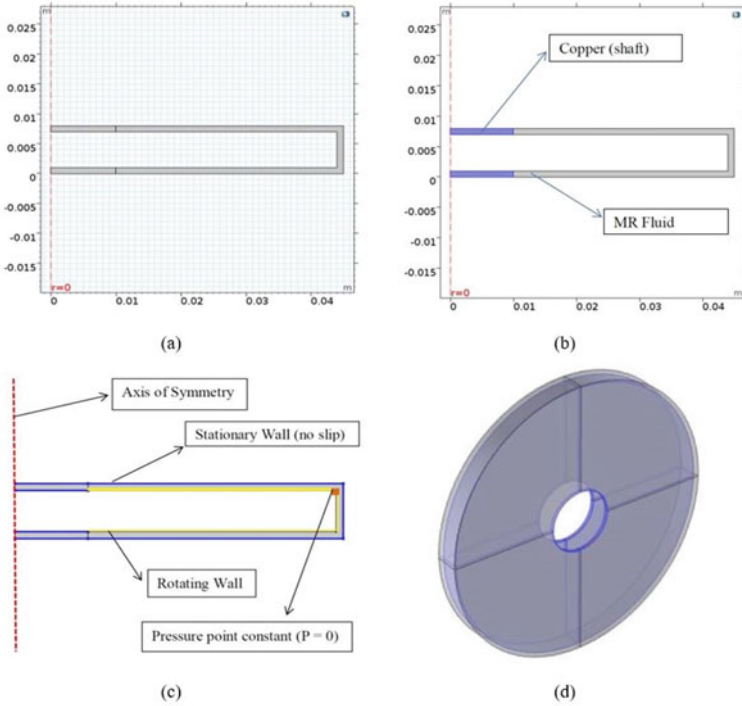
Fig. 5 **a** Geometry of MR fluid domain, **b** material specification of the MR fluid geometry, **c** applied boundary conditions of MR fluid domain and **d** 3D geometry of MR fluid
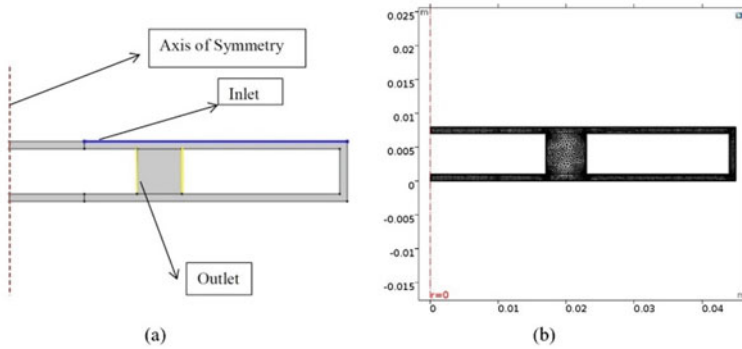
Fig. 6 **a** Applied boundary conditions of MR fluid domain, **b** MR fluid meshed geometry
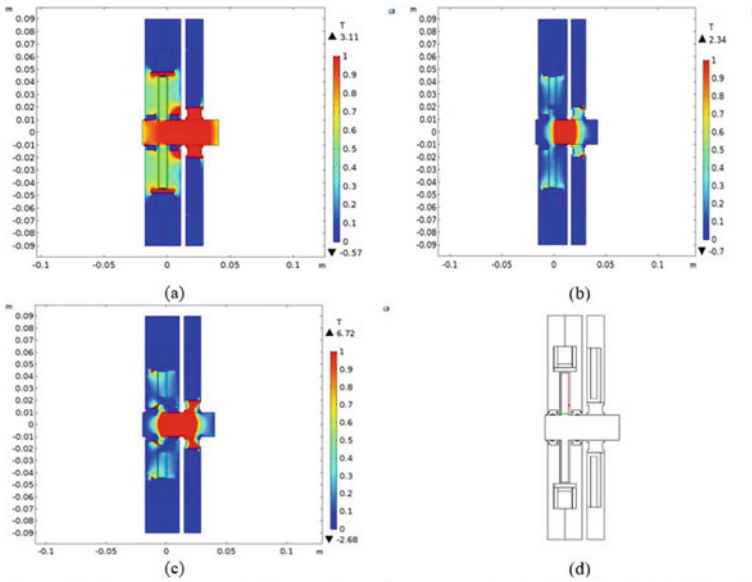
Fig. 7 **a** Surface magnetic flux density (T) in the XZ plane for the plane disc, **b** holed disc, **c** slotted disc with both (central and side) active coils and **d** cut line drawn on the MR fluid domain

as 1.5 A. The cut plane is made up of an XZ plane. The values illustrated are as follows from a maximum of 6.72(T) to a minimum of $-2.68(T)$. The negative sign indicates the induced electromagnetic force that opposes the change of magnetic flux associated with a surface. If the field points out of the surface (in the same direction as the normal), then the flux is positive. The red color portion in the geometry of MR brake indicates the higher magnetic field. Figure 7b shows the magnetic flux density on a center plane at input current 1.5 A and Fig. 7d shows the cutline drawn at MR fluid domain.

A plane along the diameter of the MR fluid domain is shown in Fig. 8a, on which the pressure and velocity profiles are drawn. To get the variation of transmittable torque along the radial direction, a cut line in MR fluid close to the rotating wall is drawn as shown in Fig. 8b. The velocity profile of the MR fluid domain with the rotor rotating at an angular speed of 300 rev/min is shown in Fig. 8c.

The iron particle movement due to compressive force on the MR fluid, the flow of dispersed phase, i.e., the iron particles through the slotted disc is presented in the MR fluid domain as presented in Fig. 9. A time-dependent study at 0, 1, 10, 60, 3600, and 7200 s is performed for the present model. It shows the variation of the MR fluid particle concentration in the MR fluid domain at 300 rpm at times 0, 0.02, 0.06, and 0.1 s. The MR fluid iron particles move from the inner rotation wall to the outer stationary wall due to the centrifugal force and then from compressive zone to expansion zone.
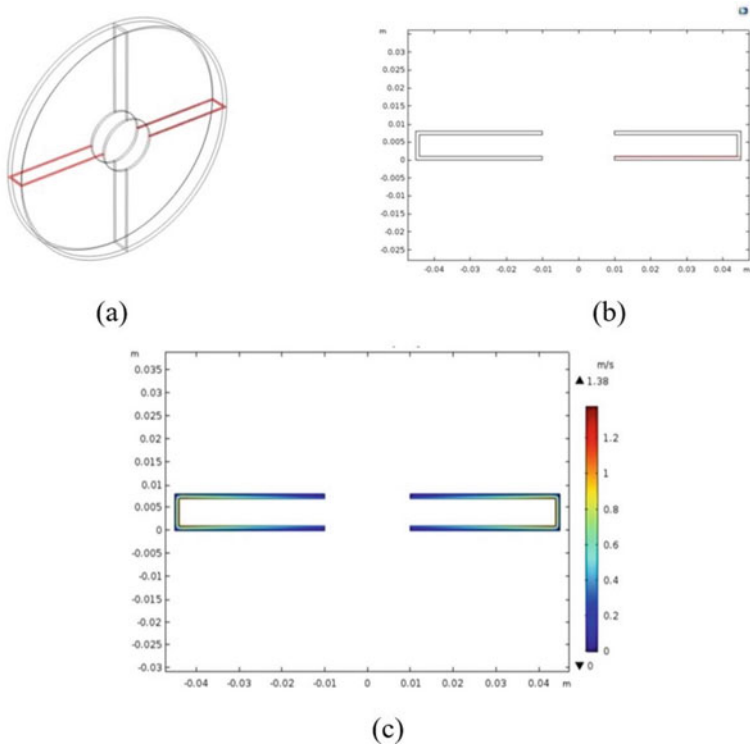
Fig. 8 **a** Cut plane drawn along the diameter of MR fluid domain, **b** cut line (MR Fluid) drawn near the rotating wall to get the brake torque and **c** velocity magnitude profile of MR fluid domain

The comparative results of simulation torque in Fig. 10 for the three different MR brake discs show that the slotted disc has a higher value of torque (4.5 Nm) than the others. It also shows the linear trend with the input current (*A*). The minimum value of torque is obtained around the groove area. It is due to lesser magnetic field occurring around the groove surface. The torque shows an increasing trend with the increased disc radius.

5   Conclusions

In this research work, a numerical tool is developed for the MR brake with a different type of brake disc. It can simulate the magnetic field distribution, MR fluid flow velocities, and MR particle migration. Three different surfaces of the texture-based rotor disc of the MR brake have been analyzed through the magnetic field distribution, CFD, and multi-phase flow approach in COMSOL Multiphysics software. It involves mixture flow analysis to predict the MR particle or dispersed phase flow in the domain
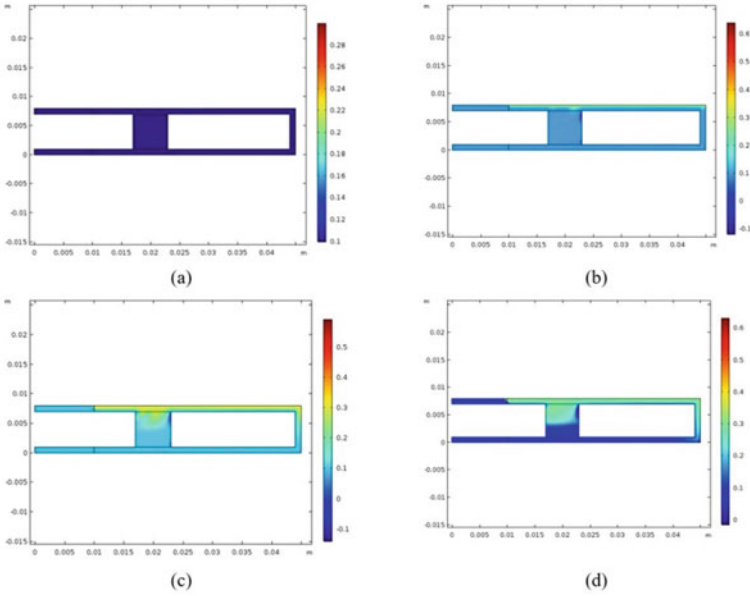
Fig. 9 Volume fraction of MR fluid particles for MR Brake rotating at 300 rpm with time **a** 0 s, **b** 0.02 s, **c** 0.06 s, **d** 0.1 s
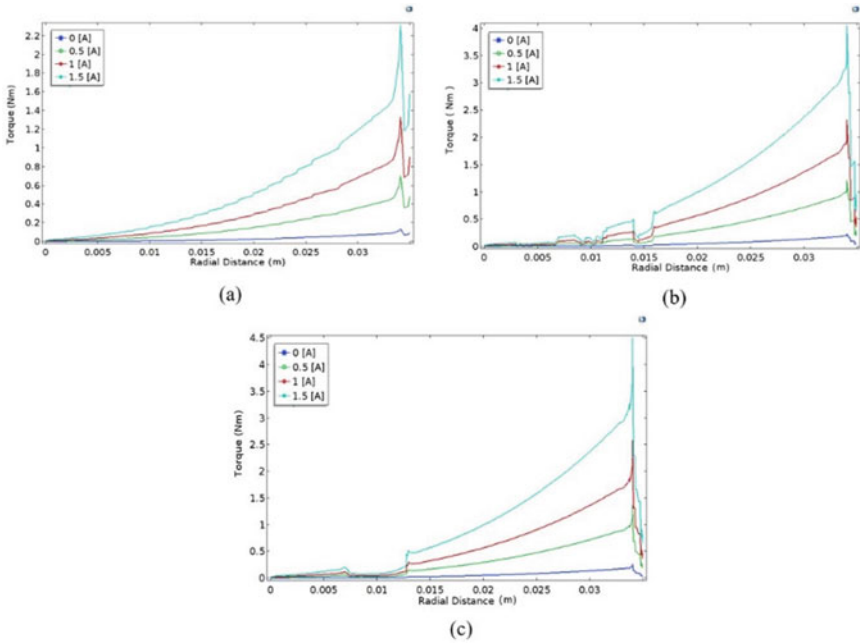
Fig. 10 Variation of MR brake torque on cut line (MR fluid) in **a** plane disc, **b** holed disc and **c** slotted disc MR brake

of MR fluid. The presented work can be successfully used for numerical simulation of MR fluids kept inside the MR brake with different types of the brake discs. The present method is limited to the simulation of steady, laminar flows of MR fluid. The effectiveness of surface modification is identified due to the higher value of torque. The individual simulation for a plane, slotted, and holed disc MR brake is performed, and the torque performance data with brake radius is plotted. The variation of torque for slotted, plane, and holed disc MR brakes is presented. The slotted disc-based MR brake has a higher value of torque than other MR brake discs. Hence, we can note that a slotted disc MR brake is recommended.

References

1. Jamadar NM, Jadhav HT (2021) A case study on effective reduction in friction brake dust by adopting electric braking system. Life Cycle Reliab Saf Eng 10(1):91–97
2. Atia MR, Haggag SA, Kamal AM (2016) Enhanced electromechanical brake-by-wire system using sliding mode controller. J Dyn Syst Meas Control 138(4):041003
3. Farris RJ, Goldfarb M (2010) Design of a multidisc electromechanical brake. IEEE/ASME Trans Mechatron 16(6):985–993
4. Dias AL, Rodrigues RDN, Bezerra RDA, Lamary P, Miranda MH (2021) Light duty automotive drum brake squeal analysis using the finite-element method. Proc Inst Mech Eng Part L J Mater Des Appl 14644207211035991
5. Thakur MK, Sarkar C (2020) Influence of graphite flakes on the strength of magnetorheological fluids at high temperature and its rheology. IEEE Trans Magn 56(5):1–10
6. Sarkar C, Hirani H (2013) Theoretical and experimental studies on a magnetorheological brake operating under compression plus shear mode. Smart Mater Struct 22(11):115032
7. Thakur MK, Sarkar C (2021) Thermal and tribological performance of graphite flake-based magnetorheological fluid under shear mode clutch. J Tribol 143(12):121806
8. Yaojung S, Kantipudi MB (2022) High torque density magnetorheological brake with multipole dual disc construction. Smart Mater Struct 31(4):045022
9. Hung NQ, Le HD, Li W, Hung NX (2021) Development of a novel magnetorheological brake with zigzag magnetic flux path. Smart Mater Struct 30(12):125028
10. Jianwei T, Li Z, Zhang J, Gao K, Liao J, Gao J (2019) Development, test, and mechanical model of the leak-proof magnetorheological damper. Frontiers Mater 6:118
11. Kuzhir P, Georges B, Victor B, Olga V (2003) Flow of magnetorheological fluid through porous media. Eur J Mech-B/Fluids 22(4):331–343
12. Recebli Z, Hüseyin K (2008) Two-phase steady flow along a horizontal glass pipe in the presence of the magnetic and electrical fields. Int J Heat Fluid Flow 29(1):263–268
13. Sarkar C, Hirani H (2017) Experimental studies on magnetorheological brake containing plane, holed and slotted discs. Ind Lubr Tribol
14. Westerberg LG, Sarkar C, Lladós JF, Lundström TS, Höglund E (2017) Lubricating grease flow in a double restriction seal geometry: a computational fluid dynamics approach. Tribol Lett 65(3):82

Estimation of Friction and Inlet Loss Coefficient in Stationary Annulus

S. Aravindan and A. John Arul

1 Introduction

Pumps are designed with very small clearance between the rotating impeller and stationary casing, to maximize the volumetric efficiency. The pumps are provided with wear rings which offer the small clearance. The differential pressure across the wear ring drives the flow through it in the axial direction and the rotation of the wear ring of the impeller will drive the flow in the circumferential direction as shown in Fig. 1.

The total pressure loss in the annulus is a combination of inlet/entry loss and friction loss. The friction loss coefficient was estimated by Yamada [1] for annulus with mean radius to radial clearance (R/C) ratio of 9.2–74. The wear rings in centrifugal pumps have R/C ratio of 250–750 [2], which is one order higher than the annulus which was studied earlier. Hence, the applicability of correlations given by Yamada for wear rings has to be verified and inlet loss coefficients have to be estimated. Estimation of inlet and friction loss coefficient in the annulus is of paramount importance towards assessment of total pressure drop in the annulus as well as rotordynamic coefficients such as stiffness and damping.

In this study, CFD analysis is carried out towards estimation of friction and inlet loss coefficients for the annulus, whose R/C ratio is 250–700.

S. Aravindan (✉) · A. J. Arul
Homi Bhabha National Institute, Indira Gandhi Centre for Atomic Research, Kalpakkam, Tamilnadu 603102, India
e-mail: aravinds@igcar.gov.in
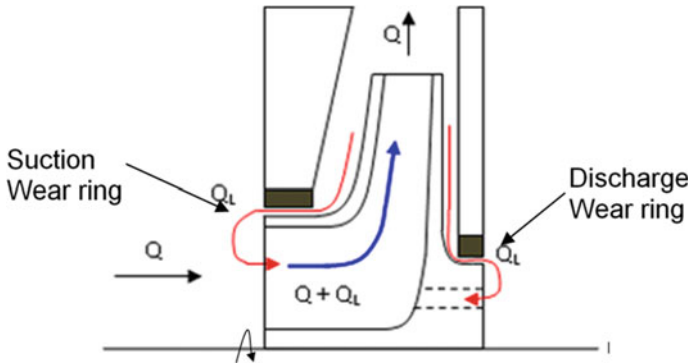
Fig. 1 Flow path in an impeller and leakage flow through wear rings

2 Literature Review and Objective

Yamada [3] has studied the resistance of water flow through co-axial cylinders, with inner cylinder under stationary and rotating condition. The flow resistance is measured for six sizes, *R/C* ranging from 9.2 to 74, for various combination of axial and rotation flows. The inner radius ranges from 28.8 to 31.7 mm in this experiment. Yamada has also derived an empirical formula for friction loss coefficient (or) friction factor (λ) based on velocity distribution on the flow between the plates, with one moving plate and 1/7th power law of turbulent flow.

The Suction Wear Ring (SWR) and Discharge Wear Ring (DWR) clearance in the pumps is governed by the API standard and the recommended *R/C* ratio of shown in Fig. 2. It can be observed that, the *R/C* ratio for API recommended wear ring design can be up to 800, which is ~ 1 order less than the *R/C* ratio for which extensive studies are available in the literature.

Fig. 2 Range of radial clearance to diameter ratio for sodium pumps
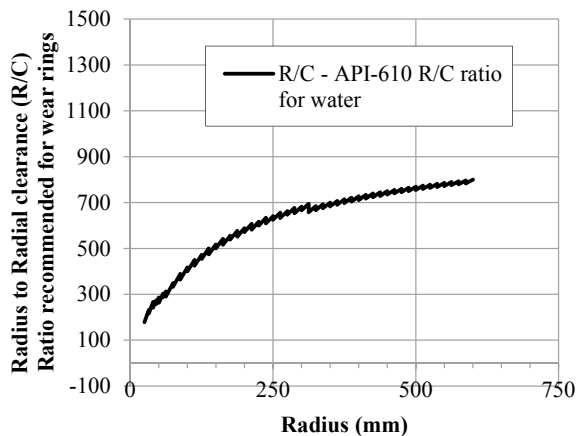
2.1 Importance of Friction Loss and Inlet Loss Coefficients

The friction factor for annulus is estimated by Yamada in 1962 [3]. The friction factor and entry loss coefficient in the annulus are used to estimate rotor dynamic coefficients of wear rings. The pressure loss in the wear rings is given by

$$\Delta P = (1 + \zeta + \sigma) \times \frac{\rho V^2}{2} \tag{1}$$

where $\frac{(1+\zeta)\rho V^2}{2}$ defines the inlet pressure drop and $\frac{\sigma \rho V^2}{2}$ defines the friction pressure drop and $\sigma = \frac{\lambda L}{2C}$ where λ is the friction factor or friction loss coefficient, L is the length of the wear ring and C is the radial clearance of the seal.

An expression is derived to estimated the rotordynamic coefficients of the seal by Childs [4] and it is given by

$$\overline{K} = \frac{2\sigma^2 E(1 - m_0)}{1 + \zeta + 2\sigma} \tag{2}$$

$$\overline{C} = \frac{2\sigma^2 B\left(\frac{1}{6} + E\right)}{2(1 + \zeta + 2\sigma)} \tag{3}$$

where $\overline{K}$ and $\overline{C}$ are non-dimensional stiffness and damping coefficients, E and B are also dimensionless coefficients, which are functions of ζ and λ. Hence, reasonably accurate estimation of inlet and friction loss coefficients are crucial for reasonably accurate estimation of stiffness and damping coefficients.

2.2 Correlations on Friction Loss and Inlet Loss Coefficients

The friction loss coefficient (λ) for annulus is estimated by Yamada [3] and it is given for laminar and turbulent flow as

$$\lambda_{\text{laminar}} = f_2 = \left(\frac{96}{Re_a}\right) \tag{4}$$

$$\lambda_{\text{turbulent}} = f_2 = 0.307\left(Re_a^{-0.24}\right)\left(1 + \left(\frac{7}{8}\right)^2\left(\frac{Re_c}{2Re_a}\right)^2\right)^{0.38} \tag{5}$$

where $Re_a = V(2C)/\nu$ and $R_\omega = U(2C)/\nu$.

However, there is no clear correlation is available in literature for entry loss coefficients. Some of the literature suggests that $\zeta = 0.1$ [5] or $\zeta = 0 \text{ to } 0.25$ [6], without providing any range of Re_a and Re_c at which it is applicable. In an example problem given by Childs [4], $\zeta = -0.5$ is taken for water seals.

Hence, in this study, the annulus is modelled in ANSYS FLUENT® towards estimation of friction and inlet loss coefficient. The validation of friction loss coefficient correlations by Yamada for annulus with large R/C ratio (250–700) is verified and the inlet loss coefficients are estimated.

3 Region of Study and Methodology

The wear ring in typical pumps will consists of two regions, namely annulus entrance region and the annulus region as shown in Fig. 1. The flow will enter from the entrance region to the annulus region, where the fluid undergoes inlet pressure loss. When the fluid is travelling in very narrow clearance in annulus, it will also experience significant friction loss compared to the entrance region.

In FLUENT, an axisymmetric model is developed to study the entry loss and friction loss in annulus. In FLUENT, the axisymmetric model with axis of rotation as X-axis is shown in Fig. 3. R_{1m} and R_{2m} represent the mean radius of annulus entrance region and annulus region. L_1, C_1 be the length and radial clearance of annulus entrance region and L_2, C_2 be the length and radial clearance of the annulus region.
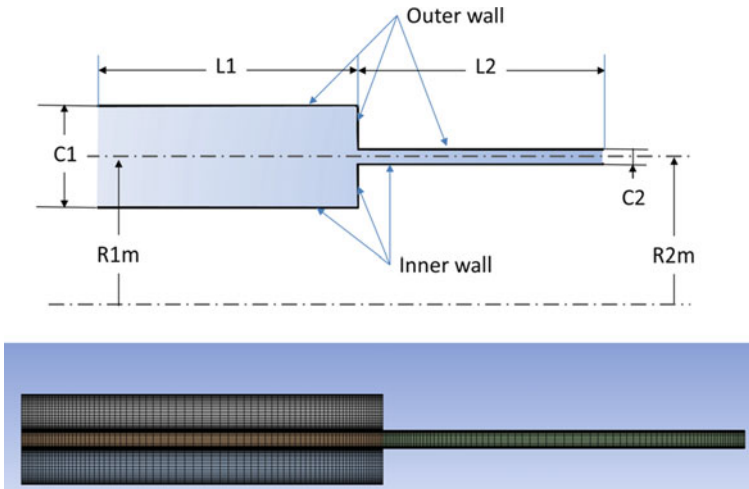
Fig. 3 Annulus entrance and annulus region with dimensions for modelling and parametric study in ANSYS FLUENT

3.1 Procedure for Estimation of Inlet and Friction Loss Coefficients

The procedure followed for obtaining friction loss coefficient and inlet loss coefficient is given below.

STEP 1: The annulus is modelled in ANSYS design modeller and it is meshed.

STEP 2: In the ANSYS FLUENT, apply the inlet velocity of the entry annulus (V_1), fluid properties (μ, ρ) and pressure at the outlet (P_{out}).

STEP 3: Solve the model using k–ω SST turbulence model, with convergence criteria for residuals of continuity, momentum, k and ω as 10^{-6}. The converged pressure and velocity fields are obtained.

STEP 4: In the post processing, define lines (a1, a2, a3, …, x1, x2, x3,…) at regular intervals on both entry and wear ring annulus as shown in Fig. 4. Compute the average pressure at these lines.

STEP 5: Compute the pressure drop per unit length ($\Delta P_{fric}/L$) at each section. The pressure drop per unit length will converge at the end of annulus, indicating a developed flow.

STEP 6: The friction drop in annulus is given by $\Delta P_{fric} = \lambda \left(\frac{L}{D_h}\right)\left(\frac{\rho V^2}{2}\right)$, where $D_h = 2C$. From the estimated pressure drop per unit length ($\Delta P_{fric}/L$), the friction factor (λ) is calculated for the entry region and wear ring annulus $\lambda = \left(\frac{\Delta P_{fric}}{L}\right)\left(\frac{4C}{\rho V^2}\right)$. The friction pressure loss is estimated in each segment using above correlations.

STEP 7: The total pressure loss in the model (ΔP_{total}) is estimated from FLUENT and the inlet loss due to sudden entry of flow to the wear ring annulus is estimated as $\Delta P_{entry} = \Delta P_{total} - \Delta P_{fric}$.

STEP 8: The inlet pressure loss is given by $\Delta P_{inlet} = (1 + \zeta)\left(\frac{\rho V^2}{2}\right)$, from which the inlet loss coefficient (ζ) is estimated.

A flow chart of the above sequence followed for estimation of friction loss and inlet pressure loss is shown in Fig. 5.
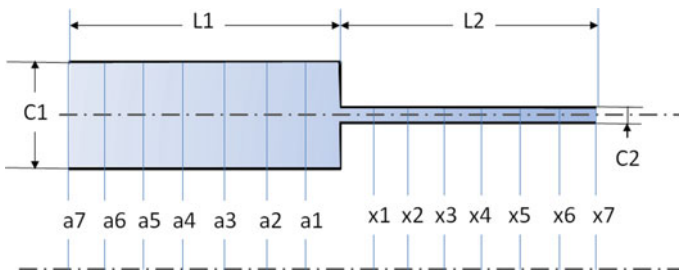
Fig. 4 Sections along the flow domain
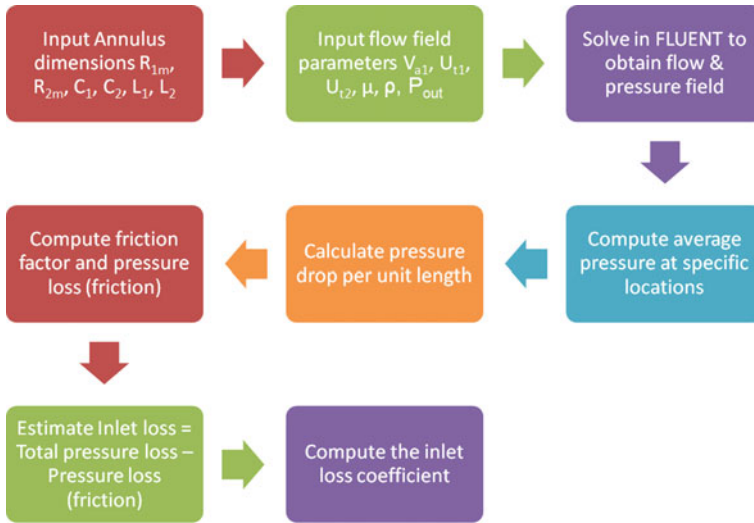
Fig. 5 Flow chart to calculate the friction loss and inlet loss coefficients

4 Results and Discussion

The friction losses and inlet losses were studied for a range of *R/C* ratios based on dimensions mentioned in Yamada [3] and API recommended wear ring clearance are given in Table 1.

4.1 Validation with Literature

The annulus with minimum *R/C* ratio studied by Yamada is modelled with *R/C* ratio of 9.2 and *L/C* of 60. The friction coefficient (λ) is estimated for a stationary annulus and the results obtained are compared with the correlations.

Table 1 Range of *R/C* and *L/C* ratio of wear rings to be studied

References	*R* (mm)	*C* (mm)	*R/C*	*L* (mm)	*L/C*
Yamada	30.494	3.315	9.2	190	57
	31.936	0.431	74	190	441
API recommended dimensions	100	0.354	282	100	282
	250	0.524	477	100	191
	500	0.781	640	100	128

Fig. 6 Friction loss coefficient in stationary annulus and comparison with expressions given in literature
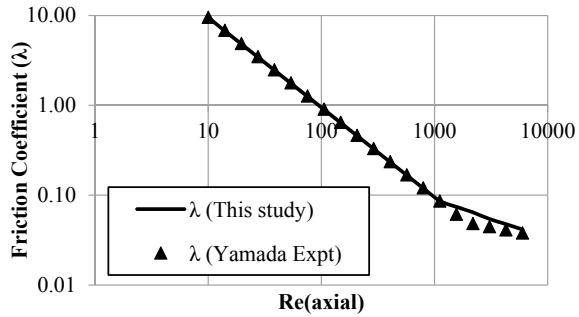
The results for friction loss coefficient (λ) obtained from FLUENT are plotted in Fig. 6, and the results are found to match well with the analytical expressions from Yamada [3].

4.2 Mesh Convergence

A mesh convergence check is carried out for estimation of friction loss coefficient and inlet loss coefficient. The element edge length defined during meshing is halved from initial value, to obtain a refined mesh. For *R/C* ratio of 9.2, for given initial element length, number of elements was 35,000. When the element edge length was reduced by half during meshing, number of elements increased to 136,000. Similarly, the process is repeated again, to get mesh size of 540,000. The results from all the three mesh are shown in Fig. 7. It was found that, the results have converged well. Similarly, the inlet loss coefficient is estimated for three mesh sizes and it is shown in Fig. 8. The results for inlet loss coefficient in turbulent zone ($Re_a > 2000$) expressed excellent convergence considering the lowest mesh size. However, in the laminar domain, deviation is observed in lowest mesh size (NOE = 35,000) compared to other two meshes (NOE = 136,000 and 540,000), indicating the significance of mesh convergence study.

4.3 Friction and Inlet Loss Coefficient for Annulus with Higher R/C Ratios

The friction loss coefficient is estimated for annulus with larger *R/C* ratios, under stationary condition are estimated and it is plotted in Fig. 9. It can be observed that the friction loss coefficient does not vary significantly for a range of *R/C* ratio from 9 to 640. The reason for the non-variation of friction coefficient is that, the friction loss depends on the Reynolds number only, which is affected only by the gap between the annulus and flow velocity. The Reynolds number does not depend on radius of

Fig. 7 Friction loss
coefficient in stationary
annulus ($R/C = 9.2$) for
various mesh size
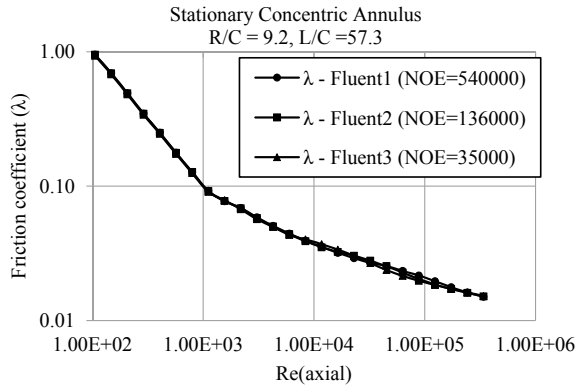
Fig. 8 Inlet loss coefficient
in stationary annulus ($R/C =$
9.2) for various mesh size
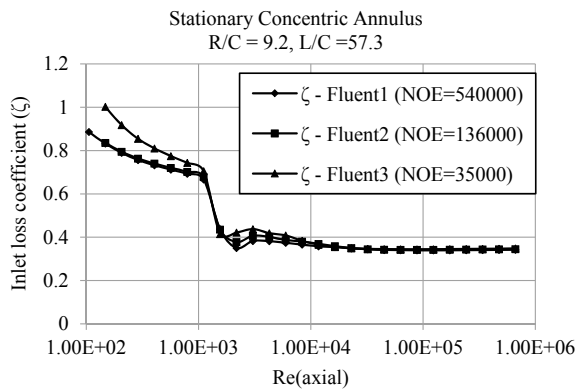
the annulus and hence, the friction coefficient does not depend on R/C ratio of the annulus.

The inlet loss coefficient is estimated and it is shown in Fig. 10. The inlet loss coefficient in turbulent zone is 0.4. However, in the laminar domain, the inlet loss coefficient varies as a function of Reynolds number as well as R/C ratio. In the laminar regime, the inlet loss coefficient is higher, because of larger vena contracta formation due to lower velocity.

The static pressure distribution in the inner and outer wall of the annulus is plotted for annulus with R/C ratio of 9.2 for $Re = \sim 200$ and ~ 300 and shown in Fig. 11. From the figure, it can be observed that though the inlet loss coefficient is turbulent, regime is less than the laminar regime, and the actual pressure loss at the inlet is high in turbulent regime.

From the results, it was observed that the friction loss coefficient results for annulus with larger R/C ratios matches well for the results published by Yamada. However, the inlet loss coefficient for wear rings in turbulent regime is ~ 0.4, whereas in laminar domain, it is estimated to be ~ 0.6 to ~ 1.2.

Fig. 9 Friction loss coefficient in stationary annulus with various *R/C* ratio
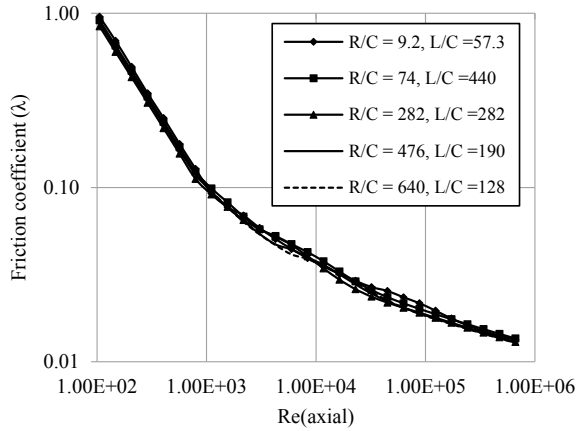
Fig. 10 Inlet loss coefficient in stationary annulus with various *R/C* ratio
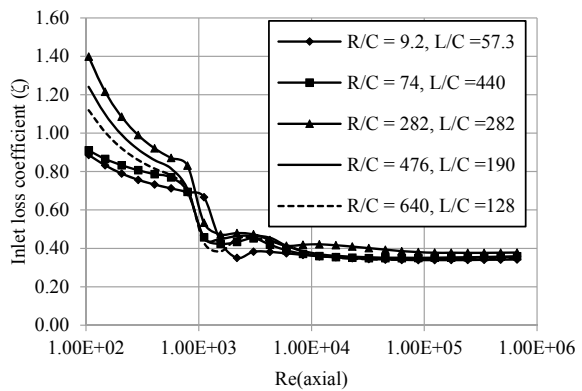
5 Conclusions

The flow in the annulus is modelled and solved using computational fluid dynamics towards estimation of friction and inlet loss coefficient. The correlations are available in literature, where annulus with *R/C* ratio of 74 is estimated using experiment. Since the annulus in pumps can have high *R/C* ratio up to 750, the annulus with higher *R/C* ratio is studied. The conclusions are:

- The correlation from Yamada for friction loss coefficient matches well with the friction loss coefficient estimated for larger *R/C* annulus. Hence, the applicability of correlations to larger *R/C* annulus is verified from this study.
- The inlet loss coefficient is estimated and it was found to decrease with increase in Reynolds number in laminar regime.
- The inlet loss coefficient was found to remain fairly constant (~ 0.4) in the turbulent regime for the annulus with *R/C* ratio from 9 to 750.
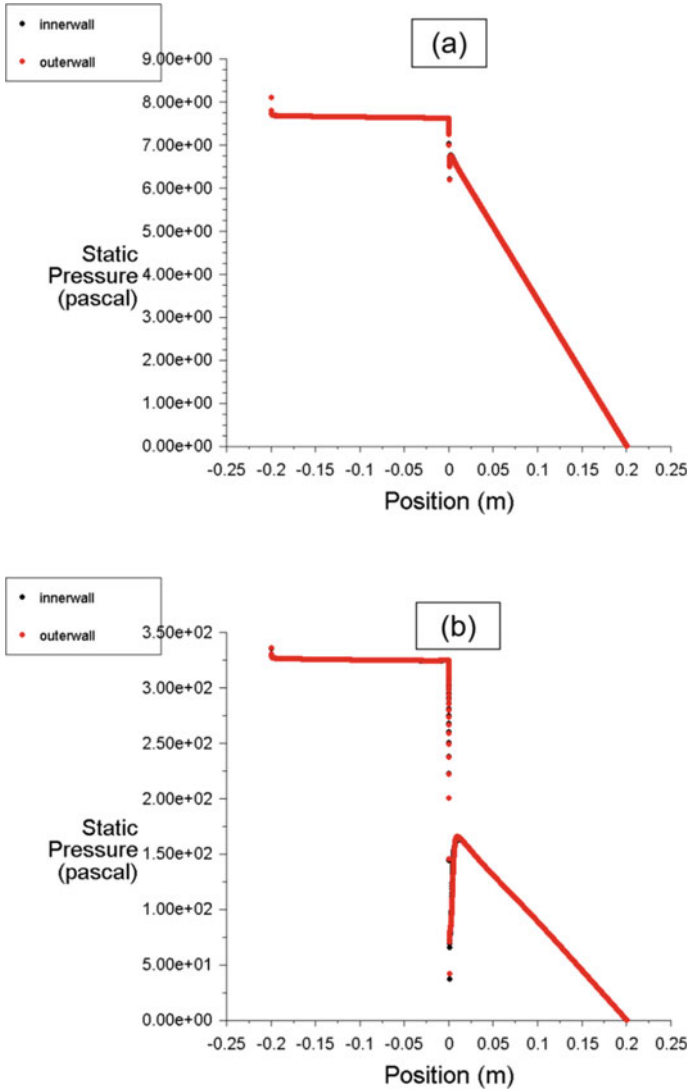
Fig. 11 Distribution of static pressure in annulus with *R/C* ratio of 9.5, for **a** *Re* = ~ 200 and **b** *Re* = ~ 3000

Nomenclature

R	Mean radius of the annulus (m)
C	Radial clearance of the annulus (m)
ζ	Inlet loss coefficient (–)
λ	Friction loss coefficient (–)
V	Velocity of flow in the annulus (m/s)
$\overline{K}$	Non-dimensional stiffness (–)
$\overline{C}$	Non-dimensional damping (–)
Re_a	Axial Reynolds number (–)
Re_c	Circumferential Reynolds number (–)
ν	Kinematic viscosity of liquid (m^2/s)
ΔP_{fric}	Friction pressure drop (Pa)
ΔP_{total}	Total pressure drop (Pa)
ΔP_{entry}	Entrance pressure drop

References

1. Yamada Y (1962) Resistance of flow through an annulus with an inner rotating cylinder. Bull JSME 5(18):302–310
2. API 610 (2010) Centrifugal pumps for petroleum, petrochemical and natural gas industries, 11th edn
3. Yamada Y (1962) Resistance of a flow through an annulus with an inner rotating cylinder. Bull JSME 5(18):302–310
4. Childs DW (1983) Dynamic analysis of turbulent annular seals based on Hirs' lubrication equation. J Lubr Technol 105(3):429–436
5. Dyrobes (2022) Liquid annular seals calculation (online). https://dyrobes.com/help1800/Rotor/html/dyro64v5.htm#:~:text=Typical%20value%20for%20the%20inlet%20loss%20factor%20is%200.1
6. San Andrés L (2010) Notes on annular pressure seals (online). https://rotorlab.tamu.edu/me626/Notes_pdf/Notes12a%20Damper%20Seals.pdf

Investigation of Experimental Data of Linkage Involving Adhesive Joint

Prashant Maheshwary, Pramod Belkhode, Sarika Modak, Ayaz Afsar, and Shubhangi Gondane

1 Introduction

Literature indicates that various properties of properly chemically treated bamboo can be significantly enhanced, so that such material can replace steel and/or plastic as a new material for machine parts. The properties that can be enhanced are (i) yield strength in tension/compression/shear [1, 2], (ii) abrasion and wear resistance [3, 4], (iii) impact resistance [5], (iv) moisture absorption resistance [6], (v) heat resistance [7, 8], (vi) dielectric strength improvement [9], etc. In this case, it is necessary to test the properly chemically treated bamboo as a new material for machine parts. It is also necessary to confirm the suitability of the developed adhesives for joining the machine parts made from bamboo.

This second aspect is the focus of the present investigation, in which a six-link planar linkage with one degree of freedom [10] is experimentally investigated to study the response of properly chemically developed adhesive joint [11] for two parts of one coupler of this linkage. The material of the links, except for the frame, is a bamboo. However, the developed adhesive is suitable for timber bamboo [12, 13], which is available in Vidarbha region of India.

P. Maheshwary
Science and Technology, Rashtrasant Tukadoji Maharaj Nagpur University, Nagpur, India

P. Belkhode (✉)
Department of General Engineering, LIT Nagpur, Nagpur 440033, India
e-mail: pnbelkhode@gmail.com

S. Modak
Department of Civil Engineering, PCE Nagpur, Nagpur 440033, India

A. Afsar
Department of Mechanical Engineering, Government Polytechnic, Amravati, India

S. Gondane
LIT Nagpur, Nagpur 440033, India

The mechanism is made up of bamboo lap joint with the application of synthesized adhesive. The lap joint of the bamboo is a crank, connecting rod and closed link. The synthesized adhesive is used to make lap joints. The significance of this mechanism is bamboo strips which are used instead of an iron bar for the linkage of this mechanism. For a small mechanical set-up, the bamboo can be used as an alternative material that is involved in the specific operation. Formulation of mathematical models in the form of relationship amongst responses and causes involved and the nature of the relationship have been focused. Various mechanisms and small set-ups are replaced with the bamboo set-ups. The analysis was carried out on bamboo strips. An experimental data-based modelling approach is proposed to study bamboo adhesive.

Analysis of six-bar mechanism is performed by varying the speed of the mechanism, in the range of 12–16 rpm, with the loading condition in the rage of 5–9.5 kg, varying the cross section area of the link, overlapping length of the joint on which adhesive is applied. The compound chain brings about rotary to oscillatory motion. The output link is sustaining the load torque organized by the dead weight W, pulley P and a rope R around pulley. The energy source is 80 W fractional HP motor operating at 12-V supply. The load torque tried is in the range of 400–640 Nm. The experimental observation recorded as per the independent variable decided as per the theory of experimentation suggested by H. Schenck Jr. An experimental data-based model is formulated based on the experimental observation. The indices of the model are the indicators of the independent pi terms which indicate the interaction of individual pi terms and dependent pi terms, i.e. the ratio of shear stress to tensile yield stress.

2 Experimental Set-Up

Mechanisms are means of power transmission as well as motion transformers. A bamboo six-bar link mechanism consists mainly of six planar links connected with six revolute joints. The input is usually given as rotary motion of a link and output can be obtained from the motion of another link or a coupler point. The bamboo species such as timber bamboo are used for the preparation of the link. The synthesized adhesives are used for the preparation of the links. The lap joints of bamboo are prepared with the application of synthesized adhesives. The bamboo strips are prepared and dry it at room temperature for seven days. For testing the mechanical properties of this link, the tensile test and compressive test are carried on the lap joints of bamboo on the UTM machine. Experimental set-up is fabricated using the bamboo links and joint with synthesized adhesive.

The schematic line diagram of the experimental set-up is shown in Fig. 1, Figure show the six-link planar chain mechanism $O_1ABO_2CO_3$ with link lengths $O_1A = 5.0$ cm; $AB = 10.0$ cm, $O_2B = 12.0$ cm, $BC = 36.0$ cm, $O_3C = 15.0$ cm and $O_1O_2O_3 = 55.0$ cm. The links O_1A, AB, O_2B, O_3C are rectangular cross sections of 3.0 cm $\times$ 2.0 cm. The link BC 36.0 cm long is in two identical pieces with adhesive joint

having dimensions 11.0 cm along BC with the height of 3.0 cm and thickness of adhesive is 0.2 cm located at in the middle of link BC as shown in Fig. 2.

The output shaft of the experimental set-up is fastened with the pulley of diameter $= 15.0$ cm wound with the rope with a dead weight W to generate resisting torque. Experimentation is performed with the varying dead weights of 5.0, 5.5, 6.0, 6.5, 7.0, 7.5, 8.0 kg at a time to the develop torque. The linkage consists of single degree of freedom (SDOF) system [10] with driving crank O_1A. The driving energy is provided with DC motor source of 12 V and 75 W. The preparation of adhesive is detailed as below: Liquification of bamboos is the first step which involved the mixture of glycerol and sulfuric acid. The mixture of 25% liquified bamboos and 75% phenol formaldehyde with the addition of 5% wheat flour is heated at 180° in oil bath for adhesive preparation. The prepared adhesive consists modulus of elasticity which

M: Motor, P: Pulley, W: Weight, R:Rope
$\angle\alpha = 12.0°$ TR = Time Ratio = 192.0/168.0 = 1.142
$O_1O_2O_3$ = 55.0 cm; O_1A = 5.0cm; AB= 10.0cm, BC = 36.0 cm, O_3C = 15.0 cm
Subscript L & R for left extreme and right extreme positions
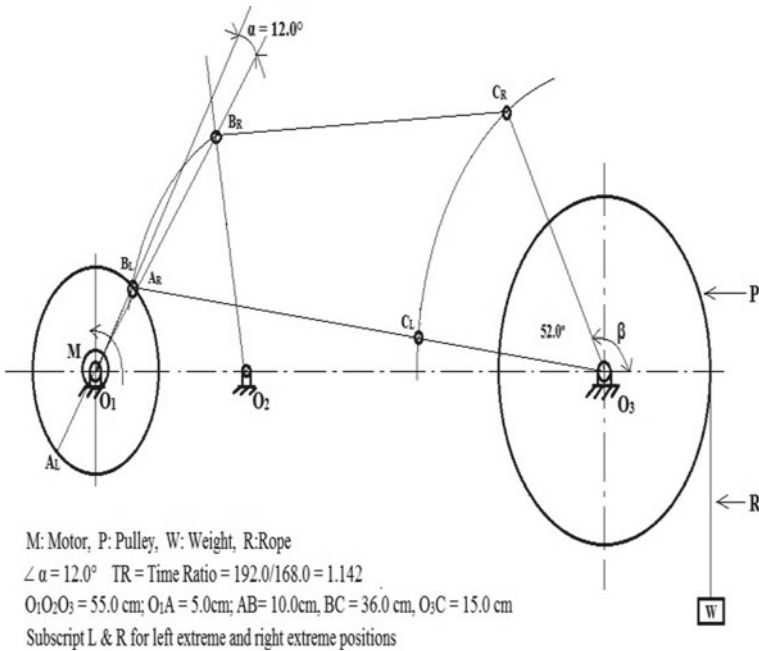
Fig. 1 Schematic diagram of an experimental set-up

Fig. 2 Sample link with adhesive layer

Top View of the Link BC

D Front View E

DE: Adhesive layer :11.0cm*3.0cm*0.2cm
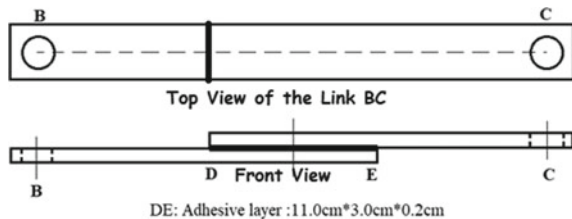
Table 1 System specifications at failure

Sr. No.	W, kg	No. of rotations	Position of O_3C, β (°)
1	5.0	18.0	137.0
2	5.5	15.0	137.0
3	6.0	13.0	138.0
4	6.5	15.0	137.0
5	7.0	14.0	137.0
6	7.5	15.5	136.0
7	8.0	16.0	135.0

Fig. 3 Photograph of the experimental set-up
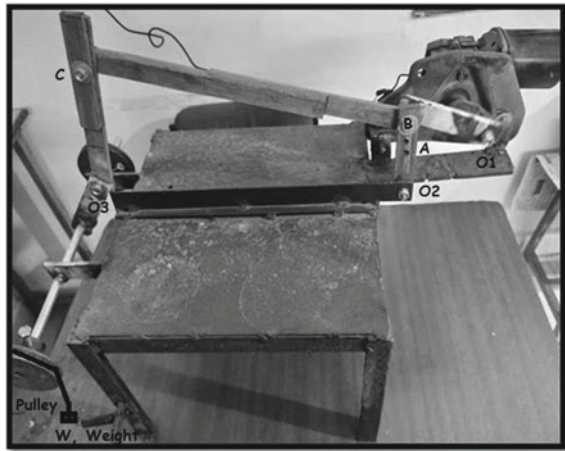
is 96 MPa. Modulus of elasticity of bamboo is 20 GPa. Table 1 gives the recorded observations when the connecting link of the fracture of coupler BC as shown in Table 1. The photograph of experimental set-up is shown in Fig. 3.

Experimentation is performed by varying the dead weight from 5 to 8 kg and the mechanism is operated for each weight till the propagation of crack in the link 5 with adhesive joint fractured. Number of rotations performed by the driving crank O_1A and approximate angular position of coupler BC at the instant of fracture is recorded in observation Table 1. The weights tried are 5.0, 5.5, 6.0, 6.5, 7.0, 7.5 and 8.0 kg for one weight only one coupler BC is tried.

Experimentation is performed on six-link planar chain mechanism consists of lap joints of bamboo coupler link BC prepared with the application of synthesized adhesives with the varying load from 5 to 8 kg on the pulley. The number of rotations of the input and the number of oscillations is recorded in Table 1. Table 1 gives that as load increases number of rotations with almost small variation in the position of O_3C. This indicates the load bearing capacity of the couple link with the lap joint.

3 Formulation of Dimensional Equations

The mechanism is made up of bamboo lap joint with the application of synthesized adhesive. The lap joint of the bamboo is a crank, connecting rod and closed link. The synthesized adhesive is used to make lap joints. The significance of this mechanism is bamboo strips which are used instead of an iron bar for the linkage of this mechanism. For a small mechanical set-up, the bamboo can be used as an alternative material that is involved in the specific operation. Formulation of mathematical models in the form of relationship amongst responses and causes involved and the nature of the relationship have been focused. Various mechanisms and small set-ups are replaced with the bamboo set-ups. The analysis was carried out on bamboo strips. An experimental data-based modelling approach is proposed to study bamboo adhesive.

a. The variables affecting the effectiveness of the phenomenon under consideration of bamboo lap joint

These independent variables have been reduced into group of π terms. Equation (1) ahead shows the relationship of Dimensionless π terms of the phenomenon.

A: Dimensional equation for fracture of adhesive joint.

π_D = Dependent π term;

$\pi_D = S/S_{ys}$;

S_{ys} = Yield strength in shear of low carbon steel, MPa.

The dependent or the response variables are

$$\text{Ratio of shear stress to the yieldstress} = f[(\pi_1)(\pi_2)(\pi_3)(\pi_4)] \qquad (1)$$

b. Dependent and independent variables for the experimental set-up involved with double four-bar model are presented in Table 2.

4 Formulation of Model

Experimental set-up is fabricated with the bamboo lap joint with adhesive applied for link BC involves in six-link planar chain operated by varying the dead weight over the pulley. The experimentation is executed for each dead weight till the failure of the bamboo link. Similarly, experimentation is executed by varying dead weight and observations were recorded given in Tables 3, 4, 5 and 6. Based on the information of Tables 3, 4, 5 and 6, four different types of models can be formed. These could be (i) exponential form of independent π terms (ii) combining all independent π terms into one independentπ term form (iii) Response Surface Modelling (RSM) and (iv) Artificial Neural Network Simulation [14]. Model is selected for the analysis by identifying independent and dependent variables. The indices of the model indicate the most influences variables that changes the dependent term. The term π_1 is related the ratio of link lengths which is constant term, $\pi_1 = 193,000,000.0$, π_2 is related the

Table 2 Independent and dependent variables

Description	Variables	Symbol	Dimension
Fixed link 1	Independent	L1	$[M^0 \, L^1 \, T^0]$
Crank	Independent	L2	$[M^0 \, L^1 \, T^0]$
Connecting link 1	Independent	L3	$[M^0 \, L^1 \, T^0]$
Fixed link 2	Independent	L4	$[M^0 \, L^1 \, T^0]$
Connecting link 2	Independent	L5	$[M^0 \, L^1 \, T^0]$
Fixed link 3	Independent	L6	$[M^0 \, L^1 \, T^0]$
Diameter of pulley	Independent	D'	$[M^0 \, L^1 \, T^0]$
Thickness or strip	Independent	T	$[M^0 \, L^1 \, T^0]$
Lap joint length	Independent	l	$[M^0 \, L^1 \, T^0]$
Modulus of elasticity of adhesive	Independent	E_{adh}	$[M^1 \, L^1 \, T^0]$
Modulus of elasticity of bamboo	Independent	E_b	$[M^1 \, L^1 \, T^0]$

Table 3 Experimental observations $W = 8$ kg, $\pi_3 = 51.94$

SN	β (°)	π_4	F65 kg	S = F65/(11.0 * 3.0)	π_D
1	114	1.988	5.000	0.1515	0.00167
2	127	2.215	5.210	0.1579	0.00175
3	134	2.337	15.000	0.4545	0.008
4	137	2.389	40.000	1.2121	0.0135
5	142	2.477	20.000	0.6061	0.007
6	147	2.573	24.000	0.7273	0.008
7	152	2.651	20.000	0.6061	0.007

ratio of elasticity of adhesives to the elasticity of bamboo which is constant term π_2 = 0.004895, π_3 is related the ratio of dead weight applied to the weight of adhesive which is constant term $\pi_3 = 51.94$ and the remaining pie terms are varied to get the dependent pie term as shown in Tables 3, 4, 5 and 6 obtained by varying the β (°) and F65 is noted when the link is instantly break.

5 Discussion of Results

Figure 2 shows highly complex patterns of variation of π_D with respect to various combinations of $\pi_1, \pi_2, \pi_3, \pi_4$. The reason becomes evident from Fig. 3. Figure 3 is corresponding to observations as presented in Table 3 and Fig. 3 is corresponding to observations as presented in Table 6. Tables 3 and 6 correspond, respectively, to weight $W = 8.0$ kg and $W = 5.0$ kg in pan for creating load torque. The corresponding ranges of variation of independent quantities are highly overlapping and hence are

Table 4 Experimental observations $W = 7.5$ kg, $\pi_3 = 48.70$

SN	β (°)	π_4	F65 kg	$S = $ F65/(11.0 * 3.0)	π_D
1	114	1.988	4.6875	0.1420	0.00158
2	127	2.215	4.884	0.1480	0.00264
3	134	2.337	14.090	0.4270	0.00474
4	137	2.389	37.580	1.1388	0.01264
5	142	2.477	18.790	0.5694	0.00632
6	147	2.573	22.548	0.6833	0.00759
7	152	2.651	18.790	0.5694	0.00632

Table 5 Experimental observations $W = 7$ kg, $\pi_3 = 45.45$

SN	β (°)	π_4	F65 kg	$S = $ F65/(11.0*3.0)	π_D
1	114	1.988	4.374	0.1325	0.00147
2	127	2.215	4.530	0.1373	0.00152
3	134	2.337	13.148	0.3984	0.00442
4	137	2.389	35.060	1.0624	0.01184
5	142	2.477	17.535	0.5314	0.00591
6	147	2.573	21.041	0.6376	0.00708
7	152	2.651	17.535	0.5314	0.0059

Table 6 Experimental observations $W = 6$ kg, $\pi_3 = 38.95$

No.	β (°)	π_4	F65 kg	$S = $ F65/(11.0 * 3.0)	π_D
1	114	1.988	3.710	0.1124	0.00124
2	127	2.215	3.900	0.1182	0.00131
3	134	2.337	11.330	0.3433	0.00381
4	137	2.389	30.127	0.9129	0.01011
5	142	2.477	14.980	0.4539	0.00504
6	147	2.573	18.070	0.5476	0.00608
7	152	2.651	15.010	0.4548	0.00504

their graphic plots. Figure2 are appearing to be extremely difficult to reason out the system behaviour. This thought led to have separate graphic presentation of the system for weights 5.0 and 8.0 kg only (as depicted in Fig. 3). The nature of this variation justifies high complexity of variations presented in Fig. 2.

In Fig. 3 over the variation of $(\pi_1 \times \pi_2 \times \pi_4)/\pi_3$ in the range 3.8×10^4 to 5.2×10^4, the variation of response π_D is also quite complex. The reason for this complexity is in fact on account of nonlinear kinematics of 6 link chain. This is so because for both the plots π_1, π_2 are constant, and even for Fig. 3, π_3 is constant at all points. Only variation is in π_4, i.e. π term related to kinematic angular position of

output link O3C, i.e. angle β. Same is true for graphic variation presented in Fig. 3. Thus, the variation in π_D in Fig. 3 is mainly due to nonlinear rigid body kinematics of output link, of 6 link compound linkage obtained by a double rocker O_2BCO_3 in series with crank rocker O_1ABO_2. Observation Table 1 gives condition of a system at the time of failure of adhesive joint. It is seen that failure has occurred when approximately $\beta = 137.0°$, i.e. when coupler BC is at 25–27° with horizontal. It is at this instant coupler BC is subjected to maximum force for specified load torque. This is of course not considering inertial force analysis as rotational speed of O_1A is very low.

6 Conclusion

Special adhesive developed and used for a coupler of a six-link kinematic chain is having sustainability of around 20 cycles of force variation when coupler maximum force is 40.0 kgf. All links are made from timber bamboo except the frame execution of experimentation is as per design of experimentation, methods of test data checking and rejection, formulation of models reliability of models and optimization of models. All these steps are included and executed as per the approach of "Theories of Engineering Experimentation" by H. Shenck Jr.

Nomenclature

M	Motor
P	Pulley
W	Weight
R	Rope
TR	Time ratio
L	Length of link, cm
D	Depth of cross section of links, cm
T	Thickness of adhesive, cm
l	Length of adhesive layer, cm
EADH	Modulus of elasticity of adhesive material MPa
E_b	Modulus of elasticity of material of bamboo from which links are manufactured, MPa
TL	Load torque on output shaft, Nm
W	Weight for creating load torque, N
D'	Diameter of pulley around which rope is placed with which weight W is attached to create load torque, m
M	Mass of adhesive, kg
β	Angular position in degrees of output link O_3C with frame $O_1O_2O_3$ measured positive counter clockwise

S   Shear stress induced in the joint, MPa
S_{ys} Yield strength in shear of low carbon steel, MPa. 1 to 6: subscripts for link members

References

1. International training workshop on sustainable bamboo management and processing techniques for small size bamboo enterprises, Hangzhou, Zhejiang of China, 2000
2. Hebel E, Javadian A, Wielopolski M, SchlesierK, Heisel F, Griebel F (2013) Process-controlled tensile properties of newly developed bamboo composite materials. In: Composites conference, 2013
3. Chaowana P (2013) Bamboo: an alternative raw material for wood and wood-based composites. J Mater Sci Res 2(20):90–102
4. Banga H, Singh VK, Kumar Choudhary S (2015) Fabrication and study of mechanical properties of bamboo fibre reinforced bio-composites. Innov Syst Des Eng l6(1):84–98
5. Al-Mosawi AI, Abdulsada SA, Hashim A (2015) Mechanical properties of recycled bamboo fibres reinforced composite. Eur J Adv Eng Technol 2(4):20–22
6. Borthakur RD, Gogoi PK (2014) Studies of dimensional stability, thermal stability and biodegradation resistance capacity of chemically treated bamboo. Asian J Biochem 9:16–29
7. Chu Y-M, Zheng P-P, Chen Y-Y (2010) Study on structure of oxidized raw bamboo fibre treated with sericin protein. JFBI 3(1):45–49
8. Chu Y-M, Zheng P-P, Chen Y-Y (2010) Study on structure of oxidized raw bamboo treated with sericin protein. JFBI 3(1):45–49
9. Kittinaovarat S, Suthamnoi W (2009) Physical properties of polyolefin / bamboo char coal composites. J Met Mater Miner 19(1):9–15
10. Hain K (1967) Applied kinematics. Mc-Graw Hill Inc.
11. Belkhode PN. Synthesis of novel adhesive for bamboo joining and comparison of its mechanical properties with adhesives available in market. Recent trends in machine learning and artificial intelligence in the field of science and technology
12. Gondane SM (2019) Analysis of different bamboo species by using existing adhesives in market. J TROI 16(1):1188–1196
13. Gondane SM (2019) Formulation of mathematical model of lap joints of strips of different types of bamboos with proper adhesives subjected to tension, compressive and shear load. IOSR J Eng. International conference on innovation and research in engineering, science and technology, ICIREST, pp 11–16
14. Black PH, Eugene Adams O (1967) Machine design, Mc-Graw Hill Inc.

Exploration of Boundary Layer Transition Through Various Roughness Patterns

Monalisa Mallick [ORCID], **Jahnvi Choudhary** [ORCID], **Abinash Mohanta** [ORCID], **and Awadhesh Kumar** [ORCID]

1 Introduction

To assess the aerodynamic performance of structures, small-scale models are usually tested in a wind tunnel under the prevailing conditions. In the natural atmospheric condition, most of the structures lie within boundary layer thickness. Generally, test section length in a wind tunnel is scanty for the development of high scale turbulence intensity and boundary layer thickness. The distance across a boundary layer from the wall to the point where the flow velocity has basically achieved the free stream velocity (u_o) is known as the boundary layer thickness (δ). This distance is measured normal to the wall. It is normally defined as the point where: boundary layer thickness is the distance from a solid surface to the point where velocity changes to 0.99 u_o in the normal direction. The thickness of the atmospheric boundary layer depends on a variety of variables including the temperature, wind speed, and roughness condition.

We are aware that boundary layer thickness cannot generate turbulence and a boundary layer with sufficient height. Generally, smooth type laminar flow is designed for application in wind tunnels, in which there is less than 4% turbulence. Many researchers employ a variety of passive tools, including vortex generators, spires, and roughness blocks, to increase the boundary layer and turbulence. The attempt has made to enhance boundary layer thickness by making different arrangements in the upstream sides, viz. increasing surface roughness, placement of grids of different configuration, spires of varying shapes and sizes, blocks of different

M. Mallick · A. Kumar
Department of Civil Engineering, National Institute of Technology Rourkela, Odisha 769008, India
e-mail: akumar@nitrkl.ac.in

J. Choudhary · A. Mohanta (✉)
School of Mechanical Engineering, Vellore Institute of Technology, Vellore, Tamil Nadu 632014, India
e-mail: abinash.mohanta@vit.ac.in

shapes, sizes, and configuration or the combination of these. Such arrangements increase turbulence that results in enhancing the boundary layer thickness that can be close to being natured conditions over the land surfaces.

In 1960s, Counihan used an elliptical shape generator in a wind tunnel to boost the turbulence and depth of the boundary layer [1]. Subsequent research led to the development of additional passive devices, some of which used jets on the wind tunnel floor and also simulate a boundary layer in a wind tunnel that has the same turbulence characteristics as an atmospheric boundary layer and use the power law equation, i.e., $u/(U) = (z/\delta)^\alpha$ for the simulation. In the above equation, u stands for average velocity, δ is the depth of the boundary layer, z is the height above the surface, and α is the roughness of the terrain, which is defined as 0.1 for open terrain to 0.35 for urban areas (above 10 m in height). There is also different ranges of α can be achieved in a wind tunnel according to terrain by using various passive devices.

2 Literature Review and Objective

Counihan [1] designed first-time triangular spires and studied the effect on boundary layer thickness in wind tunnel and found significant momentum loss in inner region than that in outer region. It produced large eddies and hence large turbulence generated at the surface. The experimental observation of the body surface and the shear flow-simulated atmospheric boundary layer with a height ten times the body dimension were provided by Castro and Robins [2]. Cook [3] simulated adiabatic atmospheric boundary layer by different roughness pattern in wind tunnel. For the velocity profile, Diffie and Hellman [4] presented a power law that depends on both the terrain's characteristics and height above the ground. Farell and Iyengar [5] used spires and barrier wall to simulate the atmospheric boundary layer and produced the boundary layer with the features of being close to urban terrain condition in wind tunnel. Guimaraes and Portugal [6] used cylindrical and rectangular rods as spires and the combinations of the two to increase the boundary layer thickness in a wind tunnel. Ten easy techniques were proposed by Hunt and Fernholz [7] for simulating a stable, neutral, and unstable atmospheric boundary layer in various types of wind tunnels. Irwin [8] developed a formula for designing triangular spires for an atmospheric boundary layer model and established a link between the altitude of triangular spires and the thickness of the boundary layer. In a wind tunnel, the turbulent structure that drives turbulence generation rate was studied by Kline et al. [9], leading to the development of boundary layer.

Jimenez-Portaz et al. [10] provided outcomes of the analysis of the turbulence generation, the Reynolds stresses, vorticity, vertical velocity skewness and the spectrum features, as well as the quadrant decomposition and demonstrating the results with respect to a closed-circuit wind tunnel that the mean flow is more uniform and the turbulence intensity is generally higher in the current open-circuit wind tunnel. Krishna et al. [11] described to determine forces and pressures on components of building or a structure as required for design purposes in IS 875 (part 3). The

researchers divided the terrain into four part and stated as: (Category-I) primarily comprises open terrain; obstacles should not be higher than 1.5 m, for instance seaside area or a field devoid of trees; (Category-II) barriers should be higher than 1.5 m but not more than 10 m, as in rural areas. (Category-III) obstruction that is greater than 10 m in height but not in a densely packed area like a suburban area. (Category-IV) densely paced area with more impediments that are higher than 10 m, such as an Indian urban region. Mueller et al. [12] studied three simulations were conducted using periodic boundary conditions. Poreh and Cermak [13] observed that if test section is larger than (>15 m) in wind tunnel, it can develop sufficient boundary layer thickness at section around 0.5 m to 1 m and at a velocity of 10 m/s. They used many configurations of triangular spires and barriers to increasing the Boundary Layer. The three main objectives of the effect of roughness on hypersonic boundary layer transition were studied by Schneider [14]. Spera and Richards [15] provided for computing power law exponents from data on surface roughness and wind speed and evaluated by comparison with wind profile data collected at several places. For the first time, Stevenson [16] proposed a parabolic law for velocity profile that was valid for heights greater than 10 m above the ground. Zasso et al. [17] described the outcomes of wind tunnel tests performed on a cone-like shaped roof. They observed that the surface roughness affects the mean pressure distribution. Kozmar [18] studied the boundary layers by varying the thickness such as ten times thicker than the typical dimension of the individual cubes. He observed the turbulence strength varied across the two trials and the normalized flow shear at the cube height was constant. This discovery made it possible to study the pressure characteristics on a wall-mounted cube exclusively in terms of the impact of the entering turbulence, independent of the flow shear, variables that had previously been shown to be significant. Qiu et al. [19] studied the effects of surface roughness and Reynolds number on the properties of aerodynamic pressures and forces on a semicircular roof and obtained simultaneous pressure measurements on smooth and rough roofs under smooth flow condition. Studies of comparison to ABL simulations produced with the regular (non-truncated) Counihan vortex generators, simulation length scales in wind tunnel research focused on wind stresses on structures may be higher when the truncated Counihan vortex generators are used which were shown by Kozmar and Laschka [20]. Broatch et al. [21] proposed a methodology to automatically generate distortion screens to reproduce a desired target velocity distribution, based on analytical relations between the porosity in a media and the total pressure loss induced by this porosity. A numerical routine is used to design a robust and easily manufactured hexahedral grid that matches the required porosity distribution. The results of the study by Catarelli et al. [22] showed that using the suggested framework in conjunction with a mechanized roughness element grid can greatly lessen the amount of trial-and-error needed to commission a BLWT while enhancing the quality of flow characterization. Saini and Shafei [23] created a simulation framework that couples computational fluid dynamics and rigid body dynamics to capture the flight paths of plate-type debris objects in atmospheric boundary layer winds.

The present research work is aimed at the assessment of boundary layer thickness under varying roughness patterns, viz. square block, diamond pattern, spire, spire

with square block, and spire with diamond pattern block. Due to momentum loss depth of boundary layer increased in wind tunnel, boundary layer depth is raised by around 80% compared to an empty boundary layer wind tunnel by using floor roughness.

3 Materials and Methods

Experiments are carried out in an open-circuit sub-sonic wind tunnel in the fluid mechanics laboratory of the Department of Civil Engineering, National Institute of Technology Rourkela, India. The wind speed varied from 6 to 25 m/s. The wind tunnel includes a plywood bottom surface, an 8-m test section, and cross-sectional measurements of 0.6 m in width and 0.6 m in height. Models are placed in the test section such that it would lie within boundary layer zone. An open-circuit wind tunnel diagram of experimental set up is shown in Fig. 1.

Arrangements of roughness elements such as the square and diamond blocks, triangular spires and their combinations are shown in Fig. 2a–e. The blocks of size 2.5 cm cube were placed at 5 cm c/c spacing in both the rectangular and the diamond arrangements. The blocks are mounted on a sheet of plywood that is 4 mm thick, 4 feet long, and the same width as the test part. The blocks are arranged in a diamond pattern with a 45° angle to the flow direction. The spires of 7 cm base of equilateral triangular section and height of 45 cm are fixed at a clear spacing of 5 cm. For the combined roughness pattern, the square and the diamond arrangement separately are placed at a distance of 0.5 m from the original placement of the spires. The floor roughness and spires aspects were set up to mimic an open landscape exposure situation. A pitot-static rake and several Turbulent Flow Instrumentation Cobra Probes were used to track the wind speed profile and turbulence characteristics with respect to height above the ground. To analyze the effects of roughness pattern on the boundary layer thickness, each arrangement is placed in the test section. Five sections are marked in

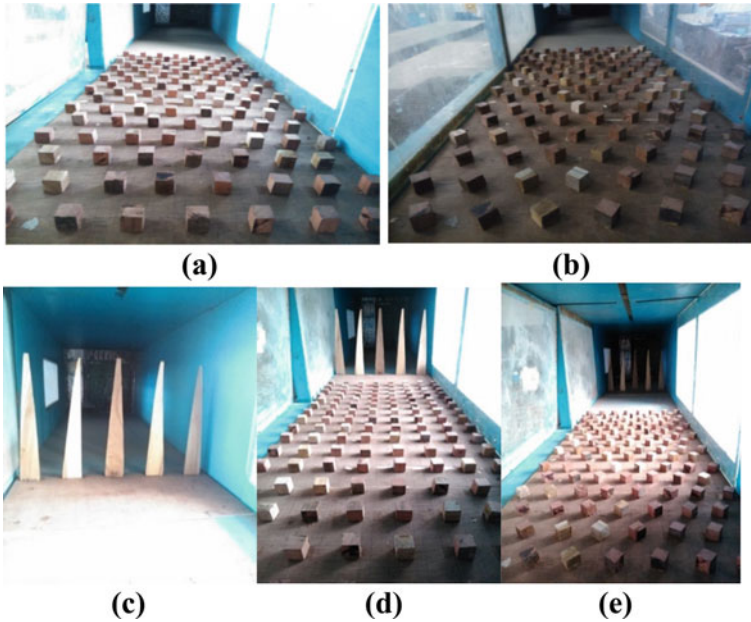**Fig. 1** Photograph of wind tunnel and model in the open-circuit wind tunnel

Fig. 2 Photocopy of roughness patterns **a** Square pattern, **b** Diamond pattern, **c** Spires, **d** Spires with square arrangement, **e** Spires with diamond arrangement

each case at distances of 20 cm, 40 cm, 60 cm, 80 cm and 100 cm from the end of the roughness patterns to obtain velocity profile and the boundary layer thickness.

At each section, the velocity is measured at a successive distance from the wind tunnel surface with the help of telescopic probe of the velocity meter connected to the trolley's arm and velocity meter. The same procedure is repeated with the different roughness pattern and configurations. The experimental data on the velocity of different cases are collected and analyzed. Details of the experiment are given in Table 1.

4 Results and Discussion

Experimental data of velocity collected at different sections for various roughness patterns are plotted separately and the typical plots are shown Figs. 3, 4, 5 and 6. The patterns used for calculating boundary layer thickness are given in Table 2. The velocity profile at the section 20 cm, and 40 cm distance from the roughness plate under different roughness pattern as square and diamond block for 11.19 m/s wind velocity are calculated and compared with a smooth surface which is shown in Figs. 3a and b, respectively. The velocity profile at the section 20 cm and 40 cm distance from the roughness plate under different roughness pattern as spires, spires square, and

Table 1 Scope of the experiment

Sl. No	Item description	Present experimental roughness
(1)	(2)	(3)
1	Roughness type	Square, diamond, triangular spires
2	Dimension of square and diamond block (cm)	2.5 × 2.5 × 2.5
3	Spacing between blocks (cm)	5
4	Dimension of triangular spires (cm) (height, base width)	45 × 7
5	Clear spacing between spires (cm)	5
6	Velocity (m/s)	7.67, 9.32 and 11.19
7	Section from the end point of roughness plate (cm)	20, 40, 60, 80 and 100
8	Temperature (°c)	27

spires diamond block for 11.19 m/s wind velocity is calculated and compared with a smooth surface which is shown in Figs. 4a and b, respectively. Figures 5a, b, and c show the velocity profiles under different roughness pattern recorded for the section of 20 cm from the distance of the roughness plate at different velocity, i.e., 11.19 m/s, 9.31 m/s, and 7.67 m/s.

Analysis is also being carried out to show the boundary layer growth under different roughness pattern as shown in Fig. 6 for various velocity conditions. Figures 3, 4, 5 and 6 show the effect of different roughness arrangement on velocity profiles against the mainstream velocity. This change can be attributed to increases in turbulence depending on the arrangement.

Figures 3, 4, 5 and 6, it is clear that diamond arrangements provide higher boundary layer depth than square arrangements do, and with increasing longitudinal distance from the end distance roughness plate, boundary layer depth rises.
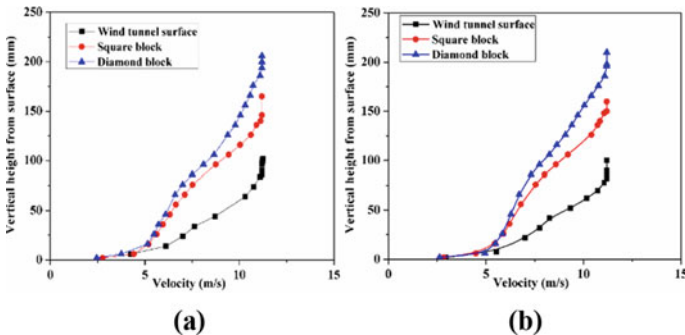

Fig. 3 Velocity profile from the distance of the roughness plate under different roughness pattern (smooth, square, and diamond block) for constant wind velocity = 11.19 m/s at the section **a** $x = 20$ cm, and **b** $x = 40$ cm
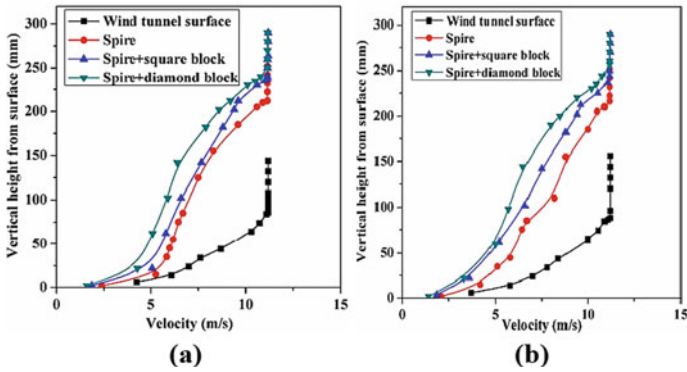
Fig. 4 velocity profile under different roughness pattern for constant velocity = 11.19 m/s on the section from the distance of the roughness plate at **a** $x = 20$ cm, and **b** $x = 40$ cm
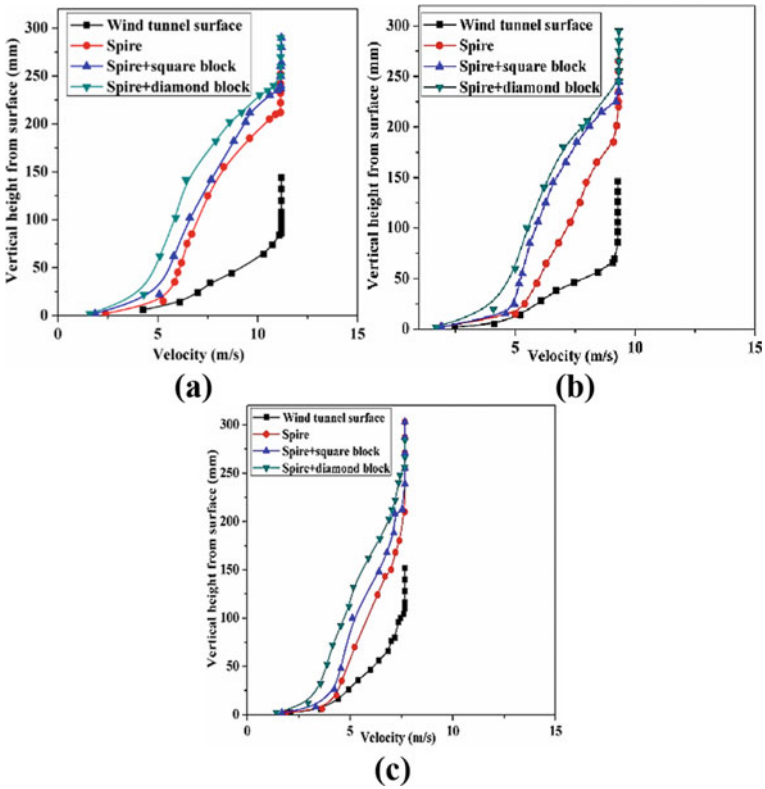

Fig. 5 Velocity profiles under different roughness pattern recorded for the section of $x = 20$ cm from the distance of the roughness plate at different velocity **a** 11.19 m/s, **b** 9.31 m/s, and **c** 7.67 m/s
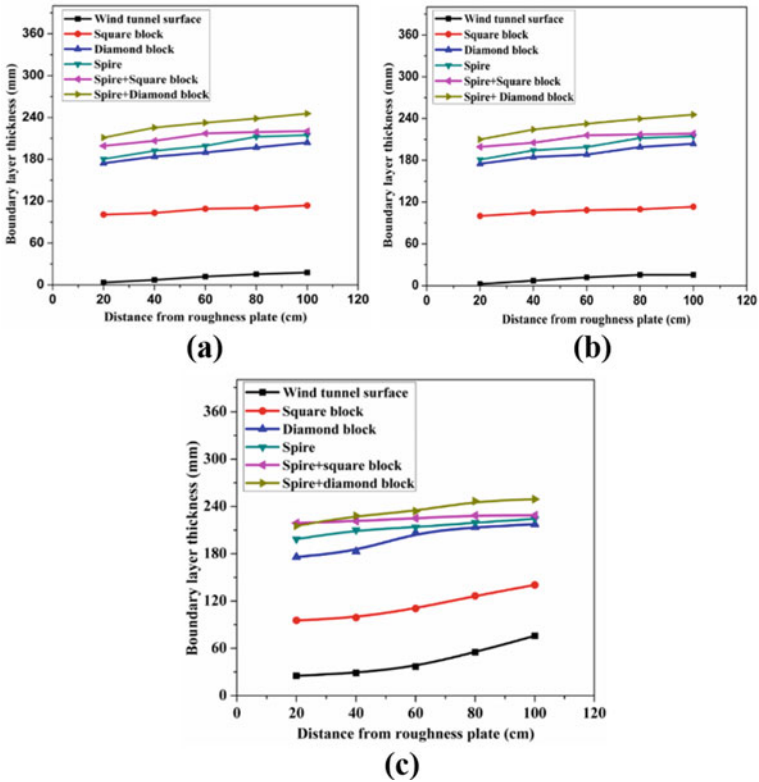
Fig. 6 Variation of boundary layer thickness at constant velocity **a** 11.19 m/s; **b** 9.32 m/s; **c** 7.67 m/s

Table 2 Roughness thickness for all configurations

Configurations in wind tunnel	Line intercept (c)	Slope of line (m)	Roughness length $\left(z_0 = e^{\frac{-c}{m}}\right)$ in mm
(1)	(2)	(3)	(4)
Square pattern of blocks	−0.5502	1.8572	1.345
Diamond pattern of blocks	−0.982	1.7638	1.745
Spires with square pattern of blocks	−1.447	1.677	2.37
Spires with diamond pattern of blocks	−1.343	1.2357	2.965

In comparison to other combinations of spire and blocks, the spire with a diamond pattern of the block enhances the maximum boundary layer thickness. Further, it has been seen that spires with blocks function efficiently at generating higher boundary layers than do simple blocks. For blocks and spire arrangements, boundary layer thickness increases due to momentum deficit and wake formations in wind tunnel.

4.1 Development of Correlation for Boundary Layer Thickness

For the development of correlation, roughness length is estimated in each case of roughness arrangement using log-law of velocity profile as:

$$U(z) = \frac{u_*}{k}[ln(z) - ln(z_0)] \tag{1}$$

where $U(z)$ represents velocity, u_* is the friction velocity, k the Karman's constant, z the height from the surface, z_0 the roughness length in mm. z_0 is estimated with the help of a graph $ln(z) vs U(z)$ and best fitting into a straight line and the equation of the straight line.

$$z_0 = e^{\frac{-c}{m}} \tag{2}$$

where c is the line intercept, m the slope of line, and z_0 the roughness length (mm)

Figure 7 shows a typical $ln(z) vs U(z)$ plot for the square arrangement of blocks as roughness pattern and the estimation of the roughness length.

Roughness lengths are obtained by seeing the best fitted line for four cases of roughness pattern as described in Fig. 7. The best fit equation and correlation coefficient are shown in Fig. 7 and the values of roughness length (z_0) are given in Table 2

Boundary layer thickness can be expressed in terms of roughness length, velocity and distance from roughness plate as

$$\delta = B\left[(z_0)^a (V)^b (X)^c\right]^d \tag{3}$$

where δ is the boundary layer thickness, B the constant, z_0 the roughness length, and a, b, and c are the exponents whose values are obtained using the experimental plots between boundary layer thickness and the roughness length as shown in Fig. 8. The values of the exponents a, b, and c are obtained from experimental plots as shown in Fig. 8 are 0.569, -0.348, and 0.065, respectively. To get the combined effect of all the variables, a correlation plot between the boundary layer thickness and the system parameter was plotted (Fig. 8d).

Now the relation of boundary layer thickness and the system parameter can be estimated as
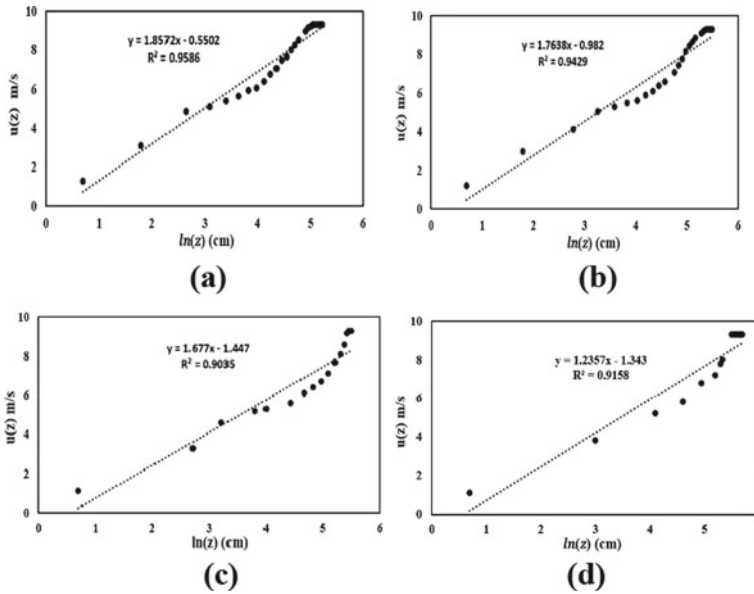
Fig. 7 Variation of roughness length for various pattern of blocks considering **a** square; **b** diamond; **c** spires with square; **d** spires with diamond

$$\delta = B\left[(z_0)^{0.5689}(V)^{-0.348}(X)^{0.0648}\right]^d \tag{4}$$

From Fig. 8d, the values of B and d are obtained as 236.94 and 0.9073, respectively. Then, Eq. (4) can be written as:

$$\delta = 236.94\left(Z_0^{0.569}V^{-0.348}X^{0.065}\right)^{0.9073} \tag{5}$$

Thus, a following final correlation is obtained.

$$\delta = 236.94\left(Z_0^{0.52}V^{0.32}X^{0.059}\right) \tag{6}$$

Comparison between the predicted values of the boundary layer thickness using developed correlation, Eq. (6) with the corresponding experimental ones is presented in Fig. 9.

A fair agreement can be seen between the predicted values of the boundary layer thickness and the corresponding experimental results.

5 Conclusions

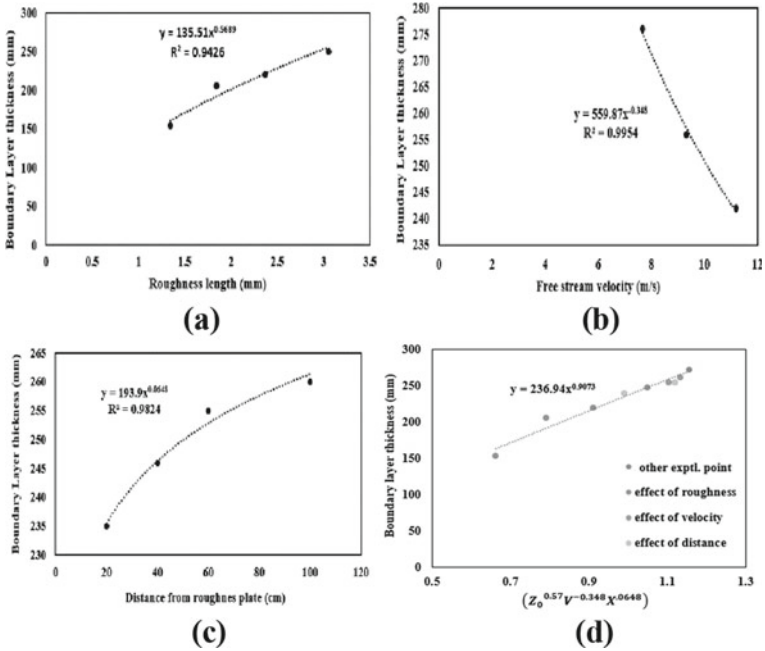From the present experimental results, the following conclusions can be drawn:
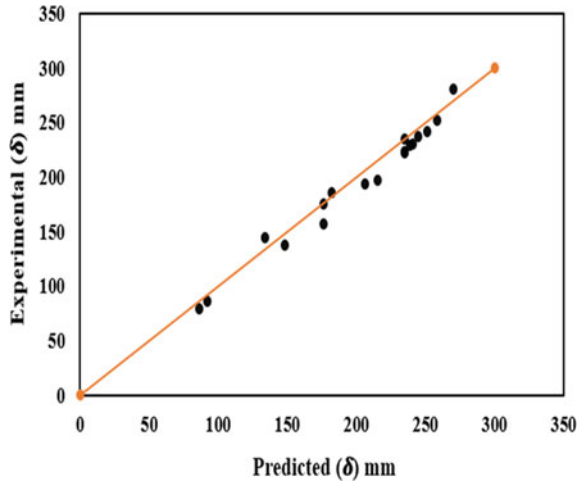
Fig. 8 Variation of boundary layer thickness with **a** roughness length for square pattern of blocks at velocity = 11.19 m/s and distance 20 cm; **b** free stream velocity for square pattern of blocks at constant roughness length 1.36 and distance 20 cm; **c** distance from roughness plate for square pattern of blocks at constant roughness length 1.36 and velocity 11.19 m/s; **d** system parameters

Fig. 9 Comparison of boundary layer thickness between the experimental and predicted using proposed equation

- Boundary layer thickness has been found to vary significantly with the roughness pattern, velocity, and position along the direction of flow.
- The formation of the boundary layer is more substantial than the plane surface of the wind tunnel due to the square, diamond, spires, and spires with square or diamond patterns.
- Roughness thickness is calculated for all arrangements of the square and diamond pattern of blocks. The sequence of the observed rise in roughness thickness has been found to be square blocks, diamond-shaped blocks, spires with square-shaped blocks, and spires with diamond-shaped blocks.
- The boundary layer thickness of the wind tunnel could be effectively formed by combining spires and different block designs. When compared to using spires alone or different block designs in the wind tunnel, this strategy is more effective in creating a thicker boundary layer.

References

1. Counihan J (1969) An improved method of simulating an atmospheric boundary layer in a wind tunnel. Atmos Environ (1967) 3(2):197–214
2. Castro IP, Robins AG (1977) The flow around a surface-mounted cube in uniform and turbulent streams. J Fluid Mech 79(2):307–335
3. Cook NJ (1978) Wind-tunnel simulation of the adiabatic atmospheric boundary layer by roughness, barrier and mixing-device methods. J Wind Eng Ind Aerodyn 3(2–3):157–176
4. Diffie W, Hellman ME (2022) New directions in cryptography, democratizing cryptography: the work of Whitfield Diffie and Martin Hellman, pp 365–390
5. Farell C, Iyengar AKS (1999) Experiments on the wind tunnel simulation of atmospheric boundary layers. J Wind Eng Ind Aerodyn 79(1–2):11–35
6. Guimaraes P, Portugal P (2010) A simple feasible procedure to fit models with high-dimensional fixed effects. Stand Genomic Sci 10(4):628–649
7. Hunt JCR, Fernholz H (1975) Wind-tunnel simulation of the atmospheric boundary layer: a report on Euromech 50. J Fluid Mech 70(3):543–559
8. Irwin H (1981) The design of spires for wind simulation. J Wind Eng Ind Aerodyn 7(3):361–366
9. Kline SJ, Reynolds WC, Schraub FA, Runstadler PW (1967) The structure of turbulent boundary layers. J Fluid Mech 30(4):741–773
10. Jimenez-Portaz M, Chiapponi L, Clavero M, Losada MA (2020) Air flow quality analysis of an open-circuit boundary layer wind tunnel and comparison with a closed-circuit wind tunnel. Phys Fluids 32(12):125120
11. Krishna P, Kumar K, Bhandari NM (2002) IS: 875 (Part3): Wind loads on buildings and structures-proposed draft & commentary, Document No.: IITK-GSDMA-Wind (2002) 02-V5
12. Mueller E, Mell W, Simeoni A (2014) Large eddy simulation of forest canopy flow for wildland fire modeling. Can J For Res 44(12):1534–1544
13. Poreh M, Cermak JE (1984) Wind tunnel simulation of diffusion in a convective boundary layer. Boundary Layer Structure, Springer, pp. 431–455
14. Schneider SP (2008) Effects of roughness on hypersonic boundary-layer transition. J Spacecr Rocket 45(2):193–209

15. Spera DA, Richards TR (1979) Modified power law equations for vertical wind profiles. In: Proceedings of the conference and workshop on wind energy characteristics and wind energy siting; 19–21 June 1979; Portland, Oregon (USA), 1979, pp 47–58
16. Stevenson T (1880) Report on simultaneous observations of the force of wind at different heights above the ground. J Scot Meteorol Soc 5(103):348–351
17. Zasso A, Giappino S, Muggiasca S (2006) Wind tunnel study of a cone-like shaped roof: Reynolds number effects. J Wind Eng Ind Aerodyn 94(5):431–444
18. Kozmar H (2021) Flow, turbulence and surface pressure on a wall-mounted cube in turbulent boundary layers. J Wind Eng Ind Aerodyn 210:104503
19. Qiu Y, Sun Y, Wu Y, San B, Tamura Y (2018) Surface roughness and Reynolds number effects on the aerodynamic forces and pressures acting on a semicylindrical roof in smooth flow. J Struct Eng 144(9):04018140
20. Kozmar H, Laschka B (2019) Wind-tunnel modeling of wind loads on structures using truncated vortex generators. J Fluids Struct 87:334–353
21. Broatch A, Margot X, Garcia-Tiscar J, Felgueroso A (2022) An automatized methodology to generate velocity distortion panels for wind tunnel testing. J Wind Eng Ind Aerodyn 227:105065
22. Catarelli RA, Fernandez-Caban PL, Masters FJ, Bridge JA, Gurley KR, Matyas CJ (2020) Automated terrain generation for precise atmospheric boundary layer simulation in the wind tunnel. J Wind Eng Ind Aerodyn 207:104276
23. Saini D, Shafei B (2021) High-fidelity prediction of flight trajectories of plate-type debris in boundary layer winds. J Wind Eng Ind Aerodyn 217:104727